MASARYK UNIVERSITY

Faculty of Science

Department of Condensed Matter Physics

Exotic Magnetism in Relativistic Transition Metal Compounds

Habilitation thesis

Brno, 2020 Jiří Chaloupka

Overview of the thesis

The thesis reviews a decade of my activities in the field of quantum magnetism of transition metal compounds containing heavier transition metal ions where a strong spin-orbit coupling leads to an on-site entanglement of spin and orbital degrees of freedom. Under certain circumstances, this may give rise to an exotic magnetic behavior, very different from the conventional Heisenberg magnets. The main focus is put on two kinds of materials – iridium Ir^{4+} and ruthenium Ru^{3+} compounds described by effective spin-$\frac{1}{2}$ models with bond-selective anisotropic interactions and on ruthenium Ru^{4+} oxides realizing soft-spin physics due to the spin length fluctuating between spinless and spinful states.

The study of such materials is at present not motivated by immediate technological applications but more fundamentally, aiming at the understanding of the basic processes driving the magnetism of these compounds and at the explanation of the experimental observations which presents a challenge per se. The potential utilization of the new unusual mechanisms of spin behavior in condensed matter encountered here is envisioned in a more distant future. Here, "topological quantum computing" may serve as an example of a particularly attractive keyword that is often used in this context.

When thinking about the structure of the thesis, I took into consideration various (sometimes conflicting) requests that appeared, as well as my limited enthusiasm to work on extensive texts. The latter was finally compensated by the convenience of having a text that may deliver the necessary knowledge to the students I supervise. The resulting thesis is composed of several parts with varying level of difficulty and the amount of details:

(i) The first part (Sec. 1) contains a "popular" introduction – a description of the emergence of magnetic models in insulating transition metals oxides (TMO) and a brief discussion of their properties targeted to a broader audience and characterized by a rather colloquial style. In the very end of this part I have tried to give a few hints on the features that make the magnetism of above iridates and ruthenates so special.

(ii) The following part including Secs. 2.1-2.4 is supposed to serve as a supplementary material for a graduate-level course on strongly correlated electron systems to be started at our faculty next year and hence may be easily skipped by expert audience. Here a lot of technical details are given and I do not avoid some illustrations of concepts from basic solid-state courses (such as the tight-binding approximation) as it often happens that the students are lacking a solid understanding of those and yet another exposition may be quite helpful. Being conceived as a study material, this part systematically guides the reader through a derivation of an effective model with localized degrees of freedom. It starts with a description of single-electron orbitals in a TMO crystal environment (Sec. 2.1), followed by a discussion of intraionic interactions and multiplet structure stemming from Coulomb repulsion of the valence electrons and spin-orbit coupling (Sec. 2.2). After the preparatory sections concerning the ionic states, in Sec. 2.3 the ions will get connected by electronic hopping captured in tight-binding approximation. The second part culminates by introducing the Mott transition and illustrating the emergence of an effective model along with a discussion of the virtual processes leading to superexchange interactions (Sec. 2.4).

(iii) The third part focuses on the two particular areas of my research – the pseudospin-$\frac{1}{2}$ materials with dominant Kitaev interactions (Sec. 3) and the soft-spin singlet-triplet systems (Sec. 4). Rather than a detailed review of the already substantial body of literature on the subject (in particular in the first area where many reviews appeared during the last few years), the goal is to show the route toward the relevant microscopic models for these materials and to give a brief introduction on their physical properties emphasizing the peculiar features not present in the

conventional magnets. Here I have also used the opportunity to partially collect the results that sometimes appear rather scattered in the attached papers and give them a coherent presentation. (iv) Finally, the closing and in fact the largest part contains reprints of the relevant papers and a brief summary of their content including remarks on the "historical" context (Secs. 5 and 6).

In conformance with the Masaryk University habilitation rules, in the following list of the attached papers I specify my contributions in terms of both quantity and content. The papers are listed in the same order as appearing in Secs. 5 and 6.

	Publication	Share	Content contribution
1.	J. Chaloupka, G. Jackeli, and G. Khaliullin, *Kitaev-Heisenberg Model on a Honeycomb Lattice: Possible Exotic Phases in Iridium Oxides* A_2IrO_3, Physical Review Letters **105**, 027204 (2010)	33%	construction of the phase diagram and exploration of its phases via exact diagonalization (ED) approach
2.	J. Chaloupka, G. Jackeli, and G. Khaliullin, *Zigzag Magnetic Order in the Iridium Oxide* Na_2IrO_3, Physical Review Letters **110**, 097204 (2013)	33%	construction of the phase diagram via ED, calculations of the magnetic susceptibility using finite-temperature Lanczos method, fitting the experimental data
3.	S. H. Chun, J. W. Kim, J. Kim, H. Zheng, C. C. Stoumpos, C. D. Malliakas, J. F. Mitchell, K. Mehlawat, Y. Singh, Y. Choi, T. Gog, A. Al-Zein, M. M. Sala, M. Krisch, J. Chaloupka, G. Jackeli, G. Khaliullin, and B. J. Kim, *Direct evidence for dominant bond-directional interactions in a honeycomb lattice iridate* Na_2IrO_3, Nature Physics **11**, 462 (2015)	6%	simulations of the diffuse magnetic X-ray scattering using ED, contributions to the theoretical model development
4.	J. Chaloupka and G. Khaliullin, *Hidden symmetries of the extended Kitaev-Heisenberg model: Implications for the honeycomb-lattice iridates* A_2IrO_3, Physical Review B **92**, 024413 (2015)	75%	development of the general method to identify hidden symmetries and its application to the particular case studied, other calculations used to interpret the experimental data, writing most of the manuscript
5.	J. Chaloupka and G. Khaliullin, *Magnetic anisotropy in the Kitaev model systems* Na_2IrO_3 *and* $RuCl_3$, Physical Review B **94**, 064435 (2016)	75%	calculations via the spin-coherent state method (including its development), part of the smaller supportive calculations, model analysis in the context of experimental data, writing most of the manuscript

6.	D. Gotfryd, J. Rusnačko, K. Wohlfeld, G. Jackeli, J. Chaloupka, and A. M. Oleś, *Phase diagram and spin correlations of the Kitaev-Heisenberg model: Importance of quantum effects*, Physical Review B **95**, 024426 (2017)	25%	methodological developments in the CMFT part, calculations of dynamic spin susceptibility, preparation of parts of the manuscript
7.	J. Rusnačko, D. Gotfryd, and J. Chaloupka, *Kitaev-like honeycomb magnets: Global phase behavior and emergent effective models*, Physical Review B **99**, 064425 (2019)	40%	symmetry analysis and derivation of emergent effective models, part of the phase-diagram calculations, writing about half of the manuscript
8.	J. Kim, J. Chaloupka, Y. Singh, J. W. Kim, B. J. Kim, D. Casa, A. Said, X. Huang, and T. Gog, *Dynamic Spin Correlations in the Honeycomb Lattice Na_2IrO_3 Measured by Resonant Inelastic x-Ray Scattering*, Physical Review X **10**, 021034 (2020)	40%	all the theoretical parts that constitute the indicated share of the manuscript – extensive numerical simulations of the RIXS spectra to identify the experimentally relevant parameter window in the global phase diagram, model interpretation of the pseudospin dynamics in the relevant regime
9.	H. Liu, J. Chaloupka, and G. Khaliullin, *Kitaev Spin Liquid in 3d Transition Metal Compounds* Physical Review Letters **125**, 047201 (2020)	25%	ED calculations of the phase diagrams and spin excitations for the microscopically obtained parameters of the extended Kitaev-Heisenberg model
10.	J. Chaloupka and G. Khaliullin, *Spin-State Crossover Model for the Magnetism of Iron Pnictides*, Physical Review Letters **110**, 207205 (2013)	75%	development of the theoretical model and its extensive analysis by a large number of methods, major part in the manuscript preparation
11.	J. Chaloupka and G. Khaliullin, *Doping-Induced Ferromagnetism and Possible Triplet Pairing in d^4 Mott Insulators*, Physical Review Letters **116**, 017203 (2016)	67%	analytical and numerical exploration of the developed theoretical model – magnetic phase diagram, calculations of the dynamic spin response and superconducting pairing, major part in the manuscript preparation
12.	A. Jain, M. Krautloher, J. Porras, G. H. Ryu, D. P. Chen, D. L. Abernathy, J. T. Park, A. Ivanov, J. Chaloupka, G. Khaliullin, B. Keimer, and B. J. Kim, *Higgs mode and its decay in a two-dimensional antiferromagnet*, Nature Physics **13**, 633 (2017)	15%	calculations of the dynamic magnetic spectra including the interplay of the Higgs mode and two-magnon continuum, part of the experimental data analysis

13.	S.-M. Souliou, J. Chaloupka, G. Khaliullin, G. Ryu, A. Jain, B. J. Kim, M. Le Tacon, and B. Keimer, *Raman Scattering from Higgs Mode Oscillations in the Two-Dimensional Antiferromagnet* Ca_2RuO_4, Physical Review Letters **119**, 067201 (2017)	40%	fitting the temperature dependent Raman spectra to extract the magnetic response, model calculations and interpretation of the data, writing a large part of the manuscript
14.	J. Chaloupka and G. Khaliullin, *Highly frustrated magnetism in relativistic* d^4 *Mott insulators: Bosonic analog of the Kitaev honeycomb model*, Physical Review B **100**, 224413 (2019)	75%	all the theoretical developments and model calculations apart from the derivation of the model itself, preparation of most of the manuscript

Contents

1 Introduction

Among the various classes of solid state materials, the transition metal compounds are probably the richest one in terms of diverse physical phenomena as well as their complexity [1–3]. To name a few prominent examples, we mention high-T_c cuprate superconductors [4, 5], colossally magnetoresistant manganites [6], multiferroics with strong magnetoelectric coupling [7], or the more recently studied exotic properties of materials with large spin-orbit coupling [8] including quantum spin liquid behavior [9,10]. The complexity of the physics of transition metal compounds stems from several key aspects:

- *Geometry* – many possible crystal lattices including those enforcing reduced dimensionality
- *Localized versus itinerant behavior* – competition of delocalization of the electrons preferring metallic state and strong Coulomb repulsion among electrons at the individual ions that supports insulating behavior
- *Multiplet structure* – we can experience many-body physics at the level of the individual transition metal ions – electrons residing in various atomic orbitals of the valence shell are subject to local correlations generated by Coulomb repulsion and Pauli principle
- *Inter-ionic interactions* – the electronic connection between the relevant ions may attain many forms due to the various bonding geometries and several valence orbitals involved. Combined with local correlations, non-trivial interactions emerge, giving rise to the multi-faceted behavior of transition metal oxides.
- *Feedback of the lattice* – the lattice does not merely provide a rigid playground for the electrons but may actively participate via electron-phonon coupling/crystal field effects. The interplay of the electronic degrees of freedom with the lattice may generate new phenomena such as Jahn-Teller effect.

In this and the following part of the thesis, we try to illustrate most the above points. Here in Sec. 1, we stay at a basic level and focus on spin systems as a prototype example of systems with localized degrees of freedom. After this initial exposition, Sec. 2 brings up the omitted "details", e.g. those related to the orbital structure. To this end, we will follow the standard scheme used when deriving an effective model for a strongly correlated electronic system with localized degrees of freedom and discuss the ingredients one mixes in.

1.1 How the transition-metal compounds are built up

The key information about a transition metal compound is provided by its chemical composition and the type of the crystal lattice formed by the ions. Apart from the transition metal elements (d-elements of the periodic table), the chemical formulas include electronegative p-elements (typically oxygen, but also other chalcogens, as well as halogens and pnictogens) and electropositive elements from the left part of the periodic table (alkali metals, alkaline earth metals, and rare-earth metals). The contrast in electronegativities has consequences for the valence/electronic occupation of the individual ions but for now let us focus solely on the structure.

Several examples of crystal lattices demonstrating the structural features of transition metal compounds are shown in Fig. 1. A common element of the selected sample lattices is a MO_6 octahedron where the central transition metal ion M is surrounded by an octahedral cage of oxygen anions O, often called ligands. Though most frequently met, this is not the only possibility, the ligands surrounding the transition metal can be found also to form a tetrahedral cage, a trigonal bipyramid etc.

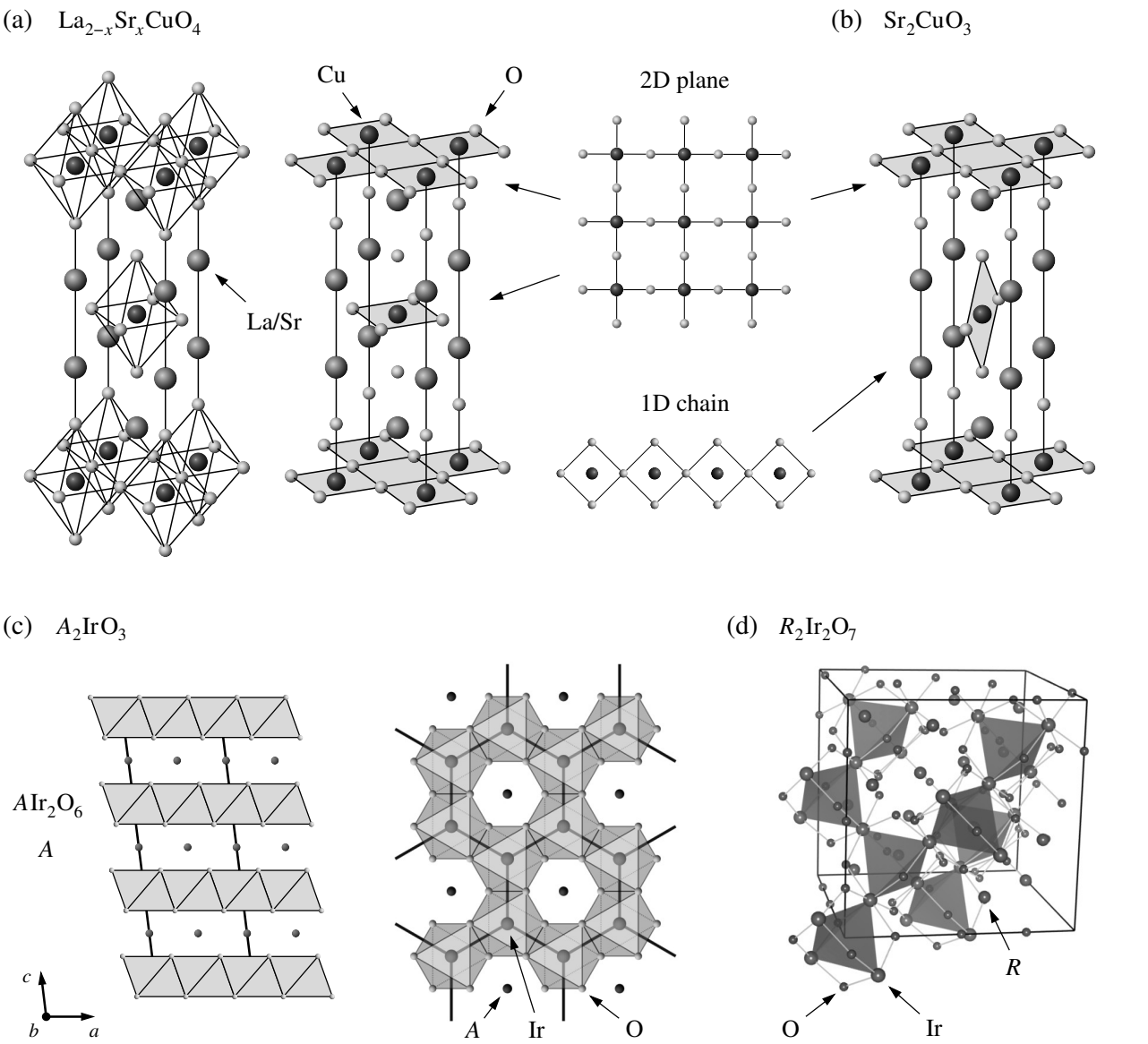

Fig. 1: Sample crystal lattices of transition metals oxides: (a) Unit cell of a high-T_c superconductor $La_{2-x}Sr_xCuO_4$ showing the octahedral cages of oxygen ions around the Cu ions (left) and the CuO_2 planes (right) as the basic constituents of the crystal lattice. Geometrically, the individual layers of corner-shared CuO_6 octahedra correspond to square lattices of copper ions with 180° Cu–O–Cu bonding. (b) Unit cell of another cuprate material Sr_2CuO_3 that contains not only CuO_2 planes in its structure but also quasi-1D chains formed by copper and oxygen ions. (c) Layered crystal structure of honeycomb iridates A_2IrO_3 where the honeycomb lattice of the iridium atoms results from placing the IrO_6 octahedra into edge-shared configurations. The side view on the left shows weakly bound AIr_2O_6 layers separated by A ions. In the top view, the honeycomb lattice of Ir ions as well as the 90° M–O–M bonds are clearly visible. (d) Pyrochlore-lattice iridate $R_2Ir_2O_7$ (adapted from [8]).

The relevant transition metal ions may form various kinds of lattices depending on the way their cages are attached to each other. Figure 1(a) and (b) illustrate the case of corner-shared octahedra using two cuprate materials. Due to their ligand cages, the transition metals are connected indirectly via oxygens in 180° M–O–M bonding geometry. The other ions, here La and Sr, fill in the voids and hold the structure together. The octahedra are not equally stacked

in all directions. Compared to M–O–M bonds, the other links are much weaker so that one can observe effectively isolated structures with reduced dimensionality which are composed of strongly bound Cu and O ions. One can thus talk about weakly coupled square-lattice CuO_2 planes [Fig. 1(a)] or even about almost decoupled one-dimensional chains [Fig. 1(b)].

A different situation occurs when the octahedra share their edges [see Fig. 1(c)]. The bonds are now due to 90° M–O–M bridges but the direct M–M bonding becomes also important. Edge-sharing of the octahedra implies a possibility of M–M bonds taking non-rectangular 60° or 120° angles so that for example triangular or honeycomb two-dimensional networks of transition metal ions can be generated. Figure 1(c) shows an example of a honeycomb iridate A_2IrO_3 where A is an alkali metal Na or Li. Here the octahedra form honeycomb layers intercalated by A ions that appear also in the voids of the honeycomb layers. Interestingly, a similar honeycomb structure is displayed by the ruthenium halide α-$RuCl_3$ but it is completely missing the A ions. These honeycomb compounds will be discussed in Sec. 3 as examples of so-called Kitaev materials.

Finally, as an example of a truly three-dimensional structure, in Fig. 1(d) we present pyrochlore-lattice iridates $R_2Ir_2O_7$ with R being a rare-earth element such as Nd, Sm, or Yb. The Ir ions in these compounds create a three-dimensional network of tetrahedra connected by their corners. A closer inspection reveals Ir–O–Ir bonds at an angle of approximately 120° in this case.

1.2 Emergence of an effective spin system

The different levels of electronegativity cause an electron transfer among the elements constituting the transition metal compound. The formal valence can be easily counted when assuming filled valence shells by all the elements other than transition metals. Each oxygen ion is expected to attract two electrons making it O^{2-} whereas the electrons are donated by ions such as Na^+, Sr^{2+} or La^{3+}. Adopting these rules, we find for the compounds shown in Fig. 1: $La^{3+}_{2-x}Sr^{2+}_xCu^{2+x}O^{2-}_4$, $Sr^{2+}_2Cu^{2+}O^{2-}_3$, $A^{+}_2Ir^{4+}O^{2-}_3$, and $R^{3+}_2Ir^{4+}_2O^{2-}_7$, respectively. Even though such a formal valence should be taken as indicative only, often it provides a reasonable starting estimate.

Being stripped of their outer s electrons and partly d electrons by the more electronegative p-element ions, the transition metal ions expose their partially filled d shells. The extent of the wave functions of the valence d orbitals turns out to be quite suitable for interesting things to happen. Staying on a qualitative level of discussion, we may evaluate this extent from two viewpoints: On one hand, d orbitals are small enough so that the Coulomb repulsion among the valence electrons is sufficiently strong, leading to strongly correlated behavior of those electrons. On the other hand, their extent still allows for a large electronic contact between the neighboring ions which gives rise to significant interactions.

We thus have two opposing mechanisms simultaneously at play – a tendency of the electrons to delocalize (travel through the crystal) and their Coulomb repulsion which tries to keep them apart. Depending on the balance between the two, we may end up with a correlated metallic state [Fig. 2(a)] or with an insulating state [Fig. 2(b)]. Note that the latter so-called Mott insulator arises due to electron-electron interactions. This is very different to conventional band insulator, where the insulating state appears when properly filling up the bands generated by periodic crystal potential. In fact, simple band theory would easily predict a Mott insulator to be metallic instead.

Both mechanisms are captured in their simplest form by a prototype model – single-band Hubbard model. It considers a single orbital per site that may be, according to Pauli principle, occupied by up to two electrons. However, a simultaneous presence of two electrons activates the Coulomb repulsion denoted as Hubbard U. The "electronic contact" is described by an amplitude t of the hopping process where an electron moves to a neighboring site. In formal terms, the

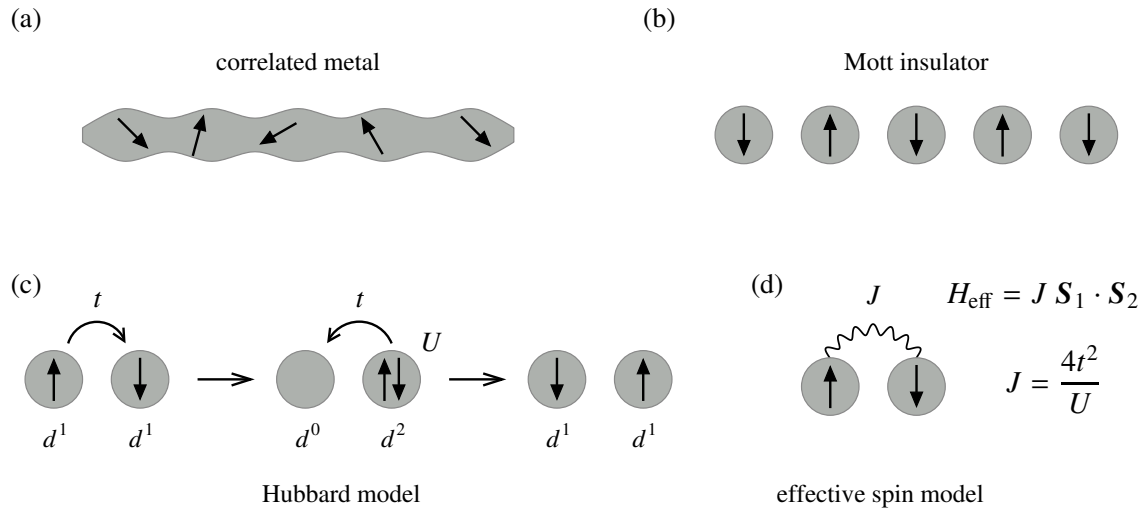

Fig. 2: Schematic pictures of (a) correlated metallic state and (b) Mott-insulating state for a system with one active orbital per site and half-filled case (on average we have one electron per site out of two possible). The arrows indicate the spin of the electrons. (c) Virtual process in the single-orbital Hubbard model that generates the exchange interaction on a bond. (d) An effective spin model that reproduces the low-energy behavior of the Hubbard model at the particular bond.

corresponding Hamiltonian reads as

$$\mathcal{H} = -t \sum_{\langle ij \rangle \sigma} (c^\dagger_{i\sigma} c_{j\sigma} + c^\dagger_{j\sigma} c_{i\sigma}) + U \sum_i n_{i\uparrow} n_{i\downarrow} \,, \tag{1.1}$$

where $c_{i\sigma}$ is the usual fermionic operator annihilating an electron of spin σ at site i, the first sum runs through all nearest-neighbor bonds $\langle ij \rangle$, and the second one in effect counts the doubly occupied sites that are penalized by the energy U. In the limit of strong repulsion compared to the electronic hopping amplitude, $U \gg t$, and for the total number of electrons being equal to the number of sites, double occupations of the sites are avoided and the system becomes a Mott insulator depicted in Fig. 2(b). In the context of the single-band Hubbard model, we talk about half-filled situation (one half of the maximum number of electrons are present), the real materials with an integer formal valence of d ions that realize Mott insulating state are usually termed "undoped". By introducing extra electrons or holes (missing electrons), the material becomes "doped" and typically turns into a metal at a sufficient doping level.

In the Mott insulating limit of a half-filled system, one does not need to give the positions of electrons, the state is sufficiently described by specifying their spins only. We arrive at an example of a model with localized degrees of freedom, here a spin model. Even though the positions are frozen, there is still some "life" left. The spins are interacting and have a particular ground-state configuration and a specific low-energy dynamics. The interactions are generated by the virtual processes of the type shown in Fig. 2(c). An electron for a short while visits its neighbor, creating a virtual excited state with an energy U, and by the second hopping in the opposite direction, the one-electron-per-site rule is restored. This process and the resulting small kinetic energy gain are possible only when the two electrons can actually meet in the same orbital – they need to be in a singlet state. In a way, the process can be understood as a formation of a bonding orbital occupied by the two electrons in a singlet state, which is caused by a weak hybridization of the localized ionic orbitals. The preference of singlets of neighboring spins is the desired spin-spin interaction. More quantitatively, the virtual processes can be accounted for

within a second-order perturbation theory giving rise to the Heisenberg Hamiltonian

$$\mathcal{H}_{\text{eff}} = J \sum_{\langle ij \rangle} \boldsymbol{S}_i \cdot \boldsymbol{S}_j \tag{1.2}$$

with the exchange constant $J = 4t^2/U$ and $\boldsymbol{S} = (S^x, S^y, S^z)$ being the spin operators describing spin-$\frac{1}{2}$ of the localized electrons.[1] The label "exchange" is explained in a pictorial way by Fig. 2(c) where the result of the virtual process is a configuration with the two spins exchanged. Formally, the operator $\boldsymbol{S}_i \cdot \boldsymbol{S}_j$ can be also written as $\frac{1}{4}(2\mathcal{P}_{ij} - 1)$ where $\mathcal{P}_{ij}$ is Dirac permutation operator that *exchanges* the quantum states of two particles [11]. For the effective model to adequately capture the low energy physics of the original Hubbard model [$\mathcal{H}$ of Eq. (1.1)], the energy scale of J needs to be well below U which is satisfied in the assumed $U \gg t$ limit. More detailed illustration of the emergence of the effective spin model will be given in Sec. 2.4 based on numerical simulations of the Hubbard model. In the next section we will briefly review the basic features of spin models.

1.3 Spin systems at a glance

As introduced in the previous section, a spin system is a system of spins residing at sites of a given lattice that are subject to spin-spin interactions. Despite the apparent simplicity compared to the underlying real material, there is still a large variability of the spin systems. One can consider various lattice geometries, interactions beyond nearest neighbors, anisotropic interactions of the general matrix form $\sum_{\alpha,\beta=x,y,z} J_{\alpha\beta} S_i^\alpha S_j^\beta$ replacing the isotropic scalar product in Eq. (1.2), or more than two-site interactions. For simplicity, here we limit ourselves to the isotropic Heisenberg Hamiltonian as appearing in Eq. (1.2). The exchange constant J came out positive for the particular mechanism discussed above but in principle it may also take a negative value favoring a triplet on the bond.

The general tendency of physical systems is an evolution towards equilibrium driven by minimization of the free energy $F = U - TS$. This contains two competing contributions – the internal energy U and the entropy term $-TS$. The balance between the two is determined by the temperature. In the low-temperature regime where the entropy does not matter, the bond interactions captured by the Hamiltonian in Eq. (1.2) and contributing to U will be optimized. The coupled spins will thus try to become aligned in the negative J case or contra-aligned for positive J. On a square lattice this leads to long-range ferromagnetic (FM) or antiferromagnetic (AF) order presented as examples in Fig. 3(a) and (b), respectively.[2] When measuring the spins or the magnetic moments, we will find a position-dependent average of the type $\langle \boldsymbol{S}_{\boldsymbol{R}} \rangle \sim \boldsymbol{m}_{\boldsymbol{R}} \sim \mathrm{e}^{i\boldsymbol{Q}\cdot\boldsymbol{R}}$ where $\boldsymbol{Q}$ is the characteristic wavevector of the ordering – the ordering vector. For a ferromagnet it is equal to zero since all the spins point in the same direction. For an antiferromagnet, the spin direction alternates with the site index n as $\mathrm{e}^{i\pi n}$ in both x and y directions and the ordering vector is $\boldsymbol{Q} = (\pi/a, \pi/a)$ where a denotes the lattice parameter.[3] The corresponding Fourier component $\boldsymbol{M}_{\boldsymbol{Q}}$ of the magnetization may serve as an order parameter determining the "strength" of the magnetic order. At elevated temperatures the order becomes gradually weakened by thermal fluctuations [see Fig. 3(c)]. This may be understood as a consequence of the term $-TS$ that now prefers a state with higher entropy, i.e. less ordered. At certain critical temperature, the magnetic order ceases to exist and the system becomes paramagnetic with zero order parameter.

[1] It is customary to work with dimensionless spin operators. We will follow this convention and use dimensionless variants (i.e. divided by $\hbar$) of all angular momentum operators through the whole text.

[2] To be precise, a strictly two-dimensional Heisenberg system considered here would not order at finite temperatures, however, in reality one encounters quasi-2D systems.

[3] The reciprocal space is often measured in units of $1/a$, in that case $\boldsymbol{Q} = (\pi, \pi)$.

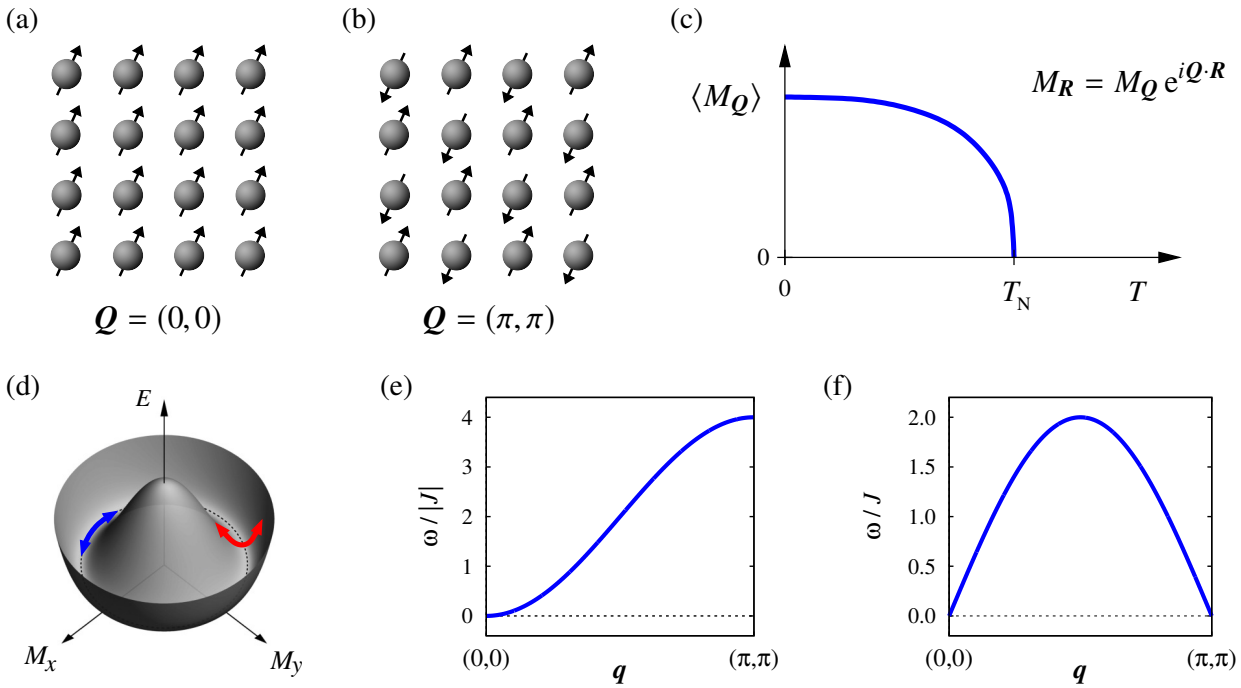

Fig. 3: (a) Ferromagnetic and (b) antiferromagnetic ordering of spins on a square lattice. The ordering vector $\boldsymbol{Q}$ is expressed in units of 1/(lattice parameter). (c) Typical temperature dependence of the order parameter (Fourier component of the magnetization at the ordering vector $\boldsymbol{Q}$). T_N stands for the Néel temperature – the critical temperature of an antiferromagnet. (d) Mexican-hat profile of the energy depending on the magnetization. Blue/red arrows indicate the direction of magnetization changes that are "for free" or cost energy, respectively. (e) Schematic spin-wave dispersion (energy ω as function of the wavevector $\boldsymbol{q}$) in the case of a ferromagnet on a square lattice. (f) The same for a square-lattice antiferromagnet.

With the order established, the behavior of the system becomes more collective and specific modes – wave-like excitations of the spins – can be observed in its low-energy dynamics. For an isotropic system, the magnetization can take any direction with the same resulting energy [see Fig. 3(d)], only its length is fixed by energy minimization. Therefore, a global simultaneous rotation of all the magnetic moments does not cost any energy and the excitations of the system that are close in nature to such a rotation will be the lowest-energy modes with the dispersion $\omega \sim q^\alpha$. More generally, these modes – called Goldstone modes – appear whenever the system spontaneously breaks a continuous symmetry as our system did when developing long-range magnetic order with certain magnetization direction. The determination of the rules for the number and type of the Goldstone modes is a deep theoretical problem [12, 13]. As a result for our particular model, the Heisenberg ferromagnet shows one Goldstone mode with $\alpha = 2$ at $\boldsymbol{Q} = (0,0)$ while in the Heisenberg antiferromagnet we find two modes with $\alpha = 1$ at $\boldsymbol{q} = (0,0)$ and the ordering $\boldsymbol{Q} = (\pi,\pi)$. The overall dispersion of the spin waves for these two cases is depicted in Figs. 3(e) and (f), respectively. When such a dispersion of spin waves for a real spin system is resolved experimentally, for example by inelastic scattering of neutrons, it brings relatively rich information enabling to narrow down the type and strength of the spin-spin interactions constituting the corresponding spin model.

Nevertheless, such a luxury is often not accessible, neutron experiments frequently suffer from low intensity, have to be performed on powders instead of monocrystals providing only direction-averaged information etc., so that alternative ways to get at least some insights into the spin-spin interactions are needed. A standard tool used to estimate the magnitude of the

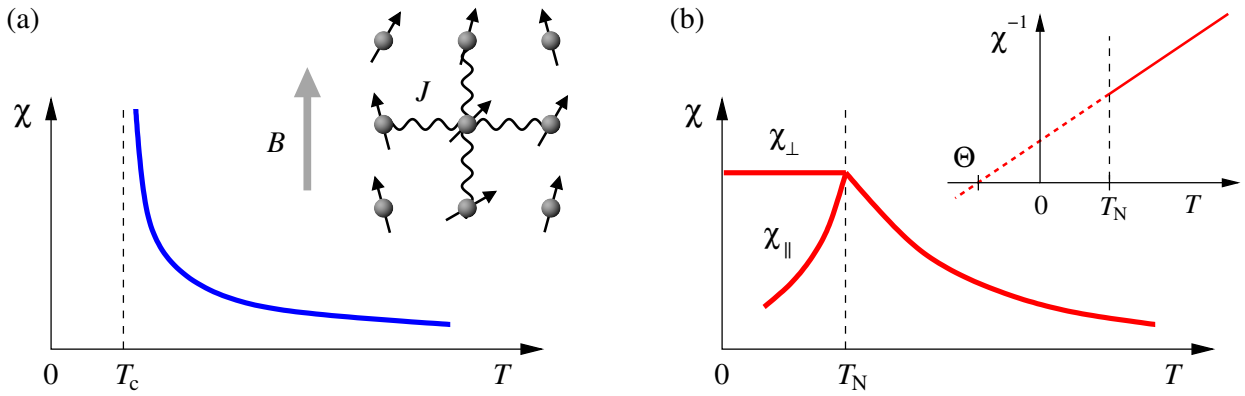

Fig. 4: (a) Schematic temperature dependence of the static spin susceptibility $\chi = \mathrm{d}M/\mathrm{d}B$ for a ferromagnet. The inset tries to suggest the physical picture behind the curve that is described in the text. (b) The same for an antiferromagnet where the susceptibility becomes anisotropic below the Néel temperature and differs for the field polarized perpendicular or parallel to the magnetization. The inset shows an extrapolation of χ^{-1} to get the Curie-Weiss scale Θ.

spin-spin interactions and one of the first experimental probes applied to freshly baked samples is the temperature dependence of the static spin susceptibility illustrated in Fig. 4. Here one uses the high-temperature behavior of the spins in homogeneous magnetic field that tries to align them in parallel fashion. Without the spin-spin interactions the high-temperature spin susceptibility would approximately follow the Curie law $\chi \sim 1/T$ for isolated moments. This is modified by the interactions that try to imprint their characteristic correlations onto the partially polarized spins. The result above the critical temperature is the Curie-Weiss law $\chi \sim 1/(T-\Theta)$ where the Curie-Weiss scale Θ combines the spin-spin interaction parameters in some way. Roughly speaking, FM $J<0$ supports the parallel alignment induced by the magnetic field and leads to positive Θ (enhances the susceptibility), AF $J>0$ works in the opposite way (suppresses the susceptibility). Going down in temperature, an anomaly at the critical temperature signals a phase transition into a magnetic ordered state. Unless a more sophisticated fitting is involved, one typically plots $\chi^{-1}(T)$ and extrapolates the linear part to get Θ as shown in Fig. 4(b).

So far we were naively discussing the spin systems as a set of arrows that want to align and this is only prevented at high temperatures by thermal fluctuations. However, the situation is more complex and the magnetic order has to fight with additional enemies. An intrinsic enemy is the very nature of spin as a quantum object. To see its consequences, we rewrite the Heisenberg Hamiltonian (1.2) in terms of the spin raising/lowering operators $S^{\pm} = S^x \pm iS^y$:

$$\mathcal{H}_{\text{eff}} = J\sum_{\langle ij\rangle} \boldsymbol{S}_i \cdot \boldsymbol{S}_j = J\sum_{\langle ij\rangle} \tfrac{1}{2}(S_i^+ S_j^- + S_i^- S_j^+) + S_i^z S_j^z \,. \tag{1.3}$$

Assuming the AF ordering with the moments along z direction, the last S^zS^z part of the interaction would be completely happy. But more energy can be gained from the resonance of configurations with flipped spins as sketched in Fig. 5(a). The degree of the ordering is thus sacrificed for a gain of "kinetic" energy. The processes bringing disorder by misaligning spins are now of quantum origin and may be thus termed as quantum fluctuations in analogy with the thermal ones. The severity of quantum fluctuations strongly depends on the spin length (with larger spins behaving more classically and spin-$\frac{1}{2}$ being the most "quantum" one), the nature of the spin-spin interactions and the dimensionality of the system (with lower-dimensional systems being more susceptible to quantum fluctuations). As an example of the level of quantum fluctuations found in quantum antiferromagnet, in Fig. 5(b) we sketch an exact ground state of a

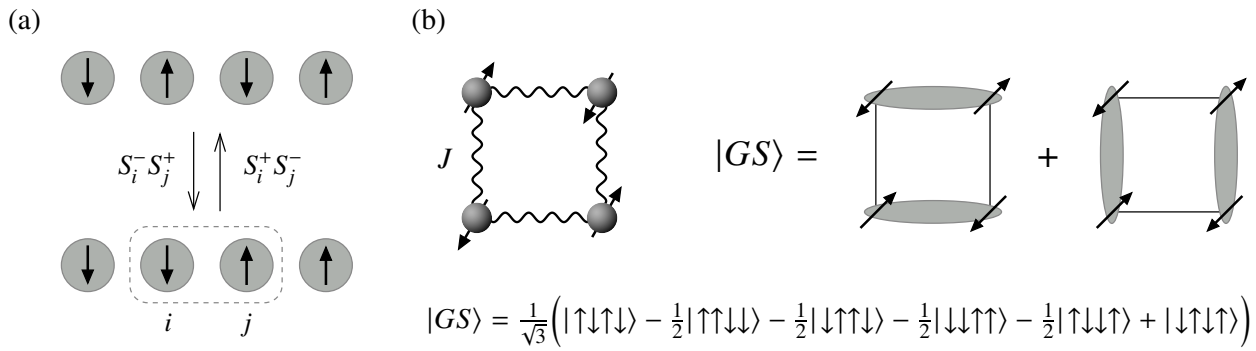

Fig. 5: (a) Resonant spin-flip processes driven by the part of the Heisenberg interaction that is perpendicular to the ordered moment direction. Spin-$\frac{1}{2}$ is considered here so that only two S_i^z eigenstates exist, those are indicated by up/down arrows. (b) Exact ground state of a Heisenberg square consisting of four spin-$\frac{1}{2}$ sites. It can be represented either as a superposition of configurations of properly aligned or misaligned spins (bottom) or via a resonance of two coverings of the square by singlets of neighboring spins (right). A singlet state of two spins is marked by a gray oval. An analogous resonance of several possible coverings is familiar from quantum chemistry of benzene and other aromatic molecules. In that case coverings by double bonds between carbon atoms are resonating.

square of four Heisenberg-interacting spins. Here the configurations with properly contra-aligned spins (Néel configurations) represent only two thirds of the whole state in terms of probability. Focusing on the topology of the bonds, the square is in fact a 1D system with periodic boundary conditions. Even though the amount of quantum fluctuations (measured by the energy gain with respect to the Néel configuration) is reduced when the 1D system grows in length, the quantum fluctuations are still strong enough to completely melt the long-range order in the case of a 1D Heisenberg chain at $T = 0$.

Sometimes the enemy is more visible – in case of *frustrated* spin systems one can explicitly see that the simple orderings of e.g. Néel type cannot satisfy the spin-spin interactions. An example of a geometric frustration is presented in Fig. 6(a) where we take a piece of so-called kagome lattice and try to populate it with AF-interacting spins. This attempt is soon over as we inevitably fail to make three interacting spins on a triangle mutually antiparallel. The nature of the ground state of the Heisenberg model on kagome lattice is still a subject of intense studies and it seems that the long-range order is indeed destroyed by the geometric frustration [14]. This is in contrast to the triangular lattice which, despite being composed from frustrated triangles as well, shows

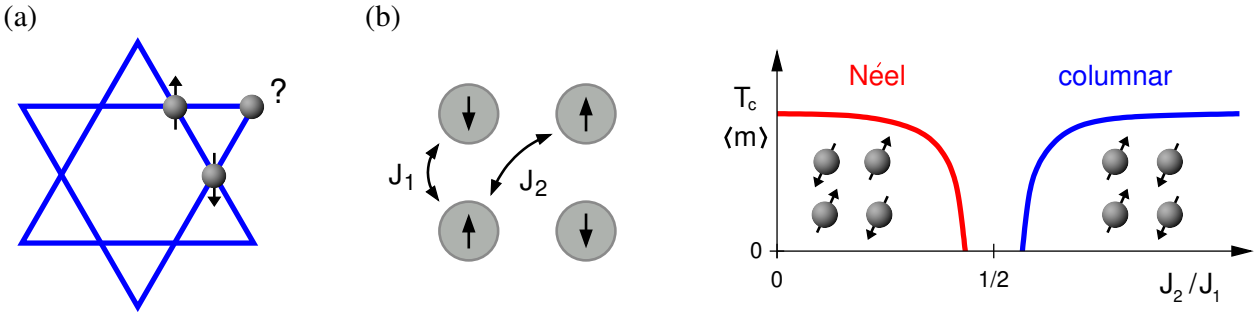

Fig. 6: (a) Frustration of spins that are subject of AF interaction when placed on a kagome lattice. (b) Competition of nearest-neighbor and next-nearest-neighbor interaction in J_1-J_2 model that, depending on the J_2/J_1 ratio shows two distinct types of spin ordering separated by a disordered phase.

a long-range order with a "compromise" angle of 120° between neighboring spins [15]. Another case of frustration is demonstrated in Fig. 6(b) for a geometrically non-frustrated square lattice. Once we activate the next-nearest-neighbor Heisenberg interaction J_2 in addition to the nearest-neighbor J_1, those two interactions start to compete as they support different spin arrangements. Depending on the ratio of J_1 and J_2, this competition leads to a reduction of the magnetic order strength or – around the balanced ratio $J_2 \approx J_1/2$ – even to a complete absence of any long-range order [16, 17].

1.4 Kitaev systems – a quick introduction

In the end of this section we briefly introduce the spin systems that are the main subject of the thesis – Kitaev-like and soft-spin systems. Both of them go in some sense far beyond the concepts of a Heisenberg magnet. Leaving a detailed discussion for the respective sections 3 and 4, here we stay at the "popular" level and address only the essential features that make those systems special.

The Kitaev-like magnets are strongly frustrated systems of spins residing on honeycomb lattice that interact predominantly via a particular bond-selective interaction introduced by Alexei Kitaev in his famous model [18]. In contrast to the isotropic Heisenberg interaction, the Kitaev interaction picks only one component of the two spins on a bond, i.e. it replaces the scalar product $\boldsymbol{S}_i \cdot \boldsymbol{S}_j$ by for example $S_i^z S_j^z$. This is not that unique yet, the same kind of anisotropy can be found in the famous Ising model which is one of the prototype models for magnetism introduced in early 1920's [19]. The key point of the Kitaev model, however, is that the interaction axis is bond-dependent and follows the pattern depicted in Fig. 7(a). Formally, the Hamiltonian of the Kitaev model can be written as

$$\mathcal{H}_{\text{Kitaev}} = -K_x \sum_{\langle ij\rangle \| x} S_i^x S_j^x - K_y \sum_{\langle ij\rangle \| y} S_i^y S_j^y - K_z \sum_{\langle ij\rangle \| z} S_i^z S_j^z \,, \tag{1.4}$$

where each of the three sums run through the bonds of a particular direction. Often an "isotropic" version of the model with $K_x = K_y = K_z = K$ is considered. The interaction constant may take both signs, in fact there is a one-to-one mapping between ferromagnetic ($K > 0$) and antiferromagnetic ($K < 0$) cases. The model can be extended to arbitrary spins but let us limit our discussion to the spin-$\frac{1}{2}$ variant proposed by Kitaev.

The honeycomb lattice is a geometrically non-frustrated lattice, the antiferromagnetic Heisenberg interaction discussed earlier would therefore establish long-range AF order similarly to the case of the square lattice depicted in Fig. 3(b). The Kitaev interaction, either ferromagnetic or antiferromagnetic, fails to do so. The reason is its intrinsic frustration stemming from a competition of the interactions at the three bond directions. As observed in Fig. 7, each site of the lattice is a member of three bonds exhausting all the possible bond directions. To optimize the energy of the attached z-bond, both spins it connects should be parallel (for positive K) or anti-parallel (for negative K) and pointing along the z direction. On the other hand, the y-bond wants them to point in the y direction, and the x-bond makes yet another request. The three options for an optimum spin direction are mutually orthogonal. An intuitive compromise might be to align spins along the $(x+y+z)/\sqrt{3}$ direction. This would bring a classical energy $3 \times \frac{1}{3}\frac{1}{4}K = \frac{1}{4}K$ which is the same as if we fully satisfied one bond direction and therefore does not seem promising. The spins choose a different way how to cope with the inherent frustration of their interactions and form so-called Kitaev quantum spin liquid. It is a exotic state where nearest-neighbor spins show well-defined correlations while further neighbors have *zero* correlations. Remarkably, this ground state can be obtained by an exact calculation making the Kitaev model one of the few examples of exactly solvable models in the field of quantum magnetism. Related to the exact

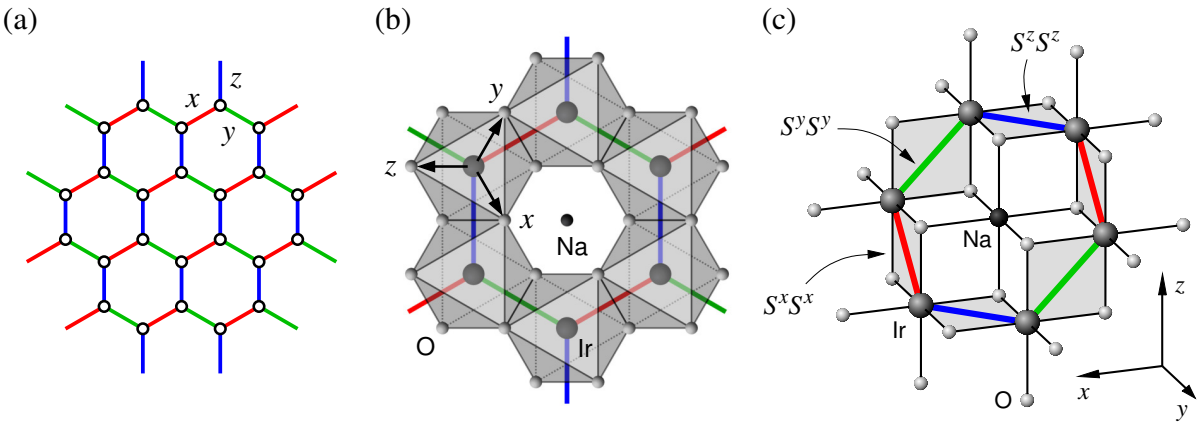

Fig. 7: (a) Honeycomb lattice with three distinct directions of bonds indicated by colors. The Kitaev interaction between nearest-neighbor spins is of the form $S_i^\alpha S_j^\alpha$ with the active component $\alpha = x, y, z$ determined by the bond direction. (b) Top view of the honeycomb lattice of edge-shared octahedra in the iridate Na_2IrO_3. More details on the structure of the compound can be found in Fig. 1(c). The main axes of the octahedra labeled by x, y, and z coincide with the spin axes of the Kitaev interaction. The active one for a particular bond is perpendicular to the bond direction. (c) A closer view on the Ir-O-Ir bonds with marked square Ir_2O_2 plaquettes where the main exchange processes happen. The Kitaev axis for the given bond is perpendicular to the corresponding plaquette.

solution are other fancy features of the model – an extensive number of conserved quantities (their number grows linearly with the system size), topological quantum order, or fractionalized elementary excitations that cannot be understood as simple wave-like rotations of the spins like it is in the case of conventional magnets.

While the original Kitaev model was introduced on purely theoretical grounds in the context of topological quantum computing, it was the proposal by George Jackeli and Giniyat Khaliullin [20] of its possible realization in Mott insulators with large spin-orbit coupling – i.e. actual materials – that attracted the attention of a broader solid state community. The possible realization of a quantum spin liquid accessible to an exact solution triggered a lot of interest and made the "Kitaev materials" one of the recent hot topics in condensed matter physics. The intense research on Na_2IrO_3 and other candidate compounds revealed that the dominant Kitaev interaction is supplemented by several other interactions that drive those materials away from the desired quantum spin liquid into a long-range ordered state, though some Kitaev-like features are preserved. In Sec. 3, after explaining the microscopic origin of the strongly anisotropic and bond-selective interactions, we will provide details on the theoretical investigations of this situation as well as the most important experimental results for the proper context.

1.5 Soft-spin systems – a quick introduction

In the soft-spin systems, the elementary building object itself is redefined. Instead of a rigid spin such as spin-$\frac{1}{2}$ appearing in the Heisenberg model of Sec. 1.2, each site carries now a superposition of various spinless and spinfull states. The balance between them brings a new degree of freedom. In the situations when this balance and thus the fraction of the spinfull states is easily changed, the average spin moment becomes "soft" and prone to fluctuations. It should be emphasized that this effect is different to spin rotations, i.e. fluctuations of the spin direction of rigid spins.

Having a basic idea of what the soft-spin systems are, we may address the question how they actually emerge in nature. The key elements are the quasidegeneracy of the above spinless and

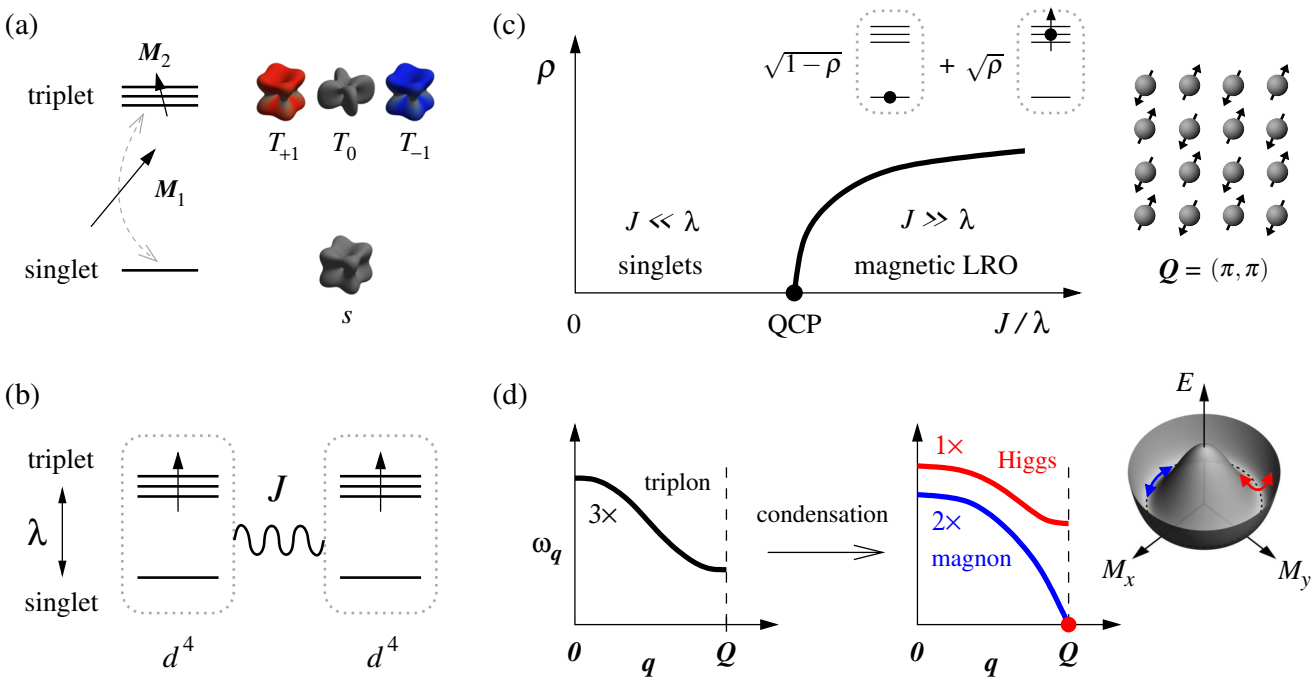

Fig. 8: (a) Schematic energy-level structure of a d^4 ion with large spin-orbit coupling. The ground state is a nonmagnetic singlet. The magnetic moment is contributed primarily by the transition between singlet and triplets ($\boldsymbol{M}_1$), only a small part of it is carried by the triplet ($\boldsymbol{M}_2$). (b) The two competing energy scales of the model – the cost of the triplet λ and the inter-ionic exchange J. (c) Quantum critical point separating the state full of singlets and a condensate of triplets established at sufficiently large J/λ. In the condensate state, singlet a triplets are mixed on-site in a quantum superposition with the relative fractions given by the condensate density ρ. The condensate carries staggered magnetic moments corresponding to long-range antiferromagnetic order. (d) Change of the excitation spectrum upon condensation. Dispersing triplet excitations touch zero energy at QCP and transform into a spin-wave like rotational mode (magnon) and an oscillation of the spin length ("Higgs" mode). Numbers indicate the degeneracy of the modes.

spinfull states and the presence of inter-ionic exchange interactions that are capable of mixing them. When these two are well balanced, the soft-spin scenario may occur. The soft-spin system that will be extensively discussed in Sec. 4 is based on transition metal ions containing four valence electrons that are subject of moderate spin-orbit coupling. The spin-orbit coupling arranges the low-energy spectrum of valence states according to the level scheme in Fig. 8(a). The lowest state is a nonmagnetic singlet, above it, separated by the spin-orbit coupling strength λ, are three excited states forming a triplet. The situation with the magnetic moment is more complicated compared to the above introductory description. The largest part of the moment sits primarily on the transition between the singlet and triplet states, while the triplet states carry only a minor contribution. Nevertheless, the essence of the soft-spin scenario remains the same. The exchange interactions between the d^4 ions under consideration are most naturally formulated as processes altering the configurations of singlets and triplets on a particular bond. When the microscopic details are considered, one finds that there are two dominant processes of similar strength – an exchange of a triplet and a singlet at the two sites and a creation or annihilation of triplet pairs on the bonds. Both bring down triplets in energy and give them dispersion. The fate of the system now depends on the ratio of the two energy scales – the triplet cost λ and the strength J of the exchange interactions [see Fig. 8(b)–(d) for a vague depiction]. Starting in the limit $\lambda \gg J$, triplets are relatively costly and the system is full of singlets

occupying most of the lattice sites. Dispersing triplets serve as elementary excitations moving in this singlet background, their dispersion is still relatively weak and the bandwidth determined by J by far does not exceed the basic energy scale λ. When increasing J, the triplet dispersion becomes more pronounced [Fig. 8(d) left] and at some critical J/λ it will touch zero level at the AF ordering vector $\boldsymbol{Q}$. Being zero energy excitations, the triplets will get incorporated into the ground state changing its nature. We just experienced a quantum phase transition – the system passed a quantum-critical point (QCP) separating the state full of singlets from the phase that could be regarded as a condensate of triplets (objects of a bosonic character). In the condensed state, each site can be imagined as a superposition of both singlet and triplet whose proportions are related to the condensate density ρ. This superposition carries a magnetic moment of $\boldsymbol{M}_1$ type [c.f. Fig. 8(a)] with the value proportional to $\sqrt{\rho\,(1-\rho)}$. The structure of the condensate imposes AF staggering of those magnetic moments so the condensation in fact created a long-range AF order. Near the QCP, the condensate is still not very rigid and shows pronounced fluctuations of its amplitude, giving rise to an unusual spectrum of magnetic excitations. This and other problems related to the peculiar AF order established by a condensation of triplets will be addressed in detail in Sec. 4.

2 Effective models with localized degrees of freedom

The purpose of this part is to expose in detail the way to arrive at an effective model for a transition metal compound where the localization tendencies discussed in Sec. 1.2 take over. The system is then effectively described as consisting of localized degrees of freedom that are subject to mutual interactions.

The derivation of the corresponding model may be a rather complex task involving several stages. First, one has to identify the localized degrees of freedom themselves. This typically consist in an inspection of the multiplet structure of the active ions that depends on their valence, the crystal environment determining single-electron orbital levels, and the intra-ionic interactions that generate the many-electron states forming the multiplet structure. The low-energy states of the multiplet structure are then used as a local basis of the effective model. We will cover these topics in the following two sections, focusing in particular on the cases of interest: d^4 and d^5 transition metal ions with strong spin-orbit coupling. Next, one has to open the communication channels between the individual ions. They are provided by the electronic hopping to be described within the framework of the tight-binding approximation in the third section of this part. Finally, as will be discussed in the last section, one combines the above pieces of information and obtains the interactions among the localized degrees of freedom by considering perturbatively the virtual processes generated by the electronic hopping.

2.1 Orbital splitting in a crystal environment

The valence electrons in transition metal ions occupy d-type orbitals. In contrast to the case of a free-standing ion, they are exposed to a crystal environment which necessarily modifies their wavefunctions and energy levels. The Coulomb interaction with the charges of the surrounding ions as well as the electronic coupling to their orbitals both imprint the symmetry of the crystal environment to the new orbitals of the ion under consideration. Leaving the intra-ionic interactions aside for a moment, we are going to inspect the restructuring of the single-electron levels by the additional crystal field. The general prediction for the symmetry of the new eigenstates depending on the symmetry of the environment can be made based on group theory. However, a more intuitive approach is to explicitly calculate the new levels when including the crystal field potential of a proper symmetry. It is handled by using first-order perturbation theory for the originally five-fold degenerate d-orbitals which leads to split energy levels corresponding to certain combinations of those orbitals. Such an approach is acceptable in particular in our case of interest where the valence electrons of the transition metal ions retain their localized character. The advantage of an explicit, though crude calculation, is that one gets an idea about the relative values of the splittings.

2.1.1 Crystal field within point-charge model

A simple picture of the crystal field is provided by so-called point-charge model where we imagine the ligands as point charges acting electrostatically on the valence electrons of the transition metal ion. In the case of the most frequent structural unit – the $M\mathrm{O}_6$ octahedron, the oxygen ions surrounding the transition metal M are supposed to carry the nominal charge $Q = -2e$ corresponding to the formal valence O^{2-}. The valence electrons with the charge $q = -e$ are then perturbed by the potential

$$V_{\mathrm{CF}}(\boldsymbol{r}) = \frac{qQ}{4\pi\epsilon_0} \sum_n \frac{1}{|\boldsymbol{r} - \boldsymbol{R}_n|} \tag{2.1}$$

with n going through the six oxygens at positions $\boldsymbol{R}_n$. These positions may form an ideal octahedron or incorporate its distortion. Both situations will be inspected later in this section. Note that the prefactor containing qQ is positive due to the repulsion of the valence electrons and the negatively charged oxygen ions. Such a treatment of the crystal environment is of course much simplified and in reality its prediction can be substantially modified, e.g. by covalency effects (electronic coupling). Nevertheless, the symmetry of the environment is properly embedded in $V_{\mathrm{CF}}(\boldsymbol{r})$. The next step is the multipole expansion of the crystal field based on the general formula

$$\frac{1}{|\boldsymbol{r}-\boldsymbol{r}'|} = \sum_{l=0}^{\infty} \frac{r_<^l}{r_>^{l+1}} P_l(\cos\alpha) = \sum_{l=0}^{\infty} \frac{r_<^l}{r_>^{l+1}} \frac{4\pi}{2l+1} \sum_{m=-l}^{+l} Y_{lm}^*(\vartheta',\varphi') Y_{lm}(\vartheta,\varphi)\,. \tag{2.2}$$

Here $r_<$ ($r_>$) is the smaller (larger) number from the pair $|\boldsymbol{r}|$ and $|\boldsymbol{r}'|$ and α is the angle between $\boldsymbol{r}$ and $\boldsymbol{r}'$. The angles ϑ, φ and ϑ', φ' are the conventional spherical angles specifying the direction of $\boldsymbol{r}$ and $\boldsymbol{r}'$, respectively. By inserting (2.2) into Eq. (2.1), we obtain the final multipole expansion

$$V_{\mathrm{CF}}(\boldsymbol{r}) = \frac{qQ}{4\pi\epsilon_0} \sum_{l=0}^{\infty} \sum_{m=-l}^{+l} A_{lm}\, r^l\, Y_{lm}(\vartheta,\varphi) \tag{2.3}$$

with the multipole coefficients A_{lm} given by

$$A_{lm} = \frac{4\pi}{2l+1} \sum_n \frac{1}{R_n^{l+1}} Y_{lm}^*(\vartheta_n,\varphi_n)\,. \tag{2.4}$$

This expansion may be also understood as a power series in r/R_n. Since the typical distance of the electron from the octahedron center is visibly less than the distance R_n of the ligands, the potential terms will weaken with increasing l. Moreover, as we will see below, only terms with $l \leq 4$ will actually contribute to the V_{CF} matrix elements between d-type orbitals due to symmetry reasons.

2.1.2 Matrix elements of the crystal field

In the absence of the crystal field, the orbitals of the d shell with the angular momentum $l = 2$ are five-fold degenerate and their wavefunctions are of the form

$$d_m(r,\vartheta,\varphi) = f(r)\, Y_{2m}(\vartheta,\varphi) \qquad (m = -2,-1,0,+1,+2)\,. \tag{2.5}$$

The radial part of the wavefunction $f(r)$ is common to all the orbitals while they differ in the angular dependence captured by the spherical harmonics. These wavefunctions will be the starting point of the perturbation theory to incorporate the crystal field. For our purposes it is sufficient to consider the first order, the resulting energy shifts and the corresponding combinations of the d_m orbitals are therefore obtained simply by diagonalizing the 5×5 matrix of the perturbation V_{CF} expressed in the unperturbed d_m basis. Employing the multipole expansion (2.3), the necessary matrix elements read as

$$\langle d_{m_1}|V_{\mathrm{CF}}|d_{m_2}\rangle = \frac{qQ}{4\pi\epsilon_0} \sum_{l=0}^{\infty} \sum_{m=-l}^{+l} A_{lm} \int_0^{\infty} r^{l+2} f^2(r)\,\mathrm{d}r \int Y_{2m_1}^* Y_{lm} Y_{2m_2}\,\mathrm{d}\Omega\,. \tag{2.6}$$

The middle integral is just the average $\langle r^l\rangle$ of some power of the radial distance. The second integral is more tricky but can be evaluated using Clebsch-Gordan coefficients[4] following the

[4]Some of the formulas involving Clebsch-Gordan coefficients would be more elegantly formulated using Wigner $3j$ symbols. However, CG coefficients will be frequently utilized in 2.2 when adding various angular momenta so we keep using them everywhere for simplicity.

formula (c.f. Eq. 3.8.73 from Ref. [21])

$$\int Y^*_{lm} Y_{l_1 m_1} Y_{l_2 m_2} \,\mathrm{d}\Omega = \sqrt{\frac{(2l_1+1)(2l_2+1)}{4\pi(2l+1)}}\, \langle l_1 l_2 00 \,|\, l0\rangle \,\langle l_1 l_2 m_1 m_2 \,|\, lm\rangle \,. \tag{2.7}$$

In our case, some of the quantum numbers are fixed and we arrive at

$$\langle d_{m_1}|V_{\mathrm{CF}}|d_{m_2}\rangle = \frac{qQ}{4\pi\epsilon_0} \sum_{l=0}^{\infty} \sum_{m=-l}^{+l} A_{lm} \langle r^l \rangle \sqrt{\frac{2l+1}{4\pi}}\, \langle l200 \,|\, 20\rangle \,\langle l2mm_2 \,|\, 2m_1\rangle \,. \tag{2.8}$$

Looking at the structure of the Clebsch-Gordan coefficients or the original integral containing spherical harmonics, we notice that we are in fact adding angular momenta with quantum numbers l and 2 and evaluating the overlap with an eigenstate of total angular momentum having the quantum number 2. To have nonzero matrix elements, this implies that the multipolar order l cannot exceed $l = 4$ (hexadecapole) as mentioned earlier.

Since the angular momentum conservation is broken by the non-spherical environment, it is not very helpful to strictly keep the corresponding eigenstates $|d_m\rangle$ of Eq. (2.5) as the working basis. Instead, it is more convenient to utilize their real combinations that are be better adjusted to the octahedral symmetry. We follow the convention by Tanabe and Sugano [22] and introduce them as

$$|\xi\rangle = \tfrac{i}{\sqrt{2}}(|d_{+1}\rangle + |d_{-1}\rangle) \qquad \sim yz \tag{2.9}$$

$$|\eta\rangle = -\tfrac{1}{\sqrt{2}}(|d_{+1}\rangle - |d_{-1}\rangle) \qquad \sim zx \tag{2.10}$$

$$|\zeta\rangle = -\tfrac{i}{\sqrt{2}}(|d_{+2}\rangle - |d_{-2}\rangle) \qquad \sim xy \tag{2.11}$$

$$|u\rangle = |d_0\rangle \qquad \sim 3z^2 - r^2 \tag{2.12}$$

$$|v\rangle = \tfrac{1}{\sqrt{2}}(|d_{+2}\rangle + |d_{-2}\rangle) \qquad \sim x^2 - y^2 \tag{2.13}$$

Here the polynomials on the right indicate the symmetry resulting from the particular combination of spherical harmonics. The matrix elements of V_{CF} obtained via Eq. (2.8) need to be converted to the basis of real harmonics leading to a new 5×5 matrix for the diagonalization. When showing the corresponding matrices in the following paragraphs, we will be always using the above order of the basis states.

2.1.3 Cubic case – t_{2g} and e_g orbitals

Let us now apply the above general results to the specific case of an ideal octahedron of oxygen ions surrounding the transition metal ions. The crystal field for this situation expressed using Eq. (2.3) and expanded up to $l = 4$ takes the form (assuming $qQ = 2e^2$)

$$V_{\mathrm{CF}}(\boldsymbol{r}) = \frac{e^2}{2\pi\epsilon_0 R} \left\{ 6 + \frac{7\sqrt{\pi}}{3} \frac{r^4}{R^4} \left[Y_{40} + \sqrt{\frac{5}{14}} \left(Y_{4,-4} + Y_{4,+4} \right) \right] \right\} \tag{2.14}$$

or, in a more familiar Cartesian representation involving the main octahedron axes [see Fig. 9(a)]

$$V_{\mathrm{CF}}(\boldsymbol{r}) = \frac{e^2}{2\pi\epsilon_0 R} \left[6 + \frac{35}{4R^4} \left(x^4 + y^4 + z^4 - \frac{3}{5} r^4 \right) \right] . \tag{2.15}$$

From the symmetry point of view, the above potential is characterized by the point group $\mathcal{O}_h$ capturing the symmetries of a cube or an octahedron. The first contribution to V_{CF} is a monopole

term from the six charges at distance R and can be ignored since it shifts all the orbitals equally. The second term with $l = 4$ is a hexadecapole potential and leads to the actual splitting of the orbitals. To see the splitting, we express the second term in the orbital basis. First using the original states $|d_{-2}\rangle$, $|d_{-1}\rangle$, $|d_0\rangle$, $|d_{+1}\rangle$, $|d_{+2}\rangle$ described by spherical harmonics, this gives us a non-diagonal matrix

$$V_{\mathrm{CF}}^{(l=4)} = \frac{e^2}{2\pi\epsilon_0 R}\,\frac{\langle r^4\rangle}{R^4}\,\frac{1}{6}\begin{pmatrix} 1 & 0 & 0 & 0 & 5 \\ 0 & -4 & 0 & 0 & 0 \\ 0 & 0 & 6 & 0 & 0 \\ 0 & 0 & 0 & -4 & 0 \\ 5 & 0 & 0 & 0 & 1 \end{pmatrix} \tag{2.16}$$

that is, however easy to diagonalize. In the Tanabe-Sugano basis (2.9)-(2.13), the matrix representing V_{CF} comes already in a diagonal form

$$V_{\mathrm{CF}}^{(l=4)} = \frac{e^2}{2\pi\epsilon_0 R}\,\frac{\langle r^4\rangle}{R^4}\,\mathrm{diag}\big(-\tfrac{2}{3},-\tfrac{2}{3},-\tfrac{2}{3},+1,+1\big) \tag{2.17}$$

separating in energy two sets of states as shown in Fig. 9(a). At the lower level we find the three states $|\xi\rangle$, $|\eta\rangle$, $|\zeta\rangle$ called t_{2g} orbitals, since they form a basis of the three-dimensional $\mathrm{T_{2g}}$ representation of the group $\mathcal{O}_h$ [23]. The upper level contains so-called e_g orbitals (forming a basis of the $\mathrm{E_g}$ representation of this group). The t_{2g}-e_g splitting

$$\Delta_{\mathrm{CF}} = E(e_g) - E(t_{2g}) = \frac{5e^2}{6\pi\epsilon_0 R}\,\frac{\langle r^4\rangle}{R^4} \tag{2.18}$$

is for historical reasons denoted as $10Dq$ with D being the prefactor in the $x^4 + y^4 + z^4$ part of the electrostatic potential and q being proportional to $e\langle r^4\rangle$. The typical value of Δ_{CF} for TMO is a few electronvolts. The shapes of the t_{2g} and e_g orbitals depicted in Fig. 9(a) enable us to intuitively understand the origin of the splitting. The e_g orbitals have their lobes oriented directly toward the negatively charged oxygen ions. Therefore they experience a larger Coulomb repulsion compared to the t_{2g} orbitals and move higher in energy.[5]

2.1.4 Further splitting due to tetragonal and trigonal distortion of the octahedra

The MO_6 octahedra in transition metal oxides are subject to various forms of distortions. Therefore their symmetry is not ideal and further splitting of orbitals occurs. We will discuss two important cases: (i) tetragonal distortion i.e. compression or elongation of the octahedron along one of its main axes, (ii) trigonal distortion where the compression or elongation happens in a direction perpendicular to one pair of faces of the octahedron.

In both cases we will consider a volume-conserving deformation – contracting or elongating the octahedron geometry by factor $(1-\varepsilon)$ in one direction and compensating this change in the remaining two directions:

$$\boldsymbol{R}' = (1-\varepsilon)\,\boldsymbol{R}_{\parallel} + \frac{1}{\sqrt{1-\varepsilon}}\,\boldsymbol{R}_{\perp}\,. \tag{2.19}$$

Here $\boldsymbol{R}_{\parallel}$ stands for the component of the ligand position $\boldsymbol{R}$ in the selected contraction ($\varepsilon > 0$) or elongation ($\varepsilon < 0$) direction and $\boldsymbol{R}_{\perp}$ is perpendicular to it.

[5] Thanks to this direct contact between the pair of e_g orbitals and the surrounding octahedral cage, strong Jahn-Teller effects may happen in the e_g orbital systems [3]. The system spontaneously distorts the octahedra in a systematic way to gain energy by e_g orbital splitting.

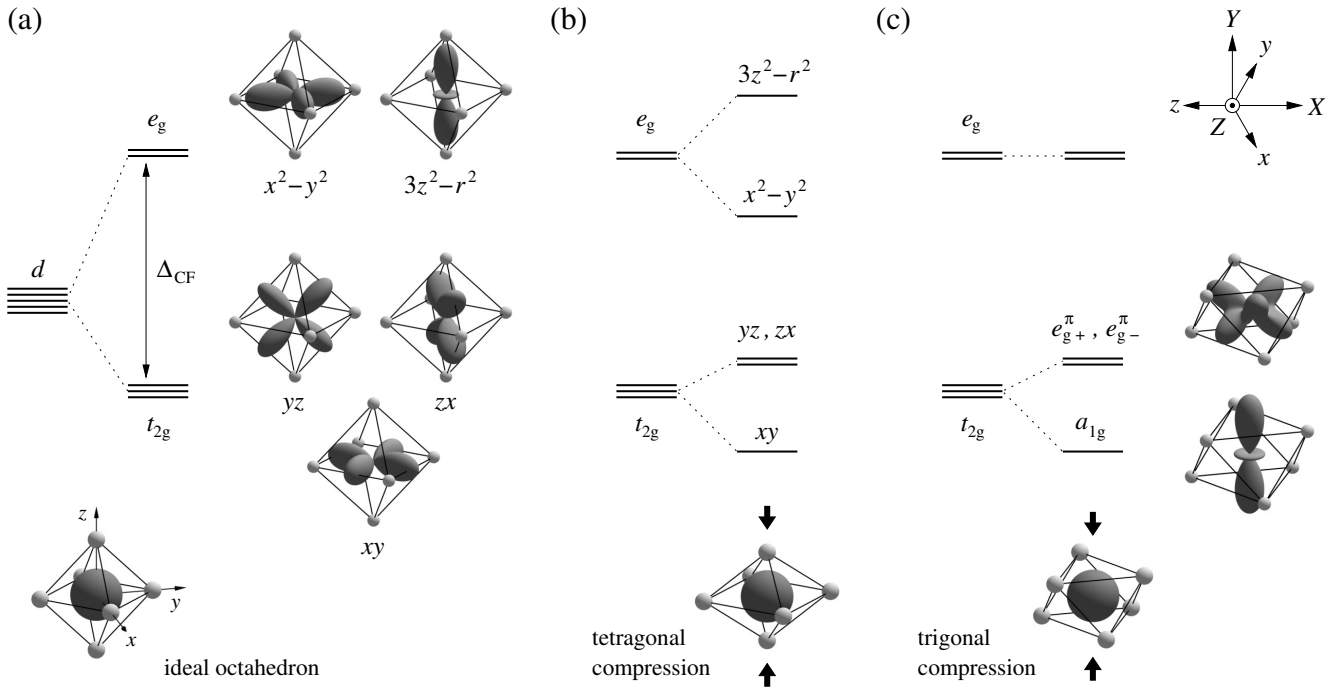

Fig. 9: (a) Splitting of d-type orbitals in a cubic field of an ideal octahedron. The crystal field of the negatively charged oxygen ions makes a distinction between the t_{2g} orbitals xy, yz, and zx whose lobes point inbetween the oxygens and e_g orbitals x^2-y^2 and $3z^2-r^2$ with their lobes oriented toward the oxygens. (b) Further splitting of the orbitals under the tetragonal compression of the octahedron. The planar orbitals xy and x^2-y^2 shift down in energy. (c) Splitting of the orbitals by the crystal field of a trigonally compressed octahedron. Upper right corner: Relation between the cubic xyz axes and trigonal XYZ axes with Z being the axis of the compression. The cubic axes and the Z axis point above the paper plane.

Let us start with the simpler case of the tetragonal distortion. Following Fig. 9(b) we select the z axis. Evaluating the matrix elements of the distorted crystal field in the Tanabe-Sugano basis, we arrive at the correction to the original matrix shown in Eq. (2.17). To linear order in the relative compression factor ε it reads as

$$\delta V_{\rm CF}^{(l\leq 4)} = \varepsilon \, \frac{e^2}{2\pi\epsilon_0 R} \left[\frac{9}{7} \frac{\langle r^2 \rangle}{R^2} \, \mathrm{diag}(1,1,-2,2,-2) + \frac{25}{42} \frac{\langle r^4 \rangle}{R^4} \, \mathrm{diag}(-2,-2,4,3,-3) \right] . \qquad (2.20)$$

The first contribution stems from the leading quadrupolar correction to the potential which is proportional to $Y_{20} \sim 3z^2 - r^2$. In the case of a compression, it supports orbitals lying in the xy plane, i.e. xy and x^2-y^2, and lifts up those that are oriented out of the xy plane. This result is natural when one considers the relative changes of the positions of the negative oxygen ions as suggested in Fig. 9(b). For completeness, we have presented also a correction to the hexadecapole which can be neglected. It merely adjusts a bit the splittings obtained from the quadrupolar term, bringing no qualitative change.

Somewhat more complicated is the case of a trigonal distortion illustrated in Fig. 9(c). We focus only on the quadrupolar contribution to the crystal field. To the linear order in ε the corresponding matrix in Tanabe-Sugano basis takes the form

$$\delta V_{\rm CF}^{(l=2)} = \varepsilon \, \frac{e^2}{2\pi\epsilon_0 R} \, \frac{\langle r^2 \rangle}{R^2} \begin{pmatrix} A & C \\ C^T & B \end{pmatrix} \qquad (2.21)$$

with the matrix blocks A, B, C given by

$$A = -\frac{6}{7}\begin{pmatrix} 0 & 1 & 1 \\ 1 & 0 & 1 \\ 1 & 1 & 0 \end{pmatrix}, \qquad B = \begin{pmatrix} 0 & 0 \\ 0 & 0 \end{pmatrix}, \quad \text{and} \quad C = \frac{2}{7}\begin{pmatrix} -\sqrt{3} & 3 \\ -\sqrt{3} & -3 \\ 2\sqrt{3} & 0 \end{pmatrix}. \tag{2.22}$$

As we can see, there is no direct trigonal splitting of the e_g orbitals, it only happens indirectly by t_{2g}-e_g mixing via the matrix elements in the C block. Such an effect is negligible if the relevant matrix elements are small compared to the t_{2g}-e_g splitting (2.18). The main effect is the splitting among the t_{2g} orbitals ξ, η, ζ. To determine it, we have to diagonalize the 3×3 matrix of the block A. A convenient choice of its eigenvectors (the convenience will become clear in the next paragraph) is as follows:

$$|a_{1g}\rangle = \tfrac{1}{\sqrt{3}}(|\xi\rangle + |\eta\rangle + |\zeta\rangle)\,, \tag{2.23}$$

$$|e^{\pi}_{g+}\rangle = +\tfrac{1}{\sqrt{3}}\left(\mathrm{e}^{+2\pi i/3}|\xi\rangle + \mathrm{e}^{-2\pi i/3}|\eta\rangle + |\zeta\rangle\right), \tag{2.24}$$

$$|e^{\pi}_{g-}\rangle = -\tfrac{1}{\sqrt{3}}\left(\mathrm{e}^{-2\pi i/3}|\xi\rangle + \mathrm{e}^{+2\pi i/3}|\eta\rangle + |\zeta\rangle\right). \tag{2.25}$$

The eigenvalue of A for the a_{1g} state is $-\frac{12}{7}$, the e^{π}_g pair of states is degenerate with the A eigenvalue $\frac{6}{7}$. The value of the splitting is thus a bit different compared to the tetragonal case but there are again a singlet and a doublet. The a_{1g} singlet has a pronounced elongated shape with the lobes pointing along the [111] direction in cubic coordinates x, y, z [see Fig. 9(c)]. For a trigonal compression ($\varepsilon > 0$) it goes down in energy since the oxygen ions move away from the lobes, relieving a bit the Coulomb repulsion. In contrast, the e^{π}_g doublet has the electron density localized closer to the plane perpendicular to [111] and gets shifted up in energy.

2.1.5 Quenched angular momentum

The particular combinations of orbitals that got split in energy by the crystal field do not form anymore the set of eigenstates of the L_z operator like it was the case of $|d_m\rangle$. By separating the t_{2g} and e_g subspaces, the original angular momentum with $l = 2$ got quenched as one can see by considering for example the e_g orbitals. One of them is $|d_m\rangle$ with $m = 0$, another one combines $m = \pm 2$. Since the magnetic quantum numbers differ by 2, all the matrix elements of L_x and L_y are zero. L_z matrix elements come zero as well so that $\boldsymbol{L}$ projected to the e_g subspace is strictly zero, i.e. the angular momentum is fully quenched. Still, remnants of the original angular momentum are present in the set of t_{2g} orbitals that are combinations of $m = \pm 1$ and $m = \pm 2$, so that it is possible to have nonzero matrix elements of $L_{x,y}$. In fact, as we explicitly show below, they host an effective angular momentum with the quantum number $l^{\mathrm{eff}} = 1$. To this end, we rearrange the basis a bit by combining

$$|a\rangle = \tfrac{1}{\sqrt{2}}(-i|\eta\rangle - |\xi\rangle)\,, \qquad |b\rangle = |\zeta\rangle\,, \qquad |c\rangle = \tfrac{1}{\sqrt{2}}(-i|\eta\rangle + |\xi\rangle)\,. \tag{2.26}$$

In the new basis consisting of a, b, c, u, v, the angular momentum operators L_x, L_y, L_z are represented by the matrices

$$L_x = \frac{1}{\sqrt{2}}\left(\begin{array}{ccc|cc} 0 & -1 & 0 & +\sqrt{3}\,i & +i \\ -1 & 0 & -1 & 0 & 0 \\ 0 & -1 & 0 & -\sqrt{3}\,i & -i \\ \hline -\sqrt{3}\,i & 0 & +\sqrt{3}\,i & 0 & 0 \\ -i & 0 & +i & 0 & 0 \end{array}\right), \quad L_y = \frac{1}{\sqrt{2}}\left(\begin{array}{ccc|cc} 0 & +i & 0 & -\sqrt{3} & +1 \\ -i & 0 & +i & 0 & 0 \\ 0 & -i & 0 & -\sqrt{3} & +1 \\ \hline -\sqrt{3} & 0 & -\sqrt{3} & 0 & 0 \\ +1 & 0 & +1 & 0 & 0 \end{array}\right),$$

$$L_z = \left(\begin{array}{ccc|cc} -1 & 0 & 0 & 0 & 0 \\ 0 & 0 & 0 & 0 & +2i \\ 0 & 0 & +1 & 0 & 0 \\ \hline 0 & 0 & 0 & 0 & 0 \\ 0 & -2i & 0 & 0 & 0 \end{array}\right) . \tag{2.27}$$

The t_{2g} subspace operators found in the indicated upper left corner show a structure precisely corresponding to $\boldsymbol{L}$ operator expressed in an $l = 1$ basis up to an overall sign change. The effective angular momentum operator may be thus defined as $\boldsymbol{L}^{\text{eff}} = -\boldsymbol{L}$ projected to the t_{2g} subspace. The states $|a\rangle$, $|b\rangle$, $|c\rangle$ then correspond to the L_z^{eff} eigenstates with $m = +1$, 0, and -1, respectively. At the same time, these states are $(\boldsymbol{L}^{\text{eff}})^2$ eigenstates corresponding to the quantum number $l^{\text{eff}} = 1$. In this basis $\boldsymbol{L}^{\text{eff}} = [L_x^{\text{eff}}, L_y^{\text{eff}}, L_z^{\text{eff}}]$ is represented by the proper set of angular momentum matrices:

$$\boldsymbol{L}^{\text{eff}} = \left[\frac{1}{\sqrt{2}} \begin{pmatrix} 0 & 1 & 0 \\ 1 & 0 & 1 \\ 0 & 1 & 0 \end{pmatrix}, \frac{1}{\sqrt{2}} \begin{pmatrix} 0 & -i & 0 \\ +i & 0 & -i \\ 0 & +i & 0 \end{pmatrix}, \begin{pmatrix} +1 & 0 & 0 \\ 0 & 0 & 0 \\ 0 & 0 & -1 \end{pmatrix} \right] . \tag{2.28}$$

The effective angular momentum $\boldsymbol{L}^{\text{eff}}$ just defined may be used to express the tetragonal splitting in a compact way. The same shifts of the t_{2g} levels as observed in Fig. 9(b) are obtained using the Hamiltonian $\Delta_{\text{tetra}}[(L_z^{\text{eff}})^2 - \frac{2}{3}]$ with Δ_{tetra} denoting the splitting value. This is not surprising, since the splitting Δ_{tetra} stems from a quadrupolar correction to the crystal field (proportional to ε) and is thus naturally captured by a quadrupolar angular momentum operator. Based on this symmetry argument, one can generalize the form of the t_{2g} splitting to other uniaxial compression/elongation directions by taking

$$\mathcal{H}_{\text{split}} = \Delta \left[(\boldsymbol{n} \cdot \boldsymbol{L}^{\text{eff}})^2 - \tfrac{2}{3} \right] , \tag{2.29}$$

where $\boldsymbol{n}$ is a unit vector along the selected direction. For example, the trigonal splitting of Fig. 9(c) corresponds to $\boldsymbol{n} = [1, 1, 1]/\sqrt{3}$. This brings us to a connection between the eigenstates in Eqs. (2.23)–(2.25) and $\boldsymbol{L}^{\text{eff}}$. Namely, the states $|a_{1g}\rangle$ and $|e^{\pi}_{g\pm}\rangle$ that split under trigonal distortion into a singlet and doublet are eigenstates of $\boldsymbol{n} \cdot \boldsymbol{L}^{\text{eff}}$ with $m = 0$ and $m = \pm 1$, respectively. Even more explicitly, we can rotate the effective angular momentum operators from the cubic coordinates xyz to the new coordinates XYZ [depicted in Fig. 9(c)] more appropriate to the trigonal case:

$$\begin{pmatrix} L_X \\ L_Y \\ L_Z \end{pmatrix}_{\text{eff}} = \begin{pmatrix} \frac{1}{\sqrt{6}} & \frac{1}{\sqrt{6}} & -\sqrt{\frac{2}{3}} \\ -\frac{1}{\sqrt{2}} & \frac{1}{\sqrt{2}} & 0 \\ \frac{1}{\sqrt{3}} & \frac{1}{\sqrt{3}} & \frac{1}{\sqrt{3}} \end{pmatrix} \begin{pmatrix} L_x \\ L_y \\ L_z \end{pmatrix}_{\text{eff}} . \tag{2.30}$$

Using the three states $|e^{\pi}_{g+}\rangle$, $|a_{1g}\rangle$, and $|e^{\pi}_{g-}\rangle$ as a basis, we find that the components L_X, L_Y, and L_Z are represented by matrices identical to those in Eq. (2.28). These states therefore play the same role as $|a\rangle$, $|b\rangle$, $|c\rangle$ of the tetragonal case.

Finally, let us comment on the off-diagonal blocks in (2.27) connecting the t_{2g} and e_g states. These are not frequently used as the two subspaces are separated by the largest crystal-field

splitting. However, in some situations they may become important. For example when considering a t_{2g} system with large spin orbit coupling, the above matrix elements may bring a sizable admixture of e_g states to the predominantly t_{2g} ones.

2.2 Local correlations and multiplet structure of transition metal ions

In the previous section we have investigated the valence shell of a d ion from the single-electron point of view, studying the orbitals and their splitting due to the crystal field. When the valence shell is occupied by more than one electron, the Coulomb repulsion among them makes their motion strongly correlated and organizes the electrons into many-body eigenstates that form the ionic multiplet structure. In the following, we first analyze the structure of the Hamiltonian capturing the Coulomb repulsion among valence electrons in d orbitals and then discuss some examples of its diagonalization arriving at the multiplet structure. Apart from the Coulomb interaction, the situation is further complicated by spin-orbit coupling that appears as a relativistic quantum mechanical effect and tries to contra-align the spins of the individual electrons and their orbital angular momenta. Such effects are of a crucial importance in iridates and ruthenates to be discussed in the next parts of the thesis, we therefore devote a substantial part of this section to a detailed exploration of the relevant ionic states restructured by the spin-orbit coupling.

2.2.1 Coulomb interactions among valence electrons

The starting point for a discussion of the many-body effects of the Coulomb repulsion among electrons in a d shell is the second-quantized form of the corresponding Hamiltonian:

$$\mathcal{H}_{\mathrm{Coul}} = \frac{1}{2} \sum_{\alpha\beta\gamma\delta} \sum_{\sigma\sigma'} V_{\alpha\beta\gamma\delta}\, \alpha^\dagger_\sigma \beta^\dagger_{\sigma'} \gamma_{\sigma'} \delta_\sigma \,. \tag{2.31}$$

Here the indices α, β, γ, δ run through the orbitals and the spin summation got restricted because we are dealing with a spin-conserving charge-charge interaction. The matrix elements of the Coulomb interaction take the form

$$V_{\alpha\beta\gamma\delta} = \frac{e^2}{4\pi\epsilon_0} \int \mathrm{d}^3\boldsymbol{r} \int \mathrm{d}^3\boldsymbol{r}'\; \psi^*_\alpha(\boldsymbol{r})\, \psi^*_\beta(\boldsymbol{r}')\, \frac{1}{|\boldsymbol{r}-\boldsymbol{r}'|}\, \psi_\gamma(\boldsymbol{r}')\, \psi_\delta(\boldsymbol{r}) \,. \tag{2.32}$$

We will again use the orbitals of the Tanabe-Sugano basis ξ, η, ζ, u, v that are described by real wavefunctions, making the above matrix elements real. They are also subject to obvious symmetry relations

$$V_{\alpha\beta\gamma\delta} = V_{\alpha\gamma\beta\delta} = V_{\delta\beta\gamma\alpha} = V_{\beta\alpha\delta\gamma} \,, \tag{2.33}$$

reducing the number of the independent values from $5^4 = 625$ to 120. This number will be further (and drastically) reduced once the symmetry of the orbitals themselves is employed.

While the use of the Cartesian orbitals is convenient to easily incorporate the crystal field splittings, the evaluation of the matrix elements is simpler when working with the spherical orbitals d_m of Eq. (2.5). In that case one considers the matrix elements

$$V_{m_1m_2m_3m_4} = \frac{e^2}{4\pi\epsilon_0} \int \mathrm{d}^3\boldsymbol{r} \int \mathrm{d}^3\boldsymbol{r}'\; d^*_{m_1}(\boldsymbol{r})\, d^*_{m_2}(\boldsymbol{r}')\, \frac{1}{|\boldsymbol{r}-\boldsymbol{r}'|}\, d_{m_3}(\boldsymbol{r}')\, d_{m_4}(\boldsymbol{r}) \tag{2.34}$$

and constructs $V_{\alpha\beta\gamma\delta}$ as linear combinations of $V_{m_1m_2m_3m_4}$. The key tool is the multipole expansion (2.2) of $1/|\boldsymbol{r}-\boldsymbol{r}'|$ with the subsequent evaluation of the angular integrals via Eq. (2.7). The radial integration is reduced to an evaluation of a set of so-called Slater-Condon parameters

$$F^{(l)} = \frac{e^2}{4\pi\epsilon_0} \int_0^\infty \mathrm{d}r\; r^2 \int_0^\infty \mathrm{d}r'\; r'^2\, \frac{r^l_<}{r^{l+1}_>}\, f(r) f(r') \,. \tag{2.35}$$

After some manipulations involving also the symmetry property of the spherical harmonics $Y^*_{lm} = (-1)^m Y_{l,-m}$, the matrix element (2.34) can be rearranged into

$$V_{m_1m_2m_3m_4} = \sum_{l=0,2,4} \frac{25\,F^{(l)}}{(2l+1)^2} \langle 2200|l0\rangle^2 \sum_{m=-l}^{+l} (-1)^{m+m_1+m_2} \langle 22, -m_1m_4|l, -m\rangle \langle 22, -m_2m_3|lm\rangle\,. \tag{2.36}$$

An important feature is the Clebsch-Gordan coefficient $\langle 2200|l0\rangle$ entering the above expression. It limits the necessary Slater-Condon parameters to three numbers $F^{(0)}$, $F^{(2)}$, $F^{(4)}$. These are most conveniently expressed via Racah parameters [24]

$$A = F^{(0)} - \tfrac{1}{9}F^{(4)} \qquad B = \tfrac{1}{49}F^{(2)} - \tfrac{5}{441}F^{(4)} \qquad C = \tfrac{5}{63}F^{(4)} \tag{2.37}$$

that lead to compact formulas for $V_{\alpha\beta\gamma\delta}$ containing round coefficients.

As we found out, all the Coulomb matrix elements $V_{\alpha\beta\gamma\delta}$ can be expressed as linear combinations of just three parameters A, B, C given by the radial part of the orbital wavefunctions. Together with the crystal field splittings, they determine the multiplet structure which therefore depends on just very few parameters. Such a huge reduction is a result of the assumed spherical symmetry i.e. it happens if the orbitals share the radial part of the wavefunction and their angular dependence is given by spherical harmonics or their combinations. While this is in general not true, in the case of localized orbitals in transition metal oxides it is still a reasonable approximation and the corresponding description of the multiplet structure is often sufficient. Going beyond this approximation, the number of independent parameters necessarily increases. For example, when assuming the cubic symmetry, we have to deal with ten of them instead of the Racah A, B, C [25].

When considering the Coulomb repulsion in a valence shell, the sum in the Hamiltonian (2.31) is usually systematically truncated. We will now discuss the set of matrix elements to be included and rearrange the selected subset of terms into the conventional form of intra-ionic interactions. The dominant matrix elements correspond to a Coulomb repulsion of two electrons sharing the same orbital. The corresponding matrix element $V_{\alpha\alpha\alpha\alpha}$ is the same for all the orbitals of the Tanabe-Sugano basis and will be termed as the intra-orbital Hubbard U. In terms of the Racah parameters, it is expressed as

$$U = A + 4B + 3C = V_{\alpha\alpha\alpha\alpha}\,. \tag{2.38}$$

The relevant contributions extracted from Eq. (2.31) may be cast to the familiar form of the intra-orbital Hubbard interaction

$$\mathcal{H}_1 = U \sum_{\alpha} n_{\alpha\uparrow} n_{\alpha\downarrow}\,. \tag{2.39}$$

The second kind of contributions to be included are two-orbital interactions with two distinct pairs of identical indices in $\alpha\beta\gamma\delta$. The corresponding matrix elements are of two types – Coulomb integral for two different orbitals

$$U_{\alpha\beta} = \frac{e^2}{4\pi\epsilon_0} \int \mathrm{d}^3\boldsymbol{r} \int \mathrm{d}^3\boldsymbol{r}'\; \psi^2_\alpha(\boldsymbol{r})\, \frac{1}{|\boldsymbol{r}-\boldsymbol{r}'|}\, \psi^2_\beta(\boldsymbol{r}') = V_{\alpha\beta\beta\alpha} = V_{\beta\alpha\alpha\beta} \tag{2.40}$$

and the exchange integral

$$J_{\alpha\beta} = \frac{e^2}{4\pi\epsilon_0} \int \mathrm{d}^3\boldsymbol{r} \int \mathrm{d}^3\boldsymbol{r}'\; \psi_\alpha(\boldsymbol{r})\psi_\beta(\boldsymbol{r})\, \frac{1}{|\boldsymbol{r}-\boldsymbol{r}'|}\, \psi_\alpha(\boldsymbol{r}')\psi_\beta(\boldsymbol{r}') = V_{\alpha\alpha\beta\beta} = V_{\beta\beta\alpha\alpha} = V_{\alpha\beta\alpha\beta} = V_{\beta\alpha\beta\alpha}\,. \tag{2.41}$$

Both can be evaluated via Eq. (2.36) with a subsequent conversion to Tanabe-Sugano orbital

$J_{\alpha\beta}$	ξ	η	ζ	u	v
ξ	–	$3B+C$	$3B+C$	$B+C$	$3B+C$
η	$3B+C$	–	$3B+C$	$B+C$	$3B+C$
ζ	$3B+C$	$3B+C$	–	$4B+C$	C
u	$B+C$	$B+C$	$4B+C$	–	$4B+C$
v	$3B+C$	$3B+C$	C	$4B+C$	–

Table 2: Exchange integrals $J_{\alpha\beta}$ in terms of Racah parameters

basis. Table 2 gives the values of the exchange integrals in terms of the Racah parameters, the Coulomb integrals may be obtained via the relation

$$U = U_{\alpha\beta} + 2J_{\alpha\beta} \tag{2.42}$$

valid for our case of orbitals derived from the spherical harmonics. After collecting all the contributions involving either $U_{\alpha\beta}$ or $J_{\alpha\beta}$, we arrive at the following two-orbital Hamiltonian:

$$\mathcal{H}_2 = \sum_{\alpha<\beta}\sum_{\sigma}\Big[(U_{\alpha\beta}-J_{\alpha\beta})\,n_{\alpha\sigma}n_{\beta\sigma} + U_{\alpha\beta}n_{\alpha\sigma}n_{\beta,-\sigma}\Big] + \sum_{\alpha\neq\beta} J_{\alpha\beta}\left(\alpha^\dagger_\uparrow\beta^\dagger_\downarrow\alpha_\downarrow\beta_\uparrow + \alpha^\dagger_\uparrow\alpha^\dagger_\downarrow\beta_\downarrow\beta_\uparrow\right). \tag{2.43}$$

To make it more transparent, it is possible to combine the spin-dependent part of the inter-orbital density-density interaction $\sum_\sigma(n_{\alpha\sigma}n_{\beta\sigma} - n_{\alpha\sigma}n_{\beta,-\sigma})$ and the second term from the right $(\alpha^\dagger_\uparrow\beta^\dagger_\downarrow\alpha_\downarrow\beta_\uparrow)$ into an inter-orbital spin-spin interaction. It is clear that these terms may only be active between two singly-occupied orbitals. For the singly-occupied orbitals we can introduce the corresponding spin operator $\boldsymbol{S}_\alpha$ (here associated with the orbital α) as

$$\boldsymbol{S}_\alpha = \left[\tfrac{1}{2}(S^+_\alpha+S^-_\alpha), \tfrac{1}{2i}(S^+_\alpha-S^-_\alpha), S^z_\alpha\right] \quad \text{with} \quad S^+_\alpha = \alpha^\dagger_\uparrow\alpha_\downarrow\,,\; S^-_\alpha = \alpha^\dagger_\downarrow\alpha_\uparrow\,,\; S^z_\alpha = \tfrac{1}{2}(n_{\alpha\uparrow}-n_{\alpha\downarrow}) \tag{2.44}$$

that enables us to bring the intra-ionic Coulomb interaction into the final form

$$\begin{aligned}\mathcal{H}_{\text{Coul}} = {} & U\sum_\alpha n_{\alpha\uparrow}n_{\alpha\downarrow} + \sum_{\alpha<\beta}(U_{\alpha\beta}-\tfrac{1}{2}J_{\alpha\beta})\,n_\alpha n_\beta \\ & - 2\sum_{\alpha<\beta} J_{\alpha\beta}\,\boldsymbol{S}_\alpha\cdot\boldsymbol{S}_\beta + \sum_{\alpha\neq\beta} J_{\alpha\beta}\,\alpha^\dagger_\uparrow\alpha^\dagger_\downarrow\beta_\downarrow\beta_\uparrow\,, \qquad (+\text{ neglected terms})\end{aligned} \tag{2.45}$$

where the individual terms represent the intra-orbital Hubbard interaction, inter-orbital Hubbard interaction, Hund's exchange, and inter-orbital pair-hopping term, respectively.

By inspecting Table 2 we notice, that the parametrization of the interactions in $\mathcal{H}_{\text{Coul}}$ simplifies when one considers a strictly t_{2g}-only or e_g-only system. In that case all relevant exchange integrals $J_{\alpha\beta}$ are equal to $J_{\text{H}} = 3B + C$ or $J_{\text{H}} = 4B + C$, respectively, and consequently $U_{\alpha\beta} = U' = U - 2J_{\text{H}}$. The resulting two-parameter Hamiltonian $\mathcal{H}_{\text{Coul}}(U, J_{\text{H}})$ is the Hubbard-Kanamori Hamiltonian [26].

There are still many non-zero matrix elements in Eq. (2.31) that were omitted when constructing (2.45). These are summarized in Table 3. Note that they always involve both t_{2g} and e_g orbitals at the same time so that they only lead to perturbative corrections for purely t_{2g} or e_g systems. However, they may become important when dealing with mixed t_{2g}-e_g situation. An important example – spin-state crossover of d^6 configuration – will be discussed in the next paragraph.

three-orbital	four-orbital
$\iint \xi^2 \frac{1}{r_{12}} u'v' = +2\sqrt{3}B$	$\iint \xi\zeta \frac{1}{r_{12}} \eta'v' = +3B$
$\iint \xi\xi' \frac{1}{r_{12}} uv' = -\sqrt{3}B$	$\iint \eta\zeta \frac{1}{r_{12}} \xi'v' = -3B$
$\iint \eta^2 \frac{1}{r_{12}} u'v' = -2\sqrt{3}B$	$\iint \xi\eta \frac{1}{r_{12}} \zeta'u' = -2\sqrt{3}B$
$\iint \eta\eta' \frac{1}{r_{12}} uv' = +\sqrt{3}B$	$\iint \eta\zeta \frac{1}{r_{12}} \xi'u' = +\sqrt{3}B$
	$\iint \xi\zeta \frac{1}{r_{12}} \eta'u' = +\sqrt{3}B$

Table 3: Nonzero matrix elements involving three or four different orbitals. The integrals are written in an abbreviated form with the prime indicating the argument $\boldsymbol{r}'$ of the corresponding orbital wavefunction while the absence of prime indicates the argument $\boldsymbol{r}$. Further, r_{12} stands for $|\boldsymbol{r} - \boldsymbol{r}'|$. Together with the symmetry property (2.33), the left and right columns of the table generate 24 and 40 $V_{\alpha\beta\gamma\delta}$ matrix elements, respectively.

2.2.2 Ionic Hubbard model and multiplet structure

Together with the energy levels of the individual orbitals discussed in the Sec. 2.1, the above Coulomb interaction Hamiltonian forms the ionic Hubbard model

$$\mathcal{H}_{\text{ion}} = \sum_{\alpha\sigma} \varepsilon_\alpha \alpha^\dagger_\sigma \alpha_\sigma + \mathcal{H}_{\text{Coul}} \,. \tag{2.46}$$

Before extending it further with the spin-orbit interaction in the next paragraph, we will inspect the resulting multiplet structure (i.e. the spectrum of eigenstates for a fixed number of electrons) in a few interesting cases.

Let us first comment on the general tendencies that can be intuitively inferred from the structure of $\mathcal{H}_{\text{ion}}$. For an isolated ion, all the orbital energies E_α are equal and the eigenstates are decided solely by the Coulomb interaction. The leading role takes the intra-orbital Hubbard repulsion (given by the dominant parameter U) which tries to place electrons to different orbitals whenever possible. The unpaired spins in singly-occupied orbitals are then organized by the ferromagnetic Hund's coupling to form the largest possible total spin. These observations are in fact the content of the first Hund's rule as discussed in standard textbooks [27]. The situation is changed by the crystal field which splits the orbital energies E_α. The primary splitting due to the octahedral crystal field is the t_{2g}-e_g one. Its value is substantial so that it may be energetically favorable to keep electrons in the lower t_{2g} levels, even though more doubly-occupied orbitals appear and this scenario thus leads to a larger Hubbard repulsion and an energy loss in Hund's coupling. On this occasion, it should be also noted that the crystal values of the model parameters are strongly affected by screening. This does not significantly modify the Hund's exchange but the Hubbard repulsion is quite reduced compared to free ions, increasing the relative importance of the crystal field splitting.

From the formal point of view, the first three terms in Eq. (2.45) do not change the distribution of electrons among the orbitals. This type of dynamics comes only due to the last term and is constrained by the necessity to transfer a complete electron pair from a doubly occupied orbital

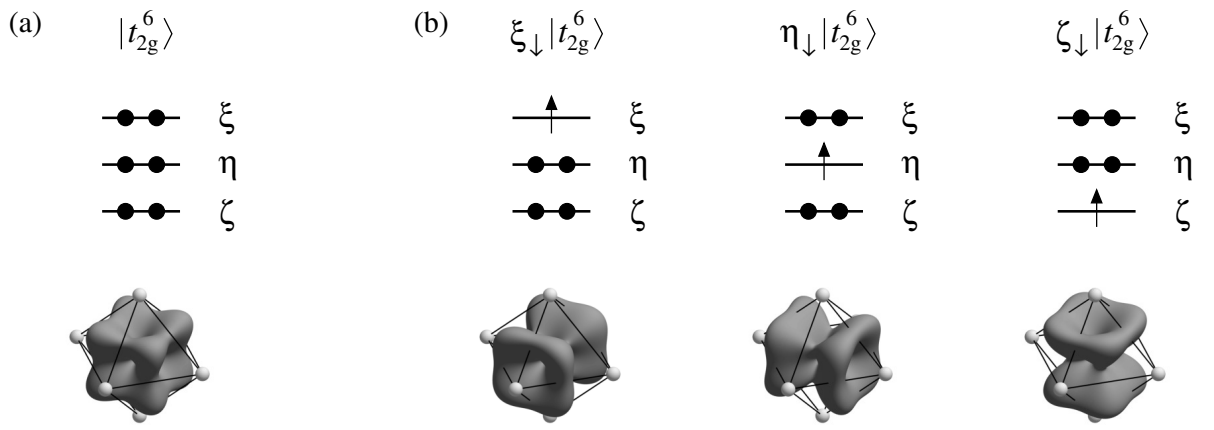

Fig. 10: (a) Schematic representation of the six-electron many-body state corresponding to the t_{2g}^6 electron configuration. The orbitals ξ, η, ζ are considered to be degenerate; in this and the following figure they are vertically separated for clarity only. In second quantization, the state depicted in panel (a) corresponds to $\xi_\uparrow^\dagger \xi_\downarrow^\dagger \eta_\uparrow^\dagger \eta_\downarrow^\dagger \zeta_\uparrow^\dagger \zeta_\downarrow^\dagger |\,\rangle$, where $|\,\rangle$ is an empty state (no electrons in the valence shell). At the bottom a visual representation of the six-electron cloud is shown. The angular distribution of the total electron density (integrated in the radial direction) is captured as a surface plot where the distance of the surface points to the origin is proportional to the integral density in the corresponding direction. (b) States of the t_{2g}^5 configuration obtained by removing a single electron from the t_{2g}^6 configuration shown in the panel (a). The electron clouds at the bottom bear some similarity to the p_x, p_y, and p_z orbitals which is related to the effective angular momentum $l^{\rm eff} = 1$ carried by the t_{2g} orbitals.

into an empty one. Thanks to the limited mixing of electron configurations, the identification of the ionic eigenstates may be relatively simple, in spite of dealing with a correlated many-body problem. The real troubles only start once we let the ions interact.

Our first illustrative example will be the t_{2g}^5 electron configuration which is relevant for the physics of Kitaev materials Na_2IrO_3 or α-$RuCl_3$. We assume that the crystal field splitting is large enough so that it practically eliminates the e_g orbitals.[6] For simplicity, we further assume that the t_{2g} orbitals are not split. The starting point is the t_{2g}^6 configuration with fully populated t_{2g} orbitals shown in Fig. 10(a). The t_{2g}^5 configurations are obtained by removing one electron from it. There are three possible choices of the corresponding orbital and two options for the spin projection, leading altogether to six-fold degeneracy. The resulting layout of electrons among orbitals allows only the Hubbard repulsion to be active so that the Coulomb energy evaluates simply to $2U + 8(U' - \frac{1}{2}J_{\rm H}) = 10(U - 2J_{\rm H})$. By observing the angular distribution of the electron clouds as presented in Fig. 10, we notice that the t_{2g}^6 configuration has a full cubic symmetry whereas the t_{2g}^5 configurations vaguely resemble the shapes of the Cartesian p_x, p_y, p_z orbitals. This visual similarity is related to the fact that by extracting a t_{2g} electron as an $l^{\rm eff} = 1$ object from the fully symmetric t_{2g}^6 configuration with total $L^{\rm eff} = 0$, we created a configuration with $L^{\rm eff} = 1$ again. A more precise symmetry classification is embedded in the usual notation of the members of the multiplet structure. Being eigenstates of some symmetric Hamiltonian, each set of degenerate eigenstates constitutes a basis for a certain representation of the respective symmetry group. In our case the rotation group $\mathcal{O}$ of a cube/octahedron is the relevant one (extending it by the spatial inversion, we get the group $\mathcal{O}_{\rm h}$). It has two one-dimensional representations A_1, A_2, one two-dimensional representation E, and two three-dimensional representations T_1, T_2. The three eigenstates presented in Fig. 10(b) are a basis for the T_2 representation of $\mathcal{O}$ [25]. When

[6] This low-spin situation is the case in the relevant Ir^{4+} ($5d$) and Ru^{3+} ($4d$) ions; the $3d$ ions usually prefer to employ the e_g orbitals to form a larger total spin and hence optimize Hund's exchange.

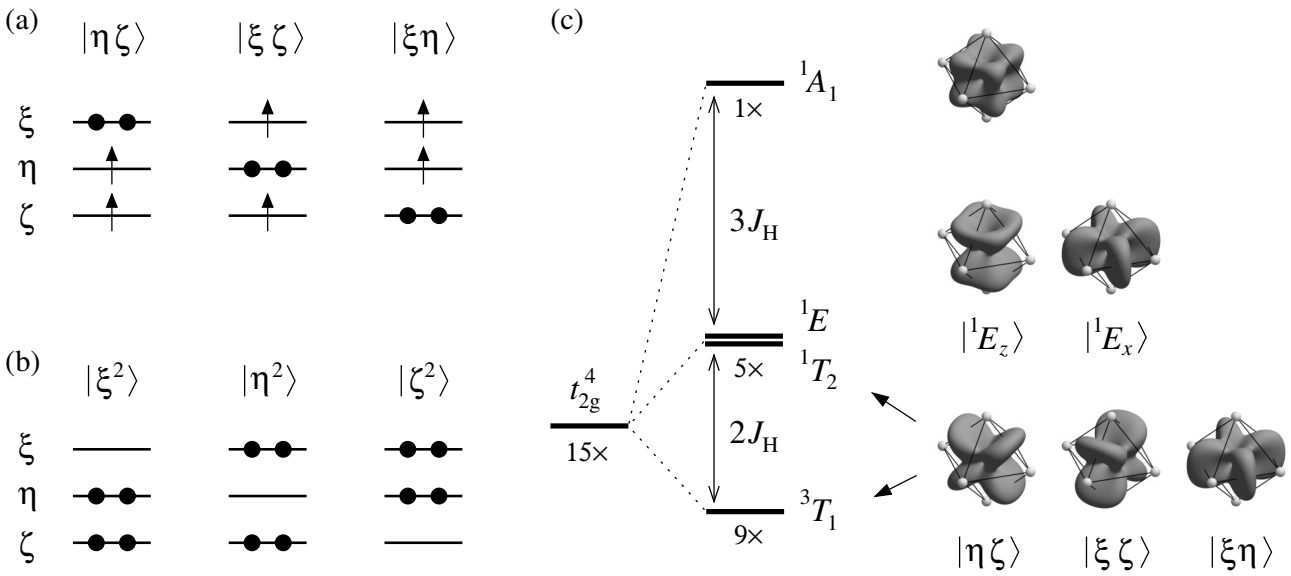

Fig. 11: (a), (b) Schematic representation of the many-body states obtained by removing two electrons from the t_{2g}^6 configuration, either from two different orbitals (a), or from the same orbital (b). In the case (a), only one of the four possible spin configurations for each electron distribution is shown. (c) Level splitting due to the Coulomb interaction. The lowest nine states are spin-triplets $^3T_1$ based on the states of the type shown in panel (a). The same three orbital populations may form also singlets $^1T_2$ that merge with the two ^1E spin-singlets to form a five-fold degenerate level. Well above the others is the fully symmetric $^1A_1$ singlet.

referring to a multiplet member, the label of the group representation comes together with the multiplicity in front. By multiplicity one means the number of possible spin projection values for the total spin of the state. Here we have three spin-$\frac{1}{2}$ doublets so the full conventional label for the six-fold degenerate t_{2g}^5 states is $^2T_2$.

The case of the t_{2g}^5 configuration discussed so far is fairly trivial. A bit more involved is the analysis of the t_{2g}^4 configuration. Here one can consider two independent classes of states presented in Fig. 11(a) and (b). The former one consists of two singly-occupied orbitals and one doubly occupied. Again there are three possibilities how to arrange them. All three configurations have the same Hubbard repulsion energy $U + 5(U' - \frac{1}{2}J_H) = 6(U - 2J_H) - \frac{1}{2}J_H$. Due to the two singly-occupied orbitals, the Hund's coupling comes now into play while the pair hopping term is clearly inactive. The two unpaired spins-$\frac{1}{2}$ can form either a triplet or a singlet state. The respective full Coulomb energies of the $^3T_1$ triplets and $^1T_2$ singlets are then $6U - 13J_H$ and $6U - 11J_H$ differing by $2J_H$. The corresponding states can be easily expressed in the second quantization formalism, for example the four states based on $|\eta\,\zeta\rangle$ of Fig. 11(a) read as:

$$|^3T_1(\eta\,\zeta, S_z{=}+1)\rangle = \xi_\uparrow^\dagger\,\xi_\downarrow^\dagger\,\eta_\uparrow^\dagger\,\zeta_\uparrow^\dagger\,|\,\rangle\,, \tag{2.47}$$

$$|^3T_1(\eta\,\zeta, S_z{=}0)\rangle = \frac{1}{\sqrt{2}}\,\xi_\uparrow^\dagger\,\xi_\downarrow^\dagger\,(\eta_\uparrow^\dagger\,\zeta_\downarrow^\dagger + \eta_\downarrow^\dagger\,\zeta_\uparrow^\dagger)\,|\,\rangle\,, \tag{2.48}$$

$$|^3T_1(\eta\,\zeta, S_z{=}-1)\rangle = \xi_\uparrow^\dagger\,\xi_\downarrow^\dagger\,\eta_\downarrow^\dagger\,\zeta_\downarrow^\dagger\,|\,\rangle\,, \tag{2.49}$$

$$|^1T_2(\eta\zeta)\rangle = \frac{1}{\sqrt{2}}\,\xi_\uparrow^\dagger\,\xi_\downarrow^\dagger\,(\eta_\uparrow^\dagger\,\zeta_\downarrow^\dagger - \eta_\downarrow^\dagger\,\zeta_\uparrow^\dagger)\,|\,\rangle\,. \tag{2.50}$$

As a consequence of having one t_{2g} orbital populated more than the others, the electron-density clouds of the twelve eigenstates $^3T_1$, $^1T_2$ become asymmetric. As shown in Fig. 11(c), they

resemble those of the d_{yz}, d_{zx}, d_{xy} orbitals. The second class of states that do not interact with the former ones is shown in Fig. 11(b). In each of these states, one of the three t_{2g} orbitals is empty while the other two are doubly occupied which makes the states singlets in terms of total spin. This configuration precludes Hund's coupling but activates the pair hopping proportional to J_{H} as well. The eigenstates are obtained by diagonalizing the pair hopping term expressed in the basis states $|\xi^2\rangle$, $|\eta^2\rangle$, and $|\zeta^2\rangle$ of Fig. 11(b):

$$J_{\mathrm{H}} \begin{pmatrix} 0 & 1 & 1 \\ 1 & 0 & 1 \\ 1 & 1 & 0 \end{pmatrix} . \tag{2.51}$$

Doing so, we get a two-fold degenerate eigenvalue $-J_{\mathrm{H}}$ and the associated ${}^1E$ states

$$|{}^1E_z\rangle = \frac{1}{\sqrt{6}} \left(|\xi^2\rangle + |\eta^2\rangle - 2|\zeta^2\rangle \right) , \tag{2.52}$$

$$|{}^1E_x\rangle = \frac{1}{\sqrt{2}} \left(|\eta^2\rangle - |\xi^2\rangle \right) , \tag{2.53}$$

and a non-degenerate eigenvalue $+2J_{\mathrm{H}}$ associated with a fully symmetric ${}^1A_1$ state

$$|{}^1A_1\rangle = \frac{1}{\sqrt{3}} \left(|\xi^2\rangle + |\eta^2\rangle + |\zeta^2\rangle \right) . \tag{2.54}$$

The Hubbard repulsion energy amounts to $2U + 4(U' - \frac{1}{2}J_{\mathrm{H}}) = 6U - 10J_{\mathrm{H}}$, by adding the eigenvalues of the pair hopping we find that ${}^1E$ merge with the ${}^1T_2$ level while ${}^1A_1$ is singled out at the top of the multiplet level scheme in Fig. 11(c).

The Cartesian formulation of the multiplet structure as demonstrated above may be convenient when considering e.g. further splitting of the orbitals in a tetragonal crystal field. However, we need to prepare ground for the inclusion of the spin-orbit coupling in the next paragraph. In this context the role of $\boldsymbol{L}^{\mathrm{eff}}$ is essential so that the multiplet structure of both t_{2g}^5 and t_{2g}^4 should be reformulated as $\boldsymbol{L}^{\mathrm{eff}}$ eigenstates. The Hamiltonian including the Coulomb interaction commutes with $\boldsymbol{L}^{\mathrm{eff}}$ and $\boldsymbol{S}$, the eigenstates will be therefore classified by the corresponding quantum numbers and denoted by $|L^{\mathrm{eff}}, L_z^{\mathrm{eff}}, S, S_z\rangle$.

To obtain compact expressions in the following, we adopt a hole picture and think about one-hole or two-hole configurations on top of the t_{2g}^6 "vacuum". The one-hole states will carry $L^{\mathrm{eff}} = 1$ and $S = \frac{1}{2}$. It is convenient to introduce the hole operators in such a way that they create states with the selected spin and $\boldsymbol{L}^{\mathrm{eff}}$ quantum numbers and give them suitable phases. For our purpose, the best choice of connecting the hole and electron operators is

$$h_{m\sigma}^{\dagger} = (-1)^m (-\sigma)\, c_{-m,-\sigma} \tag{2.55}$$

with m denoting the magnetic quantum number associated with $\boldsymbol{L}^{\mathrm{eff}}$ and $\sigma = \pm 1$ indicating the up/down configuration of spin. The logic behind the above construction is as follows: (i) To create a configuration with $m\sigma$ based on the fully symmetric ($L^{\mathrm{eff}} = 0$) and spinless ($S = 0$) t_{2g}^6 state, we need to remove an electron with the opposite quantum numbers. (ii) The phase factor $(-1)^m$ is related to a conversion between Y_{lm} and $Y_{l,-m}^*$. (iii) The factor $(-\sigma)$ is generated by reordering the fermionic operators to follow the sequence $\xi_{\uparrow}^{\dagger} \xi_{\downarrow}^{\dagger} \eta_{\uparrow}^{\dagger} \eta_{\downarrow}^{\dagger} \zeta_{\uparrow}^{\dagger} \zeta_{\downarrow}^{\dagger}$ in the final t_{2g}^5 configuration. In analogy with the notation of the a, b, c electron states in Eq. (2.26), the hole operators a, b, c will

be associated with $m = +1$, 0, and -1, respectively. Put explicitly in terms of the annihilation operators ξ_σ, η_σ, ζ_σ, they read as

$$\begin{aligned} a^\dagger_\uparrow &= +\tfrac{1}{\sqrt{2}}(i\eta_\downarrow + \xi_\downarrow)\,, & b^\dagger_\uparrow &= -\zeta_\downarrow\,, & c^\dagger_\uparrow &= +\tfrac{1}{\sqrt{2}}(i\eta_\downarrow - \xi_\downarrow)\,, \\ a^\dagger_\downarrow &= -\tfrac{1}{\sqrt{2}}(i\eta_\uparrow + \xi_\uparrow)\,, & b^\dagger_\downarrow &= +\zeta_\uparrow\,, & c^\dagger_\downarrow &= -\tfrac{1}{\sqrt{2}}(i\eta_\uparrow - \xi_\uparrow)\,. \end{aligned} \tag{2.56}$$

Defined this way, $a^\dagger_\sigma$ ($b^\dagger_\sigma$, $c^\dagger_\sigma$) acting on the state with fully occupied t_{2g} orbitals

$$|t^6_{2g}\rangle = \xi^\dagger_\uparrow \xi^\dagger_\downarrow \eta^\dagger_\uparrow \eta^\dagger_\downarrow \zeta^\dagger_\uparrow \zeta^\dagger_\downarrow |\,\rangle \tag{2.57}$$

creates the t^5_{2g} state with spin σ and the $L^{\rm eff}_z$ quantum number equal to $+1$ (0, -1). Using the systematic labeling of the eigenstates by $|L^{\rm eff}, L^{\rm eff}_z, S, S_z\rangle$, we have for example

$$\left|1, +1, \tfrac{1}{2}, +\tfrac{1}{2}\right\rangle = a^\dagger_\uparrow |t^6_{2g}\rangle\,. \tag{2.58}$$

The phases of all the six generated states follow Condon-Shortley convention so that they give canonical matrix elements of both total spin and total effective orbital momentum operators $\boldsymbol{S}$ and $\boldsymbol{L}^{\rm eff}$. This feature will be useful later when combining them following the rules for the addition of angular momenta.

The selection of $\boldsymbol{L}^{\rm eff}$ quantization axis proceeds in accordance with the potential further reduction of the octahedral symmetry. Here we have used $L^{\rm eff}_z$ for the tetragonal case, for the trigonal case one has to implement the a_{1g} and $e^\pi_{g\pm}$ states of Eqs. (2.23)–(2.25) into the definition of the hole operators to reflect the quantization in the [111] direction. Moreover, when including the spin-orbit coupling, the spin quantization axis should be consistently changed to [111] as well. The derivation of an explicit linear relation between the electron operators ξ_σ, η_σ, ζ_σ and the trigonal hole operators is a useful exercise though the relation itself has a limited use. It may be formulated as follows:

$$a^\dagger_\uparrow = A_\uparrow \mathrm{e}^{i\pi/4} \sin\theta - A_\downarrow \cos\theta \qquad a^\dagger_\downarrow = A_\uparrow \mathrm{e}^{i\pi/4} \cos\theta + A_\downarrow \sin\theta \qquad \text{with } \tan 2\theta = \sqrt{2} \tag{2.59}$$

and similarly for b, c. The operators A, B, C are defined as

$$\begin{aligned} A_\sigma &= \tfrac{1}{\sqrt{3}}(\mathrm{e}^{+2\pi i/3}\xi_\sigma + \mathrm{e}^{-2\pi i/3}\eta_\sigma + \zeta_\sigma)\,, \\ B_\sigma &= \tfrac{1}{\sqrt{3}}(\xi_\sigma + \eta_\sigma + \zeta_\sigma)\,, \\ C_\sigma &= -\tfrac{1}{\sqrt{3}}(\mathrm{e}^{-2\pi i/3}\xi_\sigma + \mathrm{e}^{+2\pi i/3}\eta_\sigma + \zeta_\sigma)\,. \end{aligned} \tag{2.60}$$

The hole operators are labeled according to [111] projections of the effective orbital momentum and spin, the electron operators use the z spin quantization axis. Equations (2.59) and (2.60) constitute a trigonal analog of Eq. (2.56). When expressing the matrices for the X, Y, and Z components of $\boldsymbol{S}$ and $\boldsymbol{L}^{\rm eff}$ operators [c.f. Fig. 9(c)], the result is identical to the matrices for the x, y, and z components in the basis given by Eq. (2.56).

Now we are going to assemble the eigenstates with two holes that will correspond to the t^4_{2g} multiplet structure. This can be achieved simply by forming $\boldsymbol{L}^{\rm eff}$ and $\boldsymbol{S}$ eigenstates of the two holes. The reason for this simplification is that the Coulomb Hamiltonian for a t_{2g}-only valence shell can be cast to a transparent form

$$\mathcal{H}_{t_{2g}} = \tfrac{1}{2}(U - 3J_{\rm H})N(N-1) + \tfrac{5}{2}J_{\rm H}N - 2J_{\rm H}\boldsymbol{S}^2 - \tfrac{1}{2}J_{\rm H}(\boldsymbol{L}^{\rm eff})^2\,, \tag{2.61}$$

where N stands for number of electrons and $\boldsymbol{S}$, $\boldsymbol{L}^{\rm eff}$ are the total spin and total effective orbital momentum as before. For a fixed number of electrons, this form of the Hamiltonian demonstrates the tendency to maximize total spin in the first place and $L^{\rm eff}$ in the second.

By combining the two $L^{\text{eff}} = 1$ holes, we can obtain the possible total $L^{\text{eff}} = 0, 1, 2$ states with the help of the tables of Clebsch-Gordan coefficients. The total spin will automatically follow by observing the symmetry of the state. Symmetric or antisymmetric states in terms of orbitals have to be of a complementary symmetry in terms of spins. This means that the symmetric orbital combinations will be spin singlets while the two holes in an antisymmetric orbital combination have to form a spin triplet. The nondegenerate topmost energy state ${}^1A_1$ shown in Fig. 11(b) is a singlet in both orbital and spin sector, i.e. it has $L^{\text{eff}} = 0$ and $S = 0$:

$$|L^{\text{eff}}, L_z^{\text{eff}}, S, S_z\rangle = |0,0,0,0\rangle = \tfrac{1}{\sqrt{3}} \left(a_\uparrow^\dagger c_\downarrow^\dagger - b_\uparrow^\dagger b_\downarrow^\dagger + c_\uparrow^\dagger a_\downarrow^\dagger\right) |t_{2g}^6\rangle \,. \tag{2.62}$$

The five-fold degeneracy of the level encompassing ${}^1T_2$ and ${}^1E$ in Fig. 11(b) is also explained, as it corresponds to $L^{\text{eff}} = 2$ and $S = 0$ with the five L_z^{eff} eigenstates given explicitly by

$$\begin{aligned}
|2,+2,0,0\rangle &= a_\uparrow^\dagger a_\downarrow^\dagger |t_{2g}^6\rangle \,, \\
|2,+1,0,0\rangle &= \tfrac{1}{\sqrt{2}} \left(a_\uparrow^\dagger b_\downarrow^\dagger + b_\uparrow^\dagger a_\downarrow^\dagger\right) |t_{2g}^6\rangle \,, \\
|2,0,0,0\rangle &= \tfrac{1}{\sqrt{6}} \left(a_\uparrow^\dagger c_\downarrow^\dagger + 2\, b_\uparrow^\dagger b_\downarrow^\dagger + c_\uparrow^\dagger a_\downarrow^\dagger\right) |t_{2g}^6\rangle \,, \\
|2,-1,0,0\rangle &= \tfrac{1}{\sqrt{2}} \left(b_\uparrow^\dagger c_\downarrow^\dagger + c_\uparrow^\dagger b_\downarrow^\dagger\right) |t_{2g}^6\rangle \,, \\
|2,-2,0,0\rangle &= c_\uparrow^\dagger c_\downarrow^\dagger |t_{2g}^6\rangle \,.
\end{aligned} \tag{2.63}$$

Finally, the low-energy triplets ${}^3T_1$ have $L^{\text{eff}} = 1$ and $S = 1$. We write down the corresponding states using an abbreviated $|L_z^{\text{eff}}, S_z\rangle$ notation:

$$\begin{aligned}
|+1,+1\rangle &= a_\uparrow^\dagger b_\uparrow^\dagger |t_{2g}^6\rangle \,, & |+1,0\rangle &= \tfrac{1}{\sqrt{2}} \left(a_\uparrow^\dagger b_\downarrow^\dagger + a_\downarrow^\dagger b_\uparrow^\dagger\right) |t_{2g}^6\rangle \,, & |+1,-1\rangle &= a_\downarrow^\dagger b_\downarrow^\dagger |t_{2g}^6\rangle \,, \\
|\,0,+1\rangle &= a_\uparrow^\dagger c_\uparrow^\dagger |t_{2g}^6\rangle \,, & |\,0,0\rangle &= \tfrac{1}{\sqrt{2}} \left(a_\uparrow^\dagger c_\downarrow^\dagger + a_\downarrow^\dagger c_\uparrow^\dagger\right) |t_{2g}^6\rangle \,, & |\,0,-1\rangle &= a_\downarrow^\dagger c_\downarrow^\dagger |t_{2g}^6\rangle \,, \\
|-1,+1\rangle &= b_\uparrow^\dagger c_\uparrow^\dagger |t_{2g}^6\rangle \,, & |-1,0\rangle &= \tfrac{1}{\sqrt{2}} \left(b_\uparrow^\dagger c_\downarrow^\dagger + b_\downarrow^\dagger c_\uparrow^\dagger\right) |t_{2g}^6\rangle \,, & |-1,-1\rangle &= b_\downarrow^\dagger c_\downarrow^\dagger |t_{2g}^6\rangle \,.
\end{aligned} \tag{2.64}$$

The phases of the t_{2g}^4 states given in Eqs. (2.62), (2.63), (2.64) are again compatible with the Condon-Shortley convention so that they generate canonical matrices of $\boldsymbol{L}^{\text{eff}}$ and $\boldsymbol{S}$ operators when used as a basis.

Having explored in detail the t_{2g}^4 and t_{2g}^5 configurations, we will now have a brief look at a combined t_{2g}-e_g situation. As an illustration, we will use a particularly rich case of d^6 ions such as Co^{3+} or Fe^{2+} well known for spin-state crossover phenomena [28]. The basic physics can be understood based on the sketches in Fig. 12(a). These show so-called low-spin (LS), intermediate-spin (IS), and high-spin (HS) configurations of a d^6 ion differing in the distribution of the six electrons among the t_{2g} and e_g levels. Placing an electron to the e_g levels costs the extra crystal-field energy Δ but doing so, we can create two unpaired spins that are subject to Hund's coupling and may therefore bring an energy gain proportional to J_{H}. For simplicity, we first ignore the differences in J_{H} for t_{2g} and e_g orbitals. More precisely, we set the Racah parameter B to zero leading to $J_{\alpha\beta} = J_{\text{H}} = C$ and vanishing matrix elements in Table 3. We will also not consider the perturbative corrections by pair hopping of t_{2g} electrons into empty e_g levels. By evaluating the Hubbard repulsion in the t_{2g}^6 configuration, we get the reference energy

$$E(t_{2g}^6) = E_0 = 15(U - 2J_{\text{H}}) \,. \tag{2.65}$$

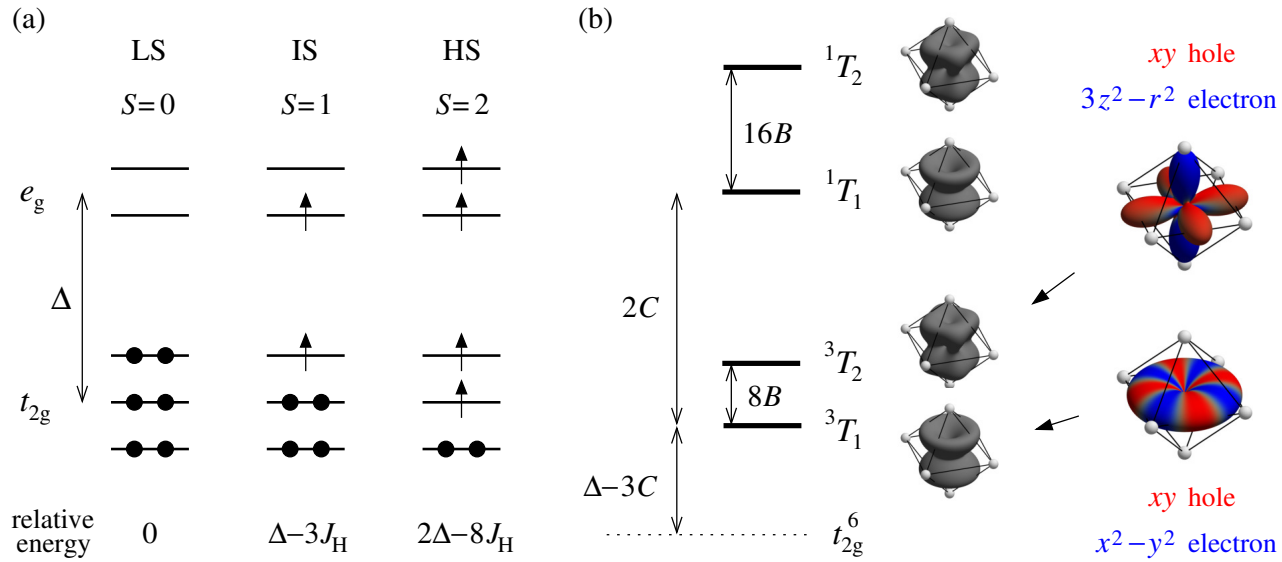

Fig. 12: (a) Schematic representation of the low-spin, intermediate-spin, and high-spin states of d^6 ion such as Co^{3+}. The relative energies of the states are determined by the balance between the crystal field splitting Δ supporting configurations with less e_g electrons and Hund's coupling that gains energy by forming the maximum total spin. (b) Multiplet structure of the $t_{2g}^5 e_g^1$ configuration. The lower two triplets ${}^3T_{1,2}$ correspond to the intermediate-spin states. The electron clouds for T_1 and T_2 slightly differ. Their internal structure can be understood in terms of a hole in t_{2g}^6 configuration combined with the e_g electrons, leading to either a triplet or a singlet total spin state. T_1 states involve e_g orbital lying in the plane defined by the t_{2g} hole, the out-of-plane e_g orbital is employed in the T_2 states.

The configuration with one e_g electron contains two unpaired spins-$\frac{1}{2}$ so that the state may be total singlet or triplet. The respective energies are $E_0 + \Delta - 3J_H$ and $E_0 + \Delta - J_H$ with the triplet state (intermediate spin $S = 1$) being supported by Hund's coupling. In case of the configurations with two e_g electrons in different e_g orbitals, we have to sort out the interaction of four unpaired spins which leads to the energy $E = E_0 + 2\Delta - [S(S+1)+2]J_H$ as function of the total spin S. The lowest state is here the high-spin $S = 2$ with the energy $2\Delta - 8J_H$ above E_0. Depending on the balance between the crystal field splitting and Hund's coupling strength, the LS, IS, and HS states may be close in energy so that the total spin of the ions may be changed by affecting slightly their crystal/ligand environment, e.g. by pressure. The low-lying excited states may also be thermally activated or brought into play by inter-ionic interactions. Later in Section 4 we will be dealing with an analogous situation created by spin-orbit coupling.

We conclude this paragraph by discussing the detailed multiplet structure of the $t_{2g}^5 e_g^1$ configuration for nonzero Racah B whose presence further splits the triplet and singlet levels. As presented in Fig. 12(b), the non-uniform interaction of the t_{2g} orbitals with the e_g ones (see Table. 2) makes an energy distinction between the various combinations of the orbitals. When one interprets the missing electron in t_{2g} orbitals as a positively charged hole, it is intuitively expected that the negatively charged e_g electron will be preferably put into the e_g orbital better matching this hole in shape. This is indeed observed in Fig. 12(b), the configurations where the e_g orbital $x^2 - y^2$ matches the plane defined by the xy hole are lower than those involving the out-of-plane $3z^2 - r^2$ orbital. Of course, the hole can be put to the other t_{2g} orbitals as well. In that case one selects other in-plane/out-of-plane combinations of the e_g orbitals. Each of the levels shown in Fig. 12(b) is thus three-fold orbitally degenerate, giving in total 24 states of the multiplet structure as it has to be for the $t_{2g}^5 e_g^1$ configuration. At this point it is important to

fully employ the matrix elements from Table 3 that we neglected in Eq. (2.45). By omitting them, we would artificially split the levels further and break the octahedral symmetry.

2.2.3 Spin-orbit coupling

Apart from the Coulomb interaction discussed in detail in the previous paragraphs, additional interactions originating in relativistic quantum mechanics come into play. In the hydrogen atom these just give the fine structure of the energy levels and can be neglected in the first approximation. This will not be the case in the heavier transition metal ions under our consideration. As we progress down through the periodic table of elements, one of the relativistic corrections – the spin-orbit coupling – becomes increasingly important and essentially rearranges the multiplet structures. Intuitively it may be understood by considering the electron in its rest frame where it is encircled by the positively charged nucleus. The magnetic field generated by the "current loop" provided by the nucleus then acts on the spin of the electron. More generally and on a quantitative level, we may estimate this effect by taking a static electrostatic field $\boldsymbol{E}$ the electron moves in (e.g. that of the nucleus), performing Lorentz transformation to the rest frame of the electron which gives the magnetic field $\boldsymbol{B}' \approx -(\boldsymbol{v} \times \boldsymbol{E})/c^2$, and letting this magnetic field act on the magnetic moment associated with the electronic spin via the usual $2\mu_\mathrm{B}\, \boldsymbol{s} \cdot \boldsymbol{B}'$. This simple estimate leads to a correct result up to a factor of 2. A proper derivation is based on an expansion of the solution of the Dirac equation up to the order v^2/c^2 and gives the interaction of the form [29]

$$\mathcal{H}_\mathrm{SOC} = \frac{e\hbar}{2m^2c^2}\, \boldsymbol{s} \cdot (\boldsymbol{E} \times \boldsymbol{p})\,. \tag{2.66}$$

Here the electron spin operator $\boldsymbol{s}$ is again dimensionless (i.e. it does not include $\hbar$). For the centrally-symmetric potential of an atom, the electric field is radial and related to the radial derivative of the potential energy V for the electron via

$$\boldsymbol{E} = -\nabla\Phi = -\frac{\boldsymbol{r}}{r}\frac{\mathrm{d}\Phi}{\mathrm{d}r} = \frac{1}{e}\frac{\boldsymbol{r}}{r}\frac{\mathrm{d}V}{\mathrm{d}r}\,. \tag{2.67}$$

The use of the above radial field in Eq. (2.66) brings the dimensionless electron angular momentum operator $\boldsymbol{l} = (\boldsymbol{r} \times \boldsymbol{p})/\hbar$ and the interaction Hamiltonian becomes

$$\mathcal{H}_\mathrm{SOC} = \frac{\hbar^2}{2m^2c^2}\frac{1}{r}\frac{\mathrm{d}V}{\mathrm{d}r}\, \boldsymbol{s} \cdot \boldsymbol{l} \tag{2.68}$$

giving the interaction its name: spin-orbit coupling. Since the binding potential for electrons is an increasing function of distance, the prefactor in (2.68) is positive so that the spin of an electron is preferably antiparallel to its orbital momentum. To make $\mathcal{H}_\mathrm{SOC}$ practical, the prefactor is approximated by its average with the main contribution apparently coming from the vicinity of the nucleus. Often it is referred to a result obtained from the scaling of the Schrödinger equation for hydrogen-like atoms with the potential $V \propto -Ze^2/r$ which gives

$$\left\langle \frac{1}{r}\frac{\mathrm{d}V}{\mathrm{d}r} \right\rangle \propto \left\langle \frac{Z}{r^3} \right\rangle = Z^4 \left\langle \frac{1}{r^3} \right\rangle_\mathrm{hydrogen} \tag{2.69}$$

suggesting the spin-orbit coupling strength proportional to Z^4. However, as argued by Landau and Lifshitz [30], one has to combine the above scaling of unscreened estimate ($\propto Z^4$) with the scaling of the probability for a valence electron being close to the nucleus ($\propto 1/Z^2$), leading to an alternative estimate of the strength proportional to Z^2. Even when considering this reduced

scaling, the spin-orbit coupling quickly increases with Z and becomes well visible in transition metal ions. We therefore have to extend our $\mathcal{H}_{\text{ion}}$ with an extra term

$$\mathcal{H}_{\text{SOC}} = \zeta \sum_i \boldsymbol{s}_i \cdot \boldsymbol{l}_i \,, \tag{2.70}$$

where the sum runs through our valence electrons and ζ is a positive constant. In $3d$ elements, ζ takes the values of tens of meV, in the heavier $5d$ elements it reaches hundreds of meV, for example $\zeta \approx 0.4\,\text{eV}$ in Ir^{4+} [31].

There are two standard schemes how to incorporate the above spin-orbit coupling into the multiplet structure. Within the framework of so-called j-j coupling scheme one first adds the spin and orbital momenta of the individual electrons to form the total angular momenta $\boldsymbol{j} = \boldsymbol{s}+\boldsymbol{l}$, diagonalizing thereby the spin-orbit interaction, and then takes care of the Coulomb interaction. The multiplet structure is then described in terms of the total angular momentum $\boldsymbol{J} = \sum \boldsymbol{j}_i$ and its constituting elements $\boldsymbol{j}_i$. This approach is more adequate for the case of a very strong spin-orbit coupling such as that encountered in lanthanides or actinides. We will use the LS coupling scheme that is appropriate for $3d$, $4d$, and with some reservations also for $5d$ transition metal ions, where the spin orbit-coupling is weaker and Hund's coupling is decisive. Here one first forms the total angular momentum $\boldsymbol{L}$ and total spin $\boldsymbol{S}$ states as we did in the previous paragraph and later mixes them via spin-orbit coupling. The formal tool to perform this operation is the Wigner-Eckart theorem. As its consequence, when working in the fixed L and fixed S subspaces, the spin orbit coupling (2.70) turns out to be equivalent to properly scaled $\boldsymbol{S} \cdot \boldsymbol{L}$ [32]. We will therefore make a replacement

$$\mathcal{H}_{\text{SOC}} = \lambda\, \boldsymbol{S} \cdot \boldsymbol{L} \qquad \text{(within a subspace with fixed } L \text{ and } S\text{)} \tag{2.71}$$

making the diagonalization of the spin-orbit coupling particularly simple. One can invoke also an intuitive argument to support this step: Hund's coupling tends to align the electrons to form states with the maximum S. In that case we can utilize the relation $\boldsymbol{s}_i = \boldsymbol{S}/2S$ with $2S$ being the number of electrons, which leads to

$$\mathcal{H}_{\text{SOC}} \approx \frac{\zeta}{2S}\, \boldsymbol{S} \cdot \sum_i \boldsymbol{l}_i = \frac{\zeta}{2S}\, \boldsymbol{S} \cdot \boldsymbol{L} \,. \tag{2.72}$$

This way we also obtained a connection between ζ and λ in a form $\lambda = \zeta/2S$ which is correct for less than half-filled t_{2g} shell. In the case of more than half-filled t_{2g} shell, the sign is opposite, $\lambda = -\zeta/2S$. We will make one more sign twist by utilizing the more convenient effective orbital momentum $\boldsymbol{L}^{\text{eff}}$ which is $-\boldsymbol{L}$ projected to t_{2g} orbitals.

As we have learned from Eq. (2.61), the J_{H} part of the Coulomb interaction for a t_{2g} shell separates the subspaces with fixed S and L^{eff}, which is the necessary prerequisite for the above replacement in $\mathcal{H}_{\text{SOC}}$. Taking all the relevant factors and signs into account, the spin-orbit coupling term to be diagonalized reads as

$$\mathcal{H}_{\text{SOC}} \approx \lambda\, \boldsymbol{S} \cdot \boldsymbol{L}^{\text{eff}} = \frac{\lambda}{2} \left[(\boldsymbol{L}^{\text{eff}} + \boldsymbol{S})^2 - (\boldsymbol{L}^{\text{eff}})^2 - \boldsymbol{S}^2 \right] = \frac{\lambda}{2} \left[\boldsymbol{J}^2 - (\boldsymbol{L}^{\text{eff}})^2 - \boldsymbol{S}^2 \right] \tag{2.73}$$

with $\lambda = \zeta$ for the t_{2g}^5 configuration and $\lambda = \zeta/2$ for t_{2g}^4. We have already incorporated the total angular momentum $\boldsymbol{J} = \boldsymbol{L}^{\text{eff}} + \boldsymbol{S}$ that enables an elegant solution of the problem by constructing the eigenstates of $\boldsymbol{J}$. The Condon-Shortley phase convention that we have consistently kept in the previous paragraph makes this task straightforward – it is sufficient to combine the L_z^{eff} and S_z eigenstates using standard tables of Clebsch-Gordan coefficients.

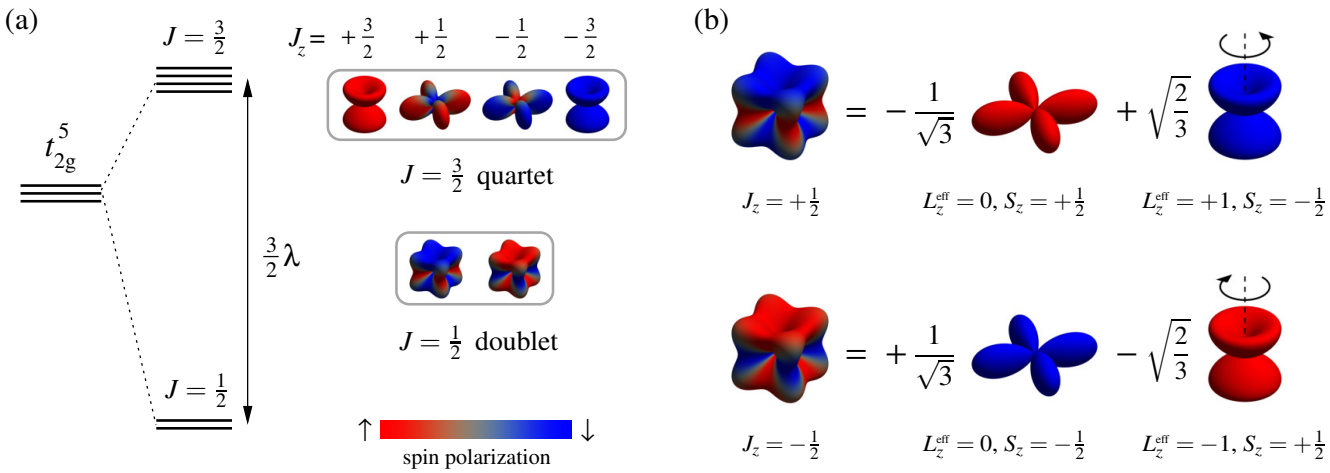

Fig. 13: (a) Energy levels of a t_{2g}^5 ion created by spin-orbit coupling. The "shapes" of the states corresponding to the upper quartet and lower doublet are depicted in a way similar to the previous orbital figures. For better clarity, we show only the part corresponding to the hole in the t_{2g}^6 configuration. The spin polarization of the hole density obtained as normalized $\rho_\uparrow - \rho_\downarrow$ is indicated by color. (b) Spin and orbital decomposition of the $J_z = \pm\frac{1}{2}$ holes. The spin polarization is again indicated by color as in panel (a), the states with nonzero effective orbital momentum have a circular arrow attached.

Let us first focus on the simpler case of the t_{2g}^5 configuration. Here we combine $L^{\rm eff} = 1$ and $S = \frac{1}{2}$ states which results in a multiplet structure consisting of a $J = \frac{1}{2}$ doublet and a $J = \frac{3}{2}$ quartet [see Fig. 13(a)]. The level splitting due to the term $\frac{1}{2}\lambda \boldsymbol{J}^2$ in $\mathcal{H}_{\rm SOC}$ amounts to $\frac{3}{2}\lambda$. The explicit wavefunctions can be written using the $|L_z^{\rm eff}, S_z\rangle$ states or the hole operators introduced e.g. in Eq. (2.56). For the lower doublet we get[7]

$$
\begin{aligned}
|J{=}\tfrac{1}{2}, J_z{=}{+}\tfrac{1}{2}\rangle &= +\sqrt{\tfrac{2}{3}}\,|{+}1,{\downarrow}\rangle - \sqrt{\tfrac{1}{3}}\,|0,{\uparrow}\rangle = \left(+\sqrt{\tfrac{2}{3}}\,a_\downarrow^\dagger - \sqrt{\tfrac{1}{3}}\,b_\uparrow^\dagger\right)|t_{2g}^6\rangle = D_{+\frac{1}{2}}^\dagger|t_{2g}^6\rangle\,, \\
|J{=}\tfrac{1}{2}, J_z{=}{-}\tfrac{1}{2}\rangle &= +\sqrt{\tfrac{1}{3}}\,|0,{\downarrow}\rangle - \sqrt{\tfrac{2}{3}}\,|{-}1,{\uparrow}\rangle = \left(+\sqrt{\tfrac{1}{3}}\,b_\downarrow^\dagger - \sqrt{\tfrac{2}{3}}\,c_\uparrow^\dagger\right)|t_{2g}^6\rangle = D_{-\frac{1}{2}}^\dagger|t_{2g}^6\rangle\,. \qquad (2.74)
\end{aligned}
$$

The "shapes" of the holes corresponding to these states depicted in Fig. 13(a) and in a decomposed form in Fig. 13(b) enable to appreciate one particular aspect of the wavefunctions influenced by spin-orbit coupling. Whenever in some part of its wavefunction the hole shows an orbital motion, the spin-orbit coupling gets activated and tries to contra-align the hole spin and the corresponding orbital momentum. This effect generates a nonuniform spatial distribution of the spin polarization of the hole (or electron) density indicated by color in Fig. 13. As we will see in Sec. 3, the resulting entanglement of spin and orbital degrees of freedom may have a crucial impact on the inter-ionic exchange interactions. For completeness, we also give explicit expressions for the states of the upper quartet, again following the Condon-Shortley phase convention:

$$
\begin{aligned}
|J{=}\tfrac{3}{2}, J_z{=}{+}\tfrac{3}{2}\rangle &= a_\uparrow^\dagger\,|t_{2g}^6\rangle = Q_{+\frac{3}{2}}^\dagger|t_{2g}^6\rangle\,, \\
|J{=}\tfrac{3}{2}, J_z{=}{+}\tfrac{1}{2}\rangle &= \left(\sqrt{\tfrac{1}{3}}\,a_\downarrow^\dagger + \sqrt{\tfrac{2}{3}}\,b_\uparrow^\dagger\right)|t_{2g}^6\rangle = Q_{+\frac{1}{2}}^\dagger|t_{2g}^6\rangle\,,
\end{aligned}
$$

[7] Let us note, that the double degeneracy of the ionic ground state for t_{2g}^5 configuration is guaranteed by Kramers theorem. Since the ionic Hamiltonian is invariant with respect to time-reversal symmetry, its ground state manifold for an odd number of electrons will be spanned by two degenerate partners related by the time-reversal operation which is well visible in Eq. (2.74) and its pictorial representation in Fig. 13(b).

$$|J{=}\tfrac{3}{2}, J_z{=}-\tfrac{1}{2}\rangle = \left(\sqrt{\tfrac{2}{3}}\, b^\dagger_\downarrow + \sqrt{\tfrac{1}{3}}\, c^\dagger_\uparrow\right)|t^6_{2g}\rangle = Q^\dagger_{-\frac{1}{2}}|t^6_{2g}\rangle\,,$$
$$|J{=}\tfrac{3}{2}, J_z{=}-\tfrac{3}{2}\rangle = c^\dagger_\downarrow\,|t^6_{2g}\rangle = Q^\dagger_{-\frac{3}{2}}|t^6_{2g}\rangle\,. \qquad (2.75)$$

In a similar way, one can include the spin-orbit interaction into the multiplet structure of the t^4_{2g} configuration. The $L^{\rm eff}=0$ and $L^{\rm eff}=2$ spin-singlets of Eqs. (2.62) and (2.63), respectively, are not affected, the spin-orbit interaction in the LS coupling scheme only reorganizes the $L^{\rm eff}=1$, $S=1$ states of Eq. (2.64). Three energy levels corresponding to $J=0$, 1, and 2 are generated within this sector as depicted in Fig. 14(a). The lowest state is a nonmagnetic singlet of total angular momentum $\boldsymbol{J}$ with fully compensated spin and orbital momentum. Written explicitly using $|L^{\rm eff}_z, S_z\rangle$ notation for the constituting parts or using the hole operators, it reads as

$$|J{=}0, J_z{=}0\rangle = \frac{1}{\sqrt{3}}\left(|{+}1,{-}1\rangle - |0,0\rangle + |{-}1,{+}1\rangle\right) = \frac{1}{\sqrt{3}}\left[a^\dagger_\downarrow b^\dagger_\downarrow - \tfrac{1}{\sqrt{2}}\left(a^\dagger_\uparrow c^\dagger_\downarrow + a^\dagger_\downarrow c^\dagger_\uparrow\right) + b^\dagger_\uparrow c^\dagger_\uparrow\right]|t^6_{2g}\rangle\,. \qquad (2.76)$$

The three components mutually compensating their spin and orbital momentum are presented in Fig. 14(b) along with the final shape of the two-hole cloud corresponding to this state. It has cubic symmetry and shows no spin polarization. The next three states separated by excitation energy $\lambda = \frac{1}{2}\zeta$ form a triplet with total angular momentum $J=1$. They carry certain magnetic moment but as it was mentioned in the introductory Sec. 1.5 and as we will see in detail in the next paragraph, the magnetism of the t^4_{2g} configuration is primarily of Van Vleck type, residing "on the transition" between the above $J=0$ state and $J=1$ triplet states. The states of the triplet can be written in a standard way using the $|L^{\rm eff}_z, S_z\rangle$ eigenstates of Eq. (2.64)

$$|J{=}1, J_z{=}{+}1\rangle = \tfrac{1}{\sqrt{2}}\left(|{+}1,0\rangle - |0,{+}1\rangle\right)\,,$$
$$|J{=}1, J_z{=}0\rangle = \tfrac{1}{\sqrt{2}}\left(|{+}1,{-}1\rangle - |{-}1,{+}1\rangle\right)\,,$$

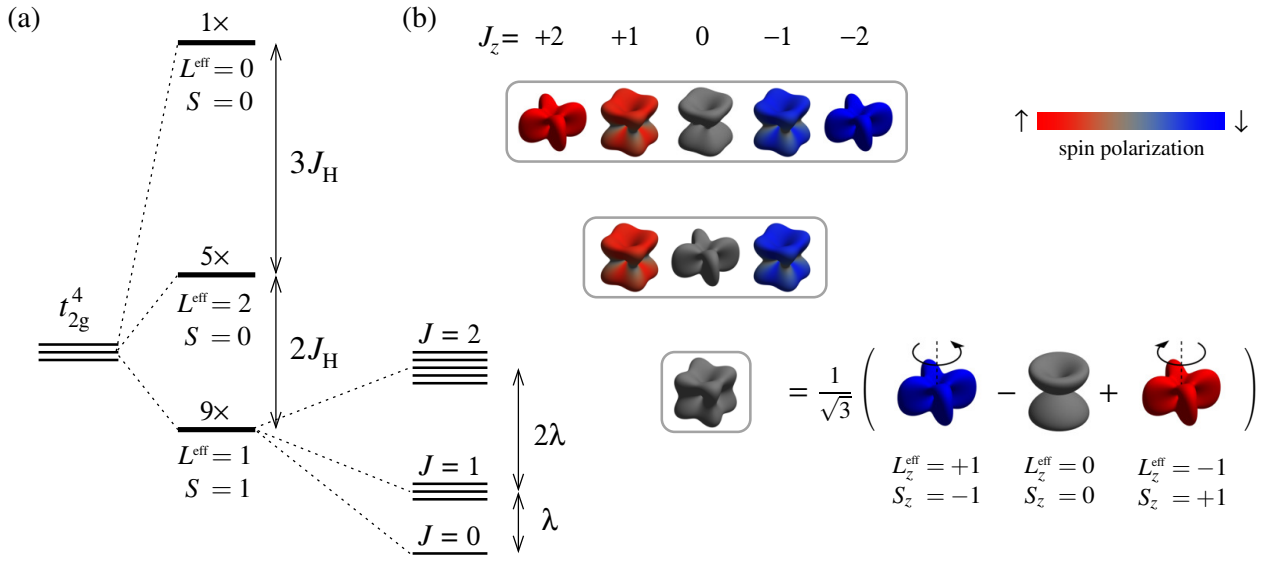

Fig. 14: (a) Final energy level scheme of t^4_{2g} configuration (LS coupling). Hund's coupling first separates the low-energy triplet sector with $L^{\rm eff}=1$ from the two singlet sectors. Spin-orbit coupling rearranges the triplet sector into three sets of $\boldsymbol{J}$ eigenstates with total angular momentum $J=0$, 1, and 2. (b) Shapes of the two-hole states corresponding to $J=0$, 1, and 2 (from bottom to top). The lowest state with $J=0$ is decomposed into its spin and orbital components.

$$|J=1, J_z=-1\rangle = \tfrac{1}{\sqrt{2}}\left(|0,-1\rangle - |-1,0\rangle\right) . \tag{2.77}$$

Finally, the topmost states generated within the $L^{\text{eff}} = 1$, $S = 1$ sector are the $J = 2$ states at the energy 3λ relative to the $J = 0$ ionic ground state. They are given by

$$\begin{aligned}
|J=2, J_z=+2\rangle &= |+1,+1\rangle , \\
|J=2, J_z=+1\rangle &= \tfrac{1}{\sqrt{2}}\left(|+1,0\rangle + |0,+1\rangle\right) , \\
|J=2, J_z=0\rangle &= \tfrac{1}{\sqrt{6}}\left(|+1,-1\rangle + 2|0,0\rangle + |-1,+1\rangle\right) , \\
|J=2, J_z=-1\rangle &= \tfrac{1}{\sqrt{2}}\left(|0,-1\rangle + |-1,0\rangle\right) , \\
|J=2, J_z=-2\rangle &= |-1,-1\rangle .
\end{aligned} \tag{2.78}$$

At this point we are ready to briefly discuss the differences between the LS and j-j coupling schemes. It should be first noted, that the spin-orbit coupling was not fully diagonalized in the above procedure. The problem is the separate consideration of each of the L^{eff}, S sectors. In fact, the spin-orbit coupling includes contributions beyond $\lambda \boldsymbol{S}\cdot\boldsymbol{L}^{\text{eff}}$ that bring additional mixing between the sectors. The conservation of the total angular momentum is respected but this still allows the mixing of the two $J = 0$ singlets of Eq. (2.62) ($L^{\text{eff}} = 0$, $S = 0$) and Eq. (2.76) ($L^{\text{eff}} = 1$, $S = 1$) or the mixing of $J = 2$ states with the same J_z projection (the $J = 1$ triplet states have no partners to mix with). To put things explicitly, by using $|L^{\text{eff}}, S; J, J_z\rangle = |1, 1; 0, 0\rangle$ and $|0, 0; 0, 0\rangle$ as the basis of the $J = 0$ subspace, the ionic Hamiltonian takes the form

$$6U - 13J_{\text{H}} + \begin{pmatrix} -\zeta & -\sqrt{2}\zeta \\ -\sqrt{2}\zeta & 5J_{\text{H}} \end{pmatrix} \tag{2.79}$$

with the diagonal part coinciding with the $J = 0$ levels shown in Fig. 14(a). As one can see, the mixing due to the spin-orbit coupling is not significant provided that ζ is much smaller than the separation of the two levels $\approx 5J_{\text{H}}$. Now we can address the same subspace using the j-j coupling scheme. To this end we take the hole operators producing the $J = \frac{1}{2}$ and $J = \frac{3}{2}$ eigenstates of a single hole (i.e. t_{2g}^5 configuration) and combine them to form two-hole states of given total angular momentum. In Eqs. (2.74) and (2.75) we have denoted the respective hole operators as $D^\dagger_{J_z}$ ($J_z = \pm\frac{1}{2}$) and $Q^\dagger_{J_z}$ ($J_z = \pm\frac{1}{2}, \pm\frac{3}{2}$). The $J = 0$ states can be obtained by combining either two $j = \frac{1}{2}$ holes

$$|j_1, j_2; J, J_z\rangle = \left|\tfrac{1}{2}, \tfrac{1}{2}; 0, 0\right\rangle = D^\dagger_{+\frac{1}{2}} D^\dagger_{-\frac{1}{2}} |t_{2g}^6\rangle \tag{2.80}$$

or two $j = \frac{3}{2}$ holes

$$|j_1, j_2; J, J_z\rangle = \left|\tfrac{3}{2}, \tfrac{3}{2}; 0, 0\right\rangle = \frac{1}{\sqrt{2}}\left(Q^\dagger_{+\frac{3}{2}} Q^\dagger_{-\frac{3}{2}} - Q^\dagger_{+\frac{1}{2}} Q^\dagger_{-\frac{1}{2}}\right) |t_{2g}^6\rangle . \tag{2.81}$$

Using these two states as the basis, we get for the matrix of the ionic Hamiltonian

$$6U - 12J_{\text{H}} + \begin{pmatrix} \frac{2}{3}J_{\text{H}} - 2\zeta & \frac{5\sqrt{2}}{3}J_{\text{H}} \\ \frac{5\sqrt{2}}{3}J_{\text{H}} & \frac{7}{3}J_{\text{H}} + \zeta \end{pmatrix} . \tag{2.82}$$

The roles of Hund's coupling and spin-orbit coupling are interchanged now. Spin-orbit coupling is diagonalized while Hund's coupling brings the mixing of the two configurations that would be neglected in the j-j coupling scheme. Nevertheless, when including the off-diagonal matrix

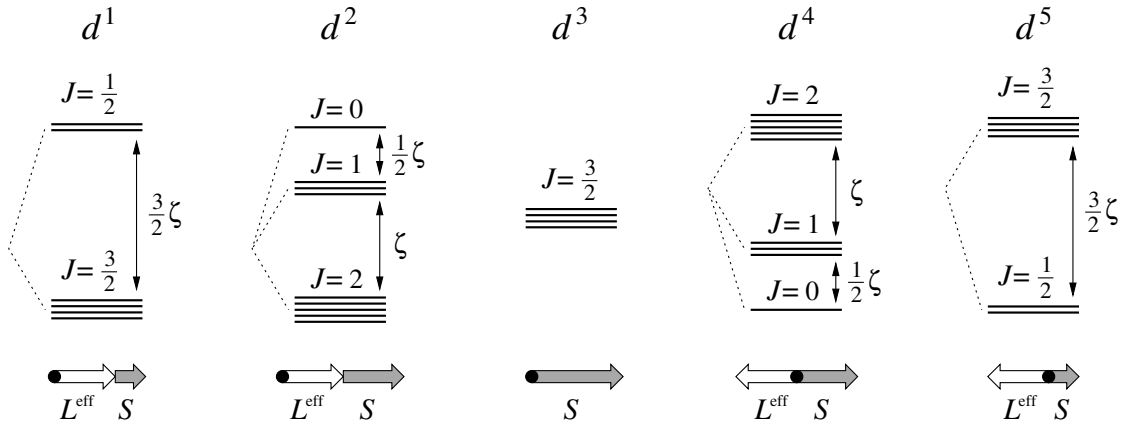

Fig. 15: Lowest energy levels for various d^n configurations composed of t_{2g} electrons only. The single-electron spin-orbit coupling constant ζ is used in all cases to indicate the splitting. The schematics at the bottom illustrate the addition of the spin and effective orbital momentum in the ground state.

elements both in Eq. (2.79) (going beyond the LS coupling scheme) and Eq. (2.82) (going beyond the j-j coupling scheme), we arrive at the same exact eigenvalues of the ionic Hamiltonian.

To conclude this paragraph, we show in Fig. 15 the low-energy level structure established by the spin-orbit coupling for all the non-trivial t_{2g}^n electron configurations with degenerate t_{2g} orbitals. The figure illustrates the reciprocity of the pairs of complementary configurations d^1–d^5, d^2–d^4 that is caused by the sign change of the spin orbit coupling λ as we increase the number of electrons. While the effective orbital momentum and spin support each other in the case of the less than half-filled configurations, they try to compensate each other in the more than half-filled case. The middle configuration with three electrons maximizes the spin but does not carry the effective orbital momentum.

2.2.4 Magnetic moment

Magnetic materials are most naturally investigated by probes that couple to magnetic moments. In the short final paragraph of this section, we will study the connection between the ionic magnetic moment and the various angular momenta used in the previous text. The magnetic moment is contributed by both the orbital momenta and spins of the individual electrons of the open valence shell that sum up to total orbital momentum and total spin

$$\boldsymbol{M} = -\mu_{\text{B}} \sum_i (\boldsymbol{l}_i + g_0 \boldsymbol{s}_i) = -\mu_{\text{B}} (\boldsymbol{L} + g_0 \boldsymbol{S}) \tag{2.83}$$

with $\mu_{\text{B}} \approx 0.05788\,\text{meV T}^{-1}$ being the Bohr magneton. The prefactors for the orbital part and spin part differ by the electron g-factor $g_0 = 2.0023\ldots$ which is well approximated by 2 for our purposes. The magnetic moments couple to magnetic fields via the Hamiltonian

$$\mathcal{H}_{\text{field}} = -\boldsymbol{B} \cdot \boldsymbol{M} = \mu_{\text{B}} \boldsymbol{B} \cdot (\boldsymbol{L} + g_0 \boldsymbol{S}) \tag{2.84}$$

analogous to the interaction of a classical magnetic dipole with magnetic field. For convenience, the magnetic moment is sometimes redefined as $\boldsymbol{M} = \boldsymbol{L} + g_0 \boldsymbol{S}$ removing the minus sign and measuring in Bohr magnetons. The interaction with the field in the form $\mu_{\text{B}} \boldsymbol{B} \cdot \boldsymbol{M}$ should be used in such a case.

Magnetic moment is a vector operator and by virtue of the Wigner-Eckart theorem, its matrix elements between the states within a subspace with fixed L, S, J are proportional to the matrix

elements of the other vector operators $\boldsymbol{L}$, $\boldsymbol{S}$, $\boldsymbol{J}$. In the case of free ions, the relation between the magnetic moment and the total angular momentum is given by the well-known Landé g-factor

$$g(LSJ) = \frac{3}{2} + \frac{S(S+1) - L(L+1)}{2J(J+1)} \,. \tag{2.85}$$

In the crystalline environment the above formula does not apply since the orbital part of the magnetic moment is fully or partially suppressed. As a first example we may start with the situation of undoped high-T_c cuprates where the Cu^{2+} ions have d^9 electron configuration with one hole in the e_g orbital of $x^2 - y^2$ symmetry. As evident from Eq. (2.27), the orbital moment of e_g orbitals is fully quenched so that the magnetic moment appears only due to the spin-$\frac{1}{2}$ of the hole made in the fully populated and thus fully symmetric d^{10} shell. A more complicated situation occurs if the t_{2g} orbitals carrying reduced $\boldsymbol{L}^{\rm eff}$ participate in the formation of the magnetic moment $\boldsymbol{M} = 2\boldsymbol{S} - \kappa\boldsymbol{L}^{\rm eff}$ (expressed within the "positive" convention). The second contribution comes with a reduction factor κ due to covalency effects between transition metal ion and oxygens, but let us ignore this in the following and set $\kappa = 1$.

For the t_{2g}^5 configuration, the spin-orbit coupling led to the $J = \frac{1}{2}$ doublet ground state. When comparing the corresponding operator matrices, we find, that within the two-dimensional $J = \frac{1}{2}$ subspace the following relations hold: $\boldsymbol{S} = -\frac{1}{3}\boldsymbol{J}$ and $\boldsymbol{L}^{\rm eff} = \frac{4}{3}\boldsymbol{J}$. The magnetic moment thus reads as

$$\boldsymbol{M} = 2\boldsymbol{S} - \boldsymbol{L}^{\rm eff} = -2\boldsymbol{J} \tag{2.86}$$

giving the g factor of -2 for the $J = \frac{1}{2}$ doublet. For the upper $J = \frac{3}{2}$ quartet of the same configuration we find $\boldsymbol{S} = \frac{1}{3}\boldsymbol{J}$ and $\boldsymbol{L}^{\rm eff} = \frac{2}{3}\boldsymbol{J}$, so that the spin and orbital contributions cancel in $2\boldsymbol{S} - \boldsymbol{L}^{\rm eff} = 0$ and the upper quartet is thus nonmagnetic. The entanglement of spin and orbital angular momentum generates also nonzero matrix elements of the magnetic moment that connect the $J = \frac{1}{2}$ and $J = \frac{3}{2}$ states, making the quartet visible in magnetic excitation spectra.

Such Van Vleck type of magnetic moment is even more interesting in the case of the t_{2g}^4 configuration. Having the future applications in Sec. 4 in mind, we will focus on the lowest energy sector consisting of the nonmagnetic $J = 0$ singlet serving as the ionic ground state and the $J = 1$ triplet. The triplet states themselves carry the magnetic moment $\boldsymbol{M} = 2\boldsymbol{S} - \boldsymbol{L}^{\rm eff} = \frac{1}{2}\boldsymbol{J}$ corresponding to a relatively small g-factor $\frac{1}{2}$. The main part of the magnetic moment is available in the transitions between the $J = 0$ and $J = 1$ states. To capture this Van Vleck moment in a transparent way we introduce the set of four operators s, T_{+1}, T_0, T_{-1} via the creation of the $J = 0, 1$ states given in Eqs. (2.76) and (2.77) [8]

$$s^\dagger \, |t_{2g}^6\rangle = |J{=}0, J_z{=}0\rangle \qquad T_m^\dagger \, |t_{2g}^6\rangle = -|J{=}1, J_z{=}m\rangle \tag{2.87}$$

and arrange the triplet ones to a Cartesian form $\boldsymbol{T} = (T_x, T_y, T_z)$ with

$$T_x = \frac{1}{i\sqrt{2}}(T_{+1} - T_{-1}) \,, \quad T_y = \frac{1}{\sqrt{2}}(T_{+1} + T_{-1}) \,, \quad T_z = iT_0 \,. \tag{2.88}$$

By observing the nonzero matrix elements of the magnetic moment operator, we find two categories:

$$\langle s| \, (2\boldsymbol{S} - \boldsymbol{L}^{\rm eff})_\alpha \, |T_\beta\rangle = -\sqrt{6}\, i \, \delta_{\alpha\beta} \qquad \text{and} \qquad \langle T_\beta| \, (2\boldsymbol{S} - \boldsymbol{L}^{\rm eff})_\alpha \, |T_{\beta'}\rangle = -\frac{i}{2}\, \epsilon_{\alpha\beta\beta'} \,. \tag{2.89}$$

[8] Note the negative sign in the triplet states in Eq. (2.87), this was introduced to have the notation compatible with the papers cited later in Sec. 4.

The magnetic moment operator reproducing these matrix elements in the selected four-dimensional $J = 0, 1$ subspace can be written down in an elegant way

$$\boldsymbol{M} = 2\boldsymbol{S} - \boldsymbol{L}^{\text{eff}} = -\sqrt{6}\, i(s^\dagger \boldsymbol{T} - \boldsymbol{T}^\dagger s) - \tfrac{1}{2}\, i(\boldsymbol{T}^\dagger \times \boldsymbol{T})\,. \tag{2.90}$$

In this form it is clear that the major potential to generate a magnetic moment have the transitions between s and $\boldsymbol{T}$ states, the second part is the already mentioned contribution of the $\boldsymbol{J}$ moment of the triplet that is equivalent to $-i(\boldsymbol{T}^\dagger \times \boldsymbol{T})$ within the $J = 0, 1$ subspace.

2.3 Electronic hopping and tight-binding approximation

So far we have been dealing with the (rather complex) physics of correlated valence shells of the individual ions. In this section we are going to activate connections between the ions in the form of electronic hopping. There will not be any many-body aspects discussed here as our main goal is just to get the matrix elements enabling a single electron to move from site to site – so-called tight-binding parameters entering a single-electron hopping Hamiltonian. As a motivating example we start by considering independent electrons moving in a crystal consisting of identical atoms arranged in a simple lattice. Their wavefunctions obey the Schrödinger equation

$$\left[-\frac{\hbar^2}{2m}\nabla^2 + \sum_{\boldsymbol{R}} V_{\text{at}}(\boldsymbol{r} - \boldsymbol{R})\right] \Psi = E\Psi\,, \tag{2.91}$$

where $V_{\text{at}}(\boldsymbol{r} - \boldsymbol{R})$ is the atomic potential for an atom placed at site $\boldsymbol{R}$. Summed through the lattices sites, the atomic potentials generate a periodic crystal potential. In the tight-binding approximation to the problem (2.91), one assumes that the relevant states are well localized so that the electron wavefunctions can be constructed as linear combinations of atomic orbitals. This concept is illustrated by Fig. 16 where we construct a virtual two-dimensional crystal made out of potential wells of circular symmetry and study the evolution of its energy levels when reducing the lattice spacing, i.e. bringing the initially isolated atoms closer to each other. At very large lattice spacing, the spectrum of energy levels has a discrete structure below the top of the crystal potential, corresponding to the individual bound states of the isolated wells. Above that threshold energy, delocalized states forming a continuum are found. As we bring the "atoms" closer and closer, the localized states start to overlap and their interaction produces energy bands of increasing bandwidth. The higher-energy bound states are forming bands sooner because they have a larger spatial extent and overlap more easily. This is an analogy of the atomic orbitals in a crystal - the valence ones form bands while the deep electron levels retain their atomic character. It is intuitively clear that in the situation with rather well localized states (the electrons are "tightly bound" to their atoms), the appropriate model Hamiltonian should be of the form

$$\mathcal{H}_{\text{TB}} = \sum_{n\boldsymbol{R}} \left[\varepsilon_n\, c^\dagger_{n\boldsymbol{R}} c_{n\boldsymbol{R}} - \sum_{n'\Delta\boldsymbol{R}} t_{nn'}(\Delta\boldsymbol{R})\, c^\dagger_{n',\boldsymbol{R}+\Delta\boldsymbol{R}}\, c_{n\boldsymbol{R}}\right]\,, \tag{2.92}$$

where the operators $c^\dagger_{n\boldsymbol{R}}$ and $c_{n\boldsymbol{R}}$ create/annihilate an electron in the state $|\phi_{n\boldsymbol{R}}\rangle$ corresponding to orbital n at site $\boldsymbol{R}$. The first part of this tight-binding Hamiltonian $\mathcal{H}_{\text{TB}}$ just counts the energies of the occupied orbitals [c.f. the energies ε_α in (2.46)], the second part captures the hopping of electrons between the orbitals located at $\boldsymbol{R}$ and $\boldsymbol{R} + \Delta\boldsymbol{R}$. The amplitudes of the hopping processes are the matrix elements of the original crystal Hamiltonian such as that of Eq. (2.91): $t_{nn'}(\Delta\boldsymbol{R}) = -\langle\phi_{n',\boldsymbol{R}+\Delta\boldsymbol{R}}|\,\mathcal{H}\,|\phi_{n\boldsymbol{R}}\rangle$. The signs are introduced in such a way that the hopping parameters t will be mostly positive. For the sake of brevity, we ignore spin that is

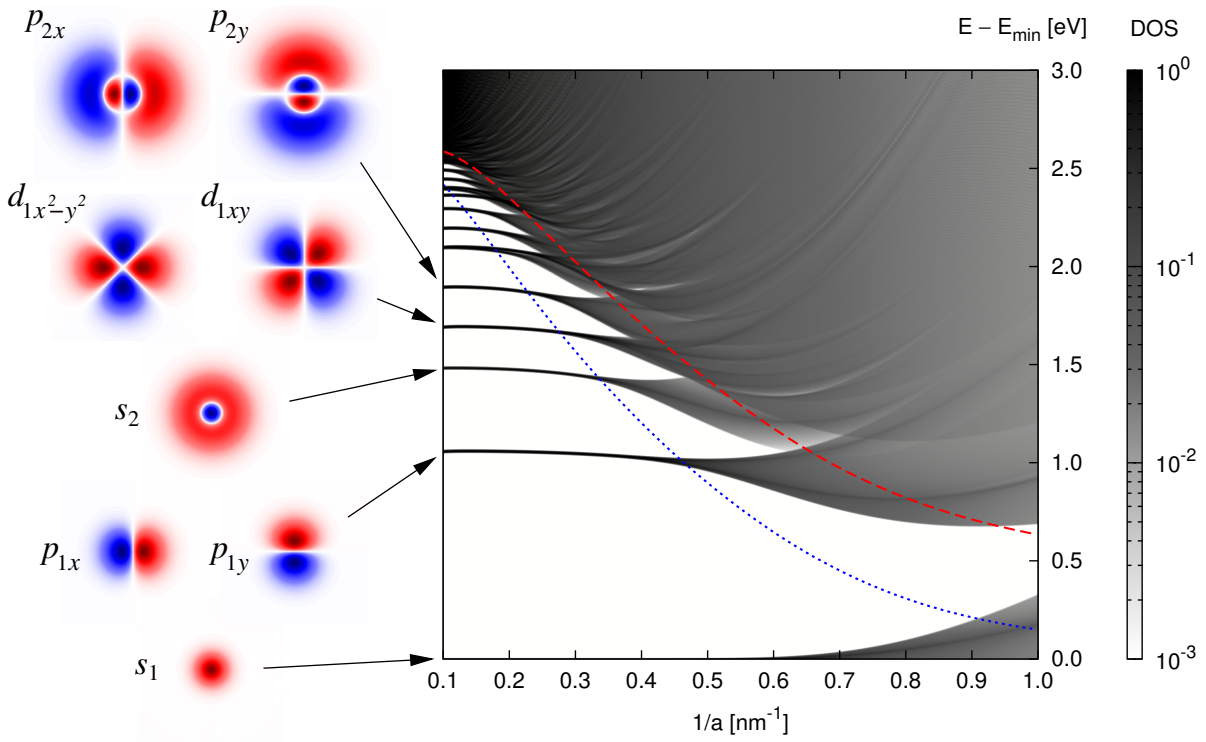

Fig. 16: (left) Wavefunctions of the lowest eigenstates in the potential well described by the 2D potential $V_{\rm at}(r) = V_0 \exp(-\kappa r)\, r_0/(r + r_0)$ with $V_0 = 5\,$eV, $\kappa = 0.5\,$nm^{-1}, $r_0 = 0.5\,$nm. The indicated levels are either non-degenerate or two-fold degenerate and they are labeled in analogy with atomic orbitals. (right) Density of states for a square lattice of the above wells as function of the inverse lattice spacing $1/a$. The energy is measured from the lowest eigenstate. For a large spacing (small $1/a$) the wells are practically isolated and the density of states shows discrete peaks at the energies of bound states. Blue dotted line indicates the average potential level, the red dashed line the top of the potential. The data to construct this figure were obtained by solving Eq. (2.91) by plane-wave expansion method.

conserved during the hopping and would come as an extra index σ together with $\sum_\sigma$. While the values of hopping amplitudes are not known yet, one can expect that the nearest-neighbor and possibly second nearest-neighbor ones will be most important and – in the case of more orbitals involved – also anticipate their symmetry structure [see Fig. 17(a) and (b) for two examples].

Owing to the periodicity of the lattice, the Hamiltonian can be easily diagonalized by employing Bloch waves assembled as linear combinations of the atomic orbitals:

$$|n\boldsymbol{k}\rangle = \frac{1}{\sqrt{N}} \sum_{\boldsymbol{R}} \mathrm{e}^{i\boldsymbol{k}\cdot\boldsymbol{R}}\, |\phi_{n\boldsymbol{R}}\rangle\,. \tag{2.93}$$

Here N denotes the total number of sites in the crystal and normalizes $|n\boldsymbol{k}\rangle$ to unity when the overlaps of orbitals at different sites are negligible. By inserting the consistently transformed electron operators $c_{n\boldsymbol{R}} = N^{-1/2} \sum_{\boldsymbol{k}} \mathrm{e}^{i\boldsymbol{k}\cdot\boldsymbol{R}} c_{n\boldsymbol{k}}$ into $\mathcal{H}_{\rm TB}$, it acquires the form with separated contributions of the individual Bloch vectors $\boldsymbol{k}$

$$\mathcal{H}_{\rm TB} = \sum_{\boldsymbol{k}} \sum_{nn'} \left[\varepsilon_n \delta_{nn'} - \sum_{\Delta\boldsymbol{R}} t_{nn'}(\Delta\boldsymbol{R})\, \mathrm{e}^{-i\boldsymbol{k}\cdot\Delta\boldsymbol{R}} \right] c^\dagger_{n'\boldsymbol{k}} c_{n\boldsymbol{k}}\,. \tag{2.94}$$

For each $\boldsymbol{k}$, it remains to diagonalize a matrix whose dimension is equal to the number of orbitals involved (no diagonalization is thus needed in case of one relevant orbital). For the two examples

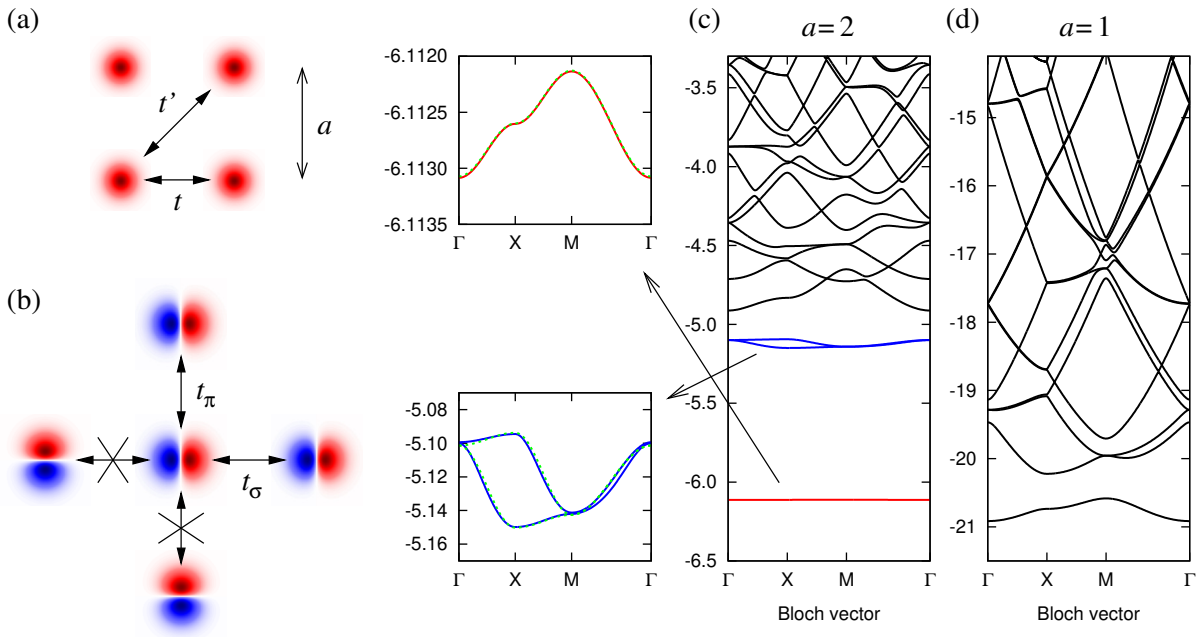

Fig. 17: (a) Hopping processes included in the simplest tight-binding approximation for the bands derived from s "orbitals" of Fig. 16 in a square lattice. Nearest-neighbor and next nearest-neighbor hopping amplitudes t and t' are indicated. (b) Hopping processes involving the p orbitals on a square lattice. The symmetry of these states makes certain hopping amplitudes to vanish, the non-zero ones depend on the relative orientation of the orbitals (t_σ and t_π). (c) Band structure obtained for the setup of Fig. 16 and the value $a = 2\,\mathrm{nm}$ of the lattice parameter. The weakly dispersing bands derived from the s_1 and p_1 levels are shown in detail on the left. The green dashed lines are fits by the corresponding nearest-neighbor tight-binding dispersion relations. The band structure is plotted along the conventional path involving $\Gamma = (0,0)$, $\mathrm{X} = (\pi/a, 0)$ and $\mathrm{M} = (\pi/a, \pi/a)$ points in the Brillouin zone. (d) Band structure for $a = 1\,\mathrm{nm}$ where even the lowest level already shows a significant dispersion. Its profile seems to be just a scaled version of that from panel (c), demonstrating the applicability of the tight-binding scheme.

in Fig. 17(a),(b) we get

$$\mathcal{H}_{\mathrm{TB}} = \sum_{\boldsymbol{k}} \left[\varepsilon_s - 2t(\cos k_x a + \cos k_y a) - 4t' \cos k_x a \cos k_y a\right] c^\dagger_{\boldsymbol{k}} c_{\boldsymbol{k}} \tag{2.95}$$

and

$$\mathcal{H}_{\mathrm{TB}} = \sum_{\boldsymbol{k}} \begin{pmatrix} c^\dagger_{p_x \boldsymbol{k}} & c^\dagger_{p_y \boldsymbol{k}} \end{pmatrix} \begin{pmatrix} \varepsilon_p - 2t_\sigma \cos k_x a - 2t_\pi \cos k_y a & 0 \\ 0 & \varepsilon_p - 2t_\pi \cos k_x a - 2t_\sigma \cos k_y a \end{pmatrix} \begin{pmatrix} c_{p_x \boldsymbol{k}} \\ c_{p_y \boldsymbol{k}} \end{pmatrix} \tag{2.96}$$

giving directly the dispersion relations of electrons. In the latter case, nonzero off-diagonal elements would be generated by next nearest-neighbor hopping, nearest-neighbor pairs of p_x and p_y orbitals are not connected due to symmetry reasons. The band structures obtained numerically by solving the full problem (2.91) are presented in Fig. 17 and contrasted to those resulting in nearest-neighbor tight-binding approximation. A remarkable agreement is obtained when choosing the proper values of the few parameters (ε_s and t or ε_p and t_σ, t_π), in particular for the s band derived from the most localized bound state.

As we have just seen, the tight-binding approximation is a useful tool well capturing the dispersion of the bands derived from localized states. Its success relies on a limited range of

significant overlaps (in the sense of the matrix element of $\mathcal{H}$) of those localized states, reaching only few nearest neighbors. Our motivational example was based on a collection of weakly coupled atoms. However, single-electron problems similar to Eq. (2.91) also arise as auxiliary problems in *ab-initio* calculations within the framework of density functional theory (DFT). There exist sophisticated approaches how to construct the local orbital bases such as maximally localized Wannier orbitals and to extract the values of the corresponding hopping matrix elements making the tight-binding scheme applicable in a broader context. In a way, by considering the limit of weakly coupled atoms, we obtain hints about the symmetry/structure of the corresponding tight-binding model, a realistic DFT calculation then fills in the actual values of the parameters.

After the initial exposition of the tight-binding approach, we will now focus in more detail on the symmetry properties of the tight-binding matrix elements $t_{nn'}(\Delta\boldsymbol{R}) = -\langle\phi_{n',\boldsymbol{R}+\Delta\boldsymbol{R}}|\,\mathcal{H}\,|\phi_{n\boldsymbol{R}}\rangle$. for transition metal compounds. The relevant ones are those connecting an oxygen ion and a transition metal ion (i.e. p and d orbitals), and two transition metal ions (only d orbitals involved). A general approach of their symmetry reduction to as few parameters as possible under the assumption of spherically symmetric atomic wavefunctions[9] was developed by Slater and Koster [33]. Let us write down the matrix element $t_{nn'}(\Delta\boldsymbol{R})$ explicitly

$$t_{nn'}(\Delta\boldsymbol{R}) = -\int \phi^*_{n'}(\boldsymbol{r}-\Delta\boldsymbol{R})\left[-\frac{\hbar^2}{2m}\nabla^2 + \sum_{\boldsymbol{R}'} V_{\mathrm{at}}(\boldsymbol{r}-\boldsymbol{R}')\right]\phi_n(\boldsymbol{r})\,\mathrm{d}^3\boldsymbol{r}\,. \tag{2.97}$$

We can ignore the on-site elements ($\Delta\boldsymbol{R} = \boldsymbol{0}$), these can be incorporated into the local level structure by renormalizing the energies ε_n. The basic trick is to use the fact that $\phi_n(\boldsymbol{r})$ and $\phi^*_{n'}(\boldsymbol{r}-\Delta\boldsymbol{R})$ are eigenstates of the atomic Hamiltonian $-\frac{\hbar^2}{2m}\nabla^2 + V_{\mathrm{at}}(\boldsymbol{r})$ or $-\frac{\hbar^2}{2m}\nabla^2 + V_{\mathrm{at}}(\boldsymbol{r}-\Delta\boldsymbol{R})$, respectively. This enables a decomposition of the integral in (2.97) into three contributions

$$\begin{aligned} t_{nn'}(\Delta\boldsymbol{R}) = &-\int \phi^*_{n'}(\boldsymbol{r}-\Delta\boldsymbol{R})\left[\tfrac{1}{2}V_{\mathrm{at}}(\boldsymbol{r}) + \tfrac{1}{2}V_{\mathrm{at}}(\boldsymbol{r}-\Delta\boldsymbol{R})\right]\phi_n(\boldsymbol{r})\,\mathrm{d}^3\boldsymbol{r} \\ &-\frac{\varepsilon_n+\varepsilon_{n'}}{2}\int \phi^*_{n'}(\boldsymbol{r}-\Delta\boldsymbol{R})\,\phi_n(\boldsymbol{r})\,\mathrm{d}^3\boldsymbol{r} - \int \phi^*_{n'}(\boldsymbol{r}-\Delta\boldsymbol{R})\sum_{\boldsymbol{R}'\neq\boldsymbol{0},\,\Delta\boldsymbol{R}} V_{\mathrm{at}}(\boldsymbol{r}-\boldsymbol{R}')\,\phi_n(\boldsymbol{r})\,\mathrm{d}^3\boldsymbol{r}\,. \end{aligned} \tag{2.98}$$

We will study just the contribution on the first line and analyze its symmetry for p-d and d-d orbital pairs and spherically symmetric V_{at}. The contributions on the second line – orbital overlaps and a sum of so-called three-center integrals – are usually neglected. In principle, they can be assumed to renormalize the tight-binding parameters.

To evaluate the two-center integrals $\frac{1}{2}\int \phi^*_{n'}(\boldsymbol{r}-\Delta\boldsymbol{R})\,[V_{\mathrm{at}}(\boldsymbol{r}) + V_{\mathrm{at}}(\boldsymbol{r}-\Delta\boldsymbol{R})]\,\phi_n(\boldsymbol{r})\,\mathrm{d}^3\boldsymbol{r}$ one observes that the term in the bracket has a rotational symmetry with $\Delta\boldsymbol{R}$ being the rotational axis. It is therefore convenient to take the decomposition of the orbitals into spherical harmonics

$$\phi_n(\boldsymbol{r}) = f(r)\sum_{m=-l}^{+l} c_m Y_{lm}(\vartheta,\varphi) \tag{2.99}$$

and rotate the angular part to the new set of spherical coordinates ϑ_{rot}, φ_{rot}, where the polar angle ϑ_{rot} is measured from $\Delta\boldsymbol{R}$. This operation amounts to a linear transformation of the set of coefficients c_m. After the transformation, the expression for the two-center integrals contains azimuthal integrals of the type $\int Y^*_{l'm'}(\vartheta'_{\mathrm{rot}},\varphi_{\mathrm{rot}})Y_{lm}(\vartheta_{\mathrm{rot}},\varphi_{\mathrm{rot}})\,\mathrm{d}\varphi_{\mathrm{rot}}$ where we have to distinguish the polar angles $\vartheta'_{\mathrm{rot}}$ and ϑ_{rot} since the origin of the spherical coordinate system differs for the

[9] This means wavefunctions of the form (common radial part) × (linear combinations of spherical harmonics) such as the case explored in Sec. 2.1.

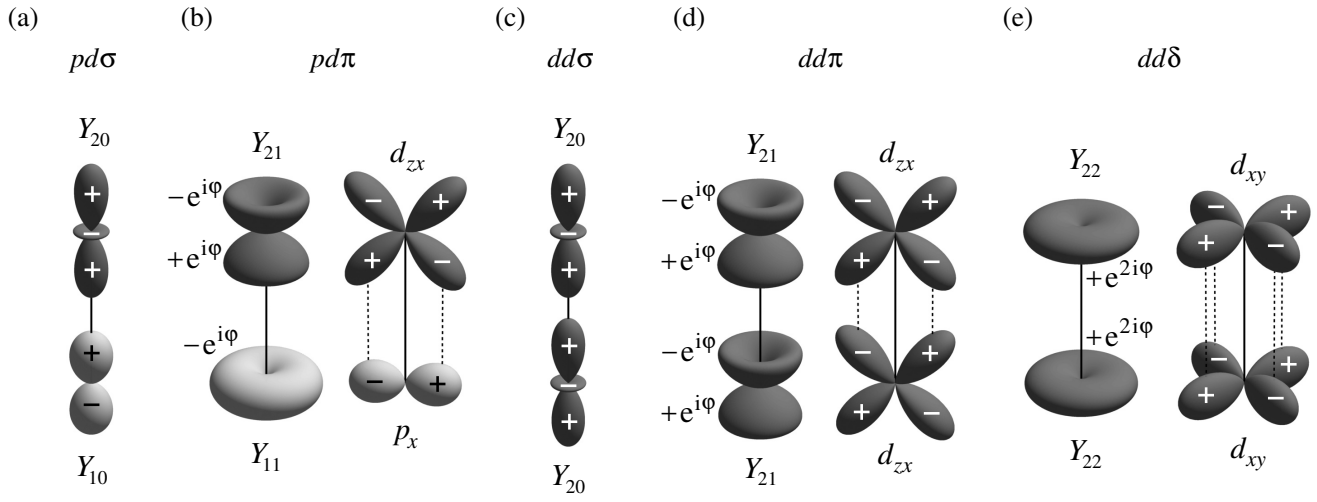

Fig. 18: Illustration of the basic Slater-Koster integrals for p-d and d-d situation. The main rotational axis is z pointing upwards. (a) ($pd\sigma$) bonding of the in-bond oriented orbitals is the strongest link between p and d orbitals. (b) ($pd\pi$) bonding is weaker and due to the phases of the spherical harmonics, it comes with an opposite sign to ($pd\sigma$). A real-orbital example is shown on the right – the integral between p orbital perpendicular to the bond and a matching d orbital is just equal to Slater-Koster ($pd\pi$), here including the sign. (c) Strongest ($dd\sigma$) bonding between two d orbitals. (d) Weaker ($dd\pi$) bonding with the same sign issues as ($pd\pi$). The integral between the two d_{zx} orbitals shown in the right example is equal to ($dd\pi$). (e) ($dd\delta$) bonding and a real-orbital example with the same value of the integral.

two orbitals. The azimuthal angle $\varphi_{\rm rot}$ can be chosen as common. The above integrals vanish for $m' \neq m$ due to the rotational symmetry of the spherical harmonics. The result can thus be expressed as a linear combination of Slater-Koster integrals $(l_1 l_2 m)$ that are defined, following Eq. (2.98), as the two-center integrals $(l_1 l_2 m) = \frac{1}{2}\int \alpha^*(\boldsymbol{r} - \Delta\boldsymbol{R})\,[V_{\rm at}(\boldsymbol{r}) + V_{\rm at}(\boldsymbol{r} - \Delta\boldsymbol{R})]\,\beta(\boldsymbol{r})\,{\rm d}^3\boldsymbol{r}$ with $\beta(\boldsymbol{r}) = f(r)Y_{l_1 m}(\vartheta_{\rm 1rot}, \varphi_{\rm rot})$ and $\alpha(\boldsymbol{r}) = f(r)Y_{l_2 m}(\vartheta_{\rm 2rot}, \varphi_{\rm rot})$. The values of $l_{1,2} = 0, 1, 2, \ldots$ are specified by the conventional letters for atomic orbitals s, p, d, ... and those of $m = 0, 1, 2$ by σ, π, δ, following the chemical bonding nomenclature. Note that the values for $+m$ and $-m$ are identical.

The basic set of Slater-Koster integrals needed for the analysis of hoppings in transition metal oxides is presented in Fig. 18. The main contribution to the Slater-Koster integrals will be presumably collected near the central area of the bond. Taking into consideration the angular distribution of the spherical harmonics, it may be expected that σ bonding is in general stronger than π bonding and that is stronger than δ bonding. One can also anticipate the signs: Since $V_{\rm at}$ is negative, the Slater-Koster integral typically has a negative sign when the closest lobes of the two orbitals have equal signs (or same complex phase). Accordingly, the indicated σ and δ Slater-Koster integrals will be probably negative while the π ones positive. Following our definition, the hopping parameters $t_{nn'}$ will be of opposite signs, for example the hopping t between s orbitals is positive which is indeed observed in Fig. 17. The above "rules of thumb" are useful when inspecting the actual hopping channels between ions as we will do soon. To have a more intuitive notation, we incorporate the anticipated signs into the newly introduced labels for hopping parameters:

$$t_{pd\sigma} = -(pd\sigma)\,, \quad t_{pd\pi} = +(pd\pi)\,, \quad t_{dd\sigma} = -(dd\sigma)\,, \quad t_{dd\pi} = +(dd\pi)\,, \quad t_{dd\delta} = -(dd\delta) \qquad (2.100)$$

that will be used below and that are not always following Eq. (2.98). In this convention the hopping parameter will be taken positively if orbital lobes of the same sign "meet" on the bond.

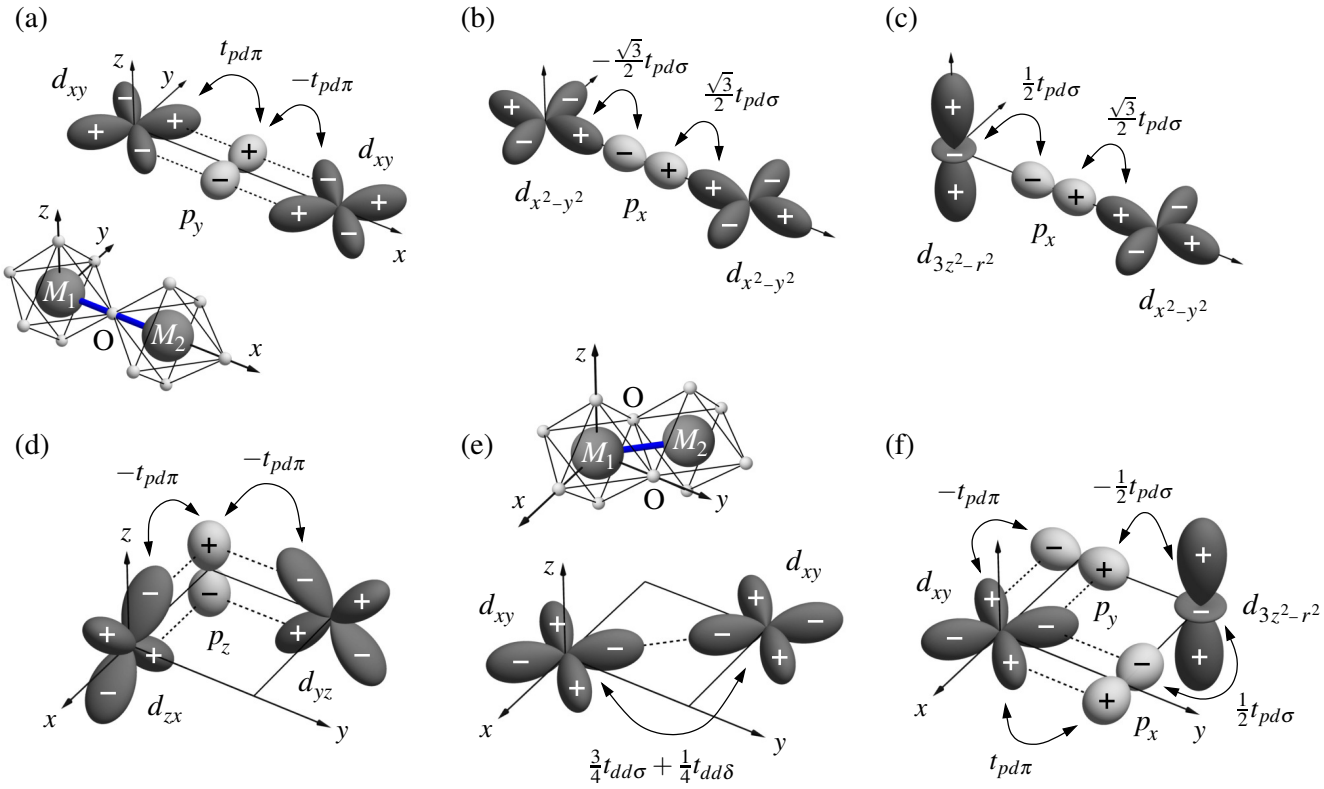

Fig. 19: Examples of hopping channels contributing to nearest-neighbor hopping between two transition metal ions in the case of 180° metal-oxygen-metal bonds (a,b,c) and 90° bonds (d,e,f). The indicated hopping amplitudes use the quantities defined by Eq. (2.100). The insets show the geometry of the connected octahedra and label the transition metal ions by $M_{1,2}$. The setup of the axes for the 90° case is identical to Fig. 7(b),(c) (z-bond). There are a few more contributing options that were not shown: (a) Connection of two d_{zx} orbitals via p_z, (b) connection of two $d_{3z^2-r^2}$ orbitals via p_x, (c) situation with interchanged d orbitals, (d) hopping between d_{zx} and d_{yz} mediated by p_z of the front oxygen of the metal$_2$-oxygen$_2$ plaquette.

When dealing with hoppings in transition metal compounds, we most frequently encounter either 180° metal-oxygen-metal bonds or 90° ones (see e.g. Fig. 1). The various options that we need to consider when connecting two transition metal ions are summarized in Fig. 19. A crucial observation is that e_g orbitals are even when mirrored by any plane containing the bond so that they can only couple to oxygen p orbitals via σ-bonding, while t_{2g} orbitals have an odd-parity mirror plane so that only the π-bonding to oxygen orbitals is possible. As a consequence, the 180° bond geometry enables only separate t_{2g}–t_{2g} and e_g–e_g hoppings, t_{2g}–e_g mixing is absent. For the 90° bond geometry, on the other hand, the t_{2g}–e_g mixing channel is the dominant one and e_g–e_g hopping is forbidden by symmetry. Most of the channels depicted in Fig. 19 correspond to second-order processes involving two successive p-d hoppings. We will now go through the individual cases and inspect the resulting d-d hoppings.

We start with the 180° bond and t_{2g} hopping channel. According to Fig. 19(a) showing an x-bond situation, a pair of d_{xy} orbitals becomes connected through the mediating p_y orbital. The same type of connection, now via p_z orbital, can be found for two d_{zx} orbitals. The remaining t_{2g} orbital d_{yz} is inactive on an x-bond. To derive the effective d-d hopping, we consider the M_1–O–M_2 bond in the initial configuration d^m–p^6–d^n corresponding to a completely filled va-

lence shell of O^{2-}. The process of hopping from the transition metal ion M_1 to M_2 needs to start with a p-d hopping from the oxygen to M_2. This creates a virtual configuration d^m–p^5–d^{n+1} with the excitation energy Δ_{pd} (to be discussed in detail later in Sec. 2.4) that can be relaxed when another electron moves from M_1 to the oxygen and fills the hole in p orbitals. The final configuration is d^{m-1}–p^6–d^{n+1} with one electron moved from M_1 to M_2. Thinking within the framework of the second-order perturbation theory, the amplitude of the whole process can be estimated as $-t_{\mathrm{O}\to 2}t_{1\to\mathrm{O}}/\Delta_{pd}$ which incorporates the amplitudes of the two successive hoppings. The corresponding term in the effective d-d hopping Hamiltonian then reads as $(+t_{\mathrm{O}\to 2}t_{1\to\mathrm{O}}/\Delta_{pd})c_2^\dagger c_1$. The extra sign originates in reordering the electron operators that appear in the sequence $(p^\dagger c_1)(c_2^\dagger p)$ when following the partial hoppings in the perturbation term. Here p, $p^\dagger$ are electron operators corresponding to the participating p orbital. A similar process can be constructed when working out the $2\to 1$ direction of the d-d hopping. Taking into account also the opposite signs of the partial hopping amplitudes observed in Fig. 19(a), we get for the t_{2g} hopping Hamiltonian on the x-bond

$$\mathcal{H}_{ij}^{(x)} = -(t_{pd\pi}^2/\Delta_{pd})(d_{xy}^\dagger d_{xy} + d_{zx}^\dagger d_{zx})_{ij} + \mathrm{H.c.} \tag{2.101}$$

Hopping Hamiltonians for the other bond directions can be obtained by cyclic permutation.

The situation is more complex for e_g orbitals on a 180° bond, where all possible combinations of e_g orbitals are connected. Shown in Fig. 19(b), (c) are two options, there is in addition a connection between two $d_{3z^2-r^2}$ orbitals. Evaluating the effective d-d hopping in this case, we arrive at the bond Hamiltonian

$$\mathcal{H}_{ij}^{(x)} = -\frac{t_{pd\sigma}^2}{\Delta_{pd}} \begin{pmatrix} d_{3z^2-r^2}^\dagger & d_{x^2-y^2}^\dagger \end{pmatrix}_i \begin{pmatrix} +\frac{1}{4} & -\frac{\sqrt{3}}{4} \\ -\frac{\sqrt{3}}{4} & +\frac{3}{4} \end{pmatrix} \begin{pmatrix} d_{3z^2-r^2} \\ d_{x^2-y^2} \end{pmatrix}_j + \mathrm{H.c.} \tag{2.102}$$

For a y-bond the hopping matrix is almost the same, the only change is an opposite sign of the off-diagonal elements as a consequence of the opposite signs of the $d_{x^2-y^2}$ orbital lobes pointing in x and y directions. For a z-bond we have essentially the situation from Fig. 18(a) giving $\mathcal{H}_{ij}^{(z)} = -(t_{pd\sigma}^2/\Delta_{pd})\,(d_{3z^2-r^2}^\dagger d_{3z^2-r^2})_{ij} + \mathrm{H.c.}$ The $d_{x^2-y^2}$ orbital is completely disconnected in that case. The partial hopping amplitude $t_{pd\sigma}$ is typically two times stronger than $t_{pd\pi}$ which makes the e_g hopping more powerful. A well known example of this type of hopping is the motion of holes in the CuO_2 planes of high-T_c cuprates. Residing in the planar $d_{x^2-y^2}$ orbital, they can fully utilize the geometry of the square lattice with Cu–O–Cu bonds.

Moving on to the 90° bond geometry and t_{2g} orbitals, we find that the hopping channel via oxygen is quite similar to the 180° case, with two orbitals out of three being active. However, the path is bent now which results in an *interchange* of t_{2g} orbitals. Specifically, for the bond along $\frac{1}{\sqrt{2}}(y-x)$ direction presented in Fig. 19(d) [the geometry coincides with the z-bonds of Fig. 7(b),(c)], we get

$$\mathcal{H}_{ij} = +(t_{pd\pi}^2/\Delta_{pd})(d_{zx}^\dagger d_{yz} + d_{yz}^\dagger d_{zx})_{ij} + \mathrm{H.c.} \tag{2.103}$$

with the two contributions being mediated separately by the two oxygen ions in the M_2O_2 plaquette. In this geometry there might also be a significant direct overlap of d_{xy} orbitals as shown in Fig. 19(e). For the other two t_{2g} orbitals, a direct hopping is also possible but weak because its matrix element contains $\frac{1}{2}(dd\pi)$ while the d_{xy} orbital uses stronger $\frac{3}{4}(dd\sigma)$. The orbitals active in oxygen-mediated hopping and direct hopping are thus basically complementary. As before, we can get the t_{2g} hoppings for the other bond directions by cyclic permutation.

Finally, let us consider the t_{2g}–e_g hopping on a 90° bond. As demonstrated in Fig. 19(f), the necessary orientation of the p orbitals is only compatible with the d_{xy} orbital. When connecting it to the e_g orbital, an interesting quantum interference effect occurs. For the $d_{3z^2-r^2}$ orbital the two

hopping channels via front and rear oxygen ions come with the same total phases accumulated from the partial p-d hoppings so that they add up to

$$\mathcal{H}_{ij} = +(t_{pd\sigma}t_{pd\pi}/\Delta_{pd})(d^\dagger_{3z^2-r^2}d_{xy} + d^\dagger_{xy}d_{3z^2-r^2})_{ij} + \text{H.c.} \tag{2.104}$$

However, for the $d_{x^2-y^2}$ orbital with alternating signs of its lobes, the amplitudes of the two channels add to zero and $d_{x^2-y^2}$ is thus disconnected. The Hamiltonians for the other bond directions may be obtained by cyclic permutation but in this case a subsequent decomposition of the resulting $d_{3x^2-r^2}$ and $d_{3y^2-r^2}$ e_g orbitals into the conventional $d_{x^2-y^2}$ and $d_{3z^2-r^2}$ pair is needed.

2.4 Mott limit and interactions emerging from residual hopping

Having explored both the physics of the individual ions as well as the way how to connect them via electronic hopping, we are now in position to assemble all together in a form of so-called multiorbital Hubbard model

$$\mathcal{H} = \sum_i \mathcal{H}_{\text{ion}}(i) + \sum_{\langle ij\rangle} \mathcal{H}_{\text{hopping}}(ij)\,. \tag{2.105}$$

The first sum goes through the lattice sites and collects the intra-ionic contributions $\mathcal{H}_{\text{ion}} = \sum_{\alpha\sigma}\varepsilon_\alpha n_{\alpha\sigma} + \mathcal{H}_{\text{Coul}} + \mathcal{H}_{\text{SOC}}$ that we have thoroughly analyzed in Secs. 2.1 and 2.2. The second sum runs through the bonds (quite often nearest-neighbor ones but further neighbors can be included if needed) and activates the various hopping channels as introduced in Sec. 2.3.

At a closer inspection the problem defined by Eq. (2.105) looks intricate and it indeed is. Without $\mathcal{H}_{\text{Coul}}$ we would be just facing a band-structure calculation on a single-electron level, readily performed by an application of the Bloch theorem. However, electron correlations due to two-body interactions contained in $\mathcal{H}_{\text{Coul}}$, that we assume to be strong, make it a genuine many-body problem.[10] We have already successfully handled the electron correlations when diagonalizing the individual $\mathcal{H}_{\text{ion}}$ which was a relatively simple task due to a limited Hilbert space of an individual ion with given number of electrons. This is no more true for a lattice of connected ions since the Hilbert space dimension grows in a terrifying way – essentially exponentially with the number of lattice sites. Moreover, the base for this exponential is not small due to several orbitals involved and combined with spin-$\frac{1}{2}$. When resorting to a fully numerical diagonalization, even the huge computational power easily accessible nowadays enables to exactly treat clusters with a few transition metal ions only.

One way out is to simplify the model by identifying the relevant ionic states – typically the low-energy multiplet states – and formulate an effective model in terms of those. The actual model may be obtained, for example, by getting rid of the high-energy states in a perturbative manner. A proper choice of the elementary objects for the model and processes to be included can make the physics behind the particular material more transparent and guide further approximations. Even though the results may be qualitative only, the insights gained are sometimes more valuable than a quantitative treatment of the original Hubbard model by some complex numerical method.

Our focus is on models with localized degrees of freedom appearing as effective models for undoped Mott insulators, the canonical example being a spin model. In the introductory section 1.2 we took a very simplistic approach to the problem of its emergence. The aim of the present section is to put it on a bit more solid ground to get ready for a derivation of "realistic" models in Secs. 3 and 4.

[10] In principle, there are also inter-ionic interactions of two-body character that could be included in the model, such as Hubbard repulsion of the electrons residing at neighboring ions, but these are only needed in special situations and we do not need to address them in our cases of interest. Consequently, the only source of correlated behavior of electrons in our models will be the intra-ionic electron-electron interactions in $\mathcal{H}_{\text{Coul}}$.

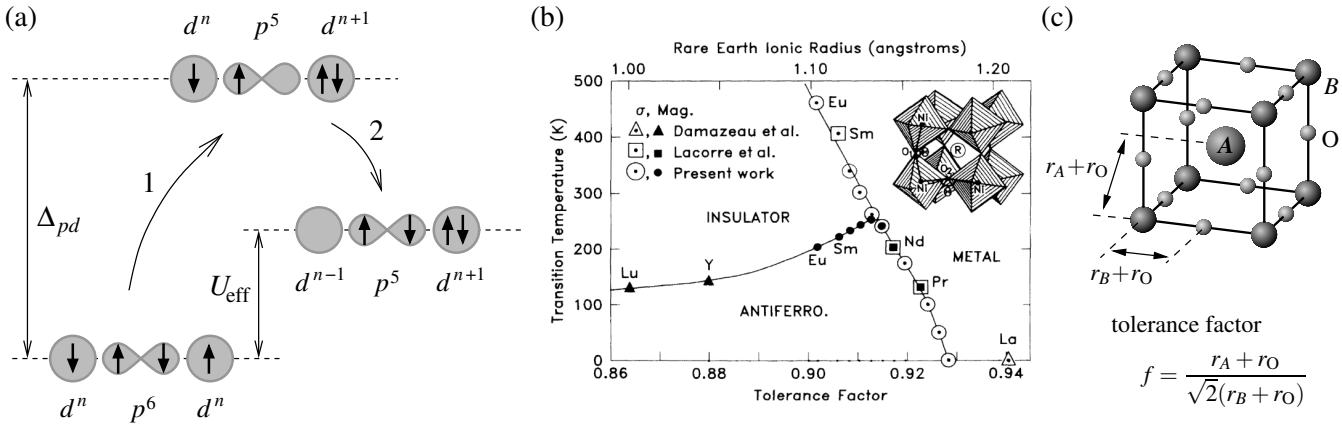

Fig. 20: (a) Hierarchy of energies of charge excitations for a undoped Mott-Hubbard insulator. The lowest elementary state is the balanced d^n-p^6-d^n configuration of metal-oxygen-metal bond with a full p shell of the O^{2-} ion. Process denoted as 1 is a charge-transfer process leading to a p-d excitation – a virtual state with the excitation energy Δ_{pd}. It may get relaxed by a backward process 1 or by process 2 producing a d-d excitation. (b) Phase diagram of the $R\mathrm{NiO}_3$ family of compounds as function of the tolerance factor and temperature (from Torrance *et al.* [34]) (c) Definition of the tolerance factor quantifying the deformations of the unit cell in $AB\mathrm{O}_3$ perovskites. The labels r_A, r_B, and r_O should bring associations with the respective ionic radii. For an ideal cube $f = 1$.

2.4.1 Metal-insulator transition

As it was emphasized in Sec. 1.2, a key element in transition metal oxides is the competition between the tendency of electrons to delocalize and form bands and Coulomb repulsion that wants to keep the electrons apart. Mott insulating state sketched in Fig. 2(b) and forming a basis for our model description appears as a consequence of the latter mechanism taking over.

Considering the details, one has to be careful because the role of the oxygen bridges between the transition metal ions may be more complex than mere mediators of d-d hopping. According to the scheme developed by Zaanen, Sawatzky, and Allen [35, 36], the insulating states may be classified as Mott-Hubbard insulators or charge-transfer insulators. The idea behind this classification is that the elementary hopping which moves an electron between p orbital of oxygen ion and d orbital of the transition metal ion may create a virtual state that is more convenient than the one generated by full d-d hopping. When "deriving" the effective d-d hopping via oxygen in Sec. 2.3 we have handled it in a bit handwaving way having the Mott-Hubbard regime in mind. Let us now analyze this issue in more detail following the scheme in Fig. 20(a) that applies to the Mott-Hubbard situation. The starting point is the most probable d^n–p^6–d^n configuration of a metal-oxygen-metal bond. Since the valence shell of O^{2-} is full in this configuration, the action may only start by moving one of its electrons to a neighboring transition metal ion via p-d hopping. This creates p-d charge excitation d^n–p^5–d^{n+1} whose energy Δ_{pd} is defined as the difference of the energies of the two states [see Fig. 20(a)]. It is contributed by the energy difference between the d and p orbitals $\varepsilon_d - \varepsilon_p$ and the Coulomb energy associated with the change $d^n \to d^{n+1}$.[11] In the next step, we can either restore the initial situation by backward p-d hopping or continue to reach d-d excitation with the configuration d^{n-1}–p^6–d^{n+1} that has an energy $U_{\rm eff}$. This is now contributed by the Coulomb energy associated with the simultaneous

[11] The changes of the Coulomb energy in the p shell of oxygen related to the $p^6 \to p^5$ process may be absorbed into the definition of $\varepsilon_d - \varepsilon_p$.

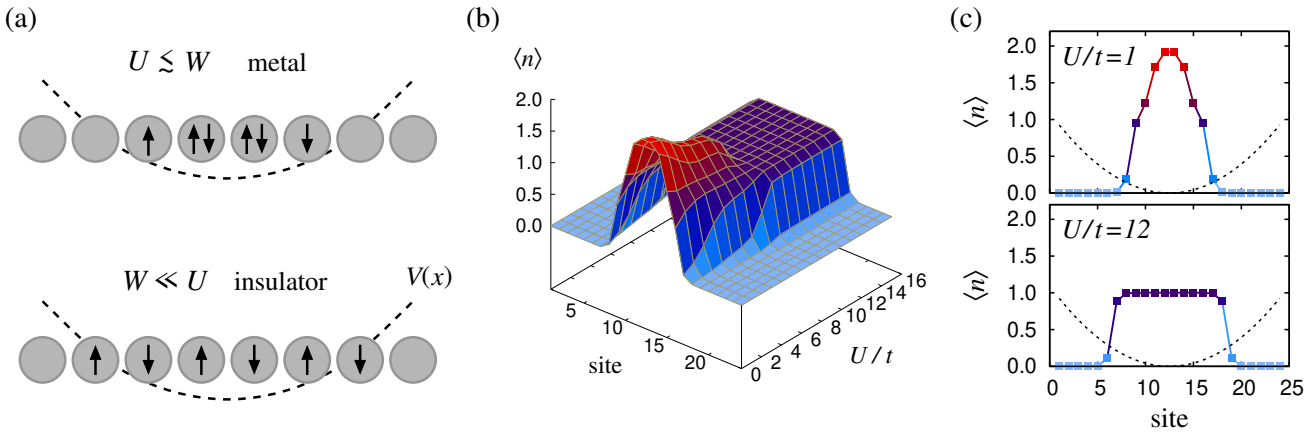

Fig. 21: (a) Two states of a Hubbard chain in a parabolic trap that can be distinguished by observing the electron density. They appear depending on the ratio between the "bandwidth" $W \propto t$ and Hubbard repulsion U. (b) Average site-dependent occupation in the ground state of the chain with 24 sites and 12 fermions ($N_\uparrow = N_\downarrow = 6$) as function of the U/t ratio. The parabolic potential reaches $30t$ at the chain ends. Mott transition can be observed around $U/t \approx 8$ in this case. (c) Density profiles well below and well above the critical U/t corresponding to the Mott transition.

changes $d^n \to d^{n+1}$ and $d^n \to d^{n-1}$. In our schematics in Fig. 20(a) it is the Hubbard U but often one encounters Hund's coupling effects in this virtual state as well. In a charge-transfer insulator, $\Delta_{pd} < U_{\rm eff}$ so that the bonds excited by p-d hopping are not eager to continue towards forming the d-d excitation and prefer to spend more time with a hole on oxygen. The resulting state of the entire system is still an insulator that looks like in Fig. 2(b) but the picture behind clearly differs from Fig. 2(c). This is the case of late $3d$ transition metal oxides like high-T_c cuprates. In a Mott-Hubbard insulator the lower excitation is the d-d one (i.e. $U_{\rm eff} < \Delta_{pd}$), so that the states with p^5 configuration of oxygen are indeed by a larger part just the mediators of the effective d-d hopping as we have implicitly assumed before. Of course, the distinction is not strict, both p-d and d-d charge excitations are in the game, but their proportion depends on the Δ_{pd} to $U_{\rm eff}$ ratio and we label the particular system according to the prevailing one.

Both insulating scenarios above require the hopping amplitudes to be substantially smaller than the the lower of the two charge-excitation gaps Δ_{pd} and $U_{\rm eff}$, otherwise the insulating state is not kept and we end up in a metallic state. Sometimes we are able to tune the balance between the competing kinetic energy and strong correlations and drive the system through the metal–insulator transition. We will now illustrate it in two examples. The first one is a set of experimental data on RNiO$_3$ family of perovskite nickelates that was assembled into a very instructive phase diagram by Torrance *et al.* [34]. The phase diagram is reproduced in Fig. 20(b). Its horizontal axis needs some explanation. The quantity shown there is so-called tolerance factor which measures how much the unit cell got deformed from an ideal cube. By changing the R cation, one can significantly influence this deformation. Thinking intuitively, the closer we are to the cubic situation with straight bonds, the larger is the overlap of the orbitals and hence the hopping. Going away from the cubic case, we may therefore experience a metal to insulator transition as indeed visible in the the phase diagram by Torrance *et al.* who collected data for various R elements and also mixed solid solutions. At low-enough temperatures the insulator develops antiferromagnetic order, consistently with our intuitive picture.

Another example that we will analyze more thoroughly is the metal-insulator transition observed in a one-dimensional Hubbard chain that is actually sketched in Fig. 2(b),(c) as a prototype system. We have simulated this system numerically using exact diagonalization for short

chains so that we can freely tune the ratio of the main parameters – hopping t and Hubbard repulsion U. The first results presented in Fig. 21 concern a Hubbard chain with an extra potential of a parabolic trap.[12] This problem was studied in the context of atoms trapped in an optical lattice [37, 38] so we should be talking about fermionic spin-$\frac{1}{2}$ atoms instead of electrons. Nevertheless, the physics of the Hubbard model works the same way. When looking at the metal-insulator transition, one should compare the bandwidth W to the Coulomb repulsion represented by Hubbard U. Here the concept of bandwidth is not well defined but we can still understand it as "some quantity proportional to the hopping t." The inhomogeneous situation due to the parabolic trap brings some specifics. We can distinguish two phases just by observing the distribution of the density of fermions $\langle n \rangle$ as sketched in Fig. 21(a) – a bell-shaped fermionic cloud with notable double occupancy replaces the metallic phase of a homogeneous system, the insulating phase is represented by a state where a Mott insulating core develops, having a flat density profile with $\langle n \rangle \approx 1$. The transition around $U/t \approx 8$ is well visible when studying the evolution of the density profile with U/t [see Fig. 21(b),(c)].

Another way of looking at the Mott transition in 1D Hubbard chain, somewhat less exotic compared to the above one, is an inspection of the spin excitations as evolving with U/t. In Fig. 22(a) we perform this inspection for a periodic chain of 16 sites, again simulated numerically by exact diagonalization. The finite-sized chain has a discrete set of wavevectors q but the shape and intensity of the spin excitation spectrum is sufficiently densely covered for our purposes. The bandwidth $W = 4t$ stemming from the dispersion $\varepsilon_k = -2t \cos ka$ is well defined in this case and appears in the metallic limit $t \ll U$ also as the bandwidth of the spin excitations. In

[12] Here our calculation reproduces the results presented in Ref. [37] that were obtained using Earth Simulator – the most powerful supercomputer in the world from 2002 to 2004. Not even two decades later, we were able to get them using a refurbished server which well demonstrates the remarkable steady progress in computer technology.

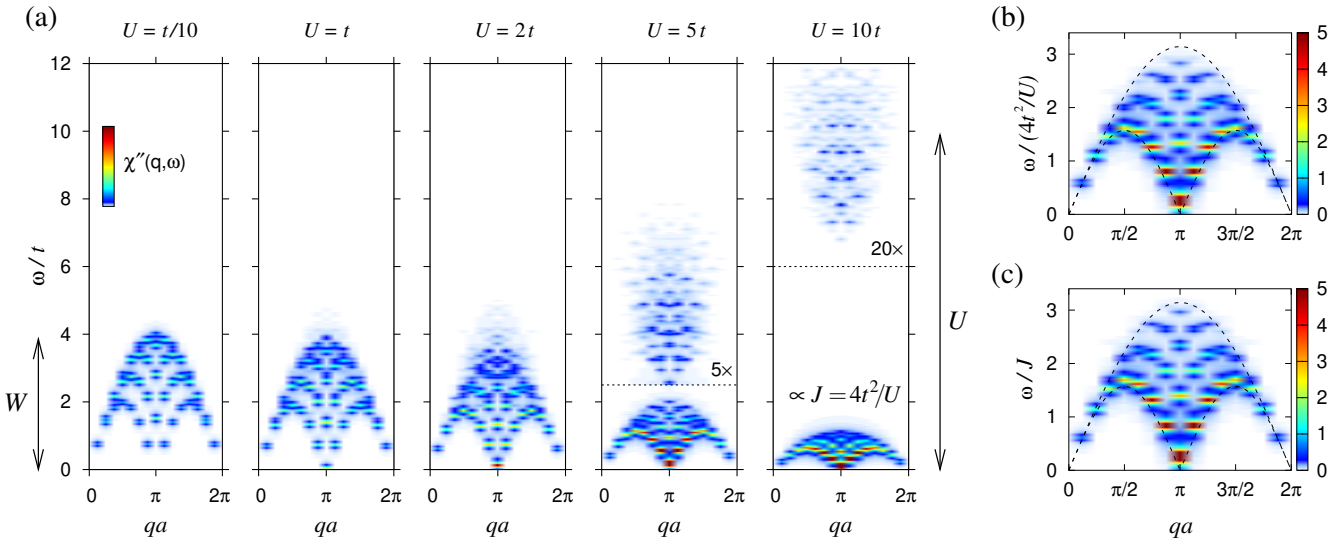

Fig. 22: (a) U/t dependence of the spin susceptibility of the one-dimensional Hubbard chain with 16 sites and periodic boundary conditions applied. Plotted is the imaginary part $\chi''(q, \omega)$ as function of one-dimensional momentum $q \in [0, 2\pi]$ and energy ω. The intensity of the upper part of the spectrum is magnified in the last two panels to make it better visible. (b) Detailed view on the low-energy part of the spin susceptibility for $U/t = 10$ with ω scaled by the anticipated exchange constant $J = 4t^2/U$. (c) Spin susceptibility obtained for the Heisenberg model on the same chain. The dotted lines indicate the lower and upper bound of the spin excitations known from the exact solution of an infinite chain by Bethe Ansatz.

this regime Fig. 22(a) essentially shows the Lindhard function for a 1D band. With increasing U there is more and more spectral weight appearing at low energies at the AF wavevector $q = \pi/a$, this is a sign of incipient AF correlations. The overall shape of the excitation spectrum remains the same, however. A dramatic change happens around $U/t \approx 5$ where the spectrum reveals a clear separation of two energy scales and a birth of an effective model. Tracing the two parts of the spectra to even higher U/t regime where the Mott insulator is well developed, we can attribute the low-energy part to an effective Heisenberg model with the excitation bandwidth proportional to the effective exchange parameter $J = 4t^2/U$. The high-energy excitations start around the energy U signifying the presence of doubly occupied sites in the participating states. With increasing U/t, their intensity gradually weakens. A conclusive test of the emergence of the Heisenberg model is provided by a comparison of the low-energy part of the spin susceptibility obtained within Hubbard model [Fig. 22(b)] and that of the Heisenberg model on the same chain [Fig. 22(c)]. Due to its one-dimensionality, the Heisenberg chain does not order magnetically and the spin excitations form a continuum instead of narrow magnon branch(es) but this difference to higher-dimensional antiferromagnets does not matter here, since we are only interested in finding signatures of the emergent model. We scale the energy axis by the exchange constant in both cases and observe an excellent agreement. There are some tiny shifts visible near the top of the two spectra in Fig. 22(b) and Fig. 22(c) but otherwise they display no noticeable differences. Therefore, the description of the Hubbard chain by an effective spin model seems to be perfectly justified in this large U/t limit with roughly $U \gtrsim 2W$.

2.4.2 Superexchange interactions

Having prepared the foundations for the effective model in a form of a Mott insulator, we now come to the question of the effective interactions. When mediated by oxygen ions or some other bridging ions, they are commonly called superexchange interactions to make a distinction between direct exchange interactions of two neighboring ions and the more complex mechanism. The first theory of superexchange interactions was proposed in 1934 by H. A. Kramers [39], later in 1950's it was refined by P. W. Anderson in his seminal works on the topic [40, 41]. In this paragraph we are going to expose the general formalism how to obtain exchange interactions and illustrate it on a relatively simple but nontrivial example of superexchange interactions in cuprates.

The exchange interactions stem from the short excursions of electrons to the neighboring ions, the simplest example being sketched in Fig. 2(c). These charge excitations are rather costly. As we have discussed in the previous paragraph, they are separated by the gap U_{eff} or Δ_{pd} that is assumed to be significantly larger than the hopping parameters t_{pd}. The problem apparently calls for a perturbative treatment of the hoppings and we will indeed proceed that way, treating the ionic part of the Hamiltonian (2.105) as the unperturbed Hamiltonian and the hopping part as a perturbation. The situation is complicated by two facts: First, we have to perform the perturbation theory to a relatively high order. Following the scheme in Fig. 20(a) for Mott-Hubbard case, we need in total four hopping processes to get to the virtual excited state and back. Second, the states we are perturbing (i.e. products of ionic multiplet states) are degenerate/quasidegenerate. The usual Rayleigh-Schrödinger perturbation theory found in textbooks is not very convenient here since it leads to relatively complex expressions. In the following derivation, we will employ the more suitable Brillouin-Wigner variant of the perturbation theory adapted for quasidegenerate levels.

We will first consider a general problem with the full Hamiltonian $\mathcal{H} = \mathcal{H}_0 + \lambda\mathcal{V}$ consisting of the unperturbed one $\mathcal{H}_0$ and the perturbation $\mathcal{V}$ accompanied by the usual expansion parameter λ to be varied from 0 to 1. The level structure for a quasidegenerate case of our interest is schematically represented in Fig. 23(a). The key concept, introduced independently by Feshbach

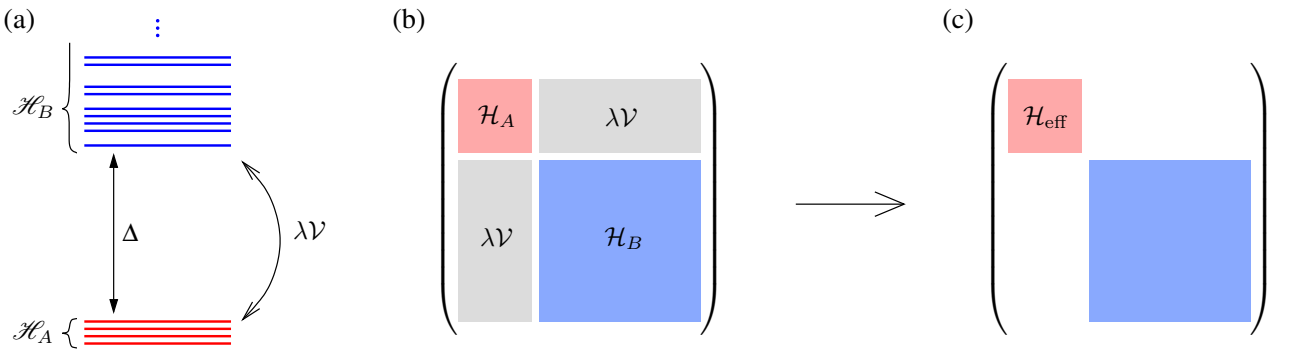

Fig. 23: (a) Level scheme of the problem to be treated by the perturbation theory. By virtue of the unperturbed Hamiltonian $\mathcal{H}_0$, the Hilbert space splits into low-energy states contained in the subspace $\mathscr{H}_A$ and high-energy states in $\mathscr{H}_B$. The states of these subspaces are separated by the energy gap Δ and connected by a weak perturbation $\lambda\mathcal{V}$. (b) Block structure of the corresponding Hamiltonian matrix. The unperturbed Hamiltonian $\mathcal{H}_0$ does not connect the two Hilbert subspaces $\mathscr{H}_A$ and $\mathscr{H}_B$. This connection is provided by the off-diagonal blocks of $\lambda\mathcal{V}$ which may also contribute to the diagonal blocks. The matrix elements of the off-diagonal blocks $\lambda\mathcal{V}$ are assumed to be significantly smaller than the energy gap Δ enabling a perturbative treatment. (c) The desired structure of the Hamiltonian. After performing a proper basis rotation, the off-diagonal blocks connecting low-energy sector to high-energy virtual states are eliminated and the effective Hamiltonian for the low-energy sector is found in the corresponding diagonal block.

[42, 43] and Löwdin [44, 45], is the partitioning of the Hilbert space. Based on unperturbed energies (i.e. the spectrum of $\mathcal{H}_0$), we single out the low-energy subspace $\mathscr{H}_A$ and let its states interact by a weak perturbation $\lambda\mathcal{V}$ with the states of the high-energy subspace $\mathscr{H}_B$. The ultimate goal is to find an effective Hamiltonian acting on states in the lower subspace but leading to the same results as the full one. To be more concrete, we introduce a decomposition of a state from the full Hilbert space utilizing the projection operators onto $\mathscr{H}_A$ and $\mathscr{H}_B$ subspaces:

$$|\psi\rangle = |\psi_A\rangle + |\psi_B\rangle = \mathcal{P}|\psi\rangle + \mathcal{Q}|\psi\rangle\,, \qquad \mathcal{Q} = 1 - \mathcal{P}\,. \tag{2.106}$$

We now want to construct the effective Hamiltonian $\mathcal{H}_{\text{eff}}$ in such a way, that a projection of the true eigenstate of $\mathcal{H}$ onto $\mathscr{H}_A$ is an eigenstate of $\mathcal{H}_{\text{eff}}$ with the same eigenvalue:

$$(\mathcal{H} - E)|\psi\rangle = 0 \qquad \rightarrow \qquad (\mathcal{H}_{\text{eff}} - E)\,\mathcal{P}|\psi\rangle = 0\,. \tag{2.107}$$

Vaguely speaking, the effective Hamiltonian has to take the low-energy component $\mathcal{P}|\psi\rangle$, complete it with the corresponding high-energy part, act with the full Hamiltonian, and return a low-energy component of the result. This "hidden" admixture of the high-energy sector that effectively eliminates $\lambda\mathcal{V}$ roughly corresponds to the basis rotation that is suggested in Fig. 23(b),(c). The above task is quite demanding and may be precisely fulfilled only by an energy-dependent $\mathcal{H}_{\text{eff}}(E)$. We are, in an indirect way, facing the inherent problem of the Brillouin-Wigner perturbation theory where the final perturbed energies themselves enter the expressions for the perturbation corrections. It is not a big issue, however, since the target energies E of interest form a relatively narrow band compared to the intermediate excitation energies so that we can make approximations easily. An explicit formula for $\mathcal{H}_{\text{eff}}(E)$ is obtained by inserting (2.106) into $(\mathcal{H} - E)|\psi\rangle = 0$ and decomposing the results by applying the projectors $\mathcal{P}$ and $\mathcal{Q}$. For the high-energy component we get

$$\mathcal{Q}\mathcal{H}\mathcal{P}|\psi\rangle + \mathcal{Q}\mathcal{H}\mathcal{Q}|\psi\rangle - E\mathcal{Q}|\psi\rangle = 0 \quad \rightarrow \quad \mathcal{Q}|\psi\rangle = \frac{1}{E - \mathcal{Q}\mathcal{H}\mathcal{Q}}\,\mathcal{Q}\mathcal{H}\mathcal{P}|\psi\rangle \tag{2.108}$$

with the operator/matrix inversion happening within the $\mathscr{H}_B$ subspace. The above expression can be used in the low-energy component of the original equation to yield $(\mathcal{H}_{\rm eff} - E)\mathcal{P}|\psi\rangle = 0$ with

$$\mathcal{H}_{\rm eff}(E) = \mathcal{P}\mathcal{H}\mathcal{P} + \mathcal{P}\mathcal{H}\mathcal{Q}\,\frac{1}{E - \mathcal{Q}\mathcal{H}\mathcal{Q}}\,\mathcal{Q}\mathcal{H}\mathcal{P}\,. \tag{2.109}$$

This result is still exact and general, though not very useful without the level separation of Fig. 23(a). By observing the structure of the full Hamiltonian matrix depicted in Fig. 23(b), we can see the correspondence of its blocks to the individual terms appearing in Eq. (2.109). The second-order effective Hamiltonian can be obtained very quickly by approximating the denominator by $-\Delta$, assuming that the relevant states from $\mathscr{H}_A$, $\mathscr{H}_B$ form narrow bands as compared to the gap Δ. To reach higher orders, we need to systematically expand the resolvent of the projected Hamiltonian:

$$\mathcal{G}(E) = \frac{1}{E - \mathcal{Q}\mathcal{H}\mathcal{Q}} \tag{2.110}$$

entering Eq. (2.109) and operating in $\mathscr{H}_B$. To this end we introduce the unperturbed resolvent

$$\mathcal{G}_0(E) = \frac{1}{E - \mathcal{Q}\mathcal{H}_0\mathcal{Q}} \tag{2.111}$$

that is related to the full one by the operator/matrix relation

$$\mathcal{G}_0^{-1}(E) - \mathcal{G}^{-1}(E) = \lambda\mathcal{Q}\mathcal{V}\mathcal{Q}\,. \tag{2.112}$$

By applying $\mathcal{G}_0(E)$ from the left and $\mathcal{G}(E)$ from the right, we get Dyson's equation

$$\mathcal{G}(E) = \mathcal{G}_0(E) + \lambda\,\mathcal{G}_0(E)\;\mathcal{Q}\mathcal{V}\mathcal{Q}\;\mathcal{G}(E) \tag{2.113}$$

that can be solved by repeated iteration, adding one order in λ in each step. When inserting the resulting series into Eq. (2.109), we obtain the perturbation series for the effective Hamiltonian in the form

$$\begin{aligned}\mathcal{H}_{\rm eff}(E) = \mathcal{P}\mathcal{H}_0\mathcal{P} + \lambda\,\mathcal{P}\mathcal{V}\mathcal{P} + \lambda^2\,\mathcal{P}\mathcal{V}\mathcal{Q}\,\frac{1}{E - \mathcal{Q}\mathcal{H}_0\mathcal{Q}}\,\mathcal{Q}\mathcal{V}\mathcal{P} + \\ + \lambda^3\,\mathcal{P}\mathcal{V}\mathcal{Q}\,\frac{1}{E - \mathcal{Q}\mathcal{H}_0\mathcal{Q}}\,\mathcal{Q}\mathcal{V}\mathcal{Q}\,\frac{1}{E - \mathcal{Q}\mathcal{H}_0\mathcal{Q}}\,\mathcal{Q}\mathcal{V}\mathcal{P} + \dots\,,\end{aligned} \tag{2.114}$$

where we have used the fact that $\mathcal{H}_0$ does not connect $\mathscr{H}_A$ and $\mathscr{H}_B$. This concludes the derivation of the general Brillouin-Wigner perturbation theory for quasidegenerate levels.

The perturbation expansion (2.114) may look intimidating at the first sight, but in the examples below we will see that it actually leads to a relatively simple and intuitive scheme for the derivation of the exchange interactions. A convenient choice of the basis are product states where each ion is in some multiplet state, which means that the ionic part of Eq. (2.105) (our $\mathcal{H}_0$) is already diagonalized. To get the total energy of the configuration, one just sums up the energies of the participating multiplet states. This makes the evaluation of $(E - \mathcal{Q}\mathcal{H}_0\mathcal{Q})^{-1}$ entering (2.114) trivial. The perturbation $\mathcal{V}$ is represented by the hopping Hamiltonian. When evaluating the second-order contribution to $\mathcal{H}_{\rm eff}$ via (2.114), we start with the initial low-energy configuration, jump into the high-energy subspace by the first hopping and leave it by the second one, reaching the final low-energy configuration. The corresponding matrix element of $\mathcal{H}_{\rm eff}$ is the product of the used hopping matrix elements divided by negatively taken excitation energy. To get the higher-order contributions, we are additionally traveling through the high-energy subspace via further hoppings, collecting the hopping matrix elements used on the way and dividing by the

excitation energies of the visited states. Here one often ignores the finer structure of the excited multiplet levels and counts only U contributions, neglecting the smaller shifts due to J_H, for example.

Let us now inspect the half-filled one-band Hubbard model as the simplest example. The second order process from Fig. 2(c) concerns only two sites, we can therefore consider an isolated bond as well. Due to the spin conservation in the hopping processes, it pays off to start with total spin eigenstates as the initial configurations. In our case, the two electrons on a bond may form a singlet and three triplet states. Due to the Pauli principle, we find that only a singlet state $|s\rangle = \frac{1}{\sqrt{2}}(c^\dagger_{1\uparrow}c^\dagger_{2\downarrow} - c^\dagger_{1\downarrow}c^\dagger_{2\uparrow})|\,\rangle$ on the bond is connected to the high-energy sector, here the relevant state is the doubly occupied combination $|d\rangle = \frac{1}{\sqrt{2}}(c^\dagger_{1\uparrow}c^\dagger_{1\downarrow} + c^\dagger_{2\uparrow}c^\dagger_{2\downarrow})|\,\rangle$ with the excitation energy U. The corresponding matrix element is $\langle d|(-t)\sum_\sigma(c^\dagger_{1\sigma}c_{2\sigma} + c^\dagger_{2\sigma}c_{1\sigma})|s\rangle = -2t$, the second-order effective Hamiltonian thus reads as

$$\mathcal{H}_{\rm eff}(E) = \frac{4t^2}{E-U}\,|s\rangle\langle s| \approx -\frac{4t^2}{U}\,|s\rangle\langle s|\,. \tag{2.115}$$

The above preference of singlet state of the two electron spins at every bond can be encoded into the final Heisenberg Hamiltonian

$$\mathcal{H} = J\sum_{\langle ij\rangle}\left(\boldsymbol{S}_i\cdot\boldsymbol{S}_j - \tfrac{1}{4}\right) \qquad \text{with} \quad J = \frac{4t^2}{U}\,. \tag{2.116}$$

A bit more involved is the evaluation of the superexchange interaction in cuprates [46] that serves as a good introductory example of a fourth-order calculation. Additional examples with more complex orbital structure will be presented in Secs. 3 and Sec. 4. Because the d shell is almost filled in this case, it is better to work with a hole representation using the configuration d^{10} as a "vacuum". In the undoped CuO_2 plane, each Cu^{2+} site with d^9 configuration is occupied by a hole that goes to the planar $d_{x^2-y^2}$ orbital. The lowest-order superexchange processes appear in fourth order in the p–d hopping and are depicted in Fig. 24. Again we need to consider one Cu–O–Cu bond only and this choice determines the active p orbital bridging the $d_{x^2-y^2}$ orbitals. To derive the superexchange, we start with singlet of the two holes $|s\rangle = \frac{1}{\sqrt{2}}(h^\dagger_{1\uparrow}h^\dagger_{2\downarrow} - h^\dagger_{1\downarrow}h^\dagger_{2\uparrow})|\,\rangle$. Here the empty state $|\,\rangle$ corresponds to the d^{10}–p^6–d^{10} bond configuration. Triplet configurations

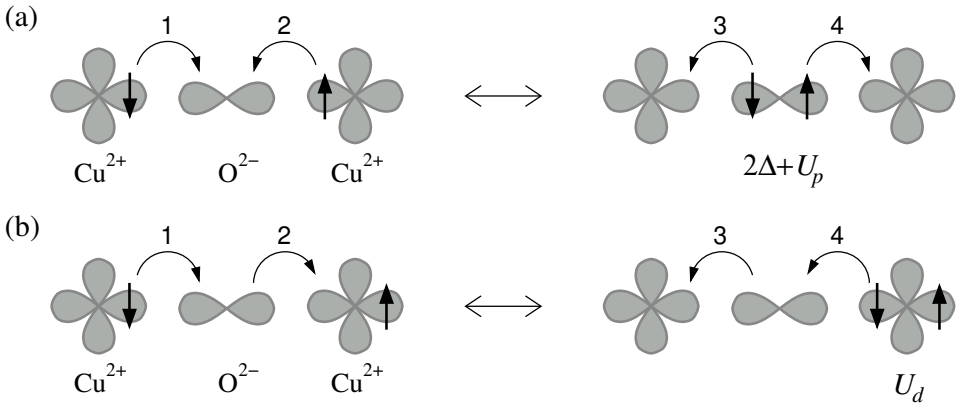

Fig. 24: (a) Virtual process of charge transfer type on a CuO_2 bond. Apart from two p-d excitations (each of the energy cost Δ_{pd}), the holes meeting in the oxygen p orbital experience Hubbard repulsion U_p. (b) Virtual process involving d-d transition. The energy cost of the intermediate state is the usual Hubbard repulsion U in the d orbital.

are again disqualified because the two holes have to meet at some point in a single orbital (either p or d). As shown in Fig. 24, after two p-d hoppings we can reach two kinds of intermediate states. In so-called charge-transfer process, the two holes meet at the oxygen ion. This state can be reached in two ways – the one shown in Fig. 24(a) and by a hopping sequence with interchanged hoppings 1 and 2. The other possibility is shown in Fig. 24(b) and corresponds to a d-d charge excitation. Here we can end up with two holes at the right Cu site (as depicted) or the left one. Collecting the possible hopping routes to get to the middle intermediate states, we obtain for the corresponding piece of the full fourth order formula

$$\mathcal{Q}\mathcal{V}\mathcal{Q}\,\frac{1}{E-\mathcal{Q}\mathcal{H}_0\mathcal{Q}}\,\mathcal{Q}\mathcal{V}\mathcal{P} = \frac{2\sqrt{2}\,t_{pd}^2}{E-\Delta_{pd}}\,|p_\uparrow p_\downarrow\rangle\langle s| + \frac{\sqrt{2}\,t_{pd}^2}{E-\Delta_{pd}}\,\big(|h_{1\uparrow}h_{1\downarrow}\rangle + |h_{2\uparrow}h_{2\downarrow}\rangle\big)\langle s|\,. \tag{2.117}$$

The intermediate state $|p_\uparrow p_\downarrow\rangle$ has energy $2\Delta_{pd}+U_p$ due to two p-d excitations and Hubbard repulsion of the two holes that meet at the bridging oxygen. The d-d excitations $|h_{1\uparrow}h_{1\downarrow}\rangle$ and $|h_{2\uparrow}h_{2\downarrow}\rangle$ have energy equal to Hubbard U_d for d orbitals. The final expression is obtained by using those energies in the denominator of the middle resolvent $\frac{1}{E-\mathcal{Q}\mathcal{H}_0\mathcal{Q}}$ of the fourth order formula and applying conjugate operator to that of (2.117) to get back to the initial state. Neglecting E in the denominators, we get for the two types of processes:

$$\mathcal{H}_{\text{eff}}^{(\text{CT})} \approx -\frac{8\,t_{pd}^4}{\Delta_{pd}^2(2\Delta_{pd}+U_p)}\,|s\rangle\langle s| \qquad \text{and} \qquad \mathcal{H}_{\text{eff}}^{(\text{dd})} \approx -\frac{4\,t_{pd}^4}{\Delta_{pd}^2 U_d}\,|s\rangle\langle s|\,, \tag{2.118}$$

which gives the superexchange constant

$$J = \frac{4t_{pd}^4}{\Delta_{pd}^2}\left(\frac{1}{\Delta_{pd}+\frac{1}{2}U_p}+\frac{1}{U_d}\right)\,. \tag{2.119}$$

Cuprates are charge-transfer insulators with $\Delta_{pd} < U_d$ (roughly by a factor of two), the first contribution to J is thus the larger one. As we can see the subdominant d-d contribution has the same form like the second-order result (2.116) with the effective d-d hopping $t = t_{pd}^2/\Delta_{pd}$.

As an illustration of the superexchange mechanism between two d^9 Cu^{2+} ions in a real material, we will discuss the interesting case of copper fluoride $KCuF_3$. Despite having a three-dimensional perovskite structure, this compound surprisingly hosts quasi one-dimensional magnetism. The key to the quasi-1D situation is the particular orbital arrangement due to Jahn-Teller

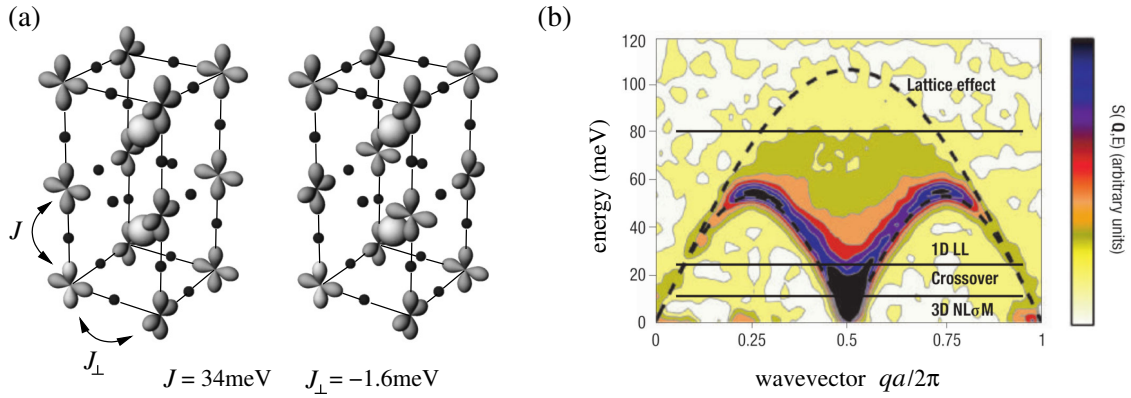

Fig. 25: (a) Two types of orbital ordering in $KCuF_3$ and the superexchange constants. The small balls represent fluorine ions, the larger ones potassium ions. Copper d-type orbitals form quasi one-dimensional chains (vertical) that are almost decoupled due to the orthogonality of orbitals. (b) Spin excitations in $KCuF_3$ measured by inelastic neutron scattering [47]. Dashed lines have the same meaning as in Fig. 22(b),(c).

effect [48]. The orbital ordering comes in two polytypes presented in Fig. 25(a). From the point of view of the superexchange mechanism, fluorine ions act similarly to oxygen ions. They have higher electronegativity and the relative energy levels change, but the physical picture shown in Fig. 24 is preserved. According to Fig. 25(a), the superexchange mechanism discussed above works only along one-dimensional chains formed by the properly oriented d orbitals. In the perpendicular direction the p-d hopping is broken due to orthogonality of the orbitals. As a consequence, the effective J between the chains is only about 5% of the intrachain one. The quasi-one-dimensionality is very clearly confirmed by the spin excitation spectrum in Fig. 25(b) obtained by inelastic neutron scattering [47]. It can be directly compared to the one calculated for a Heisenberg chain and presented in Fig. 22(c).

As a concluding remark let us note, that even though we tried to develop the perturbation expansion in a formally clean way, one should keep in mind that it frequently gives only indicative results. For example it may have problematic convergence due to insufficiently large ratio of the charge-excitation gap to the hopping amplitudes in the realistic parameter setup, the approach to the ionic states and hopping matrix elements may be too simplistic etc.

3 Kitaev materials

This part of the thesis is devoted to a more in-depth discussion of the so-called Kitaev materials that were briefly introduced in Sec. 1.4. They feature *highly anisotropic* and *bond-selective* spin interactions which result in a very peculiar magnetic behavior. Since these materials have been intensely studied in the last ten years, there already exists a large volume of literature which is pointless to review here since this task has been performed many times already and there are several review papers taking the subject from various perspectives [8–10,49–55]. Instead, we keep the "pedagogical" character of the text and focus on a few subjectively selected aspects that we consider essential.

Being armed with the tools developed in Sec. 2, we will first study the origin of the bond-selective interactions, highlighting the crucial role of the entanglement of spin and orbital degrees of freedom created by spin-orbit coupling and combined with the bond-selectivity of the hopping processes. The effective spin model derived for a simplified case will be later further extended and we will discuss its very rich phase diagram that is not fully explored up to now. In the last section of this part, we will consider the experimentally observed zigzag phase and illustrate, in the context of measured data, the specific features that appear in the regime with dominant Kitaev interaction.

3.1 Microscopic origin of the Kitaev interaction

The most heavily studied Kitaev materials Na_2IrO_3 and α-$RuCl_3$ are essentially a stack of honeycomb lattices made of edge-sharing octahedra as shown in Fig. 1(c) and Fig. 7. This is not the only option, the transition metal ions may form also three-dimensional structures such as the hyperhoneycomb [56] or harmonic honeycomb lattice [57] and other types of two-dimensional lattices, for instance the triangular [58] or kagome lattice [59], are considered theoretically as well. Two elements are common among the Mott insulating Kitaev magnets: (i) approximately 90° metal-oxygen-metal bonding, (ii) ionic ground state being a doublet generated by spin-orbit coupling. The latter is realized by the t_{2g}^5 configuration of $5d$ Ir^{4+} (see Refs. [60,61] for an interesting experimental verification of the complex spin-orbit entangled wavefunctions) or $4d$ Ru^{3+} ions with relatively large spin-orbit coupling and we will focus on this particular situation in the following, but even the $3d$ elements with smaller spin-orbit coupling may be relevant according to the recent proposals [62–64] for $t_{2g}^5 e_g^2$ Co^{2+} systems.

The above two elements generate highly anisotropic spin interactions as we will show by explicitly deriving the corresponding spin model. The local basis for the model is the $J = \frac{1}{2}$ doublet of t_{2g}^5 configuration that was thoroughly analyzed in Sec. 2.2.3. Choosing the z axis for $\boldsymbol{J}$ quantization, the two basis states read as

$$|\tilde{\uparrow}\rangle = \left(\sqrt{\tfrac{2}{3}}\, a_\downarrow^\dagger - \sqrt{\tfrac{1}{3}}\, b_\uparrow^\dagger\right)|t^6\rangle\,, \qquad |\tilde{\downarrow}\rangle = \left(\sqrt{\tfrac{1}{3}}\, b_\downarrow^\dagger - \sqrt{\tfrac{2}{3}}\, c_\uparrow^\dagger\right)|t^6\rangle\,. \tag{3.1}$$

Here we have used tilded arrows to emphasize that our local degree of freedom is $J = \frac{1}{2}$ pseudospin instead of a regular spin-$\frac{1}{2}$. The states are formulated as in Eq. (2.74) in terms of holes in t_{2g}^6 configuration created by the operators a, b, c of Eq. (2.56), corresponding to the $L_z^{\text{eff}} = +1,\, 0,\, -1$ eigenstates. The superposition of various spin and orbital labels in the pseudospin states leads to rather complex superexchange processes because the two orbital components have different fate when considering hopping on the honeycomb lattice as summarized in Fig. 26.

In the honeycomb lattice one encounters three types of bonds, each characterized by a different orientation of the square M_2O_2 plaquette with two 90° nearest-neighbor M–O–M bonds. The focus in Fig. 26(a),(b) is on a z-bond that is perpendicular to the cubic axis z. The bond direction

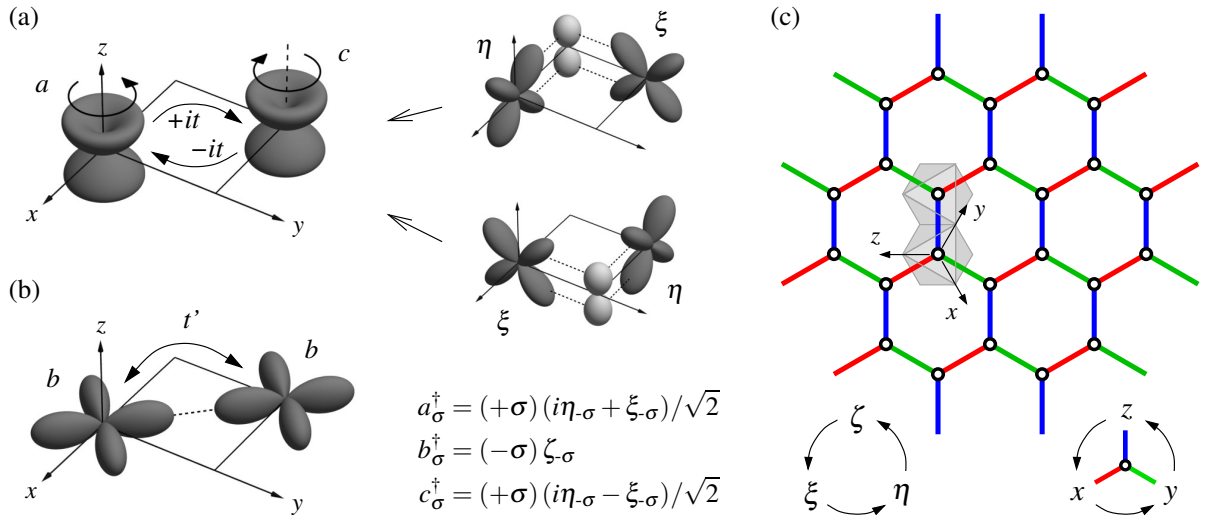

Fig. 26: (a) Oxygen-mediated hopping in the square M_2O_2 plaquette perpendicular to the cubic axis z. The two elementary bonding routes connecting ξ and η orbitals combine into imaginary hopping between a and c orbitals which changes $L_z^{\rm eff}$ by the maximum $\Delta L_z^{\rm eff} = \pm 2$. (b) Direct hopping connects primarily only b orbitals (i.e. ζ) and preserves therefore their $L_z^{\rm eff} = 0$. There is in addition a weaker $dd\pi$ and $dd\delta$ coupling between the other orbitals that we neglect. (c) Orientation of the two relevant octahedra for the z-bond used in panels (a) and (b) and cyclic exchange rules in the honeycomb lattice. When switching between the three bond directions, the definitions of a, b, c hole operators shown in the middle change by permuting the Cartesian orbitals ξ, η, ζ. This is a consequence of the corresponding rotation among the cubic axes x, y, z that can be used when the C_3 symmetry of the system is not broken.

selects the two orbitals active in the effective hopping mediated by oxygen ions, in this case they are $\xi \sim yz$ and $\eta \sim zx$ [see Fig. 26(a)]. The 90° bond geometry also allows for a significant direct overlap of the orbitals. Considering just the strongest $dd\sigma$ bonding, the direct hopping concerns only the orbital complementary to the above two [Fig. 26(b)]. In total, the electron hopping Hamiltonian on a z-bond takes the form

$$\mathcal{H}_{tt'} = t \sum_\sigma \left(\xi^\dagger_{i\sigma}\,\eta_{j\sigma} + \eta^\dagger_{i\sigma}\,\xi_{j\sigma}\right) - t' \sum_\sigma \zeta^\dagger_{i\sigma}\,\zeta_{j\sigma} + \text{H.c.}\,, \tag{3.2}$$

where $t = t^2_{pd\pi}/\Delta_{pd}$ and H.c. adds the opposite hopping direction $i \to j$. With the pseudospin basis being expressed using hole operators a, b, c, it is more convenient to switch to the hole picture and convert the above $\mathcal{H}_{tt'}$ to

$$\mathcal{H}_{tt'} = -it \sum_\sigma \left(a^\dagger_{i\sigma}\,c_{j\sigma} - c^\dagger_{i\sigma}\,a_{j\sigma}\right) + t' \sum_\sigma b^\dagger_{i\sigma}\,b_{j\sigma} + \text{H.c.} \tag{3.3}$$

For the other two bond directions, we can construct $\mathcal{H}_{tt'}$ based on Eq. (3.2) by a cyclic permutation as suggested in Fig. 26(c) or we can keep Eq. (3.3) and modify the a, b, c operators following the change of the $\boldsymbol{L}^{\rm eff}$ quantization axis from z to x or y.

Having clarified the hopping geometry, we can now proceed with the derivation of the effective pseudospin Hamiltonian following the scheme of the second-order perturbation theory as outlined in Sec. 2.4.2. Doing so we will adopt j-j coupling scheme to describe the virtual states and extend it with off-diagonal Hund's coupling. This approach is not the most practical one for the actual calculation but best exposes the internal structure of the superexchange processes. We start by considering the action of the perturbation $\mathcal{H}_{tt'}$ on a z-bond $\langle ij \rangle$ with two pseudospins up. When

including only the t contribution to the hole hopping in the direction $j \to i$, we generate d^4-d^6 intermediate state

$$|\tilde{\uparrow}\rangle_i \otimes |\tilde{\uparrow}\rangle_j = D^\dagger_{+\frac{1}{2}}|t^6\rangle_i \otimes D^\dagger_{+\frac{1}{2}}|t^6\rangle_j \xrightarrow{\text{hole hopping } j\to i \text{ via } t \text{ channel}} -it\sqrt{\tfrac{2}{3}}\, Q^\dagger_{-\frac{3}{2}} D^\dagger_{+\frac{1}{2}}|t^6\rangle_i \otimes |t^6\rangle_j \quad (3.4)$$

that we have written down using the doublet and quartet hole operators introduced in Eqs. (2.74) and (2.75) [see also Fig. 27(a) for a schematic picture]. The t_{2g}^4 state with two holes at site i can be decomposed into $|j_1, j_2; J, J_z\rangle$ states of j-j coupling scheme discussed near the end of Sec. 2.2.3. Explicitly they read as

$$\begin{aligned}
\left|\tfrac{3}{2},\tfrac{1}{2};1,-1\right\rangle &= \left(\tfrac{1}{2}\, Q^\dagger_{-\frac{1}{2}} D^\dagger_{-\frac{1}{2}} - \tfrac{\sqrt{3}}{2}\, Q^\dagger_{-\frac{3}{2}} D^\dagger_{+\frac{1}{2}}\right)|t^6\rangle\,, \\
\left|\tfrac{3}{2},\tfrac{1}{2};2,-1\right\rangle &= \left(\tfrac{\sqrt{3}}{2}\, Q^\dagger_{-\frac{1}{2}} D^\dagger_{-\frac{1}{2}} + \tfrac{1}{2}\, Q^\dagger_{-\frac{3}{2}} D^\dagger_{+\frac{1}{2}}\right)|t^6\rangle\,.
\end{aligned} \quad (3.5)$$

We can adopt a shorthand notation QD_{J,J_z} for d^4-d^6 bond configurations where the d^4 site is in the $|\frac{3}{2},\frac{1}{2};J,J_z\rangle$ state. The state at the right-hand side of Eq. (3.4) then decomposes as $\frac{it}{\sqrt{2}}QD_{1,-1} - \frac{it}{\sqrt{6}}QD_{2,-1}$. Considering now all four possible initial pseudospin configurations and including both t and t' hoppings in $\mathcal{H}_{tt'}$ in the direction $j \to i$, we arrive at the following set of d^4-d^6 intermediate states

$$\begin{aligned}
|\tilde{\uparrow}\rangle_i \otimes |\tilde{\uparrow}\rangle_j &\xrightarrow{\mathcal{H}_{tt'}(j\to i)} +\frac{it}{\sqrt{2}}\, QD_{1,-1} - \frac{it}{\sqrt{6}}\, QD_{2,-1} - \frac{t'}{3\sqrt{2}}\, QD_{1,+1} + \frac{t'}{\sqrt{6}}\, QD_{2,+1}\,, \\
|\tilde{\downarrow}\rangle_i \otimes |\tilde{\downarrow}\rangle_j &\xrightarrow{\mathcal{H}_{tt'}(j\to i)} -\frac{it}{\sqrt{2}}\, QD_{1,+1} - \frac{it}{\sqrt{6}}\, QD_{2,+1} - \frac{t'}{3\sqrt{2}}\, QD_{1,-1} - \frac{t'}{\sqrt{6}}\, QD_{2,-1}\,, \\
|\tilde{\uparrow}\rangle_i \otimes |\tilde{\downarrow}\rangle_j &\xrightarrow{\mathcal{H}_{tt'}(j\to i)} -it\sqrt{\frac{2}{3}}\, QD_{2,+2} + \frac{t'}{3}\, QD_{1,0} + \frac{t'}{3}\,(DD_0 - QD_{2,0})\,, \\
|\tilde{\downarrow}\rangle_i \otimes |\tilde{\uparrow}\rangle_j &\xrightarrow{\mathcal{H}_{tt'}(j\to i)} -it\sqrt{\frac{2}{3}}\, QD_{2,-2} + \frac{t'}{3}\, QD_{1,0} - \frac{t'}{3}\,(DD_0 - QD_{2,0})\,.
\end{aligned} \quad (3.6)$$

Here DD_0 is a shorthand notation for d^4-d^6 configuration with the site i populated by $|\frac{1}{2},\frac{1}{2};0,0\rangle$ of Eq. (2.80). These relations represent one key element of the derivation of the effective Hamiltonian using Eq. (2.114), the other being the excitation energies entering through the $(E-\mathcal{H})$ operator that acts in the subspace of high-energy virtual states. Before analyzing the latter ones, let us inspect the implications of Eqs. (3.6) themselves. In the case of purely t hopping, the virtual states are completely disconnected so that when leaving the virtual state by the second hopping, the initial pseudospin configuration will be restored. In such a case, the exchange interaction can only be of Ising-like form. This way we already arrive at the Kitaev interaction $K\widetilde{S}^z_i\widetilde{S}^z_j$ that is enabled only by differing excitation energies for $\tilde{\uparrow}\tilde{\uparrow}$, $\tilde{\downarrow}\tilde{\downarrow}$ and $\tilde{\uparrow}\tilde{\downarrow}$, $\tilde{\downarrow}\tilde{\uparrow}$ configurations because the integral matrix elements for the second order processes are equal: $(t/\sqrt{2})^2+(t/\sqrt{6})^2 = (t\sqrt{2/3})^2$. The direct hopping t' opens new possibilities and enables a cross-talk of the pseudospin configurations. The shared virtual states for the parallel pseudospin configurations $\tilde{\uparrow}\tilde{\uparrow}$ and $\tilde{\downarrow}\tilde{\downarrow}$ activate the effective process flipping both pseudospins at the same time: $\tilde{\uparrow}_i\tilde{\uparrow}_j \leftrightarrow \tilde{\downarrow}_i\tilde{\downarrow}_j$. In the case of the antiparallel configurations $\tilde{\uparrow}\tilde{\downarrow}$ and $\tilde{\downarrow}\tilde{\uparrow}$, we now have the possibility of the effective process $\tilde{\uparrow}_i\tilde{\downarrow}_j \leftrightarrow \tilde{\downarrow}_i\tilde{\uparrow}_j$ which is just a part of the usual Heisenberg exchange among the pseudospins. The parallel and antiparallel configurations remain mutually disconnected even with t' included.

When dealing with the excitation energies, we will include only U and J_H interactions, neglecting the effects of spin-orbit coupling in the virtual states. The situation is simple for the

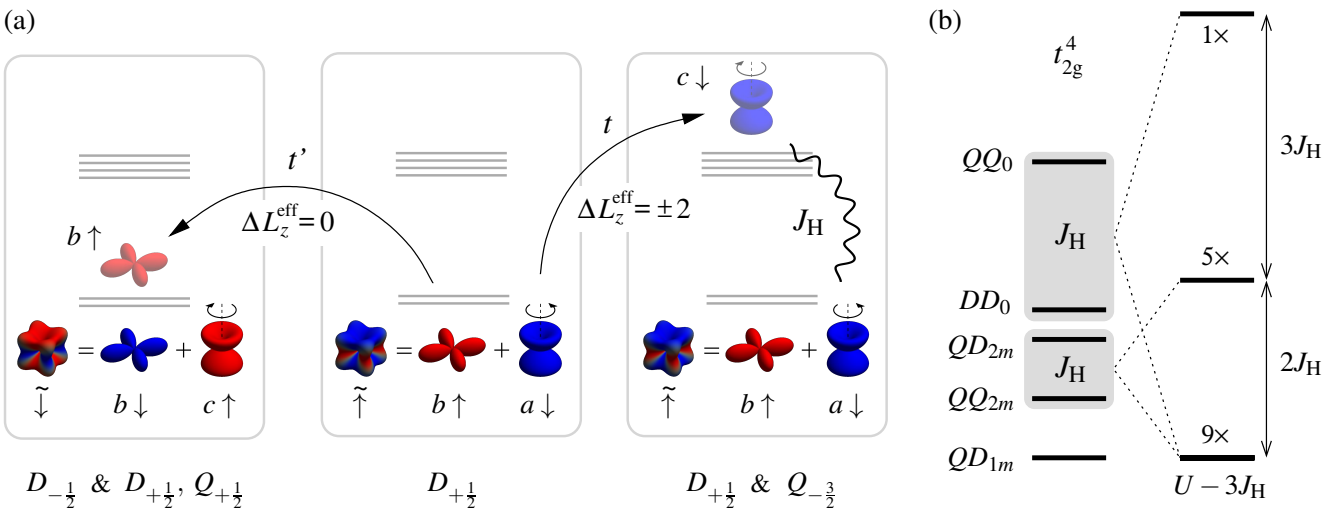

Fig. 27: (a) Virtual processes starting with a nearest-neighbor pair of $J=\frac{1}{2}$ pseudospins on a z-bond. The t' hopping operating on the b component of the pseudospins can generate usual Heisenberg exchange. The hopping t mediated by oxygens takes the a component of the pseudospin up and flips its $L_z^{\rm eff}$, producing a fully polarized quartet hole. To get back to two $J=\frac{1}{2}$ pseudospins this hole needs to be removed in the next step. If this happens via a backward t hopping, the initial pseudospin configuration is restored, enabling only Ising-type of exchange. The exchange is FM due to the Hund's coupling in the virtual state. (b) Multiplet structure of a t_{2g}^4 ion constructed by combining two $j=\frac{1}{2},\frac{3}{2}$ holes into total $\boldsymbol{J}$ eigenstates $|j_1,j_2,J,J_z\rangle$ and handling off-diagonal Hund's coupling afterwards. The lowest state is a threefold degenerate level QD_{1m} ($m=0,\pm1$) made of a quartet hole and a doublet hole that combine into total $J=1$ state. The pair of a quartet hole and a doublet hole may form also the total $J=2$ state QD_{2m} ($m=0,\pm1,\pm2$). Further possibilities include a pair of quartet holes combining into total $J=2$ state QQ_{2m} or total $J=0$ pairs DD_0 and QQ_0. Hund's coupling couples pairwise the QD_{2m} and QQ_{2m} states with the same m, as well as the pair of DD_0 and QQ_0 states (both options are marked by shading) and produces the energy levels of LS coupling scheme shown on the right. The indicated energies are excitation energies of the particular d^4-d^6 bond configuration with respect to the initial d^5-d^5 configuration of two $J=\frac{1}{2}$ pseudospins.

QD_{1m} excited states that are already composed of eigenstates of the respective ionic Hamiltonians. To evaluate the excitation energy, we need to consider the energy $6U-13J_{\rm H}$ of the t_{2g}^4 state and the energy $15(U-2J_{\rm H})$ of t_{2g}^6 configuration and compare them with the initial energy which is twice the energy $10(U-2J_{\rm H})$ of t_{2g}^5 configuration. We thus obtain

$$E_1 = U - 3J_{\rm H} \tag{3.7}$$

as the excitation energy to the QD_{1m} d^4-d^6 state. The case of QD_{2m} and DD_0 excitations is more complicated since these states are coupled via $J_{\rm H}$ to the combinations QQ_{2m} and QQ_0, respectively, that are not accessible by the hopping directly. As indicated in Fig. 27(b), this coupling restores the proper energy levels that would be simply described in LS coupling scheme. To get the effective excitation energies, we need to consider the two-dimensional subspaces spanned by the pairs QD_{2m}, QQ_{2m} and DD_0 [Eq. (2.80)], QQ_0 [Eq. (2.81)]. The latter case was already studied in Sec. 2.2.3 as an example. The corresponding Hamiltonians shifted by the energy of the d^5-d^5 configuration to give the excitation energies read as

$$H_{\rm exc} = E_1 + \frac{J_{\rm H}}{3}\begin{pmatrix} 4 & 2\sqrt{2} \\ 2\sqrt{2} & 2 \end{pmatrix} \qquad \text{and} \qquad H_{\rm exc} = E_1 + \frac{J_{\rm H}}{3}\begin{pmatrix} 5 & 5\sqrt{2} \\ 5\sqrt{2} & 10 \end{pmatrix}. \tag{3.8}$$

Since only the first member of the pair is accessed by the hopping, the matrix element $(H_{\rm exc}^{-1})_{11}$ of the inverse matrix to $H_{\rm exc}$ serves as the inverse excitation energy in the perturbation expansion (2.114). This gives us the effective excitation energies E_2 for QD_{2m} and E_0 for DD_0 state that can be inserted into the second-order perturbation term in a straightforward way. Consistently with Fig. 27(b), they are higher than E_1 and are explicitly given by $E_2^{-1} = E_1^{-1} - \Delta_2$ and $E_0^{-1} = E_1^{-1} - \Delta_0$ with the reduction factors

$$\Delta_2 = \frac{4}{3}\frac{J_{\rm H}}{(U-3J_{\rm H})(U-J_{\rm H})} \qquad \text{and} \qquad \Delta_0 = \frac{5}{3}\frac{J_{\rm H}}{(U-3J_{\rm H})(U+2J_{\rm H})}\,. \tag{3.9}$$

We are now ready to utilize Eqs. (3.6) and combine them together with the three excitation energies to obtain the effective Hamiltonian. It will have a form of a 4×4 matrix that is constructed by considering all the possible virtual connections of the four bond-basis states $\tilde{\uparrow}\tilde{\uparrow}$, $\tilde{\downarrow}\tilde{\downarrow}$, $\tilde{\uparrow}\tilde{\downarrow}$, $\tilde{\downarrow}\tilde{\uparrow}$. When doing so, we additionally multiply by two to include d^6-d^4 virtual states as well. In the final matrix, one can remove a constant shift

$$H_0 = -\frac{4}{3}\frac{t^2}{E_1} - \frac{5}{9}\frac{t'^2}{E_1} \tag{3.10}$$

found on the diagonal, since this overall kinetic energy gain is irrelevant for the pseudospin interactions. The resulting matrix contains the following nonzero matrix elements:

$$\begin{aligned} H_{11} = H_{22} &= +\frac{t'^2}{9E_1} + \frac{t^2+t'^3}{3}\,\Delta_2\,, & H_{21} = H_{12}^* &= \frac{2i\,tt'}{3}\,\Delta_2\,, \\ H_{33} = H_{44} &= -\frac{t'^2}{9E_1} + \frac{4t^2}{3}\,\Delta_2 + \frac{2t'^2}{9}\,(\Delta_2+\Delta_0)\,, & H_{34} = H_{43} &= \frac{2t'^2}{9}\left(\frac{1}{E_1} - \Delta_2 - \Delta_0\right)\,. \end{aligned} \tag{3.11}$$

To create a spin model, the effective interaction should be formulated using the pseudospin-$\frac{1}{2}$ operators $\widetilde{\boldsymbol{S}}$ acting on the $\tilde{\uparrow}$, $\tilde{\downarrow}$ basis states in the usual way. The structure of the effective Hamiltonian obtained perturbatively is reproduced if we consider the pseudospin-$\frac{1}{2}$ model

$$J\widetilde{\boldsymbol{S}}_i\cdot\widetilde{\boldsymbol{S}}_j + K\widetilde{S}_i^z\widetilde{S}_j^z + \Gamma(\widetilde{S}_i^x\widetilde{S}_j^y + \widetilde{S}_i^y\widetilde{S}_j^x)\,. \tag{3.12}$$

Expressing this Hamiltonian in the same bond basis $\tilde{\uparrow}\tilde{\uparrow}$, $\tilde{\downarrow}\tilde{\downarrow}$, $\tilde{\uparrow}\tilde{\downarrow}$, $\tilde{\downarrow}\tilde{\uparrow}$ as used above, we find

$$H_{\rm eff} = \begin{pmatrix} \frac{J+K}{4} & -i\frac{\Gamma}{2} & & \\ +i\frac{\Gamma}{2} & \frac{J+K}{4} & & \\ & & -\frac{J+K}{4} & \frac{J}{2} \\ & & \frac{J}{2} & -\frac{J+K}{4} \end{pmatrix} \tag{3.13}$$

which enables to quantify the values of the exchange parameters J, K, Γ by a comparison with the matrix elements in Eq. (3.11):

$$J = \frac{4t'^2}{9}\left(\frac{1}{E_1} - \Delta_2 - \Delta_0\right)\,, \qquad K = \left(-2t^2 + \frac{2}{3}t'^2\right)\Delta_2\,, \qquad \Gamma = \frac{4tt'}{3}\,\Delta_2\,. \tag{3.14}$$

Let us note that the derivation was performed for the particular case of the z-bond. Using the C_3 symmetry of the problem as illustrated in Fig. 26(c), the effective interaction for the other bond directions is obtained simply by cyclic permutation, for example on the level of the

pseudospin Hamiltonian (3.12) by replacing the x, y, z components of the pseudospin operators by the cyclically permuted ones.

The structure of the final expressions for the three exchange parameters highlights several aspects. First of all, the usual isotropic exchange of Heisenberg type originated only from the supposedly smaller t' hopping[13] and compared to the canonical cases (2.116) or (2.119) it is further reduced by factor of $\frac{1}{9}$ due to the relatively small participation of the relevant orbital in the pseudospin wavefunctions. There is no other contribution of the usual type t^2/U, the remaining terms are solely due to the Hund's coupling in the virtual states which brings a smallness factor of roughly $J_{\rm H}/U$. This is an important observation, suggesting that the overall energy scale of the interactions will be rather low. Among all those "small" interactions, the FM Kitaev interaction can be expected to be the dominant one, since it is generated by the larger t hopping. The off-diagonal exchange Γ resulting from a combined action of oxygen-mediated and direct hopping could be the second most important one, following our naive estimates. The interactions are thus expected to be highly anisotropic as it is indeed found experimentally.

Of course, our analysis considered only one class of virtual processes, namely the d-d transitions within the t_{2g} sector. There is a number of other contributing channels – one can additionally consider charge transfer processes and cyclic exchange (see [62] for a thorough discussion of those in the d^7 case), and involve also the e_g orbitals that are higher in energy than the t_{2g} ones but are coupled by stronger hopping amplitudes [c.f. the discussion related to Fig. 19(f)]. Moreover, the pseudospin wavefunctions become modified when including the trigonal splitting among t_{2g} orbitals that is present in the actual materials. Nevertheless, even our limited approach provided a number of insights concerning the emergence of strongly anisotropic and bond-selective spin interactions characteristic for Kitaev materials.

3.2 Extended Kitaev–Heisenberg model and its phase diagram

3.2.1 Effects of the trigonal splitting

In the previous section, we have considered an ideal case of two connected octahedra of undistorted shape and arrived at the $JK\Gamma$ model of Eq. (3.12) describing the effective interaction of $J = \frac{1}{2}$ pseudospins. A more realistic model should include also trigonal splitting of the t_{2g} orbitals that significantly modifies the pseudospin wavefunctions and brings a new interaction term that was not symmetry-allowed in the previous example. Below we will incorporate the effects of the trigonal distortion and later include also selected further-neighbor coupling to arrive at the final interaction Hamiltonian that is often used as a basic model for the magnetism of honeycomb Kitaev materials.

The trigonal splitting of orbitals arises in a twofold way. First, the structure of edge shared octahedra may be compressed (or elongated) in the direction perpendicular to the honeycomb plane, i.e. in the [111] direction in the cubic coordinate system associated with the octahedral axes. There are of course other types of possible distortion, breaking the C_3 symmetry of the lattice, but the trigonal one may be expected to have the largest impact. Second, the hopping of electrons supports the extension of their wavefunctions in the direction of the honeycomb plane, this effect thus acts similarly to the trigonal distortion. Formally, we need to amend the ionic Hamiltonian with the trigonal field that splits the a_{1g} orbital of Eq. (2.23) from the e_g^π pair of Eqs. (2.24) and (2.25). Following Eq. (2.29), this is achieved by the term $\Delta[(L_Z^{\rm eff})^2 - \frac{2}{3}]$ where Z is the out-of-plane direction as introduced in Fig. 9(c). On the level of point-charge model, the a_{1g} orbital should sink down under a trigonal compression which corresponds to positive Δ.

[13] As an example, Winter *et al.* [65] give ab-initio values $t \approx 0.25\,$eV and about ten times smaller t' for Na_2IrO_3, while for α-$RuCl_3$ the estimated t, t' are approximately the same 0.15 eV.

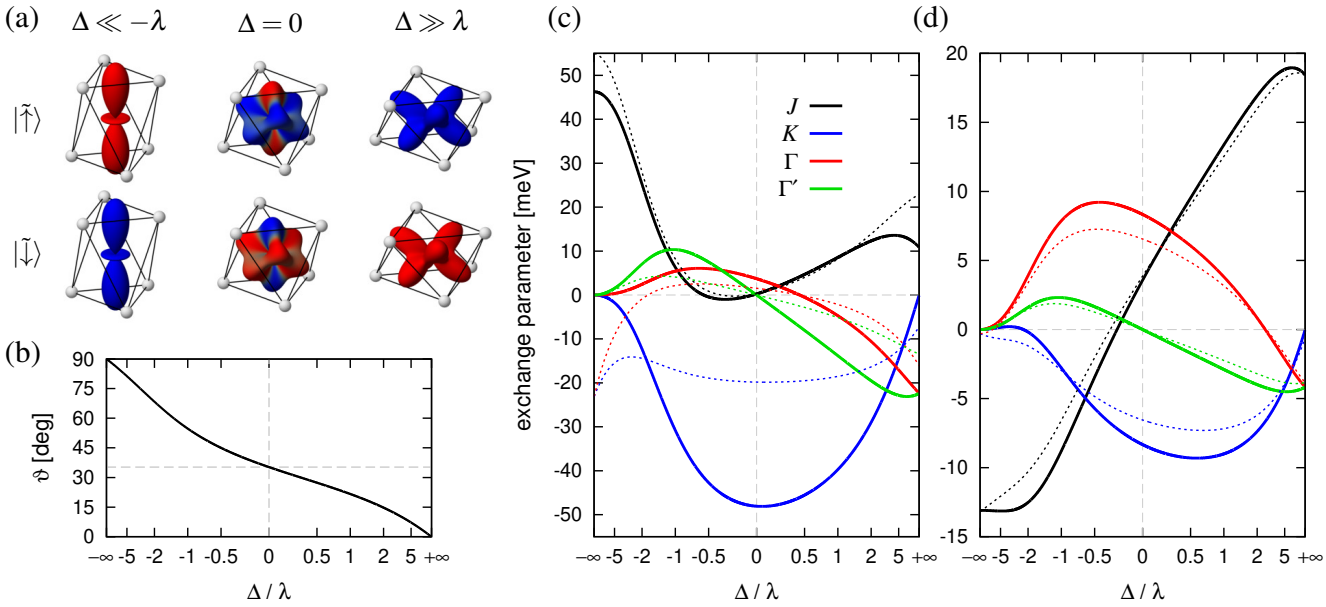

Fig. 28: (a) Pseudospin wavefunctions in the limit of large negative trigonal field Δ, cubic case with $\Delta = 0$, and the limit of large positive trigonal field Δ. The graphical representation shows the hole distribution in the same way as in Fig. 13. The shapes in the $\Delta = 0$ limit are again cubic but the spin polarization distribution is modified because of the Z quantization axis that applies to both $\boldsymbol{L}^{\text{eff}}$ and $\boldsymbol{S}$. (b) Mixing angle ϑ entering Eq. (3.15) as it depends on the trigonal field. (c) Exchange parameters resulting from second order perturbation theory with $U = 1.7\,\text{eV}$, $J_{\text{H}} = 0.3\,\text{eV}$, $\lambda = 0.4\,\text{eV}$, $t = 0.26\,\text{eV}$, $t' = 0.03\,\text{eV}$. Solid lines are calculated neglecting spin-orbit coupling in the virtual states, dotted lines include this effect. (d) The same for the values $U = 3.0\,\text{eV}$, $J_{\text{H}} = 0.6\,\text{eV}$, $\lambda = 0.15\,\text{eV}$, $t = 0.15\,\text{eV}$, $t' = 0.15\,\text{eV}$. The parameter sets are inspired by Ref. [65] and are supposed to imitate the situation in Na_2IrO_3 and α-$RuCl_3$, respectively. To have continuous evolution of the exchange parameters, we had to change the relative phase of the two pseudospin wavefunctions below $\Delta = -2.25\lambda$.

When adopting the hole picture to get the t_{2g}^5 pseudospin states, we need to revert the sign and diagonalize $\mathcal{H} = \lambda \boldsymbol{S} \cdot \boldsymbol{L}^{\text{eff}} - \Delta (L_Z^{\text{eff}})^2$. The new Hamiltonian still conserves one component of $\boldsymbol{J}$, namely J_{Z}, but does not conserve J^2 as it did before. The extra term mixes members of the $J = \frac{1}{2}$ doublet and $J = \frac{3}{2}$ quartet with matching J_Z. The wavefunctions of the lower doublet are then modified to

$$|\tilde{\uparrow}\rangle = \left(\cos\vartheta\; a_\downarrow^\dagger - \sin\vartheta\; b_\uparrow^\dagger\right)|t^6\rangle\,, \quad |\tilde{\downarrow}\rangle = \left(\sin\vartheta\; b_\downarrow^\dagger - \cos\vartheta\; c_\uparrow^\dagger\right)|t^6\rangle\,, \quad \tan 2\vartheta = \frac{2\sqrt{2}}{1 + \frac{2\Delta}{\lambda}}\,. \tag{3.15}$$

The shapes and spin polarization of the hole densities corresponding to the above pseudospin wavefunctions are presented in Fig. 28(a) and the orbital mixing angle ϑ in Fig. 28(b), covering the whole range of ratios of the trigonal field Δ to the spin-orbit coupling λ. For the cubic case with $\Delta = 0$, the mixing angle takes the "magic" value of $\vartheta = \frac{1}{2}\arctan(2\sqrt{2}) = \arctan(1/\sqrt{2}) \approx 35.26°$ that is at the same time the angle of the cubic axes to the honeycomb plane. With this value, the cubic pseudospin wavefunctions of Eq. (3.1) are reproduced. In contrast to the $J_Z = \pm\frac{1}{2}$ quartet state, the $J_Z = \pm\frac{3}{2}$ ones are unaffected by the mixing so that the quartet splits into two doublets. Such a splitting may be accessible experimentally e.g. by a resonant inelastic x-ray scattering, enabling a quantification of the trigonal field Δ [66].

Performing the same kind of perturbation calculation as in the previous section, but starting with the low-energy doublet (3.15), we can derive the effective pseudospin Hamiltonian including

now an extra anisotropic interaction Γ' that scales linearly with the trigonal splitting near the cubic limit. At a nearest-neighbor z-bond, the pseudospin interaction reads as

$$\mathcal{H}_{\langle ij\rangle\|z} = J\widetilde{\boldsymbol{S}}_i \cdot \widetilde{\boldsymbol{S}}_j + K\widetilde{S}_i^z\widetilde{S}_j^z + \Gamma(\widetilde{S}_i^x\widetilde{S}_j^y + \widetilde{S}_i^y\widetilde{S}_j^x) + \Gamma'(\widetilde{S}_i^x\widetilde{S}_j^z + \widetilde{S}_i^z\widetilde{S}_j^x + \widetilde{S}_i^y\widetilde{S}_j^z + \widetilde{S}_i^z\widetilde{S}_j^y)\,. \tag{3.16}$$

To get the interactions at other bond directions, we again apply the cyclic permutation as shown in Fig. 26(c). This form of the Hamiltonian already includes all the symmetry-allowed nearest-neighbor terms compatible with the C_3 symmetry of the lattice and is often called as the extended Kitaev-Heisenberg model. Further often employed extension consists in including further neighbor couplings that are likely to be significant due to the extended nature of $4d$ and $5d$ orbitals. Among these, Heisenberg third-neighbor coupling J_3 seems to be most important.

Before inspecting the phase diagram of the model, it is instructive to have a look at the interaction parameters as functions of the trigonal splitting presented in Fig. 28(c),(d). We use two sets of microscopic parameters that roughly correspond to the values suggested by Winter *et al.* [65] for Na_2IrO_3 and α-$RuCl_3$, respectively. Being $5d$ and $4d$ materials, they differ in the relative strength of the spin-orbit coupling and Hund's coupling. In the case of Fig. 28(c), these two energy scales are comparable, $J_H \lesssim \lambda$. This cast some doubts at the approximation made in the previous section, i.e. neglecting spin-orbit coupling in the virtual states. Indeed, if both spin-orbit coupling and Hund's coupling are incorporated in the virtual states and excitation energies, some of the newly obtained interaction parameters show a significant reduction. Most importantly, this concerns the Kitaev interaction K, which still remains dominant, however. The situation is much different in Fig. 28(d) that illustrates the $J_H \gg \lambda$ regime relevant for $4d$ Ru^{3+} ions. Here the difference caused by the neglection of spin-orbit coupling in the virtual states is rather minor. The set of parameters used in this case also assumes equal hopping amplitudes $t = t'$. As can be expected based on Eq. (3.14), this choice makes the anisotropic interactions K and Γ of the same order of magnitude.

Regarding the dependence on the trigonal field, we note that the interaction is most anisotropic near the cubic limit. The reason is that the trigonal field, either positive or negative, quenches further the orbital angular momentum and makes the interactions more Heisenberg-like. For a large trigonal compression, the pseudospin is reduced to the e_g^π doublet states having entangled spin and the only unquenched L_Z^{eff} orbital component. This leaves space for Ising-like anisotropy with differing interactions of the in-plane and out-of-plane components. When worked out, such a constraint implies $K = 0$ and $\Gamma = \Gamma'$ as can be indeed observed in Fig. 28(c),(d). In the opposite limit – large negative trigonal splitting – the orbital component is completely suppressed and we are left with spin-$\frac{1}{2}$ residing in the a_{1g} orbital. The interaction is then necessarily isotropic and only the parameter J takes a nonzero value. Note, that in this limit the wavefunctions as introduced in Eq. (3.15) bring an extra minus sign to the relative phase of $|\tilde{\uparrow}\rangle$ and $|\tilde{\downarrow}\rangle$, so that at some point we have to redefine the pseudospin to match the spin-$\frac{1}{2}$ carried by the a_{1g} orbital.

3.2.2 Phase diagram of the extended Kitaev-Heisenberg model

The main attraction of the Kitaev materials is of course the connection to the Kitaev honeycomb model for spins-$\frac{1}{2}$ [18] that appears as a special case of the pseudospin model in Eq. (3.16) when J, Γ and Γ' are zero. In this limit the model is exactly solvable and at the same time it features an exotic ground state – quantum spin liquid touched upon in the introductory Sec. 1.4. An essential element of the exact solution [18] is the exploitation of an extensive set of conserved quantities. These are associated with the individual hexagonal plaquettes of the honeycomb lattice and are constructed as a product W_p of six spin operators indicated in Fig. 29(a). The conserved quantities have eigenvalues ± 1 and by considering all the possible distributions of $+1$'s and -1's at the plaquettes of the honeycomb lattice we exhaust the Hilbert space of the model

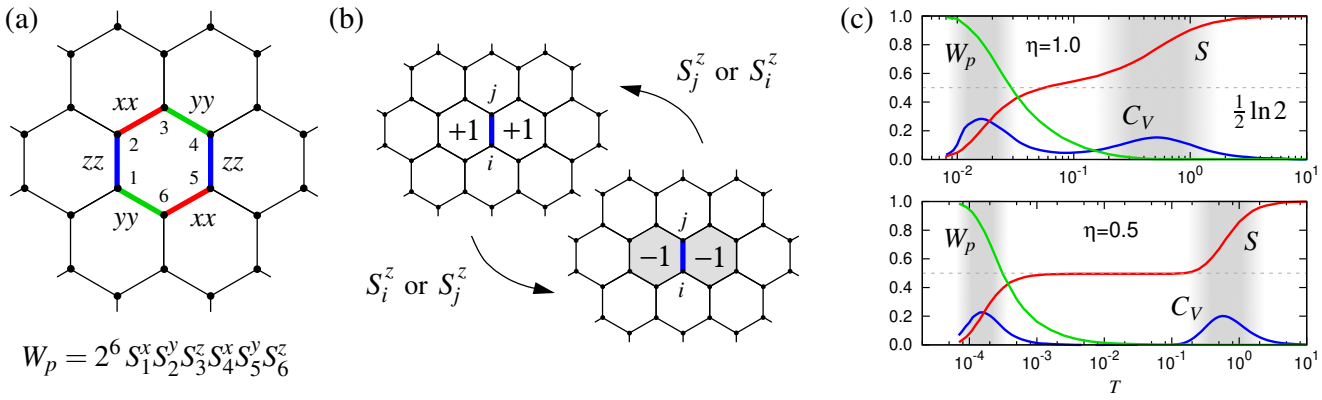

Fig. 29: (a) Conserved plaquette quantity W_p of the Kitaev model. (b) Origin of the local nature of spin correlations $\langle S_i^\alpha S_j^\beta \rangle$ that are limited to nearest-neighbor bonds. When acting by a spin operator on the flux-free ground state of the Kitaev model, two fluxes are generated at the adjacent plaquettes and need to be removed again when applying the second spin operator. Moreover, there is a link between the spin component and the orientation of the pair of the concerned plaquettes, making the correlations highly anisotropic – only the component $\langle S_i^\alpha S_j^\alpha \rangle$ is nonzero at α-bond. (c) Temperature-dependent specific heat C_V, entropy S, and thermal average of the plaquette quantities W_p for the Kitaev honeycomb model. The upper panel shows results for the isotropic version with equal Kitaev interaction strength for all bond directions, $K_x = K_y = K_z$ [c.f. Eq. (1.4)], the lower panel is for the anisotropic situation $K_x = K_y = \eta/3$, $K_z = 1 - 2\eta/3$ with $\eta = 0.5$. Shading indicates the two crossover temperature ranges. At lowest temperatures the ground-state sector without fluxes dominates, hence $\langle W_p \rangle \approx 1$. In the middle regime, the plaquette quantities W_p fluctuate and $\langle W_p \rangle \approx 0$. The entropy per site staying flat around $\frac{1}{2}\ln 2$ in certain interval of temperatures suggests the fractionalization of spins-$\frac{1}{2}$ into two parts (these are the localized and running Majorana fermions) that breaks down at higher temperatures where $S \approx \ln 2$ corresponding to spin-$\frac{1}{2}$. Panel (c) is adapted from Ref. [67].

by disconnected subspaces. When utilizing the Majorana spin representation (here for Pauli spin operators $\sigma_\alpha = 2S_\alpha$)

$$\sigma_x = ib_x c, \qquad \sigma_y = ib_y c, \qquad \sigma_z = ib_z c \tag{3.17}$$

that employs the "gauge" Majorana fermions b_α and "matter" fermions c, we find that the b_α fermions are static and become constituents of W_p quantities while c fermions are freely running on the lattice. In this representation the diagonalization of the spin Hamiltonian is thus equivalent to a problem of noninteracting Majorana fermions hopping in a magnetic background which can be easily solved. The magnetic background differs in each of the symmetry sectors, i.e. subspaces of states with different configurations of W_p's. The spin liquid ground state is found in the homogeneous sector with $W_p = +1$ at every plaquette. The above diagonalization procedure applied to this sector shows that the spectrum of excitations that inherit unusual fermionic character is gapless. However, this does not imply that we are dealing here with gapless magnetic excitations. In fact, by applying the spin operator at a selected site, we flip two plaquette quantities W_p from $+1$ to -1 as shown in Fig. 29(b). From the viewpoint of the Majorana fermion representation, we have introduced two magnetic fluxes at those plaquettes. This brings us out of the ground-state $W_p = +1$ sector and costs certain energy that appears as a spin gap in the magnetic excitation spectra [68, 69]. This feature also leads to short-range spin correlations limited to nearest neighbors. When evaluating the static correlator $\langle S_i^\alpha S_j^\beta \rangle$, the first application of the S_j^β flips W_p at two hexagons attached to site j (the particular pair is decided by β) and this defect has to be restored by the application of S_i^α which requires i to be either equal to j (trivial) or forming a nearest-neighbor bond. As a consequence, there

cannot be nonzero spin correlations beyond nearest neighbors. Despite the relatively simple exact solution, the evaluation of thermodynamic quantities for the Kitaev model is challenging. As a reward we can observe an interesting hierarchy of regimes that appear due to the combination of fermionic excitations and fluxes with finite cost [67,70]. There are two characteristic temperature scales, that can be clearly identified in the temperature-dependent specific heat or entropy as illustrated by Fig. 29(c). Below the lower one the thermodynamics is given by Majorana fermionic excitations within the flux-free ground-state sector (all $W_p = +1$). Above this temperature scale, thermally excited fluxes start to appear and disturb running Majorana fermions. These can still maintain their coherent motion, however. Finally, above the higher temperature scale the fractionalization of spins into Majorana fermions is lost and the system behaves as a thermally excited paramagnet.

While the fancy features such as spin liquid with short-range correlations or fermionic character of excitations are appealing theoretically, the actual materials do not realize the pure Kitaev limit and are less frustrated anisotropic magnets that support long-range order. Their magnetic behavior can be explained by invoking the other terms of the extended Kitaev-Heisenberg model (3.16) that "spoil" the Kitaev limit but on the other hand make the systems more approachable by methods developed for conventional spin systems.

A central issue related to the Kitaev materials, for instance Na_2IrO_3 or α-$RuCl_3$, is the identification of the relevant parameter regime. To estimate it from first principles is not a simple task since, as we have learned in Sec. 3.1, the typical leading superexchange contribution $\propto t^2/U$ is missing and the balance of the existing subleading interactions largely depends on microscopic details. Accepting the form of the extended Kitaev-Heisenberg model, we can get to the values of the model parameters by evaluating various measurable quantities within the model and comparing them to experimental data. The first experimental constraint is the presence of long-range magnetic order of zigzag type [71–74] in both abovementioned compounds.[14] This observation calls for a determination of the phase diagram of the model. Due to the high anisotropy and several participating interactions, it is quite complex in its entirety and some of its parts are still being debated. In general this concerns the more frustrated regions with potential spin liquid ground states [76,77], in most of its parameter space the extended Kitaev-Heisenberg model shows long-range orderings that are well understood. In Fig. 30 we try to give an idea of the above complexity, presenting selected sections through the phase diagram obtained by two methods.

In the first one we stay on the classical level, treating spins as regular vectors of fixed length $\frac{1}{2}$ in Eq. (3.16) and trying to optimize their orientations to minimize the resulting classical energy. One of the possible approaches, that is also used in Fig. 30(a)-(c), is the Luttinger-Tisza method first introduced in Ref. [78] when studying crystals with dipolar interactions and later conveniently reformulated to the Fourier domain [79]. Here one represents the spins on the two sublattices A, B of the honeycomb lattice by Fourier expansions $\boldsymbol{S}_{A\boldsymbol{R}} = \sum_{\boldsymbol{q}} \mathrm{e}^{i\boldsymbol{q}\boldsymbol{R}} \boldsymbol{S}_{A\boldsymbol{q}}$ and $\boldsymbol{S}_{B\boldsymbol{R}} = \sum_{\boldsymbol{q}} \mathrm{e}^{i\boldsymbol{q}\boldsymbol{R}} \boldsymbol{S}_{B\boldsymbol{q}}$ with $\boldsymbol{R}$ denoting the unit cell position. Due to the translational symmetry, the spin Hamiltonian then assumes the form

$$\mathcal{H} = \sum_{\boldsymbol{q}} \Psi_{\boldsymbol{q}}^\dagger H_{\boldsymbol{q}} \Psi_{\boldsymbol{q}}\,, \qquad \text{where} \qquad \Psi_{\boldsymbol{q}} = \begin{pmatrix} \boldsymbol{S}_{A\boldsymbol{q}} \\ \boldsymbol{S}_{B\boldsymbol{q}} \end{pmatrix}. \tag{3.18}$$

The explicit forms of the 6×6 matrices $H_{\boldsymbol{q}}$ can be found e.g. in Ref. [80]. Treating spins classically in Eq. (3.18), we would have to minimize the energy under the constraint $|\boldsymbol{S}_{A\boldsymbol{R}}|^2 = |\boldsymbol{S}_{B\boldsymbol{R}}|^2 = \frac{1}{4}$ that should be valid for each $\boldsymbol{R}$. This is complicated to achieve in the Fourier representation

[14] One can also find spiral orders such as that observed in α-Li_2IrO_3 [75], these can be still captured on the level of highly anisotropic models of extended Kitaev-Heisenberg type.

but in Luttinger-Tisza method one makes an approximation that the above constraints should be satisfied *on average* only, i.e. $\sum_{\boldsymbol{R}}(|\boldsymbol{S}_{A\boldsymbol{R}}|^2 + |\boldsymbol{S}_{B\boldsymbol{R}}|^2) = \frac{1}{4}N$ with N being the total number of spins. Minimization under this relaxed constraint which translates to the requirement of constant $\sum_{\boldsymbol{q}} \Psi_{\boldsymbol{q}}^\dagger \Psi_{\boldsymbol{q}}$ is simple, one just evaluates the eigenvalues of the matrices $H_{\boldsymbol{q}}$ and finds the lowest one among them. The solution found this way has to satisfy the original spin-length constraints otherwise the Luttinger-Tisza methods is said to fail for that parameter point. In such cases an alternative method is needed, for example Monte Carlo minimization of the classical energy for a large piece of the honeycomb lattice.

The second method is fully quantum and consists in finding the ground state of a small honeycomb cluster via exact diagonalization. For this clearly finite-size system, the symmetry cannot be spontaneously broken and instead of a single ordered state, we find a fluctuating superposition of all the degenerate possibilities. To disentangle the information about potential orderings, the ground state can be analyzed by the method of spin coherent states introduced in Ref. [81]. Here one works with the coherent spin-$\frac{1}{2}$ states that "point" in certain directions and based on them assembles a product state for the cluster that best fits its exact ground state. To put things explicitly, let us capture the direction by a unit vector $\boldsymbol{n}$ and denote by $|\boldsymbol{n}\rangle$ spin-$\frac{1}{2}$ state that is an eigenstate of $\boldsymbol{n}\cdot\boldsymbol{S}$ operator (i.e. the component of $\boldsymbol{S}$ in the direction of $\boldsymbol{n}$) with the eigenvalue $+\frac{1}{2}$. Using spherical coordinates, we get $\boldsymbol{n} = (\cos\phi\sin\theta, \sin\phi\sin\theta, \cos\theta)$ and $|\boldsymbol{n}\rangle = \mathrm{e}^{-i\phi/2}\cos\frac{\theta}{2}|\uparrow\rangle + \mathrm{e}^{-i\phi/2}\sin\frac{\theta}{2}|\downarrow\rangle$. Based on a set of spin coherent states for the individual sites we define a product state of the N-site cluster as $|\Psi\rangle = |\boldsymbol{n}_1\rangle\otimes|\boldsymbol{n}_2\rangle\otimes\ldots\otimes|\boldsymbol{n}_N\rangle$ and measure its overlap with the ground state $|\mathrm{GS}\rangle$. The ordering pattern is then detected by varying the directions $\boldsymbol{n}_i$ and trying to maximize the probability $P(\boldsymbol{n}_1\ldots\boldsymbol{n}_N) = |\langle\Psi|\mathrm{GS}\rangle|^2$. This approach provides a relatively good overview of the phase diagram including details of the ordered phases and is consistent, apart from a few problematic regions, with more advanced but less transparent numerical approaches such as DMRG [82] or tensor networks [83, 84] used to investigate certain parameter regions of the model.

The rich phase diagram of the extended Kitaev-Heisenberg model that is partially revealed by Fig. 30 contains a few phases that can be anticipated in the various limits of the model. These include the ferromagnetic (FM) and antiferromagnetic (AF) phases linked to $J < 0$ and $J > 0$ Heisenberg limit, respectively, which are very extended in contrast to the Kitaev spin liquid phases found in the Kitaev-limit areas of FM or AF character [see Fig. 30(d)]. The Kitaev spin liquid state is able to withstand only a rather limited amount of non-Kitaev perturbations and gives up soon enabling a development of a long-range order. Apart from the expected FM and AF order, there is in addition a stripy one, two types of zigzag order differing in the direction of the ordered moments, and two non-collinear orders of vortex type (only one of them appears in the sections shown in Fig. 30). The respective ordering patterns are presented in Fig. 30(g)-(k). In fact, by using nontrivial sublattice-dependent spin rotations, the model can be shown [80] to be equivalent to Heisenberg model for certain parameter combinations – points of hidden SU(2) symmetry. These hidden relations give somewhat deeper insight into the location and characteristics of the individual phases [80, 85]. The stripy and zigzag phases were found to be related to the FM and AF Heisenberg points by a four-sublattice transformation and the vortex phase seen in Fig. 30 was linked to the FM Heisenberg point by a six-sublattice transformation. A problematic part of the phase diagram for the exact diagonalization method limited to small clusters is the area indicated by the IC label. It is partially covered by incommensurate spiral phase but it may also host further spin liquid phases not directly linked to the closest Kitaev point [76, 77].

We are not going to discuss the details of the phase diagram and the (hidden) symmetry properties of the model that were thoroughly analyzed e.g. in Ref. [85]. Instead, we briefly inspect the experimentally relevant zigzag phases. As already mentioned, there are two distinct

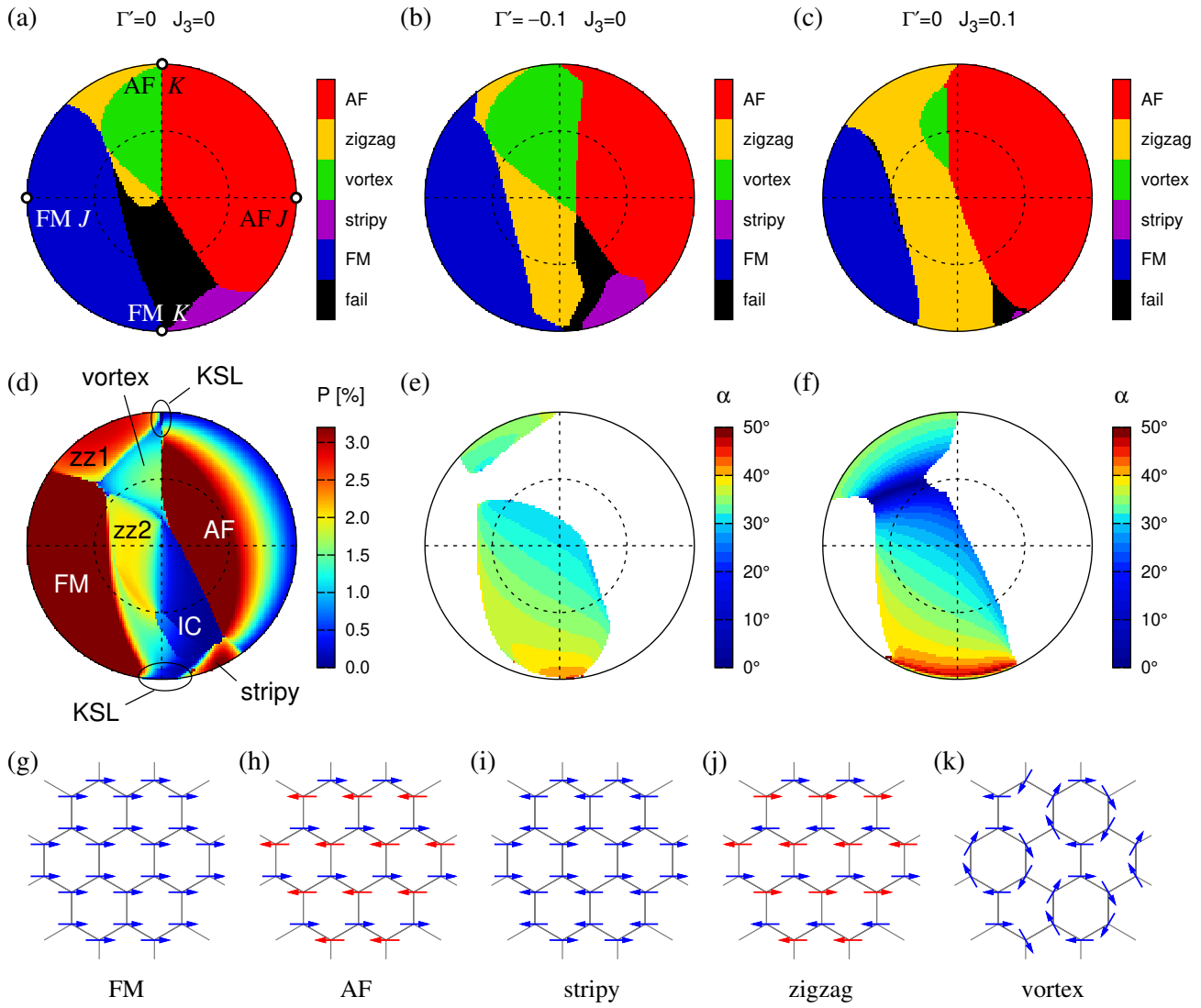

Fig. 30: (a) Classical phase diagram of the extended Kitaev-Heisenberg model as obtained by the Luttinger-Tisza method. The interactions are parametrized as $J = \sin\theta\cos\phi$, $K = \sin\theta\sin\phi$, $\Gamma = \cos\theta$ with θ being the radial coordinate in the circle (distance from the center varying from 0 up to $\pi/2$ at the outer rim) and ϕ being the conventional polar angle measured from the horizontal axis. Four points of purely Heisenberg or Kitaev character at the outer rim are indicated by dots. In the black region the Luttinger-Tisza method suggests an incommensurate order. (b) The same with fixed nonzero $\Gamma' = -0.1$. (c) The same as in (a) with fixed nonzero third-neighbor Heisenberg exchange $J_3 = 0.1$. (d) Phase diagram obtained by coherent-state analysis of the exact ground states for 24-site cluster. Shown are the added probabilities of coherent states with zigzag (unscaled), ferromagnetic (unscaled), antiferromagnetic (reduced 10 times), stripy (reduced 5 times), and vortex (reduced 10 times) patterns. The values above 3.2% are shown using the topmost color of the scale. The AF phase extends up to the outer rim, its probability gets reduced there due to increased quantum fluctuations compared to the inner part of the circle. Tiny patches of Kitaev spin liquid (KSL) phase are encircled. The large area showing almost zero probability hosts an incommensurate (IC) or large-unit-cell order. (e) Zigzag region in the phase diagram with fixed $\Gamma' = -0.1$ obtained by the same method as in panel (d). The area with $P(\text{zigzag}) \geq 0.5\%$ is highlighted. The color indicates the angle of the ordered moments to the honeycomb plane. (f) The same as in panel (e) for fixed $J_3 = 0.1$. (g–k) Pseudospin patterns of the commensurate ordered phases.

zigzag phases. They are not completely unrelated, however, according to Ref. [80] one can actually find a dual transformation of the model that converts one into another. The ordered

moments in the upper phase zz1 of Fig. 30(d) prefer one of the cubic axes x, y, z, depending on the direction of the zigzag chains. For the pattern shown in Fig. 30(j) with zigzag chains running along the x and y bonds, the ordered moments are close to (or coinciding with) the z axis. This spin arrangement is stabilized in the regime of large AF $K > 0$ that profits from the AF correlations of z pseudospin components at the vertical bonds and FM $J < 0$ interaction that, being component-insensitive, gains energy due to FM correlations at the majority of bonds (FM x and y bonds versus AF z bonds). The lower zigzag phase zz2 has the ordered moments pointing along an almost orthogonal direction, for the pattern in Fig. 30(j) they are found roughly inbetween the cubic x and y axes. In this case, the zigzag order is supported by large FM $K < 0$ that exploits the FM correlated x and y pseudospin components on the zigzag chains formed by x- and y-bonds, and large $\Gamma > 0$ interaction that contributes on the interchain z-bonds where it simultaneously utilizes the conveniently oriented x and y components of the pseudospins. The latter situation is observed experimentally, in agreement with the microscopic expectations of the ferromagnetic Kitaev interaction and positive Γ interaction (see [53] and references therein) that we have found also in Sec. 3.1 based on a simplified calculation. As illustrated in Fig. 30(e), the zigzag phase zz2 is supported by negative Γ' interaction (i.e. positive crystal field Δ). The phase zz1 does not feature the properly correlated pseudospin components compatible with the negative Γ' interaction and is supported by small positive Γ' instead. Both zigzag phases benefit from the anticipated third-nearest-neighbor Heisenberg interaction J_3 that accepts any moment direction in the zigzag arrangement [see Fig. 30(f)]. The precise ordered moment direction is decided by the balance of the anisotropic interactions K, Γ, Γ' and can be used as a guide to narrow down the relevant parameter region [81]. It is automatically resolved by the method of coherent states and indicated in Figs. 30(e),(f) to give an example of this effect.

Finally, let us note that while the qualitative appearance of the phase diagrams obtained classically [Fig. 30(a)-(c)] and by exact diagonalization of a cluster Hamiltonian [Fig. 30(d)-(f)] is quite similar, the precise positions of the phase boundaries may differ significantly. Generally speaking, the phases involving stronger quantum fluctuations (AF, zigzag) become more extended when going from the classical to the quantum calculation since the properly included quantum fluctuations bring them an energy advantage in the competition with the less fluctuating phases (FM, stripy, vortex). These trends are clearly visible in Fig. 30.

3.3 Specific features of the zigzag phase in the regime of the dominant Kitaev interaction

Focusing now on the zigzag phase, we will study a few signatures of the highly anisotropic and bond-selective pseudospin interactions that appear in static and dynamic pseudospin correlations. The component- and bond-selective Kitaev interaction induces anisotropic and bond-dependent correlations of the pseudospins. This is true not only for the ordered states, as it has been discussed in the previous section, but can be observed also in the short-range correlated state above the ordering temperature.

In the case when the model supports zigzag ordering, the state above T_N contains – in a short-range correlated form – all three possible zigzag patterns depicted in Fig. 31(a). Each of them is characterized by different preferred direction of the pseudospin moments and at the same time corresponds to different pair of characteristic wavevectors [Bragg spots shown in Fig. 31(a)]. This link enables a direct experimental proof of anisotropic bond-selective interactions in a real Kitaev material by measuring momentum-dependent correlations of the pseudospins resolved into the individual components. For example, assuming the above FM $K < 0$ situation, the zigzag pattern with FM chains along x and y bonds places pseudospins into the direction roughly inbetween the x and y cubic axes. Considering only the diagonal components of the pseudospin correlations,

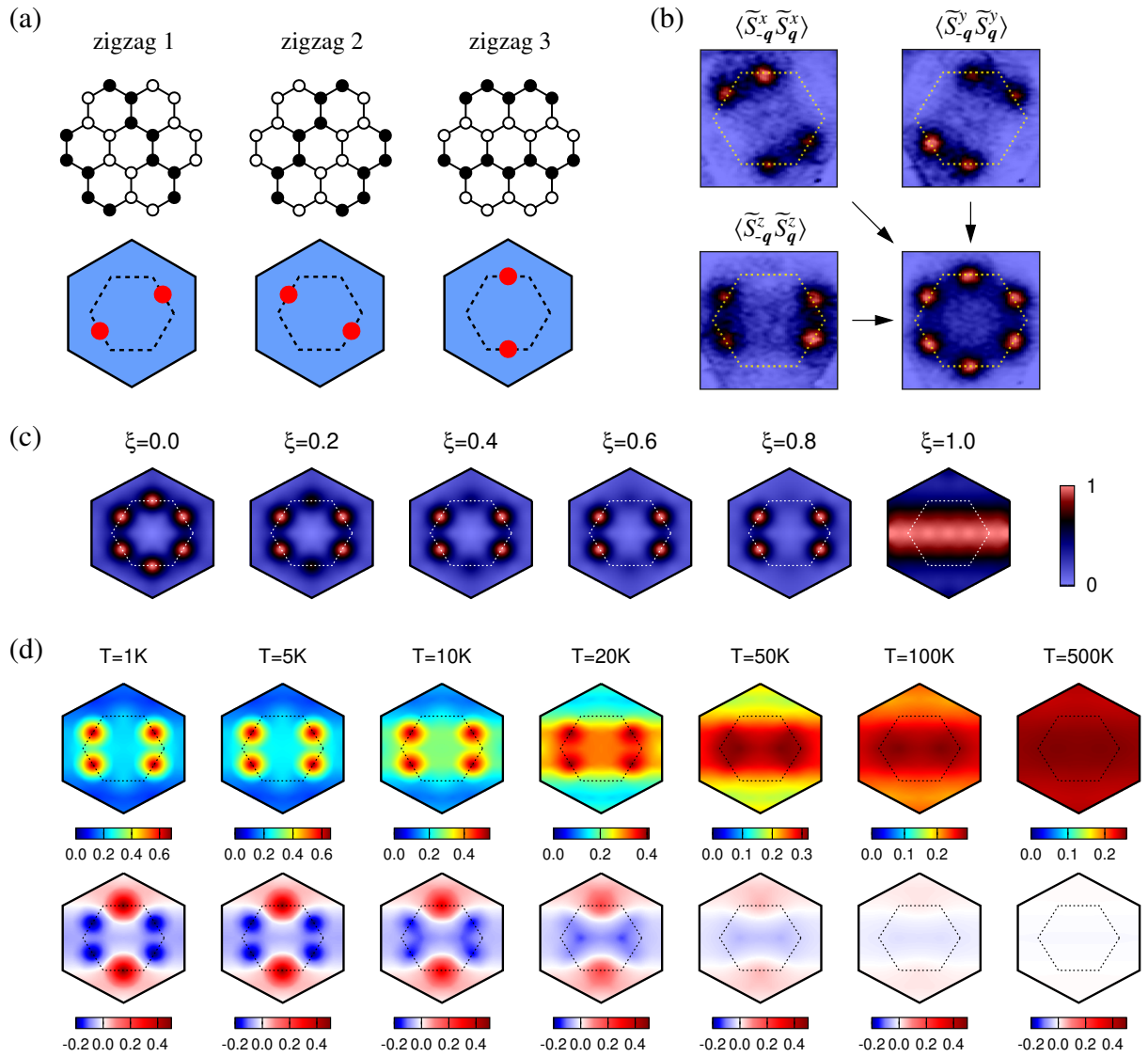

Fig. 31: (a) Three possible zigzag patterns differing in the direction of the FM zigzag chains and the corresponding Bragg spots in the reciprocal space. The inner dashed hexagons in the bottom part are Brillouin zones of the honeycomb lattice, the blue filled hexagons mark the Brillouin zone of the triangular lattice generated by filling the voids in the honeycomb lattice. (b) Component-resolved pseudospin correlations measured by diffuse magnetic x-ray scattering on Na_2IrO_3 [86]. The experiment was performed at $T = 17\,\mathrm{K}$, i.e. above $T_N \approx 12 - 15\,\mathrm{K}$ (sample dependent). The dashed hexagons have the same meaning as in panel (a). (c) Simulated pseudospin correlations $\langle \widetilde{S}^z_{-\boldsymbol{q}} \widetilde{S}^z_{\boldsymbol{q}} \rangle$ obtained by exact diagonalization on 24-site cluster when interpolating between Heisenberg and Kitaev limits of the model. With the selected parametrization $J = J_2 = J_3 = 1 - \xi$ and $K = -\xi$ for $\xi \in [0, 1]$, the ground state is of zigzag type up to ξ very close to 1 where it switches to the Kitaev spin liquid. (d) Temperature dependent pseudospin correlations uncovering the hierarchy of the energy scales. The upper row shows $\langle \widetilde{S}^z_{-\boldsymbol{q}} \widetilde{S}^z_{\boldsymbol{q}} \rangle$ correlations, the bottom row $\langle \widetilde{S}^x_{-\boldsymbol{q}} \widetilde{S}^y_{\boldsymbol{q}} \rangle$. Model parameters $J = -0.5$, $K = -5.0$, $\Gamma = 2.5$, $J_3 = 0.5$ in units of meV were adopted from Refs. [87,88]. The correlations are calculated for 24-cluster using finite-temperature Lanczos method [89,90] in LTLM variant [91].

the characteristic momenta of the above zigzag pattern should be thus visible mainly in $\langle \widetilde{S}^x_{-\boldsymbol{q}} \widetilde{S}^x_{\boldsymbol{q}} \rangle$ and $\langle \widetilde{S}^y_{-\boldsymbol{q}} \widetilde{S}^y_{\boldsymbol{q}} \rangle$ correlations. Alternatively, the $\langle \widetilde{S}^x_{-\boldsymbol{q}} \widetilde{S}^x_{\boldsymbol{q}} \rangle$ correlations should display characteristic momenta of zigzag patterns 2 and 3, but a negligible contribution from zigzag 1. Such a correspondence is indeed observed in the diffuse magnetic x-ray maps presented in Fig. 31(b). When

added together, the maps of the three components $\langle \widetilde{S}^{\alpha}_{-\boldsymbol{q}} \widetilde{S}^{\alpha}_{\boldsymbol{q}} \rangle$ ($\alpha = x, y, z$) reveal a very symmetric picture with all the zigzag momenta showing similar intensities.

To simulate these effects and estimate the amount of interaction anisotropy needed to explain the experimental observations, in Fig. 31(c) we perform exact diagonalization on a small 24-site cluster interpolating between Heisenberg and Kitaev limits of a model that supports zigzag ordering most of the time. This is achieved by using AF Heisenberg interactions of the same strength up to third nearest neighbors and complementing them by FM Kitaev interaction. Although our calculation is in principle for $T = 0$ only, the inability of the cluster ground state to spontaneously break symmetry comes as an advantage here and we get all three zigzag patterns mixed in, imitating therefore the situation just above T_{N}. As seen in Fig. 31(c), the Heisenberg limit of the model retains fully isotropic correlations so that all the zigzag points in a selected correlation component $\langle \widetilde{S}^{\alpha}_{-\boldsymbol{q}} \widetilde{S}^{\alpha}_{\boldsymbol{q}} \rangle$ are equally intense. With a relatively modest relative strength of the Kitaev interaction as compared to the Heisenberg ones, the symmetry is lost and two of the characteristic momenta start to vanish. However, to make the "unwanted" Bragg spots completely invisible (in the given color scale), a relatively large Kitaev interaction is needed, suggesting its dominance in the Na_2IrO_3 compound [86].

Another interesting fictitious experiment is performed in Fig. 31(d). Here we take a parameter set with dominant FM K and substantial $\Gamma > 0$, accompanied by small $J < 0$ and $J_3 > 0$ to

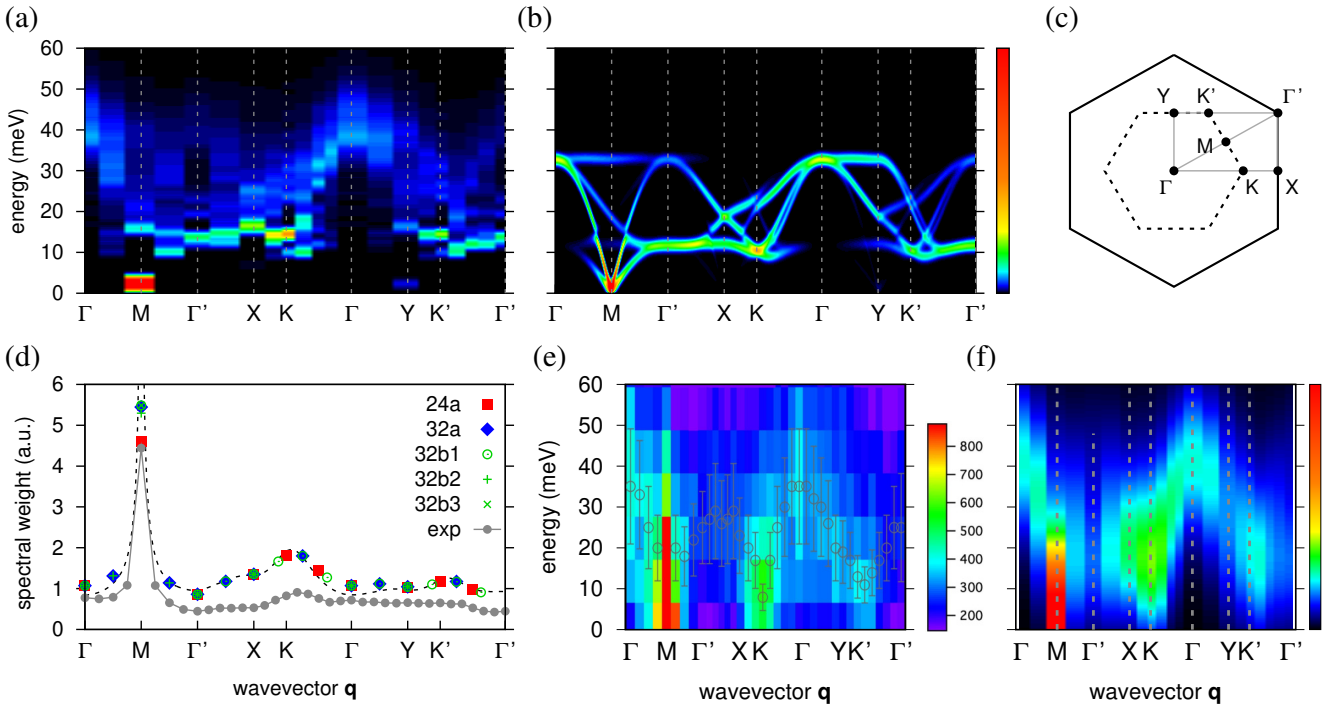

Fig. 32: (a) RIXS response calculated by exact diagonalization of the extended Kitaev-Heisenberg model on 24-site and various 32-site clusters (see Ref. [92] for details). The model parameters used are: $J \approx 10$ meV, $K \approx -15$ meV, $\Gamma \approx 16$ meV, $\Gamma' = -2.4$ meV, $J_2 = 1.2$ meV, $J_3 = 2.4$ meV. (b) The same dynamic response function evaluated within linear spin-wave approximation (LSW), averaging over all three zigzag directions. (c) Brillouin zone of the honeycomb lattice (dashed hexagon), extended Brillouin zone (solid hexagon) and positions of the high-symmetry points used in panels (a) and (b). (d) Spectral weight of the response function from panels (a), (b) as obtained by exact diagonalization for the various clusters (points), within LSW approximation (dashed line), and compared to (arbitrarily scaled) experimental data. (e) Measured RIXS response on Na_2IrO_3 at $T = 7$ K [92] compared to (f) the broadened data from panel (a).

stabilize the zigzag order, and calculate the pseudospin correlations by a finite-temperature exact diagonalization approach. By elevating the temperature, the correlations gradually reveal the hierarchy of energy scales. Requiring the support of the smallest J and J_3 interactions, the sharp zigzag correlations give up first, their degradation is clearly visible in the $10\,\mathrm{K} \approx 1\,\mathrm{meV}$ map. The Γ interaction correlating the $\widetilde{S}^x$ and $\widetilde{S}^y$ components is defeated by the thermal fluctuations in the interval $T \approx 20 - 50\,\mathrm{K}$ where the corresponding correlations almost vanish. The largest energy scale K is able to withstand higher temperatures and gives the correlations a wave-like profile in momentum space, characteristic for the nearest-neighbor Kitaev correlations.

As a final illustration of the features brought about by the dominance of the Kitaev interaction, in Fig. 32 we present dynamical correlations in a form of resonant-inelastic x-ray scattering (RIXS) spectrum that was supposed to simulate the experimental data on Na_2IrO_3 based on the extended Kitaev-Heisenberg model [92]. In contrast to gapless magnons observed for the isotropic Heisenberg model that conserves total spin, here we get a gapped spin excitation spectrum, though the gap can be quite small as it happens to be in our example. The violation of total pseudospin conservation is also manifested by large $\boldsymbol{q} = 0$ intensity at finite energies, that could not be present if $\widetilde{\boldsymbol{S}}_{\boldsymbol{q}=0}$ – which is proportional to the total pseudospin – commuted with the Hamiltonian. A comparison of exact diagonalization, here rather limited by momentum resolution, and linear spin-wave approximation reveals large decay rates due to highly anisotropic interactions. The dynamics is characterized by two energy scales with the smaller Heisenberg interactions influencing the low-energy magnons that keep to be well defined, while the large anisotropic interactions determine the overall shape of the spectrum up to the high energies that correspond to the fast dynamics of the pseudospins. This is subject to strong decay processes leading to a large broadening of the high-energy spectral features. On the other hand, being generated by the large K and Γ interactions, the high-energy spectral features survive even above T_N where the low-energy magnon features are lost [92]. As discussed before, in this regime one can imagine short-range correlated zigzag fragments, still showing their specific high-energy dynamics due to K and Γ. This effect is a dynamic analog of the gradual suppression of characteristic static correlations by elevated temperature that is captured in Fig. 31(d). Finally, the bond-selectivity of the interactions that creates links between the momentum space and pseudospin components as observed on the correlations in Fig. 31(a),(b), also enters the game here. For example, even though all the three zigzag directions are equally employed in both Fig. 32(a),(b), the particular selection of the pseudospin components entering the RIXS response makes a distinction between otherwise symmetry-equivalent points M and Y – the former hosts an intense magnon cone while the latter does not.

4 Soft-spin systems

In this part of the thesis, we will move beyond the concept of rigid spin systems, where the local moments are represented by spins or pseudospins of a given spin length, and consider soft-spin systems that were briefly introduced in Sec. 1.5. Here the magnetic ions may host several quasidegenerate spin states that are dynamically mixed by superexchange interactions. This dynamic mixing makes the magnetic moments soft, which brings specific features to e.g. spin excitation spectra. On the material side, our motivation is the ruthenate Ca_2RuO_4 that is Mott insulating below approximately 360 K [93] and shows antiferromagnetic order below $T_N \approx 110$ K [94–96]. Its crystal structure depicted in Fig. 33(a) is similar to that of high-T_c cuprates and consists of stacked RuO_2 planes where the Ru ions connected by O ions are arranged into a square lattice. The ordered magnetic moments lie within the RuO_2 planes and are oriented diagonally with respect to the square lattice.

Below we will formulate the magnetic model for this compound based on the low-energy multiplet states of Ru^{4+} ions with t_{2g}^4 configuration. As observed in Ref. [97], the orbital angular momentum of t_{2g} orbitals is largely unquenched, supporting the low-energy structure as in Fig. 14 that is formed by spin-orbit coupling. It features nonmagnetic $J = 0$ singlet ionic ground state and $J = 1$ triplet states that are separated by the energy λ. Based on this local basis, we will first formulate a singlet-triplet superexchange model serving as an introductory example. The model will be later refined to account for the tetragonal and small orthorhombic splitting in Ca_2RuO_4 and become in fact a singlet-doublet model. Finally, we will solve the model, demonstrate the peculiar antiferromagnetic order due to a condensation of $J = 1$ triplet levels and obtain spin response and Raman response that can be successfully compared to experiments on Ca_2RuO_4.

In the following, we will limit our discussion to the square lattice case applicable to Ca_2RuO_4. However, another interesting situation occurs when applying the same ideas to the honeycomb lattice case where Kitaev-like frustration of interactions may appear [98–100]. The details of the resulting frustrated singlet-triplet model are discussed in Ref. [100] attached in Sec. 6.

4.1 Singlet-triplet model

As a first step toward a microscopic model for the magnetism of Ca_2RuO_4, we will consider the multiplet structure of t_{2g}^4 configuration discussed in Sec. 2.2.3. The moderate spin-orbit coupling constant $\lambda \approx 70 - 80$ meV for Ru^{4+} ions [31, 97] leads to the hierarchy of energy scales $U \gg J_H \gg \lambda$ that fits the successive level splitting suggested by Fig. 14. A natural selection of basis states for the minimal model includes the nonmagnetic $J = 0$ ionic ground state and – to have some magnetic moment available – low-lying excited $J = 1$ states. As we will see below, these states are easily accessible by second-order superexchange processes on a bond. The $J = 2$ states at three times higher excitation energy will be ignored. It was already noted in Sec. 2.2.4 that we encounter here a special situation of predominantly Van Vleck type of magnetic moment – the largest part of the magnetic moment contained within the $J = 0, 1$ subspace is obtained from the transition between $J = 0$ and $J = 1$ states.

The local part of the singlet-triplet model embodies the energy cost of the triplet state as compared to a singlet. This is captured by the simple Hamiltonian $\lambda \sum_i n_{Ti} = E_T \sum_i n_{Ti}$ counting the number of triplet excitations with the excitation energy $E_T = \lambda$. The derivation of the bond part will follow the general scheme utilized in the previous sections. With the singlet-triplet basis selected, we could proceed similarly to Sec. 3.1 by forming all possible combinations of singlets and triplets on a bond and obtain their energy gains and mutual connections by considering the virtual processes within second-order perturbation theory. However, here we will illustrate another route to arrive at the same result. We will first obtain more general model of Kugel-

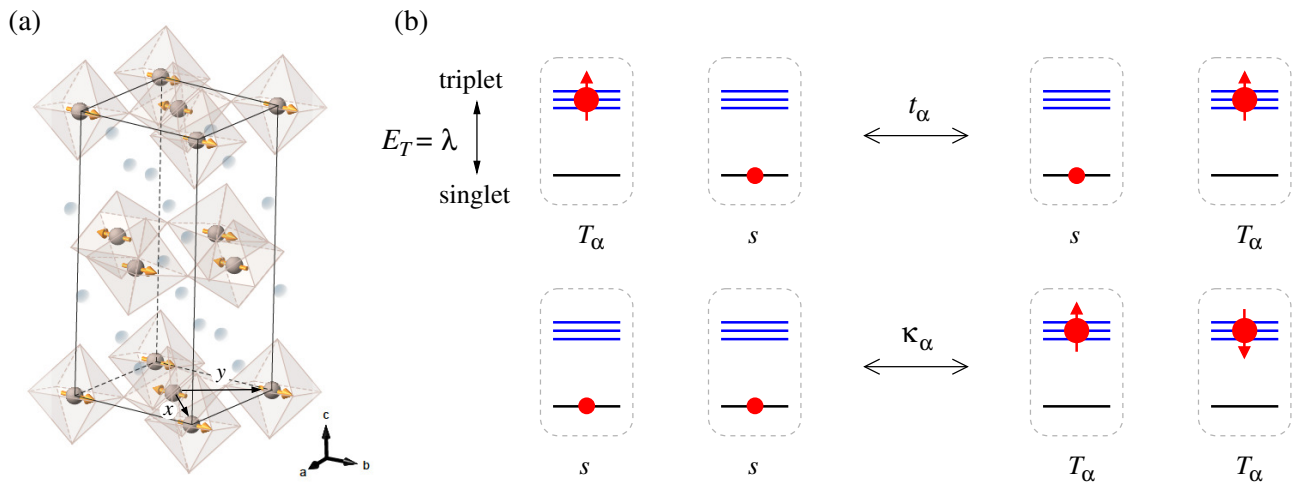

Fig. 33: (a) Crystal structure and magnetic ordering of Ca_2RuO_4. Ru^{4+} ions are depicted as gray balls surrounded by oxygen octahedra. Magnetic moments lying in the RuO_2 planes and pointing along crystallographic b axis are indicated by yellow arrows. In-plane bond directions are labeled as x and y. Adapted from Ref. [101]. (b) Schematic representation of singlet-triplet processes corresponding to the Hamiltonian terms in Eq. (4.5). Each site may host a singlet t_{2g}^4 configuration s or a triplon excitation T_α ($\alpha = x, y, z$) of the cost $E_T = \lambda$. The upper exchange process is a triplon hopping (exchange of s and T), the lower process is a creation/annihilation of a singlet pair of triplons.

Khomskii type[15] operating in the subspace involving all nine $L^{\rm eff} = 1$, $S = 1$ ionic states selected by Hund's coupling. This model will be later projected on the $J = 0, 1$ states to get the singlet-triplet model. The most natural basis for the Kugel-Khomskii model are the states of the type (2.64) that enable to easily capture the action of the two hoppings involved in the second-order virtual process by properly assembling the spin operators $\boldsymbol{S}_i$, $\boldsymbol{S}_j$ and orbital operators $\boldsymbol{L}_i^{\rm eff}$, $\boldsymbol{L}_j^{\rm eff}$ associated with the two sites of the bond $\langle ij \rangle$. Due to the spin conservation during the hopping, the spin operators may only appear in a form of the isotropic product $\boldsymbol{S}_i \cdot \boldsymbol{S}_j$. The orbital part of the interaction is not limited this way and may take various forms depending on the hopping geometry and the particular bond direction. In the case of 180° metal–oxygen–metal bonding, we have a bond-selected pair of active orbitals that are subject to oxygen-mediated hopping preserving the orbital label (i.e. it is diagonal in orbitals). For concreteness, we will consider a z-bond[16] where the hopping Hamiltonian reads as [c.f. Eq. (2.101) for an x-bond]

$$\mathcal{H}_t = -t \sum_\sigma \left(\xi_{i\sigma}^\dagger \, \xi_{j\sigma} + \eta_{i\sigma}^\dagger \, \eta_{j\sigma} \right) \; + \text{H.c.} \,, \tag{4.1}$$

with $t = t_{pd\pi}^2 / \Delta_{pd}$. In contrast to Eqs. (3.2) and (3.3) for the 90° bond geometry encountered in Sec. 3.1, here we only get diagonal hopping of a and c holes associated with $L_z^{\rm eff}$ eigenstates. Combining this information with the a, b, c composition of the basis states (2.64), we can infer that their individual $L_z^{\rm eff}$ will be mostly preserved in the superexchange process, but there is also a possibility to exchange $L_z^{\rm eff} = +1$ and $L_z^{\rm eff} = -1$ on the bond. All these observations are indeed consistent with the actual form of the effective Hamiltonian derived for the z-bond:

$$\frac{t^2}{2U} (\boldsymbol{S}_i \cdot \boldsymbol{S}_j + 1) \left\{ \frac{(L_i^+)^2 (L_j^-)^2 + (L_i^-)^2 (L_j^+)^2}{2} + \left[(L_i^z)^2 - 2 \right] \left[(L_j^z)^2 - 2 \right] + L_i^z L_j^z \right\} + \frac{t^2}{U} \left[(L_i^z)^2 + (L_j^z)^2 \right] . \tag{4.2}$$

[15] This type of spin-orbital models has been introduced by K. I. Kugel and D. I. Khomskii in Ref. [102].

[16] Note, that in the planar structure of Ca_2RuO_4 only the x- and y-bonds of M–O–M type are present, as seen in Figs. 33(a) and 34(a). The z-bond is considered here just to have a familiar notation used before.

For brevity, we denoted $\boldsymbol{L}^{\rm eff}$ by $\boldsymbol{L}$ in the above equation. Now we need to project the Hamiltonian (4.2) onto the singlet-triplet basis. This is achieved by considering the site operators such as $S_i^x(L_i^z)^2$ contained in the fragments of (4.2) and expressing them in the multiplet basis with spin-orbit coupling included. By throwing away the terms involving the $J=2$ quintuplet and keeping only s and T_α operators associated with $J=0,1$ states, we arrive at the required projection. For example, the above site operator can be written as

$$S^x(L^z)^2 = -\frac{i}{\sqrt{6}}(s^\dagger T_x - T_x^\dagger s) - \frac{i}{2}(T_y^\dagger T_z - T_z^\dagger T_y) \;+ \text{neglected terms involving } J=2 \text{ states.} \quad (4.3)$$

When converted into the singlet-triplet basis, the bond Hamiltonian (4.2) generates a large number of terms. The diagonal ones can be written as a renormalization of the triplet energy and mutual density-density interactions of triplets. To this end we first make a constant energy shift so that the energy gain of $|ss\rangle$ bond configuration becomes zero. The other energy gains can be then distributed among the local E_T shifts $\Delta E_{Tx} = \Delta E_{Ty} = -\frac{11}{6}\frac{t^2}{U}$, $\Delta E_{Tz} = -\frac{4}{3}\frac{t^2}{U}$ and the repulsion terms $V_{\alpha\alpha'} n_{T\alpha i} n_{T\alpha' j}$ with $V_{xx} = V_{yy} = V_{zz} = \frac{23}{12}\frac{t^2}{U}$, $V_{xy} = \frac{5}{3}\frac{t^2}{U}$, and $V_{xz} = V_{zx} = V_{yz} = V_{zy} = \frac{17}{12}\frac{t^2}{U}$. Note that the z-bond naturally makes a distinction between the T_z excitation and the T_x, T_y pair. For the other bond directions, all the Hamiltonian terms are obtained by a cyclic permutation. The above diagonal contributions will be later ignored, we may imagine them as being partly absorbed into renormalized E_T and partly neglected under an assumption of low density of triplet states. More interesting are the off-diagonal terms of the effective Hamiltonian that can be visualized as bond processes involving triplet excitations. These are of hardcore boson nature and will be called triplons in the following. To make the notation compact, we introduce Hubbard operators switching between s and T_α states of the t_{2g}^4 configuration:

$$\mathcal{T}_\alpha^\dagger = |T_\alpha\rangle\langle s|\,, \qquad \mathcal{T}_\alpha = |s\rangle\langle T_\alpha|\,. \quad (4.4)$$

The off-diagonal contributions quadratic in triplon operators may be summarized as (again for a z-bond)

$$t_{xy}\left(\mathcal{T}_{xi}^\dagger \mathcal{T}_{xj} + \mathcal{T}_{yi}^\dagger \mathcal{T}_{yj}\right) + t_z \mathcal{T}_{zi}^\dagger \mathcal{T}_{zj} \;-\; \kappa_{xy}\left(\mathcal{T}_{xi}^\dagger \mathcal{T}_{xj}^\dagger + \mathcal{T}_{yi}^\dagger \mathcal{T}_{yj}^\dagger\right) - \kappa_z \mathcal{T}_{zi}^\dagger \mathcal{T}_{zj}^\dagger \;+\; \text{H.c.} \quad (4.5)$$

They can be understood as hopping of triplons and their pairwise creation and annihilation depicted in Fig. 33(b). There are also terms involving three or four triplon operators – conversion of a single triplon on a bond to a pair of complementary ones, exchange of triplons on the bond, and pair-conversion terms $\propto |T_{\alpha i} T_{\alpha j}\rangle\langle T_{\alpha' i} T_{\alpha' j}|$. All these may be ignored when focusing on the cases with small enough density of triplons. Including first order corrections in $\eta = J_{\rm H}/U$, the interaction parameters in Eq. (4.5) read as

$$t_{xy} \approx \frac{t^2}{U}\left(1 - \frac{5}{6}\eta\right), \quad t_z \approx \frac{2}{3}\frac{t^2}{U}, \quad \kappa_{xy} \approx \frac{5}{6}\frac{t^2}{U}\left(1 - \frac{8}{5}\eta\right), \quad \kappa_z \approx \frac{2}{3}\frac{t^2}{U}. \quad (4.6)$$

When assuming the typical $\eta \approx 0.2$ [see e.g. the Ru parameters used in Fig. 28(d)], the values of the above parameters are relatively close to each other, so it is reasonable to simplify the singlet-triplet Hamiltonian to the isotropic form

$$\mathcal{H} = E_T \sum_i n_{Ti} + J \sum_{\langle ij\rangle}\left(\boldsymbol{\mathcal{T}}_i^\dagger \cdot \boldsymbol{\mathcal{T}}_j \;- \boldsymbol{\mathcal{T}}_i^\dagger \cdot \boldsymbol{\mathcal{T}}_j^\dagger + \text{H.c.}\right) \quad (4.7)$$

with $J \approx 2t^2/3U$ and the vector operator $\boldsymbol{\mathcal{T}} = (\mathcal{T}_x, \mathcal{T}_y, \mathcal{T}_z)$. Based on Eq. (4.7) applied to a square lattice as appropriate for Ca_2RuO_4, we could already study the competition of the triplon cost E_T and the superexchange J, the emergence of the magnetic order due to triplon condensation, and the implications for magnetic excitation spectra. However, to make the model more realistic, we will still include tetragonal splitting of the orbitals that essentially eliminates one of the triplon flavors, a small splitting due to orthorhombicity, and also consider some of the higher-order terms.

4.2 Revisions of the model to reflect tetragonal splitting

Apart from the major t_{2g}-e_g splitting, the orbitals in Ca_2RuO_4 are subject to further splittings due to tetragonal and small orthorhombic components of crystal field illustrated by Fig. 34(a),(b). The main effect is due to the tetragonal crystal field $\Delta(n_{yz}+n_{zx}-2n_{xy})/3$ that brings down the planar xy orbital for positive Δ as shown Fig. 9(b). As we will see below, the tetragonal splitting pushes the magnetic moment to the RuO_2 plane by essentially deactivating one member of the triplet states. The small orthorhombic crystal field Δ' generates in-plane anisotropy selecting the b crystallographic axis as preferential for the ordered moments.

The tetragonal splitting acts on the two-hole states $|L_z^{\rm eff}, S_z\rangle$ of Eq. (2.64) via an extra term $\Delta[(L_z^{\rm eff})^2 - \frac{2}{3}]$, changing the proportions of these states in the multiplet eigenstates. This leads to wavefunction modifications similar to what we already encountered in Eq. (3.15) for pseudospin-$\frac{1}{2}$ states of the t_{2g}^5 configuration. The wavefunction of the singlet ground state gets adjusted to the tetragonal splitting as

$$|s\rangle = \cos\vartheta_0 \, \tfrac{1}{\sqrt{2}}(|+1,-1\rangle + |-1,+1\rangle) - \sin\vartheta_0 \, |0,0\rangle \,, \qquad \tan 2\vartheta_0 = \frac{2\sqrt{2}}{1-2\delta} \tag{4.8}$$

with the crystal field being quantified by $\delta = \Delta/2\lambda = \Delta/\zeta$. For nonzero Δ, the orbital-mixing angle ϑ_0 deviates from its cubic-limit value $\arctan(1/\sqrt{2}) \approx 35.26°$ that reproduces the original $J = 0$ singlet of Eq. (2.76). The triplet states split into a degenerate pair

$$|T_{\pm1}\rangle = \mp\cos\vartheta_1 \, |\pm1,0\rangle \pm \sin\vartheta_1 |0,\pm1\rangle \,, \qquad \tan\vartheta_1 = \frac{1}{\sqrt{1+\delta^2}-\delta} \tag{4.9}$$

that is linked to $|T_x\rangle = \frac{i}{\sqrt{2}}(|T_{+1}\rangle - |T_{-1}\rangle)$ and $|T_y\rangle = \frac{1}{\sqrt{2}}(|T_{+1}\rangle + |T_{-1}\rangle)$ used in Sec. 2.2.4 to handle the magnetic moment of the t_{2g}^4 configuration, and the non-degenerate state

$$|T_0\rangle = -\tfrac{1}{\sqrt{2}}(|+1,-1\rangle - |-1,+1\rangle) \tag{4.10}$$

that is linked to the remaining $|T_z\rangle = -i|T_0\rangle$ and only shifts in energy. The above states are still eigenstates of J_z but J is not a good quantum number anymore due to the mixing of the original $J = 0, 1$ states with the $J = 2$ quintuplet states caused by the tetragonal crystal field. The energy level splitting is plotted in full in Fig. 34(c) and the two angles entering Eqs. (4.8) and (4.9) in Fig. 34(d).

The newly introduced splitting among the triplet levels should be reflected in the singlet-triplet model. As seen in Fig. 34(e) showing the ionic excitation spectrum, for positive Δ case that applies to Ca_2RuO_4, the T_0 level goes quickly up and can be omitted in the model basis, leading to a singlet-doublet model. In contrast, the excitation energy of the doublet $T_{\pm1}$ levels becomes significantly reduced compared to the original $\lambda = \zeta/2$, making them even better accessible by the superexchange processes. Ref. [101] estimates $\delta \approx 1.5$ and the corresponding reduction of the $T_{\pm1}$ excitation energy from $\lambda \approx 70 - 80$ meV to about 25 meV. When leaving out the $T_0 \sim T_z$ state, the three active basis states are conveniently described by pseudospin-1. Using the above states, we can form the basis of pseudospin-1 according to

$$|\widetilde{+1}\rangle = \tfrac{1}{\sqrt{2}}(i|T_x\rangle - |T_y\rangle) = -|T_{+1}\rangle \,, \qquad |\widetilde{0}\rangle = |s\rangle \,, \qquad |\widetilde{-1}\rangle = \tfrac{1}{\sqrt{2}}(i|T_x\rangle + |T_y\rangle) = |T_{-1}\rangle \tag{4.11}$$

defining the eigenstates of the z-projection of the pseudospin-1. The corresponding pseudospin operators that fulfill the spin-1 algebra are then expressed as

$$\widetilde{S}_x = -i(s^\dagger T_x - T_x^\dagger s) \,, \qquad \widetilde{S}_y = -i(s^\dagger T_y - T_y^\dagger s) \,, \qquad \widetilde{S}_z = -i(T_x^\dagger T_y - T_y^\dagger T_x) \,. \tag{4.12}$$

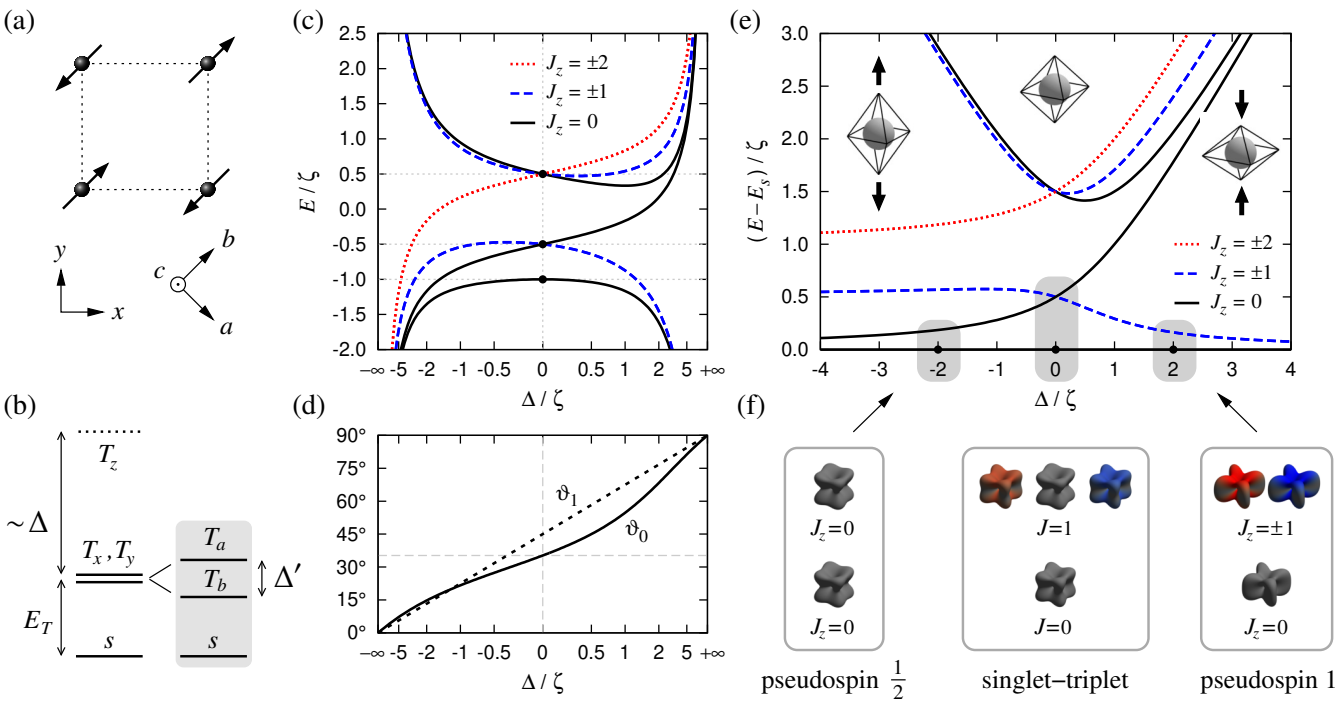

Fig. 34: (a) Coordinate systems for the RuO_2 plane. The crystallographic axes are labeled by a and b. (b) Splitting of triplet levels under crystal field of distorted octahedra. Tetragonal deformation giving rise to the Δ field lifts up the T_z triplet state, small additional orthorhombic distortion represented by the field Δ' further splits the T_x and T_y states into the combinations $T_{a,b} = \frac{1}{\sqrt{2}}(T_x \mp T_y)$. (c) Energy levels within the $L^{\rm eff} = 1$ and $S = 1$ sector depending on the ratio of the tetragonal crystal field Δ and spin-orbit coupling strength ζ. (d) Auxiliary angles ϑ_0 and ϑ_1 entering the eigenstates in Eqs. (4.8) and (4.9). (e) Excitation energies measured from the singlet ionic ground-state level. The insets illustrate the tetragonal deformation of the octahedron as connected to the sign of Δ within point-charge model. (f) Electron densities of low-energy t_{2g}^4 states including their spin polarization. The low-energy states form a basis of a singlet-triplet model (cubic limit $\Delta = 0$), effective spin-1 model (large positive Δ), or effective spin-$\frac{1}{2}$ model (large negative Δ).

Pseudospin-1 introduced this way also perfectly captures the surviving components of the magnetic moment. The x and y components of $\widetilde{\boldsymbol{S}}$ are proportional to the in-plane Van Vleck moment [see Eq. (2.90)] while the z component describes the magnetic moment hosted by the triplons themselves. The g-factors that connect magnetic moment $2\boldsymbol{S} - \boldsymbol{L}^{\rm eff}$ and pseudospin-1 operators within the pseudospin-1 subspace are plotted in Fig. 35(a). For the cubic limit, we notice the coincidence with the factors entering Eq. (2.90). At large tetragonal compression, the orbital component is suppressed as evident from Eqs. (4.8) and (4.9) and the usual spin g-factor 2 is recovered.

Adopting the pseudospin-1 notation, we will first implement the level splitting depicted in Fig. 34(b) into the local part of the new singlet-doublet model. Combining both the reduced $T_{\pm 1}$ excitation cost E_T and the in-plane anisotropy attracting the moments to the b axis, we have

$$\mathcal{H}_{\rm loc} = E_T n_T + \tfrac{1}{2}\Delta'(n_{Ta} - n_{Tb}) = E_T \widetilde{S}_z^2 + \tfrac{1}{2}\Delta'(\widetilde{S}_a^2 - \widetilde{S}_b^2) = E_T \widetilde{S}_z^2 - \Delta'(\widetilde{S}_x \widetilde{S}_y + \widetilde{S}_y \widetilde{S}_x)\,, \quad (4.13)$$

where E_T is now much smaller than λ. Still, when the experimental data on Ca_2RuO_4 are fit by the pseudospin-1 model, E_T turns out to be the dominant parameter, constraining the magnetic moments to the RuO_2 plane.

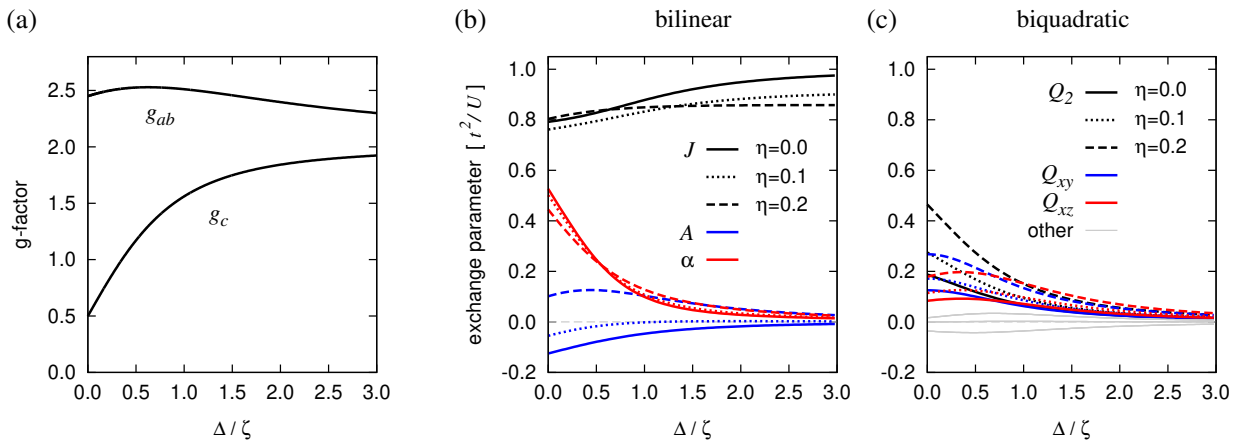

Fig. 35: (a) In-plane (g_{ab}) and out-of-plane (g_c) g-factors connecting the magnetic moment and pseudospin-1 $\widetilde{\boldsymbol{S}}$. The scaling of the in-plane and out-of-plane components is highly anisotropic near the cubic limit but the pseudospin-1 picture only starts to apply around $\Delta \approx \zeta$ where the g-factors are already rather close to their $\Delta \to \infty$ value of 2. (b),(c) Exchange parameters of the effective spin-1 model depending on the crystal field and Hund's coupling strength $\eta = J_{\mathrm{H}}/U$. Panel (b) concerns the dominant bilinear part of the interaction showing the parameters J, A, α defined by Eq. (4.14), the smaller biquadratic part is addressed in panel (c). Here we have singled out three quadrupolar interaction channels $Q_{2,i}Q_{2,j}$, $Q_{xy,i}Q_{xy,j}$, and $Q_{xz,i}Q_{xz,j}$, the other nonzero ones are indicated by thin gray lines only (shown for all three η values).

Much more demanding task is the recalculation of the superexchange part of the singlet-triplet model with the modified basis wavefunctions and its subsequent conversion to the pseudospin-1 operators. The resulting contribution of the x-bonds in RuO_2 plane can be written as

$$\mathcal{H}_x = \sum_{\langle ij\rangle \| x} \left[(J+A)\widetilde{S}_i^x \widetilde{S}_j^x + (J-A)\widetilde{S}_i^y \widetilde{S}_j^y + J(1-\alpha)\widetilde{S}_i^z \widetilde{S}_j^z + \sum_{\alpha\beta} q_{\alpha\beta}^{(x)} Q_i^\alpha Q_j^\beta \right] . \tag{4.14}$$

A similar form with interchanged x and y components is obtained for the y-bonds. Together with $\mathcal{H}_{\mathrm{loc}}$ we get the full Hamiltonian of the pseudospin-1 model, $\mathcal{H} = \mathcal{H}_{\mathrm{loc}} + \mathcal{H}_x + \mathcal{H}_y$. Let us now analyze the superexchange interaction in Eq. (4.14) in detail. The first part contains diagonal spin-spin interactions $\widetilde{S}_{\alpha i}\widetilde{S}_{\alpha j}$, each component coming with its own interaction constant. By inserting the definitions of $\widetilde{S}_x = -i(\mathcal{T}_x - \mathcal{T}_x^\dagger)$ and $\widetilde{S}_y = -i(\mathcal{T}_y - \mathcal{T}_y^\dagger)$ in terms of Hubbard operators, one finds, that the $J(\widetilde{S}_i^x \widetilde{S}_j^x + \widetilde{S}_i^y \widetilde{S}_j^y)$ part of the pseudospin-1 interaction just reproduces the $\mathcal{T}_{x,y}$ part of the quadratic interactions in the singlet-triplet model of Eq. (4.7). On top of this, we also get a bond-selective contribution associated with the parameter A [this effect was already neglected at the level of Eq. (4.7)] and $\widetilde{S}_i^z \widetilde{S}_j^z$ interaction parametrized using $J_z = J(1-\alpha)$ that was among the ignored four-triplon terms in Sec. 4.1. The respective interaction constants in units of t^2/U and with $c_{0,1} = \cos 2\vartheta_{0,1}$, $s_{0,1} = \sin 2\vartheta_{0,1}$, and $\eta = J_{\mathrm{H}}/U$ are given explicitly by

$$\begin{aligned}
J &= \frac{7-c_0+c_1-7c_0c_1-2\sqrt{2}s_0s_1}{48(1-3\eta)} + \frac{13-c_0-5c_1+29c_0c_1+13\sqrt{2}s_0s_1}{96} + \frac{9-c_0-c_1+5c_0c_1+3\sqrt{2}s_0s_1}{32(1+2\eta)} , \\
A &= \frac{5-3c_0+3c_1-5c_0c_1+2\sqrt{2}s_0s_1}{48(1-3\eta)} + \frac{-10-6c_1+4c_0c_1-7\sqrt{2}s_0s_1}{96} - \frac{2c_0+2c_0c_1+\sqrt{2}s_0s_1}{32(1+2\eta)} , \\
J_z &= \frac{1-\cos 4\vartheta_1}{24(1-3\eta)} + \frac{17-24c_1+7\cos 4\vartheta_1}{96} + \frac{7-8c_1+\cos 4\vartheta_1}{32(1+2\eta)} .
\end{aligned} \tag{4.15}$$

Ignoring the corrections due to Hund's coupling in virtual states, they reduce to

$$J = \frac{9-c_0-c_1+5c_0c_1+3\sqrt{2}s_0s_1}{16}\,, \quad A = -\frac{2c_0+2c_0c_1+\sqrt{2}s_0s_1}{16}\,, \quad J_z = \frac{7-8c_1+\cos 4\vartheta_1}{16}\,. \tag{4.16}$$

As can be seen in Fig. 35(b) where we plot J, A, α as functions of the tetragonal field Δ, the anisotropy is quickly getting marginal with increasing Δ and in the large Δ limit we approach the isotropic Heisenberg situation with $J_x = J_y = J_z = t^2/U$. This effect is a consequence of the quenched orbital component of the pseudospin-1 which then coincides with the original spin $S = 1$ of t_{2g}^4 configurations and hence may only be subject to isotropic interactions. Vanishing anisotropy can be also readily verified (for any $J_{\rm H}/U$ ratio) using the above explicit expressions when $\vartheta_0 = \vartheta_1 = \pi/2$ giving $c_0 = c_1 = -1$, $s_0 = s_1 = 0$, and $\cos 4\vartheta_1 = 1$.

Since we deal with an effective spin-1 situation, the bilinear terms of the general form $S_{\alpha i}S_{\beta j}$ may not be sufficient to fully describe the spin-spin interactions, in contrast to spin-$\frac{1}{2}$ models, and this is indeed the case here. In Eq. (4.14), we have included also biquadratic terms that are expressed using products of the five components of spin-1 quadrupolar moments:

$$Q_0 = \tfrac{1}{\sqrt{3}}(2\widetilde{S}_z^2-\widetilde{S}_x^2-\widetilde{S}_y^2)\,, \quad Q_2 = \widetilde{S}_x^2-\widetilde{S}_y^2\,, \quad Q_{xy} = \widetilde{S}_x\widetilde{S}_y+\widetilde{S}_y\widetilde{S}_x\,, \quad Q_{yz},\ Q_{zx}\ \text{(analogous)}. \tag{4.17}$$

They can be in general arbitrarily combined for the two sites of the bond leading to the superposition $\sum_{\alpha\beta} q_{\alpha\beta}^{(x)} Q_i^\alpha Q_j^\beta$ but in our case the coefficients $q_{\alpha\beta}^{(x)}$ are diagonal with the exception of Q_0 to Q_2 coupling. All the nonzero biquadratic interactions are presented in Fig. 35(c) which demonstrates that they are minor in the Δ/ζ interval of interest. In the following section we will thus consider just the bilinear part of the superexchange.

4.3 Magnetic order due to triplon condensation

Before attempting a detailed comparison of the magnetic model introduced in the previous sections and the experimental data on Ca_2RuO_4, we will demonstrate the basic features of the model phase diagram. In particular, we will focus on the long-range magnetic order supported by the model, that can be interpreted as resulting from triplon condensation. The introductory singlet-triplet model (4.7) and the refined pseudospin-1 model of Sec. 4.2 show similar overall behavior in this respect. Here we will consider the main part of the pseudospin-1 model that is contained also in Eq. (4.7) and can be written explicitly as

$$\mathcal{H} = E_T \sum_i n_{Ti} + J \sum_{\langle ij\rangle} \sum_{\alpha=x,y} \left[(T_\alpha^\dagger s)_i (s^\dagger T_\alpha)_j - (T_\alpha^\dagger s)_i (T_\alpha^\dagger s)_j + \text{H.c.}\right]. \tag{4.18}$$

The model can be easily handled in the limit $E_T \gg J$ where the intuitive picture of its ground state is a dilute gas of triplons moving on the square lattice. To obtain the dispersion of moving triplons we treat the local constraint $n_s + n_{Tx} + n_{Ty} = 1$ by adopting dynamical Gutzwiller approximation. Namely, we replace both s and $s^\dagger$ operators in Eq. (4.18) by $\sqrt{1-n_{Tx}-n_{Ty}}$ and expand the square root assuming small density of triplons. We keep terms up to quadratic order in the triplon operators T_x, T_y and regard T as regular bosonic operators afterwards. In momentum space, we get the Hamiltonian of the canonical form

$$\mathcal{H}_{\rm harm} = \sum_{\boldsymbol{q}} \sum_{\alpha=x,y} A_{\boldsymbol{q}} T_{\alpha\boldsymbol{q}}^\dagger T_{\alpha\boldsymbol{q}} - \tfrac{1}{2} B_{\boldsymbol{q}} (T_{\alpha\boldsymbol{q}} T_{\alpha,-\boldsymbol{q}} + T_{\alpha\boldsymbol{q}}^\dagger T_{\alpha,-\boldsymbol{q}}^\dagger) \tag{4.19}$$

with

$$A_{\boldsymbol{q}} = E_T + 4J\gamma_{\boldsymbol{q}}\,, \quad B_{\boldsymbol{q}} = 4J\gamma_{\boldsymbol{q}}\,, \quad \gamma_{\boldsymbol{q}} = \tfrac{1}{2}(\cos q_x + \cos q_y) \tag{4.20}$$

that is readily solved by Bogoliubov transformation giving elementary excitations with the dispersion

$$\omega_{\boldsymbol{q}} = \sqrt{A_{\boldsymbol{q}}^2 - B_{\boldsymbol{q}}^2} = \sqrt{E_T\,(E_T + 8J\gamma_{\boldsymbol{q}})}\,. \tag{4.21}$$

According to this result, the triplon excitations that start at the energy E_T in the $J \to 0$ limit gradually soften around the $\boldsymbol{q} = (\pi, \pi)$ point when J is increased [see also Fig. 36(d)]. We can continue with this solution up to a relatively modest $J_{\rm crit} = \frac{1}{8}E_T$. At this point the excitation dispersion touches zero energy, signaling a quantum phase transition to a phase with condensed triplons as it has been briefly introduced in Sec. 1.5. Let us note here, that the position of the quantum critical point is approximate only and $J_{\rm crit}$ is revised to a higher value when going beyond the harmonic approximation, i.e. including interaction effects between triplons (the density of which is no longer negligible near the critical point).

To cover the entire parameter range of the model at the same level of approximation, we utilize a trial wavefunction that allows for the condensation of triplons (as hardcore bosons) by locally mixing the s and T states:

$$|\Psi\rangle = \prod_{\boldsymbol{R}} \left(\cos\theta\; s_{\boldsymbol{R}}^\dagger + \sin\theta \sum_{\alpha=x,y} d_{\alpha\boldsymbol{R}}^* T_{\alpha\boldsymbol{R}}^\dagger \right) |{\rm vac}\rangle\,. \tag{4.22}$$

Having a condensate of vector bosons, we need to deal with its internal structure which is represented here by a position-dependent complex vector $\boldsymbol{d}_{\boldsymbol{R}}$. The local constraint $n_s + n_T = 1$ is maintained when $|\boldsymbol{d}| = 1$. By minimizing the Hamiltonian average $\langle\Psi|\mathcal{H}|\Psi\rangle$ with respect to the variational parameter θ and optimizing simultaneously the $\boldsymbol{d}_{\boldsymbol{R}}$ structure, we get the phase diagram shown in Fig. 36(a). The average can be conveniently expressed by introducing condensate density $\rho = \langle\Psi|n_T|\Psi\rangle = \sin^2\theta$ and separating the real and imaginary parts of the $\boldsymbol{d}$ vectors as $\boldsymbol{d}_{\boldsymbol{R}} = \boldsymbol{u}_{\boldsymbol{R}} + i\boldsymbol{v}_{\boldsymbol{R}}$ with the constraint $u^2 + v^2 = 1$. With this notation we obtain for the Hamiltonian average, termed also the "classical" energy of the condensate

$$E_{\rm class} = \langle\Psi|\mathcal{H}|\Psi\rangle = E_T \sum_i \rho + J \sum_{\langle ij\rangle} 4\rho(1-\rho)\,\boldsymbol{v}_i \cdot \boldsymbol{v}_j\,. \tag{4.23}$$

Up to $J = \frac{1}{8}E_T$ the minimization gives $\theta = 0$ and hence zero condensate density, recovering the above result of the harmonic approximation. Above this critical J/E_T strength, nonzero ρ appears and the structure of Eq. (4.23) forces us to maximize the $\boldsymbol{v}$ component and make it antiparallel at nearest-neighbor sites to gain energy. To uncover the magnetic nature of this type of triplon condensate, we evaluate $\langle\Psi|M_\alpha|\Psi\rangle = g_{ab}\langle\Psi|(-i)(s^\dagger T_\alpha - T_\alpha^\dagger s\,)|\Psi\rangle = -2g_{ab}v_{\alpha\boldsymbol{R}}\sqrt{\rho(1-\rho)}$ ($\alpha = x, y$) and $\langle\Psi|M_z|\Psi\rangle = g_c\langle\Psi|(-i)(T_x^\dagger T_y - T_y^\dagger T_x)|\Psi\rangle = 0$, finding that the staggered $\boldsymbol{v}_{\boldsymbol{R}}$ of the condensate translates to in-plane ordering of magnetic moments with the ordering vector $\boldsymbol{Q} = (\pi, \pi)$ [see Fig. 36(b)]. Any direction of $\boldsymbol{v}$ and therefore any normalized combination of T_x and T_y is equally good in terms of energy, this corresponds to the freedom to choose the magnetization direction in the lattice plane. For later convenience, we set $v_{x\boldsymbol{R}} = -{\rm e}^{i\boldsymbol{Q}\cdot\boldsymbol{R}}$, $v_y = 0$ giving $M_x = 2g_{ab}\sqrt{\rho(1-\rho)}{\rm e}^{i\boldsymbol{Q}\cdot\boldsymbol{R}}$, $M_y = 0$ and bringing Eq. (4.22) to its final form

$$|\Psi\rangle = \prod_{\boldsymbol{R}} \left(\sqrt{1-\rho}\; s_R^\dagger + \sqrt{\rho}\; i\,{\rm e}^{i\boldsymbol{Q}\cdot\boldsymbol{R}} T_{x\boldsymbol{R}}^\dagger \right) |{\rm vac}\rangle \tag{4.24}$$

with the optimum condensate density and θ parameter given by

$$\rho = \sin^2\theta = \frac{1}{2}\left(1 - \frac{E_T}{8J}\right) \qquad (J > J_{\rm crit} = \tfrac{1}{8}E_T)\,. \tag{4.25}$$

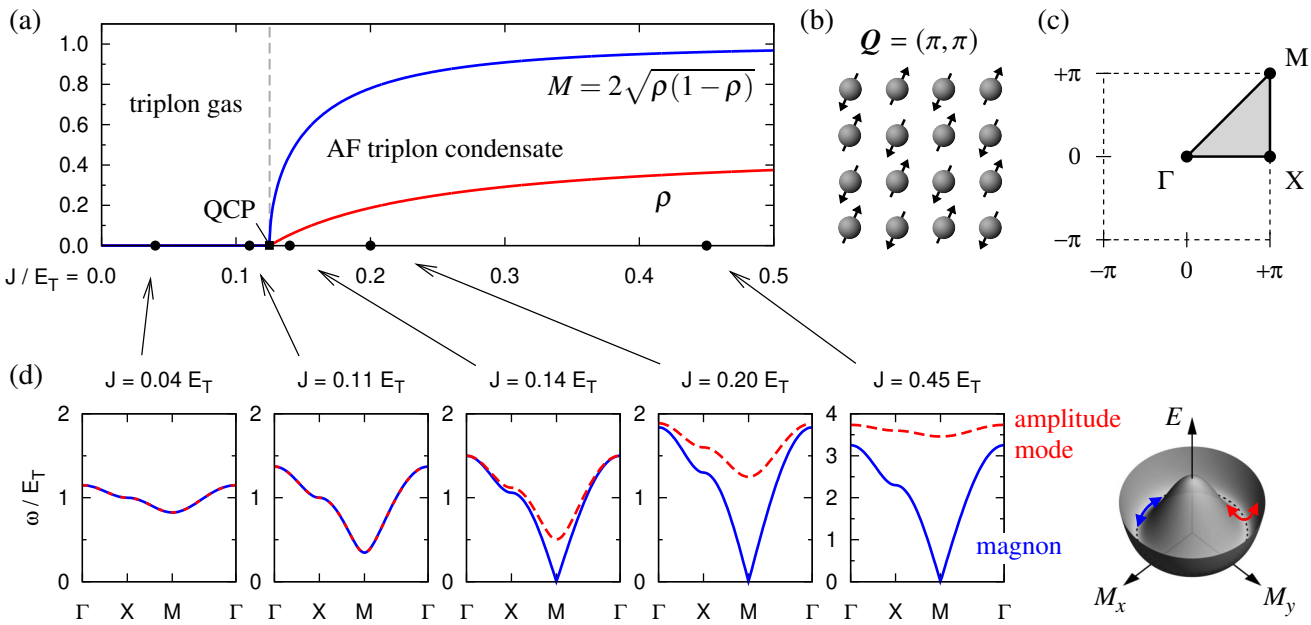

Fig. 36: (a) Condensate density and ordered moment obtained from the variational Ansatz (4.22) as functions of the J to E_T ratio. Quantum critical point at $J/E_T = \frac{1}{8}$ separating the triplon gas phase and condensed phase is indicated by the black square and the dashed line. (b) Magnetic ordering pattern in the square lattice having $\boldsymbol{Q} = (\pi, \pi)$ ordering vector. (c) Brillouin zone of the square lattice with highlighted conventional path around the irreducible Brillouin zone. (d) Dispersions of the elementary excitations at selected J/E_T points plotted along the conventional path of panel (c). Initially, we observe twofold degenerate branch of triplon excitations. After the condensation occurs, the excitation dispersion splits giving rise to a gapless magnon mode and gapful mode that can be interpreted as an amplitude mode of the triplon condensate.

Let us now inspect the evolution of the elementary excitations. To calculate their spectra we need to perform a harmonic expansion around $|\Psi\rangle$ of Eq. (4.24), similar to that used to arrive at Eqs. (4.19)-(4.21). The situation is complicated by the more complex structure of $|\Psi\rangle$ for the condensed case with nonzero ρ. This can be gauged away by performing the bosonic transformation into new bosons a, b, c according to[17]

$$\begin{pmatrix} s \\ T_x \\ T_y \end{pmatrix}_{\boldsymbol{R}} = \begin{pmatrix} \cos\theta & i\,\mathrm{e}^{i\boldsymbol{Q}\cdot\boldsymbol{R}}\sin\theta & 0 \\ i\,\mathrm{e}^{i\boldsymbol{Q}\cdot\boldsymbol{R}}\sin\theta & \cos\theta & 0 \\ 0 & 0 & 1 \end{pmatrix} \begin{pmatrix} c \\ a \\ b \end{pmatrix}_{\boldsymbol{R}} \tag{4.26}$$

which converts $|\Psi\rangle$ into a suitable form $|\Psi\rangle = \prod_{\boldsymbol{R}} c^\dagger_{\boldsymbol{R}}|\mathrm{vac}\rangle$. Now we are in a position to employ the dynamical Gutzwiller approximation for the condensed boson c via $c, c^\dagger \to \sqrt{1-n_a-n_b}$ followed by harmonic expansion in a and b operators. On the harmonic level, both a and b bosons obey the Hamiltonian of the form (4.19) with

$$A_{\boldsymbol{q}} = E_T\cos 2\theta + 8J\sin^2 2\theta + 4J\cos^2 2\theta\;\gamma_{\boldsymbol{q}}\,, \qquad B_{\boldsymbol{q}} = 4J\cos^2 2\theta\;\gamma_{\boldsymbol{q}}\,, \qquad (a\text{-bosons}) \tag{4.27}$$

$$A_{\boldsymbol{q}} = E_T\cos^2\theta + 4J\sin^2 2\theta + 4J\cos^2\theta\;\gamma_{\boldsymbol{q}}\,, \qquad B_{\boldsymbol{q}} = 4J\cos^2\theta\;\gamma_{\boldsymbol{q}}\,, \qquad (b\text{-bosons}) \tag{4.28}$$

[17] The form of the transformation matrix is chosen based on two requirements - to preserve bosonic commutation relations in general and to maintain continuity with Eqs. (4.19)-(4.21) in particular.

which leads to elementary excitations independently carried by the a and b bosons and having the dispersions $\omega_{\boldsymbol{q}} = \sqrt{A_{\boldsymbol{q}}^2 - B_{\boldsymbol{q}}^2}$ shown in Fig. 36(d). For the uncondensed case $\theta = 0$, the dispersions are degenerate and coincide with Eq. (4.21) for the moving triplons, in the condensed case they split and the corresponding excitations become two distinct species. The excitation carried by b bosons is always gapless at the wavevector $\boldsymbol{Q}$ [symmetry point M in Fig. 36(c),(d)] and corresponds to a magnon. Not surprisingly, it is linked to the boson T_y associated with the direction perpendicular to the ordered moment. At $\boldsymbol{q} = \boldsymbol{Q}$, the mode merely rotates the ordered moment among energetically equivalent positions, hence its gapless nature. A rather specific feature of the magnon dispersion is that it reaches its maximum at $\boldsymbol{q} = 0$, making it very distinct from the conventional magnon dispersion obtained within antiferromagnetic Heisenberg model. The excitation carried by a bosons can be interpreted as an amplitude fluctuation of the condensate (sometimes dubbed as the condensed-matter Higgs mode [103]). Through the oscillations in the angle θ, it effectively shakes the ratio of s and T_x in the local superposition and hence modulates the condensate density. Such a mode necessarily costs some energy and is thus gapful as seen in Fig. 36(d). Close to the quantum critical point the amplitude fluctuations are still cheap and the gap is relatively small but when increasing J in the $J > J_{\text{crit}}$ interval, making the condensate more and more robust, the amplitude mode gradually shifts to higher energies. Fig. 36(e) schematically represents the two distinct modes as oscillations in a "Mexican hat" depiction of the condensate potential. Both of them enter various dynamic response functions and can be probed experimentally as we will discuss in the next paragraph.

4.4 Excitation spectra probed by neutron and Raman scattering

The peculiar magnetic state formed by the condensation of triplon excitations should most naturally manifest itself in the dynamical magnetic susceptibility. The traditional experimental way to access this quantity is the inelastic neutron scattering whose results will be discussed in the following. Apart from the unusual magnon dispersion having a maximum at $\boldsymbol{q} = 0$, we will be mainly interested in the signatures of the amplitude mode detected in the experiments.

To be able to appreciate the inelastic neutron scattering data presented in Fig. 37, we first inspect the corresponding susceptibilities on a simplified level of the previous Sec. 4.3. We start by transforming the pseudospin $\widetilde{\boldsymbol{S}}$ or magnetic moment operators via Eq. (4.26) followed by the replacement of the condensed c boson operator. This gives us the connection of the magnetic moment components and the elementary excitations carried by a, b bosons with already known dispersions. Keeping only terms up to the quadratic order as before, we have

$$\widetilde{S}_x = M_x/g_{ab} \approx \mathrm{e}^{i\boldsymbol{Q}\cdot\boldsymbol{R}} \sin 2\theta + \cos 2\theta \, (a - a^\dagger) \,, \tag{4.29}$$

$$\widetilde{S}_y = M_y/g_{ab} \approx \cos\theta \, (b - b^\dagger) \,, \tag{4.30}$$

$$\widetilde{S}_z = M_z/g_c \approx -\mathrm{e}^{i\boldsymbol{Q}\cdot\boldsymbol{R}} \sin\theta \, (b + b^\dagger) \,. \tag{4.31}$$

Equations (4.29)-(4.31) enable us to separately assess three distinct polarizations of the magnetic modes as depicted in Fig. 37(a): the longitudinal polarization parallel to the ordered moment direction (represented here by $\widetilde{S}_x$) is complemented by in-plane and out-of-plane transverse options ($\widetilde{S}_y$ and $\widetilde{S}_z$, respectively). Note that Fig. 37(a) shows the actual situation in Ca_2RuO_4 where the ordered moments point along the b axis while we are assuming the x direction. For the moment we can ignore this inconsistency as it is irrelevant in the initial inspection of the in-plane isotropic model. What matters here is just the relative orientation of the particular magnetic component with respect to the ordered moment direction and lattice plane.

Based on Eq. (4.29) it is clear that the oscillating part of longitudinal component of the magnetic moment is directly connected to the a bosons. The corresponding excitations – the

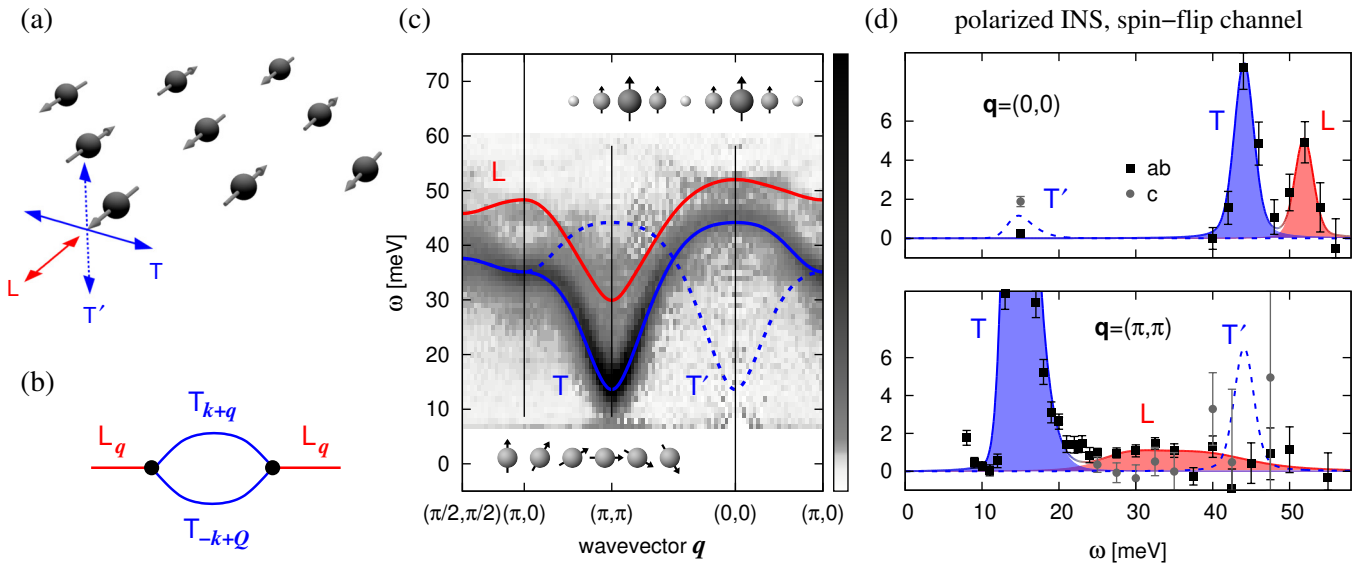

Fig. 37: (a) Polarization of the magnetic modes with respect to the ordered moment direction. Apart from the two transverse modes, in-plane T and out-of-plane T', the longitudinal mode L is visible in the experimental data. (b) Renormalization of the longitudinal mode via decay into two-magnon continuum. (c) Dynamical susceptibility as measured by unpolarized inelastic neutron scattering on Ca_2RuO_4. The lines show the theoretical dispersions of the magnetic modes including anharmonic effects. Model parameters used to fit the data: $E_T = 25$ meV, $J = 5.8$ meV, $\alpha = 0.15$, $A = 2.3$ meV, and $\Delta' = 4$ meV. The insets provide an intuitive picture of the nature of the longitudinal (top) and transverse modes (bottom). (d) Results of polarized neutron measurements (squares and dots) for two wavevectors $\boldsymbol{q} = (0,0)$ (upper panel) and $\boldsymbol{q} = (\pi,\pi)$ (lower panel) compared to the theoretical spectral profiles (shaded areas) of the modes calculated including anharmonic effects. The experimental conditions enabled to distinguish the in-plane (ab plane) response containing T and L modes and the out-of-plane (c axis) response containing the low-intensity T' mode. Details on the experiments and theoretical fits can be found in Ref. [101].

amplitude oscillations of the condensate – should therefore get imprinted into the susceptibility in a form of a longitudinal mode (L). In the harmonic approximation it will share the dispersion with the a bosons corresponding to the amplitude mode in Fig. 36(d). Similarly, the transverse in-plane component of the magnetic moment in Eq. (4.30) is linked to the b bosons that were interpreted as magnons. Finally, the transverse out-of-plane component in Eq. (4.31) is again linked to the b bosons, but it includes an extra factor $e^{i\boldsymbol{Q}\cdot\boldsymbol{R}}$ which translates to a shift in momentum space. Both transverse components of the dynamic susceptibility will therefore contain magnon-like modes T, T' but the dispersion of the out-of-plane T' mode will be shifted by $\boldsymbol{Q} = (\pi,\pi)$ compared to the original magnons.

This rough picture inferred from Eqs. (4.29)-(4.31) is consistent with the experimental observations represented by the map of unpolarized neutron scattering intensity shown in Fig. 37(c) and complemented by polarized neutron scattering spectra in Fig. 37(d). While the overall interpretation of the data in terms of the L, T, T' modes discussed above seems acceptable, the simplified approach of Sec. 4.3 apparently does not capture certain features of the experimental data. The deficiencies that are easily addressed on the theory side is the lack of the opening of the magnon gap and discrepancies in the details of the dispersions. These are remedied by the inclusion of the terms of the full pseudospin-1 model that were missing in Eq. (4.18). The low-energy magnon gap opens due to the orthorhombic field represented by Δ' term in the local

part (4.13) of the full model. It prefers the b-axis direction in the RuO_2 plane so that in-plane rotations of the ordered moments are not for free anymore.[18] The dispersions are "cured" by considering the bond-selective interaction A and the interaction of the out-of-plane pseudospin-1 components $\widetilde{S}_z$. Much more challenging is the proper treatment of the longitudinal response. The longitudinal mode is somewhat poorly visible in the unpolarized data but the polarized ones clearly suggest that its effective lifetime drastically changes through the Brillouin zone. The mode is observed as quite sharp at $\boldsymbol{q} = (0,0)$, however, in the region around the ordering vector $\boldsymbol{Q} = (\pi,\pi)$ it is subject to a strong decay. The explanation of this observation lies in the simultaneous excitation of two-magnon continuum in the longitudinal channel and its interplay with the amplitude mode. While being minor in three-dimensional cases [104,105], the interplay with Goldstone modes is of a crucial importance in our two-dimensional setting. Without going into details that can be found in the Supplementary Information to Ref. [101], we just note that the most important correction when analyzing the spin excitations beyond harmonic approximation is the coupling of the form

$$\sum_{\boldsymbol{kq}} \Gamma_{\boldsymbol{kq}}\, a_{\boldsymbol{q}}\, b_{\boldsymbol{k}}\, b_{-\boldsymbol{k}-\boldsymbol{q}-\boldsymbol{Q}} \quad \text{with} \quad \Gamma_{\boldsymbol{kq}} \propto J \sin 2\theta \left[\cos 2\theta\, \gamma_{\boldsymbol{q}} + \tfrac{1}{2}(\gamma_{\boldsymbol{k}} + \gamma_{-\boldsymbol{k}-\boldsymbol{q}-\boldsymbol{Q}})\right] \tag{4.32}$$

which generates a selfenergy for the bare L mode obtained within harmonic approximation. In the above equation, a and b should be understood as a shorthand notation for the imaginary parts of the corresponding fields associated with the operators such as $a - a^\dagger$ entering Eq. (4.29). The coupling activates a decay of the L mode into two-magnon continuum composed of pairs of T modes, the simplest example of such process being illustrated in Fig. 37(b). The selfenergy turns out to be indeed strongest for $\boldsymbol{q}$ around $\boldsymbol{Q} = (\pi,\pi)$ due to the common action of a large matrix element combined with the employment of low-energy magnons with momentum $\approx \boldsymbol{Q}$. The magnon gap due to Δ' is actually an advantage here and enables us to stay with RPA-like approximation for the two-magnon decay. Having gapless magnons, we would have to face delicate issues of infrared divergences. When renormalizing the L mode (and to a much smaller extent also the T mode) by incorporating the anharmonic corrections, we obtain a nice detailed agreement with the experimental data, including the extreme broadening of the L mode near $\boldsymbol{q} = \boldsymbol{Q}$ as demonstrated by the spectra in Fig. 37(d).

With the amplitude mode being obscured by the two-magnon continuum in the longitudinal magnetic susceptibility, we would like to find another probe allowing for a more direct access. Perhaps a bit surprising answer to this request is that the amplitude mode can be found in the typically magnetically silent channel of Raman scattering. As it has been shown in several theoretical studies, the appearance of the amplitude mode strongly depends on the symmetry of the probe used [103,106]. We have observed its large decay in the longitudinal response (that was still reduced thanks to the magnon gap) while in so-called scalar susceptibility it can maintain its coherence [107–109]. The latter situation is the case of the Raman scattering.

In formal terms, the Raman scattering on a superexchange-driven magnetic system probes dynamic correlation function of the Raman operator that is expressed within Fleury-Loudon approximation [110] as

$$\mathcal{R} \propto \sum_{\langle ij \rangle} (\epsilon_{\text{in}} \cdot \boldsymbol{r}_{ij})(\epsilon_{\text{out}} \cdot \boldsymbol{r}_{ij}) \mathcal{H}_{ij}\,. \tag{4.33}$$

Here $\mathcal{H}_{ij}$ is the superexchange Hamiltonian for the bond $\langle ij \rangle$ connecting two sites with the relative position $\boldsymbol{r}_{ij}$ and ϵ_{in} (ϵ_{out}) is the polarization vector of the incoming (outgoing) photon.

[18] Lifting the degeneracy in the subspace spanned by T_x, T_y as shown in Fig. 34(b), this field also selects a particular triplon combination $T_b = (T_x + T_y)/\sqrt{2}$ to condense. The calculation in Sec. 4.3 where we have used T_x condensation for simplicity has to be revised accordingly.

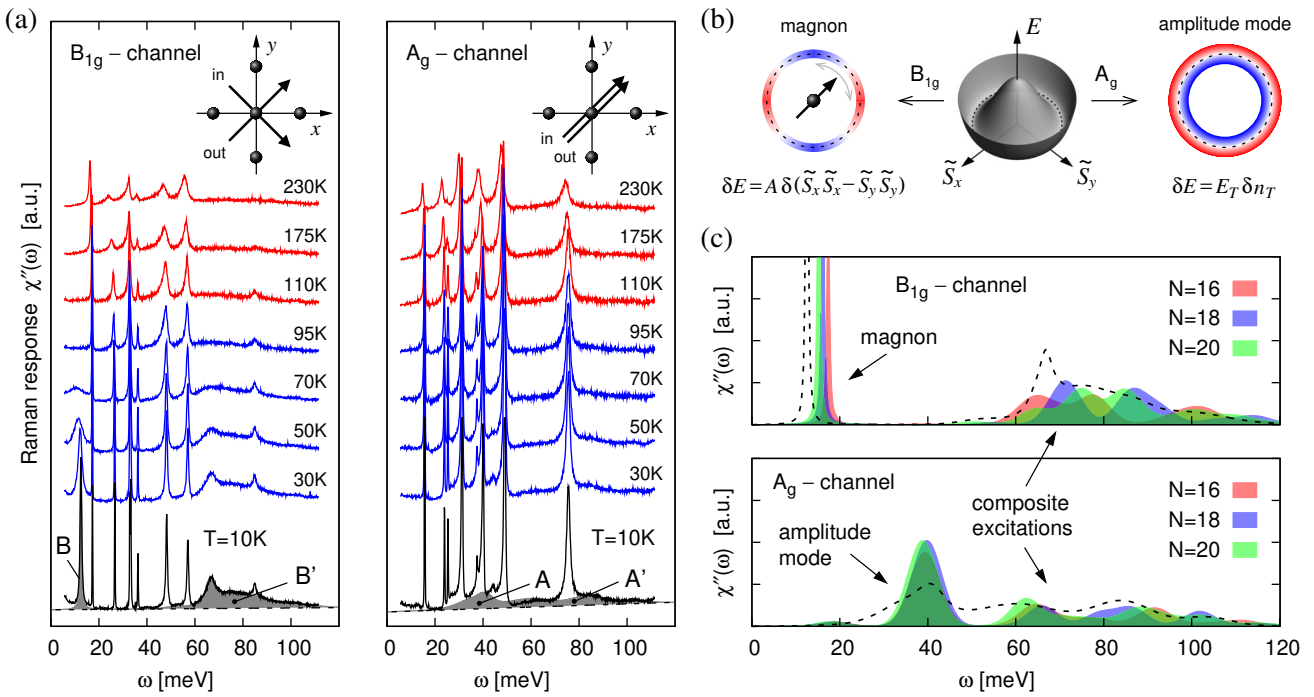

Fig. 38: (a) Temperature dependent Raman spectra of Ca_2RuO_4 sample obtained using the B_{1g} and A_g polarization setups [111]. The insets indicate the relative orientation of the in-plane polarization vectors $\epsilon_{\rm in}$, $\epsilon_{\rm out}$ with respect to the lattice. The magnetic part of the signal developing below $T_{\rm N} \approx 110\,{\rm K}$ is highlighted for the lowest $T = 10{\rm K}$ by gray shading. Sharp peaks corresponding to the phonons that are present at all temperatures were subtracted. (b) Schematic representation of the Raman excitation of the magnetic condensate via modulation of the bond energy given by Eq. (4.33). In the B_{1g} channel, the A-term deforms the bottom of the potential driving a magnon rotation. In the A_g channel, modulations via n_T lead to an isotropic oscillation of the condensate amplitude – a direct excitation of the amplitude mode occurs in this channel. (c) Raman spectra obtained by exact diagonalization on clusters with $N = 16$, 18, and 20 sites compared to experimental data. The numerical spectra for B_{1g} and A_g channels are presented in identical scales and overlayed by the magnetic signal from panel (a) (dashed lines). The calculation was performed using $E_T = 31$ meV, $J = 7.5$ meV, $\alpha = 0.15$, $A = 2.3$ meV, and $\Delta' = 4$ meV.

By playing around with various combinations of the polarizations, we can test the system in rather different ways.

For Heisenberg-like magnets the usual channel of interest is the B_{1g} one that is probed when using cross-polarized setup as shown in the inset of Fig. 38(a). It corresponds to the Raman operator of the form $\mathcal{R} \propto \mathcal{H}_x - \mathcal{H}_y$, where $\mathcal{H}_x$ and $\mathcal{H}_y$ are sums of $\mathcal{H}_{ij}$ over x- and y-bonds, respectively. In the Heisenberg case this term excites a two-magnon continuum. The same happens in our case with mostly Heisenberg-like bond interactions of pseudospins-1 as given for the x-bonds by $\mathcal{H}_x$ in Eq. (4.14). However, thanks to the bond-selective anisotropic component of the interaction $A\sum_{\langle ij\rangle}(\pm 1)(\widetilde{S}^x_i\widetilde{S}^x_j - \widetilde{S}^y_i\widetilde{S}^y_j)$, we get an additional feature that is unusual in the magnetic Raman scattering – a direct excitation of a *single* magnon. To see this we consider the A part of the Raman operator in more convenient axes, $A\sum_{\langle ij\rangle}(\widetilde{S}^a_i\widetilde{S}^b_j + \widetilde{S}^b_i\widetilde{S}^a_j)$, and approximate $\widetilde{S}^b$ which is the component along the ordered moment direction by $\widetilde{S}^b_{\boldsymbol{R}} = \langle S_\parallel\rangle\, {\rm e}^{i\boldsymbol{Q}\cdot\boldsymbol{R}}$. This way the A part of the B_{1g} Raman operator becomes $\propto A\langle S_\parallel\rangle\widetilde{S}^a_{\boldsymbol{Q}}$ and probes therefore the magnon at $\boldsymbol{q} = \boldsymbol{Q}$. Looking at the experimental data in Fig. 38(a), we can see the magnetic signal developing below $T_{\rm N}$. Consistently with the above expectations, it is composed of the two contributions – two-magnon continuum (feature B') encompassing energies around two times the magnon bandwidth

$\approx 40\,\mathrm{meV}$ observed in Fig. 37(c) and a very sharp peak (feature B) at the energy coinciding with the bottom of the magnon dispersion at $\boldsymbol{Q} = (\pi, \pi)$.

Let us now focus on the A_g channel that is normally not very interesting in magnetic Raman scattering. In this case the Raman operator can be expressed as $\mathcal{R} \propto \mathcal{H}_x + \mathcal{H}_y$ and is typically proportional to the magnetic Hamiltonian of the system itself, making this channel silent at finite frequencies. However, our Hamiltonian is equipped with a large local term $E_T n_T$ that is a source of highly interesting spectra. Finite-energy dynamics is equally well described by the Raman operator equal to the difference of scaled $\mathcal{R}$ and the Hamiltonian, $\mathcal{R}' = \mathcal{H}_x + \mathcal{H}_y - \mathcal{H} = -E_T n_T \propto n_T$, which means that in the A_{1g} channel we are in fact probing the n_T susceptibility and hence the amplitude mode. To have a more precise connection, we can take the n_T operator approximated in the same way as the longitudinal $\widetilde{S}_x$ in Eq. (4.29). It reads as

$$n_T \approx \rho - \tfrac{1}{2}\, i\, \mathrm{e}^{i\boldsymbol{Q}\cdot\boldsymbol{R}} \sin 2\theta\, (a - a^\dagger) \tag{4.34}$$

which implies that the magnetic signal in A_{1g} Raman channel (essentially the n_T susceptibility for $\boldsymbol{q} \to 0$) will contain the $\boldsymbol{q} \to \boldsymbol{Q}$ amplitude mode of Fig. 36(d) that failed to show up clearly in the longitudinal magnetic response. The experimental data for the A_g channel in Fig. 38(a) indeed show a spectral profile consisting of a peak (feature A) followed by a long tail (feature A') that resembles the unspoiled "Higgs" spectral functions found in the literature [107–109]. To have a one-to-one comparison for our particular model, Fig. 38(c) presents the theoretical Raman spectra obtained numerically for small clusters and contrasts them to the magnetic part of the signal plotted in Fig. 38(a). Overall, the magnetic Raman features in both channels are well reproduced by the model calculations including their relative intensities, successfully concluding our discussion on the singlet-triplet magnetism of Ca_2RuO_4, where the magnetic order is due to Bose-Einstein condensation of initially gapped magnetic excitations.

5 Papers addressing the Kitaev–Heisenberg model

- *Kitaev-Heisenberg Model on a Honeycomb Lattice: Possible Exotic Phases in Iridium Oxides A_2IrO_3*

  J. Chaloupka, G. Jackeli, and G. Khaliullin

  Physical Review Letters **105**, 027204 (2010) DOI: 10.1103/PhysRevLett.105.027204

  In this paper we made an initial exploration of the phase diagram of the Kitaev-Heisenberg model for honeycomb iridates that was proposed in Ref. [20]. Assuming FM Kitaev interaction and AF Heisenberg interaction, we have demonstrated that the FM Kitaev spin liquid survives the perturbation by the Heisenberg interaction up to a sizable strength, leading to a finite window of the liquid phase in the phase diagram.

- *Zigzag Magnetic Order in the Iridium Oxide Na_2IrO_3*

  J. Chaloupka, G. Jackeli, and G. Khaliullin

  Physical Review Letters **110**, 097204 (2013) DOI: 10.1103/PhysRevLett.110.097204

  This paper is a continuation of the study of the Kitaev-Heisenberg model reflecting the experimental data that appeared since the publication of the first paper in 2010. Providing microscopic arguments, we have extended the parameter regime to include further combinations of signs of the Kitaev and Heisenberg interactions and determined the parameter values that were consistent with the experimental data on Na_2IrO_3 available that time – zigzag type of the magnetic ordering, temperature-dependent static magnetic susceptibility, and powder inelastic neutron scattering.

- *Direct evidence for dominant bond-directional interactions in a honeycomb lattice iridate Na_2IrO_3*

  S. H. Chun, J. W. Kim, J. Kim, H. Zheng, C. C. Stoumpos, C. D. Malliakas, J. F. Mitchell, K. Mehlawat, Y. Singh, Y. Choi, T. Gog, A. Al-Zein, M. M. Sala, M. Krisch, J. Chaloupka, G. Jackeli, G. Khaliullin, and B. J. Kim

  Nature Physics **11**, 462 (2015) DOI: 10.1038/NPHYS3322

  By studying spin correlations above the Néel temperature using magnetic diffuse x-ray scattering, this paper brought an experimental evidence, that the spin interactions in Na_2IrO_3 are highly anisotropic and this anisotropy is bond selective. Based on a comparison to numerical simulations, we have quantified the dominance of the anisotropic interactions. Another important result of this paper is the determination of the ordered moment direction by resonant x-ray diffraction that fixed the FM sign of the Kitaev interaction in Na_2IrO_3.

- *Hidden symmetries of the extended Kitaev-Heisenberg model: Implications for the honeycomb-lattice iridates A_2IrO_3*

  J. Chaloupka and G. Khaliullin

  Physical Review B **92**, 024413 (2015) DOI: 10.1103/PhysRevB.92.024413

  This paper explored the rich hidden symmetries of the extended Kitaev-Heisenberg model (including Γ and Γ' interactions) through the method of dual transformations that map the model to an equivalent form but with different parameters. We have identified several points of hidden SU(2) symmetry where the model reduces (in a nontrivial way) to either FM or AF Heisenberg model. The complete exploration of these symmetries provided deeper insights into the global phase diagram of the model. The results were also used in the discussion of the relevant parameter regime of honeycomb iridates Na_2IrO_3 and Li_2IrO_3.

- *Magnetic anisotropy in the Kitaev model systems Na_2IrO_3 and $RuCl_3$*

  J. Chaloupka and G. Khaliullin

  Physical Review B **94**, 064435 (2016) DOI: 10.1103/PhysRevB.94.064435

  This paper is devoted to a detailed study of the ordered moment direction as a very sensitive probe of the anisotropic interactions. We have developed a method based on spin-coherent states that enabled to analyze cluster ground states obtained by exact diagonalization and precisely determine the moment direction. Utilizing the above methodology we have attempted to narrow down the parameter regime in Na_2IrO_3 and the newly discovered (at that time) α-$RuCl_3$. Doing so, we have emphasized the role of the trigonal field that brings a distinction between the pseudospin direction and those of the magnetic moment and a special vector entering the polarization dependence of the resonant x-ray scattering.

- *Phase diagram and spin correlations of the Kitaev-Heisenberg model: Importance of quantum effects*

  D. Gotfryd, J. Rusnačko, K. Wohlfeld, G. Jackeli, J. Chaloupka, and A. M. Oleś

  Physical Review B **95**, 024426 (2017) DOI: 10.1103/PhysRevB.95.024426

  In this paper we tried to quantify the role of quantum fluctuations through the phase diagram of the (non-extended) Kitaev-Heisenberg model by contrasting several methods that handle quantum fluctuations in different ways. We have illustrated and provided insights into several interesting effects, such as the striking difference of the robustness of the FM and AF Kitaev spin liquid phases against Heisenberg perturbations.

- *Kitaev-like honeycomb magnets: Global phase behavior and emergent effective models*

  J. Rusnačko, D. Gotfryd, and J. Chaloupka

  Physical Review B **99**, 064425 (2019) DOI: 10.1103/PhysRevB.99.064425

  This paper presents a comprehensive discussion of the global phase diagram of the extended Kitaev-Heisenberg model. By combining numerical simulations on small clusters and analytical techniques based on symmetry analysis of this spin Hamiltonian, we were able to thoroughly interpret the global trends in the phase diagram and uncover peculiar links to well-known simpler models on the honeycomb lattice. The paper can also serve as a methodological example how to deal with a complex spin model with bond-selective anisotropic interactions based on symmetry grounds.

- *Dynamic Spin Correlations in the Honeycomb Lattice Na_2IrO_3 Measured by Resonant Inelastic x-Ray Scattering*

  J. Kim, J. Chaloupka, Y. Singh, J. W. Kim, B. J. Kim, D. Casa, A. Said, X. Huang, and T. Gog

  Physical Review X **10**, 021034 (2020) DOI: 10.1103/PhysRevX.10.021034

  In this paper we present results of resonant inelastic x-ray (RIXS) measurements on Na_2IrO_3 utilizing a state-of-the-art setup at APS Argonne that are interpreted through an extensive set of numerical simulations. The experiment provided unique momentum and energy resolved spectra of spin excitations in this compound. These are compared to exact diagonalization calculations of the RIXS response based on the extended Kitaev-Heisenberg model. This way, important conclusions about the interactions in Na_2IrO_3 were obtained.

- *Kitaev Spin Liquid in 3d Transition Metal Compounds*

  H. Liu, J. Chaloupka, and G. Khaliullin

  Physical Review Letters **125**, 047201 (2020) DOI: 10.1103/PhysRevLett.125.047201

  This paper extends the idea of Ref. [62] that suggested a potential realization of the Kitaev honeycomb model in cobalt compounds with $3d^7$ valence configuration. Via a microscopic derivation of the exchange interactions when including the effects of the trigonal crystal field, we found that the trigonal distortion should be an efficient tool to drive the material toward the Kitaev spin liquid phase. Apart from a general discussion we tried to apply our theory to the candidate compound $Na_3Co_2SbO_6$ and estimated the parameters of the corresponding model.

PRL 105, 027204 (2010) PHYSICAL REVIEW LETTERS week ending 9 JULY 2010

Kitaev-Heisenberg Model on a Honeycomb Lattice: Possible Exotic Phases in Iridium Oxides A_2IrO_3

Jiří Chaloupka,[1,2] George Jackeli,[2,*] and Giniyat Khaliullin[2]

[1]*Department of Condensed Matter Physics, Masaryk University, Kotlářská 2, 61137 Brno, Czech Republic*
[2]*Max-Planck-Institut für Festkörperforschung, Heisenbergstrasse 1, D-70569 Stuttgart, Germany*

(Received 16 April 2010; published 9 July 2010)

We derive and study a spin one-half Hamiltonian on a honeycomb lattice describing the exchange interactions between Ir^{4+} ions in a family of layered iridates A_2IrO_3 (A = Li, Na). Depending on the microscopic parameters, the Hamiltonian interpolates between the Heisenberg and exactly solvable Kitaev models. Exact diagonalization and a complementary spin-wave analysis reveal the presence of an extended spin-liquid phase near the Kitaev limit and a conventional Néel state close to the Heisenberg limit. The two phases are separated by an unusual stripy antiferromagnetic state, which is the exact ground state of the model at the midpoint between two limits.

DOI: 10.1103/PhysRevLett.105.027204 PACS numbers: 75.10.Jm, 75.25.Dk, 75.30.Et

Magnetic systems exhibit, most commonly, long-range classical order at sufficiently low temperatures. An exception are frustrated magnets, in which the topology of the underlying lattice and/or competing interactions lead to an extensively degenerate manifold of classical states. In such systems, exotic quantum phases of Mott insulators (spin liquids, valence bond solids, etc.) can emerge as the true ground states (for reviews, see Refs. [1,2]). In quantum spin liquids, strong zero-point fluctuations of correlated spins prevent them to ''freeze'' into magnetic or statically dimerized patterns, and conventional phase transitions that break time-reversal and lattice symmetries are avoided. Spin liquids have attracted particular attention since Anderson proposed their possible connection to superconductivity of cuprates [3].

Recently, spin-liquid states of matter have been exemplified, on a quantitative level, by an exactly solvable model by Kitaev [4]. His model deals with spins one-half that live on a honeycomb lattice. The nearest-neighbor (NN) spins interact in a simple Ising-like fashion but, because different bonds use different spin components [see Fig. 1(a)], the model is highly frustrated. Its ground state is spin-disordered and supports the emergent gapless excitations represented by Majorana fermions [4]. Spin-spin correlations are, however, short-ranged and confined to NN pairs [5,6]. This may suggest the robustness of the disordered state to spin perturbations. Indeed, Tsvelik has shown [7] that there is a window of stability for the spin-liquid state in the Kitaev model perturbed by isotropic Heisenberg exchange.

Finding a physical realization of this remarkable model is a great challenge, also because of its special properties attractive for quantum computation [4]. As the key element of the model is a bond-selective spin anisotropy, one possible idea [8] is to explore Mott insulators of late transition metal ions with orbital degeneracy, in which the bond directional nature of electron orbitals can be translated into a desired anisotropy of magnetic interactions through strong spin-orbit coupling.

In this Letter, we examine the iridium oxides A_2IrO_3 from this perspective. In these compounds, the Ir^{4+} ions have an effective spin one-half moment and form weakly coupled honeycomb-lattice planes. Our analysis of the underlying exchange mechanisms shows that the spin Hamiltonian comprises two terms, ferromagnetic (FM) and antiferromagnetic (AF), in the form of Kitaev and Heisenberg models, respectively. The model has an inter-

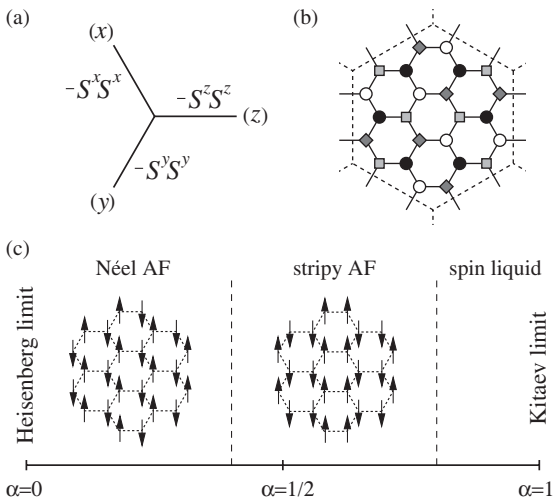

FIG. 1. (a) Three types of bonds in the honeycomb lattice and Kitaev part of the interaction. (b) The supercell of the four-sublattice system enabling the transformation of the model (1) into the Hamiltonian of a simple ferromagnet at $\alpha = \frac{1}{2}$. This supercell with periodic boundary conditions applied was used as a cluster for the exact diagonalization. (c) Schematic phase diagram: With increasing α, the ground state changes from the Néel AF order to the stripy AF state (being a fluctuation-free exact solution at $\alpha = \frac{1}{2}$) and to the Kitaev spin liquid. See the text for the critical values of α.

esting phase behavior and hosts, in addition to the spin-liquid state, an unusual AF order that is also an exact solution at a certain point in phase space.

Experimental studies of iridium compounds are rather scarce, and the nature of their insulating behavior is not yet fully understood. In fact, Na_2IrO_3 was suggested as an interesting candidate for a topological band insulator [9]. Given that high temperature magnetic susceptibilities of Na_2IrO_3 and Li_2IrO_3 obey the Curie-Weiss law with an effective moment corresponding $S = 1/2$ per Ir ion [10–13], we start here with the Mott insulator picture.

The Hamiltonian.—We recall that the Ir^{4+} ion in the octahedral field has a single hole in the threefold degenerate t_{2g} level hosting an orbital angular momentum $l = 1$. Strong spin-orbit coupling lifts this degeneracy, and the resulting ground state is a Kramers doublet with total angular momentum one-half [14], referred to as "spin" hereafter. In fact, it is predominantly of orbital origin, and this is what makes the magnetic interactions highly anisotropic due to the spin-orbit entanglement of magnetic and real spaces. In A_2IrO_3 compounds, the IrO_6 octahedra share the edges, and Ir ions can communicate through two 90° Ir-O-Ir exchange paths [8] or via direct overlap of their orbitals. Collecting the possible exchange processes (discussed below) and projecting them onto the lowest Kramers doublet with $S = 1/2$, we obtain the following spin Hamiltonian on a given NN ij bond:

$$\mathcal{H}_{ij}^{(\gamma)} = -J_1 S_i^\gamma S_j^\gamma + J_2 \boldsymbol{S}_i \cdot \boldsymbol{S}_j. \tag{1}$$

Here spin quantization axes are taken along the cubic axes of IrO_6 octahedra. In a honeycomb lattice formed by Ir ions, there are three distinct types of NN bonds referred to as γ ($=x, y, z$) bonds because they host the Ising-like J_1 coupling between the γ components of spins [see Fig. 1(a)]. The first part of Eq. (1) is thus nothing but the FM Kitaev model, and the J_2 term is a conventional AF Heisenberg model. The exchange constants J_1 and J_2 are derived from a multiorbital Hubbard Hamiltonian consisting of the local interactions and the hopping term. The latter describes $t_{pd\pi}$ hopping between Ir $5d$ and O $2p$ orbitals via the charge-transfer gap Δ_{pd}, and a direct dd overlap t' between NN Ir t_{2g} orbitals [15]. We find $J_1 = (\eta_1 + 2\eta_2)$ and $J_2 = (\eta_2 + \eta_3)$. Hereafter, we use $4t^2/9U_d$ as our energy unit, where $t = t_{pd\pi}^2/\Delta_{pd}$, and U_d stands for the Coulomb repulsion on the same d orbitals. There are three physically distinct virtual processes that determine the set of η parameters and thus the ratio J_2/J_1. The $\eta_1 = \frac{6J_H}{U_d - 3J_H}\frac{U_d}{U_d - J_H}$ term appears due to the multiplet structure of the excited levels induced by Hund's coupling J_H [8]. The processes when two holes meet at the same oxygen site (and experience U_p repulsion) and when they are cyclically exchanged around a Ir_2O_2 square plaquette bring together a $\eta_2 = \frac{U_p}{\Delta_{pd} + U_p/2}\frac{U_d}{\Delta_{pd}}$ contribution. Further, a direct dd-hopping t' between NN Ir t_{2g} orbitals contributes to the Heisenberg term with exchange coupling $\eta_3 = (t'/t)^2$. It is difficult to estimate the values of all the parameters involved; however, we expect η_1 to be the largest, of the order of 1, and $\eta_{2,3} < 1$.

We parametrize the exchange couplings as $J_1 = 2\alpha$ and $J_2 = 1 - \alpha$ and study the properties of Kitaev-Heisenberg model (1) in the whole parameter space $0 \le \alpha \le 1$.

Phase diagram.—At $\alpha = 0$, we are left with the Heisenberg model exhibiting the Néel order with a staggered moment reduced to $\langle S^z \rangle \simeq 0.24$ [16]. The opposite limit, $\alpha = 1$, corresponds to the exactly solvable Kitaev model with a short-range spin-liquid state [4], where spin correlation functions are identically zero beyond the NN distance and, on a given NN bond, only the components of spins matching the bond type are correlated [5].

Interestingly, the model is exactly solvable at $\alpha = \frac{1}{2}$, too. At this point Eq. (1) reads, e.g., on a z-type bond, as $\mathcal{H}_{ij}^{(z)} = \frac{1}{2}(S_i^x S_j^x + S_i^y S_j^y - S_i^z S_j^z)$. This anisotropic Hamiltonian can be mapped to that of a simple Heisenberg model on all bonds simultaneously [17]. Specifically, we divide the honeycomb lattice into four sublattices [see Fig. 1(b)] and introduce the rotated operators $\tilde{\boldsymbol{S}}$: While $\tilde{\boldsymbol{S}} = \boldsymbol{S}$ in one of the sublattices, $\tilde{\boldsymbol{S}}$ on the remaining three sublattices differs from the original $\boldsymbol{S}$ by the sign of two appropriate components, depending on the sublattice they belong to. In the new basis, Eq. (1) takes the form

$$\mathcal{H}_{ij}^{(\gamma)} = -2(2\alpha - 1)\tilde{S}_i^\gamma \tilde{S}_j^\gamma - (1 - \alpha)\tilde{\boldsymbol{S}}_i \cdot \tilde{\boldsymbol{S}}_j. \tag{2}$$

At $\alpha = \frac{1}{2}$, the first term vanishes and we obtain the isotropic, both in spin and real spaces, Heisenberg model $\mathcal{H}_{ij}^{(\gamma)} = -\frac{1}{2}\tilde{\boldsymbol{S}}_i \cdot \tilde{\boldsymbol{S}}_j$ with FM coupling. Thus, at $\alpha = \frac{1}{2}$, i.e., at $J_1 = 2J_2$, the exact ground state of model (1) is a fully polarized FM state in the rotated basis. Now consider the FM array of spins with, e.g., $\langle \tilde{S}^z \rangle = 1/2$, and map it back to the original spin basis. The resulting order corresponds to a stripy AF pattern of the original magnetic moments depicted in Fig. 1(c). Note that such a stripy order, despite being of AF type, is fluctuation-free at $\alpha = \frac{1}{2}$ and would thus show a fully saturated AF order parameter.

The above discussion suggests three possible ground state phases of the model (1) as shown in Fig. 1(c): (i) Néel order near $\alpha = 0$, (ii) stripy AF order around $\alpha = \frac{1}{2}$, and (iii) a spin-liquid phase close to $\alpha = 1$.

We first consider the ordered phases. Except special cases of $\alpha = 0$ and $\alpha = \frac{1}{2}$ just discussed, the Hamiltonian (1) does not have any spin-rotational symmetry. However, a spurious $SU(2)$ continuous symmetry and associated pseudo-Goldstone mode appear in a linear spin-wave (SW) description. As in the case of a similar model on a cubic lattice [18], we find that quantum fluctuations restore the underlying discrete (hexagonal) symmetry of the model, selecting thereby the direction of ordered moments along one of the cubic axes (of IrO_6 octahedra), and also open a gap in SW spectra. Considering the quantum energy

cost for rotating the order parameter by a small angle away from a cubic axis, we find a quantum SW gap $\Delta \simeq \frac{2}{\alpha}(\alpha - \frac{1}{2})^2$ for $\alpha \sim \frac{1}{2}$.

The classical phase boundary between Néel and stripy AF orderings is at $\alpha = \frac{1}{3}$, where linear SW spectra of both states develop zero-energy lines [19], reflecting the infinite degeneracy of classical states. At $\alpha = \frac{1}{3}$, Eq. (1) reads, e.g., on z-type bonds, as $\mathcal{H}_{ij}^{(z)} = \frac{2}{3}(S_i^x S_j^x + S_i^y S_j^y)$; i.e., only two spin components are coupled on a given bond. Considering Néel or stripy AF with ordered spins parallel to the z axis, one finds that flipping all the spins along a zigzag chain, formed by x- and y-type bonds, does not change classical energy. This degeneracy is again accidental (an artifact of classical treatment) and can thus be lifted by quantum fluctuations. They favor the Néel state and shift the classical phase boundary to a larger value $\alpha \simeq 0.4$. This estimate is obtained by comparing the energies of the Néel $[e_1 \simeq -\frac{3}{16}(3 - 5\alpha)]$ and the stripy $[e_2 \simeq -\frac{1}{8}(5\alpha - 3 + \frac{1}{\alpha})]$ states including quantum corrections via second-order perturbation theory and matches well the numerical result found below.

Now we discuss the phase behavior at $\frac{1}{2} < \alpha < 1$, i.e., in between two exact solutions (stripy AF at $\alpha = \frac{1}{2}$ and a Kitaev spin liquid at $\alpha = 1$). In terms of rotated spins, all the couplings are of FM nature in this region [see Eq. (2)]. Thus, the FM order (read stripy AF of the original spins) is the only possible magnetic phase here to compete with the spin-liquid state. Since the latter is stable against a weak Heisenberg-type perturbation [7], a critical value of α for the spin order/disorder transition must be located at some point less than 1. We give its naive estimate based on the energetics of these two phases. The energy of the stripy AF state is given above. The *upper* boundary for the energy of spin-liquid state is given by the expectation value of Eq. (2) using the exact result $\langle S_i^\gamma S_j^\gamma \rangle = 0.13$ at $\alpha = 1$ [5]. As a result, we find the transition from stripy AF order to a spin liquid at $\alpha \simeq 0.86$ (close to the numerical result below).

Single-magnon excitations fail to detect this transition (since, as said above, there is not any other competing magnetic state). As α increases, the lower branch of the linear SW spectrum just gradually softens, to become completely flat in the limit of $\alpha = 1$ where the classical ground state is extensively degenerate [20]. We therefore suspect that the instability responsible for the collapse of magnetic order resides in the two-magnon sector [21]. Leaving this subtle issue for a future work, we now turn to our numerical results, which describe the evolution of spin correlations across the entire phase diagram.

Numerical study.—We use the Lanczos exact diagonalization method to study a 24-site cluster [see Fig. 1(b)] with periodic boundary conditions. The cluster is compatible with the above discussed four-sublattice transformation of Eq. (1) into Eq. (2). This provides an exact reference point $\alpha = 1/2$, which is useful for the interpretation of numerical data shown in Figs. 2 and 3 in terms of the original as well as transformed spins.

Figure 2 clearly locates the two phase transitions. In particular, a pronounced maximum in the second derivative of the ground state energy [Fig. 2(c)] indicates a first-order transition from Néel to stripy AF phase at $\alpha \simeq 0.4$. The much weaker (note the *log* scale) and wider second peak at $\alpha \simeq 0.8$ suggests a second- (or a weakly first-) order transition from stripy AF to a spin-liquid state.

Figure 2(a) shows the squared total spins $\tilde{\boldsymbol{S}}_{\rm tot}^2$ and $\boldsymbol{S}_{\rm tot}^2$ normalized to $\tilde{S}(\tilde{S}+1)$ with $\tilde{S} = N/2$ that can be reached in the FM state. Although these are not conserved quantities in the model, they characterize the phase map quite well. In particular, a long tail of $\tilde{\boldsymbol{S}}_{\rm tot}^2$ above $\alpha = 0.8$ indicates a "leakage" of stripy AF correlations into a spin-liquid phase. This is also evidenced by the behavior of longer range, beyond NN, spin correlations that are still visible in a spin-liquid regime, except close to the

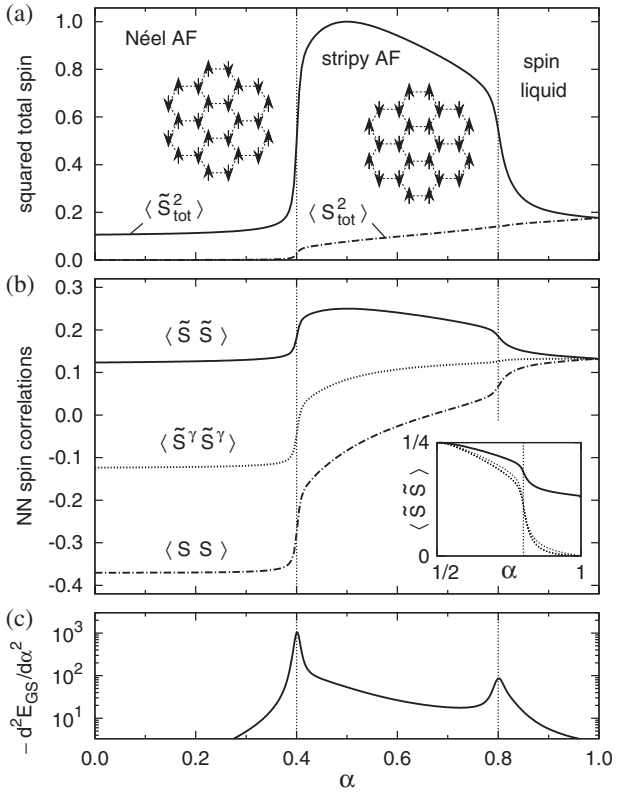

FIG. 2. (a) Squared total spin of the 24-site cluster, normalized to its value in the fully polarized FM state, as a function of α. The solid (dot-dashed) line corresponds to the rotated (original) spin basis. (b) The NN spin correlations: The solid (dot-dashed) line corresponds to a scalar product of the rotated (original) spins. The component of the correlation function matching the bond direction is indicated by a dotted line. This quantity is the same in both bases. The inset compares NN spin correlations (solid line) above $\alpha = 0.5$ with longer range spin correlations up to third-nearest neighbors (dotted lines). (c) Negatively taken second derivative of the ground state energy with respect to α. Its maxima indicate the phase transitions at $\alpha \simeq 0.4$ and 0.8.

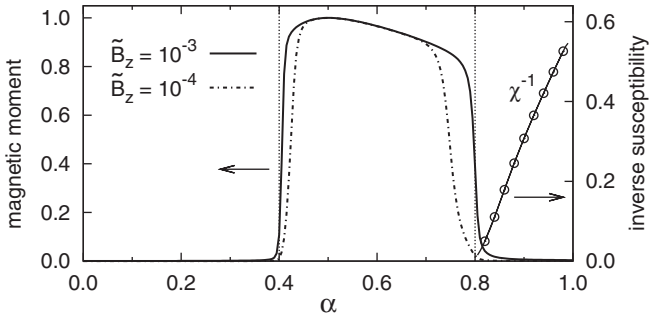

FIG. 3. Magnetic moment $2\langle \tilde{S}^z_{\rm tot}\rangle/N$ induced by field $\tilde{B}_z$ (Zeeman coupled to the rotated spins). The circles at $\alpha > 0.8$ show the inverse spin susceptibility to this field.

Kitaev limit where they vanish completely [see the inset in Fig. 2(b)].

Figure 2(b) highlights how the NN spin correlations evolve as their interactions change from one type to another. In the Néel state, where the model is more Heisenberg-like for the original spins, we reproduce $\langle \boldsymbol{S}_i \cdot \boldsymbol{S}_j\rangle \simeq -0.37$ [16]. At the "hidden" FM Heisenberg point $\alpha = 1/2$, one finds $\langle \tilde{\boldsymbol{S}}_i \cdot \tilde{\boldsymbol{S}}_j\rangle = \frac{1}{4}$, equally contributed by all three components of the rotated spin $\tilde{\boldsymbol{S}}$. Things change dramatically in the spin-liquid phase: Here, a particular component of spin correlations $\langle \tilde{S}^\gamma_i \tilde{S}^\gamma_j\rangle$, dictated by the Kitaev model, dominates. Its value of 0.132 that we find at $\alpha = 1$ agrees well with the exact result 0.131 for an infinite lattice [5].

Finally, we discuss the response to a weak magnetic field $\tilde{B}^z$ which, in terms of original spins, linearly couples to the stripy AF order parameter. Figure 3 shows that even a very weak field induces a nearly saturated moment in the entire region of the stripy AF phase. As the system switches to the Néel phase, a response to the "stripy field" $\tilde{B}^z$ drops abruptly to zero, as expected. The induced moment sharply reduces near $\alpha = 0.8$, too, but remains finite in a spin-liquid phase. Here the magnetization curve shows a linear dependence on $\tilde{B}^z$, and we may extract from its slope the susceptibility $\chi = \langle \tilde{S}^z_{\rm tot}\rangle/N\tilde{B}_z$. Shown in Fig. 3 is the inverse value of χ as a function of α. This quantity scales with the energy gap between the ground state and the excited states that are accessible by the magnetic field. According to Kitaev's solution [4], these states must belong to the flux sectors located at energies of the order of 1. The observed $\chi^{-1} \propto (\alpha - 0.8)$ behavior shows that this characteristic (spin) gap gradually softens towards the $\alpha \simeq 0.8$ critical point, as the spin correlations beyond the NN distances start to grow [see Fig. 2(b), inset].

Experimental data [10–13] are rather insufficient to conclusively locate the position of A_2IrO_3 compounds in our phase diagram. Also, Na/Ir site disorder [13] has to be kept in mind: Often, nonmagnetic impurities induce local moments [22], and this has been shown to happen in the Kitaev model as well [23].

In conclusion, we have examined the interactions and possible magnetic states in iridates A_2IrO_3. The obtained Kitaev-Heisenberg model shows rich behavior including a spin liquid and unusual stripy AF phases. We hope that these results will motivate experimental studies of layered iridates and similar compounds of late transition metal ions, where the physics of the Kitaev model might be within reach.

We thank B. Keimer, A. Schnyder, S. Trebst, and M. Zhitomirsky for discussions. We are grateful to H. Takagi and A. M. Tsvelik for valuable discussions and for communicating the unpublished results. Support from MSM0021622410 (J. C.) and GNSF/ST09-447 (G. J.) is acknowledged.

*Also at Andronikashvili Institute of Physics, 0177 Tbilisi, Georgia.

[1] L. Balents, Nature (London) **464**, 199 (2010).
[2] G. Misguich and C. Lhuillier, in *Frustrated Spin Systems*, edited by H. T. Diep (World Scientific, Singapore, 2005).
[3] P. W. Anderson, Science **235**, 1196 (1987).
[4] A. Kitaev, Ann. Phys. (N.Y.) **321**, 2 (2006).
[5] G. Baskaran, S. Mandal, and R. Shankar, Phys. Rev. Lett. **98**, 247201 (2007).
[6] H.-D. Chen and Z. Nussinov, J. Phys. A **41**, 075001 (2008).
[7] A. M. Tsvelik (unpublished).
[8] G. Jackeli and G. Khaliullin, Phys. Rev. Lett. **102**, 017205 (2009).
[9] A. Shitade *et al.*, Phys. Rev. Lett. **102**, 256403 (2009).
[10] I. Felner and I. M. Bradarić, Physica (Amsterdam) **311B**, 195 (2002).
[11] H. Kobayashi *et al.*, J. Mater. Chem. **13**, 957 (2003).
[12] H. Takagi (private communication).
[13] Y. Singh and P. Gegenwart, arXiv:1003.0973.
[14] B. J. Kim *et al.*, Science **323**, 1329 (2009).
[15] On a Ir_2O_2 plaquette, e.g., in the xy plane, the hopping term reads as $-t_{pd\pi}p^\dagger_{1(2),z}(d_{i,xz(yz)} + d_{j,yz(xz)}) - t' d^\dagger_{i,xy} d_{j,xy}$ + H.c., where $p_{1(2),z}$ refers to a $2p_z$ orbital of oxygen 1(2) shared by NN Ir ions i and j.
[16] J. B. Fouet, P. Sindzingre, and C. Lhuillier, Eur. Phys. J. B **20**, 241 (2001).
[17] G. Khaliullin, Prog. Theor. Phys. Suppl. **160**, 155 (2005).
[18] G. Khaliullin, Phys. Rev. B **64**, 212405 (2001).
[19] The details of SW analysis will be given elsewhere.
[20] G. Baskaran, D. Sen, and R. Shankar, Phys. Rev. B **78**, 115116 (2008).
[21] Preliminary calculations indicate that two-magnon bound states form at large α. In case of the Kitaev toric code model, the relevance of multimagnon bound states to a quantum phase transition has been discussed by J. Vidal, R. Thomale, K. P. Schmidt, and S. Dusuel, Phys. Rev. B **80**, 081104(R) (2009).
[22] G. Khaliullin, R. Kilian, S. Krivenko, and P. Fulde, Phys. Rev. B **56**, 11 882 (1997).
[23] A. J. Willans, J. T. Chalker, and R. Moessner, Phys. Rev. Lett. **104**, 237203 (2010).

PRL 110, 097204 (2013) PHYSICAL REVIEW LETTERS week ending 1 MARCH 2013

Zigzag Magnetic Order in the Iridium Oxide Na_2IrO_3

Jiří Chaloupka,[1,2] George Jackeli,[1,*] and Giniyat Khaliullin[1]

[1]*Max Planck Institute for Solid State Research, Heisenbergstrasse 1, D-70569 Stuttgart, Germany*

[2]*Central European Institute of Technology, Masaryk University, Kotlářská 2, 61137 Brno, Czech Republic*

(Received 23 September 2012; published 28 February 2013)

We explore the phase diagram of spin-orbit Mott insulators on a honeycomb lattice, within the Kitaev-Heisenberg model extended to its full parameter space. Zigzag-type magnetic order is found to occupy a large part of the phase diagram of the model, and its physical origin is explained as due to interorbital $t_{2g} - e_g$ hopping. The magnetic susceptibility, spin wave spectra, and zigzag order parameter are calculated and compared to the experimental data, obtaining thereby the spin coupling constants in Na_2IrO_3 and Li_2IrO_3.

DOI: 10.1103/PhysRevLett.110.097204 PACS numbers: 75.10.Jm, 75.25.Dk, 75.30.Et

In the quest for materials with novel electronic phases, iridium oxide Na_2IrO_3 came into focus recently [1–7] due to theoretical predictions [8,9] that this system may host Kitaev model physics and the quantum spin Hall effect.

Na_2IrO_3 is an insulator with a sizable and temperature independent optical gap $\simeq 0.35$ eV [7], and shows Curie-Weiss type susceptibility [1,6] with moments corresponding to an effective spin one-half Ir^{4+} ion with a t_{2g}^5 configuration [10]. These facts imply that Na_2IrO_3 is a Mott insulator with well-localized Ir moments.

Collective behavior of local moments in Mott insulators is governed by three distinct and often competing forces: (i) orbital-lattice [Jahn-Teller (JT)] coupling, (ii) virtual hopping of electrons across the Mott gap resulting in exchange interactions, and (iii) relativistic spin-orbit coupling (see Ref. [11] for extensive discussions). The corresponding energy scales E_{JT}, J, and λ vary broadly depending on the type of magnetic ions and chemical bonding [12]. When $\lambda > (E_{\mathrm{JT}}, J)$, as often realized for Co, Rh, and Ir ions in an octahedral environment, local moments acquire a large orbital component which may result in a strong departure from spin-only Heisenberg models [8,11]. The direct observation of large spin-orbit splitting $3\lambda/2 \sim 0.6$–0.7 eV in insulating iridates Sr_2IrO_4 [13], $Sr_3Ir_2O_7$ [14], and Na_2IrO_3 [15] made it certain that $\lambda > (E_{\mathrm{JT}}, J)$. Thus, the low-energy physics of Na_2IrO_3 is governed by interactions among the spin-orbit entangled Kramers doublets of Ir ions.

It is also established now [3–5] that Ir moments in Na_2IrO_3 undergo antiferromagnetic (AF) order at $T_N \simeq 15$ K. The fact that T_N is much smaller than the paramagnetic Curie temperature (-125 K) [6] and spin-wave energies [4] implies that the underlying interactions are strongly frustrated. This is natural in the so-called Kitaev-Heisenberg (KH) model [16] where long range order is suppressed by the proximity to the Kitaev spin-liquid (SL) state. However, the observed ''zigzag'' magnetic pattern [ferromagnetic (FM) zigzag chains, AF coupled to each other] came as a surprising challenge to this simple and attractive model. To resolve the ''zigzag puzzle'', a number of proposals, ranging from various modifications of the KH model [4,6,17–19] to a complete denial [20] of a local moment picture in Na_2IrO_3, have been put forward.

In this Letter, we show that the zigzag order is in fact a natural ground state (GS) of the KH model, in a previously overlooked parameter range. Next, we identify the exchange process that supports a zigzag-phase regime. Further, we calculate spin-wave spectra, the ordered moment, and magnetic susceptibility of the model in the zigzag phase, and find a nice agreement with experiment. This lends strong support to the KH model as a dominant interaction in Na_2IrO_3 and related oxides.

The model.—Nearest-neighbor (NN) interaction between isospin one-half Kramers doublets of Ir^{4+} ions, coupled via 90°-exchange bonds, reads as follows (the exchange processes are described later):

$$\mathcal{H}_{ij}^{(\gamma)} = 2KS_i^\gamma S_j^\gamma + J\boldsymbol{S}_i \cdot \boldsymbol{S}_j. \tag{1}$$

Here, $\gamma(= x, y, z)$ labels 3 distinct types of NN bonds of a honeycomb lattice [16] of Ir ions in Na_2IrO_3, and spin axes oriented along the Ir-O bonds of IrO_6 octahedron. The bond-dependent Ising coupling between the γ components of spins is nothing but the Kitaev model [21], and the second term stands for the Heisenberg exchange.

Let us introduce the energy scale $A = \sqrt{K^2 + J^2}$ and the angle φ via $K = A\sin\varphi$ and $J = A\cos\varphi$; the model (1) takes then the following form:

$$\mathcal{H}_{ij}^{(\gamma)} = A(2\sin\varphi S_i^\gamma S_j^\gamma + \cos\varphi \boldsymbol{S}_i \cdot \boldsymbol{S}_j). \tag{2}$$

We let the ''phase'' angle φ vary from 0 to 2π, uncovering, thereby, additional phases of the model that escaped attention previously [16], including its zigzag ordered state which is of a particular interest here.

It is instructive to introduce, following Refs. [11,16], 4 sublattices with the fictitious spins $\tilde{\boldsymbol{S}}$, which are obtained from $\boldsymbol{S}$ by changing the sign of its two appropriate

components depending on the sublattice index. This transformation results in the $\tilde{S}$ Hamiltonian of the same form as (1), but with effective couplings $\tilde{K} = K + J$ and $\tilde{J} = -J$, revealing a hidden $SU(2)$ symmetry of the model at $K = -J$ (where the Kitaev term $\tilde{K}$ vanishes). For the angles, the mapping reads as $\tan\tilde{\varphi} = -\tan\varphi - 1$.

Phase diagram.—In its full parameter space, the KH model accommodates 6 different phases, best visualized using the phase-angle φ as in Fig. 1(a). In addition to the previously discussed [16,22,23] Néel-AF, stripy-AF, and SL states near $\varphi = 0$, $-\frac{\pi}{4}$, and $-\frac{\pi}{2}$, respectively, we observe 3 more states. First one is "AF" ($K > 0$) Kitaev spin-liquid near $\varphi = \frac{\pi}{2}$. Second, the FM phase broadly extending over the third quadrant of the φ circle. The FM and stripy-AF states are connected [see Fig. 1(a)] by the 4-sublattice transformation, which implies their identical dynamics. Finally, near $\varphi = \frac{3}{4}\pi$, the most wanted phase, zigzag AF, appears occupying almost a quarter of the phase space. Thanks to the above mapping, it is understood that the zigzag and Néel states are isomorphic, too.

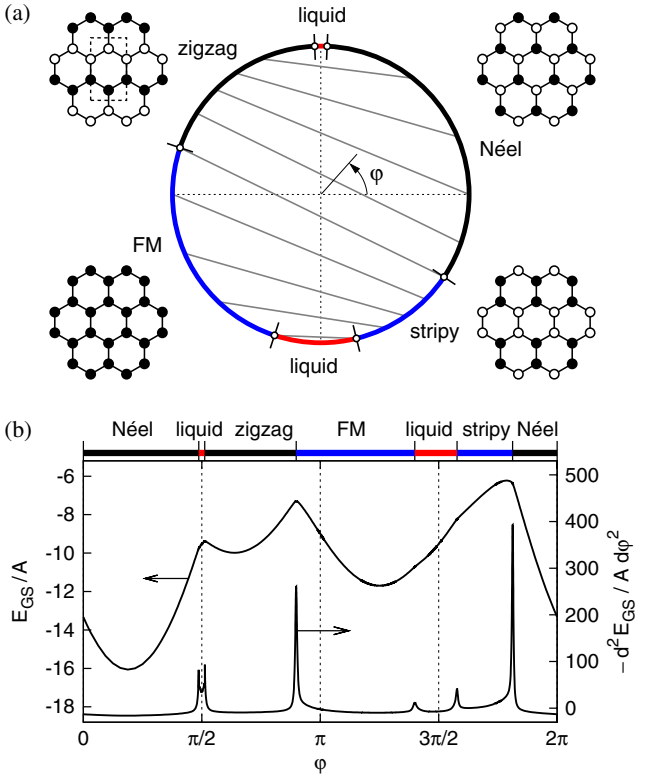

FIG. 1 (color online). (a) Phase diagram of the Kitaev-Heisenberg model containing 2 spin-liquid and 4 spin-ordered phases. The transition points (open dots on the φ circle) are obtained by an exact diagonalization. The gray lines inside the circle connect the points related by the exact mapping (see text). Open and solid circles in the insets indicate up and down spins. The rectangular box in the zigzag pattern (top-left) shows the magnetic unit cell. (b) Ground-state energy $E_{\rm GS}$ and its second derivative $-d^2E_{\rm GS}/d\varphi^2$ revealing the phase transitions.

In particular, the $\varphi = \frac{3}{4}\pi$ zigzag state is identical to the Heisenberg-AF state of the fictitious spins [24].

To obtain the phase boundaries, we have diagonalized the model numerically, using a hexagonal 24-site cluster with periodic boundary conditions. The cluster is compatible with the above 4-sublattice transformation and $\varphi \leftrightarrow \tilde{\varphi}$ mapping. As seen in Fig. 1(b), the second derivative of the GS energy $E_{\rm GS}$ with respect to the φ well detects the phase transitions. Three pairs of linked transition points are found: $\simeq (88°, 92°)$ and $(-76°, -108°)$ for the spin liquid-order transitions around $\pm\frac{\pi}{2}$, and $(162°, -34°)$ or the transitions between ordered phases.

The transitions from zigzag-AF to FM, and from stripy-AF to Néel-AF are expected to be of first order by symmetry; the corresponding peaks in Fig. 1(b) are indeed very sharp. The spin liquid-order transitions near $\varphi = -\frac{\pi}{2}$ lead to wider and much less pronounced peaks, suggesting a second- (or weakly first-) order transition [16]. On the contrary, liquid-order transitions around $\varphi = \frac{\pi}{2}$ show up as very narrow peaks; on the finite cluster studied, they correspond to real level crossings. The nature of these phase transitions remains to be clarified [25].

While at $J = 0$ (i.e., $\varphi = \pm\frac{\pi}{2}$) the sign of K is irrelevant [21], the stability of the AF- and FM-type Kitaev spin liquids against J perturbation is very different: the SL phase near $\frac{\pi}{2}$ ($-\frac{\pi}{2}$) is less (more) robust. This phase behavior is related to a different nature of the competing ordered phases: for the $\frac{\pi}{2}$ SL, these are highly quantum zigzag and Néel states, while the SL near $-\frac{\pi}{2}$ is sandwiched by more classical (FM and "fluctuation free" stripy [16]) states which are energetically less favorable than the quantum SL state.

Exchange interactions in Na_2IrO_3.—Having fixed the parameter space ($K > 0$, $J < 0$) for the zigzag phase, we turn now to the physical processes behind the model (1). Exchange interactions in Mott insulators arise due to virtual hoppings of electrons. This may happen in many different ways, depending sensitively on chemical bonding, intra-ionic electron structure, etc. The case of present interest (i.e., strong spin-orbit coupling, t_{2g}^5 configuration, and 90°-bonding geometry) has been addressed in several papers [8,11,16,26]. There are the following four physical processes that contribute to K and J couplings.

Process 1: Direct hopping t' between NN t_{2g} orbitals. Since no oxygen orbital is involved, 90° bonding is irrelevant; the resulting Hamiltonian is $H_1 = I_1 \boldsymbol{S}_i \cdot \boldsymbol{S}_j$ with $I_1 \simeq (\frac{2}{3}t')^2/U$ [16]. Here, U is the Coulomb repulsion between t_{2g} electrons. Typically, one has $t'/t < 1$, when compared to the indirect hopping t of t_{2g} orbitals via oxygen ions.

Process 2: Interorbital NN $t_{2g} - e_g$ hopping $\tilde{t}$. This is the dominant pathway in 90° bonding geometry since it involves strong $t_{pd\sigma}$ overlap between oxygen-$2p$ and e_g orbitals; typically, $\tilde{t}/t \sim 2$. The corresponding Hamiltonian is [11]

$$H_2^{(\gamma)} = I_2(2S_i^\gamma S_j^\gamma - \boldsymbol{S}_i \cdot \boldsymbol{S}_j). \quad (3)$$

This is nothing but the model (1) with $K = -J = I_2 > 0$, i.e., at its $SU(2)$ symmetric point $\varphi = \frac{3}{4}\pi$ inside the zigzag phase; see Fig. 2. For the Mott-insulating iridates (as opposed to charge-transfer cobaltates [11]), we estimate $I_2 \simeq \frac{4}{9}(\tilde{t}/\tilde{U})^2 \tilde{J}_H$, where $\tilde{U}$ is the (optically active) excitation energy associated with $t_{2g} - e_g$ hopping, and $\tilde{J}_H$ is Hund's interaction between the t_{2g} and e_g orbitals. The physics behind this expression is clear: $(\tilde{t}/\tilde{U})^2$ measures the amount of t_{2g} spin which is transferred to the NN e_g orbital; once arrived, it encounters the "host" t_{2g} spin and has to obey the Hund's rule.

For its remarkable properties, the Hamiltonian H_2 (3) deserves a few more words. On a triangular lattice, it shows a nontrivial spin vortex ground state [11,27]; however, the elementary excitations are simple $SU(2)$ magnons of a conventional Heisenberg-AF state. When regarded as the "J" part of a doped $t - J$ model, it leads to an exotic pairing [11,28].

Process 3: Indirect hopping t between NN t_{2g} orbitals via oxygen ions. This gives rise to the Kitaev model $H_3^{(\gamma)} = -I_3 S_i^\gamma S_j^\gamma$, with $I_3 \simeq \frac{8}{3}(t^2/U)(J_H/U)$ [8], where J_H is Hund's coupling between t_{2g} electrons. This process supports $\varphi = -\frac{\pi}{2}$ SL state; see Fig. 2.

Process 4: Mechanisms involving pd charge-transfer excitations with energy Δ_{pd}. Two holes may meet at an oxygen and experience Coulomb U_p and Hund's J_H^p interactions, or cycle around a Ir_2O_2 plaquette (Fig. 2). The resulting Hamiltonian H_4 has the form of H_2 (3). The coupling constant $I_4 \simeq \frac{8}{9} t^2 (\frac{2}{2\Delta_{pd} + U_p - J_H^p} - \frac{1}{\Delta_{pd}})$ is negative

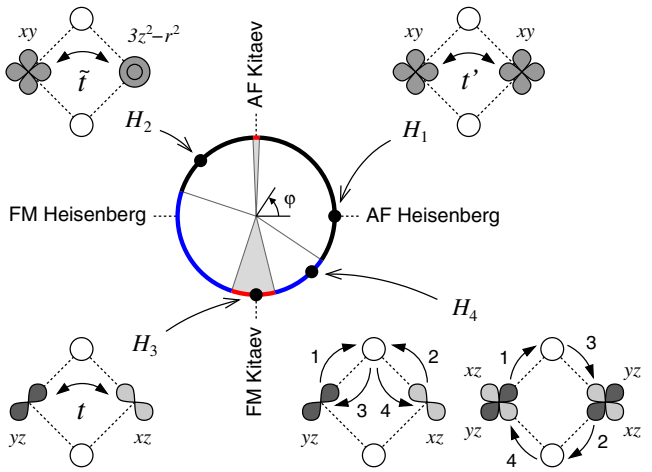

FIG. 2 (color online). Schematics of four different exchange processes (see text for details), arranged around the φ phase diagram of Fig. 1(a). Taken separately, the Hamiltonians H_1, H_2, H_3, and H_4 would favor "pure" Néel-AF, zigzag-AF, Kitaev-SL, and stripy-AF states, respectively, as indicated by arrows connecting H_i with the dots on the φ circle. The circle is divided into the phase sectors by gray lines; SL phases are shaded.

[29], supporting the stripy-AF state not observed in Na_2IrO_3.

Putting things together, we observe that it is the interorbital $t_{2g} - e_g$ hopping H_2 process that uniquely supports zigzag order in Na_2IrO_3. This implies in general that multiorbital Hubbard-type models, when applied to iridates with 90°-bonding geometry, must include e_g states as well, even though the moments reside predominantly in the t_{2g} shell.

Up to this point, we neglected trigonal field splitting Δ of the t_{2g} level due to the c axis compression present in Na_2IrO_3. This approximation is valid as long as Δ is much smaller than the spin-orbit coupling $\lambda \simeq 0.4$ eV [13,15,30] and seems to be justified, since the recent *ab initio* calculations [20] suggest that $\Delta \simeq 75$ meV only [31].

We have also examined the longer-range couplings, using the hopping matrix of Ref. [20], and found that the second-NN interaction has the form of (3) (as previously noticed Refs. [32,33]), while the third-NN coupling is of the AF-Heisenberg type [the corresponding coupling constants are $\frac{4}{9}(t_{2,3}^2/U)$]. The second (third)-NN interaction would oppose (support) zigzag order; however, we believe that these couplings are not significant in Na_2IrO_3 because the hoppings t_2 and t_3 are small [34].

We do not attempt here to evaluate the parameters involved in $H_1 - H_4$; *ab-initio* calculations as in Ref. [35] might be more useful in this regard. Instead, having obtained a zigzag order in our model (1) and identified the physical process driving this order, we turn now to the experimental data. The J and K values in Na_2IrO_3 and Li_2IrO_3 will be extracted below from analysis of the neutron scattering and magnetic susceptibility data.

Spin waves in the zigzag phase.—Consider a single domain zigzag state, e.g., with FM chains running perpendicular to z-type bonds. Following Ref. [4], we introduce a rectangular $a \times b$ magnetic unit cell [$\sqrt{3}a_0 \times 3a_0$ in terms of hexagon-edge a_0; see Fig. 1(a)], and define the ab-plane wave vector $\mathbf{q}$ in units of (h, k) as $\mathbf{q} = (\frac{2\pi}{a}h, \frac{2\pi}{b}k)$. Standard spin-wave theory gives four dispersive branches:

$$\omega_{1,2}^2(h,k) = [K^2 + (K+J)^2]c_h^2 - KJ(1 - s_h s_k) \pm |(K+J)c_h| \sqrt{(2K-J)^2 - (2Ks_h - Js_k)^2}, \quad (4)$$

and $\omega_{3,4}(h,k) = \omega_{1,2}(-h,k)$, with $c_h = \cos\pi h$, $s_h = \sin\pi h$, and $s_k = \sin\pi k$. If $K = -J$, i.e., at the $\varphi = \frac{3}{4}\pi$ point of hidden $SU(2)$ symmetry, two branches are degenerate ($\omega_1 = \omega_2$) and become true Goldstone modes. Away from this special point, the small magnon gap is expected to open by quantum effects not considered here. For $\mathbf{q}$ with $h = k$, the dispersions (4) simplify to $\omega_1(h,h) = \sqrt{2K(2K+J)}|c_h|$ and $\omega_2(h,h) = \sqrt{2}|Jc_h|$, revealing two different energy scales in the magnon spectra set by K and J couplings.

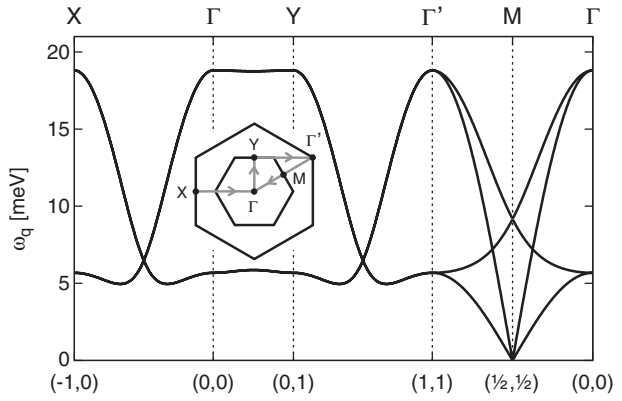

FIG. 3. Magnon spectra in the zigzag phase calculated using Eq. (4) with $(J, K) = (-4.0, 10.5)$ meV. The inset shows the path along the symmetry directions in the reciprocal space; the notation of Ref. [4] is used.

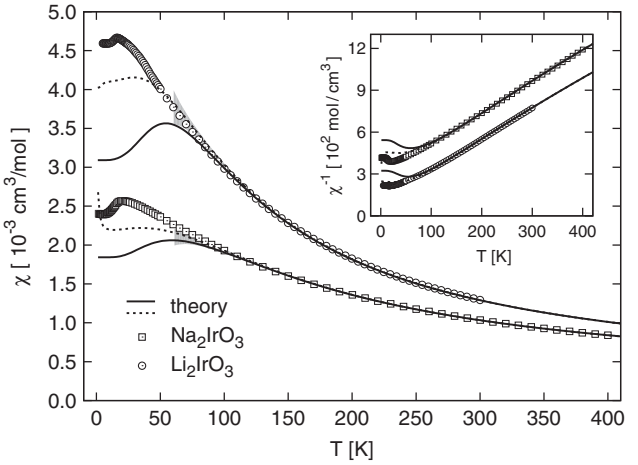

FIG. 4. Experimental magnetic susceptibilities $\chi(T)$ for Na_2IrO_3 [1,6] (squares) and Li_2IrO_3 [6] (circles) fitted by the theoretical calculations. Exact χ of the 8-site (14-site) cluster is shown as solid (dashed) lines. Lanczos results for the 24-site cluster are indicated by shading [37]. Their comparison suggests that the calculated χ gives the thermodynamic limit down to $T \approx 100$ K where the finite-size effects become significant.

While the bandwidth of the lowest dispersive mode (set by J) is already known to be about 5–6 meV [4], we are not aware of the high energy magnon data to estimate K in Na_2IrO_3. We have therefore examined (see below) the magnetic susceptibility data [1,6], and obtained $(J, K) \simeq (-4.0, 10.5)$ meV that well fit the susceptibility as well as the neutron scattering data [4]. With this, we predict the magnon spectra for Na_2IrO_3 shown in Fig. 3. The lowest dispersive (J) mode is as observed [4], indeed. However, mapping out entire magnon spectra is highly desirable to quantify the Kitaev term K directly.

Magnetic susceptibility.—We have calculated the uniform magnetic susceptibility $\chi(T)$ of the model (1) on 8- and 14-site clusters by exact diagonalization, and on 24-site cluster using the finite-temperature Lanczos method [36,37]. The parameters are varied such that $J = A\cos\varphi$ is consistent with the neutron data [4] while φ stays within the zigzag sector of Fig. 1(a); this strongly narrows the possible K window. For the data fits, we let the g factor of the Ir^{4+} ion deviate from 2 (due to the covalency effects [10]), and include the T-independent Van Vleck term χ_0. The result for $J = -4.0$ meV, $K = 10.5$ meV, $g = 1.78$, $\chi_0 = 0.16 \times 10^{-3}$ cm^3/mol fits the Na_2IrO_3 data nicely (Fig. 4); deviations occur at low temperatures only, when correlation length exceeds the size of the cluster used. The fit is quite robust: similar results can be found for small only variations, locating Na_2IrO_3 near $\varphi = 111 \pm 2°$ of the model phase diagram Fig. 1(a). The spin couplings obtained are reasonable for the 90°-exchange bonds (as expected [8,11], they are much smaller than in 180°-bond perovskites [13,14]). The magnitude of the Van Vleck term also agrees with our estimate $\chi_0 \simeq \frac{8}{3\lambda}\mu_B^2 N_A \simeq 0.2 \times 10^{-3}$ cm^3/mol for the Ir^{4+} ion, considering spin-orbit coupling $\lambda \simeq 0.4$ eV [13,15,30].

Dominance of the Kitaev term ($2K/J \sim 5$ in Na_2IrO_3) implies strong frustration hence enhanced quantum fluctuations; this explains the reduced ordered moment $m \simeq 0.22\mu_B$ [5]. With the J, K, and g values above, we calculated the leading order spin-wave correction to m and obtained $m \simeq 0.33\mu_B$ [38].

For the sake of curiosity, we have also fitted the $\chi(T)$ data of Li_2IrO_3 [6], a sister compound of Na_2IrO_3. Acceptable results have been found for the angle window $\varphi = 124 \pm 6°$; a representative plot for $J = -5.3$ meV, $K = 7.9$ meV, $g = 1.94$, $\chi_0 = 0.14 \times 10^{-3}$ cm^3/mol is shown in Fig. 4. It is worth noticing that the value of J, which controls the bandwidth of the softest spin-wave mode (see Fig. 3), appears to be similar in both compounds. This may explain why they undergo magnetic transition at similar $T_N \simeq 15$ K, despite very different high temperature susceptibilities.

To conclude, we have clarified the origin of zigzag magnetic order in Na_2IrO_3 in terms of nearest-neighbor Kitaev-Heisenberg model for localized Ir moments. The model well agrees with the low-energy magnon and high temperature magnetic susceptibility data. A general implication of this work is that the interactions considered here should hold a key for understanding the magnetism of a broad class of spin-orbit Mott insulators with 90°-exchange bonding geometry, including triangular, honeycomb, and hyperkagome lattice iridates.

We thank R. Coldea, Y. Singh, H. Takagi, and I. I. Mazin for discussions. J. C. acknowledges support by the Alexander von Humboldt Foundation, ERDF under Project No. CEITEC (CZ.1.05/1.1.00/02.0068), and the EC 7th Framework Programme (286154/SYLICA). G. J. is supported by Grant No. GNSF/ST09-447 and in part by the NSF under Grant No. NSF PHY11-25915.

*Also at Andronikashvili Institute of Physics, 0177 Tbilisi, Georgia.

[1] Y. Singh and P. Gegenwart, Phys. Rev. B **82**, 064412 (2010).

[2] H. Takagi (unpublished).

[3] X. Liu, T. Berlijn, W.-G. Yin, W. Ku, A. Tsvelik, Y.-J. Kim, H. Gretarsson, Y. Singh, P. Gegenwart, and J. P. Hill, Phys. Rev. B **83**, 220403 (2011).

[4] S. K. Choi, R. Coldea, A. N. Kolmogorov, T. Lancaster, I. I. Mazin, S. J. Blundell, P. G. Radaelli, Y. Singh, P. Gegenwart, K. R. Choi, S.-W. Cheong, P. J. Baker, C. Stock, and J. Taylor, Phys. Rev. Lett. **108**, 127204 (2012).

[5] F. Ye, S. Chi, H. Cao, B. C. Chakoumakos, J. A. Fernandez-Baca, R. Custelcean, T. F. Qi, O. B. Korneta, and G. Cao, Phys. Rev. B **85**, 180403 (2012).

[6] Y. Singh, S. Manni, J. Reuther, T. Berlijn, R. Thomale, W. Ku, S. Trebst, and P. Gegenwart, Phys. Rev. Lett. **108**, 127203 (2012).

[7] R. Comin, G. Levy, B. Ludbrook, Z.-H. Zhu, C. N. Veenstra, J. A. Rosen, Y. Singh, P. Gegenwart, D. Stricker, J. N. Hancock, D. van der Marel, I. S. Elfimov, and A. Damascelli, Phys. Rev. Lett. **109**, 266406 (2012).

[8] G. Jackeli and G. Khaliullin, Phys. Rev. Lett. **102**, 017205 (2009).

[9] A. Shitade, H. Katsura, J. Kuneš, X.-L. Qi, S.-C. Zhang, and N. Nagaosa, Phys. Rev. Lett. **102**, 256403 (2009).

[10] A. Abragam and B. Bleaney, *Electron Paramagnetic Resonance of Transition Ions* (Clarendon Press, Oxford, 1970).

[11] G. Khaliullin, Prog. Theor. Phys. Suppl. **160**, 155 (2005).

[12] J. B. Goodenough, *Magnetism and the Chemical Bond* (Interscience, New York, 1963).

[13] J. Kim, D. Casa, M. H. Upton, T. Gog, Y.-J. Kim, J. F. Mitchell, M. van Veenendaal, M. Daghofer, J. van den Brink, G. Khaliullin, and B. J. Kim, Phys. Rev. Lett. **108**, 177003 (2012).

[14] J. Kim, A. H. Said, D. Casa, M. H. Upton, T. Gog, M. Daghofer, G. Jackeli, J. van den Brink, G. Khaliullin, and B. J. Kim, Phys. Rev. Lett. **109**, 157402 (2012).

[15] H. Gretarsson, J. P. Clancy, X. Liu, J. P. Hill, E. Bozin, Y. Singh, S. Manni, P. Gegenwart, J. Kim, A. H. Said, D. Casa, T. Gog, M. H. Upton, H.-S. Kim, J. Yu, V. M. Katukuri, L. Hozoi, J. van den Brink, Y.-J. Kim, arXiv:1209.5424.

[16] J. Chaloupka, G. Jackeli, and G. Khaliullin, Phys. Rev. Lett. **105**, 027204 (2010).

[17] I. Kimchi and Y.-Z. You, Phys. Rev. B **84**, 180407 (2011).

[18] S. Bhattacharjee, S.-S. Lee, and Y. B. Kim, New J. Phys. **14**, 073015 (2012).

[19] C. H. Kim, H. S. Kim, H. Jeong, H. Jin, and J. Yu, Phys. Rev. Lett. **108**, 106401 (2012).

[20] I. I. Mazin, H. O. Jeschke, K. Foyevtsova, R. Valenti, and D. I. Khomskii, Phys. Rev. Lett. **109**, 197201 (2012).

[21] A. Kitaev, Ann. Phys. (Amsterdam) **321**, 2 (2006).

[22] H.-C. Jiang, Z.-C. Gu, X.-L. Qi, and S. Trebst, Phys. Rev. B **83**, 245104 (2011).

[23] J. Reuther, R. Thomale, and S. Trebst, Phys. Rev. B **84**, 100406 (2011).

[24] After initial submission of this work, we became aware of the recent derivation [Y. Yu, L. Liang, Q. Niu, and S. Qin, Phys. Rev. B **87**, 041107(R) (2013)] of the KH model and zigzag phase from a single band Hubbard model with the spin- and link-dependent NN-hoppings. However, such hoppings are not present in the hexagonal iridates A_2IrO_3 [8,9].

[25] C. C. Price and N. B. Perkins, [Phys. Rev. Lett. **109**, 187201 (2012)] demonstrated the highly nontrivial phase behavior of the KH model also at finite temperatures.

[26] G. Chen and L. Balents, Phys. Rev. B **78**, 094403 (2008).

[27] I. Rousochatzakis, U. K. Rössler, J. van den Brink, and M. Daghofer, arXiv:1209.5895.

[28] G. Khaliullin, W. Koshibae, and S. Maekawa, Phys. Rev. Lett. **93**, 176401 (2004).

[29] The results for I_4 of Refs. [8,11,26] were incomplete.

[30] O. F. Schirmer, A. Forster, H. Hesse, M. Wohlecke, and S. Kapphan, J. Phys. C **17**, 1321 (1984).

[31] Typically, "noncubic" corrections to the interactions between Kramers doublets scale as $(\frac{3\cos 2\theta - 1}{2})^2$ [28], which is about 0.01 if $\Delta = 75$ meV. [θ is given by $\tan 2\theta = 2\sqrt{2}\lambda/(\lambda + 2\Delta)$]. The case of $\Delta > \lambda$ can be excluded also on the grounds that, in this limit, the interactions become *bond-independent* and support either Ising-FM or xy-AF states [11], instead of zigzag order observed.

[32] J. Reuther, R. Thomale, and S. Rachel, Phys. Rev. B **86**, 155127 (2012).

[33] M. Kargarian, A. Langari, and G. A. Fiete, Phys. Rev. B **86**, 205124 (2012).

[34] The second-NN hopping $t_2 \simeq 75$ meV is about 4 times less than NN hopping t via oxygen, and $t_3 \simeq 30$ meV [20].

[35] V. M. Katukuri, H. Stoll, J. van den Brink, and L. Hozoi, Phys. Rev. B **85**, 220402(R) (2012).

[36] J. Jaklič and P. Prelovšek, Adv. Phys. **49**, 1 (2000).

[37] We used $M = 100$ Lanczos steps and $N_{st} = 1024$ random sampling vectors. The values of χ and their statistical error are presented in Fig. 4 in the form of 3σ intervals estimated by taking many sets of the sampling vectors.

[38] Hybridization of the Ir-5d and O-2p orbitals on antiferromagnetic bonds [5], as well as the higher order quantum corrections may further reduce m.

LETTERS
PUBLISHED ONLINE: 11 MAY 2015 | DOI: 10.1038/NPHYS3322
nature physics

Direct evidence for dominant bond-directional interactions in a honeycomb lattice iridate Na_2IrO_3

Sae Hwan Chun[1], Jong-Woo Kim[2], Jungho Kim[2], H. Zheng[1], Constantinos C. Stoumpos[1], C. D. Malliakas[1], J. F. Mitchell[1], Kavita Mehlawat[3], Yogesh Singh[3], Y. Choi[2], T. Gog[2], A. Al-Zein[4], M. Moretti Sala[4], M. Krisch[4], J. Chaloupka[5], G. Jackeli[6,7], G. Khaliullin[6] and B. J. Kim[6]*

Heisenberg interactions are ubiquitous in magnetic materials and play a central role in modelling and designing quantum magnets. Bond-directional interactions[1-3] offer a novel alternative to Heisenberg exchange and provide the building blocks of the Kitaev model[4], which has a quantum spin liquid as its exact ground state. Honeycomb iridates, A_2IrO_3 (A = Na, Li), offer potential realizations of the Kitaev magnetic exchange coupling, and their reported magnetic behaviour may be interpreted within the Kitaev framework. However, the extent of their relevance to the Kitaev model remains unclear, as evidence for bond-directional interactions has so far been indirect. Here we present direct evidence for dominant bond-directional interactions in antiferromagnetic Na_2IrO_3 and show that they lead to strong magnetic frustration. Diffuse magnetic X-ray scattering reveals broken spin-rotational symmetry even above the Néel temperature, with the three spin components exhibiting short-range correlations along distinct crystallographic directions. This spin- and real-space entanglement directly uncovers the bond-directional nature of these interactions, thus providing a direct connection between honeycomb iridates and Kitaev physics.

Iridium (IV) ions with pseudospin-1/2 moments form in Na_2IrO_3, a quasi-two-dimensional (2D) honeycomb network, which is sandwiched between two layers of oxygen ions that frame edge-shared octahedra around the magnetic ions and mediate superexchange interactions between neighbouring pseudospins (Fig. 1a). Owing to the particular spin–orbital structure of the pseudospin[5,6], the isotropic part of the magnetic interaction is strongly suppressed in the 90° bonding geometry of the edge-shared octahedra[2,3], thereby allowing otherwise subdominant bond-dependent anisotropic interactions to play the main role and manifest themselves at the forefront of magnetism. This bonding geometry, common to many transition-metal oxides, in combination with the pseudospin that arises from strong spin–orbit coupling gives rise to an entirely new class of magnetism beyond the traditional paradigm of Heisenberg magnets. On a honeycomb lattice, for instance, the leading anisotropic interactions take the form of the Kitaev model[3], which is a rare example of exactly solvable models with non-trivial properties such as Majorana fermions and non-Abelian statistics, and with potential links to quantum computing[4].

Realization of the Kitaev model is now being intensively sought out in a growing number of materials[7–13], including 3D extensions of the honeycomb Li_2IrO_3, dubbed 'hyper-honeycomb'[7] and 'harmonic-honeycomb'[8], and 4*d* transition-metal analogues such as $RuCl_3$ (ref. 12) and Li_2RhO_3 (ref. 13). Although most of these are known to magnetically order at low temperature, they exhibit a rich array of magnetic structures, including zigzag[14–16], spiral[17] and other more complex non-coplanar structures[18,19] that are predicted to occur in the vicinity of the Kitaev quantum spin liquid (QSL) phase[20–23], which hosts many degenerate ground states frustrated by three bond-directional Ising-type anisotropies. All of these magnetic orders are captured in an extended version of the Kitaev model written as

$$H = \sum_{\langle ij \rangle_\gamma} \left[K S_i^\gamma S_j^\gamma + J \mathbf{S}_i \cdot \mathbf{S}_j + \Gamma (S_i^\alpha S_j^\beta + S_i^\beta S_j^\alpha) \right]$$

which includes, in addition to the Kitaev term K, the Heisenberg exchange J, which may be incompletely suppressed in the superexchange process and/or arise from a direct exchange process[21], and the symmetric off-diagonal exchange term Γ, which is symmetry-allowed even in the absence of lattice distortions[23–25]. This 'minimal' Hamiltonian couples pseudospins $\mathbf{S}$ (hereafter referred to as 'spin') only on nearest-neighbour bonds $\langle ij \rangle$, neglecting further-neighbour couplings, which may be non-negligible. The bond-directional nature of the K and Γ terms is reflected in the spin components $[\alpha \neq \beta \neq \gamma \in (x, y, z)]$ which they couple for a given bond ($\gamma \in x$-, y-, z-bonds; Fig. 1a). For example, the K term couples only the spin component normal to the Ir_2O_6 plaquette containing the particular bond. Despite these extra terms that may account for finite-temperature magnetic orders in the candidate materials, the fact that the Kitaev QSL phase has a finite window of stability against these perturbations[20,25] calls for investigation of competing phases and a vigorous search for the Kitaev QSL phase.

Although the notion of magnetic frustration induced by competing bond-directional interactions is compelling, it remains a theoretical construct without an existence proof for such interactions in a real-world material. Moreover, theories for iridium compounds based on itinerant electrons suggest alternative pictures[26–28]. In principle, measurement of the dynamical structure factor through inelastic neutron scattering (INS) or resonant

[1]Materials Science Division, Argonne National Laboratory, Argonne, Illinois 60439, USA. [2]Advanced Photon Source, Argonne National Laboratory, Argonne, Illinois 60439, USA. [3]Indian Institute of Science Education and Research (IISER) Mohali, Knowledge City, Sector 81, Mohali 140306, India. [4]European Synchrotron Radiation Facility, BP 220, F-38043 Grenoble Cedex, France. [5]Central European Institute of Technology, Masaryk University, Kotlářská 2, 61137 Brno, Czech Republic. [6]Max Planck Institute for Solid State Research, Heisenbergstraße 1, D-70569 Stuttgart, Germany. [7]Institute for Functional Matter and Quantum Technologies, University of Stuttgart, Pfaffenwaldring 57, D-70569 Stuttgart, Germany. *e-mail: bjkim@fkf.mpg.de

NATURE PHYSICS DOI: 10.1038/NPHYS3322 LETTERS

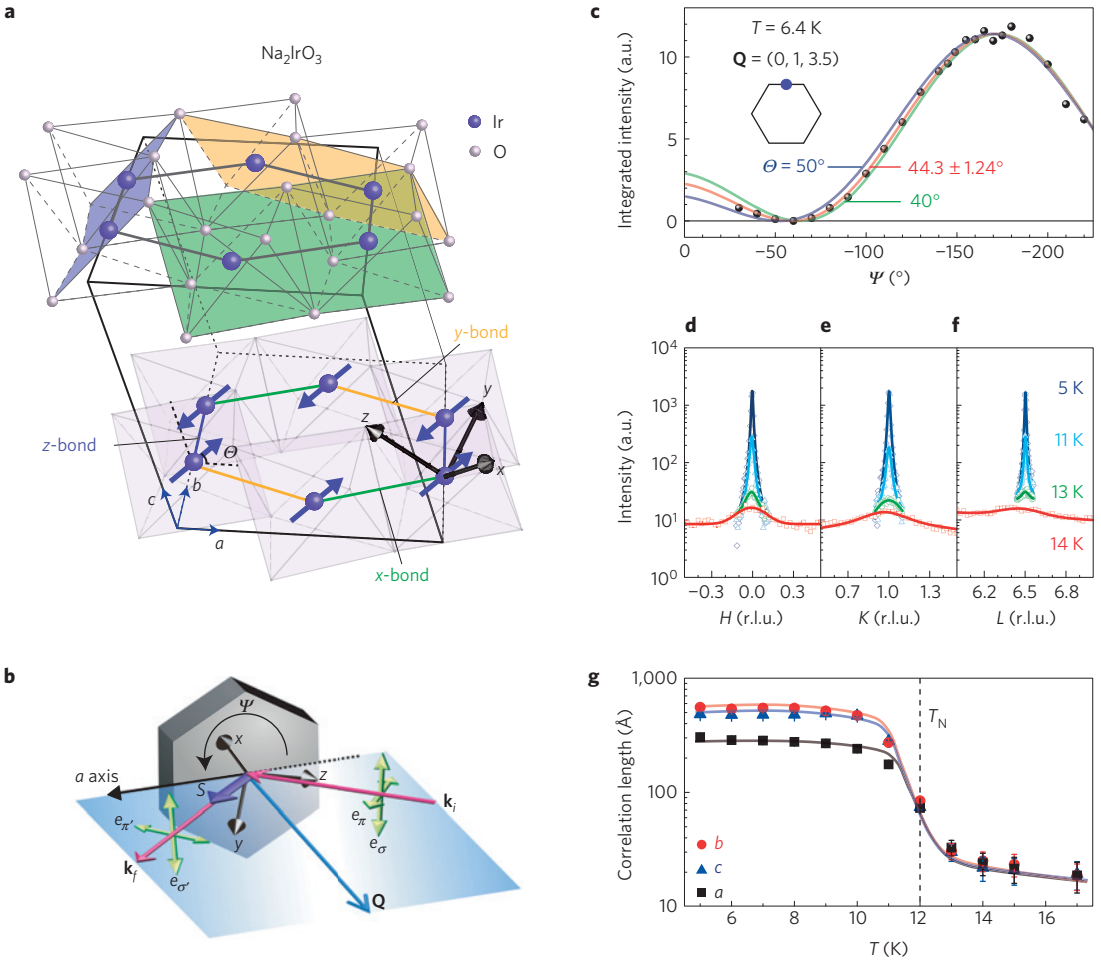

Figure 1 | Magnetic easy axis and temperature dependence of the zigzag order. a, Honeycomb layers of Ir^{4+} in the monoclinic Bravais lattice. Green, yellow and blue planes show Ir_2O_6 plaquettes normal to the local *x*-, *y*- and *z*-axes (black arrows), respectively, which point along three nearest-neighbour Ir–O bonds in an octahedron. Ir–Ir bonds are labelled following the plaquettes they belong to. Na^+ is not shown for clarity. Blue arrows show the spins in the static zigzag order propagating along the *b* direction. Spins are antiparallel between the layers (not shown). **b**, Illustration of the scattering geometry. Shown in blue is the scattering plane defined by the incident ($\mathbf{k}_i$) and outgoing ($\mathbf{k}_f$) wavevector (red arrows). Green arrows show the X-ray polarizations. The azimuth, Ψ, is defined as the angle between the *a*-axis and the scattering plane. **c**, Ψ-dependence of the magnetic Bragg peak (blue filled circle) intensity at (0, 1, 3.5) measured in the σ–π' channel. The black hexagon is the Brillouin zone of the honeycomb net. The red solid line shows the best fitting result to the data with $\Theta = 44.3°$, with a standard error of $\pm 1.24°$. We note that the actual error may be larger owing to systematic errors arising from factors such as changes in the beam footprint on the sample. Green and blue lines shows the calculated Ψ dependence for $\Theta = 40°$ and 50°, respectively. **d**–**f**, *H*, *K* and *L* scans, respectively, of the magnetic Bragg peak at (0, 1, 6.5) for selected temperatures. **g**, Temperature dependence of the correlation lengths along the *a*-, *b*- and *c*-axes from Gaussian fitting to the scans. Error bars represent the standard deviation in the fitting procedure. The solid lines are guides to the eye.

inelastic X-ray scattering (RIXS) provides the most direct access to the Hamiltonian describing the magnetic interactions. However, a fully momentum- and energy-resolved dynamical structure factor thus far remains elusive for any of the candidate materials; RIXS suffers from insufficient energy resolution[29] and INS is at present limited by unavailability of large-volume single crystals[15]. In this Letter, we take a new approach using diffuse magnetic X-ray scattering to provide direct evidence for predominant bond-directional interactions in Na_2IrO_3 through the measurement of equal-time correlations of spin components above the ordering temperature ($T_N = 12$–15 K, see Supplementary Fig. 1).

We start by establishing the spin orientation in the static zigzag order[14–16] below T_N, as shown in Fig. 1a, using standard resonant magnetic X-ray diffraction. In this measurement, the X-ray polarization projects out a certain spin component; the intensity depends on the spin orientation through the relation $I \propto |\mathbf{k}_f \cdot \mathbf{S}|^2$ for the σ–π' channel measured, where $\mathbf{k}_f$ is the scattered X-ray wavevector (Fig. 1b). Figure 1c shows the intensity variation as the sample is rotated about the ordering wavevector $\mathbf{Q} = (0, 1, 3.5)$ by an azimuthal angle Ψ, which causes $\mathbf{S}$ to precess around $\mathbf{Q}$. Earlier studies[14,16] have established that $\mathbf{S}$ is constrained to lie in the *ac*-plane, so this measurement of $I(\Psi)$ determines the spin orientation by resolving the tilting angle Θ of $\mathbf{S}$ with respect to the *a*-axis. The best fitting result with $\Theta = 44.3°$ indicates that the magnetic easy axis is approximately half way between the cubic *x*- and *y*-axes (Fig. 1a). This static spin orientation is a compromise among all anisotropic interactions present in the system, and is strongly tied to the magnetic structure because of their bond-directional nature. To see this point, consider, for example, the *K* term: in the zigzag structure propagating along the *b* direction, where the spins are antiferromagnetically aligned on the *z*-bond and ferromagnetically aligned on the *x*-bond and *y*-bond, a ferromagnetic (antiferromagnetic) *K* favours spins pointing perpendicular to (along) the *z*-axis for a pair of spins on the *z*-bond, and along (perpendicular to) the *x*-axis and *y*-axis for the pairs on the *x*-bond and *y*-bond, respectively.

The zigzag order is one of the many magnetic states (including the aforementioned spiral and non-coplanar structures) that are

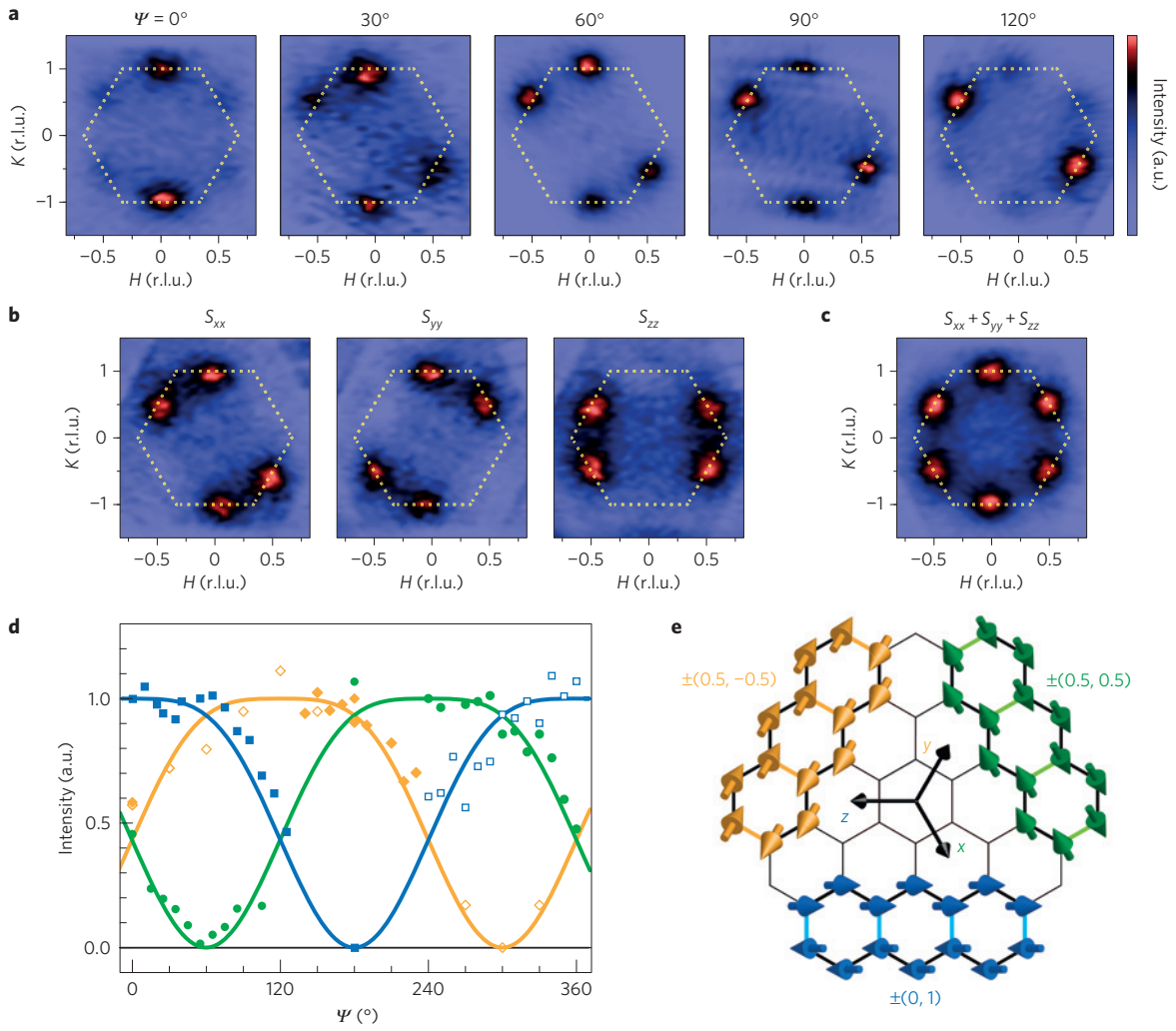

Figure 2 | Diffuse magnetic X-ray scattering intensities above T_N. a, Intensity plots in the *HK*-plane (*L* varying between 6.5 and 7) measured at $T = 17$ K for selected azimuth angles summing π-σ' and π-π' channels, sensitive to spin components parallel to $\mathbf{k}_i$ and perpendicular to the scattering plane, respectively. For example, $\Psi = 0°$ measures the sum of correlations S_{xx} and S_{yy}. The dashed hexagon indicates the first Brillouin zone of the honeycomb net. **b**, Spin-component-resolved equal-time correlations extracted from **a**. **c**, Spin-component-integrated equal-time correlations extracted from **a**. Peaks are located at $\mathbf{Q} = \pm(0,1)$, $\pm(0.5, 0.5)$, and $\pm(0.5, -0.5)$. **d**, Ψ-dependence of the diffuse peak intensities for Samples 1 (open symbol) and 2 (closed symbol). Solid lines show the calculated Ψ-dependence for *x*-, *y*- and *z*-zigzag states shown in **e** for the π-σ' and π-π' polarization channels summed. **e**, Zigzag orders propagating along three equivalent directions. Blue zigzag is the static structure, and green and yellow zigzags are generated by 120° rotation of the blue zigzag.

classically degenerate in the pure Kitaev limit[30] and comprise the micro-states in the QSL phase. Away from the pure Kitaev limit, depending on their energy separations, signatures of other magnetic states and their associated magnetic anisotropies may become observable in the paramagnetic phase through diffuse magnetic scattering. In particular, zigzag orders propagating in two other directions, ±120° rotated from the static one, are expected for a honeycomb net with C_3 symmetry. (The actual 3D crystal structure has an only approximate C_3 symmetry because of a monoclinic distortion, which singles out one propagation direction for the long-range ordered state (along *b* direction) out of the three possible under the ideal C_3 symmetry[15].)

With other magnetic correlations possibly emerging at high temperature in mind, we follow the temperature evolution of the zigzag order. Figure 1d–f shows *H*, *K* and *L* scans, respectively, of the magnetic Bragg peak at $\mathbf{Q} = (0, 1, 6.5)$ for selected temperatures. Figure 1g shows the correlation lengths along the *a*-, *b*- and *c*-axes as a function of temperature. As the temperature increases above T_N, the zigzag correlations diminish rather isotropically, despite dominant 2D couplings in the honeycomb net. This 3D characteristic of the magnetic correlations contrasts with that of the quasi-2D Heisenberg antiferromagnet Sr_2IrO_4, which exhibits 2D long-range correlations well above T_N (ref. 31), and implies that the critical temperature in Na_2IrO_3 is limited by the anisotropic interactions rather than the interlayer coupling; the Mermin–Wagner theorem requires either the symmetry to be lower than SU(2) or the dimension to be higher than 2D for a finite-temperature phase transition. The zigzag correlations survive on a length scale of several nanometres (approximately three unit cells wide) above T_N, but the peak intensities drop by two orders of magnitude. To isolate such small signals from the background, we used an experimental set-up that maximizes the signal-to-noise ratio, as described in the Methods.

Figure 2a maps the diffuse scattering intensity over a region in momentum space encompassing a full Brillouin zone of the honeycomb net, at several different Ψ angles to resolve the spin components (see Supplementary Fig. 2). These maps integrate the dynamic structure factor over the range $0 \leq \omega \leq 100$ meV,

NATURE PHYSICS DOI: 10.1038/NPHYS3322 LETTERS

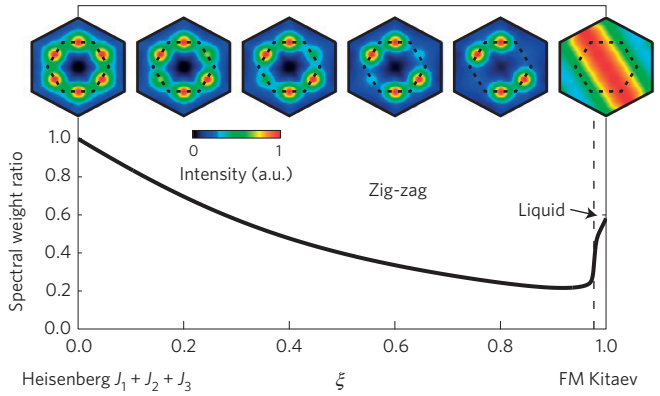

Figure 3 | Simulation of diffuse scattering using exact diagonalization. The Kitaev–Heisenberg model including up to third nearest-neighbour Heisenberg interactions was considered. ξ interpolates between the pure Heisenberg model and the pure Kitaev model via $J_1 = J_2 = J_3 = 1 - \xi$ and $K = -\xi$. A ferromagnetic K with finite J_1, J_2 and J_3 stabilizes the zigzag state for most values of ξ. The black curve shows the spectral asymmetry, defined as the ratio of spectral weight at $\mathbf{Q} = (0.5, 0.5)$ to that at $\mathbf{Q} = (0, 1)$. Images show equal-time correlations $\langle S^x_{\mathbf{Q}} S^x_{-\mathbf{Q}} \rangle$ obtained by exact diagonalization using a 24-site cluster and plotted in the extended Brillouin zone for selected ξ. The correlations for y and z components (not shown) can be generated by $\pm 120°$ rotations of the images shown.

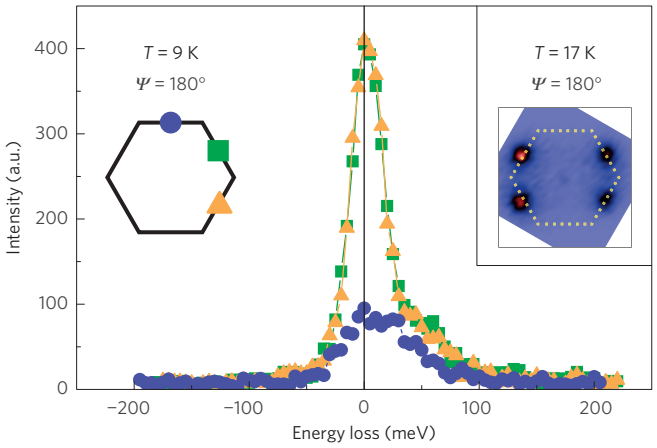

Figure 4 | Resonant inelastic X-ray scattering spectra below T_N. RIXS spectra recorded at $T = 9$ K and $\Psi = 180°$. $\mathbf{Q} = (0, 1)$, $(0.5, 0.5)$ and $(0.5, -0.5)$, shown as blue, green and yellow filled symbols, respectively, marked on the Brillouin zone of the honeycomb net and colour-coded with the spectra. At this Ψ angle, $\mathbf{S}$ lies approximately along $\mathbf{k}_f$ and π-σ' and π-π' channels measure the two spin components transverse to $\mathbf{S}$. For comparison, the inset shows the diffuse map at $T = 17$ K for the same Ψ angle, generated by rotating the $\Psi = 60°$ data shown in Fig. 2a clockwise by 120°.

covering the entire range of magnetic excitations, and serve as an excellent approximation for the equal-time correlation $S_{\alpha\alpha} \equiv \langle S^\alpha_{\mathbf{Q}} S^\alpha_{-\mathbf{Q}} \rangle$ $(\alpha = x, y, z)$. When averaged over the three spin components, the intensity map (Fig. 2c) indeed shows three zigzag correlations above T_N, with peaks at $\mathbf{Q} = \pm(0, 1)$, $\pm(0.5, 0.5)$ and $\pm(0.5, -0.5)$ of equal intensities, confirming the near-ideal C_3 symmetry. However, the spin-component-resolved maps, shown in Fig. 2b, manifestly break the C_3 symmetry. The system is left invariant only when C_3 rotation is performed simultaneously in the real space and in the spin space—that is, cyclic permutation of spin indices. This 'global' C_3 symmetry implies a strong entanglement between the real space and the spin space. Specifically, the full azimuthal dependence of each zigzag state, shown in Fig. 2d, closely follows the curves simulated for spin orientation fixed relative to the propagation direction, as depicted in Fig. 2e. In other words, specifying a spin component amounts to fixing the momentum direction and vice versa. This one-to-one correspondence between the spin space and the real space is a direct consequence of the bond-dependent nature of the anisotropic exchange terms.

Qualitatively, it is immediately seen that the anisotropic interactions dominate over the isotropic interactions and the system is very far away from the pure Heisenberg limit, in which case the spatial correlations must be spin-component-independent with three zigzag peaks having equal intensities by symmetry (as in the spin-averaged correlation shown in Fig. 2c preserving C_3 symmetry). A measure of how close the system is to either the Heisenberg or the Kitaev limits is provided by the intensity ratio of the weakest peak to the two bright peaks in the spin-component-resolved correlations (Fig. 2b). To quantify this measure, represented by a variable linearly interpolating between these two limits, ξ, requires specifying the Hamiltonian, which is not precisely known. For an estimation at a semi-quantitative level, we adopt a simple Hamiltonian that neglects all anisotropic terms beyond the K term. (This in turn requires including further-neighbour Heisenberg couplings J_2 and J_3 to stabilize the zigzag order[32], which we take to be equal to J_1 for simplicity.) Figure 3 shows the simulated patterns for selected ξ. It is clear that the observed diffuse pattern is consistent with the simulated pattern for the large ξ limit. In fact, the observed intensity ratio of ≈ 0.2 is even smaller than calculated (Fig. 3) for the largest ξ in the zigzag phase, which confirms the predominant anisotropic interactions.

Interpreted within this model, our calculations would imply that the system is very close to the Kitaev limit. However, it is becoming increasingly evident that other anisotropic terms beyond the Kitaev interaction do play a role[22,23]. This is, in fact, evident from the static spin not pointing along one of the cubic axes favoured by the K term; all other anisotropic terms conspire to rotate the spin away from the principal axes. This in turn suggests that the zigzag structure is further stabilized by other anisotropic terms. The zigzag correlations survive at least up to ~70 K (see Supplementary Fig. 3), which is in accord with the observation that coherent spin waves[15] disperse up to ≈ 5 meV. This energy scale coincides with the temperature scale (≈ 100 K) below which the magnetic susceptibility deviates from the Curie–Weiss behaviour[33]. This energy scale is, however, still far too small in comparison with the energy (≈ 100 meV) spanned by the magnetic excitations (Fig. 4), suggesting that the zigzag order is an emergent phenomenon. Despite the macroscopic degeneracy in the Kitaev QSL phase being reduced down to three zigzags, the high-energy Kitaev interactions leave their signature in the low-energy sector: the three spin components, each carrying its own zigzag, compete and melt the long-range order at a temperature much lower than that suggested by the Weiss temperature (Θ_W), leading to a large frustration parameter[33] ($\equiv \Theta_W / T_N$) approximately equal to 8.

The fluctuations among three zigzag states remain even below T_N, albeit with subtle spectral changes (Supplementary Fig. 3d), implying that they are primarily quantum rather than thermal fluctuations. At $\Psi = 180°$ (Fig. 4), the intensity remains highest at $\mathbf{Q} = \pm(0.5, 0.5)$ and $\mathbf{Q} = \pm(0.5, -0.5)$, away from the Bragg peaks at $\mathbf{Q} = \pm(0, 1)$, and peaked at zero energy within the energy resolution of 24 meV. Note that this scattering geometry probes two spin components transverse to the static component. A profound consequence of the unusual nature of the fluctuations is that the soft excitations are located away from the Bragg peak[15]. This is a notable exception to the universality held in conventional magnets that spin waves emanate from Bragg peaks by virtue of the Goldstone theorem, and magnetic anisotropy is manifested as a spin-wave gap, even in systems with extremely large magnetic anisotropy[34]. By contrast, the spin gap in our system is small (unresolved in our

spectra and estimated to be smaller than 2 meV from INS data[15]) in comparison with the overall energy scale of the system, despite the fact that the magnetism is dominated by the anisotropic terms. Rather, the anisotropy is manifested as the separation of the long-wavelength spin waves from the Bragg peaks, which is a natural consequence of each spin component exhibiting its own real-space correlations. Our results directly reveal the key building blocks of the Kitaev model in Na_2IrO_3, and establish a new design strategy for the long-sought quantum spin liquids via the bond-directional magnetic coupling.

Methods

Methods and any associated references are available in the online version of the paper.

Received 11 January 2015; accepted 1 April 2015; published online 11 May 2015

References

1. van Vleck, J. H. On the anisotropy of cubic ferromagnetic crystals. *Phys. Rev.* **52,** 1178–1198 (1937).
2. Khaliullin, G. Orbital order and fluctuations in Mott insulators. *Prog. Theor. Phys. Suppl.* **160,** 155–202 (2005).
3. Jackeli, G. & Khaliullin, G. Mott insulators in the strong spin–orbit coupling limit: From Heisenberg to a quantum compass and Kitaev models. *Phys. Rev. Lett.* **102,** 017205 (2009).
4. Kitaev, A. Anyons in an exactly solved model and beyond. *Ann. Phys.* **321,** 2–111 (2006).
5. Kim, B. J. *et al.* Novel $J_{\rm eff}=1/2$ Mott state induced by relativistic spin–orbit coupling in Sr_2IrO_4. *Phys. Rev. Lett.* **101,** 076402 (2008).
6. Kim, B. J. *et al.* Phase-sensitive observation of a spin–orbital Mott state in Sr_2IrO_4. *Science* **323,** 1329–1332 (2009).
7. Takayama, T. *et al.* Hyper-honeycomb iridate β-Li_2IrO_3 as a platform for Kitaev magnetism. *Phys. Rev. Lett.* **114,** 077202 (2015).
8. Modic, K. A. *et al.* Realization of a three-dimensional spin-anisotropic harmonic honeycomb iridate. *Nature Commun.* **5,** 4203 (2014).
9. Kimchi, I. & Vishwanath, A. Kitaev–Heisenberg models for iridates on the triangular, hyperkagome, kagome, fcc, and pyrochlore lattices. *Phys. Rev. B* **89,** 014414 (2014).
10. Hermanns, M. & Trebst, S. Quantum spin liquid with a Majorana Fermi surface on the three-dimensional hyperoctagon lattice. *Phys. Rev. B* **89,** 235102 (2014).
11. Lee, S. B., Jeong, J-S., Hwang, K. & Kim, Y. B. Emergent quantum phases in a frustrated J_1–J_2 Heisenberg model on the hyperhoneycomb lattice. *Phys. Rev. B* **90,** 134425 (2014).
12. Plumb, K. W. *et al.* α-$RuCl_3$: A spin–orbit assisted Mott insulator on a honeycomb lattice. *Phys. Rev. B* **90,** 041112 (2014).
13. Luo, Y. *et al.* Li_2RhO_3: A spin-glassy relativistic Mott insulator. *Phys. Rev. B* **87,** 161121 (2013).
14. Liu, X. *et al.* Long-range magnetic ordering in Na_2IrO_3. *Phys. Rev. B* **83,** 220403 (2011).
15. Choi, S. K. *et al.* Spin waves and revised crystal structure of honeycomb iridate Na_2IrO_3. *Phys. Rev. Lett.* **108,** 127204 (2012).
16. Ye, F. *et al.* Direct evidence of a zigzag spin-chain structure in the honeycomb lattice: A neutron and X-ray diffraction investigation of single-crystal Na_2IrO_3. *Phys. Rev. B* **85,** 180403 (2012).
17. Reuther, J., Thomale, R. & Rachel, S. Spiral order in the honeycomb iridate Li_2IrO_3. *Phys. Rev. B* **90,** 100405 (2014).
18. Biffin, A. *et al.* Noncoplanar and counterrotating incommensurate magnetic order stabilized by Kitaev interactions in γ-Li_2IrO_3. *Phys. Rev. Lett.* **113,** 197201 (2014).
19. Biffin, A. *et al.* Unconventional magnetic order on the hyperhoneycomb Kitaev lattice in β-Li_2IrO_3: Full solution via magnetic resonant X-ray diffraction. *Phys. Rev. B* **90,** 205116 (2014).
20. Chaloupka, J., Jackeli, G. & Khaliullin, G. Kitaev–Heisenberg model on a honeycomb lattice: Possible exotic phases in iridium oxides A_2IrO_3. *Phys. Rev. Lett.* **105,** 027204 (2010).
21. Chaloupka, J., Jackeli, G. & Khaliullin, G. Zigzag magnetic order in the iridium oxide Na_2IrO_3. *Phys. Rev. Lett.* **110,** 097204 (2013).
22. Lee, E. K-H. & Kim, Y. B. Theory of magnetic phase diagrams in hyperhoneycomb and harmonic-honeycomb iridates. *Phys. Rev. B* **91,** 064407 (2015).
23. Rau, J. G., Lee, E. K-H. & Kee, H-Y. Generic spin model for the honeycomb iridates beyond the Kitaev limit. *Phys. Rev. Lett.* **112,** 077204 (2014).
24. Katukuri, V. M. *et al.* Kitaev interactions between $j=1/2$ moments in honeycomb Na_2IrO_3 are large and ferromagnetic: Insights from *ab initio* quantum chemistry calculations. *New J. Phys.* **16,** 013056 (2014).
25. Yamaji, Y., Nomura, Y., Kurita, M., Arita, R. & Imada, M. First-principles study of the honeycomb-lattice iridates Na_2IrO_3 in the presence of strong spin–orbit interaction and electron correlations. *Phys. Rev. Lett.* **113,** 107201 (2014).
26. Shitade, A. *et al.* Quantum spin Hall effect in a transition metal oxide Na_2IrO_3. *Phys. Rev. Lett.* **102,** 256403 (2009).
27. Mazin, I. I., Jeschke, H. O., Foyevtsova, K., Valenti, R. & Khomskii, D. I. Na_2IrO_3 as a molecular orbital crystal. *Phys. Rev. Lett.* **109,** 197201 (2012).
28. Kim, C. H., Kim, H. S., Jeong, H., Jin, H. & Yu, J. Topological quantum phase transition in 5*d* transition metal oxide Na_2IrO_3. *Phys. Rev. Lett.* **108,** 106401 (2012).
29. Gretarsson, H. *et al.* Magnetic excitation spectrum of Na_2IrO_3 probed with resonant inelastic X-ray scattering. *Phys. Rev. B* **87,** 220407 (2013).
30. Price, C. & Perkins, N. B. Finite-temperature phase diagram of the classical Kitaev–Heisenberg model. *Phys. Rev. B* **88,** 024410 (2013).
31. Fujiyama, S. *et al.* Two-dimensional Heisenberg behavior of $J_{\rm eff}=1/2$ isospins in the paramagnetic state of the spin–orbital Mott insulator Sr_2IrO_4. *Phys. Rev. Lett.* **108,** 247212 (2012).
32. Kimchi, I. & You, Y-Z. Kitaev–Heisenberg-J_2-J_3 model for the iridates A_2IrO_3. *Phys. Rev. B* **84,** 180407 (2011).
33. Singh, Y. & Gegenwart, P. Antiferromagnetic Mott insulating state in single crystals of the honeycomb lattice material Na_2IrO_3. *Phys. Rev. B* **82,** 064412 (2010).
34. Kim, J. *et al.* Large spin-wave energy gap in the bilayer iridate $Sr_3Ir_2O_7$: Evidence for enhanced dipolar interactions near the Mott metal–insulator transition. *Phys. Rev. Lett.* **109,** 157402 (2012).

Acknowledgements

Work in the Materials Science Division of Argonne National Laboratory (sample preparation, characterization, and contributions to data analysis) was supported by the US Department of Energy, Office of Science, Basic Energy Sciences, Materials Science and Engineering Division. Use of the Advanced Photon Source, an Office of Science User Facility operated for the US Department of Energy (DOE) Office of Science by Argonne National Laboratory, was supported by the US DOE under Contract No. DE-AC02-06CH11357. K.M. acknowledges support from UGC-CSIR, India. Y.S. acknowledges DST, India for support through Ramanujan Grant #SR/S2/RJN-76/2010 and through DST grant #SB/S2/CMP-001/2013. J.C. was supported by ERDF under project CEITEC (CZ.1.05/1.1.00/02.0068) and EC 7th Framework Programme (286154/SYLICA).

Author contributions

B.J.K. conceived the project. S.H.C., J-W.K., J.K. and B.J.K. performed the experiment with support from Y.C., T.G., A.A-Z., M.M.S. and M.K. H.Z. and K.M. grew the single crystals; C.C.S., C.D.M. and K.M. characterized the samples under the supervision of J.F.M. and Y.S. S.H.C., J-W.K. and B.J.K. analysed the data. J.C. performed the numerical calculations. J.C., G.J. and G.K. developed the theoretical model. All authors discussed the results. B.J.K. led the manuscript preparation with contributions from all authors.

Additional information

Supplementary information is available in the online version of the paper. Reprints and permissions information is available online at www.nature.com/reprints. Correspondence and requests for materials should be addressed to B.J.K.

Competing financial interests

The authors declare no competing financial interests.

NATURE PHYSICS DOI: 10.1038/NPHYS3322

Methods

Single-crystal growth. Single crystals of Na_2IrO_3 were grown following two different recipes using Na_2CO_3 flux (Sample 1) and self-flux (Sample 2). For Sample 1, a mixture of Na_2CO_3 and IrO_2 with a molar ratio of 50:1 was melted at 1,050 °C for 6 h followed by fast cooling at a rate of 100 °C h^{-1} down to 1,000 °C, slow cooling at a rate of 1 °C h^{-1} down to 800 °C and furnace cooling to room temperature in sequence. Hexagonal pillar-shaped crystals with typical dimensions of 0.2 mm × 0.2 mm × 0.4 mm were obtained after dissolving Na_2CO_3 flux in acetone and water. For Sample 2, powders of Na_2CO_3 were mixed with 10–20% excess IrO_2 and were calcined at 700 °C for 24 h. Single crystals were grown on top of a powder matrix in a subsequent heating at 1,050 °C. Plate-like crystals with typical dimensions of 5 mm × 5 mm × 0.1 mm were physically extracted.

Resonant X-ray scattering. Incident X-rays were tuned to the Ir L_3 edge (11.2145 keV). The resonant X-ray diffraction experiments were carried out at the 6 ID-B beamline of the Advanced Photon Source. The polarization analysis was performed in the vertical scattering geometry using a pyrolytic graphite analyser probing the $\sigma-\pi'$ channel. The RIXS was performed at ID20 of the European Synchrotron Radiation Facility. The total instrumental energy resolution of 24 meV was achieved with a monochromator and a diced spherical analyser made from Si (844) and a position-sensitive area detector placed on a Rowland circle with a 2 m radius. The diffuse magnetic scattering was performed using the RIXS spectrometers at the 9 ID, 27 ID and 30 ID (MERIX) beamlines of the Advanced Photon Source, where a monochromator of 90 meV bandwidth was used for an order-of-magnitude higher incident photon flux than that from the Si (844) monochromator. In these experiments, a horizontal scattering geometry was used with the π-incident X-ray polarization measuring the sum of $\pi-\sigma'$ and $\pi-\pi'$ channels. The 2θ angle was fixed at 90° to minimize the contribution from Thompson elastic scattering. As a result, L values in the HK maps shown in Fig. 2a vary in the range between 6.5 and 7. The in-plane momentum resolution of the RIXS spectrometer was ± 0.048 Å^{-1}. The use of RIXS spectrometers rejecting all inelastically scattered X-rays outside of the 100 meV energy window centred at the elastic line led to a significant improvement in the signal-to-noise ratio. A typical counting time of 2 h was required for a map shown in Fig. 2.

nature physics

SUPPLEMENTARY INFORMATION

DOI: 10.1038/NPHYS3322

Direct evidence for dominant bond-directional interactions in a honeycomb lattice iridate Na_2IrO_3

A. Sample characterization

The powder x-ray diffraction patterns of both Sample #1 and #2 were consistent with the crystal structure in the C2/m space group as previous reported[15]. Sample #1 had a slightly lower T_N=12 K compared to Sample #2 with T_N=15 K, as measured by SQUID magnetometry (Fig. S1a) and by resonant x-ray diffraction through the magnetic Bragg peaks at Q = (0 1 n+$\frac{1}{2}$) (n: integer) (Fig. S1b). Sample #1 was found to be of multi domains but had a superior crystallinity with 0.1° mosaicity (as compared to 0.5° mosaicity of Sample #2) (Fig. S1c), and thus was used for the resonant diffraction experiment (polarization analysis and measurement of the magnetic correlation length.) Sample #2 was found to be of a single domain and was used for the RIXS measurement. Both Sample #1 and #2 were used for the diffuse scattering measurement and gave identical results.

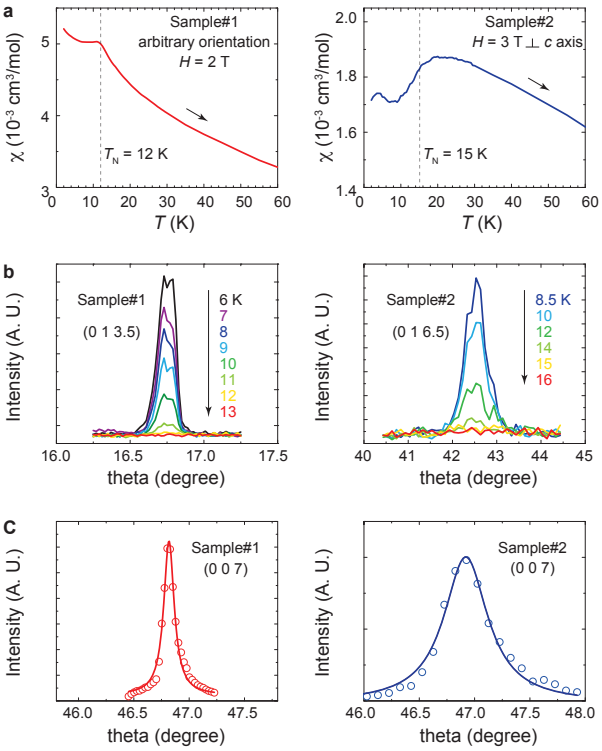

Supplementary Figure 1. Characterization of Sample #1 and Sample #2. (a) Temperature dependence of magnetic susceptibility. Dotted lines indicate T_N. Black arrows indicate that the data were measured while warming after zero-field cooling. (b) Temperature dependence of the magnetic Bragg peaks. (c) Sample mosaicity.

B. Extraction of the spin-component resolved equal-time correlators

The x-ray scattering intensity measured without using a polarization analyzer contains contributions from both π-σ' and π-π' channels, probing spin components along $\mathbf{k}_i$ and perpendicular to the horizontal scattering plane, respectively. In other words, two spin components perpendicular to $\mathbf{k}_f$ are measured in the 90° horizontal scattering geometry used. For example, when Ψ=0°, the z local cubic axis points approximately along $\mathbf{k}_f$ (Fig. S2), and thus the scattering

SUPPLEMENTARY INFORMATION DOI: 10.1038/NPHYS3322

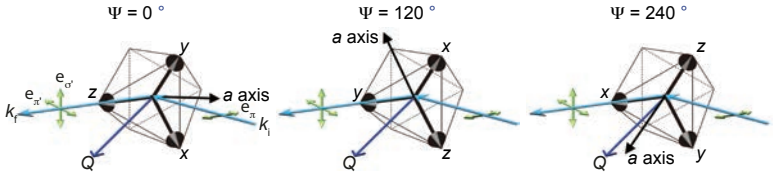

Supplementary Figure 2. Scattering configurations. (a) Ψ= 0°, (b) Ψ = 120°, and (c) Ψ = 240°. The azimuth Ψ is the angle between the a axis and the scattering plane. Thick black arrows denote the local x, y, and z axes in the IrO_6 octahedron. a axis is indicated by a thin black arrow. Cyan arrows are the incident and scattered x-rays with the wave vectors $\mathbf{k}_i$ and $\mathbf{k}_f$, respectively. Green arrows indicate the x-ray polarizations. **Q** (dark blue arrow) is the momentum transfer.

intensity measures the correlation $S_{xx}+S_{yy}$. Likewise, Ψ=120°(Ψ=240°) measures $S_{xx}+S_{zz}$($S_{yy}+S_{zz}$). Then, S_{xx}, S_{yy}, and S_{zz} can be extracted by solving a set of linear equations.

C. Temperature dependence of the diffuse magnetic peak and RIXS spectra

The short-range zig-zag order is observable at least up to T≈70 K (Fig. S3a). The magnetic correlation length (1.6-1.8 nm) along the a axis does not vary significantly in the measured temperature region. Figs. S3b and S3c plot the diffuse map at T=50 K for Ψ=0° and Ψ=30°, respectively, which is similar to the diffuse map recorded at T=17 K (shown in Fig. 2a) apart from thermal broadenings. Fig. S3d depicts the RIXS spectra at **Q**=(0.5 0.5) and (0.5 -0.5) for Ψ=180°, which show subtle spectral change in the temperature range, 9 K-17 K, below and above T_N.

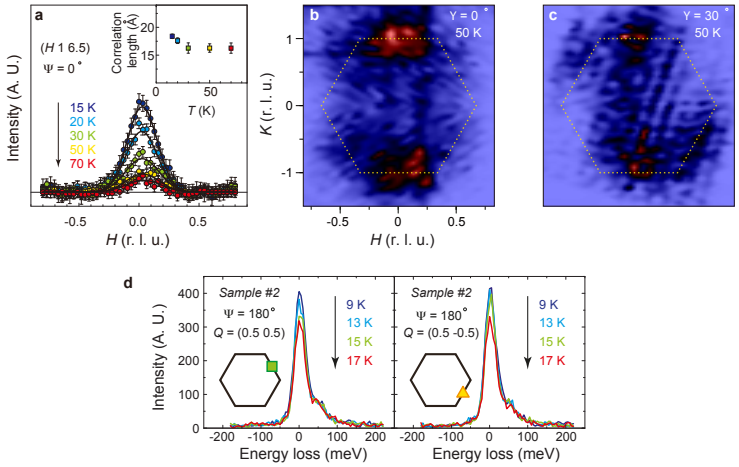

Supplementary Figure 3. Diffuse magnetic x-ray scattering intensities above T_N and RIXS spectra below and above T_N. (a) H profiles of the diffuse peak at **Q**=(0 1). Shown in the inset is the magnetic correlation length along the a axis derived from Gaussian fitting (solid curves)of the data for Sample #1. (b,c) Diffuse maps at T=50 K for Ψ=0° and Ψ=30°. The dashed hexagon indicates the first Brillouin zone of the honeycomb net. (d) Temperature evolution (9 K-17 K) of RIXS spectra at **Q**=(0.5 0.5) and **Q**=(0.5 -0.5) for Ψ=180°.

DOI: 10.1038/NPHYS3322

D. Calculated azimuthal angle dependence for all polarization channels

In order to facilitate comparison between the two azimuth angle dependence curves shown in Fig. 1c and Fig. 2d measured with different analyzer settings, we provide in Fig. S4 calculated azimuth angle dependence for all polarization channels for the two measured **Q** positions.

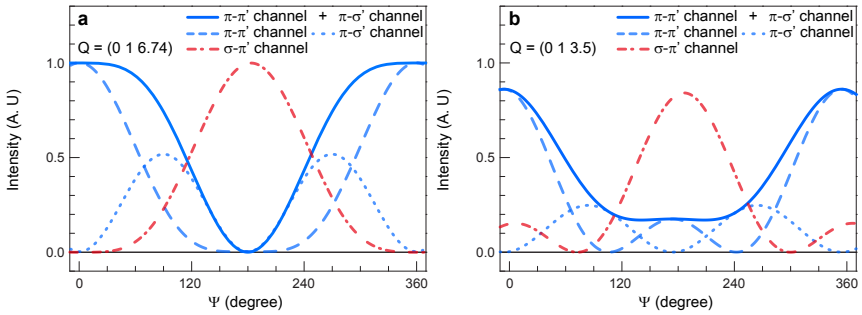

Supplementary Figure 4. Azimuthal angle dependence for all polarization channels. (a) For **Q**=(0 1 6.74) (b) For **Q**=(0 1 3.5).

PHYSICAL REVIEW B **92**, 024413 (2015)

Hidden symmetries of the extended Kitaev-Heisenberg model: Implications for the honeycomb-lattice iridates A_2IrO_3

Jiří Chaloupka[1] and Giniyat Khaliullin[2]

[1]*Central European Institute of Technology, Masaryk University, Kotlářská 2, 61137 Brno, Czech Republic*

[2]*Max Planck Institute for Solid State Research, Heisenbergstrasse 1, D-70569 Stuttgart, Germany*

(Received 19 February 2015; revised manuscript received 5 May 2015; published 13 July 2015)

We have explored the hidden symmetries of a generic four-parameter nearest-neighbor spin model, allowed in honeycomb-lattice compounds under trigonal compression. Our method utilizes a systematic algorithm to identify all dual transformations of the model that map the Hamiltonian on itself, changing the parameters and providing exact links between different points in its parameter space. We have found the complete set of points of hidden SU(2) symmetry at which a seemingly highly anisotropic model can be mapped back on the Heisenberg model and inherits therefore its properties such as the presence of gapless Goldstone modes. The procedure used to search for the hidden symmetries is quite general and may be extended to other bond-anisotropic spin models and other lattices, such as the triangular, kagome, hyperhoneycomb, or harmonic-honeycomb lattices. We apply our findings to the honeycomb-lattice iridates Na_2IrO_3 and Li_2IrO_3, and illustrate how they help to identify plausible values of the model parameters that are compatible with the available experimental data.

DOI: 10.1103/PhysRevB.92.024413 PACS number(s): 75.10.Jm, 75.25.Dk, 75.30.Et

I. INTRODUCTION

When relativistic spin-orbit coupling dominates over the exchange and orbital-lattice interactions, the orbital moment $\boldsymbol{L}$ of an ion remains unquenched and a total angular momentum $\boldsymbol{J} = \boldsymbol{S} + \boldsymbol{L}$ is formed. This was known to happen in compounds of late transition metal ions such as of cobalt (see, e.g., Ref. [1]); however, the "cleanest" examples of spin-orbit coupled magnets emerged more recently: these are the iridium oxides Sr_2IrO_4 and Na_2IrO_3 with perovskite and honeycomb-lattice structures, correspondingly.

By construction, magnetic ordering in these systems necessarily involves interactions between orbital moments $\boldsymbol{L}$, in addition to a conventional Heisenberg exchange among the spin part of total angular momentum $\boldsymbol{J}$ [2]. Since the L moment, hosted by t_{2g} orbital in a crystal, is only an "effective" one [3], it need not be conserved during the electron hoppings; thus the L-moment exchange interactions are generally not SU(2) invariant [4]. Moreover, the orbital moments have a "shape" and hence the L interactions are anisotropic in real space, too, and thus strongly frustrated even on simple cubic lattices. Altogether, this results in nontrivial L Hamiltonians and orderings, including, e.g., noncoplanar (multi-Q) states, "hidden" Goldstone modes, etc. [5,6]. Via the spin-orbit coupling, these peculiar features of orbital physics are inherited by the "pseudospin-J" wave functions and interactions [6–14]. In essence, the frustrated nature and quantum behavior of t_{2g}-orbital moments [15,16] are transferred to those of low-energy pseudospins J.

Depending on the electron configuration of ions, the ground state pseudospin may take different values $J = 0, 1/2, 1, \ldots$, and a variety of magnetic Hamiltonians with different symmetries and diverse behavior emerge in each case, because of different admixture of non-Heisenberg L interactions. Perhaps the most radical departure from a conventional magnetism is realized in compounds with apparently "nonmagnetic" $J = 0$ ions, where a competition between spin-orbit and exchange interactions results in a nonmagnetic-magnetic quantum phase transition [17–20].

The case of pseudospin $J = 1/2$ iridates is of special interest. This is because Sr_2IrO_4 perovskite was found [22–24] to host cuprate-like magnetism, and honeycomb-lattice iridates A_2IrO_3 (A = Na, Li) have been suggested [9] as a candidate material where the Kitaev model [25] physics might be realized. Following this proposal, a subsequent work [11] has introduced the minimal magnetic Hamiltonian for iridates A_2IrO_3: the Kitaev-Heisenberg model (KH model)—a frustrated spin model with many attractive properties. Most importantly, its phase diagram contains a finite window of a quantum spin-liquid phase which emanates from the pure Kitaev point of the model with a known exact solution [25]. To reflect the later experimental findings in iridates, such as the zigzag (Na_2IrO_3 [26–28]) and spiral (Li_2IrO_3 [29]) type magnetic orderings, the initially proposed model was modified by including longer-range Heisenberg [28,30] or anisotropic [31] interactions, extending the parameter range [32–34], by considering further anisotropic terms in the Hamiltonian [35–42], or by including spatial anisotropy of the model parameters [43]. An alternative picture based on an itinerant approach has been also suggested [44].

Despite the extensive efforts, no consensus concerning the minimal model for the honeycomb-lattice iridates has thus far been reached. A reliable microscopic derivation of the exchange interactions is difficult and does not lead to a conclusive suggestion for the minimal Hamiltonian and its parameters. On the experimental side, the richest information about the underlying spin model would be provided by mapping momentum-resolved spin excitation spectrum. However, due to the lack of large enough monocrystals, the inelastic neutron scattering (INS) has been performed on powders only [28]. Another possible probe—resonant inelastic x-ray scattering (RIXS)—suffers from a small resolution at present. While it could be successfully applied in the case of perovskite iridates [23], here the limitation comes from the much smaller energy scale of the excitations to be studied in detail by RIXS; however, the overall strength of magnetic interactions in Na_2IrO_3 has been quantified [45,46].

Nevertheless, the experimental data collected to date puts rather strong constraints on the possible models. First, the RIXS-derived magnetic energies [45,46] (of the order of 40 meV) are much higher than the ordering temperature (∼15 K), suggesting strong frustration. Second, the magnetic scattering intensity, measured by RIXS at zero momentum, $\boldsymbol{Q} = 0$, is as strong as elsewhere in the Brillouin zone, which implies a dominance of anisotropic, non-Heisenberg spin interactions. Third, the recent resonant x-ray scattering data [46] have revealed nearly ideal C_3 symmetry of the spin correlations in momentum space. Moreover, inelastic neutron scattering data [28] have indicated that a spin gap, if present, would be relatively small (less than 2 meV). All these observations taken together imply that the dominant pseudospin interactions in iridates are strongly frustrated, highly anisotropic in spin space, and yet highly symmetric in real space. By very construction, all these features are in fact the intrinsic properties of the KH model and its extended versions.

The KH model, supplemented by other C_3 symmetry allowed terms (see below), is therefore physically sound and plausible. However, there is a problem of its large parameter space (four parameters even within the nearest-neighbor model) resulting in complex phase diagrams, which makes the analysis of experimental data and the extraction of the model parameters a difficult task. In such cases, clarification of the underlying symmetry properties of the model is often of a great help. In general, the spin-orbital models in Mott insulators possess peculiar symmetries [6,14] which are rooted in the bond-directional nature of orbitals. In this context, a special four-sublattice rotation [6] within spin space has proved itself as an extremely useful tool in the case of the original two-parameter KH model [11,32,47–50]. It maps the Hamiltonian on itself but changes the Hamiltonian parameters, connecting thereby different points in the parameter space. Being an exact transformation, it transfers the complete knowledge about some point in the phase diagram, including the ground state, excitation spectrum, response functions, etc., to its partner. Based solely on this self-duality of the model, the entire phase diagram could be sketched and the deep relations between the phases understood. In addition, it also reveals points of hidden SU(2) symmetry, where the system is exactly equivalent to a Heisenberg model for the rotated spins. Given its usefulness, it is highly desirable to find and analyze similar transformations for the extended versions of the KH model.

In this paper, we introduce a systematic method to derive dual transformations of bond-anisotropic spin Hamiltonians and demonstrate its results and their physical implications in the case of honeycomb iridates adopting the full nearest-neighbor model [36,37,39]. We find all the hidden SU(2)-symmetry points of the model, the most peculiar one being characterized by a "vortex"-like pattern with a six-site unit cell, and demonstrate how the characteristics of the hidden Heisenberg magnet manifest themselves in the anisotropic situations. By identifying the SU(2) points we characterize all the possible gapless Goldstone modes that may be encountered within the model. This is relevant in the context of real materials as the spin gap was found to be well below 2 meV [28,29], suggesting a connection to some of the SU(2) points. Finally, using a self-duality of the model, we will provide a link between our fits of the earlier Na_2IrO_3 data [32] and the recent experimental observation of the ordered moment direction [46]. We argue that this observation provides a direct access to the strength of the additional terms "extending" the KH model, and quantify the spin easy axis direction in terms of this "departure" from the pure KH model. This allows us to suggest plausible values of the model parameters that are compatible with the current data. While we focus here on the case of a honeycomb lattice as realized in Na_2IrO_3 and more recently in $RuCl_3$ [51], the method is general and expected to produce interesting results also in the context of the new structural families of iridates—recently synthesized hyperhoneycomb [52,53] and harmonic-honeycomb lattices [54,55], or the theoretically proposed hyperoctagon lattice [56].

The paper is organized as follows. Section II introduces the Hamiltonian and discusses its parameters. Sections III and IV introduce the method and derive and discuss the main results of the paper—the hidden symmetries of the model. Section V and Appendix B discuss the implications of the results for honeycomb iridates.

II. EXTENDED KITAEV-HEISENBERG MODEL

We start by specifying the model Hamiltonian including all symmetry-allowed spin interactions on nearest-neighbor bonds. An ideal, undistorted structure of the honeycomb $NaIr_2O_6$ plane is shown in Fig. 1(a). We will utilize its rotational C_3 symmetry and the three sets of parallel mirror

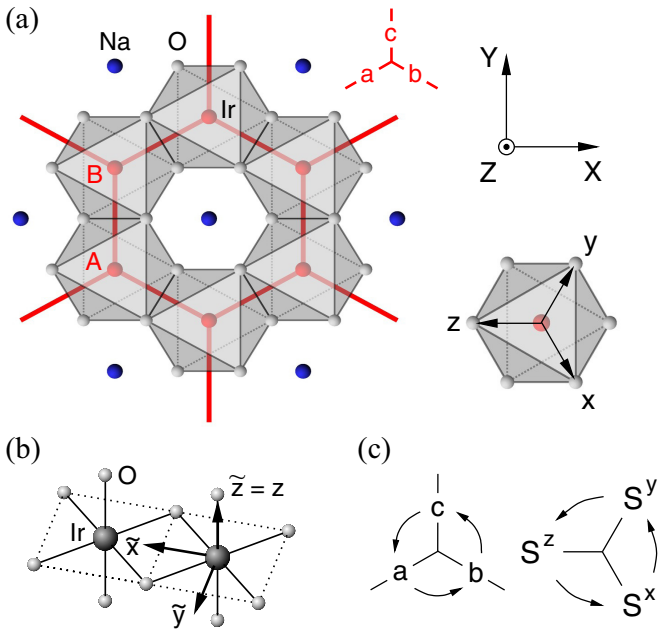

FIG. 1. (Color online) (a) Top view of the honeycomb $NaIr_2O_6$ plane, the definition of global X,Y,Z axes, and the xyz reference frame for the spin components. The X and Y directions coincide with the crystallographic **a** and **b** axes. The three bond directions of the honeycomb lattice are labeled as a, b, and c; its two sublattices are labeled by A and B. (b) Two edge-shared IrO_6 octahedra of a c bond and the definition of the local spin axes $\tilde{x}$, $\tilde{y}$, $\tilde{z}$ [used in Eq. (1)]. (c) Simultaneous cyclic permutation of the Ir-Ir bond directions a, b, c and the spin components x, y, z when applying a C_3 rotation to the model.

planes containing the shared edges of the IrO_6 octahedra and cutting the Ir-Ir bonds into halves. The C_3 symmetry links the interactions for different bond directions while the presence of the mirror planes restricts the possible interactions for a given bond direction. A trigonal distortion (compression or elongation along the Z axis) fully preserves these symmetries so that our Hamiltonian applies in that case as well. Furthermore, recent experiments [46] indicate a nearly ideal C_3 symmetry of the spin properties and hence suggest that additional terms, possibly induced by a monoclinic distortion present in Na_2IrO_3, can be neglected. Physically, this observation implies the robustness of the pseudospin wave functions against weak monoclinic distortions.

The bond Hamiltonian is most compactly expressed in a local, bond-dependent $\tilde{x}\tilde{y}\tilde{z}$ reference frame for spins, presented in Fig. 1(b) for a c bond. Due to the mirror symmetry, the in-bond $S^{\tilde{x}}$ component is forbidden to interact with the $S^{\tilde{y}}$ and $S^{\tilde{z}}$ components [36]. Following the notation of Ref. [36] we arrange the allowed terms into the form

$$\mathcal{H}_{\langle ij\rangle\parallel c} = J\,\boldsymbol{S}_i\cdot\boldsymbol{S}_j + K\,S_i^{\tilde{z}}S_j^{\tilde{z}} + D\left(S_i^{\tilde{x}}S_j^{\tilde{x}} - S_i^{\tilde{y}}S_j^{\tilde{y}}\right) + C\left(S_i^{\tilde{y}}S_j^{\tilde{z}} + S_i^{\tilde{z}}S_j^{\tilde{y}}\right). \quad (1)$$

This four-parameter Hamiltonian extends the KH model (J and K terms) by the D term bringing further anisotropy among the diagonal components of the interaction, and the C term determining the only symmetry-allowed nondiagonal element in the exchange interaction tensor. Parameter C would vanish for an isolated pair of undistorted octahedra; it becomes finite due to a trigonal distortion and/or due to the extended nature of orbitals in a crystal ("recognizing" the fact that the octahedra are canted relative to the crystal axis Z).

To capture the C_3 symmetry, it is convenient to switch to cubic axes xyz, introduced in Fig. 1(a) and pointing from an Ir ion to neighboring O ion positions in an ideal structure. The c-bond Hamiltonian in the cubic reference frame, as derived in Ref. [37], reads then as

$$\mathcal{H}_{\langle ij\rangle\parallel c} = J\,\boldsymbol{S}_i\cdot\boldsymbol{S}_j + K\,S_i^zS_j^z + \Gamma\left(S_i^xS_j^y + S_i^yS_j^x\right) + \Gamma'\left(S_i^xS_j^z + S_i^zS_j^x + S_i^yS_j^z + S_i^zS_j^y\right), \quad (2)$$

with the correspondence $\Gamma = -D$ and $\Gamma' = \frac{1}{\sqrt{2}}C$, often used below. For the other bond directions, the Hamiltonian is obtained by a cyclic permutation [see Fig. 1(c)], resulting in one-to-one correspondence between the three types of bonds and interactions, as required by C_3 symmetry. Physically, each type of bond favors its own distinct "orbital setup" to optimize the hopping energy, and this is fingerprinted in pseudospin interactions via spin-orbit coupling. For completeness, Appendix A shows the Hamiltonian in the global axes XYZ; it has certain advantages moving the bond dependence from the operator forms to the coupling constants.

A few comments are in order concerning the model parameters. In general, calculation of exchange integrals in transition metal compounds with 90° $d-p-d$ bonding geometry is an intricate task, because more hopping pathways are allowed as compared to a simpler case of 180° $d-p-d$ bonding in perovskites (where theory [9] has correctly predicted the strength of dominant exchange constants). For instance, t_{2g} orbitals may also overlap directly, in addition to oxygen-mediated hoppings; there is a large overlap between orbitals of t_{2g} and e_g symmetries (forbidden in perovskites), etc., resulting in a number of competing ferromagnetic and antiferromagnetic contributions which are difficult to evaluate, in particular in compounds with small Mott and/or charge-transfer excitation gaps. The uncertainties in interaction parameters U and J_H further affect the theoretical estimates.

Initial consideration [6] of the pseudospin one-half exchange interactions in 90°-bonding geometry resulted in $K = -2J$ [hitting a "hidden" SU(2) point by chance] in the cubic limit; later work [8,9,11] using different approximations has changed this estimate both in terms of the signs and values of J and K, illustrating the difficulties described above. It was also found that the nondiagonal element Γ allowed in cubic symmetry may take sizable values [36,37,39,40]. Further, Γ' is expected to become as large as the other parameters if trigonal splitting Δ of the t_{2g} orbital level, caused by a compression along the Z axis, becomes comparable to spin-orbit coupling λ; also, the trigonal field suppresses the parameter K. These trends are easy to understand: large trigonal field suppresses the in-plane components of orbital moment L_X and L_Y, leaving the axial L_Z component the only unquenched one; thus the pseudospin one-half Hamiltonian, written most conveniently in global axes in this limit, may not contain anything but $XX+YY$ and ZZ type terms: $J_{XY}(S_i^XS_j^X + S_i^YS_j^Y) + J_ZS_i^ZS_j^Z$, identical for all bonds. This is what has indeed been found by explicit calculations [6,35] in the limit of $\Delta \gg \lambda$. This implies $K=0$ and $\Gamma' = \Gamma$ in this limit (see also Appendix A), while $J_{XY} = (J-\Gamma)$ and $J_Z = (J+2\Gamma)$ may take any values depending on the microscopic details. Although this limit is not very realistic for the Ir^{4+} ion with large spin-orbit constant $\lambda \sim 0.4$ eV [3,57], we may expect sizable values of both Γ and Γ' in Na_2IrO_3 where Δ seems to exceed 0.1 eV [58,59]. The role of Γ and Γ' terms should further increase in other compounds based on pseudospin-1/2 Co^{4+}, Ru^{3+}, and Rh^{4+} ions with smaller λ.

In general, the high-energy behavior of spins and orbitals in transition metal compounds is well captured by the Kugel-Khomskii models [4] and their descendants [6]. However, the low-energy physics and ultimate magnetic "fixed-point" are heavily influenced by many "unpleasant" details originating from orbital-lattice coupling and distortions, unavoidable in real materials. In perovskites, the Kugel-Khomskii energy scale is given by $4t^2/U$ independent of spin-orbit coupling; however, this leading term drops out for pseudospins-1/2 in the edge-shared, 90°-bonding geometry [6,9], so the "high-energy" scale is set up by the subleading terms. In iridates, the hope [9] is that the Kitaev-type coupling is the leading one among these subleading terms. Since this coupling is itself a correction to $4t^2/U$, this expectation may or may not hold in reality.

To summarize up to now: in real materials even with an ideal C_3 symmetry, all four of the exchange parameters may play a significant role. This motivates us to regard the Hamiltonian (1) and (2) as an effective model with arbitrary parameters, and look for some general symmetry arguments that may help to identify plausible parameter windows in the analysis of experimental data.

III. SYSTEMATIC CONSTRUCTION OF DUAL TRANSFORMATIONS

Having fixed the model Hamiltonian, we are ready to explore its dual transformations. By a dual transformation we mean a prescription for site-dependent rotations in the spin space, $\boldsymbol{S}_i' = \mathcal{R}_i \boldsymbol{S}_i$, which transforms a spin Hamiltonian $\mathcal{H}(\boldsymbol{S})$ into a formally new Hamiltonian $\mathcal{H}'(\boldsymbol{S}')$. We are interested in self-dual transformations of $\mathcal{H}$ that map the model onto itself, preserving all its symmetry properties. That is, the rotated partner $\mathcal{H}'$ (i) has the same four terms albeit with different parameters $J'K'D'C'$, and (ii) it respects the C_3 rotation rules encoded in Fig. 1(c), hence preserving the original distribution of the three types of bond-dependent interactions on a lattice.

Starting with the $JKDC$ Hamiltonian expressed as $\mathcal{H}(\boldsymbol{S}) = \sum_{\langle ij\rangle} \boldsymbol{S}_i^T H_{ij} \boldsymbol{S}_j$ where H_{ij} are 3×3 matrices, we obtain $\mathcal{H}(\boldsymbol{S}) = \mathcal{H}'(\boldsymbol{S}') = \sum_{\langle ij\rangle} \boldsymbol{S}_i'^T H_{ij}' \boldsymbol{S}_j'$ with $H_{ij}' = \mathcal{R}_i H_{ij} \mathcal{R}_j^T$. For a self-dual transformation, the matrices H_{ij}' are identical to H_{ij}, but the parameters $JKDC$ are replaced by $J'K'D'C'$, and the one-to-one correspondence between the bond directions and interactions remains intact. These two points in the parameter space are linked by the transformation and knowing the solution at one of the points, we may "rotate" it to the other one.

In this section we give an algorithm to find the self-dual transformations for the extended KH model that map it onto itself. We have found a single self-dual transformation $JKDC \leftrightarrow J'K'D'C'$ operating in full parameter space of the model; we will show it shortly below and return to it later when discussing experimental data.

However, studying the hidden symmetries of the model, we have identified a number of *restricted* self-dual transformations that operate only in some regions of the parameter space, where constants J,K,D,C are all finite but obey certain relations, or some of them are simply zero. Our primary interest is in the special class of such transformations of the type $J_0 \leftrightarrow JKDC$, which convert the Heisenberg model into the full $JKDC$ model and vice versa. These transformations, to be discussed in the next section, reveal points of hidden SU(2) symmetry; by inverting the transformation the anisotropic model with the parameters $JKDC$ can be exactly mapped back to the Heisenberg model with the exchange constant J_0.

A. Algorithm

A systematic search for the dual transformations seems to be an intricate task. Fortunately, it can be easily performed by computer on a finite cluster of the lattice using the following simple algorithm. We give it specifically for the case of a self-dual transformation:

(A) As a first step, we choose two rotation matrices $\mathcal{R}_i$, $\mathcal{R}_j$ on a selected bond $\langle ij\rangle$. They have to preserve the $JKDC$ form given by (1), which leaves us with only a few choices, each having only one free angular parameter.

(B) Next, we randomly choose nonzero values of the initial parameters $JKDC$ and use the relation $H_{ij}' = \mathcal{R}_i H_{ij} \mathcal{R}_j^T$ together with the C_3 symmetry to determine the new Hamiltonian matrices for the three bond directions.

(C) Knowing all the bond Hamiltonians, we may now determine further rotation matrices by utilizing relations of the type $\mathcal{R}_j = (H_{ij}')^{-1} \mathcal{R}_i H_{ij}$ and proceeding neighbor-by-neighbor. To fully determine the rotation matrices, about two thirds of the bonds need to be used.

(D) The bonds of the remaining third are used to check consistency; the Hamiltonian matrix determined by using the rotation matrices belonging to the bond has to be identical to that determined in step B. If the total difference on all the remaining bonds equals zero, we have just constructed a self-dual transformation. By scanning through the entire interval of the free parameter introduced in step A, we find all the self-dual transformations.

The above procedure may be easily adapted to find the dual transformations such as $J_0 \leftrightarrow JKDC$. In this case, in step A of the algorithm, we use the symmetry of the Heisenberg model and choose $\mathcal{R}_i$ as an identity matrix. The choice of the second matrix $\mathcal{R}_j$ is restricted by the requirement that $H_{ij}' = \mathcal{R}_i H_{ij} \mathcal{R}_j^T = J\mathcal{R}_j^T$ be of the $JKDC$ form.

By inspecting the rotation matrices of the cluster, we can identify the particular unit cell of the transformation. Note that even if our cluster is smaller than this unit cell, we do not miss the corresponding transformation, so that the method is completely systematic [60].

B. Self-duality of the extended Kitaev-Heisenberg model

The systematic procedure described above has identified only a single self-dual transformation $JKDC \leftrightarrow J'K'D'C'$. This is not surprising given the complexity of the model. The corresponding parameter transformation may be written in a matrix form

$$\begin{pmatrix} J' \\ K' \\ D' \\ C' \end{pmatrix} = \begin{pmatrix} 1 & +\frac{4}{9} & +\frac{4}{9} & +\frac{2\sqrt{2}}{9} \\ 0 & -\frac{1}{3} & -\frac{4}{3} & -\frac{2\sqrt{2}}{3} \\ 0 & -\frac{4}{9} & +\frac{5}{9} & -\frac{2\sqrt{2}}{9} \\ 0 & -\frac{2\sqrt{2}}{9} & -\frac{2\sqrt{2}}{9} & +\frac{7}{9} \end{pmatrix} \begin{pmatrix} J \\ K \\ D \\ C \end{pmatrix}. \tag{3}$$

For convenience, we also give the transformation of the parameters $JK\Gamma\Gamma'$ entering the Hamiltonian (2):

$$\begin{pmatrix} J \\ K \\ \Gamma \\ \Gamma' \end{pmatrix}' = \begin{pmatrix} 1 & +\frac{4}{9} & -\frac{4}{9} & +\frac{4}{9} \\ 0 & -\frac{1}{3} & +\frac{4}{3} & -\frac{4}{3} \\ 0 & +\frac{4}{9} & +\frac{5}{9} & +\frac{4}{9} \\ 0 & -\frac{2}{9} & +\frac{2}{9} & +\frac{7}{9} \end{pmatrix} \begin{pmatrix} J \\ K \\ \Gamma \\ \Gamma' \end{pmatrix}. \tag{4}$$

In terms of the spins, the transformation, labeled for future reference as $\mathcal{T}_1$, is simply a global π rotation about the Z axis defined in Fig. 1(a). The individual S^X, S^Y, and S^Z components transform according to

$$\mathcal{T}_1: \quad (X',Y',Z') = (-X,-Y,Z) \tag{5}$$

at every site. By applying the transformation twice, we get an identity and the matrices in (3) and (4) are thus self-inverse. Despite its apparent triviality, this transformation will play an essential role when discussing the real materials; see Sec. V below.

IV. POINTS OF HIDDEN SU(2) SYMMETRY

In this paragraph we find and characterize all the points of hidden SU(2) symmetry present in the extended KH model. At these special points in the parameter space, the anisotropic

TABLE I. Parameter values for the SU(2) points in units of the exchange constant J_0 of the hidden Heisenberg model.

	J/J_0	K/J_0	$(\Gamma \equiv -D)/J_0$	$(\Gamma' \equiv \frac{1}{\sqrt{2}}C)/J_0$
$\mathcal{T}_2$	$-1/3$	0	$2/3$	$2/3$
$\mathcal{T}_4$	-1	2	0	0
$\mathcal{T}_6$	0	-1	-1	0
$\mathcal{T}_1\mathcal{T}_4$	$-1/9$	$-2/3$	$8/9$	$-4/9$
$\mathcal{T}_2\mathcal{T}_6$	$-2/3$	1	$1/3$	$-2/3$

model can be mapped back to a Heisenberg ferromagnet or antiferromagnet. The SU(2) points of the original KH model have been identified [11] by virtue of the four-sublattice transformation introduced in Ref. [6]. The corresponding ordering patterns on the honeycomb lattice are of stripy and zigzag type. A similar symmetry analysis of the KH model was performed for other relevant lattices [47].

The extended KH model of course inherits the SU(2) points of the KH model and contains several new ones in addition. They are identified by dual transformations of the type $J_0 \leftrightarrow JKDC$ which is less general than $JKDC \leftrightarrow J'K'D'C'$. Because of this, we obtain a relatively rich set of dual transformations characterized by two-, four-, and six-sublattice structure of the rotations. In terms of parameters, all the nontrivial SU(2) points are listed in Table I. We now proceed with the detailed description of the corresponding transformations.

A. Summary of the SU(2) points and the corresponding rotations on the sublattices

We first give a summary of the transformations as represented by rotations in the real space. Each of them generates an infinite number of orderings, since the ordered moment direction in the underlying Heisenberg model can be chosen arbitrarily. Figure 2 shows a few important examples.

The simplest transformation $\mathcal{T}_2$ is π rotation about the Z axis at one of the two sublattices of the honeycomb lattice:

$$\begin{aligned} \mathcal{T}_2: \quad & (X',Y',Z') = (X,Y,Z) \quad \text{(sublattice A)}, \\ & (X',Y',Z') = (-X,-Y,Z) \quad \text{(sublattice B)}. \end{aligned} \tag{6}$$

Its physical relevance is small due to the dominance of $\Gamma'(\equiv \frac{1}{\sqrt{2}}C)$ and the complete absence of K (corresponding to the case of strong trigonal field splitting, as explained above). As a curiosity, if we choose the spins to lie in the honeycomb plane, $\mathcal{T}_2$ converts the FM pattern to AF and vice versa. We may thus have an AF/FM ordered pattern, but the hidden nature revealing itself, e.g., in the spin dynamics is that of Heisenberg FM/AF, respectively.

The next transformation $\mathcal{T}_4$ has a four-sublattice structure depicted in Fig. 2(a) with π rotations about cubic x, y, and z axes applied at sublattices 1, 2, and 3, respectively, and no rotation involved at sublattice 4. Written explicitly:

$$\begin{aligned} \mathcal{T}_4: \quad & (x',y',z') = (x,-y,-z) \quad \text{(sublattice 1)}, \\ & (x',y',z') = (-x,y,-z) \quad \text{(sublattice 2)}, \\ & (x',y',z') = (-x,-y,z) \quad \text{(sublattice 3)}, \\ & (x',y',z') = (x,y,z) \quad \text{(sublattice 4)}. \end{aligned} \tag{7}$$

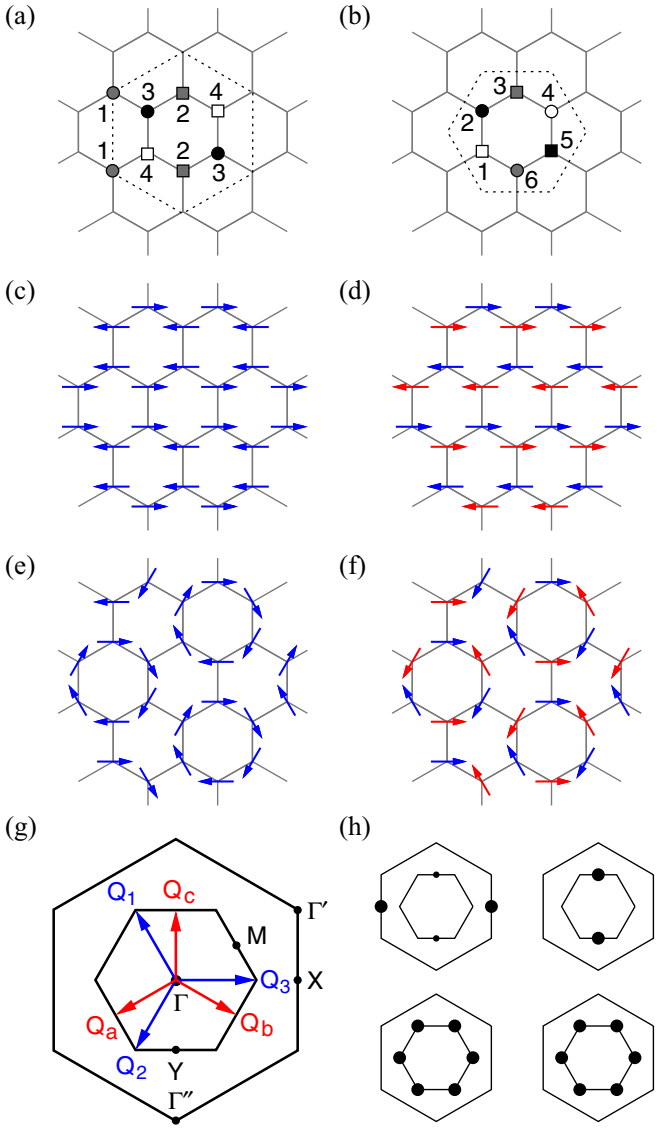

FIG. 2. (Color online) (a), (b) Unit cells for the four- and six-sublattice transformations. (c), (d) Stripy and zigzag patterns related to the FM and AF order of a hidden Heisenberg magnet via the four-sublattice transformation $\mathcal{T}_4$. The spins take the z-axis direction. (e), (f) "Vortex"-like patterns generated by the six-sublattice transformation $\mathcal{T}_6$. The spins are lying in the lattice plane in the case presented. The colors of the arrows in panels (d) and (f) indicate the sublattices of the hidden AF order. (g) Brillouin zones of the honeycomb (inner hexagon) and the completed triangular lattice (outer hexagon). The characteristic vectors $\boldsymbol{Q}_{a,b,c}$ of the four-sublattice transformation and $\boldsymbol{Q}_{1,2,3}$ of the six-sublattice transformation are shown in red and blue, respectively. (h) Bragg spots of the patterns in panels (c)–(f). The dot size is proportional to $|S_{\boldsymbol{Q}}|$.

This transformation, introduced earlier in Ref. [6], is a self-dual transformation of the original two-parameter KH model and has been already heavily used in this context. Applying the transformation to an ordered Heisenberg FM/AF with the moments pointing along the z axis, we get the stripy/zigzag order shown in Figs. 2(c) and 2(d).

Perhaps the most surprising SU(2) point of the model is linked to the six-sublattice transformation $\mathcal{T}_6$. Its rotations are

most conveniently described in the cubic coordinates. On the lattice sites 1, 3, and 5 [see Fig. 2(b)] they correspond to cyclic permutations among the spin components. On the lattice sites 2, 4, and 6 the rotations correspond to anticyclic permutations which have to be followed by a spin inversion. Altogether the transformation can be written as

$$\begin{aligned}
\mathcal{T}_6: \quad & (x',y',z') = (x,y,z) && \text{(sublattice 1)},\\
& (x',y',z') = (-y,-x,-z) && \text{(sublattice 2)},\\
& (x',y',z') = (y,z,x) && \text{(sublattice 3)},\\
& (x',y',z') = (-x,-z,-y) && \text{(sublattice 4)},\\
& (x',y',z') = (z,x,y) && \text{(sublattice 5)},\\
& (x',y',z') = (-z,-y,-x) && \text{(sublattice 6)}. \qquad (8)
\end{aligned}$$

It is easy to see that for $K = \Gamma(\equiv -D)$ and $J = \Gamma' = 0$, these rotations lead to the isotropic Heisenberg Hamiltonian. As an example, we consider the c bond $1-2$ of Fig. 2(b). By exchanging x and y at site 2, the nondiagonal Γ term in (2) becomes diagonal and the inversion ensures its proper sign. Sample patterns generated by $\mathcal{T}_6$ and showing a "vortex"-like structure are presented in Figs. 2(e) and 2(f). The peculiarity of the SU(2) points is now best demonstrated: the Hamiltonian is completely anisotropic containing K and $\Gamma(\equiv -D)$ terms only, the ordered spins form a very unusual pattern, yet the hidden nature of the system is exactly that of the Heisenberg FM or AF, including, e.g., the presence of gapless Goldstone modes.

Apart from revealing a hidden SU(2) point of the present model, the $\mathcal{T}_6$ transformation has a remarkable property that deserves special attention. Namely, applying $\mathcal{T}_6$ to the Kitaev Hamiltonian, we notice that it redistributes three types of Ising-interactions on a honeycomb lattice such that at each hexagon a Kekulé-type pattern is formed [61]. We thus arrive at the so-called Kekulé-Kitaev model [62]. In other words, the Kitaev and Kekulé-Kitaev models are exact dual partners linked via the $\mathcal{T}_6$ transformation. This observation should be helpful in studying both models, in particular of their extended versions including a Heisenberg term [62,63].

Two more transformations providing SU(2) points are obtained as the combinations $\mathcal{T}_1\mathcal{T}_4$ and $\mathcal{T}_2\mathcal{T}_6$. They share the sublattice structure with $\mathcal{T}_4$ and $\mathcal{T}_6$, respectively. Adopting the extended KH model, the former one is probably the SU(2) point closest to the real situation in Na_2IrO_3 as will be discussed in Sec. V.

B. Implications for the phase diagram

After examining the nature of the individual SU(2) points, we want to visualize now their positions in the parameter space, get a sketch of the phase diagram, and infer the relations between the individual phases. The result can be compared with the published phase diagrams of Refs. [37] and [38], obtained by classical analysis and partly complemented by exact diagonalization. For this reason, we adopt the representation of the parameter space introduced in Ref. [37]. The overall energy scale irrelevant for the phase diagram is removed and J, K, Γ are parametrized using "spherical" angles θ and ϕ via $J = \sin\theta\cos\phi$, $K = \sin\theta\sin\phi$, and $\Gamma = -D = \pm\cos\theta$,

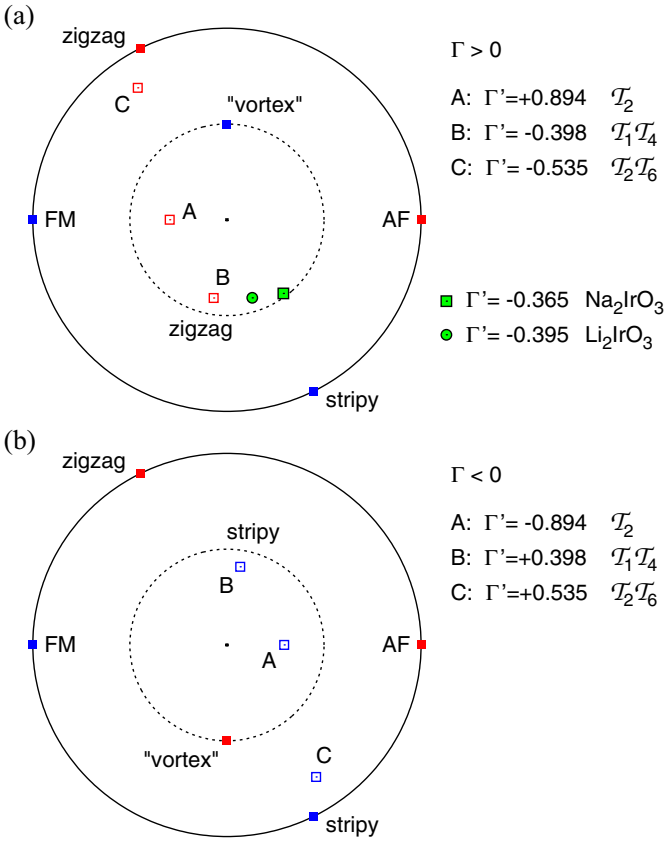

FIG. 3. (Color online) (a) Depiction of the SU(2) points using the parametrization of Ref. [37], $J = \sin\theta\cos\phi$, $K = \sin\theta\sin\phi$, $\Gamma = \cos\theta$. The distance from the center of the circle corresponds to θ going from 0 (center) through $\pi/4$ (dashed circle) to $\pi/2$ (solid circle). The polar angle is ϕ. Filled squares show the SU(2) points with $\Gamma' = 0$, open squares those with nonzero Γ' values given on the right along with the transformation label. The color of the points indicates their hidden FM (blue) or AF (red) nature. The green square (circle) shows the parameter values specified in Sec. V when discussing Na_2IrO_3 (Li_2IrO_3). (b) The same as in panel (a) but with $\Gamma = -\cos\theta$.

keeping $\Gamma'(\equiv \frac{1}{\sqrt{2}}C)$ as a separate parameter of the phase portrait.

Shown in Fig. 3 is the complete set of SU(2) points of the extended KH model. The outer rings correspond to the original KH model and contain the trivial SU(2) points and the two well-known $\mathcal{T}_4$ hidden SU(2) points of the KH model characterized by a stripy and zigzag pattern. Still within the $JK\Gamma$ plane is the "vortex" $\mathcal{T}_6$ point associated with a "vortex"-like pattern. The corresponding phases determined by these SU(2) points can be observed in Figs. 2 and 3 of Ref. [37], with the $\mathcal{T}_6$ point lying in their 120° phase.

Three more SU(2) points A, B, and C characterized by a nonzero value of Γ' are shown as projected onto the $JK\Gamma$ plane. For the $\Gamma > 0$ case presented in Fig. 3(a), they are of AF character; one of them appears for positive (point A) and two for negative (points B and C) values of Γ'. The point A (given by $\mathcal{T}_2$) of hidden AF nature can possess FM pattern as discussed in the previous paragraph. The region between the true FM Heisenberg point and the point A in the phase diagram obtained classically is therefore filled by the

FM phase extending as Γ' increases (see panels (c) and (e) of Fig. 2 of Ref. [38]). However, the (hidden) nature of this phase changes from FM to AF which should manifest itself, e.g., on the character of the magnon dispersion. Similarly, the presence of the points B ($\mathcal{T}_1\mathcal{T}_4$) and C ($\mathcal{T}_2\mathcal{T}_6$) of zigzag and "vortex" character, respectively, explains the enlarged region of the corresponding phases in the classical phase diagram for $\Gamma' < 0$ (see panels (a) and (d) of Fig. 2 of Ref. [38]). We also observe an intimate relation between the zigzag phase emanating from the B ($\mathcal{T}_1\mathcal{T}_4$) point and that connected to the zigzag SU(2) point of the original KH model (given by $\mathcal{T}_4$). Due to the additional $\mathcal{T}_1$ rotation, their ordered moment directions are related by π rotation about the global Z axis. This point will be further discussed in Sec. V. Finally, similar conclusion as for the $\Gamma > 0$ case presented in Fig. 3(a) can be drawn for the $\Gamma < 0$ case shown in Fig. 3(b). The SU(2) points are related by inversion with respect to the center of the circle and the opposite FM/AF nature.

In summary, we have illustrated that the gross features of the phase diagram of the extended, four-parameter KH model can be deduced solely by inspecting the nature of the points of hidden SU(2) symmetry and their location in the parameter space.

C. Spin excitation spectra

We proceed further by inspecting the spin excitation spectra at the SU(2) points associated with $\mathcal{T}_4$ and $\mathcal{T}_6$ transformations, and see how they are related to those of the simple Heisenberg model. To this end, the dual transformations have to be expressed in Fourier space and relations between the Fourier components $\boldsymbol{S}_{\boldsymbol{q}}$ of the dual partners have to be established. The situation is somewhat complicated by the two-sublattice structure of the honeycomb lattice, requiring us to introduce an additional index [see the labels A and B in Fig. 1(a) for the convention used below].

In both cases, it is convenient to use the cubic axes xyz. The four-sublattice transformation has three characteristic vectors $\boldsymbol{Q}_{a/b} = (\mp\pi/\sqrt{3}, -\pi/3)$ and $\boldsymbol{Q}_c = (0, 2\pi/3)$ touching the Brillouin zone boundary in the middle of its edges [see Fig. 2(g)]. The rotation matrices have a simple diagonal form, reflecting only the sign changes of the respective components

$$\mathcal{R}_{A/B} = \mathrm{diag}\,(\pm e^{i\boldsymbol{Q}_a\cdot\boldsymbol{R}}, \pm e^{i\boldsymbol{Q}_b\cdot\boldsymbol{R}}, e^{i\boldsymbol{Q}_c\cdot\boldsymbol{R}}). \tag{9}$$

The six-sublattice transformation written in Fourier representation has a full matrix structure

$$\mathcal{R}_{A/B} = \pm\tfrac{1}{3}(I + M_{A/B}\gamma + M^*_{A/B}\gamma^*) \tag{10}$$

with the factor $\gamma = \frac{1}{3}(e^{i\boldsymbol{Q}_1\cdot\boldsymbol{R}} + e^{i\boldsymbol{Q}_2\cdot\boldsymbol{R}} + e^{i\boldsymbol{Q}_3\cdot\boldsymbol{R}})$ and the matrices

$$I = \begin{pmatrix} 1 & 1 & 1 \\ 1 & 1 & 1 \\ 1 & 1 & 1 \end{pmatrix}, \quad M_A = \begin{pmatrix} 1 & c^* & c \\ c & 1 & c^* \\ c^* & c & 1 \end{pmatrix},$$
$$M_B = \begin{pmatrix} c & 1 & c^* \\ 1 & c^* & c \\ c^* & c & 1 \end{pmatrix}, \tag{11}$$

where $c = e^{2\pi i/3}$. The characteristic vectors $\boldsymbol{Q}_{1,2} = (-2\pi/3\sqrt{3}, \pm 2\pi/3)$ and $\boldsymbol{Q}_3 = (4\pi/3\sqrt{3}, 0)$ shown in Fig. 2(g) again touch the boundary of the Brillouin zone, now in its corners. The dual transformation takes a general form $\boldsymbol{S}'_{A\boldsymbol{R}} = \sum_{\boldsymbol{Q}} e^{i\boldsymbol{Q}\cdot\boldsymbol{R}}\mathcal{R}_{A\boldsymbol{Q}}\boldsymbol{S}_{A\boldsymbol{R}}$ (here for sublattice A) which translates into

$$\boldsymbol{S}'_{A\boldsymbol{q}} = \sum_{\boldsymbol{Q}} \mathcal{R}_{A\boldsymbol{Q}}\boldsymbol{S}_{A,\boldsymbol{q}-\boldsymbol{Q}}; \tag{12}$$

i.e., the Fourier components get shifted by the characteristic vectors. As a side result, the above relation gives the Bragg spots derived from the Bragg spots of Heisenberg FM/AF ($\boldsymbol{S}_{A,\boldsymbol{q}=0} = \pm\boldsymbol{S}_{B,\boldsymbol{q}=0} = 1$) and presented in Fig. 2(h).

To study the spin excitations, we employ the spin susceptibility tensor defined as

$$\chi_{\alpha\beta}(\boldsymbol{q},\omega) = i\int_0^\infty \langle[S^\alpha_{\boldsymbol{q}}(t), S^\beta_{-\boldsymbol{q}}(0)]\rangle\, e^{i(\omega+i\delta)t}\, dt. \tag{13}$$

It is evaluated at the SU(2) points by first decomposing $S_{\boldsymbol{q}}$ into the A- and B-sublattice contributions via

$$\boldsymbol{S}_{\boldsymbol{q}} = \frac{1}{\sqrt{2}}\, e^{i\sqrt{3}q_x/2}(e^{iq_y/2}\boldsymbol{S}_{A\boldsymbol{q}} + e^{-iq_y/2}\boldsymbol{S}_{B\boldsymbol{q}}), \tag{14}$$

applying the dual transformation in the Fourier form of Eq. (12) to get back to the underlying Heisenberg model, and using the spin susceptibility for the Heisenberg model obtained within linear-spin-wave (LSW) approximation. In the case of $\mathcal{T}_4$, this brings simple $\boldsymbol{q}$ shifts by $\boldsymbol{Q}_a$, $\boldsymbol{Q}_b$, and $\boldsymbol{Q}_c$ for the individual components. For $\mathcal{T}_6$, the corresponding expressions are somewhat more involved containing a nonshifted contribution and shifted contributions combining pairs of the characteristic vectors $\boldsymbol{Q}_1$, $\boldsymbol{Q}_2$, and $\boldsymbol{Q}_3$. Without going into details, the presence of both shifted and nonshifted parts can be easily understood based on Eq. (10).

Presented in Fig. 4 are the traces of the spin susceptibility tensor of the Heisenberg model and the extended KH model at the two hidden SU(2) points under consideration. For completeness, we demonstrate both hidden FM and AF cases characterized by quadratic and linearly dispersing Goldstone modes, respectively. The situation is more transparent for the four-sublattice patterns—stripy (hidden FM) and zigzag (hidden AF)—since the spin wave dispersions are just shifted with the $\boldsymbol{q} = M$ points replacing the Goldstone points Γ and Γ' of the Heisenberg case. In our example, we have chosen the z axis as the ordered moment direction. For the magnons, which are in fact deviations of the ordered moment in x and y directions, only $\boldsymbol{Q}_a$ and $\boldsymbol{Q}_b$ shifts are active, selecting four out of the six M points in total. The remaining two are the Bragg spots reached from Γ and Γ' by $\boldsymbol{Q}_c$ shifts active for the ordered z spin component. The Bragg spots and the Goldstone points are thus complementary in this case. The spin excitations associated with the six-sublattice patterns are significantly more complicated. They contain both shifted Goldstone modes [in Fig. 4(c) such a mode appears at $\boldsymbol{q} = K$ point coinciding with $\boldsymbol{Q}_3$] and Goldstone modes at the characteristic momenta $\boldsymbol{q} = \Gamma$ and $\boldsymbol{q} = \Gamma'$ of the underlying Heisenberg model. In the latter case just the intensity of the modes has been transferred by the dual transformation, making, e.g., the linear Goldstone mode at $\boldsymbol{q} = \Gamma$ the most intense one in the hidden AF case.

A similar analysis of the spin excitations as presented here for $\mathcal{T}_4$ and $\mathcal{T}_6$ SU(2) points can be performed for the remaining SU(2) points. Due to the nature of the relevant transformations,

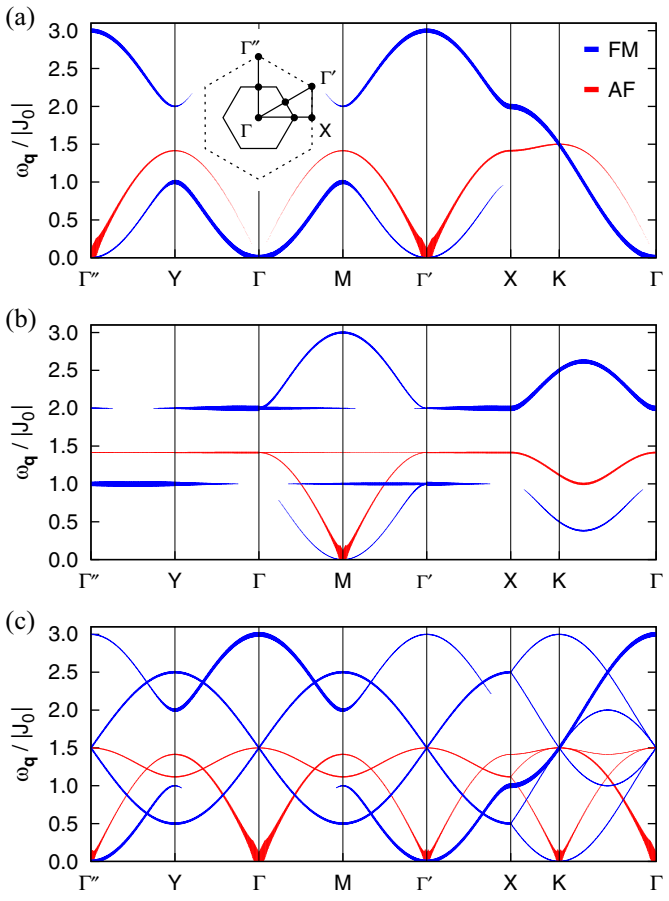

FIG. 4. (Color online) (a) LSW dispersion of the Heisenberg FM (blue) and AF (red) on the honeycomb lattice. The width of the lines indicates the trace of the spin susceptibility tensor, $\sum_\alpha \chi''_{\alpha\alpha}(\boldsymbol{q},\omega)$, calculated in the LSW approximation. (b) The same for the stripy and zigzag state presented in Figs. 2(c) and 2(d). Energy is scaled by J_0 of the hidden Heisenberg magnet. (c) The same for the "vortex"-like patterns presented in Figs. 2(e) and 2(f).

no other characteristic vectors appear. Therefore, $\boldsymbol{q} = \Gamma$, $\boldsymbol{q} = \Gamma'$ and their counterparts shifted by the vectors $\boldsymbol{Q}_{a,b,c}$ and $\boldsymbol{Q}_{1,2,3}$ entering the transformations $\mathcal{T}_4$ and $\mathcal{T}_6$ constitute the entire set of the wave vectors of the Goldstone modes that can be observed within the extended KH model.

V. APPLICATION TO THE REAL MATERIALS

The aim of this work was to study the basic symmetry properties of the extended KH model—a promising spin Hamiltonian for the magnetism of honeycomb iridates. Below we illustrate how this knowledge, taken together with the experimental data, helps to locate the plausible windows in otherwise very large parameter space even for this nearest-neighbor (NN) model. We will show that, despite having only a single result, the search for full self-dual transformations $JKDC \leftrightarrow J'K'D'C'$ of the extended KH model provides us with a surprisingly useful tool in the context of Na_2IrO_3. This utility of $\mathcal{T}_1$ emerges due to the recent observation of the magnetic moment direction [46] which, as we see shortly, imposes an important constraint on the model parameters. This is because, in general, the data on magnetic easy axes in a crystal, along with the magnon gaps and torque magnetometry data, provide direct information on the symmetry and strength of the anisotropy terms in spin Hamiltonians, and the case of Na_2IrO_3 is of course not at all special in this sense.

To begin with, we recall that Na_2IrO_3 shows so-called zigzag order, where the spins on a and b bonds are parallel and form ferromagnetic chains that run along the X direction and couple antiferromagnetically along the Y axis. This relatively simple collinear magnetic structure has been first explained [28,30] as due to 2nd-NN J_2 and 3rd-NN J_3 Heisenberg couplings (which are often relevant in compounds with 90°-bonding geometry; a well-known example is quasi-one-dimensional cuprates). This model emphasizes a geometrical frustration which is realized at large values of $J_{2,3}$ and resolved by the C_3 symmetry breaking zigzag formation.

However, as argued in the Introduction, more recent data [45,46] suggest that the origin of frustrations is largely related to the non-Heisenberg-type interactions which are bond-dependent and hence highly frustrated even on the level of NN models. A minimal NN model of this sort is the KH model, which has been shown [32] to host zigzag order in its phase diagram indeed. We follow this way of reasoning and explore below the extended version of the KH model as the basic NN model for iridates. On the way, we will also see the point where the data may require the presence of additional terms $J_{2,3}$ too, suggesting that the both "zigzag theories" above are the part of a full story.

In Ref. [32], the available experimental data on Na_2IrO_3 have been fitted using the two-parameter KH model, regarding it as a phenomenological spin Hamiltonian with arbitrary parameters. For $K = 21$ meV and $J = -4$ meV, the model was found consistent with experiments in terms of the type of magnetic ordering, the temperature dependence of static magnetic susceptibility, and the low-energy spin-excitation spectrum being compared to powder INS. Later, RIXS experiments [45,46] confirmed the presence of a high-energy branch of spin excitations, with an even better agreement obtained if the LSW calculation of Ref. [32] is replaced by a more suitable exact diagonalization [65].

However, the recent data [46] on the moment direction came about as an unexpected surprise, challenging at first glance the above coherent description of Na_2IrO_3. The point is that within the original two-parameter KH model, the zigzag order is characterized by the spins pointing towards one of the oxygen ions [see Fig. 1(a)]. This expectation is generic and guaranteed by the "order-from-disorder" physics [66] which typically selects one of the high-symmetry cubic axes as the easy one, when a spin Hamiltonian contains the compass-type or Kitaev-type bond-dependent anisotropy [11,16,40,67], independently of parameter values. The resonant magnetic x-ray diffraction data [46] show instead that the magnetic easy axis is in fact far away from any of the Ir-O bond directions: it is oriented "nowhere" slightly below a midpoint between the two, x and y, oxygen ions in Figs. 1(a) and 5(a). This is a clear indication of the significance of the D and C terms in the spin Hamiltonian [68].

To reconcile all the data at hand using now the full four-parameter model, we first notice that the above two easy axis directions—the one observed in Na_2IrO_3 and the one expected from the KH model as used in Ref. [32]—are roughly

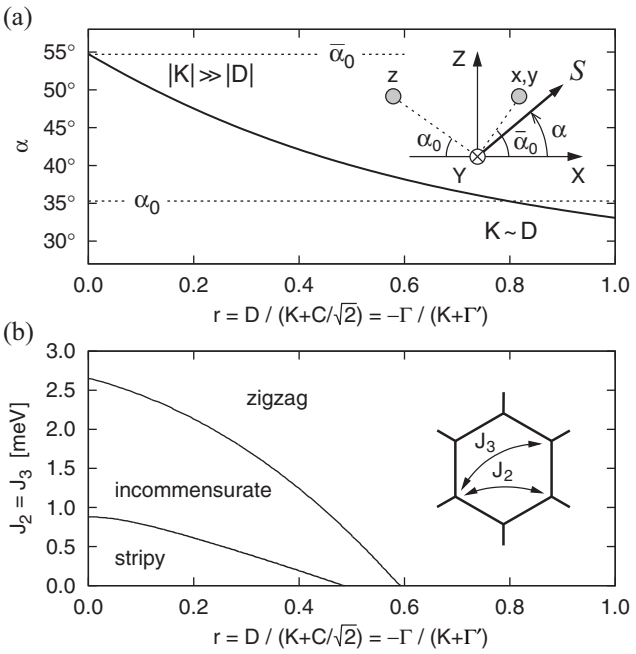

FIG. 5. (a) Pseudospin angle α relative to the XY plane (see inset) as a function of the parameter $r = D/(K + C/\sqrt{2}) = -\Gamma/(K + \Gamma')$. Dashed lines show the "magic" angle $\alpha_0 \simeq 35^\circ$ and its complement $\bar{\alpha}_0 \simeq 55^\circ$, determined by the z axis and xy plane, respectively, as sketched in the inset. (b) The phase diagram as a function of long-range couplings $J_2 = J_3$ and anisotropy parameter r. Starting with the "bare," $\mathcal{T}_1$-derived values of $J = 5.3$ meV, $K = -7.0$ meV, $D = -9.3$ meV, and $C = -6.6$ meV, we have scaled D and C simultaneously to vary r. To stay within the zigzag phase at the smaller values of $r \lesssim 0.59$, one needs to have finite $J_{2,3}$ couplings. Otherwise, the NN-only extended KH model with negative $K < 0$ switches to the incommensurate and "stripy" [11,32,69] ground states. The inset shows the exchange bonds J_2 and J_3.

related to each other simply by a π rotation about the Z axis. This observation gives an immediate hint of how to obtain a starting parameter point when fitting the current data set for Na_2IrO_3 within the extended, four-parameter KH model in an appealingly easy way, and resolve the above apparent problem with the moment direction.

As discussed in Sec. IV B, the $\mathcal{T}_4$-associated zigzag phase of the KH model with $K > 0$ is related to the zigzag phase connected to the SU(2) point B ($\mathcal{T}_1\mathcal{T}_4$) of Fig. 3(a) via $\mathcal{T}_1$. Remarkably, due to the nature of $\mathcal{T}_1$—a global π rotation of the magnetic moments about the Z axis—all the aforementioned consistent results [32] of the two-parameter KH model are fully preserved if we apply Eq. (3) to the parameters K and J of Ref. [32] given above; the only change is the spin easy axis being rotated to the proper direction as in experiment. The corresponding set of parameters obtained via (3) is $J = 5.3$ meV, $K = -7.0$ meV, $D \equiv -\Gamma = -9.3$ meV, $C \equiv \sqrt{2}\Gamma' = -6.6$ meV. We would like to emphasize that these numbers should not be taken literally; rather, they fix the signs of the parameters involved and put an upper limit for D and C, as we explain below.

For the representative parameters given above, the pseudospin makes a "magic" angle of $\alpha_0 \simeq 35^\circ$ from the XY plane, as follows from $\mathcal{T}_1$ construction. This is slightly lower than observed [46,70]. Now, we inspect how the angle α varies as a function of the anisotropy parameters. The result is illustrated in Fig. 5(a) and shows that the exact value of α heavily influences the "departure" from the KH model quantified by the parameter $r = D/(K + C/\sqrt{2}) = -\Gamma/(K + \Gamma')$. [The corresponding Eqs. (B13), (B14), and (B16) for the spin direction are derived in the Appendix B by minimizing the classical energy]. The "magic" angle $\alpha = \alpha_0$ appears at $r = 0.8$ – as obtained for the above parameters. Yet, as observed in Fig. 5(a), by increasing α for example by 10° only, we already find $r \simeq 0.3$ and get closer to the $|K| \gg |D|$ regime. Therefore, more detailed measurements and fits of the ordered spin direction are highly desirable to get the actual values of the parameters D and C relative to the Kitaev term K. Doing so, it is crucial to take into account the fact that the pseudospin direction and magnetic moment direction are not the same in general; while they coincide in the cubic limit, a sizable trigonal-field splitting might be present in Na_2IrO_3 [45,59]. It is thus important to quantify this splitting by independent measurements.

At this point, longer-range couplings $J_{2,3}$ become a part of the full spin model for iridates, for the following reason. As a $\mathcal{T}_1$ partner of the zigzag phase of Ref. [32], the present NN-model with large D is well in its zigzag ordered state. But this is not so at smaller values of D (e.g., for $r \sim 0.5$), which are required to get the spin angles $\alpha \sim 40^\circ$ or above; see Fig. 5(a). Incorporating moderate J_2 and J_3 couplings into the model, we can however stabilize the zigzag phase, see Fig. 5(b), and hence obtain the ordered spin angles above the "magic" one. The values of $J_{2,3}$ of the order of 1–2 meV are indeed suggested by *ab initio* calculations [39]. This shows again the key importance of the experimental data on moment directions for quantifying the balance between the two zigzag-supporting mechanisms discussed above: based on $J_{2,3}$ geometrical frustration, and on frustration driven by the non-Heisenberg nature of interactions in spin-orbit coupled magnets. Recent observations [46] of a pronounced spin-space anisotropy on one hand, and an "intermediate" spin direction that requires finite $J_{2,3}$ values on the other hand, suggest that both mechanisms are at play in Na_2IrO_3.

Altogether, the present analysis using the symmetry properties of the model, taking into account the recent data on moment direction [46], as well as considering the role of the $J_{2,3}$ couplings, suggests a plausible window in the parameter space of an effective spin model for Na_2IrO_3: $J_{2,3} < J \sim |C| < |D| < |K|$, with positive (AF) Heisenberg couplings $J_{2,3}$ and J. The leading anisotropy terms $K < 0$ and $D < 0$ are both negative, while a smaller term C may in principle take any sign. This parameter window is globally consistent with experimental observations on Na_2IrO_3 we are aware of to date, and may be used as a guide in future analysis, in particular once $\boldsymbol{q}$-resolved spin response becomes available, and the ordered pseudospin and magnetic moment directions (they differ in general) are obtained and confirmed by independent measurements.

Even though this general result still leaves quite a freedom, it is of great help by fixing the signs of most relevant couplings and their hierarchy. This is the main outcome of the present theory in the context of real materials. Further, we note that the Kitaev coupling K can be deduced from overall magnetic

energy scale, and the spin and magnetic moment directions should determine the parameter r hence D. From a careful analysis of the zigzag stability condition, magnon gaps and dispersions, paramagnetic susceptibility data, etc., one should be able to quantify all the model parameters including C, J, and $J_{2,3}$.

Considering this result in the context of microscopic theories, we notice first that the signs of $J > 0$ and $K < 0$ above are consistent with the original calculations of these parameters for honeycomb iridates [9,11] as well as with the later studies [36–40]. Next, we may conclude that a contribution from t_{2g}-e_g hopping that favors pseudospin interaction with $K > 0$ [6] is not significant in iridates; this is also consistent with the recent calculations [36,73]. Further, the present symmetry analysis resolves an apparent conflict with the theoretical $K < 0$ [9,11] and the positive $K > 0$ that follows from the best data fit using the KH model [32]: in fact, the pure KH model with $K > 0$ and the extended one with $K < 0$ and sizable D,C terms are $\mathcal{T}_1$-dual partners (the latter one being physical).

More surprisingly, a relatively large D ($\equiv -\Gamma$) anisotropy term is required to "turn" the moment direction well away from the pure KH model position. A positive implication of this observation is that this term makes it much easier to stabilize the zigzag order (the pure KH model with large $K < 0$ would require large long-range $J_{2,3}$ couplings otherwise). In a view of the discussion in Sec. II, this suggests a presence of sizable trigonal field effects in Na_2IrO_3. Eventually, an unusual—out of any crystal symmetry axis—orientation of pseudospins [46] should originate from a competition among the several anisotropy terms K, D, and C of different symmetry and physical origin.

To conclude our discussion of Na_2IrO_3: it seems that the extended KH model, likely further "extended" by moderate longer-range couplings, is indeed a good candidate model for this compound. Even though these extensions (to be still quantified by future experiments) reduce the chances for "pure" Kitaev-model physics in iridates, the model itself is highly interesting due to its rich internal structure and hidden symmetries that we have uncovered in this work.

Motivated by the above, we further consider the case of Li_2IrO_3. Since the data are limited here, the discussion will be brief and suggestive only. Due to the smaller Curie-Weiss temperature and more "ferromagnetic" behavior of its spin susceptibility [74,75], this compound was located closer to the SU(2) point of the KH model [32]. Even though the parameters $K = 15.8$ meV and $J = -5.3$ meV given in Ref. [32] correspond to the zigzag phase while Li_2IrO_3 shows a spiral magnetic ordering [29], these parameters can be used to get a hint of the direction in the parameter space to consider. We therefore transform the above parameters using (3) to obtain $J = 1.7$ meV, $K = -5.3$ meV, $D \equiv -\Gamma = -7.0$ meV, $C \equiv \sqrt{2}\Gamma' = -5.0$ meV. Representing the parameters for Na and Li compounds obtained via the $\mathcal{T}_1$ transformation (3) in Fig. 3, we see that both are close to the SU(2) point B ($\mathcal{T}_1\mathcal{T}_4$), with Li being closer, as expected. To approach the spiral state observed in Li_2IrO_3, we first note that, in first approximation, $K \sim D < 0$ in both cases and that Li compound is characterized by a much smaller J. For simplicity, we set $J = 0$ meV, assume $K = D = -10$ meV to roughly preserve the overall energy scale, and reduce the parameter C associated with the trigonal

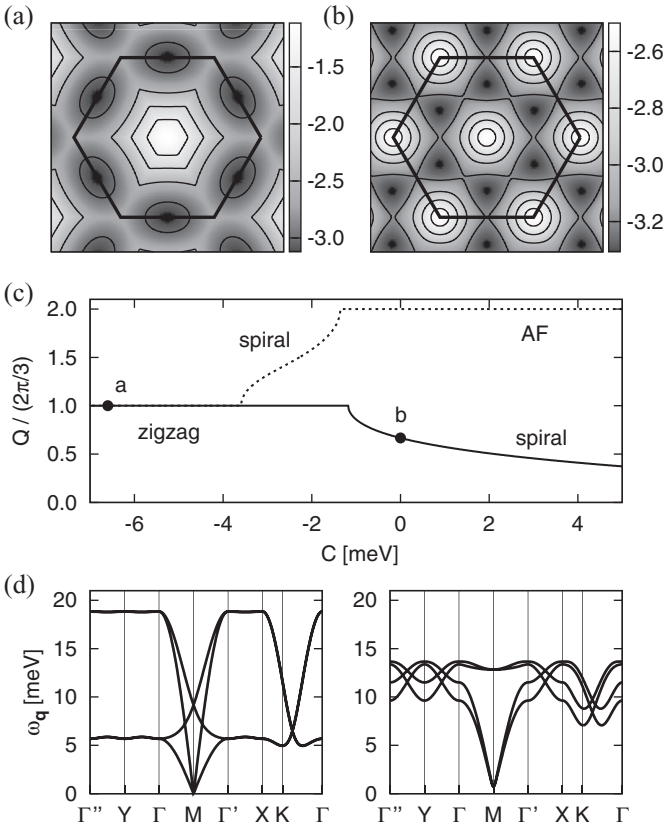

FIG. 6. (a) Map of the $\boldsymbol{q}$-dependent classical energy (per site, in units of meV) obtained by Luttinger-Tisza method [71,72] for the "bare," i.e., $\mathcal{T}_1$-derived parameters $J = 5.3$ meV, $K = -7.0$ meV, $D = -9.3$ meV, $C = -6.6$ meV relevant for Na_2IrO_3. The hexagon indicates the first Brillouin zone. (b) The same for the parameters $K = D = -10$ meV, $J = C = 0$ relevant to Li_2IrO_3. (c) Length of the ordering vector for varying C, keeping the other parameter values unchanged. The dashed (solid) line was calculated using the above parameters JKD relevant to Na_2IrO_3 (Li_2IrO_3). Points a and b show the C values used in panels (a) and (b), respectively. (d) LSW dispersions for the parameters used in panel (a) (left) and panel (b) (right). In the latter case, we have taken $C \simeq -1.2$ meV instead of $C = 0$ meV to stay in the zigzag phase at the border to the spiral phase.

distortion, which is expected to be much smaller in Li_2IrO_3 with the bond angles being closer to 90°. The Luttinger-Tisza [71,72] maps of the classical energy for the Na and Li case presented in Figs. 6(a) and 6(b) confirm the zigzag and incommensurate magnetic ordering, respectively. For $C = 0$ the incommensurate ordering wave vector is obtained as $\boldsymbol{Q} \simeq \frac{2}{3}\boldsymbol{Q}_c$ [see Figs. 6(b) and 6(c)]; this would predict a magnetic Bragg peak in powder neutron diffraction experiments at a $|\boldsymbol{Q}|$ value that could be consistent with experiments on powder Li_2IrO_3 [29]. Finally, Fig. 6(d) compares the spin excitations obtained using the LSW approximation. In the case of Na_2IrO_3, the dispersion is identical to that presented in Fig. 3 of Ref. [32], possessing low- and high-energy branches. As the parameter J is reduced, these two branches gradually merge, leading to a steeper dispersion compared to Na_2IrO_3, which might be consistent with powder inelastic neutron scattering experiments on powder Li_2IrO_3 [29]. The predicted dispersion

is illustrated in Fig. 6(d) for a point on the boundary between the zigzag and the spiral phase. A further minor reduction of C to enter the spiral phase and get the proper ordering vector should not affect this result dramatically, apart from the changes at low energies forming an "hour-glass" shape characteristic of spiral magnets (see, e.g., Ref. [76]).

VI. CONCLUSIONS

To summarize, we have analyzed nontrivial symmetries of the extended Kitaev-Heisenberg model on the honeycomb lattice. As a main result, we have identified the complete set of points in the parameter space where this bond-anisotropic model can be transformed to a simple Heisenberg model and is therefore characterized by hidden SU(2) symmetry. Such a dual transformation can be performed using a particular choice of sublattice rotations of the spins, specific for each of the SU(2) points. The sublattice structure of the transformations creates a number of ordering patterns which together with the location of the hidden SU(2) points in the parameter space give a good overview of the global phase diagram of the model. In terms of the spin excitations, the hidden SU(2) symmetry manifests itself by the presence of Goldstone modes inherited from the SU(2) symmetric Heisenberg FM/AF on the honeycomb lattice. Their characteristic vectors and even the full spin excitation spectra are easily obtained by an explicit transformation of the FM/AF case.

One of the special transformations linked to the hidden SU(2) points reveals at the same time an exact duality between the Kitaev and Kekulé-Kitaev models; this result should be useful in theoretical studies of these and related models.

We emphasize that, adopting the extended KH model, all the above results are necessary consequences of its symmetry which is in turn dictated by the underlying C_3 symmetry of the lattice.

Having the results of the general symmetry analysis at hand, we were able to find the region of the parameter space that is consistent with the observed properties of the honeycomb lattice iridates Na_2IrO_3 and Li_2IrO_3. Further, a relation between the ordered moment direction and the model parameters is derived, which may help to quantify these parameters from future experiments.

Finally, our method to systematically explore the hidden symmetries is general and can be applied to other bond-anisotropic models as well. In the context of the iridate materials, the symmetry analysis of the extended KH model on hyperhoneycomb and harmonic-honeycomb lattices is of a great interest.

ACKNOWLEDGMENTS

We would like to thank B. J. Kim for sharing with us the experimental data [46] which motivated this study, and R. Coldea, G. Jackeli, I. Kimchi, N. B. Perkins, S. Trebst, and S. E. Sebastian for helpful discussions and comments. J.C. acknowledges support by ERDF under project CEITEC (CZ.1.05/1.1.00/02.0068), EC 7th Framework Programme (286154/SYLICA), and Czech Science Foundation (GAČR) under Project No. 15-14523Y.

APPENDIX A: *XYZ* FORM OF THE HAMILTONIAN

The Hamiltonian expressed in terms of the spin components S^X, S^Y, and S^Z, corresponding to the XYZ reference frame in Fig. 1(a), takes the form

$$\begin{aligned}\mathcal{H}_{\langle ij\rangle\parallel\gamma} = {} & J_{XY}\left(S_i^X S_j^X + S_i^Y S_j^Y\right) + J_Z S_i^Z S_j^Z \\ & + A\left[c_\gamma\left(S_i^X S_j^X - S_i^Y S_j^Y\right) - s_\gamma\left(S_i^X S_j^Y + S_i^Y S_j^X\right)\right] \\ & - B\sqrt{2}\left[c_\gamma\left(S_i^X S_j^Z + S_i^Z S_j^X\right) + s_\gamma\left(S_i^Y S_j^Z + S_i^Z S_j^Y\right)\right].\end{aligned} \tag{A1}$$

Here the C_3 symmetry of the model is embodied in the factors $c_\gamma \equiv \cos\phi_\gamma$ and $s_\gamma \equiv \sin\phi_\gamma$, where the angles ϕ_γ are determined by the bond directions: $\phi_\gamma = 0, \frac{2\pi}{3}, \frac{4\pi}{3}$ for the c, a, and b bonds, respectively. In terms of the original parameters $JK\Gamma\Gamma'$, the exchange constants entering (A1) read as

$$A = \tfrac{1}{3}K + \tfrac{2}{3}(\Gamma - \Gamma'), \tag{A2}$$

$$B = \tfrac{1}{3}K - \tfrac{1}{3}(\Gamma - \Gamma'), \tag{A3}$$

$$J_{XY} = J + B - \Gamma', \tag{A4}$$

$$J_Z = J + A + 2\Gamma'. \tag{A5}$$

Note that it is the A and B terms which bring about the bond directionality of the interactions, and hence they naturally support C_3 symmetry breaking orderings such as zigzag in the present model. Physically, these terms arise from the exchange processes that involve the in-plane components of orbital momentum L_X and L_Y which "know" the bond directions, like the orbitals do in the Kugel-Khomskii models.

It is also noticed that the A and B terms change the Z component of total angular momentum by ± 2 and ± 1, correspondingly. This is because the t_{2g}-orbital angular momentum L is not a conserved quantity in a crystal, and this commonly shows up in effective spin Hamiltonians due to the spin-orbit coupling.

A strong trigonal field splits the t_{2g} level such that the lowest Kramers doublet (pseudospin) wave functions $|\tilde{\uparrow}\rangle, |\tilde{\downarrow}\rangle$ become simple products of $L_Z = \pm 1$ and spin $|\downarrow\rangle$, $|\uparrow\rangle$ states, correspondingly; i.e., there will be a one-to-one correspondence between the real spin and pseudospin directions. Since the total spin is conserved during the hoppings, pseudospin is then conserved, too. Thus, the spin-nonconserving terms A and B must vanish in this limit, which implies $K \to 0$ and $\Gamma \to \Gamma'$ simultaneously. Physically, a strong compression along the trigonal axis dictates that this axis becomes the "easy" (or "hard") one for moments. Since this limit is not realized in iridates, we will not use the XYZ form of the Hamiltonian in this paper; however, it might be useful for pseudospin-1/2 Co^{4+}, Rh^{4+}, and Ru^{3+} compounds where the spin-orbit and crystal field effects may strongly compete.

APPENDIX B: ANALYSIS OF THE CLASSICAL ENERGY AND MOMENT DIRECTION

In this Appendix we show the expressions used in the classical energy analysis. We first give the Hamiltonian in its momentum space form utilized within the Luttinger-Tisza

method. By minimizing the classical energy in the zigzag phase we then find the ordered moment direction.

Transforming the spin operators via $\boldsymbol{S}_{A\boldsymbol{R}} = \sum_{\boldsymbol{q}} e^{i\boldsymbol{q}\cdot\boldsymbol{R}} \boldsymbol{S}_{A\boldsymbol{q}}$ and similarly for the B sublattice, we cast the Hamiltonian into the form

$$\mathcal{H} = \sum_{\boldsymbol{q}} \Psi_{\boldsymbol{q}}^{\dagger} H_{\boldsymbol{q}} \Psi_{\boldsymbol{q}} \quad \text{with} \quad \Psi_{\boldsymbol{q}} = \begin{pmatrix} \boldsymbol{S}_{A\boldsymbol{q}} \\ \boldsymbol{S}_{B\boldsymbol{q}} \end{pmatrix}, \tag{B1}$$

where the $\boldsymbol{q}$ vectors cover the first Brillouin zone of the triangular lattice of $\boldsymbol{R}$. The simplest expressions for the 6×6 matrices $H_{\boldsymbol{q}}$ of the momentum-space Hamiltonian (B1) are obtained using the cubic axes x, y, z. Complementing the interactions in Eq. (2) by long-range J_2 and J_3, we arrive at

$$H_{\boldsymbol{q}} = N_{\text{site}} \begin{pmatrix} F_{\boldsymbol{q}} & G_{\boldsymbol{q}} \\ G_{\boldsymbol{q}}^{\dagger} & F_{\boldsymbol{q}} \end{pmatrix} \quad \text{with} \quad F_{\boldsymbol{q}} = \tfrac{1}{2} J_2 \begin{pmatrix} 1 & 0 & 0 \\ 0 & 1 & 0 \\ 0 & 0 & 1 \end{pmatrix} \eta_{2\boldsymbol{q}} \tag{B2}$$

and

$$\begin{aligned} G_{\boldsymbol{q}} = {} & \tfrac{1}{4}(J_1 \eta_{1\boldsymbol{q}} + J_3 \eta_{3\boldsymbol{q}}) \begin{pmatrix} 1 & 0 & 0 \\ 0 & 1 & 0 \\ 0 & 0 & 1 \end{pmatrix} \\ & + \tfrac{1}{4} K \begin{pmatrix} e_1 & 0 & 0 \\ 0 & e_2 & 0 \\ 0 & 0 & 1 \end{pmatrix} + \tfrac{1}{4} \Gamma \begin{pmatrix} 0 & 1 & e_2 \\ 1 & 0 & e_1 \\ e_2 & e_1 & 0 \end{pmatrix} \\ & + \tfrac{1}{4} \Gamma' \begin{pmatrix} 0 & e_1 e_2 & e_1 + 1 \\ e_1 e_2 & 0 & e_2 + 1 \\ e_1 + 1 & e_2 + 1 & 0 \end{pmatrix}. \end{aligned} \tag{B3}$$

Here the momentum-dependent factors read as

$$e_{1,2} = e^{-i\frac{1}{2}(\pm\sqrt{3}q_x + 3q_y)}, \tag{B4}$$

$$\eta_{1\boldsymbol{q}} = 1 + 2\cos\tfrac{\sqrt{3}q_x}{2}\, e^{-i\frac{3}{2}q_y}, \tag{B5}$$

$$\eta_{2\boldsymbol{q}} = \cos\sqrt{3}q_x + 2\cos\tfrac{\sqrt{3}q_x}{2}\cos\tfrac{3q_y}{2}, \tag{B6}$$

$$\eta_{3\boldsymbol{q}} = e^{-i3q_y} + 2\cos\sqrt{3}q_x. \tag{B7}$$

In the Luttinger-Tisza method [71,72], the matrices $H_{\boldsymbol{q}}/2N_{\text{site}}$ for $\boldsymbol{q}$ running through the Brillouin zone are diagonalized. The $\boldsymbol{q}$ vector and the eigenvector corresponding to the minimum eigenvalue then determine the ordering resulting on a classical level and the minimum eigenvalue itself gives the classical energy per site. This approach relaxes the spin-length constraint which should be checked afterward.

Next, we evaluate the classical energy for the zigzag state with the ordering vector $\boldsymbol{Q} = \boldsymbol{Q}_c = (0, 2\pi/3)$ and an arbitrary ordered moment direction given by a unit vector $\boldsymbol{u}$. The corresponding zigzag pattern is captured by $\Psi_{\boldsymbol{Q}} = (+\frac{1}{2}\boldsymbol{u}, -\frac{1}{2}\boldsymbol{u})^T$. Using (B1), we get for the classical energy per site

$$E_{\text{class}} = \tfrac{1}{8}(J_1 - K - 2J_2 - 3J_3) + \tfrac{1}{8}\boldsymbol{u}^T M \boldsymbol{u} \tag{B8}$$

with the matrix

$$M = \begin{pmatrix} 2K & -\Gamma + 2\Gamma' & \Gamma \\ -\Gamma + 2\Gamma' & 2K & \Gamma \\ \Gamma & \Gamma & 0 \end{pmatrix} \tag{B9}$$

or equivalently

$$M = \begin{pmatrix} 2K & D + \sqrt{2}C & -D \\ D + \sqrt{2}C & 2K & -D \\ -D & -D & 0 \end{pmatrix}. \tag{B10}$$

The ordered moment direction can now be obtained as the eigenvector of M corresponding to its lowest eigenvalue. However, as will be clear in a moment, it is more convenient to switch to the reference frame which coincides with the local $\tilde{x}$, $\tilde{y}$, $\tilde{z}$ axes for c bonds [see Fig. 1(b)]. The matrix M is then transformed to

$$\tilde{M} = \begin{pmatrix} 2K - D - \sqrt{2}C & 0 & 0 \\ 0 & 2K + D + \sqrt{2}C & -\sqrt{2}D \\ 0 & -\sqrt{2}D & 0 \end{pmatrix}, \tag{B11}$$

which can be readily diagonalized and the angle α of the ordered pseudospin to the XY plane can be found.

As discussed in the main text, if we rotate the spins by 180° around the global Z axis, the observed moment would come close to the $\tilde{z}$ axis. Since the latter is an attractive point for the two-parameter KH model [11], we guess that this rotation will transform the actual J, K, D, C Hamiltonian ($K < 0$, large D) for Na_2IrO_3 into an effective J', K', D', C' one, with $K > 0$ and small only D' and C' values, i.e., into a nearly two-parameter KH model (which guarantees that the corresponding effective easy axis is close to $\tilde{z}$). We therefore first apply the $\mathcal{T}_1$ transformation via Eq. (3), calculate the moment direction for effective J', K', D', C', and later make use of the expected smallness of the transformed D'. The first two steps yield an analytical expression for the angle α:

$$\alpha = \alpha_0 + \frac{1}{2}\arctan\left(\frac{2\sqrt{2}D'}{2K' + D' + \sqrt{2}C'}\right) \tag{B12}$$

with the first contribution being the "magic" angle $\alpha_0 = \arcsin(1/\sqrt{3}) \simeq 35.3°$ of the $\tilde{z}$ axis to the XY plane and the second contribution supposed to be small. Now, we return to the original spin axes by applying the $\mathcal{T}_1$ transformation again. This does not alter the angle α but rotates the moment into its physical position: below a midpoint between two oxygen ions [46]. In terms of the original parameters we have

$$\alpha = \alpha_0 + \frac{1}{2}\arctan\left(2\sqrt{2}\,\frac{4K - 5D + 2\sqrt{2}C}{14K + 23D + 7\sqrt{2}C}\right). \tag{B13}$$

For $D = C = 0$, this equation gives the moment direction towards a midpoint of two oxygens, as expected for negative K values of the Kitaev coupling [46] on a classical level (but it will turn to either the x or y oxygen direction once the order-by-disorder mechanism is switched on [11,40]). The moment moves down from this position once the model is extended by D and C terms of a proper sign. At the parameter set given in the main text, the moment takes the "magic" angle. By expanding the arctangent near this point, we arrive at the following formula for the deviation from α_0:

$$\delta\alpha = \frac{1}{2}\arctan\left(\frac{4\sqrt{2}}{7}\,\frac{1 - \frac{5}{4}r}{1 + \frac{23}{14}r}\right) \approx \frac{2\sqrt{2}}{7}\,\frac{1 - \frac{5}{4}r}{1 + \frac{23}{14}r} \tag{B14}$$

with the single parameter

$$r = \frac{D}{K + \frac{1}{\sqrt{2}}C} = -\frac{\Gamma}{K + \Gamma'}. \tag{B15}$$

This parameter quantifies the "departure" from the KH model and can be measured by resonant x-ray [46] or neutron diffraction experiments; as mentioned in the main text, care has to be taken in the fits by considering the crystal field effects on pseudospin wave functions.

In terms of the parameter r, Eq. (B13) can be rewritten as

$$\tan 2\alpha = 4\sqrt{2}\,\frac{1+r}{7r-2}. \tag{B16}$$

Note that this and the previous equations for α hold at finite $J_{2,3}$ Heisenberg corrections as well, since the easy axis is determined solely by the anisotropy terms.

[1] W. J. L. Buyers, T. M. Holden, E. C. Svensson, R. A. Cowley, and M. T. Hutchings, J. Phys. C: Solid State Phys. **4**, 2139 (1971).
[2] R. J. Elliott and M. F. Thorpe, J. Appl. Phys. **39**, 802 (1968).
[3] A. Abragam and B. Bleaney, *Electron Paramagnetic Resonance of Transition Ions* (Clarendon Press, Oxford, 1970).
[4] K. I. Kugel and D. I. Khomskii, Sov. Phys. Usp. **25**, 231 (1982).
[5] G. Khaliullin and S. Okamoto, Phys. Rev. Lett. **89**, 167201 (2002); Phys. Rev. B **68**, 205109 (2003).
[6] G. Khaliullin, Prog. Theor. Phys. Suppl. **160**, 155 (2005).
[7] G. Khaliullin, W. Koshibae, and S. Maekawa, Phys. Rev. Lett. **93**, 176401 (2004).
[8] G. Chen and L. Balents, Phys. Rev. B **78**, 094403 (2008).
[9] G. Jackeli and G. Khaliullin, Phys. Rev. Lett. **102**, 017205 (2009).
[10] A. Shitade, H. Katsura, J. Kuneš, X.-L. Qi, S.-C. Zhang, and N. Nagaosa, Phys. Rev. Lett. **102**, 256403 (2009).
[11] J. Chaloupka, G. Jackeli, and G. Khaliullin, Phys. Rev. Lett. **105**, 027204 (2010).
[12] S. Okamoto, Phys. Rev. Lett. **110**, 066403 (2013).
[13] W. Witczak-Krempa, G. Chen, Y. B. Kim, and L. Balents, Annu. Rev. Condens. Matter Phys. **5**, 57 (2014).
[14] Z. Nussinov and J. van den Brink, Rev. Mod. Phys. **87**, 1 (2015).
[15] G. Khaliullin and S. Maekawa, Phys. Rev. Lett. **85**, 3950 (2000).
[16] G. Khaliullin, Phys. Rev. B **64**, 212405 (2001).
[17] G. Chen, L. Balents, and A. P. Schnyder, Phys. Rev. Lett. **102**, 096406 (2009).
[18] G. Khaliullin, Phys. Rev. Lett. **111**, 197201 (2013).
[19] O. N. Meetei, W. S. Cole, M. Randeria, and N. Trivedi, Phys. Rev. B **91**, 054412 (2015).
[20] More specifically, some ions with an even number of electrons (e.g., d^4-Ru in Ca_2RuO_4 [18] or d^6-Fe in $FeSc_2S_4$ [17]) adopt a singlet $J = 0$ ground state. When the exchange interactions become comparable to the spin-orbit induced singlet-triplet splitting, magnetic order emerges as a condensation of the excited levels with $J = 1$. At the transition, the spin-length fluctuations diverge; the ordered state is characterized by "soft" moments and the associated amplitude (Higgs) mode, in addition to the usual transverse magnons [18]. In essence, this is similar to the spin-state crossover physics and "soft" magnetism realized in some compounds of Co^{3+} and Fe^{2+} ions, where the ground state has $S = 0$ (due to large covalency and crystal field effects) while the $S \neq 0$ levels are not too high; for details, see the recent work [21] and references therein.
[21] J. Chaloupka and G. Khaliullin, Phys. Rev. Lett. **110**, 207205 (2013); Prog. Theor. Phys. Suppl. **176**, 50 (2008).
[22] B. J. Kim, H. Ohsumi, T. Komesu, S. Sakai, T. Morita, H. Takagi, and T. Arima, Science **323**, 1329 (2009).
[23] J. Kim, D. Casa, M. H. Upton, T. Gog, Y.-J. Kim, J. F. Mitchell, M. van Veenendaal, M. Daghofer, J. van den Brink, G. Khaliullin, and B. J. Kim, Phys. Rev. Lett. **108**, 177003 (2012).
[24] S. Fujiyama, H. Ohsumi, T. Komesu, J. Matsuno, B. J. Kim, M. Takata, T. Arima, and H. Takagi, Phys. Rev. Lett. **108**, 247212 (2012).
[25] A. Kitaev, Ann. Phys. **321**, 2 (2006).
[26] X. Liu, T. Berlijn, W.-G. Yin, W. Ku, A. Tsvelik, Y.-J. Kim, H. Gretarsson, Y. Singh, P. Gegenwart, and J. P. Hill, Phys. Rev. B **83**, 220403(R) (2011).
[27] F. Ye, S. Chi, H. Cao, B. C. Chakoumakos, J. A. Fernandez-Baca, R. Custelcean, T. F. Qi, O. B. Korneta, and G. Cao, Phys. Rev. B **85**, 180403(R) (2012).
[28] S. K. Choi, R. Coldea, A. N. Kolmogorov, T. Lancaster, I. I. Mazin, S. J. Blundell, P. G. Radaelli, Y. Singh, P. Gegenwart, K. R. Choi, S.-W. Cheong, P. J. Baker, C. Stock, and J. Taylor, Phys. Rev. Lett. **108**, 127204 (2012).
[29] R. Coldea, presentation at SPORE13, Dresden, 2013 (unpublished); S. Choi, R. Coldea *et al.* (unpublished).
[30] I. Kimchi and Y.-Z. You, Phys. Rev. B **84**, 180407(R) (2011).
[31] J. Reuther, R. Thomale, and S. Rachel, Phys. Rev. B **90**, 100405(R) (2014).
[32] J. Chaloupka, G. Jackeli, and G. Khaliullin, Phys. Rev. Lett. **110**, 097204 (2013).
[33] Y. Yu, L. Liang, Q. Niu, and S. Qin, Phys. Rev. B **87**, 041107(R) (2013).
[34] S. Okamoto, Phys. Rev. B **87**, 064508 (2013).
[35] S. Bhattacharjee, S.-S. Lee, and Y. B. Kim, New J. Phys. **14**, 073015 (2012).
[36] V. M. Katukuri, S. Nishimoto, V. Yushankhai, A. Stoyanova, H. Kandpal, S. Choi, R. Coldea, I. Rousochatzakis, L. Hozoi, and J. van den Brink, New J. Phys. **16**, 013056 (2014).
[37] J. G. Rau, E. K.-H. Lee, and H.-Y. Kee, Phys. Rev. Lett. **112**, 077204 (2014).
[38] J. G. Rau and H.-Y. Kee, arXiv:1408.4811.
[39] Y. Yamaji, Y. Nomura, M. Kurita, R. Arita, and M. Imada, Phys. Rev. Lett. **113**, 107201 (2014).
[40] Y. Sizyuk, C. Price, P. Wölfle, and N. B. Perkins, Phys. Rev. B **90**, 155126 (2014).
[41] K. Shinjo, S. Sota, and T. Tohyama, Phys. Rev. B **91**, 054401 (2015).
[42] I. Kimchi, R. Coldea, and A. Vishwanath, Phys. Rev. B **91**, 245134 (2015).
[43] E. Sela, H.-C. Jiang, M. H. Gerlach, and S. Trebst, Phys. Rev. B **90**, 035113 (2014).

[44] I. I. Mazin, H. O. Jeschke, K. Foyevtsova, R. Valentí, and D. I. Khomskii, Phys. Rev. Lett. **109**, 197201 (2012).

[45] H. Gretarsson, J. P. Clancy, Y. Singh, P. Gegenwart, J. P. Hill, J. Kim, M. H. Upton, A. H. Said, D. Casa, T. Gog, and Y.-J. Kim, Phys. Rev. B **87**, 220407(R) (2013).

[46] S. H. Chun, J.-W. Kim, Jungho Kim, H. Zheng, C. Stoumpos, C. Malliakas, J. F. Mitchell, K. Mehlawat, Y. Singh, Y. Choi, T. Gog, A. Al-Zein, M. Moretti Sala, M. Krisch, J. Chaloupka, G. Jackeli, G. Khaliullin, and B. J. Kim, Nat. Phys. **11**, 462 (2015).

[47] I. Kimchi and A. Vishwanath, Phys. Rev. B **89**, 014414 (2014).

[48] I. Rousochatzakis, U. K. Rössler, J. van den Brink, and M. Daghofer, arXiv:1209.5895.

[49] M. Becker, M. Hermanns, B. Bauer, M. Garst, and S. Trebst, Phys. Rev. B **91**, 155135 (2015).

[50] K. Li, S.-L. Yu, and J.-X. Li, New J. Phys. **17**, 043032 (2015).

[51] K. W. Plumb, J. P. Clancy, L. J. Sandilands, V. V. Shankar, Y. F. Hu, K. S. Burch, H.-Y. Kee, and Y.-J. Kim, Phys. Rev. B **90**, 041112(R) (2014).

[52] T. Takayama, A. Kato, R. Dinnebier, J. Nuss, H. Kono, L. S. I. Veiga, G. Fabbris, D. Haskel, and H. Takagi, Phys. Rev. Lett. **114**, 077202 (2015).

[53] A. Biffin, R. D. Johnson, S. Choi, F. Freund, S. Manni, A. Bombardi, P. Manuel, P. Gegenwart, and R. Coldea, Phys. Rev. B **90**, 205116 (2014).

[54] K. A. Modic, T. E. Smidt, I. Kimchi, N. P. Breznay, A. Biffin, S. Choi, R. D. Johnson, R. Coldea, P. Watkins-Curry, G. T. McCandless, J. Y. Chan, F. Gandara, Z. Islam, A. Vishwanath, A. Shekhter, R. D. McDonald, and J. G. Analytis, Nat. Commun. **5**, 4203 (2014).

[55] A. Biffin, R. D. Johnson, I. Kimchi, R. Morris, A. Bombardi, J. G. Analytis, A. Vishwanath, and R. Coldea, Phys. Rev. Lett. **113**, 197201 (2014).

[56] M. Hermanns and S. Trebst, Phys. Rev. B **89**, 235102 (2014).

[57] B. N. Figgis and M. A. Hitchman, *Ligand Field Theory and Its Applications* (Wiley-VCH, New York, 2000).

[58] H. Gretarsson, J. P. Clancy, X. Liu, J. P. Hill, E. Bozin, Y. Singh, S. Manni, P. Gegenwart, J. Kim, A. H. Said, D. Casa, T. Gog, M. H. Upton, H.-S. Kim, J. Yu, V. M. Katukuri, L. Hozoi, J. van den Brink, and Y.-J. Kim, Phys. Rev. Lett. **110**, 076402 (2013).

[59] A relative strength of the trigonal field splitting Δ/λ in Na_2IrO_3 can be deduced from a splitting $\Delta_{BC} \sim 0.1$ eV [58] of the excited $J = 3/2$ quartet, using a relation $\Delta_{BC}/\lambda = \frac{1}{\sqrt{2}} \tan^{-1}\theta - 1$, where the angle θ is given by $\tan 2\theta = 2\sqrt{2}/(1 + \frac{2\Delta}{\lambda})$. This gives $\Delta/\lambda \simeq 3/8$. With this ratio, we obtain the pseudospin g factors (see Ref. [3] for details) $g_c \simeq -2.6$ and $g_{ab} \simeq 1.7$ for out-of-plane and in-plane directions, correspondingly, in fair agreement with the observed values $|g_c| \simeq 2.7$ and $|g_{ab}| \simeq 1.9$ [74].

[60] Unfortunately, the requirement of the Hamiltonian being represented by nonsingular matrices prevents us from finding all the hidden Kitaev points by using the transformations $K_0 \leftrightarrow JKDC$. We can only reveal a part of them by using $J_0K_0 \leftrightarrow JKDC$ and setting $J_0 = 0$.

[61] M. Kamfor, S. Dusuel, J. Vidal, and K. P. Schmidt, J. Stat. Mech: Theory Exp. (2010) P08010.

[62] E. Quinn, S. Bhattacharjee, and R. Moessner, Phys. Rev. B **91**, 134419 (2015).

[63] Recently we came across a preprint [64] which also introduces the six-sublattice transformation, and claims that it maps the extended KH model onto itself. We emphasize again that this transformation is not self-dual in general; is becomes such only at the special parameter setup for this model (linking $J_0 \leftrightarrow K = \Gamma$). In most of the phase space, it breaks the bond distribution pattern dictated by the C_3 rotation rules in Fig. 1(c).

[64] J. Lou, L. Liang, Y. Yu, and Y. Chen, arXiv:1501.06990.

[65] J. Chaloupka, G. Jackeli, and G. Khaliullin, presentation at SPORE13, Dresden, 2013 (unpublished).

[66] For a discussion of the order-from-disorder phenomena in frustrated spin systems, see A. M. Tsvelik, *Quantum Field Theory in Condensed Matter Physics* (Cambridge University Press, Cambridge, 1995), Chap. 17, and references therein.

[67] Regarding the terminology used here, we have in mind that the compass-type and Kitaev-type interactions are very distinct in their physical appearance and origin. While the compass-spins (pseudodipoles) as introduced in Ref. [4] align themselves *along* the bond direction as real compasses do (hence the name), the spins in the Kitaev honeycomb model tend rather to avoid the bond directions. Placed on a honeycomb lattice, the bond-directional compasses would feel much less frustrated than the Kitaev spins, and show "order-from-disorder" behavior instead. As to the physical origin, the compass-type and Kitaev-type spin anisotropy terms arise in compounds with distinct chemical bonding geometries—corner-shared [16,9] and edge-shared [6,9] structures, correspondingly.

[68] In general, obtaining the right moment orientation is a crucial test for the completeness of the model Hamiltonians used. For instance, the compass-type anisotropy (only allowed for spin-1/2 in an ideal perovskite) favors the easy spin axis along a bond direction (say [100]), but in real perovskites it often takes a "wrong" direction (e.g., [110] in Sr_2IrO_4), due to (orthorhombic) distortions and/or other factors not included in idealized "Heisenberg plus compass" type spin models. Similarly, an unexpected easy axis direction in Na_2IrO_3 is a manifestation of the other anisotropy terms beyond the "Heisenberg plus Kitaev" spin model.

[69] H.-C. Jiang, Z.-C. Gu, X.-L. Qi, and S. Trebst, Phys. Rev. B **83**, 245104 (2011).

[70] Ref. [46] has estimated the angle $\alpha \simeq 44^\circ$ based on the fits that did not account for a trigonal field splitting. Positive (negative) Δ values may decrease (increase) the actual value of α from this estimate.

[71] J. M. Luttinger and L. Tisza, Phys. Rev. **70**, 954 (1946).

[72] D. B. Litvin, Physica **77**, 205 (1974).

[73] K. Foyevtsova, H. O. Jeschke, I. I. Mazin, D. I. Khomskii, and R. Valentí, Phys. Rev. B **88**, 035107 (2013).

[74] Y. Singh and P. Gegenwart, Phys. Rev. B **82**, 064412 (2010).

[75] Y. Singh, S. Manni, J. Reuther, T. Berlijn, R. Thomale, W. Ku, S. Trebst, and P. Gegenwart, Phys. Rev. Lett. **108**, 127203 (2012).

[76] J.-H. Kim, A. Jain, M. Reehuis, G. Khaliullin, D. C. Peets, C. Ulrich, J. T. Park, E. Faulhaber, A. Hoser, H. C. Walker, D. T. Adroja, A. C. Walters, D. S. Inosov, A. Maljuk, and B. Keimer, Phys. Rev. Lett. **113**, 147206 (2014).

PHYSICAL REVIEW B **94**, 064435 (2016)

Magnetic anisotropy in the Kitaev model systems Na_2IrO_3 and $RuCl_3$

Jiří Chaloupka[1,2] and Giniyat Khaliullin[3]

[1]*Central European Institute of Technology, Masaryk University, Kamenice 753/5, 62500 Brno, Czech Republic*

[2]*Department of Condensed Matter Physics, Faculty of Science, Masaryk University, Kotlářská 2, 61137 Brno, Czech Republic*

[3]*Max Planck Institute for Solid State Research, Heisenbergstrasse 1, D-70569 Stuttgart, Germany*

(Received 19 July 2016; revised manuscript received 10 August 2016; published 31 August 2016)

We study the ordered moment direction in the extended Kitaev-Heisenberg model relevant to honeycomb lattice magnets with strong spin-orbit coupling. We utilize numerical diagonalization and analyze the exact cluster ground states using a particular set of spin-coherent states, obtaining thereby quantum corrections to the magnetic anisotropy beyond conventional perturbative methods. It is found that the quantum fluctuations strongly modify the moment direction obtained at a classical level and are thus crucial for a precise quantification of the interactions. The results show that the moment direction is a sensitive probe of the model parameters in real materials. Focusing on the experimentally relevant zigzag phases of the model, we analyze the currently available neutron-diffraction and resonant x-ray-diffraction data on Na_2IrO_3 and $RuCl_3$ and discuss the parameter regimes plausible in these Kitaev-Heisenberg model systems.

DOI: 10.1103/PhysRevB.94.064435

I. INTRODUCTION

Due to their intermediate spatial extension, d electrons in transition-metal compounds comprise both the localized and itinerant features. This duality is manifested in a rich variety of metal-insulator transitions [1,2]. Even deep in the Mott-insulating phase, the d electrons partially retain their kinetic energy, by making virtual hoppings to the neighboring sites and forming the covalent bonds. The internal structure of these bonds is dictated by the orbital shape of d electrons as well as by Pauli principle and Hund's interactions among spins. This results in an intimate link between the nature of chemical bonds ("orbital order") and magnetism [3], which can be cast in terms of phenomenological Goodenough-Kanamori rules.

The Kugel-Khomskii models [4] form a theoretical framework where the "spin physics" and "orbital chemistry" are treated on equal footing. A special feature of these models is that the d orbital is spatially anisotropic and hence cannot satisfy all the bonds simultaneously. In high-symmetry crystals, this results in a picture of fluctuating orbitals [5,6], where the frustration among different covalent bonds is resolved by virtue of their quantum superposition, lifting the orbital degeneracy without a static order.

It might seem that a relativistic spin-orbit coupling, which lifts the orbital degeneracy already on a single ion level [3,4], will readily eliminate the orbital frustration problem. This coupling does indeed greatly reduce the initially large spin-orbital Hilbert space of d ions, leaving often just a twofold degenerate Kramers level with an effective ("pseudo") spin one-half [7]. It turns out, however, that the pseudospins still well "remember" the orbital frustration, by inheriting the bond-directional nature of orbital interactions via the spin-orbit entanglement [6].

The bond-directional nature of pseudospin interactions has profound consequences for magnetism (as well as for the properties of doped systems [8]). The most remarkable example, pointed out in Ref. [9], is a possible realization of Kitaev's honeycomb model [10] in materials with the $d^5(t_{2g})$ electronic configuration such as Na_2IrO_3. This theoretical proposal has sparked a broad interest in honeycomb lattice pseudospin systems (see the recent review paper [11] and references therein).

There is a direct experimental evidence [12] that the Kitaev-type interactions are indeed dominant in Na_2IrO_3. Unusual features pointing towards the Kitaev model have been observed [13] also in spin excitation spectra of $RuCl_3$ (this compound was suggested [14] to host pseudospin physics, too). On the other hand, it is also clear that there are terms in the pseudospin Hamiltonian that take these systems away from the Kitaev spin-liquid phase window [15]. The identification of these "undesired" interactions and clarification of their dependence on material parameters is an important issue that has been in the focus of many recent studies.

Experimentally, the strength of a dominant Kitaev coupling $|K|$ can readily be evaluated from an overall bandwidth of spin excitations; however, the determination of its sign and quantification of the subdominant terms is not straightforward and needs a theory support. The aim of this paper is to show that the direction of the ordered moments, which can be extracted from the neutron-diffraction and x-ray-diffraction data, contains valuable information on the model parameters, including the sign of K. Considering a symmetry dictated form of the model Hamiltonian, we calculate the pseudospin direction fully including quantum fluctuations which are expected to be crucial in frustrated spin models. We will point out that the pseudospin itself is not directly probed by neutrons; rather, they detect the direction of the *magnetic* moment which is not the same as that of the pseudospin. Similarly, we will describe how to extract the pseudospin direction from resonant x-ray-scattering (RXS) data.

The paper is organized as follows. Section II introduces the model Hamiltonian. Section III briefly discusses the pseudospin easy axis direction on a classical level. Section IV introduces the method of deriving the moment direction from exact diagonalization (ED) data. Section V presents the ED results on moment direction as a function of model parameters. Section VI considers a relation between the pseudospins and magnetic moments probed by neutron-diffraction and RXS experiments, and discusses implications of the theory for

Na_2IrO_3 and $RuCl_3$. Appendix A compares the method of Sec. IV with the standard approach. Appendix B derives the equations used in the analysis of RXS data. Finally, Appendix C discusses how the trigonal field can be extracted from $J = 3/2$ magnetic excitation spectra.

II. EXTENDED KITAEV-HEISENBERG MODEL

To describe the interactions among the pseudospins (referred to as "spins" below), we adopt a model containing all symmetry allowed nearest-neighbor (NN) terms and the longer-range Heisenberg interactions:

$$\mathcal{H} = \sum_{\langle ij\rangle\in \mathrm{NN}} \mathcal{H}_{ij}^{(\gamma)} + \sum_{\langle ij\rangle\notin \mathrm{NN}} J_{ij}\boldsymbol{S}_i\cdot\boldsymbol{S}_j. \tag{1}$$

The nearest-neighbor contribution is the extended Kitaev-Heisenberg model [16–18] that, apart from the Heisenberg interaction, includes all the bond-anisotropic interactions compatible with the symmetries of a trigonally distorted honeycomb lattice. Its z-bond contribution (see Fig. 1 for the definitions of the bonds and spin axes) takes the following form:

$$\mathcal{H}_{ij}^{(z)} = K\,S_i^zS_j^z + J\,\boldsymbol{S}_i\cdot\boldsymbol{S}_j + \Gamma\left(S_i^xS_j^y + S_i^yS_j^x\right) + \Gamma'\left(S_i^xS_j^z + S_i^zS_j^x + S_i^yS_j^z + S_i^zS_j^y\right). \tag{2}$$

The Hamiltonian contributions for the other bonds (x and y) are obtained by a cyclic permutation among S_x, S_y, S_z. The resulting alternation of the local easy axis directions from bond to bond, imposed by the Ising-like term K, brings about a strong frustration which, as discussed above, can be traced back to the orbital frustration problem in Kugel-Khomskii type models. An extensive discussion of the above Hamiltonian and its nontrivial symmetry properties can be found in Ref. [19].

With the Kitaev-coupling K alone, the model has a spin-liquid ground state. Both Na_2IrO_3 and $RuCl_3$ show spin order where the zigzag-type ferromagnetic (FM) chains, running along the a direction, are coupled to each other antiferromagnetically [see Fig. 1(b)]. This order becomes a ground state of the Kitaev model with $K > 0$ [antiferromagnetic (AF) sign], when a small FM $J < 0$ Heisenberg coupling is added [20]. If the Kitaev coupling is negative, $K < 0$ (FM sign), then zigzag order emerges due to longer-range AF couplings [21,22] and/or Γ, Γ' terms [17–19]. Given that the stability of the Kitaev-liquid phase against perturbations strongly depends on the sign of K [20], which scenario is realized in a given compound becomes an important issue.

Leaving aside the "orbital chemistry" aspects that decide the sign of K as well as the other model parameters, we just mention that various *ab initio* estimates (see, e.g., [16,23,24]) generally support the FM $K < 0$ regime, most likely reflecting the decisive role of Hund's coupling effect on K emphasized earlier [9,15]. However, we take here a phenomenological approach, considering the model with free parameter values including both signs of K. The J, Γ, and Γ' values are varied such that the ground state stays within the zigzag phase. Based on a recent result [24] that third-NN Heisenberg coupling J_3 is more significant than second-NN J_2 in both Na_2IrO_3 and $RuCl_3$, we replace J_{ij} in Eq. (1) by J_3, reducing thereby the parameter space.

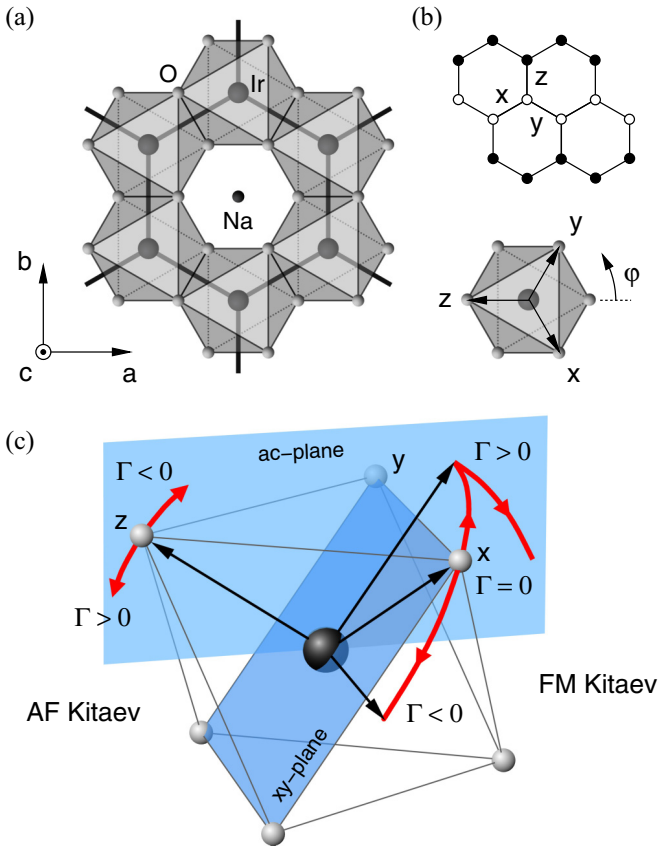

FIG. 1. (a) Top view of the honeycomb lattice of the edge-shared IrO_6 octahedra in Na_2IrO_3. (b) Three types of bonds and zigzag-AF state where x and y bonds connecting similar dots are FM, while the z bonds are AF (top), and the orientation of the cubic axes x, y, z with respect to the octahedra (bottom). (c) The possible directions of the ordered moment in the above zigzag state. In the AF Kitaev case the moment is tied to the cubic z axis and deviates from it only slightly with nonzero Γ. In the FM Kitaev case with $\Gamma = 0$, it is constrained to the xy plane classically, and pinned to a cubic x or y axis when quantum fluctuations are included. Nonzero $\Gamma < 0$ gradually pushes the moment direction towards the b axis in the honeycomb plane, while positive Γ drives it first towards the ac plane [which is reached at $\Gamma \approx 0.05|K|$, see Fig. 3(a)], and then rotates the moment within the ac plane towards the a axis.

The magnetic anisotropy in the present model is a nontrivial problem, since the leading term K is anisotropic by itself, and, on top of this highly frustrated interaction, the other terms which eventually drive a magnetic order in real compounds have a strong impact on magnetic energy profile. As illustrated in Fig. 1(c) and discussed in detail below, the ordered moment direction is very sensitive to the model parameters, and it shows a qualitatively different behavior in case of FM and AF Kitaev couplings. We note that the "moment direction" in this figure refers to that of pseudospin; Sec. VI explains how it is related to the magnetic moments probed by neutron-diffraction and x-ray-diffraction experiments.

III. CLASSICAL MOMENT DIRECTION

Let us briefly mention the results of a classical analysis (for details see Appendix B of Ref. [19]) assuming the zigzag order with antiferromagnetic z bonds as shown in Fig. 1(b). On this level, the moment direction is determined solely by the anisotropy parameters K, Γ, and Γ' and corresponds to the eigenvector of the matrix

$$M = \begin{pmatrix} 2K & -\Gamma+2\Gamma' & \Gamma \\ -\Gamma+2\Gamma' & 2K & \Gamma \\ \Gamma & \Gamma & 0 \end{pmatrix} \tag{3}$$

that has the lowest eigenvalue. This minimizes the anisotropic contribution in the classical energy per site of the zigzag phase, $E_{\rm class} = \frac{1}{8}(J-K-3J_3) + \frac{1}{8}\boldsymbol{m}^T M \boldsymbol{m}$, where $\boldsymbol{m}$ is a unit vector. The dominant Kitaev interaction contributing by the diagonal terms makes the main choice—it prefers either the xy plane (FM $K<0$) or the z axis (AF $K>0$). The smaller Γ and Γ' terms lead to a finer selection of the ordered moment direction.

In the case of the zigzag order stabilized by AF $K>0$ and FM $J<0$, the ordered moment direction is close to the z axis being slightly tilted in the ac plane mainly by virtue of Γ [see Fig. 1(c)].

The FM $K<0$ case, where the zigzag order is stabilized by Γ and J_3 terms, is more complex. With $\Gamma=\Gamma'=0$, the entire xy plane is degenerate on a classical level. Further selection depends on the sign of $\Gamma-2\Gamma'$, with the positive and negative sign making the moment to jump into the ac plane or the b axis in the honeycomb plane, respectively. In the former case, an increasing Γ further pushes the moment closer to the honeycomb plane. As it has been found earlier [15,25] and discussed below, the Kitaev term generates an additional magnetic anisotropy due to quantum and/or thermal fluctuations, pinning the moment direction to the cubic axes. This will turn the above jumps into a gradual rotation of the easy axis with changing Γ, along the path shown in Fig. 1(c).

IV. EXTRACTION OF THE MOMENT DIRECTION FROM A CLUSTER GROUND STATE

To determine the ground state of the Hamiltonian (1) and obtain the moment direction as a function of model parameters more rigorously than in the previous perturbative methods, we have performed an exact diagonalization using a hexagon-shaped 24-site supercell covering the honeycomb lattice. This cluster is highly symmetric and compatible with all the hidden symmetries of the model [19] so that no bias induced by the cluster geometry is expected.

Since the cluster ground state does not spontaneously break the symmetry and corresponds to a superposition of all possible degenerate orderings, the identification of the ordered moment direction is not straightforward. One possibility is to evaluate the 3×3 correlation matrix $\langle S^\alpha_{-\boldsymbol{Q}} S^\beta_{\boldsymbol{Q}}\rangle$ $(\alpha,\beta=x,y,z)$ at the ordering vector $\boldsymbol{Q}$ and to take the direction of the eigenvector corresponding to its largest eigenvalue. Because of specific problems of this standard approach in the present context (see Appendix A for details), we have developed here another method that brings a more intuitive picture of the exact ground state by "measuring" the presence of the classical states with a varying moment direction. As a basic building block, we utilize the spin-$\frac{1}{2}$ coherent state

$$|\theta,\phi\rangle = \mathcal{R}_z(\phi)\mathcal{R}_y(\theta)|{\uparrow}\rangle = e^{-i\phi S^z} e^{-i\theta S^y}|{\uparrow}\rangle \tag{4}$$

that is fully polarized along the (θ,ϕ) direction [26]. Here the cubic axes are used as a convenient reference frame and θ and ϕ are the conventional spherical angles. A spin-coherent state on the cluster is constructed as a direct product

$$|\Psi\rangle = \prod_{j=1}^{N} |\theta_j,\phi_j\rangle \tag{5}$$

with the unit vectors $\boldsymbol{m}_j = (\cos\phi\sin\theta, \sin\phi\sin\theta, \cos\theta)_j$ forming the desired pattern. In this fully polarized classical state $\langle\Psi|S^\alpha_i S^\beta_j|\Psi\rangle = \frac{1}{4}m^\alpha_i m^\beta_j$ and the energy $\langle\Psi|\mathcal{H}|\Psi\rangle$ is thus equal to the classical energy. We consider only collinear states of FM, AF, and zigzag type. For example, a FM state with the moment direction (θ,ϕ) is explicitly expressed as

$$|\Psi\rangle = \prod_{j=1}^{N} \left(e^{-i\phi/2}\cos\tfrac{\theta}{2}\,|{\uparrow}\rangle_j + e^{+i\phi/2}\sin\tfrac{\theta}{2}\,|{\downarrow}\rangle_j\right). \tag{6}$$

By varying θ and ϕ and evaluating the overlap with the exact cluster ground state $|\mathrm{GS}\rangle$, we obtain the probability map $P(\theta,\phi) = |\langle\Psi|\mathrm{GS}\rangle|^2$. The ordered moment direction is then identified by locating the maxima of $P(\theta,\phi)$.

There is an intrinsic width of the peaks in $P(\theta,\phi)$ due to the nonzero overlap of the spin-coherent states, namely, $|\langle\Psi|\Psi'\rangle|^2 = \cos^{2N}(\frac{1}{2}\Omega)$, where Ω is the angle between the directions (θ,ϕ) and (θ',ϕ'). This gives an approximate half width at half maximum of $\sqrt{2/N}$ (in terms of the angular distance from the maximum), evaluating to about 17° for $N=24$. Despite this sizable intrinsic width, the ordered moment direction can be detected with a high accuracy (limited only by the accuracy of the ground-state vector), as we see below.

V. MOMENT DIRECTION—EXACT DIAGONALIZATION RESULTS

A. Testing the method: Nearly Heisenberg limit

Before discussing in detail the ordered moment direction in the zigzag phases, relevant for actual compounds Na_2IrO_3 and $RuCl_3$, let us demonstrate the above method by considering the Kitaev-Heisenberg model close to the Heisenberg limit, $|J| \gg |K|$, with both signs of J. In such a situation, the FM or AF order is established by the dominant isotropic interaction, while the anisotropic Kitaev interaction merely selects the easy axis direction via an order-from-disorder mechanism [27].

We start with the FM case $J<0$. Figure 2(a) is the corresponding probability map obtained by the method of Sec. IV for $K/J=0.2$. The probability is clearly peaked at the directions of the cubic axes attaining there the maximum value $P_{\max}$ slightly less than $\frac{1}{6}$. This is due to the cluster ground state being a superposition of six possible classical states and a small contribution of quantum fluctuations. The width of the peaks matches well the intrinsic width estimated in Sec. IV.

That the K term favors cubic axes for the ordered moment follows also from simple analytical calculations. By treating the quantum fluctuations within second-order perturbation

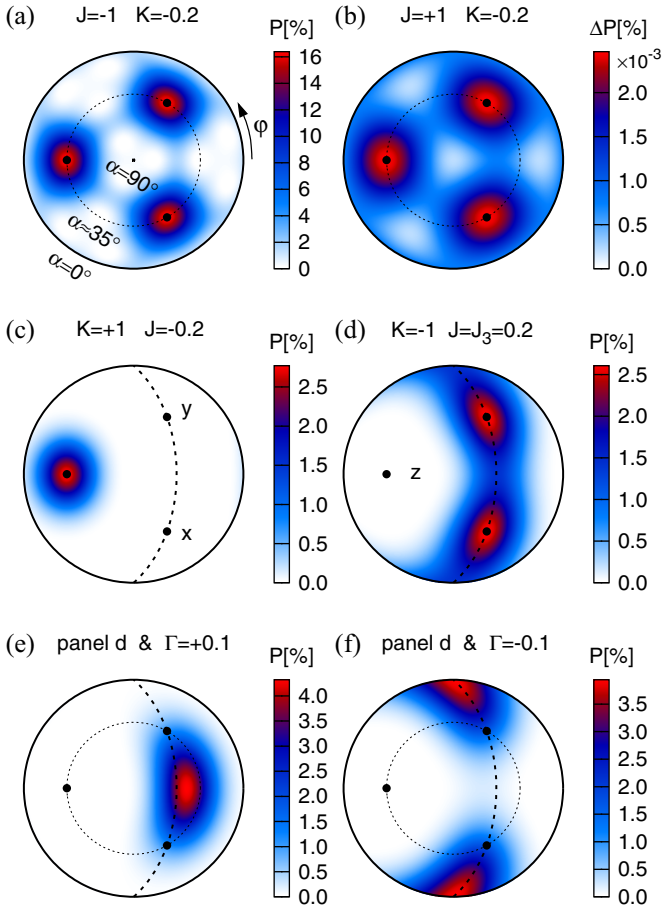

FIG. 2. (a) Map of the probability of the spin-coherent state given by Eq. (6) in the FM ground state of the KH model near the Heisenberg limit. The radial coordinate gives the angle α to the honeycomb plane; the polar angle φ matches that defined in Fig. 1(b). (b) Probability map for the AF ground state obtained using small K and dominant $J > 0$. Only the variation ΔP on top of $P_0 = 2.923\%$ is shown. (c) Probability map for the zigzag phase of the KH model with $K > 0$, $J < 0$ reveals a strong pinning to the z axis. The coherent state corresponding to the zigzag pattern in Fig. 1(b) was used. Directions lying in the xy plane are indicated by the dashed line. (d) Soft xy plane for FM $K < 0$ zigzag stabilized by J_3. Cubic axes x and y are selected but the moment strongly fluctuates in the plane. (e,f) The same as in panel (d) but extended by a sizable Γ term forcing the moment into the ac plane (left) or the b axis (right).

expansion (see Ref. [28] for details), we obtain the magnetic anisotropy energy

$$\delta E^{(2)}_{\rm FM} \approx \frac{K^2}{64|J|}\left(1 - m_x^4 - m_y^4 - m_z^4\right), \qquad (7)$$

depending on the moment direction given by a unit vector $\boldsymbol{m} = (m_x, m_y, m_z)$. This quantum correction on top of the isotropic classical energy is minimized for $\boldsymbol{m}$ pointing along the cubic axes x, y, and z that become the easy axes, consistent with the ED result.

The case of the AF $J > 0$ is rather different due to the presence of large quantum fluctuations already in the Heisenberg limit. This is manifested in an almost flat probability profile with P of about 3% [see Fig. 2(b)]. Nevertheless, the probability maxima again precisely locate the x, y, and z directions for the ordered moments, consistent with the "order-from-disorder" calculations [15,25,28–30] in the models containing compass- or Kitaev-type bond-directional anisotropy.

B. Moment direction in the zigzag phases

Having verified the method, we now move to the zigzag phases observed in Na_2IrO_3 and $RuCl_3$. We first inspect the case of $\Gamma, \Gamma' = 0$ when the anisotropy is due to the Kitaev term alone. Shown in Fig. 2(c) is the probability map for AF $K > 0$ and FM $J < 0$, where the z axis is selected already on the classical level as discussed in Sec. III [31]. The probability is indeed strongly peaked at the direction of the z axis. The small $P_{\rm max}$ of about 3% is again a signature of large quantum fluctuations in the ground state. Note that this number contains an overall reduction factor of $\frac{1}{6}$ due to the six possible zigzag states being superposed in the cluster ground state.

The probability map Fig. 2(d) for the FM $K < 0$ zigzag case reveals the moment being constrained to the vicinity of the xy plane, as expected from classical considerations. Within this plane, the order-from-disorder mechanism selects the cubic axes x and y where the probability reaches its maxima. Concluding the survey of the probability maps, we show P calculated including a large enough Γ that leads to the selection of a direction within the ac plane [$\Gamma > 0$, Fig. 2(e)] or the b axis [$\Gamma < 0$, Fig. 2(f)].

The above three examples for the FM K zigzag indicate a rather complex behavior of the moments in this case, as already suggested in Fig. 1(c). In the following, we therefore focus on the full Γ dependence presented in Fig. 3(a) in the form of the angles $\alpha(\Gamma)$ (the angle to the honeycomb plane) and $\varphi(\Gamma)$ (polar angle of the projection into the honeycomb plane). Instead of the jump in $\alpha(\Gamma)$ obtained on a classical level, we find a finite window $|\Gamma| \lesssim 0.05|K|$ of an order-from-disorder stabilized phase, where the moment direction gradually moves from the cubic axis ($\Gamma = 0$) to either the b axis ($\Gamma < 0$) or the ac plane ($\Gamma > 0$). Once the critical value of Γ is reached, the moment either stays along the b axis or is pushed down within the ac plane closer to the honeycomb plane. Figure 3(b) illustrates the evolution of $\alpha(\Gamma)$ for different values of J_3 stabilizing the zigzag order. For small J_3, the dominant directional Kitaev term makes the moment more pinned to the cubic axes, which is manifested by a significantly reduced slope of $\alpha(\Gamma)$ near $\Gamma = 0$ compared to the large-J_3 case. On the other hand, the critical values of Γ are only slightly affected by J_3.

The above crossover behavior near $\Gamma = 0$ may be easily understood and even semiquantitatively reproduced by considering a competition of the classical energy and the order-from-disorder potential as follows. Keeping the moment $\boldsymbol{m} = (\cos\phi, \sin\phi, 0)$ within the xy plane preferred by $K < 0$, we can evaluate the classical energy per site:

$$E_{\rm class} = \tfrac{1}{8}(K - 3J_3 + J) - \tfrac{1}{8}(\Gamma - 2\Gamma')\sin 2\phi. \qquad (8)$$

In this contribution, the anisotropy is due to the Γ and Γ' terms only. $E_{\rm class}$ is complemented by an order-from-disorder potential $E_{\rm fluct}(\phi)$ that should contain four equivalent minima at $\phi = 0, \frac{1}{2}\pi, \pi, \frac{3}{2}\pi$ corresponding to the cubic axes (supported by the K term). Such a potential can be represented by the

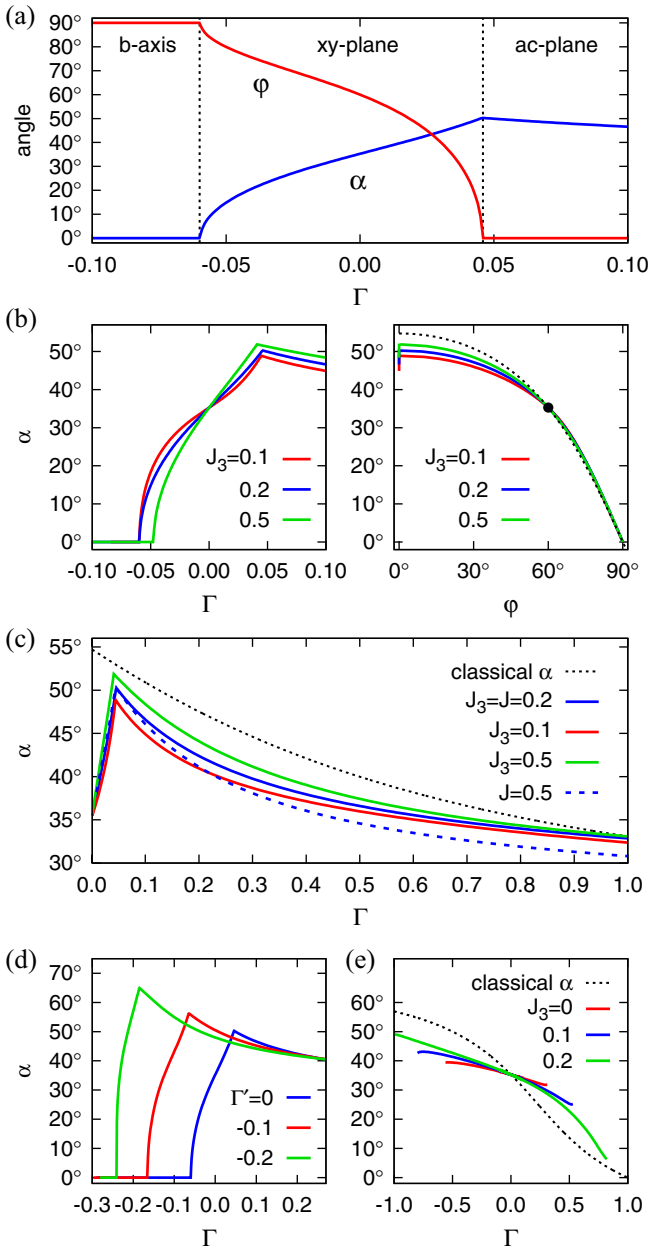

FIG. 3. (a) Γ-dependent angles α, φ specifying the moment direction reveal three regimes for FM K zigzag supported by small J_3. The values $K=-1$ and $J=J_3=0.2$ were used. At $\Gamma=0$, the angles give the direction towards an oxygen ion. A crossover in the interval $|\Gamma| \lesssim 0.05$ corresponds to the path shown in Fig. 1(c). (b) Left panel shows the angle α for $K=-1$, $J=0.2$ and several J_3 values manifesting a stronger pinning to the cubic axis at smaller J_3. The same data are presented as $\alpha(\varphi)$ in the right panel together with $\alpha(\varphi)$ corresponding to the xy plane (dashed). The black dot indicates the cubic axis direction. (c) The angle α for larger values of $\Gamma>0$ compared to the classical result of Ref. [19] (dotted). The blue solid curve is a continuation of that of panel (a), red and green curves are calculated using different J_3 values used in panel (b), and the blue dashed curve denotes a larger J value. (d) The angle α for the parameters $K=-1$, $J=J_3=0.2$, and several Γ' values. (e) Γ-dependent α in the AF $K=+1$ case with $J=-0.2$ and several J_3 values compared to the classical result of Ref. [19] (dotted). The endpoints of the curves are determined by a sharp drop of the probability of the classical zigzag state indicating a phase boundary.

following form:

$$E_{\text{fluct}} = V \sin^2 2\phi, \tag{9}$$

approximating $E_{\text{fluct}}(\phi)$ by its lowest harmonic. This function is characterized by a single unknown parameter—the barrier height V, determined mainly by the dominant K. Assuming $\Gamma'=0$, the minimization of the total energy $E_{\text{class}}+E_{\text{fluct}}$ gives $\phi(\Gamma)=\frac{1}{2}\arcsin\frac{\Gamma}{16V}$ and the critical value $\Gamma_{\text{crit}}=16V$. This enables us to extract effective V from our numerical data. By taking $\Gamma_{\text{crit}}\approx 0.05|K|$ observed in Figs. 3(a) and 3(b) we get $V\approx 0.003|K|$. Furthermore, converting ϕ in the xy plane to the angle α to the honeycomb plane, we obtain "phenomenological" $\alpha(\Gamma)=\arcsin\sqrt{\frac{1}{3}(1+\frac{\Gamma}{16V})}$ that roughly approximates the numerical $\alpha(\Gamma)$ data. The agreement between these two $\alpha(\Gamma)$ profiles improves with increasing J_3, when the order-from-disorder potential becomes more harmonic and the deviation of the moment direction from the xy plane for $\Gamma>0$ reduces [see Fig. 3(b)]. In fact, Eqs. (8) and (9), together with the value of $V\approx 0.003|K|$ extracted from the ED data, may be used for a semiquantitative determination of the easy axis direction within the xy plane.

For curiosity, we have evaluated the potential barrier V also analytically, by two slightly different methods. First, as in Sec. V A, we estimated quantum corrections for the zigzag phase along the lines of Ref. [28]. This reproduced the above form (9) of the anisotropy potential, and provided a consistent estimate of $V\approx 0.005|K|$. An alternative evaluation of the anisotropy potential within the linear spin-wave framework resulted in zero-point energy of the same form as Eq. (9) again, but with an overestimated value of $V\approx 0.014|K|$.

In Na_2IrO_3 the moment direction was found [12] in the ac plane suggesting that $\Gamma>\Gamma_{\text{crit}}$ for this material. We thus focus on this particular case and investigate how the precise value of α is affected by the model parameters in more detail. Already on a classical level, finite $\Gamma>0$ rotates the moment within the ac plane from $\alpha\approx 54.7^\circ$ (corresponding to the xy plane) toward the honeycomb plane ($\alpha=0$). Such an effect is well visible also in Figs. 3(a) and 3(b). Presented in Fig. 3(c) are a few representative $\alpha(\Gamma)$ curves for larger values of Γ up to $|K|$ that serve as a test of the classical prediction

$$\tan 2\alpha = 4\sqrt{2}\,\frac{1+r}{7r-2} \quad \text{with} \quad r=-\frac{\Gamma}{K+\Gamma'} \tag{10}$$

derived in Ref. [19]. As we find, the quantum fluctuations included in the exact ground state push the ordered moments much closer to the honeycomb plane. The difference is substantial and needs to be considered when trying to quantify the model parameters based on the experimental data.

So far, we have considered $\Gamma'=0$ only, while a small negative Γ' is expected to be generated by a trigonal compression [18,19,32]. Based on Eq. (8), Γ' is expected to effectively shift the value of Γ in the first approximation. Indeed, as shown in Fig. 3(d), the rough three-phase picture as in Fig. 3(a) is preserved and the negative Γ' shifts the $\alpha(\Gamma)$ curve in the negative direction. This enables α to reach higher values, even above the xy-plane angle 54.7°.

Finally, in Fig. 3(e) we briefly analyze the AF K situation with the moment near the z axis. In contrast to the FM K case, small Γ has a relatively little effect here, because the z axis

is classically selected by the dominant $K > 0$ itself. Quantum fluctuations are found to generate an even stronger pinning to the z axis, compared to the classical solution of Ref. [19]. Only a very large Γ coupling is able to take the spin away from the z axis.

VI. COMPARISON TO EXPERIMENT

A. Extracting pseudospin direction from resonant x-ray and neutron-scattering data

Having quantified the pseudospin easy axis direction as a function of the Hamiltonian parameters, we consider now how this "pseudomoment" direction is related to that of real magnetic moments measured by neutron-scattering and x-ray scattering experiments. To this end, we first define the pseudospin one-half wave functions including crystal field of trigonal symmetry. The latter splits the t_{2g} manifold into an orbital singlet $a_{1g} = \frac{1}{\sqrt{3}}(xy + yz + zx)$ and the e'_g doublet $\{\frac{1}{\sqrt{6}}(yz + zx - 2xy)\,;\ \frac{1}{\sqrt{2}}(zx - yz)\}$. Denoting this splitting by Δ and using the hole representation, we have

$$H = \Delta\, \tfrac{1}{3}[2n(a_{1g}) - n(e'_g)]. \tag{11}$$

Within a point-charge model, positive (negative) Δ would correspond to a compression (elongation) of octahedra along the trigonal c axis. The actual value of Δ in real material is decided by various factors, but this issue is not relevant in the present context.

In terms of the effective angular momentum $l = 1$ of the t_{2g} shell, the a_{1g} state corresponds to the $l_c = 0$ state, while the e'_g doublet hosts the $l_c = \pm 1$ states, using the quantization axis c suggested by the trigonal crystal field. Explicitly,

$$|0\rangle = \frac{1}{\sqrt{3}}(|yz\rangle + |zx\rangle + |xy\rangle), \tag{12}$$

$$|\pm 1\rangle = \pm\frac{1}{\sqrt{3}}(e^{\pm 2\pi i/3}|yz\rangle + e^{\mp 2\pi i/3}|zx\rangle + |xy\rangle). \tag{13}$$

Via these l_c states, pseudospin-$\frac{1}{2}$ wave functions are defined as

$$\left|+\tfrac{1}{2}\right\rangle = +\sin\vartheta\ |0,\uparrow\rangle - \cos\vartheta\ |+1,\downarrow\rangle, \tag{14}$$

$$\left|-\tfrac{1}{2}\right\rangle = -\sin\vartheta\ |0,\downarrow\rangle + \cos\vartheta\ |-1,\uparrow\rangle, \tag{15}$$

where $\uparrow$ and $\downarrow$ refer to the projections of the hole spin on the trigonal c axis. The spin-orbit "mixing" angle $0 \leqslant \vartheta \leqslant \pi/2$ is given by $\tan 2\vartheta = 2\sqrt{2}/(1+\delta)$, where $\delta = 2\Delta/\lambda$.

Using the wave functions (14) and (15), we may express the spin $\boldsymbol{s}$ and orbital $\boldsymbol{l}$ moments of a hole via the pseudospin $\boldsymbol{S}$. In a cubic limit, i.e., $\Delta = 0$, one has $\boldsymbol{s} = -\frac{1}{3}\boldsymbol{S}$, $\boldsymbol{l} = \frac{4}{3}\boldsymbol{S}$, and total magnetic moment $\boldsymbol{M} = (2\boldsymbol{s} - \boldsymbol{l}) = -2\boldsymbol{S}$ (note a negative g factor $g = -2$). These relations imply that the pseudospin easy axis direction is identical to that of spin, orbital, and magnetic moments when the trigonal field is zero. However, this is no longer valid at finite Δ. For instance, strong compression ($\vartheta = 0$) would completely suppress the ab-plane components of magnetic moments, so the pseudospin and magnetic moment will not be parallel anymore (unless pseudospin is ordered along the c axis).

The x rays and neutrons couple initially to the spin and orbital moments, and the scattering operator has to be projected onto the pseudospin basis. We first consider an effective RXS operator. For pseudospin one-half in a trigonal field, it has to have a form $\hat{R} \propto i f_{ab}(P_a S_a + P_b S_b) + i f_c P_c S_c$, where $\boldsymbol{P} = \boldsymbol{\varepsilon} \times \boldsymbol{\varepsilon}'$ and $\boldsymbol{\varepsilon}$ ($\boldsymbol{\varepsilon}'$) is the polarization of the incoming (outgoing) photon. This can be written as $\hat{R} \propto i\,\boldsymbol{P} \cdot \boldsymbol{N}$, introducing a vector $\boldsymbol{N} = (f_a S_a, f_b S_b, f_c S_c)$ with $f_a = f_b \equiv f_{ab}$. The RXS data determine a direction of this auxiliary vector $\boldsymbol{N}$; in Na_2IrO_3, it was found to make an angle $\alpha_N \approx 44.3^\circ$ to the ab plane [12]. However, this is not yet the pseudospin direction, since $f_{ab} \neq f_c$ and hence $\alpha_S \neq \alpha_N$, unless the trigonal field is exactly zero (unlikely in real materials). To access the pseudospin angle α_S and quantify the model parameters, one has to know the "RXS factors" f_{ab} and f_c.

We have derived the f factors (see Appendix B for details). For the L_3 edge, they read as

$$f_{ab} = \frac{1}{2} + \frac{5}{6\sqrt{2}}\, s_{2\vartheta} - \frac{1}{6}\, c_{2\vartheta}, \tag{16}$$

$$f_c = 1 + \frac{2}{3}\, c_{2\vartheta} - \frac{1}{3\sqrt{2}}\, s_{2\vartheta}. \tag{17}$$

Here, $s_{2\vartheta} = 2\sqrt{2}/r$, $c_{2\vartheta} = (1+\delta)/r$, and $r = \sqrt{8 + (1+\delta)^2}$. Figure 4(a) shows the f factors as a function of trigonal field parameter δ. In the cubic limit, one has $f_{ab} = f_c$ and hence $\boldsymbol{N}$ is parallel to $\boldsymbol{S}$, as expected.

For completeness, we show also the f factors for the L_2 edge:

$$f_{ab} = 2f_c = -\tfrac{3}{2} + \tfrac{1}{2}\, c_{2\vartheta} + \sqrt{2}\, s_{2\vartheta}, \tag{18}$$

which vanish at the $\delta = 0$ limit, as a consequence of the spin-orbit entangled nature of pseudospins [33].

In neutron-diffraction experiments, the magnetic moment $\boldsymbol{M} = (g_a S_a, g_b S_b, g_c S_c)$ is probed. For the pseudospins as defined above, the g factors are (neglecting covalency effects [7])

$$g_{ab} = -(1 + \sqrt{2}\, s_{2\vartheta} - c_{2\vartheta}), \tag{19}$$

$$g_c = -(1 + 3\, c_{2\vartheta}). \tag{20}$$

The g-factor anisotropy can quantify the strength of the trigonal field, as illustrated in Fig. 4(b). Again, magnetic moment direction is in general different from that of pseudospin, and to access the latter one needs to know the g factors.

These considerations imply that the orientations of the (x-ray) $\boldsymbol{N}$ vector and magnetic moment $\boldsymbol{M}$ differ from each other, and also from that of pseudospin $\boldsymbol{S}$ which enters the model Hamiltonian. As we show in Fig. 4(c), their relative angles come in the order $\alpha_M > \alpha_N > \alpha_S$ for positive Δ, and in reversed order $\alpha_S > \alpha_N > \alpha_M$ for negative Δ. Ideally, having measured both $\boldsymbol{N}$ and $\boldsymbol{M}$ directions in the same compound, one could extract the crystal-field parameter δ using the above equations, and uniquely fix the pseudospin easy axis angle α_S. In principle, the g-factor anisotropy provides the same information on δ, but obtaining g factors in magnetically concentrated systems is a somewhat nontrivial task. Alternatively, one could extract the value and sign of Δ directly from the splitting and anisotropy of the high-energy $J = 3/2$ quartet in single crystals (see Appendix C for details).

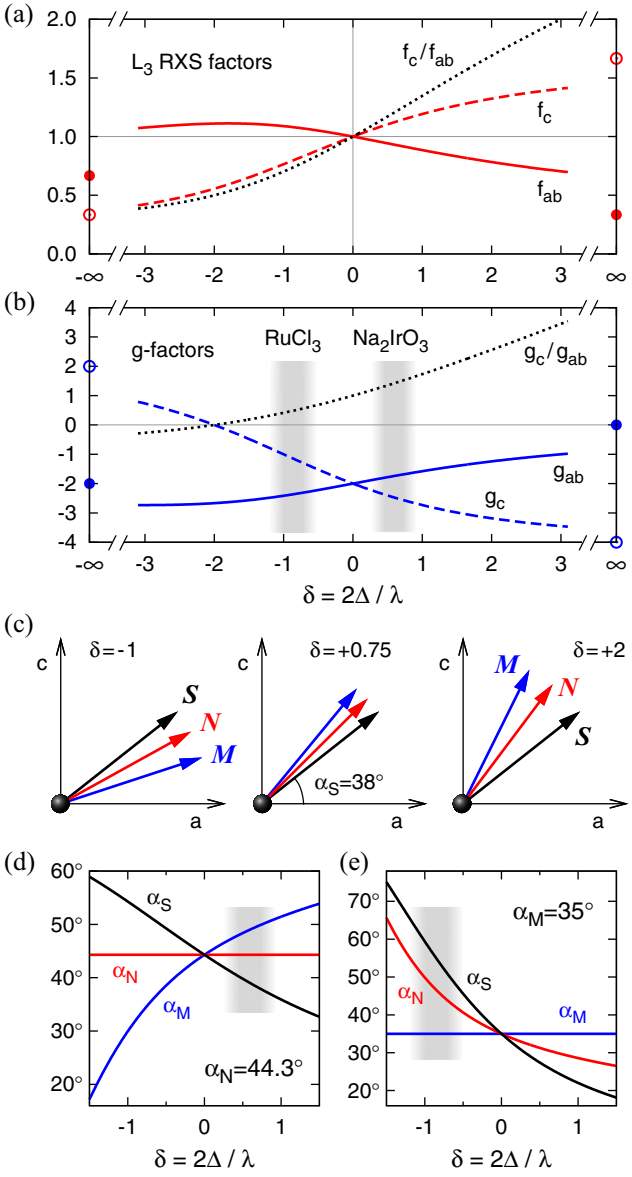

FIG. 4. (a) Factors f entering the relation between the pseudospin $\boldsymbol{S}$ and L_3 RXS vector $\boldsymbol{N}$ presented as functions of the trigonal field. (b) g factors as functions of the trigonal field. Intervals of δ consistent with the g factors suggested by the experimental data on $RuCl_3$ [34,35] and Na_2IrO_3 [36,37] are indicated by shading. (c) Directions of the $\boldsymbol{S}$, $\boldsymbol{N}$, and $\boldsymbol{M}$ vectors for sample values of the trigonal field parameter δ and a fixed pseudospin angle $\alpha_S = 38°$. The case with the negative $\delta = -1$ could be relevant for $RuCl_3$, while positive $\delta = +0.75$ with the reverse order of the vectors $\boldsymbol{M}$, $\boldsymbol{N}$, and $\boldsymbol{S}$ for Na_2IrO_3. (d),(e) Angles α_S, α_N, and α_M of the vectors $\boldsymbol{S}$, $\boldsymbol{N}$, and $\boldsymbol{M}$ to the honeycomb plane as functions of δ keeping fixed $\alpha_N = 44.3°$ (d) or $\alpha_M = 35°$ (e). The shaded δ intervals are the same as in panel (b).

B. Implications for Na_2IrO_3 and $RuCl_3$

Armed with the above relations between different moments, and using the results of Sec. V B, let us now analyze the available experimental data on Na_2IrO_3 and $RuCl_3$.

Starting with the case of Na_2IrO_3, we utilize the value $\alpha_N \approx 44.3°$ determined recently by RXS [12]. Keeping this experimental constraint, in Fig. 4(d) we plot the remaining angles α_M and α_S as functions of the relative strength of the trigonal crystal field δ. In Ref. [19], the value $\Delta/\lambda \approx 3/8$ was deduced based on the splitting $\Delta_{BC} \approx 0.1$ eV of the $J = 3/2$ quartet [37]. As seen in Fig. 4(b), the corresponding $\delta \approx 0.75$ is also roughly consistent with the anisotropy of the g factors, $g_c/g_{ab} \approx 1.4$, obtained by fitting the temperature-dependent magnetic susceptibilities $\chi_c > \chi_{ab}$ [36]. The data in Fig. 4(d) then suggest that the magnetic moment takes an angle of about $\alpha_M \approx 50°$ to the honeycomb plane, while the pseudospin angle α_S is roughly 38–40°. Such a deviation of the pseudospin from the xy plane ($\alpha \approx 54.7°$) implies a sizable Γ value. Based on Fig. 3(c) we may naively expect the $\Gamma/|K|$ ratio in the range 0.3–0.5. We emphasize, however, that this conclusion relies on the above estimate of the trigonal field, that should be verified by measuring the "magnetic" angle α_M directly by neutron scattering.

Compared to Na_2IrO_3, $RuCl_3$ shows an opposite magnetic anisotropy behavior with $\chi_c \ll \chi_{ab}$ [34]. The magnetic structure has been recently investigated by neutron scattering [38], with the result $\alpha_M \approx 35°$ and φ being equal to either 0 or 180°. Similarly to Fig. 4(d), in Fig. 4(e) we keep the measured angle, now α_M, fixed at its experimental value, and plot α_S and α_N for varying $\delta = 2\Delta/\lambda$. This parameter could be obtained from the anisotropy of $J = 3/2$ transitions in single crystals (see Appendix C). We are not aware of such a direct measurement in $RuCl_3$, so the trigonal field is best assessed by considering the anisotropy of the g factors. References [34,35] reported in-plane and out-of-plane magnetization curves measured for high fields up to 60 T. Even though the saturation was not reached, the data indicate the value $g_c/g_{ab} \approx 0.4$–0.5. A similar ratio was also found by Yadav *et al.* [39] using quantum chemistry methods and by fitting the high-field data of Ref. [35]. The corresponding δ puts the pseudospin angle α_S at relatively high values of about $\alpha_S \gtrsim 50°$ [see Fig. 4(e)]. Adopting this estimate, we will try to identify a consistent parameter window.

Unfortunately, the present neutron experiment [38] could not directly resolve the orientation of the moments with respect to the a axis, i.e., whether $\varphi = 0$ or 180°. The absence of this most conclusive evidence for the sign of the Kitaev interaction requires us to consider both possibilities.

We assume first FM $K < 0$ as obtained in two recent *ab initio* calculations of the exchange interactions in $RuCl_3$ [24,39]. Figure 3(c) gives a hint that the estimated $\alpha_S \gtrsim 50°$ can be reached for small Γ only. As seen in Fig. 3(d), by including small negative Γ' that shifts the crossover towards negative Γ, the pseudospin direction may rotate even far above the xy plane. Interestingly, the corresponding parameter regime $J \sim -\Gamma \sim -\Gamma' \sim 0.2|K|$ matches well the prediction by quantum chemistry calculations [39].

Now we analyze the AF $K > 0$ case, proposed for $RuCl_3$ in Refs. [13,38,40]. In this case, the zigzag order is obtained on the level of the two-parameter Kitaev-Heisenberg model [20] alone, and this simplicity makes the AF K scenario particularly attractive. In the zigzag phase of the two-parameter model, the pseudospins point along the cubic z axis leading to $\alpha_S \approx 35°$. This can be reconciled with the experimental value $\alpha_M \approx 35°$ only in a nearly cubic situation with a small trigonal distortion. Considering, however, the large anisotropy of the g factors

discussed above and the resulting $\alpha_S \gtrsim 50^\circ$, it seems that the AF Kitaev interaction needs to be supplemented by other anisotropic interactions lifting the pseudospin considerably up. This scenario is addressed in Fig. 3(e). We have found that Γ' does not influence α_S much so that we focus on the Γ dependence. Since the AF K zigzag phase becomes fragile if the other anisotropy terms are included, the model has to be additionally extended by J_3. Based on the data of Fig. 3(e), we may conclude that large negative Γ comparable to K is needed to obtain $\alpha_S \gtrsim 50^\circ$. It should be carefully checked if such a substantially extended model is still consistent with other experimental data, in particular with the spin excitation spectrum with only small gaps [13].

We would like to stress again that our analysis of $RuCl_3$ for both $K < 0$ and $K > 0$ heavily relied on the relative trigonal field strength Δ/λ inferred solely from the magnetization anisotropy in high magnetic fields. It is thus highly desirable to measure the complementary angle α_N by RXS and quantify Δ/λ more precisely, as suggested in the previous subsection. As discussed in Appendix C, measuring the anisotropy of $J = 3/2$ states by inelastic neutron scattering in single crystals would be also very helpful.

To summarize this section, in Na_2IrO_3, the measured moment direction [12] with $\varphi = 0^\circ$ well fixes the FM sign of the Kitaev interaction, and our analysis of its angle from the ab plane suggests that $\Gamma \sim 0.3 - 0.5|K|$ coupling is present. Concerning $RuCl_3$, the current ambiguity in the angle φ (0 or 180°) leaves open the issue of the sign of K. There is also an uncertainty in the trigonal field value Δ; based so far on the g-factor anisotropy, we found that FM $K < 0$ with relatively small Γ and Γ' values would be consistent with the data, while the AF $K > 0$ situation requires large $\Gamma < 0$ couplings comparable to K.

VII. CONCLUSIONS

We have investigated the ordered moment direction in the zigzag phases of the extended Kitaev-Heisenberg model for honeycomb lattice magnets. Our method analyzes the exact cluster ground states using a particular set of spin coherent states and as such fully accounts for the quantum fluctuations. The interplay among the various anisotropic interactions leads to a complex behavior of the ordered moment direction as a function of the model parameters. We have found substantial corrections to the results of a classical analysis that are important when quantifying the exchange interactions based on the experimental data.

We have pointed out that, away from the ideal cubic situation, the notion of the "ordered moment direction" has to be precisely specified. Assuming a trigonal field relevant to the layered honeycomb systems, we have derived relations among the directions of (i) the pseudospins entering the model Hamiltonian, (ii) the magnetic moments measured by neutron diffraction, and (iii) the moment direction as probed by resonant magnetic x-ray scattering. These relations and a combination of neutron and x-ray data should enable a reliable quantification of the trigonal field as well as the pseudospin direction in future experiments.

Using the above results, we have analyzed the currently available experimental data on Na_2IrO_3 and $RuCl_3$ and identified plausible parameter regimes in these compounds.

ACKNOWLEDGMENTS

We would like to thank G. Jackeli, B. J. Kim, S. E. Nagler, and J. Rusnačko for helpful discussions. J.C. acknowledges support by Czech Science Foundation (GAČR) under Project No. GJ15-14523Y and MŠMT ČR under NPU II project CEITEC 2020 (Project No. LQ1601).

APPENDIX A: COMPARISON OF NUMERICAL METHODS

As mentioned in the main text, the standard method to obtain the ordered moment direction using the ED ground state is to evaluate the spin-spin correlation matrix $\langle S^\alpha_{-\boldsymbol{Q}} S^\beta_{\boldsymbol{Q}}\rangle$ $(\alpha,\beta = x,y,z)$ at the ordering vector $\boldsymbol{Q}$ and to find its eigenvector corresponding to the largest eigenvalue. However, there are two main problems associated with this simple method, both emerging since the cluster ground state is a linear superposition of degenerate orderings where the individual orderings have equal weights.

(i) If there are several equivalent easy axis directions associated with the selected ordering vector $\boldsymbol{Q}$, they will be characterized by the same eigenvalue. This leads to a degenerate eigenspace and prevents us from resolving such directions. The most severe cases are those with a dominant Heisenberg interaction presented in Figs. 2(a) and 2(b). Here we have three degenerate easy axes x, y, and z which makes the correlation matrix proportional to a unit matrix and thus isotropic. In the FM $K < 0$ zigzag situation shown in Fig. 2(d) and the entire middle phase in Fig. 3(a), two degenerate moment directions for a particular zigzag pattern (selected by $\boldsymbol{Q}$) are possible and the correlation matrix therefore just uncovers the softness of the xy plane. Only after these two directions merge for a large enough $|\Gamma|$, the moment direction can be identified.

(ii) The zigzag pattern to be probed is selected by choosing the ordering vector $\boldsymbol{Q}$. In contrast to an infinite lattice, at a finite cluster this separation of the three zigzag directions is

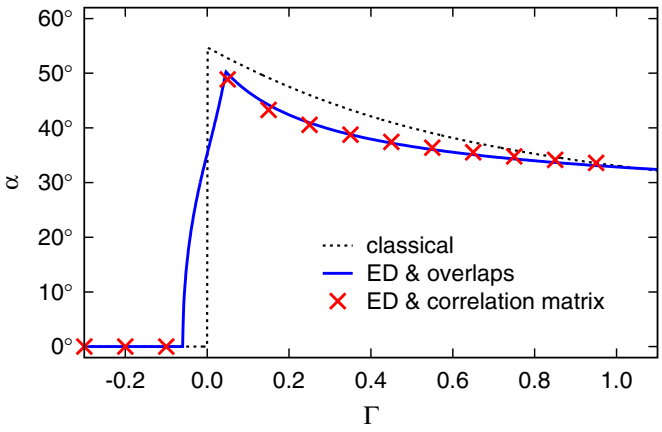

FIG. 5. Comparison of the angle α of the pseudospin direction to the ab plane obtained using various methods. The parameters $K = -1$ and $J = J_3 = 0.2$ were used. The blue curve is identical to the one shown in Figs. 3(a)–3(d).

not perfect. The range of spin correlations is limited by the size of the cluster and the corresponding momentum space peaks become broad. The correlation matrix at given $\boldsymbol{Q}$ is thus "polluted" by small contributions of the two other zigzags in the ground state, that are associated with the remaining ordering vectors.

Our method introduced in Sec. IV does not suffer from the above problems and is able to handle all the situations encountered. This is due to the full resolution of the various degenerate orderings present in the cluster ground state by using a prescribed ordering pattern and by a construction of a full directional map.

If applicable, the standard method gives results very similar to our method. We demonstrate this in Fig. 5 that compares the two methods for the parameters $K = -1$, $J = J_3 = 0.2$ and varying Γ used in Fig. 3. The slight deviations observed for $\Gamma > 0$ can be interpreted as a manifestation of the second problem discussed above.

APPENDIX B: DERIVATION OF THE L-EDGE RXS OPERATOR

Resonant x-ray scattering is conceptually similar to the Raman light scattering, in a sense that both processes involve the intermediate states created and subsequently eliminated by incoming and outgoing photons. However, the nature of the intermediate states in these two cases is radically different: while the Raman light scattering involves intersite d-d transitions, the x rays create the high-energy on-site p-d transitions. As a result, the Raman light scattering probes intersite (two-magnon) spin flips, while the presence of a strong spin-orbit coupled $2p$-core hole in the RXS intermediate states makes single-ion spin flips a dominant magnetic scattering channel (see the recent review [41] and references therein for details).

A complex time dynamics of the intermediate states makes the x-ray-scattering process hard to analyze microscopically. However, as far as one is concerned with the low-energy excitations in Mott insulators, the problem of the intermediate states can be disentangled and cast in the form of frequency-independent phenomenological constants [42–44]. This results is an effective RXS operator formulated in terms of low-energy (orbital, spin, etc.) degrees of freedom alone. The form of this operator is dictated by symmetry. In essence, this approach is similar to that of Fleury and Loudon [45] widely used in the theories of Raman light scattering in quantum magnets.

While the RXS operator used in the main text follows from an underlying trigonal symmetry, the ratio between f_{ab} and f_c constants requires specific calculations. This can be easily done, with some routine modifications of the previous work for the case of tetragonal symmetry [46,47], as outlined below.

In cubic axes x, y, and z (see Fig. 1), a dipolar $2p$ to $5d$ transition operator reads as

$$D = \varepsilon_x T_x + \varepsilon_y T_y + \varepsilon_z T_z, \tag{B1}$$

where $\varepsilon_{x,y,z}$ are the polarization factors, and $T_x = d^\dagger_{zx} p_z + d^\dagger_{xy} p_y$, $T_y = d^\dagger_{xy} p_x + d^\dagger_{yz} p_z$, $T_z = d^\dagger_{yz} p_y + d^\dagger_{zx} p_x$. Here and below, it is implied that d and p operators carry also the spin quantum numbers $(\uparrow, \downarrow)$ over which summation is taken.

In the quantization axes a, b, and c, suggested by the trigonal crystal field, this operator takes the following form:

$$D = \frac{1}{\sqrt{6}}(\varepsilon_a T_a + \varepsilon_b T_b + \varepsilon_c T_c), \tag{B2}$$

where

$$\begin{aligned} T_a &= (d^\dagger_0 + 2d^\dagger_{-1})p_1 + (d^\dagger_1 - d^\dagger_{-1})p_0 + (2d^\dagger_1 - d^\dagger_0)p_{-1}, \\ iT_b &= (-d^\dagger_0 + 2d^\dagger_{-1})p_1 + (d^\dagger_1 + d^\dagger_{-1})p_0 - (2d^\dagger_1 + d^\dagger_0)p_{-1}, \\ T_c &= \sqrt{2}\,(2d^\dagger_0 p_0 - d^\dagger_1 p_1 - d^\dagger_{-1} p_{-1}). \end{aligned} \tag{B3}$$

Here, the indices 0 and ± 1 stand for the l_c orbital quantum numbers of d and p electrons.

Within the above Fleury-Loudon-like approach to the x-ray-scattering problem, the effective RXS operator is given by $D^\dagger(\varepsilon')D(\varepsilon)$, and its part responsible for the magnetic scattering reads as $\hat{R} \propto i(\boldsymbol{\varepsilon} \times \boldsymbol{\varepsilon}') \cdot (\boldsymbol{T}^\dagger \times \boldsymbol{T})$.

Next, the core-hole operators p in Eq. (B3) are expressed in terms of spin-orbit split $j = 1/2$ and $3/2$ eigenstates of the $2p$ level, resulting in two sets of $\boldsymbol{T}$ operators active in L_2 and L_3 edges, correspondingly. After "integrating out" these $2p_{\frac{1}{2}}$ and $2p_{\frac{3}{2}}$ operators, the product $(\boldsymbol{T}^\dagger \times \boldsymbol{T})$ becomes a simple quadratic form of d operators. Finally, projecting this form onto a pseudospin doublet [given by Eqs. (14) and (15) of the main text], we arrive at the RXS operator $\hat{R} \propto i f_{ab}(P_a S_a + P_b S_b) + i f_c P_c S_c$, with the f factors shown in the main text. Via the pseudospin wave functions, the RXS f factors are sensitive to a trigonal field strength.

APPENDIX C: DETERMINATION OF THE TRIGONAL FIELD FROM $J = 3/2$ MAGNETIC EXCITATION SPECTRA

Under spin-orbit coupling λ and trigonal crystal field Δ, t_{2g}-hole states split into three levels A, B, and C [see Fig. 6(a)]. The A level hosts a Kramers pseudospin one-half (corresponding to $J = 1/2$ in the cubic limit), with the wave functions

$$|A_+\rangle = +\sin\vartheta\,|0,\uparrow\rangle - \cos\vartheta\,|+1,\downarrow\rangle, \tag{C1}$$

$$|A_-\rangle = -\sin\vartheta\,|0,\downarrow\rangle + \cos\vartheta\,|-1,\uparrow\rangle, \tag{C2}$$

as were given by Eqs. (14) and (15) of the main text. The upper Kramers doublets B and C are derived from the spin-orbit $J = 3/2$ quartet. The former correspond to pure $J_c = \pm 3/2$ states of $J = 3/2$ moment:

$$|B_+\rangle = |+1,\uparrow\rangle, \tag{C3}$$

$$|B_-\rangle = |-1,\downarrow\rangle, \tag{C4}$$

while the C level wave functions are given by

$$|C_+\rangle = \cos\vartheta\,|0,\uparrow\rangle + \sin\vartheta\,|+1,\downarrow\rangle, \tag{C5}$$

$$|C_-\rangle = \cos\vartheta\,|0,\downarrow\rangle + \sin\vartheta\,|-1,\uparrow\rangle, \tag{C6}$$

corresponding to $J_c = \pm 1/2$ states of the $J = 3/2$ quartet in the cubic limit, and containing some admixture of

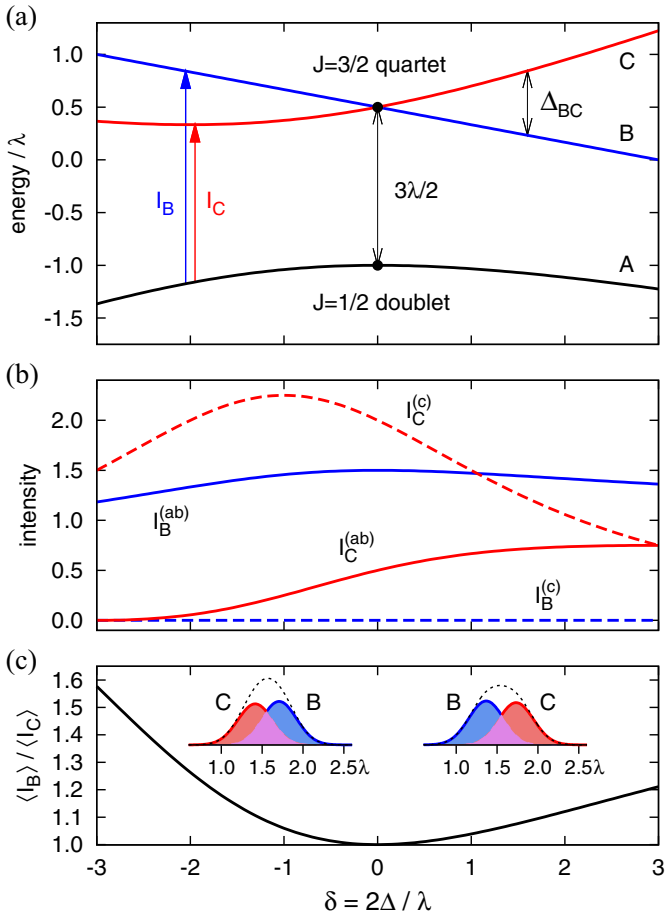

FIG. 6. (a) Level structure of a $d^5(t_{2g})$ ion upon trigonal field splitting characterized by $\delta = 2\Delta/\lambda$ (hole picture). (b) Intensities of the magnetic transitions $A \to B$ and $A \to C$ for the ab-plane and c-axis components of the dynamical spin structure factor as given by Eqs. (C11) and (C13). (c) Ratio of the powder-averaged intensities. The insets show the broadened (HWHM $= \frac{1}{4}\lambda$) peak structure assuming $\delta = -1$ (left) and $\delta = +1$ (right), respectively.

the original $J = 1/2$ doublet at finite Δ. The energies of these states are $E_{A,C}/\lambda = \frac{1}{4}[\mp\sqrt{8+(1+\delta)^2} - 1] + \frac{1}{12}\delta$ and $E_B/\lambda = \frac{1}{2} - \frac{1}{6}\delta$.

Transitions from the ground-state A level to B and C states are magnetically active; their spectral weights in the dynamical spin structure factor are determined by matrix elements of the magnetic moment $\boldsymbol{M} = 2\boldsymbol{s} - \boldsymbol{l}$:

$$\mp\langle B_\pm|M_a|A_\pm\rangle = \frac{1}{i}\langle B_\pm|M_b|A_\pm\rangle = \cos\vartheta + \frac{1}{\sqrt{2}}\sin\vartheta, \tag{C7}$$

$$\pm\langle C_\mp|M_a|A_\pm\rangle = \frac{1}{i}\langle C_\mp|M_b|A_\pm\rangle = \frac{1}{2}(s_{2\vartheta} + \sqrt{2}c_{2\vartheta})\,. \tag{C8}$$

Out-of-plane moment M_c matrix elements between A and B vanish (independent of the spin-orbit mixing angle ϑ), while

$$\langle C_\pm|M_c|A_\pm\rangle = \tfrac{3}{2}s_{2\vartheta}\,. \tag{C9}$$

In the magnetic excitation spectra, a transition $A \to B$ gives a peak at the energy

$$E_B - E_A = \frac{\lambda}{4}[\sqrt{8+(1+\delta)^2} + 3 - \delta], \tag{C10}$$

with the following intensities for different components of the dynamical spin structure factor:

$$I_B = \begin{cases} \frac{1}{4}(3 + c_{2\vartheta} + 2\sqrt{2}s_{2\vartheta}) & (ab \text{ plane}) \\ 0 & (c \text{ axis}) \end{cases}. \tag{C11}$$

The second transition $A \to C$ is peaked at the energy

$$E_C - E_A = \frac{\lambda}{2}\sqrt{8+(1+\delta)^2} \tag{C12}$$

and has the intensity

$$I_C = \begin{cases} \frac{1}{4}(s_{2\vartheta} + \sqrt{2}c_{2\vartheta})^2 & (ab \text{ plane}) \\ \frac{9}{4}s_{2\vartheta}^2 & (c \text{ axis}) \end{cases}. \tag{C13}$$

The B and C peaks are separated by $\Delta_{BC}/\lambda = \frac{1}{4}[\sqrt{8+(1+\delta)^2} - 3 + \delta]$; at small trigonal splitting $\Delta \ll \lambda$, this can be approximated as $\Delta_{BC} \approx \frac{2}{3}\Delta$. At positive (negative) Δ, the B peak position is lower (higher) than that of the C peak [see Fig. 6(a)].

Figure 6(b) shows that the intensities of both transitions are highly anisotropic with respect to ab-plane and c-axis polarizations, with the opposite behavior of B and C contributions. The out-of-plane response is due to the C transition exclusively, while the B peak dominates the ab-plane intensity. This should enable one to distinguish them and determine thereby both the sign and value of trigonal field parameter δ from single-crystal spin-polarized neutron-scattering data.

On the other hand, the powder averaged intensities of B and C peaks are nearly the same for realistic values of δ [see Fig. 6(c)]. Even at $|\delta| = 1$, the two peaks may overlap to give a single broad line, leaving an ambiguity in the sign of parameter δ.

[1] N. F. Mott, *Metal-Insulator Transitions* (Taylor and Francis, London, 1974).
[2] M. Imada, A. Fujimori, and Y. Tokura, Rev. Mod. Phys. **70**, 1039 (1998).
[3] J. B. Goodenough, *Magnetism and the Chemical Bond* (Interscience, New York, 1963).
[4] K. I. Kugel and D. I. Khomskii, Sov. Phys. Usp. **25**, 231 (1982).
[5] G. Khaliullin and S. Maekawa, Phys. Rev. Lett. **85**, 3950 (2000).
[6] G. Khaliullin, Prog. Theor. Phys. Suppl. **160**, 155 (2005).
[7] A. Abragam and B. Bleaney, *Electron Paramagnetic Resonance of Transition Ions* (Clarendon, Oxford, 1970).
[8] G. Khaliullin, W. Koshibae, and S. Maekawa, Phys. Rev. Lett. **93**, 176401 (2004).

[9] G. Jackeli and G. Khaliullin, Phys. Rev. Lett. **102**, 017205 (2009).
[10] A. Kitaev, Ann. Phys. **321**, 2 (2006).
[11] J. G. Rau, E. K.-H. Lee, and H.-Y. Kee, Annu. Rev. Condens. Matter Phys. **7**, 195 (2016).
[12] S. H. Chun, J.-W. Kim, Jungho Kim, H. Zheng, C. C. Stoumpos, C. D. Malliakas, J. F. Mitchell, K. Mehlawat, Y. Singh, Y. Choi, T. Gog, A. Al-Zein, M. Moretti Sala, M. Krisch, J. Chaloupka, G. Jackeli, G. Khaliullin, and B. J. Kim, Nat. Phys. **11**, 462 (2015).
[13] A. Banerjee, C. A. Bridges, J.-Q. Yan, A. A. Aczel, L. Li, M. B. Stone, G. E. Granroth, M. D. Lumsden, Y. Yiu, J. Knolle, S. Bhattacharjee, D. L. Kovrizhin, R. Moessner, D. A. Tennant, D. G. Mandrus, and S. E. Nagler, Nat. Mater. **15**, 733 (2016).
[14] K. W. Plumb, J. P. Clancy, L. J. Sandilands, V. V. Shankar, Y. F. Hu, K. S. Burch, H.-Y. Kee, and Y.-J. Kim, Phys. Rev. B **90**, 041112(R) (2014).
[15] J. Chaloupka, G. Jackeli, and G. Khaliullin, Phys. Rev. Lett. **105**, 027204 (2010).
[16] V. M. Katukuri, S. Nishimoto, V. Yushankhai, A. Stoyanova, H. Kandpal, S. Choi, R. Coldea, I. Rousochatzakis, L. Hozoi, and J. van den Brink, New J. Phys. **16**, 013056 (2014).
[17] J. G. Rau, E. K.-H. Lee, and H.-Y. Kee, Phys. Rev. Lett. **112**, 077204 (2014).
[18] J. G. Rau and H.-Y. Kee, arXiv:1408.4811.
[19] J. Chaloupka and G. Khaliullin, Phys. Rev. B **92**, 024413 (2015).
[20] J. Chaloupka, G. Jackeli, and G. Khaliullin, Phys. Rev. Lett. **110**, 097204 (2013).
[21] I. Kimchi and Y.-Z. You, Phys. Rev. B **84**, 180407(R) (2011).
[22] S. K. Choi, R. Coldea, A. N. Kolmogorov, T. Lancaster, I. I. Mazin, S. J. Blundell, P. G. Radaelli, Y. Singh, P. Gegenwart, K. R. Choi, S.-W. Cheong, P. J. Baker, C. Stock, and J. Taylor, Phys. Rev. Lett. **108**, 127204 (2012).
[23] Y. Yamaji, Y. Nomura, M. Kurita, R. Arita, and M. Imada, Phys. Rev. Lett. **113**, 107201 (2014).
[24] S. M. Winter, Y. Li, H. O. Jeschke, and R. Valentí, Phys. Rev. B **93**, 214431 (2016).
[25] Y. Sizyuk, P. Wölfle, and N. B. Perkins, Phys. Rev. B **94**, 085109 (2016).
[26] A. Auerbach, *Interacting Electrons and Quantum Magnetism* (Springer, New York, 1994).
[27] For a discussion of the order-from-disorder phenomena in frustrated spin systems, see A. M. Tsvelik, *Quantum Field Theory in Condensed Matter Physics* (Cambridge University, Cambridge, England, 1995), Chap. 17, and references therein.
[28] G. Jackeli and A. Avella, Phys. Rev. B **92**, 184416 (2015).
[29] G. Khaliullin, Phys. Rev. B **64**, 212405 (2001).
[30] Z. Nussinov and J. van den Brink, Rev. Mod. Phys. **87**, 1 (2015).
[31] However, the separation of the individual zigzag chain directions is an order-from-disorder effect, since a linear combination of different zigzag patterns is a classical ground state as well.
[32] S. Bhattacharjee, S.-S. Lee, and Y. B. Kim, New J. Phys. **14**, 073015 (2012).
[33] B. J. Kim, H. Ohsumi, T. Komesu, S. Sakai, T. Morita, H. Takagi, and T. Arima, Science **323**, 1329 (2009).
[34] Y. Kubota, H. Tanaka, T. Ono, Y. Narumi, and K. Kindo, Phys. Rev. B **91**, 094422 (2015).
[35] R. D. Johnson, S. C. Williams, A. A. Haghighirad, J. Singleton, V. Zapf, P. Manuel, I. I. Mazin, Y. Li, H. O. Jeschke, R. Valentí, and R. Coldea, Phys. Rev. B **92**, 235119 (2015).
[36] Y. Singh and P. Gegenwart, Phys. Rev. B **82**, 064412 (2010).
[37] H. Gretarsson, J. P. Clancy, X. Liu, J. P. Hill, E. Bozin, Y. Singh, S. Manni, P. Gegenwart, J. Kim, A. H. Said, D. Casa, T. Gog, M. H. Upton, H.-S. Kim, J. Yu, V. M. Katukuri, L. Hozoi, J. van den Brink, and Y.-J. Kim, Phys. Rev. Lett. **110**, 076402 (2013).
[38] H. B. Cao, A. Banerjee, J.-Q. Yan, C. A. Bridges, M. D. Lumsden, D. G. Mandrus, D. A. Tennant, B. C. Chakoumakos, and S. E. Nagler, Phys. Rev. B **93**, 134423 (2016).
[39] R. Yadav, N. A. Bogdanov, V. M. Katukuri, S. Nishimoto, J. van den Brink, and L. Hozoi, arXiv:1604.04755.
[40] H.-S. Kim, Vijay Shankar V., A. Catuneanu, and H.-Y. Kee, Phys. Rev. B **91**, 241110(R) (2015).
[41] L. J. P. Ament, M. van Veenendaal, T. P. Deveraux, J. P. Hill, and J. van den Brink, Rev. Mod. Phys. **83**, 705 (2011).
[42] L. J. P. Ament and G. Khaliullin, Phys. Rev. B **81**, 125118 (2010).
[43] M. W. Haverkort, Phys. Rev. Lett. **105**, 167404 (2010).
[44] L. Savary and T. Senthil, arXiv:1506.04752.
[45] P. A. Fleury and R. Loudon, Phys. Rev. **166**, 514 (1968).
[46] L. J. P. Ament, G. Khaliullin, and J. van den Brink, Phys. Rev. B **84**, 020403(R) (2011).
[47] J. Kim, D. Casa, M. H. Upton, T. Gog, Y.-J. Kim, J. F. Mitchell, M. van Veenendaal, M. Daghofer, J. van den Brink, G. Khaliullin, and B. J. Kim, Phys. Rev. Lett. **108**, 177003 (2012).

PHYSICAL REVIEW B **95**, 024426 (2017)

Phase diagram and spin correlations of the Kitaev-Heisenberg model: Importance of quantum effects

Dorota Gotfryd,[1,2] Juraj Rusnačko,[3,4] Krzysztof Wohlfeld,[1] George Jackeli,[5,6] Jiří Chaloupka,[3,4] and Andrzej M. Oleś[2,6]

[1]*Institute of Theoretical Physics, Faculty of Physics, University of Warsaw, Pasteura 5, PL-02093 Warsaw, Poland*

[2]*Marian Smoluchowski Institute of Physics, Jagiellonian University, prof. S. Łojasiewicza 11, PL-30348 Kraków, Poland*

[3]*Central European Institute of Technology, Masaryk University, Kamenice 753/5, CZ-62500 Brno, Czech Republic*

[4]*Department of Condensed Matter Physics, Faculty of Science, Masaryk University, Kotlářská 2, CZ-61137 Brno, Czech Republic*

[5]*Institute for Functional Matter and Quantum Technologies, University of Stuttgart, Pfaffenwaldring 57, D-70569 Stuttgart, Germany*

[6]*Max Planck Institute for Solid State Research, Heisenbergstrasse 1, D-70569 Stuttgart, Germany*

(Received 16 August 2016; revised manuscript received 28 November 2016; published 23 January 2017)

We explore the phase diagram of the Kitaev-Heisenberg model with nearest neighbor interactions on the honeycomb lattice using the exact diagonalization of finite systems combined with the cluster mean field approximation, and supplemented by the insights from analytic approaches: the linear spin-wave and second-order perturbation theories. This study confirms that by varying the balance between the Heisenberg and Kitaev term, frustrated exchange interactions stabilize in this model either one of four phases with magnetic long range order: Néel phase, ferromagnetic phase, and two other phases with coexisting antiferromagnetic and ferromagnetic bonds, zigzag and stripy phase, or one of two distinct spin-liquid phases. Out of these latter disordered phases, the one with ferromagnetic Kitaev interactions has a substantially broader range of stability as the neighboring competing ordered phases, ferromagnetic and stripy, have very weak quantum fluctuations. Focusing on the quantum spin-liquid phases, we study spatial spin correlations and dynamic spin structure factor of the model by the exact diagonalization technique, and discuss the evolution of gapped low-energy spin response across the quantum phase transitions between the disordered spin liquid and phases with long range magnetic order.

DOI: 10.1103/PhysRevB.95.024426

I. INTRODUCTION

Frustration in magnetic systems occurs by competing exchange interactions and leads frequently to disordered spin-liquid states [1–3]. Recent progress in understanding transition metal oxides with orbital degrees of freedom demonstrated many unusual properties of systems with active t_{2g} degrees of freedom—they are characterized by anisotropic hopping [4–8] which generates Ising-like orbital interactions [9–17], similar to the orbital superexchange in e_g systems [18,19]. Particularly challenging are $4d$ and $5d$ transition metal oxides, where the interplay between strong electron correlations and spin-orbit interaction leads to several novel phases [20,21]. In iridates the spin-orbit interaction is so strong that spins and orbital operators combine to new $S = 1/2$ pseudospins at each site [22], and interactions between these pseudospins decide about the magnetic order in the ground state.

The A_2IrO_3 ($A =$ Na, Li) family of honeycomb iridates has attracted a lot of attention as these compounds have t_{2g} orbital degree of freedom and lie close to the exactly solvable $S = 1/2$ Kitaev model [23]. This model has a number of remarkable features, including the absence of any symmetry breaking in its quantum Kitaev spin-liquid (KSL) ground state, with gapless Majorana fermions [23] and extremely short-ranged spin correlations confined to nearest neighbors [24]. We emphasize that below we call a KSL also disordered spin-liquid states which arise near the Kitaev points in presence of perturbing Heisenberg interactions $\propto J$.

By analyzing possible couplings between the Kramers doublets it was proposed that the microscopic model adequate to describe the honeycomb iridates includes Kitaev interactions accompanied by Heisenberg exchange in the form of the Kitaev-Heisenberg (KH) model [25]. Soon after the experimental evidence was presented that several features of the observed zigzag order are indeed captured by the KH model [26–34]. Its parameters for A_2IrO_3 compounds are still under debate at present [35,36]. One finds also a rather unique crossover from the quasiparticle states to a non-Fermi-liquid behavior by varying the frustrated interactions [37]. Unfortunately, however, it was recently realized that this model is not sufficient to explain the observed direction of magnetic moments in Na_2IrO_3, and its extension is indeed necessary to describe the magnetic order in real materials [38,39]. For example, bond-anisotropic interactions associated with the trigonal distortions have to play a role to explain the differences between Na_2IrO_3 and Li_2IrO_3 [40], the two compounds with quite different behavior reminiscent of the unsolved problem of $NaNiO_2$ and $LiNiO_2$ in spin-orbital physics [19]. On the other hand, the KH model might be applicable in another honeycomb magnet α-$RuCl_3$, see, e.g., a recent study of its spin excitation spectrum [41].

Understanding the consequences of frustrated Heisenberg interactions on the honeycomb lattice is very challenging and has stimulated several studies [42–45]. The KH model itself is highly nontrivial and poses an even more interesting problem in the theory [25,34,46,47]: The Kitaev term alone has intrinsic frustration due to directional Ising-like interactions between the spin components selected by the bond direction [23]. In addition, these interactions are disturbed by nearest neighbor Heisenberg exchange which triggers long-range order (LRO) sufficiently far from the Kitaev points [25,34,46,47]. In general, ferromagnetic (FM) and antiferromagnetic (AF) interactions coexist and the phase diagram of the KH model is quite rich as shown in several previous studies [25,34,46–49]. Finally, the KH model has also a very interesting phase diagram on the triangular lattice [50–53]. These studies motivate better

understanding of quantum effects in the KH model on the honeycomb lattice in the full range of its competing interactions.

The first purpose of this paper is to revisit the phase diagram of the KH model and to investigate it further by comparing the exact diagonalization (ED) result [34] with the self-consistent cluster mean field theory (CMFT), supplemented by the insights from the linear spin-wave theory (LSWT) and the second-order perturbation theory (SOPT). The main advantage of CMFT is that it goes beyond a single site mean field classical theory and gives not only the symmetry-broken states with LRO, but partly includes quantum fluctuations as well, namely the ones within the considered clusters [43,54,55]. In this way the treatment is more balanced and may allow for disordered states in cases when frustration of interactions dominates.

We present below a complete CMFT treatment of the phase diagram which includes also the Kitaev term in MF part of the Hamiltonian and covers the entire parameter space (in contrast to the earlier prototype version of CMFT calculation on a single hexagon for the KH model [56]). Note that the CMFT complements the ED which is unable to get symmetry breaking for a finite system, but nevertheless can be employed to investigate the phase transitions in the present KH model by evaluating the second derivative of the ground state energy to identify phase transitions by its characteristic maxima [25,34]. The ED result can be also used to recognize the type of magnetic order by transforming to reciprocal space and computing spin-structure factor. The second purpose is to investigate further the difference between quantum KSL regions around both Kitaev points mentioned in Ref. [34] and LRO/KSL boundaries.

The paper is organized as follows: In Sec. II we introduce the KH model and define its parameters. In Sec. III we present three methods of choice: (i) the exact diagonalization in Sec. III A, (ii) the self-consistent CMFT in Sec. III B, and (iii) linear spin wave theory in Sec. III D. An efficient method of solving the self-consistence problem obtained within the CMFT is introduced in Sec. III C. The numerical results are presented and discussed in Sec. IV: (i) the phase transitions and the phase diagram are introduced in Sec. IV A, and (ii) the phase boundaries, the values of the ground state energies, and the magnetic moments obtained by different methods are presented and discussed in Secs. IV B and IV C, and (iii) we discuss the impact of the Kitaev interaction on different spin ordered states in Sec. IV C. Spin correlations obtained for various phases are presented in Sec. V. The dynamical spin susceptibility and spin structure factor are introduced and analyzed for different phases in Sec. VI. Finally, in Sec. VII we present the main conclusions and short summary. The paper is supplemented with the Appendix where we explain the advantages of the linearization procedure implemented on the CMFT on the example of a single hexagon.

II. KITAEV-HEISENBERG MODEL

We start from the KH Hamiltonian with nearest neighbor interactions on the honeycomb lattice in a form,

$$\mathcal{H} \equiv K \sum_{\langle ij\rangle\parallel\gamma} S_i^\gamma S_j^\gamma + J \sum_{\langle ij\rangle} \boldsymbol{S}_i \cdot \boldsymbol{S}_j, \tag{2.1}$$

where $\gamma = x,y,z$ labels the bond direction. The Kitaev term $\propto K$ favors local bond correlations of the spin component interacting on the particular bond. The superexchange J is of Heisenberg form and alone would generate a LRO state, antiferromagnetic or ferromagnetic, depending on whether $J > 0$ or $J < 0$. We fix the overall energy scale,

$$J^2 + K^2 = 1, \tag{2.2}$$

and choose angular parametrization:

$$K = \sin\varphi, \quad J = \cos\varphi, \tag{2.3}$$

varying φ within the interval $\varphi \in [0,2\pi]$. This parametrization exhausts all the possibilities for nearest neighbor interactions in the KH model.

While zigzag AF order was observed in Na_2IrO_3 [28–32], its microscopic explanation has been under debate for a long time. The *ab initio* studies [35,57] give motivation to investigate a broad regime of parameters K and J, see Eqs. (2.3). Further motivation comes from the honeycomb magnet α-$RuCl_3$ [41]. Note that we do not intend to identify the parameter sets representative for each individual experimental system, but shall concentrate instead on the phase diagram of the model Eq. (2.1) with nearest neighbor interactions only.

III. CALCULATION METHODS

A. Exact diagonalization

We perform Lanczos diagonalization for an $N = 24$-site cluster with periodic boundary conditions (PBC). This cluster respects all the symmetries of the model, including hidden ones. Among the accessible clusters it is expected to have the minimal finite-size effects.

B. Cluster mean field theory

A method which combines ED with an explicit breaking of Hamiltonian's symmetries is the so-called self-consistent CMFT. It has been applied to several models with frustrated interactions, including the Kugel-Khomskii model [54,55]. The method was also extensively used by Albuquerque *et al.* [43] as one of the means to establish the full phase diagram of the Heisenberg-J_2-J_3 model on the honeycomb lattice.

Within CMFT the internal bonds of the cluster [connecting the circles in Fig. 1(a)] are treated exactly. The corresponding part $H_{\rm IN}$ of the Hamiltonian is the nearest neighbor KH Hamiltonian, Eq. (2.1). The external bonds that connect the boundary sites (•) with the corresponding boundary sites of periodic copies of the cluster (□) are described by the MF part of the Hamiltonian,

$$H_{\rm MF} \equiv K \sum_{[ij]\parallel z} \langle S_i^z\rangle S_j^z + J \sum_{[ij]} \langle S_i^z\rangle S_j^z, \tag{3.1}$$

where $[ij]$ marks the external bonds. Since the ordered moments in the KH model align always along one of the cubic axes x, y, z (see, e.g., Ref. [25]), we have put

$$\langle \vec{S}_i\rangle \cdot \vec{S}_j \equiv \langle S_i^z\rangle S_j^z \tag{3.2}$$

in $H_{\rm MF}$ to simplify the calculations.

The averages $\langle S_i^z\rangle$ generate effective magnetic fields acting on the boundary sites of the cluster. The total Hamiltonian

$$\mathcal{H} \equiv H_{\rm IN} + H_{\rm MF} \tag{3.3}$$

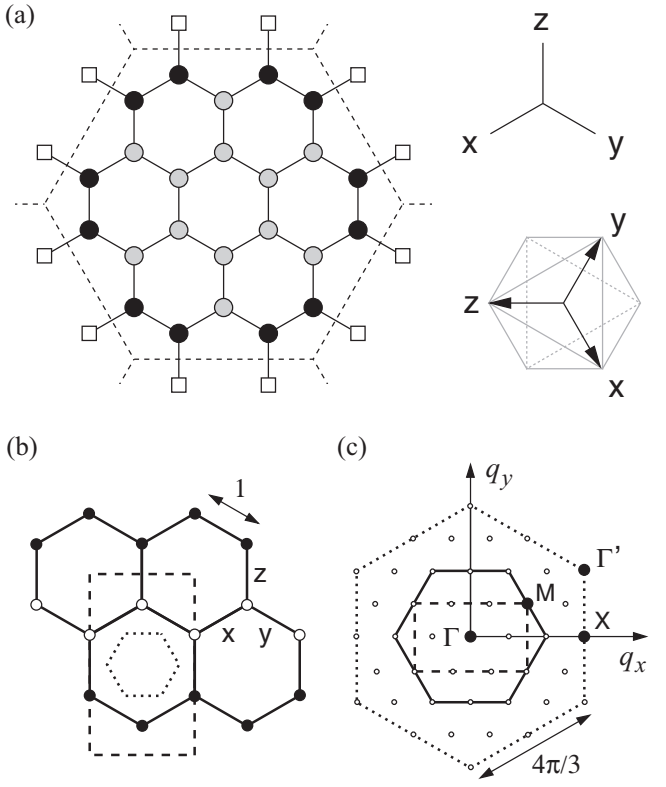

FIG. 1. (a) 24-site cluster and the introduction of the mean fields. Gray (black) circles indicate internal (boundary) sites. In CMFT the internal bonds of the cluster are treated exactly while the external bonds crossing the cluster boundary (dashed) are treated on the MF level. The sites marked by □ generate effective magnetic fields on the boundary sites •. Labels x, y, and z stand for three inequivalent bond directions determining the active products $S_i^\gamma S_j^\gamma$ in the Kitaev part of the Hamiltonian (2.1), e.g., bonds of x direction contribute with the $S_i^x S_j^x$ product to the Hamiltonian, etc. The pseudospin axes used here are parallel to the cubic axes indicated in the top view of a single octahedron. (b) Unit cells: for honeycomb lattice (coinciding with a single hexagon of that lattice), for triangular lattice (inner dotted hexagon), and zigzag magnetic unit cell (dashed rectangle). Black and white circles stand for up/down spin and indicate one of three equivalent zigzag patterns. (c) Corresponding Brillouin zones and special $\boldsymbol{q}$ points for the lattice constant $a = 1$. The $\boldsymbol{q}$ vectors compatible with the 24-site cluster in (a) are also shown.

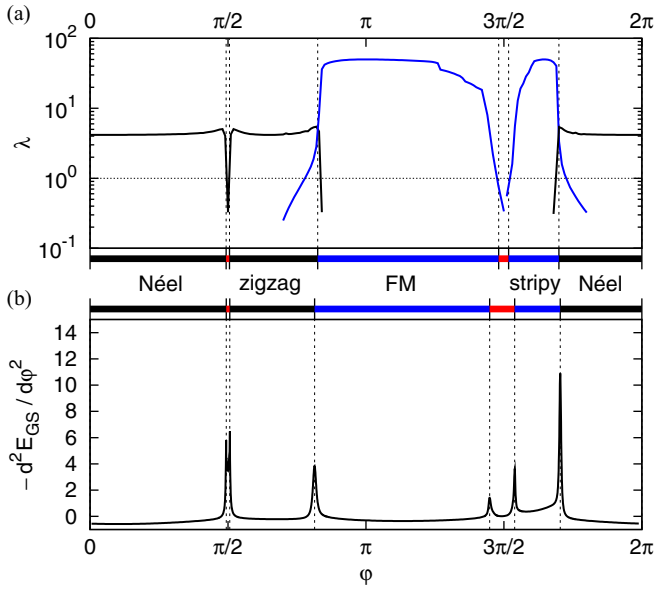

FIG. 2. (a) The values of λ obtained by the linearization of CMFT for an embedded cluster of $N = 24$ sites with fixed magnetic order patterns: FM, AF, stripy, and zigzag. Leading $\lambda > 1$ indicates the order that sets in. The disordered KSL phases near $\varphi = \pi/2$ and $3\pi/2$ are indicated by red. (b) Second derivative of the ground state energy, $-d^2E_0(\varphi)/d\varphi^2$, obtained by ED. Adopted from Ref. [34].

is diagonalized in a self-consistent manner, taking a slightly different approach than the one presented in Ref. [43]: Instead of starting with a random wave function our algorithm begins with expectation values $\langle S_i^z\rangle_{\rm in}$ on each boundary site i of the cluster. These can represent a certain pattern (zigzag, stripy, Néel, FM) or be set randomly to have a "neutral" starting point. After diagonalizing the Hamiltonian (3.3) (again by the ED Lanczos method) the ground state of the system is obtained and we recalculate the expectation values $\langle S_i^z\rangle$ to be used in the second iteration. The procedure is repeated until self-consistency is reached.

C. Linearized cluster mean field theory

A single iteration of the self-consistent MF calculation may be viewed as a nonlinear mapping of the set of initial averages $\{\langle S_i^z\rangle_{\rm in}\}$ to the resulting averages $\{\langle S_i^z\rangle_{\rm fin}\}$. The self-consistent solution is then a stable stationary point of such a mapping. To find the leading instability, we may consider the case of small initial averages in the CMFT calculation and identify the pattern characterized by the fastest growth during the iterations. To this end we linearize the above mapping.

In the lowest order the mapping corresponds to the multiplication of the vector of the averages $\{\langle S_i^z\rangle_{\rm in}\}$ by the matrix,

$$F_{ij} = \frac{\partial\langle S_i^z\rangle_{\rm fin}}{\partial\langle S_j^z\rangle_{\rm in}}, \tag{3.4}$$

where i and j run through the cluster boundary sites. During iterations, the patterns corresponding to the individual eigenvectors of the matrix F grow as λ^n after n iterations for a particular eigenvalue λ. The ordering pattern obtained by CMFT is then given by the eigenvector with largest $\lambda_{\rm max} > 1$. In the quantum KSL regimes, all the eigenvalues are less than 1 and no magnetic order emerges. An example of linearized CMFT applied to a single hexagon with PBC can be found in the Appendix.

A modified version of this method, used to obtain Fig. 2(a), assumes a particular ordered pattern (Néel, zigzag, FM, or stripy phase) and uses a single spin average $\langle S^z\rangle_{\rm in}$ distributed along the boundary sites outside the cluster, with the signs consistent with this pattern. The resulting values, $\langle S_i^z\rangle_{\rm fin}$, are then averaged correspondingly. In this case the matrix F is reduced to a single value λ plotted in Fig. 2(a). We observe that the largest eigenvalue either drops below 1 when the disordered

KSL state takes over, or interchanges with another eigenvalue at a quantum phase transition to a different ordered phase.

D. Linear spin-wave theory

The LSWT is a basic tool to determine spin excitations and quantum corrections in systems with LRO [58]. For systems with coexisting AF and FM bonds quantum corrections are smaller than for the Néel phase on the same lattice but are still substantial for $S = 1/2$ spins [59]. For the KH model the LSWT [25,29,34] has to be implemented separately for each of the four ordered ground states: Néel (N), zigzag (ZZ), FM, or stripy (ST). Then for a particular ground state the Hamiltonian is rewritten in terms of the Holstein-Primakoff bosons [29,60] and only quadratic terms in bosonic operators are kept. The spectrum of such a quadratic Hamiltonian is finally obtained using the successive Fourier and Bogoliubov transformations.

While the spin wave dispersion relations are usually of prime interest [25,29,34,60], there are also two other quantities which can easily be calculated using LSWT and which will be important in the discussion that follows: (i) the value of the total ordered moment $\langle M\rangle$ per site, and (ii) the total energy per site $\langle E\rangle$. These observables are calculated in a standard way [58,59] and expressed in terms of the eigenvalues, i.e., spin-wave energies $\omega_{\mathbf{k}\alpha}$, and the eigenvector components $\{v_{\mathbf{k}\alpha\lambda}\}$ of the bosonic Hamiltonian *before* the Bogoliubov transformation:

$$\langle M\rangle = S - \frac{1}{LV}\sum_{\alpha,\lambda=1,\ldots,L}\int_{\mathbf{k}\in BZ}|v_{\mathbf{k}\alpha,\lambda}|^2\, d^2\mathbf{k}, \tag{3.5}$$

and

$$\langle E\rangle = E_{\rm cl}\,[S^2 \to S(S+1)] + \frac{S}{2LV}\sum_{\alpha=1,\ldots,L}\int_{\mathbf{k}\in BZ}\omega_{\mathbf{k}\alpha}\, d^2\mathbf{k}, \tag{3.6}$$

where the choice of the sign of the eigenvalues and the normalization of their eigenvectors is described in Ref. [58]. Here $E_{\rm cl}$ is the classical ground state energy per site, e.g.,

$$E_{\rm cl} = -JzS^2/2, \tag{3.7}$$

with $z = 3$ for the Néel phase at $K = 0$ and $S = 1/2$ is the value of spin quantum number. L in Eqs. (3.5)–(3.6) is the number of the eigenvalues of the problem (spin-wave modes) and α enumerates these modes. For all cases except for the zigzag order [25], the integrals go over the two-sublattice ($L = 2$) rectangular Brillouin zone (BZ) [61] with its volume $V = 8\pi^2/3\sqrt{3}$ and $-\pi/\sqrt{3} \leqslant k_x \leqslant \pi/\sqrt{3}$, $-2\pi/3 \leqslant k_y \leqslant 2\pi/3$ (as already mentioned we assume the lattice constant $a = 1$). For the zigzag state $L = 4$ and the rectangular BZ can be chosen as: $-\pi/\sqrt{3} \leqslant k_x \leqslant \pi/\sqrt{3}$ and $-\pi/3 \leqslant k_y \leqslant \pi/3$ and its volume is $V = 4\pi^2/3\sqrt{3}$.

IV. QUANTUM PHASE TRANSITIONS

A. Phase diagram

Here we supplement the ED-based phase diagram for the KH model Eq. (2.1) established in Ref. [34] with the one obtained within CMFT. Figure 3 displays the phase boundaries obtained with ED [34], within CMFT, as well as classical

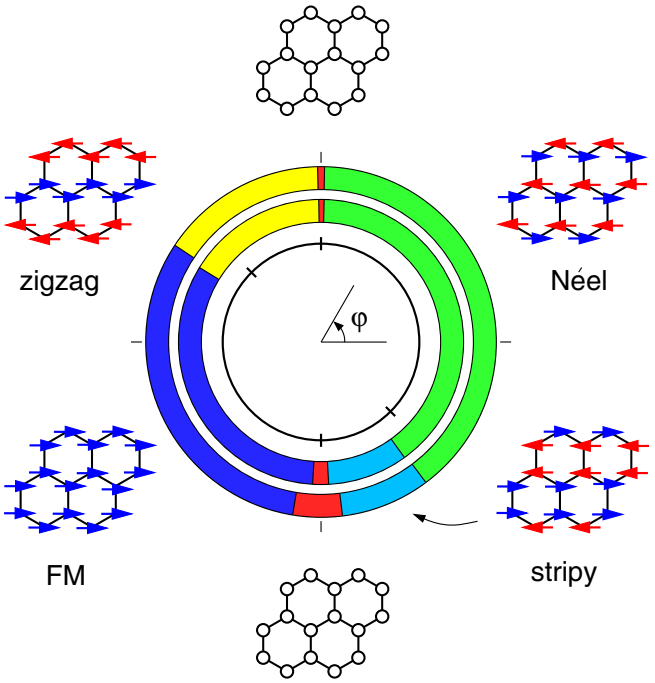

FIG. 3. $T = 0$ phase diagram for KH model. The outer ring is composed from ED data for the 24-site cluster, reproducing the result from Ref. [34] in the new parametrization, the middle ring shows CMFT results also for 24-site cluster and the inner black circle represents the classical result. The convention used for the angular parameter φ which determines coupling constants [see Eqs. (2.3)] is shown in the center of the inner circle. The colors represent particular phases, shown also as mini drawings next to suitable regions of the phase diagram. Starting from $\varphi = 0$ green colored region corresponds to Néel order, red—KSL, yellow—zigzag order, dark blue—FM, red—KSL, light blue—stripy phase, and again green—Néel phase.

(Luttinger-Tisza) phase boundaries. The latter are included for completeness and to highlight the fact that the quantum fluctuations stabilize the KSL phases beyond single points, see below. To examine them in more detail it is instructive to analyze the data in Fig. 2(a) for the boundaries obtained from linearized CMFT and Fig. 2(b) for the peaks in the second derivative of energy, $-{\rm d}^2E_0(\varphi)/{\rm d}\varphi^2$, giving phase boundaries in ED [34].

It is clearly visible that all the methods that include quantum fluctuations give quantum versions of the four classically established magnetic phases: Néel, zigzag, FM, and stripy. As the most important effect we note that when quantum fluctuations are included within a classical phase, the energy is generally lowered and that the emerging phase is expected to expand beyond the classical boundaries, but only in cases when a phase which competes with it has weaker quantum fluctuations. This implies that phases of AF nature will expand at the expense of the FM ones as the latter phases have lower energy gains by quantum fluctuations (which even vanish exactly for the FM order at $K = 0$ and $J < 0$).

We summarize the phase boundaries obtained within different methods in Table I. One finds substantial corrections to the quantum phase transitions which follow from quantum fluctuations. These corrections are quite substantial in both KSLs at the Kitaev points ($K = +1$, $\varphi = \frac{1}{2}\pi$ and $K = -1$,

TABLE I. Phase boundaries for the KH model, parameterized by the angle φ (in units of π), see Eqs. (2.3). Columns: classical Luttinger-Tisza approximation, second-order perturbation theory (SOPT), exact diagonalization (ED), and self-consistent cluster mean field theory (CMFT).

Boundary	Classical	SOPT	ED	CMFT
Néel/KSL	0.5	0.492	0.494	0.496
KSL/zigzag	0.5	0.507	0.506	0.505
zigzag/FM	0.75	0.813	0.814	0.825
FM/KSL	1.5	1.463	1.448	1.478
KSL/stripy	1.5	1.530	1.539	1.519
stripy/Néel	1.75	1.705	1.704	1.699

$\varphi = \frac{3}{2}\pi$, first column of Table I). Indeed, in the classical approach massively degenerate ground states exist just at isolated points, but they are replaced by disordered spin-liquid states that extend to finite intervals of φ when quantum fluctuations are included, see the second, third, and fourth column in Table I. The expansion of Néel and zigzag phases beyond classical boundaries is given by particularly large corrections and is well visible.

The most prominent feature in the phase diagram described above is however the difference in size between two KSL regions, already addressed before using ED [34] and also visible now in the CMFT data. Therefore, the CMFT result supports the claim from Ref. [34] that the stability of KSL perturbed by relatively small Heisenberg interaction depends on the nature of the phases surrounding the spin liquid and the amount of quantum fluctuations that they carry. In the following we discuss the above issues more thoroughly, examining: (i) ground state energy curves emerging from ED, CMFT, SOPT within the linked cluster expansion and LSWT, (ii) the ordered moment given by various methods, (iii) the spin-spin correlation functions, and (iv) the spin structure factor as well as the dynamical spin susceptibility in the vicinity of the Kitaev points.

B. Quantum corrections: Energetics

We start the discussion of quantum corrections to the energy of the ordered phases by noting that, even though it properly captures finite order parameters, the CMFT looses quantum energy on the external bonds and would therefore not provide a reliable estimate of the ground-state energy. However, if one calculates instead the energy based on the correlations on the bonds of the central hexagon, the estimate is significantly improved. Here we choose the energy obtained using the ED calculations [see Fig. 4(a)] as a reference value because of all the bonds treated in an exact manner. This observation is also supported by the fact that the ED phase boundaries were roughly confirmed by tensor networks (iPEPS) [49] and density matrix renormalization group (DMRG) results [48]: The iPEPS phase boundaries agree with ED for AF KSL/LRO transitions and the boundaries between different LRO phases differ only slightly from those found in ED (iPEPS: zigzag/FM—0.808π, stripy/Néel—1.708π). For FM KSL/LRO transition however the iPEPS result deviates more, i.e., KSL/stripy—1.528π. On the other hand, DMRG boundaries agree perfectly with ED and due to four-sublattice dual transformation [10,25] one can reproduce the FM/zigzag as well as FM/KSL boundaries. Only the extent of the AF spin-liquid phase cannot be extracted from this result, but that is already confirmed by iPEPS.

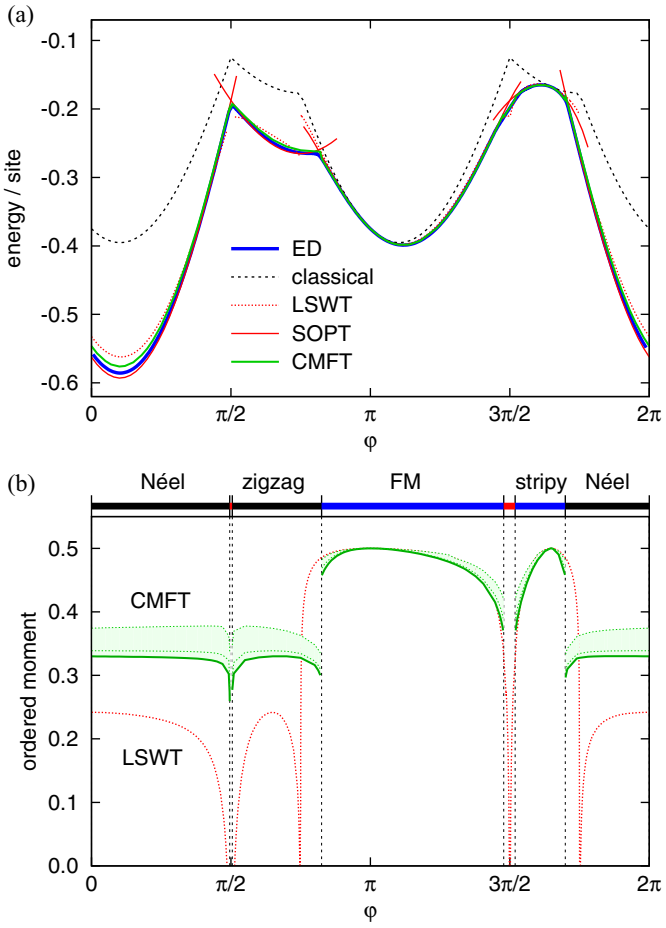

FIG. 4. (a) Comparison between ground state energies per site obtained using various methods: classical Luttinger-Tisza approximation (dashed black), SOPT (solid red), LSWT (dashed red), ED for 24-site cluster (solid blue, see Ref. [34] for this result in a different parametrization), and CMFT (energy given by the central hexagon, solid green). (b) Ordered moment obtained from CMFT (solid green line for the central hexagon, dashed green line for the value for intermediate and boundary sites) and LSWT (dashed red line).

Figure 4(a) shows a quite remarkable agreement between the energy values and critical values of φ obtained by the simplest SOPT [25] and our reference ED results. This suggests that this analytical method can be utilized to get better insight to the quantum contributions to the ground state energy. For a phase X with LRO, the energy per site $\mathcal{E}_X$, written as a sum of the classical energy E_{cl} and the quantum fluctuation contribution ΔE_X, is obtained as:

$$\mathcal{E}_N = -\frac{1}{8}(K+3J) - \frac{1}{16}(K+3J), \tag{4.1}$$

$$\mathcal{E}_{ZZ} = -\frac{1}{8}(K-J) - \frac{1}{16}(K-J), \tag{4.2}$$

$$\mathcal{E}_{FM} = +\frac{1}{8}(K+3J) + \frac{1}{16}\frac{K^2}{K+2J}, \tag{4.3}$$

$$\mathcal{E}_{\rm ST} = +\frac{1}{8}(K-J) + \frac{1}{16}\frac{(K+2J)^2}{K}. \tag{4.4}$$

In addition, to get the LRO/KSL phase boundary points in Table I, we estimate the energy of the KSL phase as

$$\mathcal{E}_{\rm KSL} \simeq \tfrac{3}{2}(K+J)\langle S^\gamma S^\gamma\rangle_{\rm Kitaev}, \tag{4.5}$$

using the analytical result for the Kitaev points [24], $\langle S^\gamma S^\gamma\rangle_{\rm Kitaev} \approx \pm 0.131$.

The two spin-liquid phases in the phase diagram of the KH model differ strongly in their extent, despite the formal equivalence of the FM ($K=-1$) and AF ($K=1$) Kitaev points provided by an exact mapping of the Kitaev Hamiltonian [23]. As mentioned earlier, this is due to the fact that the two KSLs compete with LRO phases of a distinct nature. Here we give a simple interpretation based on the strength of the quantum corrections of the LRO phases estimated using Eqs. (4.1)–(4.4). Later, in Secs. V and VI we illustrate the different nature of the transitions between FM and AF KSL and the surrounding it LRO phases in terms of spin correlations and spin dynamics.

Let us now compare the quantum fluctuation contribution and the classical one. For the LRO phases surrounding the AF spin liquid—Néel and zigzag—we always have $\Delta E/E_{\rm cl} = \frac{1}{2}$ as deduced from Eqs. (4.1) and (4.2), i.e., only $\frac{2}{3}\mathcal{E}_{\rm N}$ and $\frac{2}{3}\mathcal{E}_{\rm ZZ}$ are found in the classical approach. This guarantees that the quantum phase transition between these two types of order occurs at the same value of $\varphi = \pi/2$ in SOPT and in the classical approach that do not capture the spin-liquid phase in between these ordered states, see Fig. 4(a). In contrast, the phases neighboring to the FM spin liquid—FM and stripy—would reach the value of $\Delta E/E_{\rm cl} = \frac{1}{2}$ only at the FM Kitaev point with $J=0$ and away from this point the contribution of quantum fluctuations decreases rapidly allowing for a large extent of the FM spin-liquid phase. Note that both these latter phases contain a point which is exactly fluctuation free—for the FM phase when frustration is absent ($K=0$), and for the stripy phase it is related to the FM one by the interaction transformation [39] at $K=-2J$.

Moving to the CMFT energy analysis one should also keep in mind that within the CMFT method the external bonds between $\langle S_i^z\rangle$ and S_j^z do not include quantum fluctuations fully. This implies a worse estimate of the energy (of the whole cluster) for regions of the phase space that allow quantum fluctuations. As a consequence the region of stability of FM spin-liquid phase is smaller than that obtained in the ED. Significantly better energy estimate is given by the central hexagon, for which all the bonds experience exact interactions. As a result, this CMFT energy curve [green line in Fig. 4(a)] lies almost as close to ED energy as the SOPT one. Finally, the estimates obtained from LSWT, which represents a harmonic approximation to the quantum fluctuations, are not as good as those from central hexagon via CMFT and SOPT, see dashed red lines in Fig. 4(a). As expected, the energy obtained from the LSWT agrees well with ED curve for phases with less quantum fluctuations, FM and stripy phase, and starts to diverge when these phases are unstable beyond quantum phase transitions within Néel and zigzag phases.

C. Quantum corrections: Ordered moment

As usual, getting the correct value of the ordered moment turns out to be a more difficult task than estimating the ground state energy. This is primarily due to the fact that the ED does not capture the symmetry-broken states and the ordered moment can only be indirectly extracted from the m^2; moreover, the SOPT may not be reliable here. Hence, we are mostly left with the results obtained with CMFT and LSWT. We discuss the corresponding data [shown in Fig. 4(b)] together with the several values given already in the literature.

Let us begin with the Heisenberg AF point $\varphi = 0$: Here it is expected that the ordered moment should be strongly reduced by quantum fluctuations. LSWT estimates the ordered moment value at 0.248 [61]. Similar values were extracted from m^2 in quantum Monte Carlo (0.268 [62–64]) and ED (0.270 [43]) calculations. In the last case however the authors admit that the set of clusters for finite size scaling was chosen so as to make the best agreement with quantum Monte Carlo. Another method—series expansion (high order perturbation theory) [47] sets ordered moment value at a somewhat higher value of 0.307. While all the above results seem roughly consistent, CMFT value obtained from the boundary sites seems to stand out (0.374 for $\varphi = 0$). Nevertheless, the central-hexagon value (0.330 for $\varphi = 0$) lies much closer to the results from the methods mentioned above. Moreover, one should note that the ordered moment estimated from m^2 for 24-site cluster ED equals 0.45 [43] which is above the CMFT value. This suggests that at this point the finite size scaling is important.

Before moving to the frustrated regime we briefly mention that the trivial ordered moment value at $\varphi = \pi$ is here correctly reproduced by both CMFT and LSWT. Besides, for the regions around the fluctuation-free FM (and stripy) point the ordered moments predicted by CMFT and LSWT also match. Following the ground state energy analysis, LSWT gives the correct result because quantum fluctuations contribution is small compared to the classical state. The further one moves towards the Kitaev points, however, the more incorrect the LSWT approximation should be because of the strong reduction of the ordered moment due to increasing frustration.

In contrast, the lack of quantum fluctuations on the external bonds generates systematic errors within CMFT except for FM and stripy phases. The ordered moment obtained from the boundary sites experiences the errors discussed above. However, the ordered moment values for intermediate sites and the central hexagon become largely reduced in the whole Néel and zigzag regions due to the fact that for the internal part of the cluster the fluctuations are fully included. Still, the best estimate comes from the central hexagon where quantum fluctuations on the bonds are included and CMFT gives more realistic results than LSWT in frustrated parts of the phase diagram. Here it is also important to stress that the series expansion captures correctly the fluctuation-free point at $\varphi = \pi$ (FM) and $\varphi = -\arctan 2$ (stripy) and predicts a broader region of the FM KSL phase [47]. The order parameter is also qualitatively correctly estimated and is reduced more to $m \simeq 0.3$ for both Néel and zigzag phases [47]. However, while the ordered moment values obtained by CMFT are

consistent with the four-sublattice dual transformation, the ordered moment data from the high-order perturbation theory [47] are not as the values of ordered moment differ at the points connected by the mapping. Unfortunately the largest difference appears near the FM LRO/KSL boundaries. This observation uncovers certain shortcomings of the high-order perturbation theory.

D. Quantum corrections: Naive interpretation

Let us conclude the discussion of the quantum corrections with the following more general observation: Developing the argumentation presented by Iregui, Corboz, and Troyer [49], the dependence of the quantum corrections to the energy and to the ordered moment on the angle φ suggests that the Kitaev interaction is less "compatible" with the FM/stripy ground states than with the Néel/zigzag ones. This can be understood in the simple picture of the KH model on a four-site segment of the honeycomb lattice consisting of three bonds attached to a selected lattice site, as presented below.

Starting with $\varphi = \pi$ (FM ground state, e.g. along the z quantization axis), increasing φ leads to gradual increase of the FM Kitaev term which favors ferromagnetically aligned spins along the x, y, and z quantization axes for the x, y, and z directional bonds, respectively. It can easily be seen that, e.g., for the x bond, the eigenstate of the FM Kitaev-only Hamiltonian on that bond ($|\uparrow_x\uparrow_x\rangle$) has a 25% overlap with the FM ground state, $|\langle\uparrow_z\uparrow_z|\uparrow_x\uparrow_x\rangle|^2 = \frac{1}{4}$. While again a similar situation happens for the y bond, the overlap between such states for the z bond is maximal, i.e., these states are identical (we assume the same phase factors 1).

Next, we perform a similar analysis for $\varphi = 0$ and firstly assume that we deal with a *classical* Néel ground state, $|\uparrow_z\downarrow_z\rangle$. In this case for the "unsatisfied" bonds from the point of view of the increasing AF Kitaev interaction we also obtain that the eigenstate of the AF Kitaev-only Hamiltonian ($|\uparrow_x\downarrow_x\rangle$) on that bond has a 25% overlap with the classical Néel ground state—e.g., $|\langle\uparrow_z\downarrow_z|\uparrow_x\downarrow_x\rangle|^2 = \frac{1}{4}$. However, this situation changes once we consider that the spin quantum fluctuations dress the classical Néel ground state. This can be best understood if we assumed the unrealistic but insightful case of very strong quantum fluctuations destroying the classical Néel ground state: then for the x bond a singlet could be stabilized and the overlap between such a state and the state "favored" by the Kitaev term increases to 50%: $|\langle 0|\uparrow_x\downarrow_x\rangle|^2 = \frac{1}{2}$. This suggests that the Néel ground state, which *contains* quantum spin fluctuations, is more "compatible" with the states "favored" by the Kitaev terms than the FM ground state, resulting in more stable values of ordered moment for Néel phase. It seems that the above difference is visible in CMFT data but not in LSWT ones. We shall discuss this issue further by analyzing spin correlations below.

V. SPIN CORRELATIONS

Additional information about the ground state is given by spin-spin correlation functions. In Fig. 5(a) one can observe isotropic stable $\langle S_i^\gamma S_j^\gamma\rangle$ correlations in almost the entire AF phase (with $\langle \boldsymbol{S}_i \cdot \boldsymbol{S}_j\rangle \approx -0.36$ for $\varphi = 0$), while for the FM phase the anisotropy quickly develops when moving away from the FM Heisenberg point $\varphi = \pi$ (here $\langle \boldsymbol{S}_i \cdot \boldsymbol{S}_j\rangle$ reaches

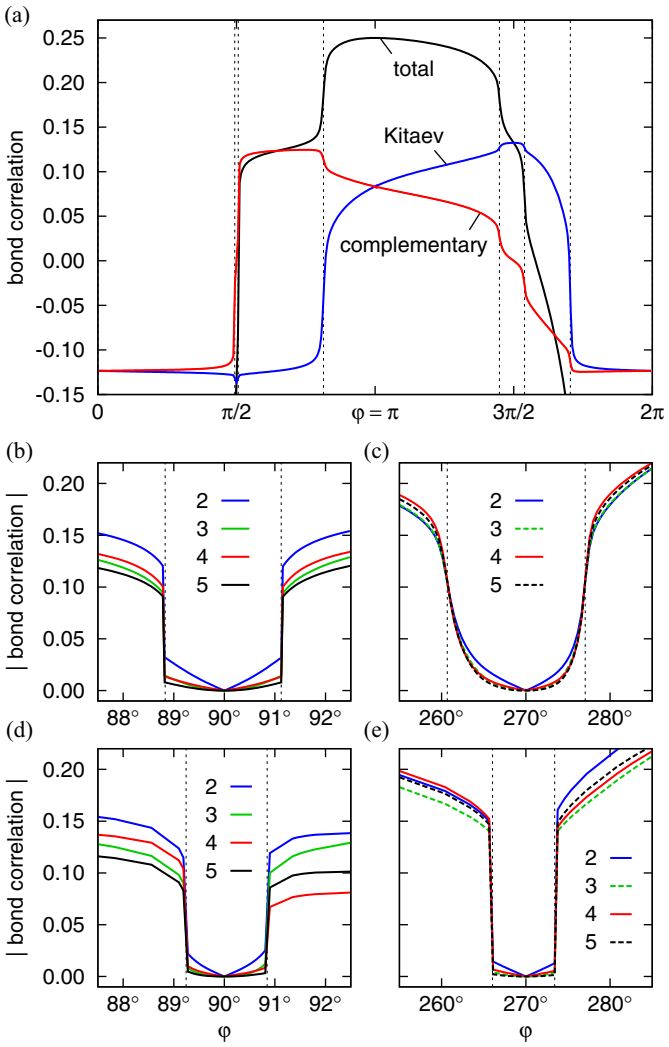

FIG. 5. (a) Spin correlations $\langle \boldsymbol{S}_i \cdot \boldsymbol{S}_j\rangle$ obtained within ED for the bonds between nearest neighbors (black line), spin correlations of the components active in the Kitaev interaction, $\langle S_i^\gamma S_j^\gamma\rangle$ (blue line), and complementary spin components, $\langle S_i^{\tilde\gamma} S_j^{\tilde\gamma}\rangle$ (red line). Below further neighbor spin correlations $|\langle \boldsymbol{S}_i \cdot \boldsymbol{S}_j\rangle|$ are shown (colors correspond here to different neighbors). ED: (b) near the AF spin-liquid phase, and (c) for the angle φ interval including the FM spin-liquid phase. CMFT—the neighborhood of the: (d) AF spin-liquid, and (e) FM spin-liquid region.

the classical value 0.25). This again demonstrates that the AF (and zigzag) phase is more robust and uniform than the FM (and stripy) phase.

Moreover, spin-spin correlations allow us to confirm the disordered regions around the Kitaev points as critical cases of quantum spin liquid [65]. At the Kitaev points ($J = 0$) we observe the expected undisturbed KSL pattern: nonzero values of nearest neighbor correlations between spin components active in the Kitaev interaction [blue curve in Fig. 5(a)] and vanishing correlations between complementary components (red curve). In contrast, the next nearest and further neighbor correlations disappear, see Figs. 5(b) and 5(c). While moving away from the Kitaev points the absolute values of the correlations enter the regions of slow growth—these are signatures of the critical spin-liquid phases and they look

similar in AF and FM spin liquid cases. At some point however proceeding further results in rapidly growing absolute values which mark KSL/LRO boundaries.

Furthermore, Figs. 5(b) and 5(c) prove that there is a qualitative difference between the two spin-liquid regimes. This is observed in the rapid growth of spin correlations at the onset of LRO: The steplike jump visible in Fig. 5(b) contrasts with the smoother crossover seen in Fig. 5(c). Below we investigate this distinct behavior by analyzing the dynamical spin susceptibility for various available phases. After Fourier transformation of the z-component correlations, we obtain the spin structure factor to be discussed in the context of the spin susceptibility also in Sec. VI.

As a supplement we present the further neighbor spin correlations obtained via CMFT [Figs. 5(d) and 5(e)]. One should remark that within KSL the averages $\langle S_i^z \rangle$ are 0 and CMFT is thus equivalent to ED for an isolated cluster (open boundary conditions). This leads to stronger finite size effects and larger inhomogeneity of the correlations. Nevertheless, considering the central part of the cluster, the emergence of the longer-range correlations away from the Kitaev point presented in Figs. 5(d) and 5(e) is almost identical to that calculated by ED, see Figs. 5(b) and 5(c).

VI. SPIN SUSCEPTIBILITY AND EXCITATIONS IN THE VICINITY OF THE KITAEV POINTS

Below we study the spin dynamics within the KH model by analyzing the dynamical spin susceptibility at $T = 0$,

$$\chi_{\alpha\alpha}(\boldsymbol{q},\omega) = i \int_0^\infty \langle \Phi_0 | \left[S^\alpha_{\boldsymbol{q}}(t), S^\alpha_{-\boldsymbol{q}}(0) \right] | \Phi_0 \rangle \, \mathrm{e}^{i\omega t} \, \mathrm{d}t, \qquad (5.1)$$

with the Fourier-transformed spin operator defined via

$$S^\alpha_{\boldsymbol{q}} = \frac{1}{\sqrt{N}} \sum_{\boldsymbol{R}} \mathrm{e}^{-i\boldsymbol{q}\cdot\boldsymbol{R}} S^\alpha_{\boldsymbol{R}}, \qquad (5.2)$$

and $|\Phi_0\rangle$ denoting the cluster ground state. For $\omega > 0$, the imaginary part of $\chi(\boldsymbol{q},\omega)_{\alpha\alpha}$ reads as

$$\chi''_{\alpha\alpha}(\boldsymbol{q},\omega) = -\mathrm{Im} \, \langle \Phi_0 | \, S^\alpha_{\boldsymbol{q}} \, \frac{1}{\omega + E_{\mathrm{GS}} - \mathcal{H} + i\delta} \, S^\alpha_{-\boldsymbol{q}} \, | \Phi_0 \rangle, \qquad (5.3)$$

which can be conveniently expressed as a sum over the excited states $\{|\nu\rangle\}$,

$$\chi''_{\alpha\alpha}(\boldsymbol{q},\omega) = \pi \sum_{|\nu\rangle} \left| \langle \nu | S^\alpha_{-\boldsymbol{q}} | \Phi_0 \rangle \right|^2 \delta(\omega - E_\nu), \qquad (5.4)$$

where the excitation energy E_ν is measured relative to the ground state energy E_{GS}. We have evaluated $\chi_{\alpha\alpha}(\boldsymbol{q},\omega)$ by ED on a hexagonal cluster of $N = 24$ sites. In the ED approach, the exact ground state of the cluster $|\Phi_0\rangle$ is found by Lanczos diagonalization, the operator $S^\alpha_{-\boldsymbol{q}}$ is applied, and the average of the resolvent $1/(z - \mathcal{H})$ is determined by Lanczos method using normalized $S^\alpha_{-\boldsymbol{q}}|\Phi_0\rangle$ as a starting vector [66].

In our case of the KH model, the calculation generally requires a relatively large number of Lanczos steps (up to one thousand) to achieve convergence of the dense high-energy part of the spectrum. Having the advantage of being exact, the method is limited by the $\boldsymbol{q}$ vectors accessible for a finite cluster and compatible with the PBC, and by finite-size effects due to small N. These concern mainly the low-energy part of χ'' and lead, e.g., to an enlarged gap of spin excitations in LRO phases of AF nature. Nevertheless, a qualitative understanding can still be obtained.

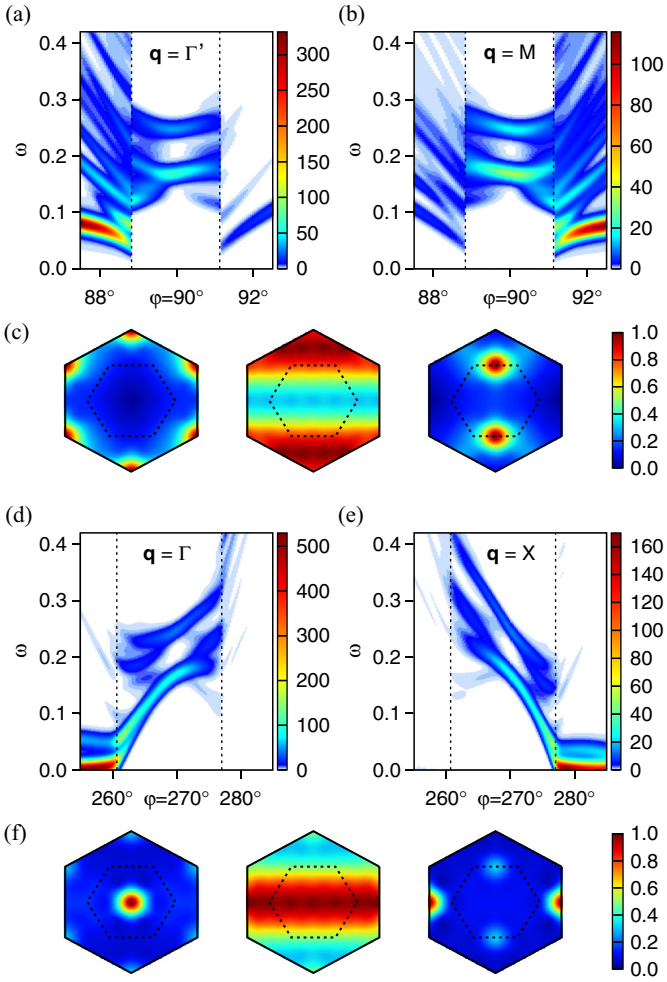

FIG. 6. (a) Dynamical spin susceptibility $\chi''(\boldsymbol{q},\omega)$ obtained by ED near the AF KSL phase at the characteristic wave vector of the AF order, $\boldsymbol{q} = \Gamma'$. (b) The same for the zigzag wave vector $\boldsymbol{q} = M$. (c) Brillouin zone portraits of the spin-structure factor $\langle S^z_{-\boldsymbol{q}} S^z_{\boldsymbol{q}} \rangle$ at $\varphi = 87.5°$, 90°, and 92.5° (interpolated from the ED data). The inner hexagon is the Brillouin zone of the honeycomb lattice; the outer one corresponds to the triangular lattice with the missing sites filled in. (d), (e) The same as in panels (a), (b) but for the interval containing the FM ($\boldsymbol{q} = \Gamma$) and stripy ($\boldsymbol{q} = X$) phase. (f) Brillouin zone portraits of the spin-structure factor obtained at $\varphi = 255°$, 270°, and 285°.

The evolution of numerically obtained $\chi''(\boldsymbol{q},\omega)_{\alpha\alpha}$ (5.4) with varying φ is presented in Figs. 6(a) and 6(b) for the region including AF spin-liquid phase, as well as in Figs. 6(d) and 6(e) for the region including the FM spin-liquid phase. The transitions are well visible at the characteristic $\boldsymbol{q}$ vectors of the individual LRO phases. The structure factor pattern, see Figs. 6(c) and 6(f), changes accordingly between the sharply peaked one in LRO phases and a wavelike form characteristic for nearest neighbor correlations in the spin-liquid phases.

After entering the spin-liquid phase, further changes of the spin response are very different for the AF and FM case. In the

AF case, there is a sharp transition—a level crossing for our cluster, so that the ground state changes abruptly. The original intense pseudo-Goldstone mode as well as many other excited states become inactive in the spin-liquid phase. The observed low-energy gap in $\chi''(\boldsymbol{q},\omega)_{\alpha\alpha}$ varies only slightly with φ.

In contrast, when entering the FM spin-liquid phase the excitation that used to be the gapless magnon mode is characterized by a gradually increasing gap which culminates at the Kitaev point. Starting from the Kitaev point, the gradual reduction of the low-energy gap in $\chi''(\boldsymbol{q},\omega)_{\alpha\alpha}$ due to the Heisenberg perturbation manifests itself by a development of finite spin correlations beyond nearest neighbors (already reported in Fig. 2 of Ref. [25]) and an increase of the static susceptibility to the magnetic field Zeeman coupled to the order parameter of the neighboring LRO phase. This susceptibility then diverges at the transition point (see also Fig. 3 of Ref. [25]).

VII. SUMMARY AND CONCLUSIONS

In the present paper we report a study of the phase diagram of the Kitaev-Heisenberg model by a combination of exact diagonalization and cluster mean field theory (CMFT), supplemented by the insights from linear spin-wave theory and the second-order perturbation theory. Both methods allowed to stabilize previously known phases with long range order: Néel, zigzag, FM, and stripy. Moreover, the ordered moment analysis provided by cluster mean field approach demonstrates Néel-zigzag and FM-stripy connections described before [34]. Compared to the previous CMFT studies utilizing $N = 6$ site cluster (see Ref. [56] or the Appendix), we have used a sufficiently large cluster of $N = 24$ sites preserving the lattice symmetries and improving the ratio between internal and boundary bonds. This led to a balanced approach which allowed us to treat both ordered and disordered (spin-liquid) states on equal footing.

As the main result, the present study uncovers a fundamental difference between the onset of broken symmetry phases in the vicinity of Kitaev points with antiferromagnetic or ferromagnetic interactions. While the spin liquids obtained at $K = +1$ and $K = -1$ are strictly equivalent and can be transformed one into the other in the absence of Heisenberg interactions (at $J = 0$), spin excitations and quantum phase transitions emerging at finite J are very different in both cases. For the antiferromagnetic Kitaev spin liquid phase ($K \simeq 1$) one finds that a gap opens abruptly in $\chi''(\boldsymbol{q},\omega)$ at $\boldsymbol{q} = \Gamma'$ and $\boldsymbol{q} = M$ when the ground state changes to the critical Kitaev quantum spin liquid. This phase transition is abrupt and occurs by level crossing. In contrast, for ferromagnetic spin liquid $K \simeq -1$ the gaps in $\chi''(\boldsymbol{q},\omega)$ at $\boldsymbol{q} = \Gamma$ and $\boldsymbol{q} = X$ open gradually from the points of quantum phase transition from ordered to disordered phase. With much weaker quantum corrections for ordered phases in the regime of ferromagnetic Kitaev interactions, the spin liquid is more robust near $K = -1$ as a phase that contains quantum fluctuations and survives in a broader regime than near $K = 1$ when antiferromagnetic Kitaev interactions are disturbed by increasing (antiferromagnetic or ferromagnetic) Heisenberg interactions. This behavior is reminiscent of the ferromagnetic Kitaev model in a weak magnetic field [65].

ACKNOWLEDGMENTS

We thank Giniyat Khaliullin for insightful discussions. We kindly acknowledge support by Narodowe Centrum Nauki (NCN, National Science Center) under Project No. 2012/04/A/ST3/00331. The CMFT spin-spin correlations were calculated at the Interdisciplinary Centre for Mathematical and Computational Modelling (ICM) of the University of Warsaw under Grant No. G66-22. J.R. and J.C. were supported by Czech Science Foundation (GAČR) under Project No. GJ15-14523Y and by the project CEITEC 2020 (LQ1601) with financial support from the Ministry of Education, Youth and Sports of the Czech Republic under the National Sustainability Programme II. Access to computing and storage facilities owned by parties and projects contributing to the National Grid Infrastructure MetaCentrum, provided under the program "Projects of Large Research, Development, and Innovations Infrastructures" (CESNET LM2015042), is acknowledged. G.J. is supported in part by the National Science Foundation under Grant No. NSF PHY11-25915.

APPENDIX: COMPARISON BETWEEN CMFT AND LINEARIZED CMFT FOR A SINGLE HEXAGON

Here we compare linearization results for a single hexagon with full CMFT to see how well linearized CMFT performs as a shortcut method. It is important to realize that this cluster is not compatible with stripy or zigzag order because of their four-site magnetic unit cell, see Fig. 1(b), and they are suppressed within vast regions of φ compared to the 24-site case. The size of the system allows for quick CMFT computations and enables detailed comparison between the two approaches. Moreover, specific problems linked to the above incompatibility make the $N = 6$-site cluster a good test case to illustrate the linearized CMFT.

Following the procedure described in Sec. III C, 6 eigenvalues λ_i are produced for each value of φ parameter. The corresponding spin patterns are inferred by inspecting the eigenvectors. Only the patterns associated with $\lambda_i > 1$ are able to grow during iterations and eventually stabilize as a

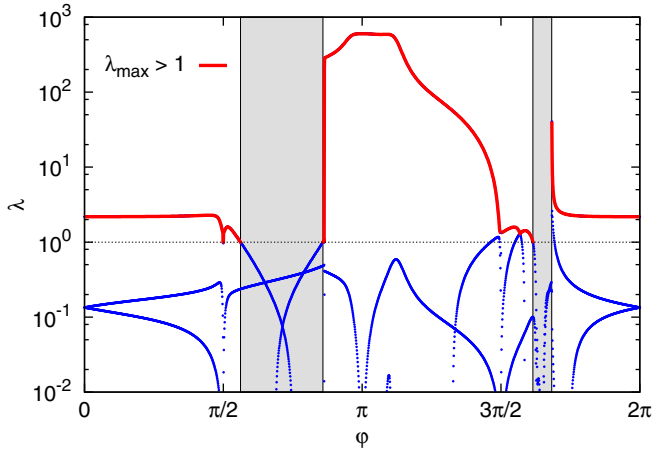

FIG. 7. Full linearized CMFT result for a single hexagon. Blue lines represent all emerged positive eigenvalues λ, while maximal λ larger than 1 is indicated in red.

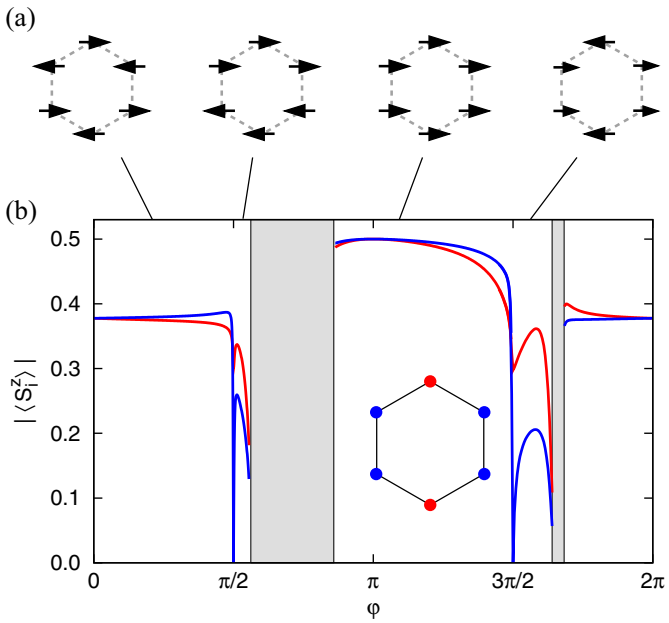

FIG. 8. (a) Spin patterns obtained for a single hexagon by CMFT. From the left: Néel, zigzag, FM, and stripy. (b) Phase diagram for a single hexagon determined by $|\langle S_i^z \rangle|$. Red and blue sites (see inset) are nonequivalent in the present CMFT due to the approximation given by Eq. (3.2) which generates the terms $\propto J$ that add to the Kitaev term only on the vertical bonds $\langle ij \rangle \parallel z$ in the MF part of the Hamiltonian (2.1).

self-consistent solution of full CMFT. Comparison of both methods presented in Figs. 7 and 8 provides the phase diagram for a single hexagon: Néel phase for $\varphi \in [0,0.5)\pi$, KSL for $\varphi = \frac{\pi}{2}$, zigzag phase for $\varphi \in (0.5,0.555)\pi$, disordered region I for $\varphi \in (0.555,0.864)\pi$, FM phase for $\varphi \in (0.864,1.5)\pi$, KSL for $\varphi = \frac{3}{2}\pi$, stripy phase for $\varphi \in (1.5,1.62)\pi$ (linearization), $\varphi \in (1.5,1.64)\pi$ (CMFT), disordered region II for $\varphi \in (1.62,1.684)\pi$ (linearization) and $\varphi \in (1.64,1.684)\pi$ (CMFT), and Néel phase for $\varphi \in (1.684,2]\pi$. In contrast to $N = 24$ cluster the two spin-liquid regions are replaced by single points $\varphi = \frac{\pi}{2}$ and $\varphi = \frac{3}{2}\pi$.

Striking difference between phase diagrams for 24-site and 6-site clusters is the reduction of the zigzag and stripy phases and the emergence of two regions of disorder indicated by two gray-shaded regions. Here all $\lambda_i < 1$ and no spin pattern is strong enough to stabilize. Zigzag pattern emerges from CMFT with random initial values of $\langle S_i^z \rangle$ without additional help. Stripy pattern however is more difficult to catch. As one can see in Fig. 7, two different λ_i corresponding to two stripy patterns exchange at $\varphi = 1.568\pi$. Unfortunately, huge parasitic oscillations make these patterns extremely difficult to stabilize within CMFT. These stem from a large negative λ_i that previously corresponded to FM pattern and decreased rapidly for $\varphi > 1.5\pi$. If one recalls that the equivalent of one iteration in the linearized version of CMFT is in fact multiplication by λ_i, one can easily see that large negative λ_i would cause oscillations with an exponentially growing amplitude when performing the iterations of the self-consistent loop. To overcome this issue we introduce a damping into a self-consistent loop by taking $(1-d)\langle S_i^z \rangle_{\text{fin}} + d\langle S_i^z \rangle_{\text{in}}$ as the new averages. Here $d < 1$ is a suitably chosen damping factor. With this modification CMFT produces one finite stripy order suggested by linearization. However since the parasitic negative λ_i grows enormously in magnitude as we approach the phase boundary an extreme damping has to be included making the phase boundary hard to determine by using CMFT.

In conclusion, it is evident that the ordered patterns suggested by linearization were reproduced by CMFT within regions dictated by the maximal $\lambda_i > 1$. Moreover, the linearized procedure indicated possible difficulties with stabilizing stripy phases that had to be cured by a strong damping introduced into the self-consistent loop.

[1] Bruce Normand, Cont. Phys. **50**, 533 (2009).
[2] Leon Balents, Nature (London) **464**, 199 (2010).
[3] L. Savary and L. Balents, Rep. Prog. Phys. **80**, 016502 (2017).
[4] G. Khaliullin and S. Maekawa, Phys. Rev. Lett. **85**, 3950 (2000); G. Khaliullin, P. Horsch, and A. M. Oleś, *ibid.* **86**, 3879 (2001).
[5] A. B. Harris, T. Yildirim, A. Aharony, O. Entin-Wohlman, and I. Ya. Korenblit, Phys. Rev. Lett. **91**, 087206 (2003).
[6] M. Daghofer, K. Wohlfeld, A. M. Oleś, E. Arrigoni, and P. Horsch, Phys. Rev. Lett. **100**, 066403 (2008); K. Wohlfeld, M. Daghofer, A. M. Oleś, and P. Horsch, Phys. Rev. B **78**, 214423 (2008).
[7] M. Daghofer, A. Nicholson, A. Moreo, and E. Dagotto, Phys. Rev. B **81**, 014511 (2010); A. Nicholson, W. Ge, X. Zhang, J. Riera, M. Daghofer, A. M. Oleś, G. B. Martins, A. Moreo, and E. Dagotto, Phys. Rev. Lett. **106**, 217002 (2011).
[8] P. Wróbel and A. M. Oleś, Phys. Rev. Lett. **104**, 206401 (2010); P. Wróbel, R. Eder, and A. M. Oleś, Phys. Rev. B **86**, 064415 (2012).
[9] S. Di Matteo, G. Jackeli, C. Lacroix, and N. B. Perkins, Phys. Rev. Lett. **93**, 077208 (2004); S. Di Matteo, G. Jackeli, and N. B. Perkins, Phys. Rev. B **72**, 024431 (2005).
[10] G. Khaliullin, Prog. Theor. Phys. Suppl. **160**, 155 (2005).
[11] G. Jackeli and D. A. Ivanov, Phys. Rev. B **76**, 132407 (2007).
[12] G. Jackeli and D. I. Khomskii, Phys. Rev. Lett. **100**, 147203 (2008).
[13] F. Krüger, S. Kumar, J. Zaanen, and J. van den Brink, Phys. Rev. B **79**, 054504 (2009).
[14] Gia-Wei Chern and N. Perkins, Phys. Rev. B **80**, 220405(R) (2009).
[15] A. van Rynbach, S. Todo, and S. Trebst, Phys. Rev. Lett. **105**, 146402 (2010).
[16] F. Trousselet, A. Ralko, and A. M. Oleś, Phys. Rev. B **86**, 014432 (2012).
[17] G. Chen and L. Balents, Phys. Rev. Lett. **110**, 206401 (2013).
[18] M. Daghofer, A. M. Oleś, and W. von der Linden, Phys. Rev. B **70**, 184430 (2004).
[19] A. Reitsma, L. F. Feiner, and A. M. Oleś, New J. Phys. **7**, 121 (2005).
[20] W. Witczak-Krempa, G. Chen, Y. B. Kim, and L. Balents, Annu. Rev. Condens. Matter Phys. **5**, 57 (2014).

[21] W. Brzezicki, A. M. Oleś, and M. Cuoco, Phys. Rev. X **5**, 011037 (2015); W. Brzezicki, M. Cuoco, and A. M. Oleś, J. Supercond. Novel Magn. **29**, 563 (2016); **30**, 129 (2017).
[22] G. Jackeli and G. Khaliullin, Phys. Rev. Lett. **102**, 017205 (2009).
[23] A. Kitaev, Ann. Phys. (NY) **321**, 2 (2006).
[24] G. Baskaran, S. Mandal, and R. Shankar, Phys. Rev. Lett. **98**, 247201 (2007).
[25] J. Chaloupka, G. Jackeli, and G. Khaliullin, Phys. Rev. Lett. **105**, 027204 (2010).
[26] Y. Singh and P. Gegenwart, Phys. Rev. B **82**, 064412 (2010); F. Trousselet, G. Khaliullin, and P. Horsch, *ibid.* **84**, 054409 (2011).
[27] X. Liu, T. Berlijn, W.-G. Yin, W. Ku, A. Tsvelik, Y.-J. Kim, H. Gretarsson, Y. Singh, P. Gegenwart, and J. P. Hill, Phys. Rev. B **83**, 220403(R) (2011).
[28] Y. Singh, S. Manni, J. Reuther, T. Berlijn, R. Thomale, W. Ku, S. Trebst, and P. Gegenwart, Phys. Rev. Lett. **108**, 127203 (2012).
[29] S. K. Choi, R. Coldea, A. N. Kolmogorov, T. Lancaster, I. I. Mazin, S. J. Blundell, P. G. Radaelli, Y. Singh, P. Gegenwart, K. R. Choi, S.-W. Cheong, P. J. Baker, C. Stock, and J. Taylor, Phys. Rev. Lett. **108**, 127204 (2012).
[30] F. Ye, S. Chi, H. Cao, B. C. Chakoumakos, J. A. Fernandez-Baca, R. Custelcean, T. F. Qi, O. B. Korneta, and G. Cao, Phys. Rev. B **85**, 180403 (2012).
[31] R. Comin, G. Levy, B. Ludbrook, Z.-H. Zhu, C. N. Veenstra, J. A. Rosen, Y. Singh, P. Gegenwart, D. Stricker, J. N. Hancock, D. van der Marel, I. S. Elfimov, and A. Damascelli, Phys. Rev. Lett. **109**, 266406 (2012).
[32] H. Gretarsson, J. P. Clancy, X. Liu, J. P. Hill, E. Bozin, Y. Singh, S. Manni, P. Gegenwart, J. Kim, A. H. Said, D. Casa, T. Gog, M. H. Upton, H.-S. Kim, J. Yu, V. M. Katukuri, L. Hozoi, J. van den Brink, and Y.-J. Kim, Phys. Rev. Lett. **110**, 076402 (2013).
[33] F. Trousselet, M. Berciu, A. M. Oleś, and P. Horsch, Phys. Rev. Lett. **111**, 037205 (2013).
[34] J. Chaloupka, G. Jackeli, and G. Khaliullin, Phys. Rev. Lett. **110**, 097204 (2013).
[35] V. M. Katukuri, S. Nishimoto, V. Yushankhai, A. Stoyanova, H. Kandpal, S. Choi, R. Coldea, I. Rousochatzakis, L. Hozoi, and J. van den Brink, New. J. Phys. **16**, 013056 (2014).
[36] S. M. Winter, Y. Li, H. O. Jeschke, and R. Valentí, Phys. Rev. B **93**, 214431 (2016).
[37] F. Trousselet, P. Horsch, A. M. Oleś, and W.-L. You, Phys. Rev. B **90**, 024404 (2014).
[38] S. H. Chun, J.-W. Kim, J. Kim, H. Zheng, C. C. Stoumpos, C. D. Malliakas, J. F. Mitchell, K. Mehlawat, Y. Singh, Y. Choi, T. Gog, A. Al-Zein, M. Moretti Sala, M. Krisch, J. Chaloupka, G. Jackeli, G. Khaliullin, and B. J. Kim, Nat. Phys. **11**, 462 (2015).
[39] J. Chaloupka and G. Khaliullin, Phys. Rev. B **92**, 024413 (2015).
[40] J. G. Rau and H. Y. Kee, arXiv:1408.4811.
[41] A. Banerjee, C. A. Bridges, J.-Q. Yan, A. A. Aczel, L. Li, M. B. Stone, G. E. Granroth, M. D. Lumsden, Y. Yiu, J. Knolle, S. Bhattacharjee, D. L. Kovrizhin, R. Moessner, D. A. Tennant, D. G. Mandrus, and S. E. Nagler, Nat. Mater. **15**, 733 (2016).
[42] J. Reuther, D. A. Abanin, and R. Thomale, Phys. Rev. B **84**, 014417 (2011).
[43] A. F. Albuquerque, D. Schwandt, B. Hetényi, S. Capponi, M. Mambrini, and A. M. Laüchli, Phys. Rev. B **84**, 024406 (2011).
[44] D. C. Cabra, C. A. Lamas, and H. D. Rosales, Phys. Rev. B **83**, 094506 (2011); A. Kalz, M. Arlego, D. Cabra, A. Honecker, and G. Rossini, *ibid.* **85**, 104505 (2012); H. D. Rosales, D. C. Cabra, C. A. Lamas, P. Pujol, and M. E. Zhitomirsky, *ibid.* **87**, 104402 (2013).
[45] X. Y. Song, Y. Z. You, and L. Balents, Phys. Rev. Lett. **117**, 037209 (2016).
[46] J. G. Rau, Eric Kin-Ho Lee, and H. Y. Kee, Phys. Rev. Lett. **112**, 077204 (2014).
[47] J. Oitmaa, Phys. Rev. B **92**, 020405(R) (2015).
[48] H.-C. Jiang, Z.-C. Gu, X.-L. Qi, and S. Trebst, Phys. Rev. B **83**, 245104 (2011); J. Reuther, R. Thomale, and S. Trebst, *ibid.* **84**, 100406 (2011); I. Kimchi and Y. Z. You, *ibid.* **84**, 180407 (2011); R. Schaffer, S. Bhattacharjee, and Y. B. Kim, *ibid.* **86**, 224417 (2012); Y. Yu, L. Liang, Q. Niu, and S. Qin, *ibid.* **87**, 041107 (2013); E. Sela, H.-C. Jiang, M. H. Gerlach, and S. Trebst, *ibid.* **90**, 035113 (2014).
[49] J. Osorio Iregui, P. Corboz, and M. Troyer, Phys. Rev. B **90**, 195102 (2014).
[50] K. Li, S.-L. Yu, and J.-X. Li, New J. Phys. **17**, 043032 (2015).
[51] M. Becker, M. Hermanns, B. Bauer, M. Garst, and S. Trebst, Phys. Rev. B **91**, 155135 (2015).
[52] G. Jackeli and A. Avella, Phys. Rev. B **92**, 184416 (2015).
[53] I. Rousochatzakis, U. K. Rössler, J. van den Brink, and M. Daghofer, Phys. Rev. B **93**, 104417 (2016).
[54] W. Brzezicki, J. Dziarmaga, and A. M. Oleś, Phys. Rev. Lett. **109**, 237201 (2012); Phys. Rev. B **87**, 064407 (2013).
[55] W. Brzezicki and A. M. Oleś, Phys. Rev. B **83**, 214408 (2011).
[56] D. Gotfryd and A. M. Oleś, Acta Phys. Polon. A **127**, 318 (2015).
[57] K. Foyevtsova, H. O. Jeschke, I. I. Mazin, D. I. Khomskii, and R. Valentí, Phys. Rev. B **88**, 035107 (2013).
[58] L. R. Walker, *Spin Waves and Other Magnetic Modes in Magnetism* (Academic Press, New York and London, 1963).
[59] M. Raczkowski and A. M. Oleś, Phys. Rev. B **66**, 094431 (2002).
[60] P. A. Maksimov and A. L. Chernyshev, Phys. Rev. B **93**, 014418 (2016).
[61] Zheng Weihong, J. Oitmaa, and C. J. Hamer, Phys. Rev. B **44**, 11869 (1991).
[62] J. D. Reger, J. A. Riera, and A. P. Young, J. Phys.: Condens. Matter **1**, 1855 (1989).
[63] E. V. Castro, N. M. R. Peres, K. S. D. Beach, and A. W. Sandvik, Phys. Rev. B **73**, 054422 (2006).
[64] U. Löw, Condens. Matter Phys. **12**, 497 (2009).
[65] K. S. Tikhonov, M. V. Feigel'man, and A. Yu. Kitaev, Phys. Rev. Lett. **106**, 067203 (2011).
[66] P. Fulde, *Electron Correlations in Molecules and Solids*, Springer Series in Solid-State Sciences, Vol. 100 (Springer-Verlag, Berlin/Heidelberg/New York, 1995).

PHYSICAL REVIEW B **99**, 064425 (2019)

Kitaev-like honeycomb magnets: Global phase behavior and emergent effective models

Juraj Rusnačko,[1,2] Dorota Gotfryd,[3,4] and Jiří Chaloupka[1,2]

[1]*Central European Institute of Technology, Masaryk University, Kamenice 753/5, CZ-62500 Brno, Czech Republic*

[2]*Department of Condensed Matter Physics, Faculty of Science, Masaryk University, Kotlářská 2, CZ-61137 Brno, Czech Republic*

[3]*Institute of Theoretical Physics, Faculty of Physics, University of Warsaw, Pasteura 5, PL-02093 Warsaw, Poland*

[4]*Marian Smoluchowski Institute of Physics, Jagiellonian University, Łojasiewicza 11, PL-30348 Kraków, Poland*

(Received 14 October 2018; revised manuscript received 28 January 2019; published 19 February 2019)

Compounds of transition metal ions with strong spin-orbit coupling recently attracted attention due to the possibility to host frustrated bond-dependent anisotropic magnetic interactions. In general, such interactions lead to complex phase diagrams that may include exotic phases, e.g., the Kitaev spin liquid. Here we report on our comprehensive analysis of the global phase diagram of the extended Kitaev-Heisenberg model relevant to honeycomb lattice compounds Na_2IrO_3 and α-$RuCl_3$. We have utilized recently developed method based on spin coherent states that enabled us to resolve arbitrary spin patterns in the cluster ground states obtained by exact diagonalization. Global trends in the phase diagram are understood in combination with the analytical mappings of the Hamiltonian that uncover peculiar links to known models—Heisenberg, Ising, Kitaev, or compass models on the honeycomb lattice—or reveal entire manifolds of exact fluctuation-free ground states. Finally, our study can serve as a methodological example that can be applied to other spin models with complex bond-dependent non-Heisenberg interactions.

DOI: 10.1103/PhysRevB.99.064425

I. INTRODUCTION

In contrast to simple examples of Heisenberg magnets discussed in standard textbooks, frustrated spin systems [1] offer much wider range of phenomena, including the exotic spin-liquid behavior [2,3] or the emergence of effective monopoles in spin-ice pyrochlores [4,5]. The usual sources of frustration are frustrated geometry of the lattice (e.g., kagome [6]) or the presence of longer-range interactions competing with the nearest-neighbor ones (as, e.g., in J_1-J_2 model [7–9]) and possibly among themselves. Within the last decade, pseudospin-$\frac{1}{2}$ systems with frustrated bond-dependent non-Heisenberg interactions emerging in Mott insulators as a consequence of spin-orbit coupling (SOC) became a subject of intense research [10–16]. While one of the main motivations has been a possible realization of the Kitaev honeycomb model [17], the presence of additional interactions leads to very rich magnetic behavior that is particularly attractive as well as challenging to study.

The basic element enabling the realization of the above models possessing bond-dependent anisotropic interactions has been well known for a long time. It relies on a d^5 valence configuration of heavy transition-metal ions with large SOC, which combines the spin $s = \frac{1}{2}$ and effective orbital angular momentum $l_{\text{eff}} = 1$ of the hole in the t_{2g}^5 configuration into $J_{\text{eff}} = \frac{1}{2}$ Kramers doublet ground state [18,19]. A direct experimental evidence for the spin-orbital entangled multiplet structure [20] was obtained, e.g., by resonant x-ray scattering on Sr_2IrO_4 [21] containing d^5 Ir^{4+} ions. It was the seminal theoretical proposal by Jackeli and Khaliullin [22] that suggested how to exploit the $J_{\text{eff}} = \frac{1}{2}$ pseudospins in Mott insulators with large SOC. Two lines of intense research followed. The first one focuses on the square lattice case with the resulting Heisenberg interactions among the pseudospins—a situation appealingly analogous to undoped cuprates. Cupratelike magnetism was indeed found in perovskite iridates [23] and certain observations support the idea to extend the analogy to the doped case [24,25]. Yet bigger excitement was initiated by a proposal that the honeycomb $J_{\text{eff}} = \frac{1}{2}$ compounds may be close to the Kitaev limit where Ising-like bond-dependent interactions lead to a spin-liquid ground state. Such an exotic effective spin system may naturally arise when translating the bond-anisotropic interactions of the d orbitals appearing in Kugel-Khomskii models [26] into the pseudospin space via the SOC-induced spin-orbital entanglement [19,27].

In the search of materials close to the Kitaev limit, much attention has been paid to the honeycomb iridates Na_2IrO_3, α-Li_2IrO_3, and the ruthenate α-$RuCl_3$ [28] that is claimed to show signatures of Kitaev physics in the excitation spectra [29–32]. However, these compounds were found to host long-range magnetic order instead—zigzag type in Na_2IrO_3 [33–35] and α-$RuCl_3$ [29,36,37] and spiral type in α-Li_2IrO_3 [38]. Only very recently, an evidence for a liquid state was found in a related compound $H_3LiIr_2O_6$ [39]. Even though the zigzag phase is present in the phase diagram of the originally proposed Kitaev-Heisenberg model [40], later experiments on Na_2IrO_3 showed that it gives an inconsistent ordered moment direction [41] and additional bond-anisotropic and/or further-neighbor interactions have to be invoked [42–47]. In the resulting extended Kitaev-Heisenberg models, the highly anisotropic interactions lead to complex phase behavior (see Refs. [15,42,43] for examples) or unusual spin excitation spectra showing, e.g., a breakdown of the magnon picture even in the long-range ordered phase away from the Kitaev limit [48] or topological features [49,50].

The (extended) Kitaev-Heisenberg models are not limited to the honeycomb lattice. A large number of other situations have been discussed, including triangular [19,51–54] and kagome [55] lattices and suitable types of three-dimensional structures such as experimentally realized hyperhoneycomb [56–60], harmonic honeycomb [57,59,61–63], hyperkagome [27,64], fcc [65–67], and pyrochlore lattices [68,69], or hypothetical hyperoctagon lattice [70]. Finally, the concept of Kitaev interactions in pseudospin $J_{\rm eff} = \frac{1}{2}$ systems has been recently extended to d^7 compounds such as those containing Co^{2+} [71,72].

In general, a thorough inspection of an extended Kitaev-Heisenberg model in terms of spin structures, excitations, etc. through the parameter space is desired. Apart from theoretical interest, this is mostly in order to establish it as an effective model for a concrete material and to narrow down the parameter regime. Methodologically, the inspection is complicated by the new kind of frustration stemming from the bond dependence of the interactions. Since exotic features such as spin-liquid ground states and fractionalized excitations are "around," simple approaches—for instance, the Luttinger-Tisza method [73] or linear spin waves—often have a limited success and one has to resort to unbiased numerical methods fully incorporating quantum effects. Of a great value are also exact symmetry properties, such as dual mappings of the Hamiltonian utilizing sublattice spin rotations [11,19,69,74,75] that proved surprisingly powerful when establishing and interpreting the phase diagram.

The aim of this paper is to perform a detailed analysis of the phase diagram of the extended Kitaev-Heisenberg model (EKH) relevant for honeycomb materials. Portions of the phase diagram have been reported before by several studies, both on the classical level [42,46,76] as well as including the quantum effects [15,47,77–79]. Here we take a global view of the phase diagram, trying to understand its trends based on the competition/cooperation of the interactions and general symmetry properties. We also analyze the internal structure of the phases including the ordered moment direction that is useful when fixing the model parameters based on experimental data [41,80]. To this end, we build on previous work [80] and use exact diagonalization combined with ground-state analysis based on spin-1/2 coherent states and complemented by cluster mean-field theory. This allows us to determine the spin structures through the phase diagram, including the noncollinear ones and estimate the amount of quantum fluctuations. The global analysis revealed two surprising features that underline the richness of the EKH model and enable a deeper understanding of its phase behavior: (i) sets of exact fluctuation-free ground states forming entire manifolds in the parameter space and (ii) possibility to map part of the phase space of the EKH model to a model characterized by a single bond-dependent interaction axis. This way several models of separate interest "emerge" from the EKH model: Ising, Kitaev, and compass [11,26] models as well as their combinations.

The paper is organized as follows: The model and numerical methods are introduced in Secs. II and III, respectively. Section IV contains the phase diagram of the model along with a discussion of its phases. Section V analyzes the manifolds of fluctuation-free ground states. Finally, Sec. VI is devoted to the study of the Ising-Kitaev-compass case and its links to EKH model.

II. EXTENDED KITAEV-HEISENBERG MODEL

A. Model Hamiltonian

According to the currently available prevailing evidence for honeycomb materials [15] and following Ref. [80], we choose to study the nearest-neighbor extended Kitaev-Heisenberg model [42–44] complemented by third-nearest neighbor Heisenberg exchange. The nearest-neighbor (NN) part of the model contains—in addition to the usual Heisenberg exchange—all possible anisotropic terms that are allowed by symmetry of the trigonally distorted honeycomb lattice [44,75]. It is most conveniently expressed in cubic coordinates x, y, z introduced in Fig. 1(a) that allow to easily incorporate the discrete rotational C_3 symmetry. For a bond of c direction, the Hamiltonian contribution reads as

$$\mathcal{H}_{ij}^{(c)} = J\,\boldsymbol{S}_i\cdot\boldsymbol{S}_j + K\,S_i^zS_j^z + \Gamma\left(S_i^xS_j^y + S_i^yS_j^x\right) + \Gamma'\left(S_i^xS_j^z + S_i^zS_j^x + S_i^yS_j^z + S_i^zS_j^y\right), \tag{1}$$

whereas the contributions for the other bond directions are obtained by a cyclic permutation of the spin components S^x, S^y, and S^z. The J and K terms alone constitute the Kitaev-Heisenberg model [22,74] that has been subject to extensive studies [40,74,81–88] and still serves as a prototype model to capture a departure from the Kitaev physics. In light of experimental data [41], it has been generally recognized that further anisotropic terms are needed, leading to the addition of the Γ and Γ' terms introduced in Refs. [42–44]. When studying the phase diagram we keep signs of J and K flexible and fix the signs $\Gamma > 0$ and $\Gamma' < 0$ following the *ab initio* calculations as well as the perturbative evaluation of the effective interactions [43,47]. According to the latter one, small negative Γ' should correspond to a trigonal compression of the

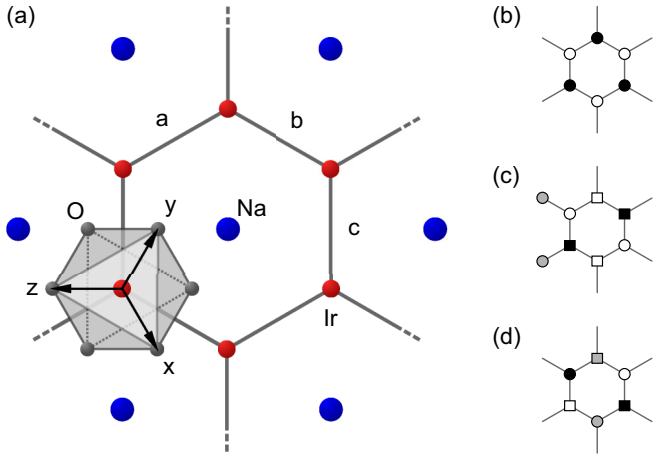

FIG. 1. (a) Honeycomb $NaIr_2O_6$ layer. Iridium ions form a honeycomb lattice with a sodium atom in the middle of each hexagon. Each iridium atom is surrounded by an octahedron of oxygens; the neighboring octahedra share an edge. The figure shows also the definition of cubic x, y, z axes and the bond directions a, b, c. [(b)–(d)] Sublattices of the two-, four- and six-sublattice transformations $\mathcal{T}_2$, $\mathcal{T}_4$, $\mathcal{T}_6$ that reveal the points of hidden SU(2) symmetry.

lattice [43], observed in Na_2IrO_3 [34,35]. Moreover, several *ab initio* studies have evaluated the importance of further-neighbor couplings (see, e.g., Refs. [45,47]). In Ref. [47], the effective spin Hamiltonians for Na_2IrO_3, α-$RuCl_3$, and α-Li_2IrO_3 were constructed using a combination of DFT and cluster exact diagonalization that equally treated interactions up to third nearest neighbors. Among the further-neighbor interactions, a significant value of $J_3 > 0$ was found for all three compounds, which leads us to the complete model considered here

$$\mathcal{H} = \sum_{\langle ij\rangle\in \mathrm{NN}} \mathcal{H}_{ij}^{(\gamma)} + \sum_{\langle ij\rangle\in 3^{\mathrm{rd}}\ \mathrm{NN}} J_3 \boldsymbol{S}_i \cdot \boldsymbol{S}_j \,. \tag{2}$$

B. Hidden symmetries of the model

The NN part of the above model ($J_3 = 0$) has rich symmetry properties explored in detail in the previous work [75]. First, it supports a self-dual transformation $\mathcal{T}_1$ that corresponds to a global π rotation of the spins around the axis perpendicular to the honeycomb plane. Such a transformation fully preserves the form of the Hamiltonian but replaces the values of the parameters $JK\Gamma\Gamma'$ by another set of values. Second, Ref. [75] has also identified a number of special parameter combinations—the points of "hidden" SU(2) symmetry in the parameter space—for which the NN model maps to ferromagnetic (FM) or antiferromagnetic (AF) Heisenberg model on the honeycomb lattice. This is achieved by employing either two-, four-, or six-sublattice coverings of the honeycomb lattice as depicted in Figs. 1(b)–1(d) and performing selected sublattice-dependent rotations of the spins. The neighboring spins that belong to different sublattices are therefore rotated in a different fashion and the interaction among those spins takes a modified form, in certain cases, the simple Heisenberg one. For these particular cases, the seemingly anisotropic model is thus exactly equivalent to the Heisenberg model on the honeycomb lattice. By using the same transformation backwards, we can exploit the known properties of Heisenberg model obtaining thereby, e.g., the ordering pattern or excitation spectra at the points of "hidden" SU(2) symmetry. Due to the sublattice structure of the transformation, the simple ordering patterns of Heisenberg FM or AF transform to more complex ones such as stripy, zigzag, or even noncollinear vortex pattern.

As a well-known example, we can consider the Kitaev-Heisenberg model with the parameters satisfying the relation $K = -2J$ and the four-sublattice covering shown in Fig. 1(c). Keeping the spins at the sites marked by □ unrotated, and applying π rotations around the x, y, or z axes to the spins at the sites attached to the □ sites by the a, b, or c bond, respectively, we obtain the Heisenberg Hamiltonian $\mathcal{H} = -J\sum_{\langle ij\rangle} \boldsymbol{S'}_i \cdot \boldsymbol{S'}_j$ in the rotated spin variables $\boldsymbol{S}'$. In the notation of Ref. [75], this transformation is called $\mathcal{T}_4$. The other possibilities include two-sublattice transformation $\mathcal{T}_2$, the six-sublattice $\mathcal{T}_6$, and the combinations $\mathcal{T}_1\mathcal{T}_4$ and $\mathcal{T}_2\mathcal{T}_6$. All these points of "hidden" SU(2) symmetry summarized in Table I and Fig. 3 of Ref. [75] provide exact reference points in the parameter space and will be extensively utilized in the present study.

III. METHODS

To solve the model, we use the standard Lanczos exact diagonalization (ED) technique employing a finite cluster [89]. The calculated cluster ground state is subsequently analyzed utilizing spin-1/2 coherent states [80] as detailed below. The ED technique is complemented by the cluster mean-field theory (CMFT). This combination is useful for a global characterization of the phase diagram—ED gives the ground-state characteristics such as energies and spin correlations, the analysis based on spin-1/2 coherent states enables to better assess the ordering patterns and the direction of magnetic moments, and CMFT supplements this information by the length of the ordered moments, which is not directly accessible by ED.

In both cases, we use a hexagonal 24-site cluster with periodic boundary conditions applied. This cluster has a fully symmetric shape and supports all the phases with hidden SU(2) symmetry [75]. It is therefore expected to provide a fair environment for the competition of the phases, with the exception of the possible spiral phases that are forced to fit the periodic boundary conditions and may be thus slightly suppressed. In this specific case, we have extended our ED analysis to 32-site clusters.

A. Spin-1/2 coherent states for noncollinear phases

The analysis of the exact ground state of the cluster obtained by ED presents a challenge—the cluster ground state does not spontaneously break symmetry but instead contains a linear combination of all the degenerate spin configurations. To resolve the dominant configuration and obtain the direction of the pseudospins from the ED ground state, we follow Ref. [80] and employ spin-1/2 coherent states. Such a state, polarized in a direction given by spherical angles θ and ϕ is given by

$$|\theta,\phi\rangle = e^{-i\phi S^z} e^{-i\theta S^y} |\uparrow\rangle, \tag{3}$$

where we make a standard choice of cubic z direction as the quantization axis. The cluster spin-coherent state is then a direct product of coherent states on each site j:

$$|\Psi\rangle = \prod_{j=1}^{N} |\theta_j,\phi_j\rangle. \tag{4}$$

This state can be understood as a classical (fluctuation-free) spin pattern with the individual spins pointing in the directions determined by the angles θ_j and ϕ_j. By calculating the overlap $\langle\Psi|\mathrm{GS}\rangle$ and maximizing its absolute value by varying the angles, we can identify the classical pattern that best fits the exact ground state $|\mathrm{GS}\rangle$.

For collinear phases (in the case of EKH model, these are FM, AF, zigzag, and stripy) the cluster spin-coherent state is captured by a single pair (θ,ϕ), which makes it easy to find the moment direction by inspecting the probability map $P(\theta,\phi) = |\langle\Psi|\mathrm{GS}\rangle|^2$ and finding the maximum. However, already the analysis of hidden SU(2) points revealed the existence of several noncollinear "vortex" phases in the phase diagram of the EKH model [75]. In the general case, the probability $P = |\langle\Psi|\mathrm{GS}\rangle|^2$ has to be maximized with respect to all $2N$ angles. For our cluster with $N = 24$ sites, this poses

a nontrivial computational problem of global optimization in 48-dimensional space. To this end, we use the particle swarm method for global optimization, which yields a result further refined by a local optimization algorithm.

The demanding task can be partly avoided by estimating in advance the parameter windows where noncollinear phases can be found. This can be achieved by first finding the optimal spin configuration among the collinear ones and calculating the full Hessian matrix of second derivatives (with respect to all 48 angular parameters) for such a configuration. The potential instability of the collinear phase can be identified by analyzing the eigenvalues of this Hessian matrix.

B. Cluster mean-field theory

Similarly to ED, within CMFT we periodically cover the lattice by copies of a given cluster. The bonds connecting the cluster copies (external bonds) are treated in a mean-field approximation, replacing the contributions to the bond Hamiltonian according to the recipe

$$S_i^\alpha S_j^\beta \approx \langle S_i^\alpha \rangle S_j^\beta + S_i^\alpha \langle S_j^\beta \rangle - \langle S_i^\alpha \rangle \langle S_j^\beta \rangle, \tag{5}$$

while the internal bonds of the cluster are kept fully quantum [81]. The mean-field approximation generates effective magnetic fields acting at the outer sites of the cluster and polarizing the cluster ground state to be determined by ED. The polarizing fields depend on the averages $\langle S_i^\alpha \rangle$ measured on the polarized ground state, which leads to a selfconsistent problem with much higher computational demands than the pure ED. On the other hand, by explicitly breaking the ground-state symmetry, the CMFT method allows to directly determine the ordering pattern and estimate the ordered moment length.

The introduction of the mean-field boundary makes the sites of the cluster nonequivalent. In combination with the highly anisotropic bond-dependent interactions, the spin structures show a tendency towards various forms of artificial canting. To prevent this, we limit ourselves to the case of collinear spin structures and follow the approach described in Ref. [81], where an averaged ordered moment through the cluster is taken and distributed on the boundary sites following a particular ordering pattern.

IV. GLOBAL PHASE DIAGRAM

By optimizing the spin configurations using the methods described in the previous section and evaluating the corresponding probabilities, we are able to construct a detailed phase diagram of the model. We present the slices through the phase diagram using a common parametrization for the main interactions [42], that is $J = \cos\varphi \sin\theta$, $K = \sin\varphi \sin\theta$, $\Gamma = \cos\theta$ with $\varphi \in [0, 2\pi]$ and $\theta \in [0, \pi/2]$. This way all the J, K sign combinations and interaction strength ratios for positive $\Gamma \geqslant 0$ are explored. The remaining model parameters Γ' and J_3 are kept fixed for a given slice. Figure 2(a) shows the phase diagram for $\Gamma' = J_3 = 0$, which is the special case of the $JK\Gamma$ model, first analyzed in Ref. [42]. We shall now use this diagram to survey the main properties of the phases and move on to their evolution with Γ' and J_3 afterwards. The reader may also consult Appendix C containing an extensive set of phase diagram slices for selected Γ' values.

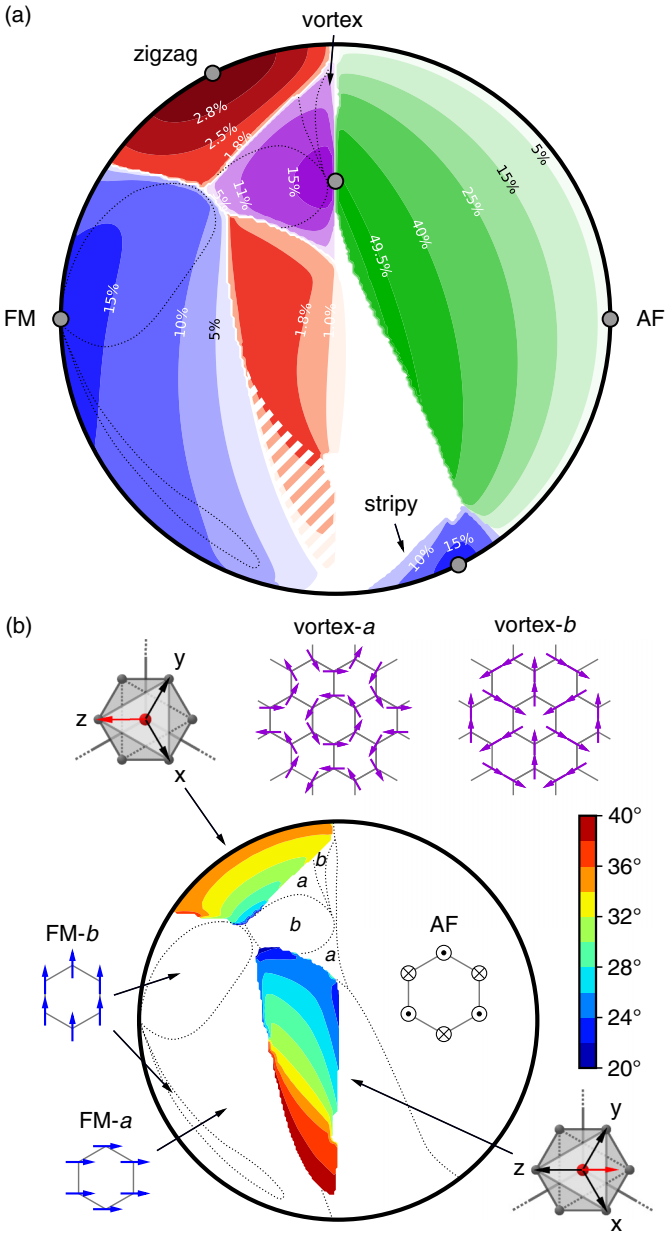

FIG. 2. (a) Phase diagram of the extended Kitaev-Heisenberg model with $\Gamma' = J_3 = 0$ using the parametrization $J = \cos\varphi \sin\theta$, $K = \sin\varphi \sin\theta$, and $\Gamma = \cos\theta$ with $\varphi \in [0, 2\pi]$ being the azimuthal angle and $\theta \in [0, \pi/2]$ the radial coordinate measured as a distance from the center of the circle. Color intensity and contours show the probabilities of classical spin patterns for the respective phases. Dashed lines separate distinct regions within one phase. White areas represent regions where no clear signatures of a long-range ordered phase were detected using the 24-site cluster. The gray dots indicate points of (hidden) SU(2) symmetry. The hatched part of the central region with a large probability of the zigzag pattern shows a tendency to form a noncollinear spin arrangement. (b) The angle of the ordered moments to the honeycomb plane for the zigzag phase—in the upper region, the moment points near the cubic z direction (assuming zigzags running along a and b bonds), whereas in the central region it is located between x and y axes. The panel also depicts the in-plane spin patterns for distinct regions (labeled as a and b) within vortex and FM phases and the out-of-plane pattern of the AF phase. Further details can be found in Fig. 9(e) of Appendix C.

A. Collinear phases of the $JK\Gamma$ model

We first focus on the simpler collinear phases which occupy most of the phase diagram. Two phases, FM and AF, dominating Fig. 2(a) are directly linked to Heisenberg points. Though they may seem trivial at the first sight, our inspection revealed their interesting internal structure due to the complex interplay of the bond-anisotropic interactions. We start with the FM phase, which is expected to be most accessible due to the small amount of quantum fluctuations. In the JK limit (the outer circle of the diagram), the ordered moments point along one of the three cubic directions x, y, z selected by virtue of the "order-from-disorder" mechanism on top of isotropic classical energy [80,90]. Since the cluster ground state is a superposition of the six degenerate possibilities, the probability approaching the value $1/6$ near the FM point indicates vanishing quantum fluctuations. With the presence of the Γ term, the magnetic moment is quickly pushed into the honeycomb plane, lying either directly within the plane or close to it [with $\lesssim 10^\circ$ deviation, see also Fig. 9(e) in Appendix C]. This can be understood by evaluating the classical energy for the FM phase: $E_{\text{class}} \propto 3J + K - \Gamma + \Gamma(n_x + n_y + n_z)^2$, where the unit vector $\boldsymbol{n} = (n_x, n_y, n_z)$ represents the moment direction. The honeycomb plane is thus preferred by Γ interaction on a classical level which makes it easy to outweigh the fluctuation-selected cubic axis. A small Γ value of the order 10^{-2} to 10^{-1} of the dominant JK is typically sufficient to achieve this with the value dropping even lower near the FM Heisenberg point. Within the honeycomb plane, moments point either in the bond direction, or perpendicular to the bond in two separate regions of the FM phase [see Fig. 2(b)]. In accord with the intuition, departing from the FM Heisenberg point, quantum fluctuations intensify, lowering thus the plotted probability.

Linked to the FM phase by means of the four-sublattice transformation ($\mathcal{T}_4$ in the notation of Ref. [75]) is the stripy phase. Its hidden FM nature is manifested by a large probability, reaching $1/6$ at the hidden SU(2) point $K = -2J < 0$ that is an image of the FM Heisenberg point in the $\mathcal{T}_4$ mapping. In contrast to the FM phase, the magnetic moment direction is tied to the vicinity of the cubic axes throughout the stripy phase, lifting a bit with increasing Γ instead of moving to the honeycomb plane. This is because the Γ interaction is not compatible with the $\mathcal{T}_4$ transformation and acts differently here.

In the AF phase, the moment direction is classically degenerate in the JK limit, and the cubic directions are chosen again by the "order-from-disorder" mechanism. The addition of the Γ anisotropy fixes now the moments in the (111) direction—perpendicular to the honeycomb plane. This state minimizes the classical energy including Γ contribution: $E_{\text{class}} \propto -3J - K + \Gamma - \Gamma(n_x + n_y + n_z)^2$. Similarly to the FM phase, the fluctuation energy selecting the cubic directions is small and the change to the (111) direction occurs already at a minute Γ of the order 10^{-4} to 10^{-2} of the dominant JK with the critical value of Γ decreasing to zero at the AF Heisenberg point. Going deeper into the AF phase, the probability of the classical Néel configuration increases with Γ steadily, peaking at $1/2$ on a line near the circle center that starts at the $K = \Gamma$ hidden SU(2) symmetry point. For the (111) AF state, there are two equivalent configurations of the moments, meaning that the peaking probability of 50% represents a classical state without any quantum fluctuations. Indeed, as we later explicitly demonstrate in Sec. V, terms that would lead to quantum fluctuations are present but their remarkable cancellation for the particular order causes the highly anisotropic model to support a fluctuation-free AF state on an entire manifold of its parameter space. The same AF phase may thus be represented by fluctuation-free ground states as well as those with significant quantum fluctuations, depending on the location in the parameter space.

Analogous to the FM/stripy case, $\mathcal{T}_4$ maps the AF Heisenberg point to the hidden SU(2) point $K = -2J > 0$. The top zigzag region of the phase diagram extends around this point; in the JK limit, the moment direction coincides again with one of the cubic directions. Adding further anisotropy with increasing Γ, the moments are pushed continuously towards the honeycomb plane, as shown in Fig. 2(b).

Of a greater experimental relevance is the second zigzag phase near the center of the phase diagram. It is also linked to a hidden SU(2) point which, however, occurs at finite $\Gamma' < 0$ [75]. In this phase, the moment direction is located roughly between the cubic x and y axes, near the direction found experimentally [41]. We will show later, that it is this zigzag region that largely expands and dominates the phase diagram after the inclusion of Γ' and/or J_3 coupling terms. A comprehensive discussion of the moment direction in both zigzag phases in the context of the experimental data can be found in Ref. [80].

B. Vortex phase

The vortex phase is a noncollinear phase "emanating" from the most peculiar hidden SU(2) symmetry point of the model that is revealed by a six-sublattice spin rotation $\mathcal{T}_6$ of Ref. [75]. $\mathcal{T}_6$ maps the ferromagnetic $J < 0$ Heisenberg model to EKH model at the parameter point $J = 0$, $K = \Gamma > 0$ indicated in Fig. 2(a). Owing to its hidden FM nature and six degenerate spin configurations, the optimized probabilities reach $1/6$ in the vicinity of this exact vortex point, and continuously decrease with the departure away from it.

The phase comprises regions with two different most probable classical configurations of moments labeled as vortex-a and vortex-b in Fig. 2(b). Let us note, however, that these two patterns have very close probabilities and are continuously connected, implying a presence of a soft mode oscillating between them. In partial agreement with the classical treatment [42], spins are found to lie within or close to the honeycomb plane. The vortex-b pattern is always planar while in the vortex-a regions near the boundary with AF or zigzag phase, the spins start to tilt away from the honeycomb plane in a staggered AF fashion. The tilt is largest in the right part of the vortex phase [see Fig. 9(e)] which we interpret as the proximity effect of the robust AF order with the moments perpendicular to the honeycomb plane.

A deeper understanding of the internal structure of the vortex phase is possible by utilizing four reference points where the EKH maps to simpler models. One of them is the vortex SU(2) point in $\Gamma' = 0$ slice. The freedom associated with the selection of the ordered moment direction in the hidden FM at this point creates a continuous family of degenerate

patterns including vortex-a and vortex-b. Another hidden SU(2) symmetry point but of AF nature is found for $\Gamma' \approx -0.5$ at the opposite edge of the vortex phase [see Fig. 9(j) of Appendix C]. It is associated with $\mathcal{T}_2\mathcal{T}_6$ transformation of Ref. [75]. For a planar structure, the staggering of the hidden AF order is compensated by the two-sublattice π rotation $\mathcal{T}_2$ such that this point supports the same vortex-a and vortex-b patterns as for the $\Gamma' = 0$ hidden FM point associated with just $\mathcal{T}_6$. However, in contrast to the latter point, the corresponding state has pronounced quantum fluctuations because of the hidden AF nature. Departing away from the hidden FM point or the hidden AF point, the degeneracy is lifted and one of the configurations is chosen as the energetically most favorable. Here the proximity to the remaining two reference points decides. As we find in Sec. VI, the point $K = \Gamma = -J > 0$ (the "meeting" point of four phases) corresponds to a FM compass model on the honeycomb lattice while at another nearby point with $K > 0$, $J = \Gamma > 0$, and $\Gamma' < 0$, the model maps to AF compasslike model with the interaction direction perpendicular to the bond. These two compass(like) models prefer patterns vortex-b and vortex-a, respectively, which qualitatively explains the location of vortex-a,b subphases.

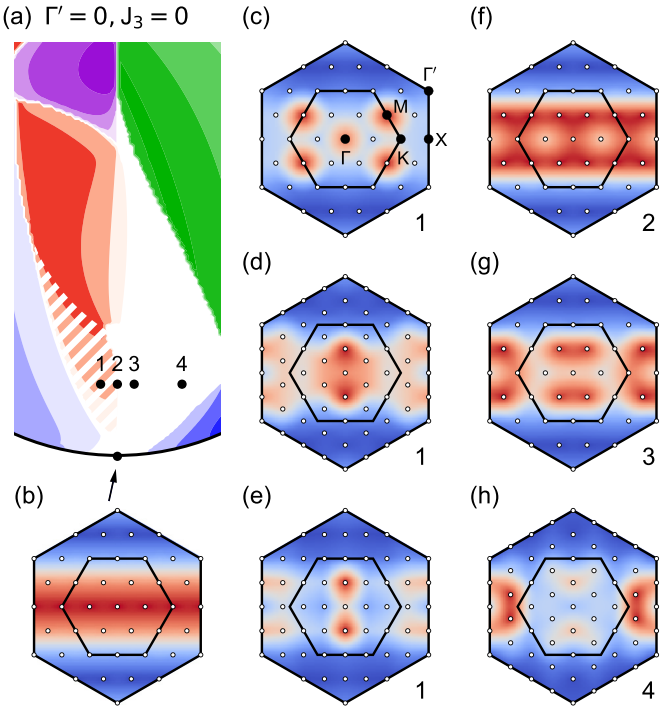

FIG. 3. (a) Position of the four selected points 1–4 in the phase diagram. In addition, the FM Kitaev point is taken as a reference. [(b)–(h)] $\langle S^z_{-\boldsymbol{q}} S^z_{\boldsymbol{q}} \rangle$ correlations at the selected parameter points calculated for the 24-site cluster [(b), (c), (f), and (g)] and 32-site clusters of hexagonal [(d) and (h)] and rectangular shape (e). The nearest-neighbor correlations in the liquid state are manifested by a wavelike pattern (b)—such a pattern seems to be present as a "background" in the other maps [(c)–(h)] as well. At point 1, the larger 32-site clusters already support incommensurate correlations [(d) and (e)], while the 24-site cluster shows zigzaglike correlations (c) though collinear zigzag is not the most probable configuration anymore. Incommensurate correlations are visible at the 24-site cluster for point 3 (g) and merge with the zigzag ones on the K-Γ line (f). Deeper in the white region, the incommensurate wave vector moves out of the first Brillouin zone (h). All the panels (b)–(h) show the available $\boldsymbol{q}$ resolution for the given cluster. In (c), the high-symmetry points in the Brillouin zone are labeled.

C. Remaining phases of the $JK\Gamma$ model

The remaining parts of the phase diagram slice for $\Gamma' = 0$ and $J_3 = 0$ [kept white in Fig. 2(a)] are to a small extent occupied by the two known Kitaev spin liquids associated with the FM and AF Kitaev points. Here the optimization of spin-1/2 coherent states described in Sec. III A finds a large number of configurations consisting of aligned/contra-aligned pairs of the nearest-neighbor spins, as appearing in classical $S \to \infty$ limit of the Kitaev model [91,92] (see also Appendix A for several details concerning the behavior of the method in the presence of Kitaev spin liquids).

However, much bigger portion of the phase diagram is taken by the white region in the lower central part which shows a particularly puzzling behavior. Parts of it were suggested earlier to host incommensurate phases [42,78]. The vertical $J = 0$ line seems to play a special role as it clearly separates the middle zigzag as well as the vortex region from the other phases on the right [see Fig. 2(a) and the detail in Fig. 3(a)]. The K-Γ model corresponding to the $J = 0$ line has been recently studied separately and its ground state for ferromagnetic K was found to bear signatures of a spin liquid [93,94].

Using the method of Sec. III A for the above region, we find tendencies to form complex spin structures, though the probability of such configurations is quite small, hinting towards a possibility of phase(s) without a long-range order. Interestingly, the region with a large probability of the collinear zigzag structure is also partially unstable towards a formation of a noncollinear spin arrangement—see the hatched pattern in Fig. 2(a) or 3(a). Although the clusters accessible to ED are not in general large enough to properly capture potential spin orderings with large unit cells, we still try to provide a further analysis based on momentum-space correlations. Here we utilize two more clusters in ED, a 32-site cluster of a hexagonal shape and a rectangular one ($4\sqrt{3} \times 6$ in lattice spacings), in addition to our default 24-site cluster.

Figure 3(a) shows the positions of four parameter points selected for a comparison: 1 in the unstable zigzag region, 2 on the K-Γ boundary, 3 in the expected spiral phase close to $J = 0$ line, and point 4 deeper in the expected spiral phase. The FM Kitaev point is added for reference. Plotted in Figs. 3(b)–3(h) are the maps of the equal-time spin-spin correlation function $\langle S^z_{-\boldsymbol{q}} S^z_{\boldsymbol{q}} \rangle$. It should be emphasized, that the cluster ground states do not spontaneously break symmetry and contain, e.g., a linear combination of several ordering patterns that differ by the direction of the ordering wave vector and hence the ordered moment direction. The selection of the spin component of the correlation function then provides access to various components of this combination. For the hexagonal clusters, where a rotation by $2\pi/3$ is in effect just a cyclic permutation among the S^x, S^y, and S^z components,

the other correlation functions $\langle S^x_{-\boldsymbol{q}} S^x_{\boldsymbol{q}} \rangle$ and $\langle S^y_{-\boldsymbol{q}} S^y_{\boldsymbol{q}} \rangle$ are merely $2\pi/3$-rotated copies of the maps shown in Fig. 3.

By combining various sets of maps from Fig. 3, several trends can be illustrated. (i) The wavelike background identical to momentum-represented nearest-neighbor correlations of the Kitaev liquid [Fig. 3(b)] is universally present at all points, less apparently in the case of peaked structures on top of the background because of an extended color scale range.

(ii) Panels (c)–(e) show the influence of the cluster size and shape at the parameter point 1 that we demonstrate now to be in the incommensurate region. For the smallest 24-site cluster, the correlation map in Fig. 3(c) still includes peaks located at the M momenta, which corresponds to a zigzag arrangement. However, using the method of Sec. III A, the zigzag pattern is found unstable which already hints towards another type of ordering. This is fully revealed by the larger 32-site clusters. By providing a denser momentum-space coverage, they enable the preferred incommensurate state to develop [Figs. 3(d) and 3(e)]. The difference between Figs. 3(d) and 3(e) is an effect of the cluster shape. The symmetric hexagonal 32-site cluster [panel (d)] supports three degenerate directions for the ordering wave vector that coexist in the ground state (two of them visible aside the main maxima near the Brillouin zone center), while the rectangular shape of the second 32-site cluster selects only one of those directions [panel (e)].

(iii) Panels (c), (f), and (g) demonstrate, for the 24-site cluster, the evolution from commensurate correlations [point 1, Fig. 3(c)] to incommensurate ones [point 3, Fig. 3(g)] found in the white region. At the boundary point 2 with $J = 0$, the corresponding states show a level crossing and we obtain the average spin-correlation pattern displayed in Fig. 3(f) resembling that of the Kitaev point.

(iv) Panels (d) and (h) illustrate, for the symmetric 32-site cluster, the transfer of the incommensurate wave vector from the inside of the first Brillouin zone [point 1, Fig. 3(d)] to the outside [point 4, Fig. 3(h)] when moving in the direction of positive J. This trend was also obtained by classical Monte Carlo simulations [43].

In conclusion, the studied region of the phase diagram shows a complex behavior with the spin correlations indicating tendencies towards various incommensurate orders. However, the common wavelike background to the spin correlations suggests a presence of strong liquidlike features.

D. Effect of nonzero Γ' and J_3 parameters

We shall now investigate the evolution of the phases found in the $\Gamma' = J_3 = 0$ slice of the phase diagram when the parameters Γ' and J_3 are varied. As argued in Sec. II, we limit ourselves to the experimentally most relevant case of small $\Gamma' < 0$ and $J_3 > 0$. Additional data to establish a fuller picture are presented in Appendix C. The observed trends can be successfully explained either simply by considering the classical energy or, more fundamentally, correlated with the positions of the points of special symmetry in the parameter space, as inspected in Ref. [75] (points of hidden SU(2) symmetry) and the following Secs. V and VI.

Figures 4(a) and 4(b) shows phase diagrams for two moderate values of $\Gamma' < 0$. Most notable effect of negative Γ' is the large expansion of the vortex phase and mainly of the

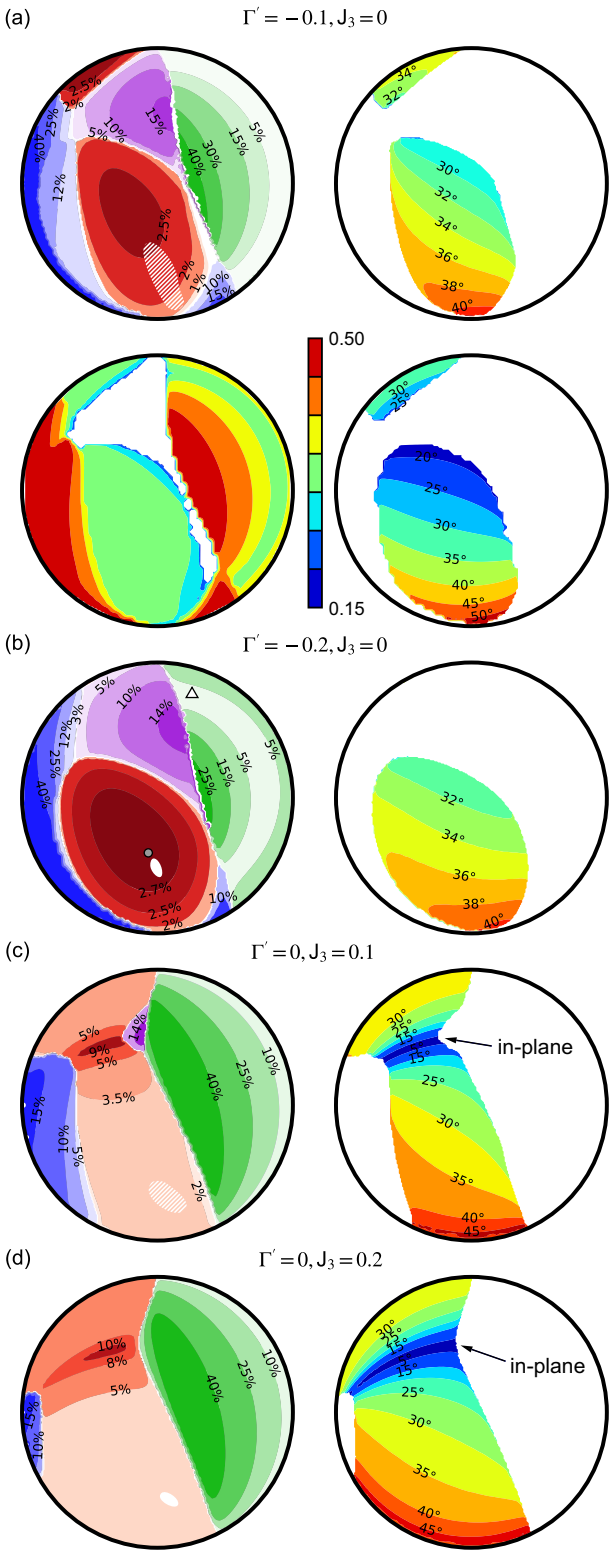

FIG. 4. Phase diagrams for nonzero values of Γ' and J_3 represented by probabilities of optimized collinear and vortex spin patterns in the ED ground state (left) and, focusing on zigzag phases, by the angle of the moments to the honeycomb plane (right). Hatched/white areas in the zigzag phase indicate the instability of the collinear pattern. Bottom part of (a) also shows the ordered moment length calculated by CMFT (left) and the angle to the honeycomb plane in zigzag phases (right). Shown in (b) are projected positions of a hidden SU(2) point (gray •) and a compasslike point (△).

central zigzag phase. The former trend can be understood as a proximity effect of the point where the EKH model maps to AF compasslike model (to be analyzed in Sec. VI). Its position is at $\Gamma' \approx -0.6$ in the chosen parametrization and the projection to $JK\Gamma$ plane is indicated in Fig. 4(b). Though the difference in Γ' is still quite large, this special point efficiently enforces the vortexlike correlations of type a so that the vortex phase not only grows but also becomes dominated by vortex-a pattern (cf. Appendix C). The expansion of the central zigzag phase is linked to approaching the hidden SU(2) point that is an image of the AF Heisenberg point in $\mathcal{T}_1\mathcal{T}_4$ transformation. This point, having $\Gamma' \approx -0.4$ and the projection onto $JK\Gamma$ plane as indicated in Fig. 4(b), enforces the zigzag order with the moment direction consistent with experiments and may be actually regarded as the source of the central zigzag phase. On the other hand, the top zigzag region related to the SU(2) point in the $\Gamma' = 0$ plane is suppressed with $\Gamma' < 0$, to the extent that it is not even discernible already for $\Gamma' = -0.2$.

The FM and AF phases develop more complex internal structure when $\Gamma' < 0$ is added. This is due to the competition of the energy contributed by Γ and Γ' that are decisive for the moment direction at a classical level. The anisotropic part of these contributions is proportional to $\pm(\Gamma + 2\Gamma')(n_x + n_y + n_z)^2$ for FM and AF, respectively. In the FM phase, $\Gamma' < 0$ creates a new subphase where the moments pushed originally to the honeycomb plane due to $\Gamma > 0$ [Fig. 2(b)] take the direction perpendicular to the honeycomb plane. This subphase extends near the outer rim of the FM phase where Γ is sufficiently weak. An opposite effect is observed in the AF phase. Here, in addition, the absence of the moment confinement by anisotropic classical energy in the case of $\Gamma + 2\Gamma' = 0$ leads to an enhancement of quantum fluctuations and the probability plotted in e.g., Fig. 4(b) therefore drops at the corresponding circle.

Based on the data presented so far, the probabilities of the best-fitting classical configurations represent a good measure of quantum fluctuations in the ground state. To have an independent quantification and to cross-check our results, we compare them to a complementary approach, namely CMFT described in Sec. III B. Its advantage is the ability to estimate the ordered moment length that we plot in Fig. 4(a). The phase boundaries of the collinear phases are in a good agreement with the method based on ED and the moment length reveals the less fluctuating FM and stripy phases, and the gradual decrease of quantum fluctuations when going deeper into the AF phase. The data on the moment angle to the honeycomb plane show a somewhat larger spread but the trend is identical.

The evolution of the phases with increasing third nearest-neighbor coupling J_3 is illustrated in Figs. 4(c) and 4(d). As expected already at the level of the classical energy, the antiferromagnetic $J_3 > 0$ coupling further favors zigzag and AF phases. The stripy and vortex phases of hidden FM nature as well as the FM phase get quickly suppressed and the two zigzag regions merge filling the entire left half of the phase diagram. In both zigzag and AF phases, the third nearest-neighbor bonds have contra-aligned spins favorable for AF J_3 interaction. The energy gain brought by J_3 therefore does not visibly shift the zigzag/AF boundary. The two zigzag regions have incompatible moment directions. When merging them, the system makes a compromise by pushing the moment direction to the honeycomb plane so that it can easily flip between z and $(x + y)/\sqrt{2}$ directions projected onto honeycomb plane [cf. Fig. 2(b)]. Near the boundary between the zigzag subphases where the moment lies in the honeycomb plane, the quantum fluctuations are significantly suppressed.

We reach the conclusion that both $\Gamma' < 0$ and $J_3 > 0$—expected to be present in real materials—strongly stabilize the central zigzag phase that is consistent with experimental observations in Na_2IrO_3 in both the magnetic ordering and direction of magnetic moment. As for the precise moment direction (figures in the right column of Fig. 4), the evolution seems to be dictated by K, Γ, while Γ', J_3 influence mostly the extent of the phase. We note that one has to distinguish the real pseudospin direction and the moment direction as probed by various techniques such as neutron or resonant x-ray scattering [80]. Based solely on the moment direction with the experimental data [41] translating to the pseudospin angle of about 38°–40° [80], it seems that the FM $K < 0$ should be the largest interaction, followed by possibly still large $\Gamma > 0$. Being in accord with the conclusions of Ref. [80], this also falls in line with *ab initio* estimates of dominant ferromagnetic K and comparable $J > 0$, $\Gamma > 0$, $\Gamma' < 0$, and $J_3 > 0$ [15].

Finally, small hatched/white areas in the zigzag phase shown in Fig. 4 again indicate the instability of the collinear zigzag pattern that may be interpreted as a protrusion of the possible incommensurate phase. They appear at small Γ' and J_3 which together with the link between Γ' and trigonal distortion suggests an explanation for the spiral order in less distorted α-Li_2IrO_3 compared to Na_2IrO_3 with zigzag order. This point was analyzed at a basic classical level in Ref. [75].

V. FLUCTUATION-FREE MANIFOLDS

As noticed in Sec. IV A when inspecting the phase diagram of the $JK\Gamma$ model [Fig. 2(a)], the AF phase contains an unusual line of fluctuation-free ground states located near the center of the phase diagram. The distance to this line seems to determine the magnitude of quantum fluctuations throughout the entire AF phase—the probability of the Néel state in the ground state increases more or less monotonously starting from the outer rim and approaching the line radially inwards. In fact, similar lines are present also for nonzero Γ' slices in a certain Γ' range and form thus an entire surface in the parameter space. This is quite unexpected since at those parameter points, all the interactions are active and there is no apparent cancellation leading to the absence of quantum fluctuations. What is more, a manifold of fluctuation-free ground states is found also in part of the FM phase away from the trivially fluctuation-free FM Heisenberg point. This is demonstrated in Fig. 5(a) for two values of $\Gamma' < 0$. Below we address both cases, starting with the simpler FM one.

A. FM phase

A common feature of the fluctuation-free ground states is the moment direction being perpendicular to the honeycomb plane, suggesting to rewrite the Hamiltonian into the XYZ reference frame [Fig. 5(b)] where this perpendicular direction is singled out. The Hamiltonian contributions for all the bond

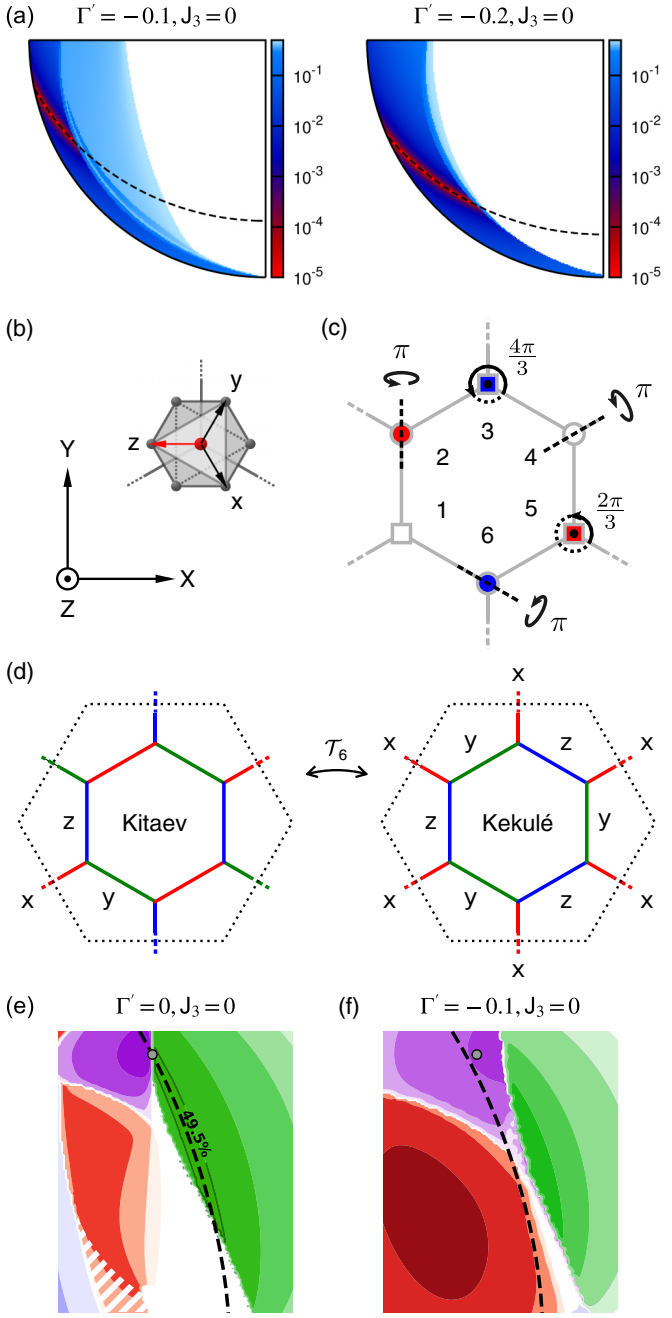

FIG. 5. (a) Lower left quadrant of the phase diagram for $\Gamma' = -0.1$ and -0.2 showing the FM phase. The color indicates the difference $P_{\max} - P$ between the probability P of the classical state in the ED ground state and its maximum value of $P_{\max} = 1/2$. The maximum probability, corresponding to a fluctuation-free ground state, is reached in the FM subphase with the moments perpendicular to the honeycomb plane (darker color) at the line given by $K + 2\Gamma - 2\Gamma' = 0$ (dashed). (b) Coordinate frames used to express spin interactions. (c) Schematic representation of the $\mathcal{T}_6$ transformation on the honeycomb lattice. At each of the six sublattices, a different rotation of spin components is applied. (d) Correspondence between the bonds and interaction Hamiltonians $\mathcal{H}^{(x)}$, $\mathcal{H}^{(y)}$, and $\mathcal{H}^{(z)}$ for the EKH model and extended Kekulé-Kitaev-Heisenberg model obtained when performing the $\mathcal{T}_6$ transformation. (e) The fluctuation-free line in the AF phase of the $JK\Gamma$ model. The line is determined by $3J + K - \Gamma - 2\Gamma' = 0$ and crosses the hidden SU(2) symmetric vortex point (gray •). (f) Shifted line for a case of nonzero Γ': the line no longer enters the AF phase.

directions can be cast to a common form [75]:

$$\begin{aligned}\mathcal{H}_{ij}^{(\gamma)} = {} & J_{XY}\left(S_i^X S_j^X + S_i^Y S_j^Y\right) + J_Z S_i^Z S_j^Z \\ & + A\left[\left(S_i^X S_j^X - S_i^Y S_j^Y\right)\cos\phi_\gamma - \left(S_i^X S_j^Y + S_i^Y S_j^X\right)\sin\phi_\gamma\right] \\ & - B\left[\left(S_i^X S_j^Z + S_i^Z S_j^X\right)\cos\phi_\gamma + \left(S_i^Y S_j^Z + S_i^Z S_j^Y\right)\sin\phi_\gamma\right].\end{aligned} \tag{6}$$

The bond-dependence of the interactions is expressed via the trigonometric factors containing the angles of the bonds measured from the Y axis, i.e., $\phi_\gamma = 0, \frac{2\pi}{3}, \frac{4\pi}{3}$ for the c, a, and b bonds, respectively. Equation (6) is obtained by inserting into Eq. (1) the transformation relations

$$\begin{pmatrix} S^x \\ S^y \\ S^z \end{pmatrix} = \begin{pmatrix} \frac{1}{\sqrt{6}} & -\frac{1}{\sqrt{2}} & \frac{1}{\sqrt{3}} \\ \frac{1}{\sqrt{6}} & \frac{1}{\sqrt{2}} & \frac{1}{\sqrt{3}} \\ -\sqrt{\frac{2}{3}} & 0 & \frac{1}{\sqrt{3}} \end{pmatrix} \begin{pmatrix} S^X\cos\phi_\gamma + S^Y\sin\phi_\gamma \\ -S^X\sin\phi_\gamma + S^Y\cos\phi_\gamma \\ S^Z \end{pmatrix}, \tag{7}$$

which represent a conversion from the cubic xyz to XYZ reference frame for a c bond as well as the necessary cyclic permutation among xyz (rotation around Z axis), and using the fact that $\cos 2\phi_\gamma = \cos\phi_\gamma$, $\sin 2\phi_\gamma = -\sin\phi_\gamma$ for the allowed values of ϕ_γ.

The interaction parameters in (6) expressed in terms of the original J, K, Γ, and Γ' read as

$$J_{XY} = J + \tfrac{1}{3}(K - \Gamma - 2\Gamma'), \tag{8}$$

$$J_Z = J + \tfrac{1}{3}(K + 2\Gamma + 4\Gamma'), \tag{9}$$

$$A = \tfrac{1}{3}(K + 2\Gamma - 2\Gamma'), \tag{10}$$

$$B = \tfrac{\sqrt{2}}{3}(K - \Gamma + \Gamma'). \tag{11}$$

Let us now consider a FM state polarized in the Z direction and inspect the terms that could lead to quantum fluctuations. As in usual Heisenberg magnets, the J_{XY} interaction containing $S_i^+ S_j^-$ and $S_i^- S_j^+$ does not act on the polarized state. The above state is an eigenstate of the S_i^Z operators, the action of B terms in the Hamiltonian therefore sums up to

$$-B\sum_{\text{sites}}\left[S_i^X\sum_{\gamma=a,b,c}\cos\phi_\gamma + S_i^Y\sum_{\gamma=a,b,c}\sin\phi_\gamma\right], \tag{12}$$

which drops out since both $\sum_\gamma \cos\phi_\gamma$ and $\sum_\gamma \sin\phi_\gamma$ are zero. Only the remaining A terms containing $S_i^+ S_j^+$ and $S_i^- S_j^-$ are active. Setting $A = 0$, all the S_i^- or $S_i^- S_j^-$ terms that could lead to quantum fluctuations are cut off by zero prefactors and we are left with an exact eigenstate. The two conditions for a fluctuation-free FM ground state, i.e., moments being perpendicular to the honeycomb plane and $A = 0$ translating to

$$K + 2\Gamma - 2\Gamma' = 0, \tag{13}$$

are checked in Fig. 5(a). Approaching the line given by Eq. (13) within the (111) polarized FM phase, the probability indeed reaches the maximum value of 1/2, reflecting the two degenerate configurations (moments along Z or $-Z$) being

superposed in the cluster ground state. Exactly at this line, we find a doubly degenerate ground state. Finally, let us note that the ground state remains fluctuation-free even in the presence of J_3 provided that the (111) polarized FM pattern is preserved.

B. AF phase

A more complex situation is encountered in the case of (111) polarized AF phase. Here the fluctuation-free manifold is attached to the vortex point of hidden SU(2) symmetry hosting an infinite number of fluctuation-free states. The (111) polarized AF state is one of them, the others being e.g., the vortex-a and vortex-b configurations shown in Fig. 2(b). The connection to the SU(2) vortex point suggests a special role of the $\mathcal{T}_6$ transformation which we discuss in more detail here.

The $\mathcal{T}_6$ transformation is a six-sublattice mapping that rotates the spins according to the recipe:

$$\begin{aligned}
&\text{sublattice 1:} && (S^{x'}, S^{y'}, S^{z'}) = (S^{x}, S^{y}, S^{z}),\\
&\text{sublattice 2:} && (S^{x'}, S^{y'}, S^{z'}) = (-S^{y}, -S^{x}, -S^{z}),\\
&\text{sublattice 3:} && (S^{x'}, S^{y'}, S^{z'}) = (S^{y}, S^{z}, S^{x}),\\
&\text{sublattice 4:} && (S^{x'}, S^{y'}, S^{z'}) = (-S^{x}, -S^{z}, -S^{y}),\\
&\text{sublattice 5:} && (S^{x'}, S^{y'}, S^{z'}) = (S^{z}, S^{x}, S^{y}),\\
&\text{sublattice 6:} && (S^{x'}, S^{y'}, S^{z'}) = (-S^{z}, -S^{y}, -S^{x}).
\end{aligned} \tag{14}$$

For a better understanding, the transformation is depicted in Fig. 5(c). On sites 1, 3, and 5 marked by a square symbol, the spins are rotated around the (111) axis, on sites 2, 4, and 6 marked by a circle, the mapping consists of π rotations around axes lying in the honeycomb plane. This in effect changes the (111) polarized AF pattern into (111) polarized FM one, making a first step towards the understanding of the AF fluctuation-free line.

The second step involves the transformation of the Hamiltonian. Performing the $\mathcal{T}_6$ spin rotations, we find that the resulting model is similar to EKH in the sense that three types of bond interactions of the form of Eq. (1) appear, $\mathcal{H}^{(x)} \equiv \mathcal{H}^{(a)}$, $\mathcal{H}^{(y)} \equiv \mathcal{H}^{(b)}$, and $\mathcal{H}^{(z)} \equiv \mathcal{H}^{(c)}$, with the parameters modified according to

$$(J, K, \Gamma, \Gamma')_{\text{Kekulé}} = (-\Gamma, -J - K + \Gamma, -J, -\Gamma'). \tag{15}$$

However, the assignment of $\mathcal{H}^{(x,y,z)}$ to the bonds is not simply by the bond direction anymore. Instead, as shown in Fig. 5(d), a network of benzene-like rings governed by alternating $\mathcal{H}^{(y)}$ and $\mathcal{H}^{(z)}$ is formed. They are interconnected by bonds possessing the $\mathcal{H}^{(x)}$ type of interactions. This way, the $\mathcal{T}_6$ transformation maps the EKH model to an extended variant of Kekulé-Kitaev model [95].

We are now in position to combine the result of $\mathcal{T}_6$ transformation with the argumentation of Sec. V A. Since the transformation led to (111) polarized FM pattern and in the new model each site is a member of three bonds governed by $\mathcal{H}^{(x)}$, $\mathcal{H}^{(y)}$, and $\mathcal{H}^{(z)}$, the cancellation of the terms leading to quantum fluctuations proceeds exactly the same way. Substituting the parameters in Eq. (13) according to (15), we thus arrive at the condition for the fluctuation-free AF state:

$$3J + K - \Gamma - 2\Gamma' = 0. \tag{16}$$

As demonstrated in Fig. 5(e), this line coincides with the region where the probability of Néel state peaks at 1/2. For a negative Γ', the line quickly gets out of the AF phase. However, going in the positive Γ' direction, the fluctuation-free line gets even deeper into the AF phase (cf. Appendix C). At the special point $J = \Gamma = \Gamma' > 0$, $K = 0$ on the fluctuation-free manifold, the model even reduces to AF Ising model with the (111) Ising axis, as can be seen from Eqs. (6)–(11). Unlike in the previous FM case, the addition of J_3 spoils the fluctuation-free nature of the ground state since the J_3 interaction generates terms of A type under the $\mathcal{T}_6$ transformation.

VI. ISING-KITAEV-COMPASS MODEL

In this section, we address yet another feature of the model that enables further insights into its phase behavior. Namely, we find points in the parameter space where the four interactions $JK\Gamma\Gamma'$ can be combined into a single one, characterized by a single interacting spin component (interaction axis) that depends on the bond direction. This way, the model in Eq. (6) may realize combinations of Ising, Kitaev, or compass model on the honeycomb lattice.

A. Compass point in the phase diagram

Inspecting the $JK\Gamma$ phase diagram, we find a degenerate point, in which several phases seem to meet: vortex, ferromagnet, and both zigzag phases. Writing the interaction as $\mathcal{H} = \sum_{ij} \boldsymbol{S}_i^T H_{ij} \boldsymbol{S}_j$, we find that the Hamiltonian matrices in this parameter point $K = \Gamma = -J > 0$, $\Gamma' = 0$ have a symmetrical block shape:

$$H_a = \begin{pmatrix} J+K & \Gamma' & \Gamma' \\ \Gamma' & J & \Gamma \\ \Gamma' & \Gamma & J \end{pmatrix} = \begin{pmatrix} 0 & 0 & 0 \\ 0 & -K & K \\ 0 & K & -K \end{pmatrix}, \tag{17}$$

$$H_b = \begin{pmatrix} J & \Gamma' & \Gamma \\ \Gamma' & J+K & \Gamma' \\ \Gamma & \Gamma' & J \end{pmatrix} = \begin{pmatrix} -K & 0 & K \\ 0 & 0 & 0 \\ K & 0 & -K \end{pmatrix}, \tag{18}$$

$$H_c = \begin{pmatrix} J & \Gamma & \Gamma' \\ \Gamma & J & \Gamma' \\ \Gamma' & \Gamma' & J+K \end{pmatrix} = \begin{pmatrix} -K & K & 0 \\ K & -K & 0 \\ 0 & 0 & 0 \end{pmatrix}. \tag{19}$$

The matrices can be diagonalized by a change of basis to the rotating coordinate frame $\tilde{x}_\gamma, \tilde{y}_\gamma, \tilde{z}_\gamma$, $\gamma \in \{a, b, c\}$, where $\tilde{x}_\gamma$ axis points in the bond direction, $\tilde{y}_\gamma$ is perpendicular to the bond direction and lies in the honeycomb plane, and $\tilde{z}_\gamma$ points out of the honeycomb plane—see Fig. 6(a) for a sketch of this coordinate system. After the change of basis, all three interaction matrices have the same form for all bond directions a, b, c:

$$\widetilde{H} = \begin{pmatrix} -2K & 0 & 0 \\ 0 & 0 & 0 \\ 0 & 0 & 0 \end{pmatrix}, \tag{20}$$

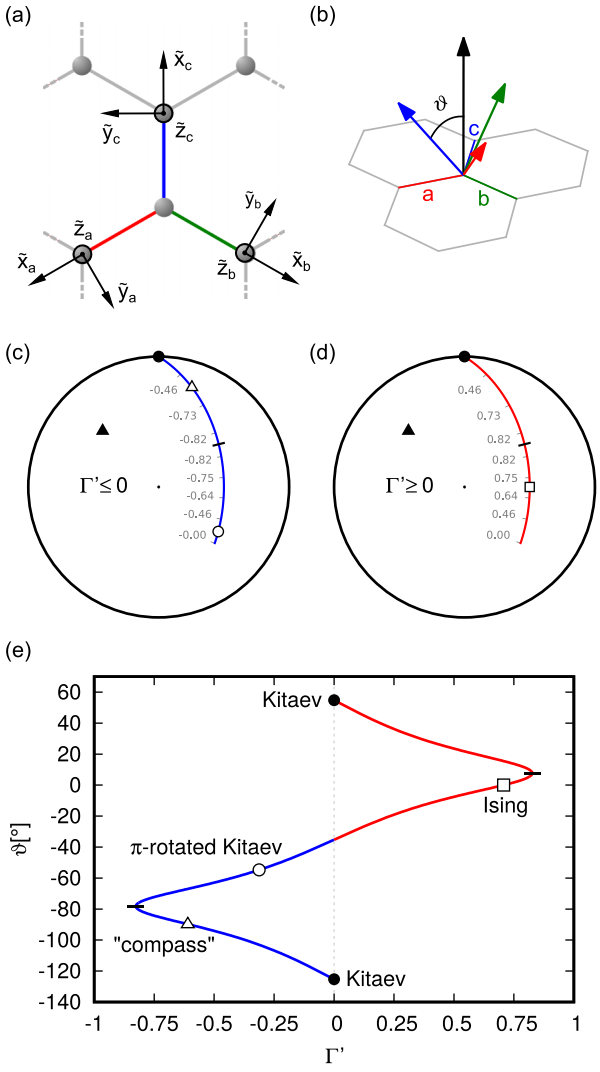

FIG. 6. (a) Rotating coordinate system $\tilde{x}_\gamma, \tilde{y}_\gamma, \tilde{z}_\gamma$ on a honeycomb lattice: color distinguishes three bond types a, b, c. (b) The direction of the interaction axis for each bond. All of them are at an angle ϑ with the Ising (111) direction shown in black. [(c) and (d)] Ising-Kitaev-compass parameter line in the phase diagram and the corresponding values of the Γ' parameter. The Ising point (□) emerges for positive Γ', while the π-rotated Kitaev point (○) and the perpendicular "compass" point (△) are found for negative Γ' values. The true compass point (▲) appears for $\Gamma' = 0$. (e) The angle ϑ of the interaction axis to the (111) direction depending on the position on the parameter line. $\varphi = \pi/2$ is assumed. The Kitaev point (●) is connected to the π-rotated Kitaev point (○) by the $\mathcal{T}_1$ dual transformation [75]—a π rotation around the (111) axis.

which represents FM interaction in the bond direction, concisely written as

$$\mathcal{H} = \sum_{\langle ij\rangle\in \mathrm{NN}} -2K(\boldsymbol{S}_i \cdot \boldsymbol{r}_{ij})(\boldsymbol{S}_j \cdot \boldsymbol{r}_{ij}), \tag{21}$$

where the unit vector $\boldsymbol{r}_{ij}$ points from site i to site j. This form of interaction is known in the literature as the 120° honeycomb compass model [11,96–98]. Similar to the Kitaev model, it features frustration due to competing interactions for the three bond directions. However, the exact ground state is not known in this case and its nature is in fact not clear, as several past works came to inconsistent conclusions. One study found a Néel state [96], others suggested a stabilization of a dimer pattern [97], a superposition of dimer coverings [98], or a quantum spin liquid state [99]. With the link to the compass model, the apparent special role of the $-J = K = \Gamma$ point marked by a competition of four long-range ordered phases in its vicinity is confirmed. This competition was noticed also in the tensor-network analysis of the $JK\Gamma$ model [77], which claimed a small region surrounding this point to harbor a valence bond solid phase.

B. Ising-Kitaev-compass line in the phase diagram

Motivated by the previous example, we now demonstrate that the EKH model provides also a more general case of a single interaction axis lying anywhere between the honeycomb plane and the perpendicular (111) direction. Dictated by the C_3 symmetry of the EKH model, the interaction axis has to rotate together with the bond direction as shown in Fig. 6(b). Representing the bond-dependent interaction axis by a unit vector $\boldsymbol{n}_\gamma$, the Hamiltonian of the single-axis model hidden in the EKH model has to be of the form

$$\mathcal{H}_{\mathrm{IKc}} = \sum_{\langle ij\rangle\in \mathrm{NN}} \widetilde{K}(\boldsymbol{n}_\gamma \cdot \boldsymbol{S}_i)(\boldsymbol{n}_\gamma \cdot \boldsymbol{S}_j). \tag{22}$$

We specify the interaction-axis direction by the deviation ϑ from the (111) direction and the azimuthal angle φ measured from the bond. In the rotating reference frame $\tilde{x}_\gamma\tilde{y}_\gamma\tilde{z}_\gamma$, we have

$$\boldsymbol{n}_\gamma = (\sin\vartheta\cos\varphi, \sin\vartheta\sin\varphi, \cos\vartheta), \tag{23}$$

while in the XYZ reference frame of Fig. 5(b)

$$\boldsymbol{n}_\gamma = (-\sin\vartheta\sin(\varphi+\phi_\gamma), \sin\vartheta\cos(\varphi+\phi_\gamma), \cos\vartheta), \tag{24}$$

with ϕ_γ being the bond angles defined in Sec. V. In the direction of increasing ϑ, the Hamiltonian (22) encompasses Ising model ($\vartheta = 0$), Kitaev model [$\vartheta = \arccos(1/\sqrt{3})$, $\varphi = \pi/2$], and compass model ($\vartheta = \pi/2$, $\varphi = 0$). Note that the physical properties do not depend on φ so that it is sufficient to focus on ϑ as the relevant parameter. For example, true compass model has $\varphi = 0$ (the interaction axis coincides with the bond direction) but $\varphi = \pi/2$ (the in-plane interaction axis is perpendicular to the bonds) leads to the same ground state, apart from a trivial rotation. We thus call the latter one "compass" to suggest a small only distinction.

We now establish the link to EKH model by converting its interactions into main axes. This is most conveniently performed in the rotating reference frame where the Hamiltonian is represented by a matrix common to all bond directions. If two of its eigenvalues are zero, we are left with the single interaction axis corresponding to the model of Eq. (22). In Sec. VI A, we have already encountered a situation in which the Hamiltonian was readily diagonalized merely by casting it into the rotating frame and the only nonzero eigenvalue for the in-bond direction generated the compass interaction. The general inspection is left for Appendix B, here we only summarize the results presented in Figs. 6(c)–6(e). It turns out that the compass case with $\boldsymbol{n}_\gamma = \tilde{x}_\gamma$ ($\varphi = 0$) is singular for $\Gamma \gtrless 0$ and in the other cases the interaction axis is found in

the perpendicular $\tilde{y}_\gamma\tilde{z}_\gamma$ plane ($\varphi = \pi/2$)—Fig. 6(b) contains a sketch of such a bond-dependent interaction axis.

Assuming $\Gamma > 0$, the diagonalized interaction has only one nonzero component on the line determined by

$$J = \Gamma,\ J(J+K) = \Gamma'^2,\ J > 0,\ J+K > 0, \qquad (25)$$

which is indicated in Figs. 6(c) and 6(d). In our parametrization, it covers the range $|\Gamma'| \leqslant \frac{1}{2}\sqrt{1+\sqrt{3}} \approx 0.83$. Figure 6(e) shows how the deviation ϑ of the interaction axis from (111) direction evolves on the parameter line (25); the colors differentiate the two branches for $\Gamma' > 0$ and $\Gamma' < 0$, respectively, and correspond to colors in Figs. 6(c) and 6(d). The interaction constant $\tilde{K} = 3J + K$ is always positive, hence the interaction is antiferromagnetic. Several distinct points are labeled in the figure: the limit $\vartheta = 0$ achieved for $J = \Gamma = \Gamma' = \frac{1}{3}\tilde{K}$, $K = 0$ corresponds to an antiferromagnetic Ising point that lies at the same time at the fluctuation-free manifold discussed in Sec. V. The "compass" limit $\vartheta = \pm\pi/2$ is reached for $J = \Gamma = \frac{1}{6}\tilde{K}$, $K = \frac{1}{2}\tilde{K}$, and $\Gamma' = -\frac{1}{3}\tilde{K}$. By varying the model parameters, one can arbitrarily interpolate between these two limits. A special role is played by the Kitaev case $\vartheta \approx \pm 54.7^\circ$ that is characterized by a spin-liquid ground state. It can be found either at AF Kitaev point $K = \tilde{K}$, $J = \Gamma = \Gamma' = 0$ with $\vartheta = \arccos(1/\sqrt{3})$ or, less trivially, in a form rotated by π about the (111) axis: $J = \Gamma = \frac{4}{9}\tilde{K}$, $K = -\frac{1}{3}\tilde{K}$, $\Gamma' = -\frac{2}{9}\tilde{K}$ with $\vartheta = -\arccos(1/\sqrt{3})$. In general, the parameters for ϑ and $-\vartheta$ are related by the $\mathcal{T}_1$ transformation of Ref. [75] that corresponds to a π rotation about the (111) axis (for details see Appendix B).

C. Phases of Ising-Kitaev-compass model

Having identified the line in the phase diagram where the EKH model effectively interpolates between Ising, Kitaev, and "compass" model captured by Eq. (22) (all AF for $\Gamma > 0$), we now briefly address the phase diagram on this line for varying ϑ. Let us note, that the corresponding type of model (dubbed "tripod") has been studied before using tensor networks [100], although with the axis in the $\tilde{x}_\gamma\tilde{z}_\gamma$ plane and not in connection with the EKH model. As before, we apply the method of Sec. III A combined with an analysis of the spin correlations.

The resulting phase diagram is shown in Fig. 7. We formally plot it as a function of $|\vartheta|$. For negative values of ϑ it covers the range Ising—π-rotated Kitaev—"compass" that is continuously visible in Fig. 6(e). The phase diagram for positive ϑ is identical, even though corresponding to different line in the parameter space of the EKH model.

More than half of the phase diagram is occupied by the AF Ising phase with the moments pointing in the (111) direction. It starts as fluctuation free at the Ising point $\vartheta = 0^\circ$ and gradually acquires more quantum fluctuating nature until $|\vartheta| \approx 49.5^\circ$ where a transition to a spin-liquid associated with the (π-rotated) Kitaev point at $|\vartheta| \approx 54.7^\circ$ happens. The increasing content of quantum fluctuations is manifested by decreasing spin correlations [Fig. 7(a)] or the probability of Néel state in the ground state, which follows a similar curve. At approximately 62° the spin liquid state breaks down. Compared to the tensor network study [100], we find a significantly wider spin liquid window: (49.5°, 62°) versus (52.7°, 57.6°). The reason for this discrepancy is not clear, an earlier tensor-network study of the Kitaev-Heisenberg model [85] was in a good agreement with ED. One possibility is that a different procedure of finding the level crossings or extrapolating the bond dimension has been used for the two tensor networks studies.

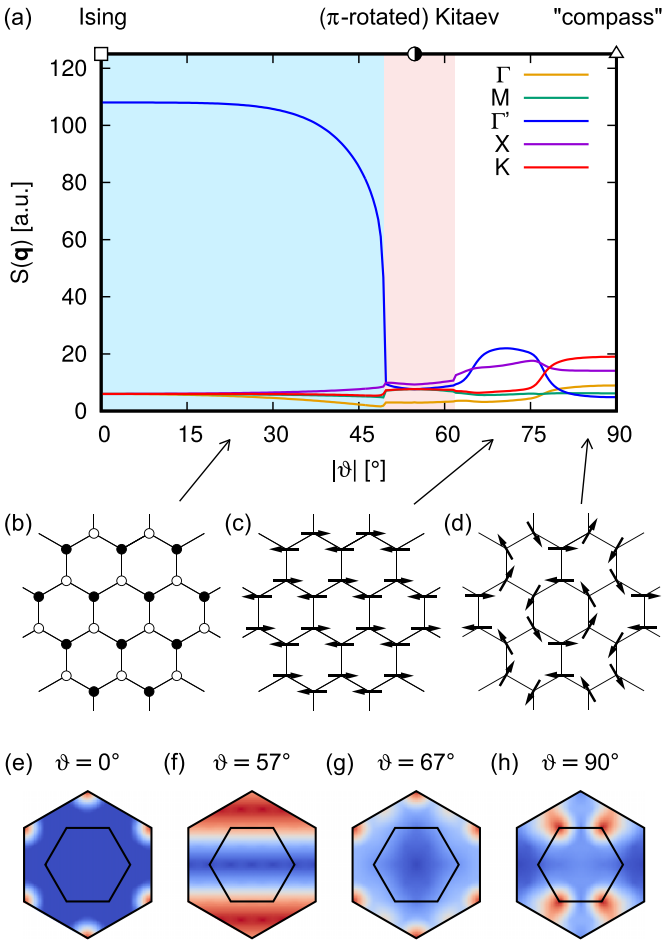

FIG. 7. (a) Trace of the spin structure factor $S(\boldsymbol{q}) = \sum_\alpha \langle S^\alpha_{-\boldsymbol{q}} S^\alpha_{\boldsymbol{q}} \rangle$ obtained by ED using hexagonal 24-site cluster. The calculation reveals an Ising antiferromagnet and a Kitaev liquid phase; for high values of $|\vartheta|$ (interaction axis near the honeycomb plane), the correlations show a mixture of contributions mainly at Γ', X, and K points. [(b)–(d)] Most probable spin configurations determined by the method of spin-1/2 coherent states (using $\varphi = \pi/2$). The Néel state is out of plane in (b) and only slightly tilted from the plane in (c). The spin arrangement (d) is the same as the vortex-a configuration shown in Fig. 2(b). [(e)–(h)] Spin-spin correlations $\langle S^z_{-\boldsymbol{q}} S^z_{\boldsymbol{q}} \rangle$ for a few selected values of ϑ and $\varphi = \pi/2$. In (f), the typical cosine wave pattern characterizing a spin liquid state appears.

For $|\vartheta| \gtrsim 62^\circ$, the ground state is characterized by peaks in the structure factor at the Γ' and X point [see Fig. 7(g)], while around $|\vartheta| \approx 77^\circ$ the correlations at Γ' point drop and the K point becomes dominant [Fig. 7(h)]. In the first part of this interval, the method of spin-1/2 coherent states finds a Néel state with the moment direction slightly tilted ($\lesssim 5^\circ$) from the honeycomb plane [Fig. 7(c)] and the amount

of quantum fluctuations comparable to the ground state of the AF Heisenberg model. After a transition at about 77°, a vortex-*a* pattern is found [Fig. 7(d)], but with a probability $P \approx 3\%$ significantly smaller than observed earlier inside the vortex phase. This suggests that the second phase might be possibly disordered, as claimed previously by Refs. [98,99] for the compass model. The absence of visible changes in the correlations in the region of the second phase indicates that the features of "compass" limit $|\vartheta| = 90°$ are kept throughout this phase. Similarly to the vortex phase, the most probable pattern (vortex-*a*) is accompanied by the complementary pattern (vortex-*b*) having a very close probability ($P \approx 3.16\%$ versus 3.05% in the AF "compass" limit). The same pair but with the swapped probabilities is found for FM compass point discussed in Sec. VI A. This is natural since the two models as well as the two patterns are linked by a simple 90° rotation of the spins (interchanging the in-bond and perpendicular components), followed by a 180° rotation at every second site (converting AF to FM and vice versa).

Finally, we note that the presence of two distinct phases between the spin liquid phase and the compass limit is at odds with the conclusion of Ref. [100] that the whole interval is occupied by a dimer phase. To check the reliability of our phase diagram, we have performed an additional ED for 32-site clusters of two different shapes, confirming the existence of the Néel phase for those clusters as well.

VII. CONCLUSIONS

We have performed a detailed numerical investigation of the global phase diagram of the extended Kitaev-Heisenberg model including the analysis of the internal structure of the individual phases. To this end, we have used mainly exact diagonalization combined with a recently developed ground-state analysis based on spin-1/2 coherent states.

In the context of real materials such as Na_2IrO_3 or α-$RuCl_3$, our results are useful when judging the extent of the experimentally observed zigzag phase and comparing the direction of the ordered moments, fixing thereby the relevant window in the parameter space.

In more general terms, we have interpreted the trends in the phase diagram based on several types of symmetry features found in the extended Kitaev-Heisenberg model, providing a number of reference points of expected behavior. They include points of hidden SU(2) symmetry, manifolds of fluctuation-free ground states, and mappings to other models: Ising, compass, and hidden Kitaev. We have demonstrated that while being in principle simple results of linear algebra, these symmetry features have far-reaching consequences and well fix the overall structure of the global phase diagram. As we believe, our symmetry-guided study can serve as a methodological template that can be applied to other spin models with bond-dependent non-Heisenberg interactions emerging in the field of Mott insulators with strong spin-orbit coupling.

Among the unusual symmetry properties brought about by the bond-dependent non-Heisenberg interactions, we have highlighted two interesting features that, to the best of our knowledge, escaped attention so far:

(i) Fluctuation-free ground states on entire manifolds of parameter points, possessing both FM and AF ordering patterns. These are enabled due to a partial cancellation of interactions for the particular spin structure. However, above the ground state, these interactions are fully active and shall lead to excitation spectra quite distinct from those of e.g., Heisenberg FM.

(ii) Models with bond-dependent non-Heisenberg interactions may realize not only the sought-after Kitaev model but also other models with a single bond-dependent interacting spin component ("interaction axis"). In the case of the extended Kitaev-Heisenberg model, they range from the simple Ising model, through Kitaev, to the 120° compass model on honeycomb lattice, whose ground-state nature is still debated in the literature. The above models are continuously connected in the parameter space of the extended Kitaev-Heisenberg model and the corresponding line in the phase diagram contains both trivial (Ising limit) as well as highly nontrivial phases—perturbed Kitaev spin liquid and the phase associated with the perturbed compass model. Such links to the extended Kitaev-Heisenberg model may motivate a search for candidate materials realizing, e.g., a compass model.

ACKNOWLEDGMENTS

We would like to thank Giniyat Khaliullin, Andrzej M. Oleś, Krzysztof Wohlfeld, and Kurt Hingerl for helpful discussions. J.C. and J.R. acknowledge support from the Ministry of Education, Youth and Sports of the Czech Republic within the project CEITEC 2020 (LQ1601) under the National Sustainability Programme II, European Research Council via project TWINFUSYON (No. 692034), Czech Science Foundation (GAČR) under project No. GJ15-14523Y, and Masaryk University internal projects MUNI/A/1310/2016 and MUNI/A/1291/2017. J.R. is Brno Ph.D Talent Scholarship Holder—Funded by the Brno City Municipality. D.G. was supported by Polish National Science Center (NCN) under projects 2012/04/A/ST3/00331 and 2016/23/B/ST3/00839. Computational resources were provided by the CESNET LM2015042 and the CERIT Scientific Cloud LM2015085, provided under the programme "Projects of Large Research, Development, and Innovations Infrastructures". The CMFT calculations were performed at the Interdisciplinary Centre for Mathematical and Computational Modelling (ICM) of the University of Warsaw under Grant Nos. G66-22 and G72-9.

APPENDIX A: OPTIMIZED SPIN-1/2 COHERENT STATES IN THE PRESENCE OF SPIN LIQUID PHASES

In contrast to the ordered phases, the ground states of Kitaev spin liquid (KSL) phases are highly entangled and cannot be well described by a spin-1/2 coherent state (4) that is a simple product of spin-1/2 states. This is indeed observed when applying the method of Sec. III A to the spin-liquid ground state. Nevertheless, the spin-liquid ground state still has a significant overlap with the configurations found in the classical $S \to \infty$ limit of the Kitaev model. Shown in Figs. 8(a) and 8(b) are the most probable configurations found in the exact ground state of the 24-site cluster near the AF or FM Kitaev point, respectively. They are characterized by spins pointing along the cubic axes x, y, z and forming aligned (FM case) or contra-aligned (AF case) pairs on nearest-neighbor

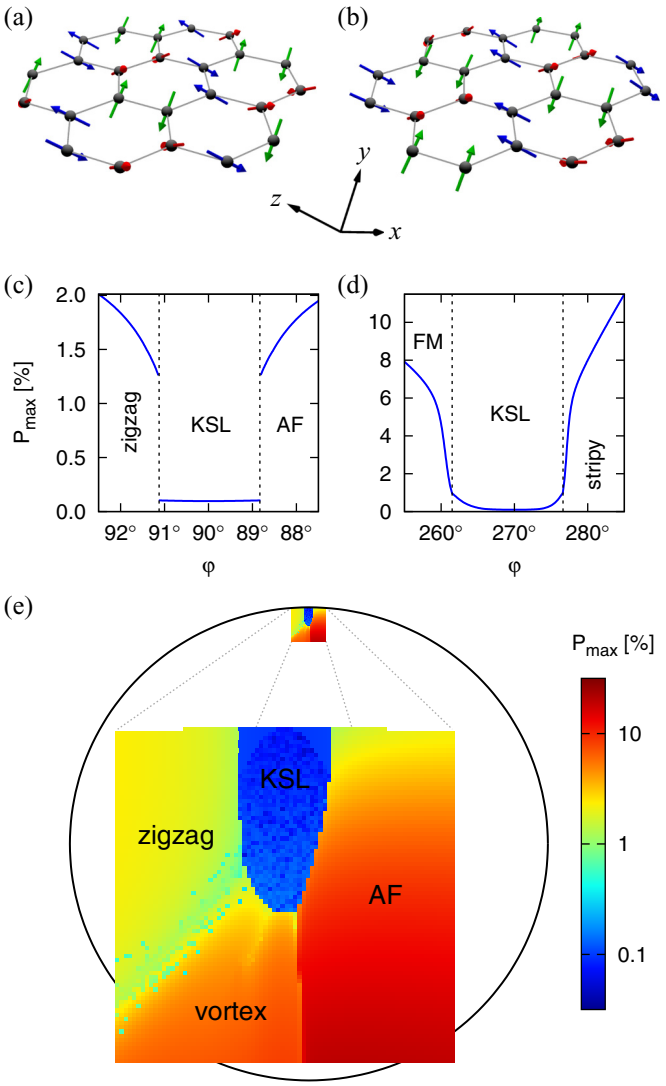

FIG. 8. Most probable configurations near the (a) AF and (b) FM Kitaev points. Spins pointing along the x, y, and z cubic axes are marked by red, green, and blue color, respectively. (c) Probability $P_{\max}$ of the optimized configuration near the AF Kitaev point in the Kitaev-Heisenberg model parametrized as $J = \cos\varphi$ and $K = \sin\varphi$. Phase transitions to the neighboring ordered phases are indicated by dashed lines. (d) The same for the region around the FM Kitaev point. (e) Map of $P_{\max}$ in a small area near the AF Kitaev spin liquid phase in the extended Kitaev-Heisenberg model with $\Gamma' = J_3 = 0$ (belongs to the same slice as shown in Fig. 2).

bonds. Their orientation is determined by the bond direction which is linked to the active spin component in the Kitaev interaction.

It is instructive to inspect the evolution of probability $P_{\max}$ of the optimized spin-1/2 coherent state when going from the KSL phase through a quantum phase transition to the neighboring ordered phases. This is done in Fig. 8(c) for the case of AF Kitaev model perturbed by Heisenberg interaction. While the KSL is characterized by small $P_{\max} \approx 0.1\%$, at the phase boundary either to zigzag or to AF ordered phase $P_{\max}$ jumps by about one order of magnitude to values above 1% typically encountered in the main text for the ordered phases with significant quantum fluctuations. A different behavior is found in the FM case. Here the probability rises near the phase boundaries to FM and stripy phases and continuously connects to $P_{\max}$ of their ground states. However, a discontinuity still appears in the derivative with respect to model parameters, with $P_{\max}$ shooting up after crossing the phase boundary. This is yet another manifestation of the different nature of the phase transitions involving AF and FM KSL phases that shows up, e.g., in the behavior of the spin-excitation gap [81].

Finally, in Fig. 8(e), we consider a larger portion of the phase diagram near the AF KSL phase which also involves the nonzero $\Gamma > 0$ parameter case. The AF KSL phase can be easily distinguished again by a drop of $P_{\max}$. The case of FM KSL phase at the bottom of the corresponding phase diagram slice is more complicated by the less pronounced transition and more complex phase behavior in the surrounding region as discussed in Sec. IV C. Fig. 8(e) also illustrates the difficulties of the global optimization in the complete 48-dimensional space of θ and ϕ parameters corresponding to the 24-site cluster. As seen in Fig. 8(e), the danger of getting trapped in a local maximum increases e.g., near the zigzag/vortex phase boundary or in the KSL phase characterized by competing configurations.

APPENDIX B: ISING-KITAEV-COMPASS MODEL: DERIVATION

The EKH Hamiltonian has a single matrix form for all bond directions when written in the rotating reference frame $\tilde{x}_\gamma, \tilde{y}_\gamma, \tilde{z}_\gamma$:

$$\widetilde{H} = \begin{pmatrix} J-\Gamma & 0 & 0 \\ 0 & J+\frac{2K}{3}+\frac{\Gamma}{3}-\frac{4\Gamma'}{3} & \frac{\sqrt{2}}{3}(K-\Gamma+\Gamma') \\ 0 & \frac{\sqrt{2}}{3}(K-\Gamma+\Gamma') & J+\frac{K}{3}+\frac{2\Gamma}{3}+\frac{4\Gamma'}{3} \end{pmatrix}. \tag{B1}$$

The matrix consists of two blocks, therefore one principal axis is $\tilde{x}_\gamma$ and the other two lie in the $\tilde{y}_\gamma\tilde{z}_\gamma$ plane. The eigenvalues of this matrix are

$$\begin{aligned} \lambda_1 &= J-\Gamma, \\ \lambda_2 &= J+\tfrac{1}{2}(K+\Gamma+\sqrt{(K-\Gamma)^2+8\Gamma'^2}), \\ \lambda_3 &= J+\tfrac{1}{2}(K+\Gamma-\sqrt{(K-\Gamma)^2+8\Gamma'^2}). \end{aligned} \tag{B2}$$

If only the first eigenvalue $\lambda_1 = J = \Gamma$ is nonzero, we obtain the 120° honeycomb compass model, the situation discussed in Sec. VI A. For $\Gamma > 0$, one can find a parameter region where only λ_2 is nonzero:

$$J = \Gamma,\ J(J+K) = \Gamma'^2,\ J > 0,\ J+K > 0. \tag{B3}$$

Analogous to this case, for $\Gamma < 0$ only λ_3 is nonzero in the region given by

$$J = \Gamma,\ J(J+K) = \Gamma'^2,\ J < 0,\ J+K < 0. \tag{B4}$$

The sole nonzero eigenvalue in both of these cases equals $3J+K$ and its sign is the same as the sign of Γ, hence in the case $\Gamma > 0$ used in the main text $3J+K > 0$ and the interaction is antiferromagnetic. The parameter region (B3) [or (B4)] can be parametrized by a single variable, which we choose as the angle ϑ between the $\tilde{z}_\gamma = Z$ axis and the

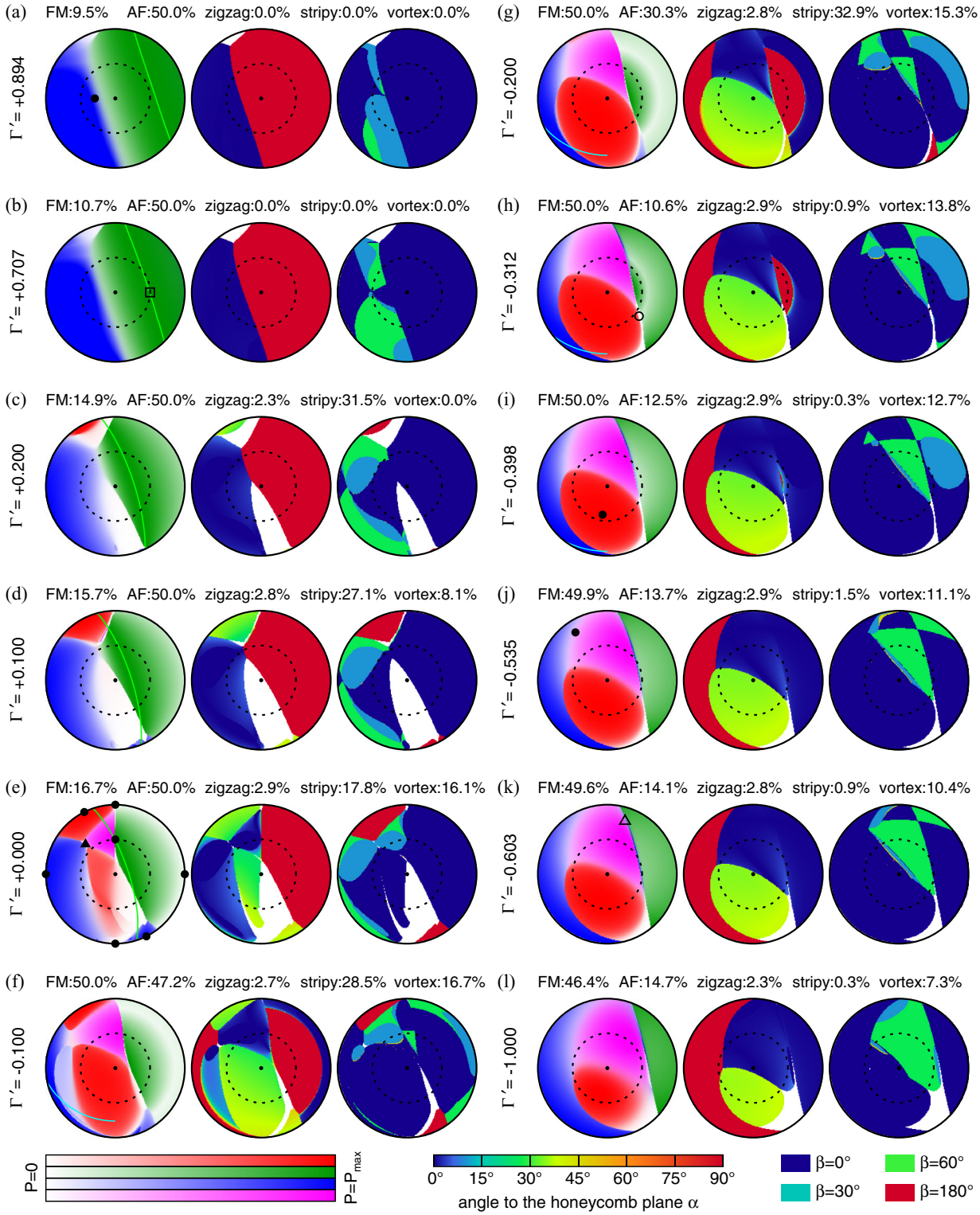

FIG. 9. Phase diagram slices for selected Γ' values and $J_3 = 0$. Left circle in each panel shows a color map of the probabilities of the patterns: FM (blue), AF (green), zigzag (red), stripy (blue), and vortex (violet). The ranges of the corresponding scales (bottom left) are determined by the maximum probability $P_{\max}$ as given at the top of the individual panels. Middle circles show the angle to the honeycomb plane (common scale at bottom center). Right circles show the azimuthal angle φ within the honeycomb plane. Fluctuation-free lines given by Eq. (13) (FM phase, light blue) and (16) (AF phase, light green) are indicated along with the special points: (hidden) SU(2) symmetry points [• in (a), (e), (i), and (j)], Kitaev points [• in (e), ○ in (h)], Ising point [□ in (b)], compass point [▲ in (e)] and compass-like point [△ in (k)].

interaction direction. In terms of the model parameters, ϑ is given by

$$\tan 2\vartheta = 2\sqrt{2}\left(\frac{9\Gamma'}{J-K+8\Gamma'}-1\right). \tag{B5}$$

It is also easy to obtain the parameters J, K, Γ, and Γ' realizing the model (22) with arbitrary ϑ and $\varphi = \pi/2$:

$$J = \Gamma = \tilde{K}\,\tfrac{1}{6}[1+\cos\vartheta(\cos\vartheta-\sqrt{8}\sin\vartheta)], \tag{B6}$$

$$K = \tilde{K}\,\tfrac{1}{2}[1-\cos\vartheta(\cos\vartheta-\sqrt{8}\sin\vartheta)], \tag{B7}$$

$$\Gamma' = \tilde{K}\,\tfrac{1}{3}\left[\cos 2\vartheta+\tfrac{1}{\sqrt{8}}\sin 2\vartheta)\right]. \tag{B8}$$

Finally, as demonstrated in Ref. [75], the nearest-neighbor EKH model preserves its form under global rotation of the spin axes by π around the (111) direction. This transformation, labeled as $\mathcal{T}_1$ in Ref. [75], maps the model parameters $JK\Gamma\Gamma'$ onto another set according to Eq. (4) of Ref. [75]. In the context of the Ising-Kitaev-compass model, the rotation by π around (111) axis corresponds to a sign change $\vartheta \to -\vartheta$. Indeed, inserting the transformed set of parameters into Eq. (B5), one observes the sign change. Obviously, the $\mathcal{T}_1$ transformation does not have any effect in the Ising ($\vartheta = 0$) and compass/"compass" ($\vartheta = \pm\pi/2$) case. Apart from these cases, it connects various pairs of points on the curves in Figs. 6(c)–6(e), most importantly, the Kitaev model and its π-rotated variant.

APPENDIX C: DETAILED EVOLUTION OF THE PHASE DIAGRAM FOR NONZERO Γ′

Figure 9 presents a detailed evolution of the phases of the nearest neighbor model ($J_3 = 0$) with the parameter Γ' attaining both positive and negative values. It was obtained using the method of Sec. III A for the hexagon-shaped 24-site cluster. The Γ' values were selected to include all the special symmetry points discussed in Ref. [75] and in the present paper. The lines of fluctuation-free ground states discussed in Sec. V are also indicated.

The plots use the same parametrization of the interactions as that of Fig. 2 and show also the moment direction in the form of an angle to the honeycomb plane α and an azimuthal angle in the honeycomb plane β. Using the XYZ reference frame of Fig. 5(b), the moment direction in the collinear phases is given by

$$\boldsymbol{n} = (\cos\alpha\cos\beta, \cos\alpha\sin\beta, \sin\alpha). \tag{C1}$$

For the moments lying in the honeycomb plane, $\beta = 0°$ corresponds to the direction perpendicular to a bond while $\beta = 30°$ is in-bond direction. The values $\beta = 60°$ and $\beta = 180°$ are used in the out-of-plane cases where a further distinction is necessary. In the vortex phase, the directions of the moments at the six sublattices marked in Fig. 5(c) are

$$\boldsymbol{n}_k = (\cos\alpha\cos\beta_k, \cos\alpha\sin\beta_k, (-1)^{k-1}\sin\alpha), \tag{C2}$$

where $\beta_k = (-1)^{k-1}\beta - 60°k$ and $k = 1, 2, \ldots, 6$ labels the sublattice. This ansatz, depicted in Fig. 10, captures both patterns vortex-a ($\beta = 0°$ or $60°$) and vortex-b ($\beta = 30°$) shown in Fig. 2(b) and AF staggering in the direction perpendicular to the honeycomb plane (nonzero α).

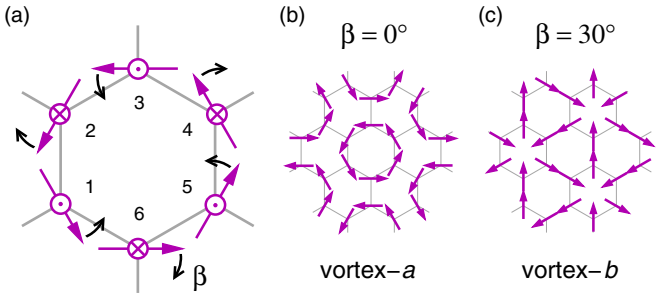

FIG. 10. (a) Moment directions defined by Eq. (C2) capturing vortex in-plane structure and out-of-plane AF staggering. For the in-plane deviation angle $\beta = 0°$ and $30°$, we get the patterns (b) vortex-a and (c) vortex-b of Fig. 2(b), respectively.

Not indicated in Fig. 9 are the regions of the instability of the zigzag phase observed in Figs. 2(a), 4(a), and 4(b). Apart from the ones shown earlier, the regions with noncollinear tendencies appear for large negative $\Gamma' \lesssim -0.5$ near the meeting point of the zigzag phase with FM and vortex phases and, to a smaller extent, also at the bottom near the white region in Figs. 9(j)–9(l). Since the smaller zigzag phase visible in Figs. 9(c)–9(f) is a copy of the larger zigzag phase linked by the exact $\mathcal{T}_1$ transformation, it also contains such patches of instability. Similarly, the top and bottom white areas hosting incommensurate orderings [visible in Figs. 9(a)–9(c) and Figs. 9(c)–9(f), respectively] are linked by the $\mathcal{T}_1$ transformation. The white area of Figs. 9(j)–9(l) maps to the $\Gamma < 0$ case.

[1] *Introduction to Frustrated Magnetism*, edited by C. Lacroix, P. Mendels, and F. Mila (Springer, Berlin, 2011).
[2] L. Balents, Nature (London) **464**, 199208 (2010).
[3] L. Savary and L. Balents, Rep. Prog. Phys. **80**, 016502 (2017).
[4] S. T. Bramwell and M. J. P. Gingras, Science **294**, 14951501 (2001).
[5] C. Castelnovo, R. Moessner, and S. L. Sondhi, Annu. Rev. Condens. Matter Phys. **3**, 35 (2012).
[6] M. R. Norman, Rev. Mod. Phys. **88**, 041002 (2016).
[7] P. Chandra and B. Doucot, Phys. Rev. B **38**, 9335 (1988).
[8] S. Chakravarty, B. I. Halperin, and D. R. Nelson, Phys. Rev. B **39**, 2344 (1989).
[9] B. Schmidt and P. Thalmeier, Phys. Rep. **703**, 1 (2017).
[10] W. Witczak-Krempa, G. Chen, Y. B. Kim, and L. Balents, Annu. Rev. Condens. Matter Phys. **5**, 57 (2014).
[11] Z. Nussinov and J. van den Brink, Rev. Mod. Phys. **87**, 1 (2015).
[12] J. G. Rau, E. K.-H. Lee, and H.-Y. Kee, Annu. Rev. Condens. Matter Phys. **7**, 195 (2016).
[13] R. Schaffer, E. K.-H. Lee, B.-J. Yang, and Y. B. Kim, Rep. Prog. Phys. **79**, 094504 (2016).

[14] S. Trebst, arXiv:1701.07056.
[15] S. M. Winter, A. A. Tsirlin, M. Daghofer, J. van den Brink, Y. Singh, P. Gegenwart, and R. Valentí, J. Phys.: Condens. Matter **29**, 493002 (2017).
[16] M. Hermanns, I. Kimchi, and J. Knolle, Annu. Rev. Condens. Matter Phys. **9**, 17 (2018).
[17] A. Kitaev, Ann. Phys. **321**, 2 (2006).
[18] A. Abragam and B. Bleaney, *Electron Paramagnetic Resonance of Transition Ions* (Clarendon Press, Oxford, 1970).
[19] G. Khaliullin, Prog. Theor. Phys. Suppl. **160**, 155 (2005).
[20] B. J. Kim, H. Jin, S. J. Moon, J.-Y. Kim, B.-G. Park, C. S. Leem, J. Yu, T. W. Noh, C. Kim, S.-J. Oh, J.-H. Park, V. Durairaj, G. Cao, and E. Rotenberg, Phys. Rev. Lett. **101**, 076402 (2008).
[21] B. J. Kim, H. Ohsumi, T. Komesu, S. Sakai, T. Morita, H. Takagi, and T. Arima, Science **323**, 1329 (2009).
[22] G. Jackeli and G. Khaliullin, Phys. Rev. Lett. **102**, 017205 (2009).
[23] J. Kim, D. Casa, M. H. Upton, T. Gog, Y.-J. Kim, J. F. Mitchell, M. van Veenendaal, M. Daghofer, J. van den Brink, G. Khaliullin, and B. J. Kim, Phys. Rev. Lett. **108**, 177003 (2012).
[24] Y. K. Kim, O. Krupin, J. D. Denlinger, A. Bostwick, E. Rotenberg, Q. Zhao, J. F. Mitchell, J. W. Allen, and B. J. Kim, Science **345**, 187 (2014).
[25] Y. K. Kim, N. H. Sung, J. D. Denlinger, and B. J. Kim, Nat. Phys. **12**, 37 (2016).
[26] K. I. Kugel and D. I. Khomskii, Sov. Phys. Usp. **25**, 231 (1982).
[27] G. Chen and L. Balents, Phys. Rev. B **78**, 094403 (2008).
[28] K. W. Plumb, J. P. Clancy, L. J. Sandilands, V. V. Shankar, Y. F. Hu, K. S. Burch, H.-Y. Kee, and Y.-J. Kim, Phys. Rev. B **90**, 041112(R) (2014).
[29] A. Banerjee, C. A. Bridges, J.-Q. Yan, A. A. Aczel, L. Li, M. B. Stone, G. E. Granroth, M. D. Lumsden, Y. Yiu, J. Knolle, S. Bhattacharjee, D. L. Kovrizhin, R. Moessner, D. A. Tennant, D. G. Mandrus, and S. E. Nagler, Nat. Mater. **15**, 733 (2016).
[30] K. Ran, J. Wang, W. Wang, Z.-Y. Dong, X. Ren, S. Bao, S. Li, Z. Ma, Y. Gan, Y. Zhang, J. T. Park, G. Deng, S. Danilkin, S.-L. Yu, J.-X. Li, and J. Wen, Phys. Rev. Lett. **118**, 107203 (2017).
[31] A. Banerjee, J. Yan, J. Knolle, C. A. Bridges, M. B. Stone, M. D. Lumsden, D. G. Mandrus, D. A. Tennant, R. Moessner, and S. E. Nagler, Science **356**, 1055 (2017).
[32] S.-H. Do, S.-Y. Park, J. Yoshitake, J. Nasu, Y. Motome, Y. S. Kwon, D. T. Adroja, D. J. Voneshen, K. Kim, T.-H. Jang, J.-H. Park, K.-Y. Choi, and S. Ji, Nat. Phys. **13**, 1079 (2017).
[33] X. Liu, T. Berlijn, W.-G. Yin, W. Ku, A. Tsvelik, Y.-J. Kim, H. Gretarsson, Y. Singh, P. Gegenwart, and J. P. Hill, Phys. Rev. B **83**, 220403(R) (2011).
[34] F. Ye, S. Chi, H. Cao, B. C. Chakoumakos, J. A. Fernandez-Baca, R. Custelcean, T. F. Qi, O. B. Korneta, and G. Cao, Phys. Rev. B **85**, 180403(R) (2012).
[35] S. K. Choi, R. Coldea, A. N. Kolmogorov, T. Lancaster, I. I. Mazin, S. J. Blundell, P. G. Radaelli, Y. Singh, P. Gegenwart, K. R. Choi, S.-W. Cheong, P. J. Baker, C. Stock, and J. Taylor, Phys. Rev. Lett. **108**, 127204 (2012).
[36] R. D. Johnson, S. C. Williams, A. A. Haghighirad, J. Singleton, V. Zapf, P. Manuel, I. I. Mazin, Y. Li, H. O. Jeschke, R. Valentí, and R. Coldea, Phys. Rev. B **92**, 235119 (2015).
[37] J. A. Sears, M. Songvilay, K. W. Plumb, J. P. Clancy, Y. Qiu, Y. Zhao, D. Parshall, and Y.-J. Kim, Phys. Rev. B **91**, 144420 (2015).
[38] S. C. Williams, R. D. Johnson, F. Freund, S. Choi, A. Jesche, I. Kimchi, S. Manni, A. Bombardi, P. Manuel, P. Gegenwart, and R. Coldea, Phys. Rev. B **93**, 195158 (2016).
[39] K. Kitagawa, T. Takayama, Y. Matsumoto, A. Kato, R. Takano, Y. Kishimoto, S. Bette, R. Dinnebier, G. Jackeli, and H. Takagi, Nature (London) **554**, 341345 (2018).
[40] J. Chaloupka, G. Jackeli, and G. Khaliullin, Phys. Rev. Lett. **110**, 097204 (2013).
[41] S. H. Chun, J.-W. Kim, Jungho Kim, H. Zheng, C. C. Stoumpos, C. D. Malliakas, J. F. Mitchell, K. Mehlawat, Y. Singh, Y. Choi, T. Gog, A. Al-Zein, M. Moretti Sala, M. Krisch, J. Chaloupka, G. Jackeli, G. Khaliullin, and B. J. Kim, Nat. Phys. **11**, 462 (2015).
[42] J. G. Rau, E. K.-H. Lee, and H.-Y. Kee, Phys. Rev. Lett. **112**, 077204 (2014).
[43] J. G. Rau and H.-Y. Kee, arXiv:1408.4811.
[44] V. M. Katukuri, S. Nishimoto, V. Yushankhai, A. Stoyanova, H. Kandpal, S. Choi, R. Coldea, I. Rousochatzakis, L. Hozoi, and J. van den Brink, New J. Phys. **16**, 013056 (2014).
[45] Y. Yamaji, Y. Nomura, M. Kurita, R. Arita, and M. Imada, Phys. Rev. Lett. **113**, 107201 (2014).
[46] Y. Sizyuk, C. Price, P. Wölfle, and N. B. Perkins, Phys. Rev. B **90**, 155126 (2014).
[47] S. M. Winter, Y. Li, H. O. Jeschke, and R. Valentí, Phys. Rev. B **93**, 214431 (2016).
[48] S. M. Winter, K. Riedl, P. A. Maksimov, A. L. Chernyshev, A. Honecker, and R. Valentí, Nat. Commun. **8**, 1152 (2017).
[49] P. A. McClarty, X.-Y. Dong, M. Gohlke, J. G. Rau, F. Pollmann, R. Moessner, and K. Penc, Phys. Rev. B **98**, 060404(R) (2018).
[50] D. G. Joshi, Phys. Rev. B **98**, 060405(R) (2018).
[51] M. Becker, M. Hermanns, B. Bauer, M. Garst, and S. Trebst, Phys. Rev. B **91**, 155135 (2015).
[52] I. Rousochatzakis, U. K. Rössler, J. van den Brink, and M. Daghofer, Phys. Rev. B **93**, 104417 (2016).
[53] K. Li, S.-L. Yu, and J.-X. Li, New J. Phys. **17**, 043032 (2015).
[54] A. Catuneanu, J. G. Rau, H.-S. Kim, and H.-Y. Kee, Phys. Rev. B **92**, 165108 (2015).
[55] K. Morita, M. Kishimoto, and T. Tohyama, Phys. Rev. B **98**, 134437 (2018).
[56] T. Takayama, A. Kato, R. Dinnebier, J. Nuss, H. Kono, L. S. I. Veiga, G. Fabbris, D. Haskel, and H. Takagi, Phys. Rev. Lett. **114**, 077202 (2015).
[57] E. K.-H. Lee and Y. B. Kim, Phys. Rev. B **91**, 064407 (2015).
[58] H.-S. Kim, E. K.-H. Lee, and Y. B. Kim, Europhys. Lett. **112**, 67004 (2015).
[59] E. K.-H. Lee, J. G. Rau and, Y. B. Kim, Phys. Rev. B **93**, 184420 (2016).
[60] V. M. Katukuri, R. Yadav, L. Hozoi, S. Nishimoto, and J. van den Brink, Sci. Rep. **6**, 29585 (2016).
[61] K. A. Modic, T. E. Smidt, I. Kimchi, N. P. Breznay, A. Biffin, S. Choi, R. D. Johnson, R. Coldea, P. Watkins-Curry, G. T. McCandless, J. Y. Chan, F. Gandara, Z. Islam, A. Vishwanath, A. Shekhter, R. D. McDonald, and J. G. Analytis, Nat. Commun. **5**, 4203 (2014).

[62] A. Biffin, R. D. Johnson, I. Kimchi, R. Morris, A. Bombardi, J. G. Analytis, A. Vishwanath, and R. Coldea, Phys. Rev. Lett. **113**, 197201 (2014).
[63] I. Kimchi, J. G. Analytis, and A. Vishwanath, Phys. Rev. B **90**, 205126 (2014).
[64] Y. Okamoto, M. Nohara, H. Aruga-Katori, and H. Takagi, Phys. Rev. Lett. **99**, 137207 (2007).
[65] G. Cao, A. Subedi, S. Calder, J.-Q. Yan, J. Yi, Z. Gai, L. Poudel, D. J. Singh, M. D. Lumsden, A. D. Christianson, B. C. Sales, and D. Mandrus, Phys. Rev. B **87**, 155136 (2013).
[66] A. M. Cook, S. Matern, C. Hickey, A. A. Aczel, and A. Paramekanti, Phys. Rev. B **92**, 020417(R) (2015).
[67] A. A. Aczel, A. M. Cook, T. J. Williams, S. Calder, A. D. Christianson, G.-X. Cao, D. Mandrus, Y.-B. Kim, and A. Paramekanti, Phys. Rev. B **93**, 214426 (2016).
[68] H. Kuriyama, J. Matsuno, S. Niitaka, M. Uchida, D. Hashizume, A. Nakao, K. Sugimoto, H. Ohsumi, M. Takata, and H. Takagi, Appl. Phys. Lett. **96**, 182103 (2010).
[69] I. Kimchi and A. Vishwanath, Phys. Rev. B **89**, 014414 (2014).
[70] M. Hermanns and S. Trebst, Phys. Rev. B **89**, 235102 (2014).
[71] H. Liu and G. Khaliullin, Phys. Rev. B **97**, 014407 (2018).
[72] R. Sano, Y. Kato, and Y. Motome, Phys. Rev. B **97**, 014408 (2018).
[73] J. M. Luttinger and L. Tisza, Phys. Rev. **70**, 954 (1946).
[74] J. Chaloupka, G. Jackeli, and G. Khaliullin, Phys. Rev. Lett. **105**, 027204 (2010).
[75] J. Chaloupka and G. Khaliullin, Phys. Rev. B **92**, 024413 (2015).
[76] L. Janssen, E. C. Andrade, and M. Vojta, Phys. Rev. B **96**, 064430 (2017).
[77] J. Lou, L. Liang, Y. Yu, and Y. Chen, arXiv:1501.06990.
[78] K. Shinjo, S. Sota, and T. Tohyama, Phys. Rev. B **91**, 054401 (2015).
[79] S. Nishimoto, V. M. Katukuri, V. Yushankhai, H. Stoll, U. K. Rössler, L. Hozoi, I. Rousochatzakis, and J. van den Brink, Nat. Commun. **7**, 10273 (2016).
[80] J. Chaloupka and G. Khaliullin, Phys. Rev. B **94**, 064435 (2016).
[81] D. Gotfryd, J. Rusnačko, K. Wohlfeld, G. Jackeli, J. Chaloupka, and A. M. Oleś, Phys. Rev. B **95**, 024426 (2017).
[82] C. C. Price and N. B. Perkins, Phys. Rev. Lett. **109**, 187201 (2012).
[83] R. Schaffer, S. Bhattacharjee, and Y. B. Kim, Phys. Rev. B **86**, 224417 (2012).
[84] J. Reuther, R. Thomale, and S. Trebst, Phys. Rev. B **84**, 100406(R) (2011).
[85] J. Osorio Iregui, P. Corboz, and M. Troyer, Phys. Rev. B **90**, 195102 (2014).
[86] M. Gohlke, R. Verresen, R. Moessner, and F. Pollmann, Phys. Rev. Lett. **119**, 157203 (2017).
[87] F. Trousselet, M. Berciu, A. M. Oleś, and P. Horsch, Phys. Rev. Lett. **111**, 037205 (2013).
[88] F. Trousselet, P. Horsch, A. M. Oleś, and W.-L. You, Phys. Rev. B **90**, 024404 (2014).
[89] *Strongly Correlated Systems: Numerical Methods*, edited by A. Avella and F. Mancini (Springer, Berlin, 2013).
[90] For a discussion of the order-from-disorder phenomena in frustrated spin systems, see A. M. Tsvelik, *Quantum Field Theory in Condensed Matter Physics* (Cambridge University Press, Cambridge, 1995), Chap. 17, and references therein.
[91] G. Baskaran, D. Sen, and R. Shankar, Phys. Rev. B **78**, 115116 (2008).
[92] I. Rousochatzakis, Y. Sizyuk, and N. B. Perkins, Nat. Commun. **9**, 1575 (2018).
[93] M. Gohlke, G. Wachtel, Y. Yamaji, F. Pollmann, and Y. B. Kim, Phys. Rev. B **97**, 075126 (2018).
[94] P. P. Stavropoulos, A. Catuneanu, and H.-Y. Kee, Phys. Rev. B **98**, 104401 (2018).
[95] E. Quinn, S. Bhattacharjee, and R. Moessner, Phys. Rev. B **91**, 134419 (2015).
[96] E. Zhao and W. V. Liu, Phys. Rev. Lett. **100**, 160403 (2008).
[97] C. Wu, Phys. Rev. Lett. **100**, 200406 (2008).
[98] J. Nasu, A. Nagano, M. Naka, and S. Ishihara, Phys. Rev. B **78**, 024416 (2008).
[99] C.-C. Chen, L. Muechler, R. Car, T. Neupert, and J. Maciejko, Phys. Rev. Lett. **117**, 096405 (2016).
[100] H. Zou, B. Liu, E. Zhao, and W. V. Liu, New J. Phys. **18**, 053040 (2016).

PHYSICAL REVIEW X **10,** 021034 (2020)

Dynamic Spin Correlations in the Honeycomb Lattice Na_2IrO_3 Measured by Resonant Inelastic x-Ray Scattering

Jungho Kim,[1,*] Jiří Chaloupka,[2,3,†] Yogesh Singh,[4] J. W. Kim,[1] B. J. Kim,[5,6] D. Casa,[1] A. Said,[1] X. Huang,[1] and T. Gog[1]

[1]*Advanced Photon Source, Argonne National Laboratory, Argonne, Illinois 60439, USA*
[2]*Central European Institute of Technology, Masaryk University, Kamenice 753/5, CZ-62500 Brno, Czech Republic*
[3]*Department of Condensed Matter Physics, Faculty of Science, Masaryk University, Kotlářská 2, CZ-61137 Brno, Czech Republic*
[4]*Department of Physical Sciences, Indian Institute of Science Education and Research Mohali, Knowledge City, Sector 81, Mohali 140306, India*
[5]*Department of Physics, Pohang University of Science and Technology, Pohang 790-784, Republic of Korea*
[6]*Center for Artificial Low Dimensional Electronic Systems, Institute for Basic Science (IBS), 77 Cheongam-Ro, Pohang 790-784, Republic of Korea*

(Received 16 April 2019; revised manuscript received 14 March 2020; accepted 23 March 2020; published 13 May 2020)

A Kitaev quantum spin liquid is a prime example of novel quantum magnetism of spin-orbit entangled pseudospin-1/2 moments in a honeycomb lattice. Most candidate materials such as Na_2IrO_3 have many competing exchange interactions beyond the minimal Kitaev-Heisenberg model whose small variations in the strength of the interactions produce huge differences in low-energy dynamics. Our incomplete knowledge of dynamic spin correlations hampers identification of a minimal model and quantification of the proximity to the Kitaev quantum spin-liquid phase. Here, we report momentum- and energy-resolved magnetic excitation spectra in a honeycomb lattice Na_2IrO_3 measured using a resonant inelastic x-ray scattering spectrometer capable of 12 meV resolution. Measured spectra at a low temperature show that the dynamic response lacks resolution-limited coherent spin waves in most parts of the Brillouin zone but has a discernible dispersion and spectral weight distribution within the energy window of 60 meV. A systematic investigation using the exact diagonalization method and direct comparison of high-resolution experimental spectra and theoretical simulations allow us to confine a parameter regime in which the extended Kitaev-Heisenberg model reasonably reproduces the main feature of the observed magnetic excitations. Hidden Kitaev quantum spin-liquid and Heisenberg phases found in the complex parameter space are used as references to propose the picture of renormalized magnons as explaining the incoherent nature of magnetic excitations. Magnetic excitation spectra are taken at elevated temperatures to follow the temperature evolution of the resonant inelastic x-ray scattering dynamic response in the paramagnetic state. Whereas the low-energy excitation progressively diminishes as the zigzag order disappears, the broad high-energy excitation maintains its spectral weight up to a much higher temperature of 160 K. We suggest that the dominant nearest-neighbor interactions keep short-range correlations up to quite high temperatures with a specific short-range dynamics which has a possible connection to a proximate spin-liquid phase.

DOI: 10.1103/PhysRevX.10.021034

Subject Areas: Condensed Matter Physics, Magnetism, Strongly Correlated Materials

I. INTRODUCTION

A Kitaev quantum spin liquid (KQSL) is a topological phase of matter resulting from an exactly solvable Hamiltonian of nearest-neighbor bond-directional interactions between half-integer spins in a honeycomb lattice [1,2]. Their long-range quantum entanglement and topologically protected fractional excitations are of particular interest for potential quantum computing platforms [3]. It has been pointed out that the bond-directional Kitaev

*jhkim@aps.anl.gov
†chaloupka@physics.muni.cz

interactions arise naturally in a honeycomb magnet with strong spin-orbit coupling, which triggered a wave of searching for a material realization of the KQSL [4]. The Kitaev-Heisenberg model and related spin models indicate extended stability of the spin-liquid phase away from the pure Kitaev limit [5–10], which widens the scope of candidate materials.

Na_2IrO_3 is one of the first and most extensively studied candidate materials despite having a conventional symmetry-breaking magnetic order as in other honeycomb magnets [11–14]. A zigzag antiferromagnetic (AFM) order was found by resonant x-ray magnetic scattering and inelastic neutron scattering [12–14]. It has been shown that the inclusion of small Heisenberg terms, omnipresent in all materials, can explain the zigzag order [13,14]. Subsequently, many other models were proposed which may be more realistic but are of increased complexity [6–10]. Resonant magnetic x-ray scattering measurements provide important constraints on the minimal model and the sign of the Kitaev term [15]. It was found that the ordered magnetic moment direction approximately bisects the angle between the cubic x and y axes and that two other dynamically fluctuating zigzag orders related to the static one by the approximate C_3 symmetry of the lattice have their corresponding moment directions [15]. These results imply a dominant ferromagnetic Kitaev term (K) with a non-negligible off-diagonal exchange (Γ), which is supported by quantum chemistry [16] and other *ab initio* calculations [17,18]. The off-diagonal exchange which is symmetry allowed can be sizable when direct exchange is effective [7]. At a classical level, a spin-liquid phase is theoretically found in models with a large off-diagonal exchange [19]. The infinite density matrix renormalization group study on the K-Γ model found strong numerical evidence for the existence of a quantum spin liquid for ferrolike Kitaev interactions [20].

The materials search for the KQSL led to the discovery of many other honeycomb materials [21–26]. For example, Cu_2IrO_3 and hydrogen-intercalated $H_3LiIr_2O_6$ are found to bear no sign of a magnetic order down to the lowest temperatures [24,25]. The 4d compound α-$RuCl_3$ is found to be a $J_{\mathrm{eff}} = 1/2$ Mott insulator despite having a much smaller magnitude of spin-orbit coupling and has received much attention recently [26]. Dynamic spin correlations of α-$RuCl_3$ have been extensively studied by inelastic neutron scattering (INS) [27–30]. The dynamical structure factor through INS reveals a highly unusual intensity distribution over a large energy interval around the zone center [29,30]. Although incoherent excitations originating from strong magnetic anharmonicity can naturally occur in a highly anisotropic frustrated magnet [31,32], several theoretical works support that the broad feature is a dynamic response of Majorana fermions—a salient nonlocal feature of the Kitaev quantum spin-liquid phase [33–37].

Phenomenologically, Na_2IrO_3 and α-$RuCl_3$ share several common features: an unusual broad continuum in their Raman scattering spectra [38,39]; magnetic entropy recovered or released in two widely separated temperature scales in heat capacity measurements [30,40]; and high-field evolution of the zigzag-ordered phase to a nonmagnetic phase in magnetic torque measurements [41,42]. However, measurement of the dynamical structure factor providing the most direct information thus far remains elusive for Na_2IrO_3, because resonant inelastic x-ray scattering (RIXS) suffers from insufficient energy resolution and INS is difficult for Ir compounds due to their high neutron absorption. The INS measurement on polycrystalline Na_2IrO_3 samples at a low temperature observes spin-wave excitations with a sinusoidal-like low-momentum dispersion, which can be best understood by including substantial further-neighbor exchanges that stabilize the zigzag magnetic order [14]. Previous RIXS measurement on single-crystal Na_2IrO_3 observed only a broad low-energy excitation interpreted as containing signals of magnetic and phonon origins [43], which limits a detailed comparison with theoretical calculations. A more recent RIXS measurement rules out the phonon interpretation of the low-energy excitation by showing different peak energies of isostructural Na_2IrO_3 and Li_2IrO_3 and suggests a magnetic origin of the broad excitation [44], which is phenomenologically similar to the unusual broad scattering in α-$RuCl_3$ [29,30]. Both RIXS works can observe only the broad excitation and do not provide detailed information on the magnetic ground state.

Here, we report magnetic excitation spectra in a honeycomb lattice Na_2IrO_3 measured by the state-of-the-art RIXS spectrometer providing an unprecedented energy resolution of 12 meV. The measurements are carried out along all high-symmetry paths including the second Brillouin zone (BZ) center. The 25 meV resolution spectra at $T = 7$ K reveal a discernible dispersion and spectral distribution within the energy window of 60 meV. The 12 meV resolution allows us to characterize the spectral width of the excitation peak and better define the low-energy excitation feature [45,46]. The zone center spectrum lacks a resolution-limited peak typical of a coherent collective excitation and has a broad feature only at high energy. The incoherent feature persists over the whole BZ. As approaching the zone boundary, a spectral weight shifts toward lower energy. Remarkably, a sharp collective excitation peak whose width is comparable to the spectrometer resolution is resolved at the K point of the honeycomb BZ. An exact diagonalization method on finite-size clusters is used to find the relevant parameter regime of the extended Kitaev-Heisenberg model which captures the main features of the measured magnetic excitation spectra at a low temperature in terms of spectral dispersion and intensity. Hidden KQSL and Heisenberg phases found in the complex parameter space of the model

provide useful references for the nature of the magnetic excitations appearing in the measured spectra. We present the temperature evolution of the RIXS dynamic response up to 280 K, which reveals an anomalous behavior of the broad high-energy excitation.

The paper is organized as follows: Section II presents experimental RIXS spectra at low temperatures. Section III describes the simulations of the low-temperature RIXS data based on the extended Kitaev-Heisenberg model and discusses the nature of the observed magnetic excitations. The zigzag phase of the model is systematically explored, and several kinds of differing pseudospin dynamics are observed. Comparing directly the experiment and theoretical RIXS spectra, this observation is used to identify the parameter regime consistent with the experimental data. A picture of renormalized magnons is proposed to explain the main spectral features in this regime. Section IV presents experimental RIXS spectra at high temperatures and discusses the anomalous higher-energy spectral intensities in the context of Kitaev systems at a finite temperature. Section V concludes the paper and presents a perspective on a RIXS probe for higher-order correlations that detects the full continuum of the Majorana fermions of the KQSL. The Appendixes provide details of our experimental setup, the description of the numerical computations, and a discussion of the hidden-symmetry points of the extended Kitaev-Heisenberg model that are utilized in Sec. III.

II. MAGNETIC EXCITATION SPECTRA AT A LOW TEMPERATURE

A. RIXS scatterings over the entire Brillouin zone

Figure 1(d) shows a RIXS intensity map recorded at $T = 7$ K along the Γ-M-Γ'-X-K-Γ-Y-K'-Γ' path of the in-plane

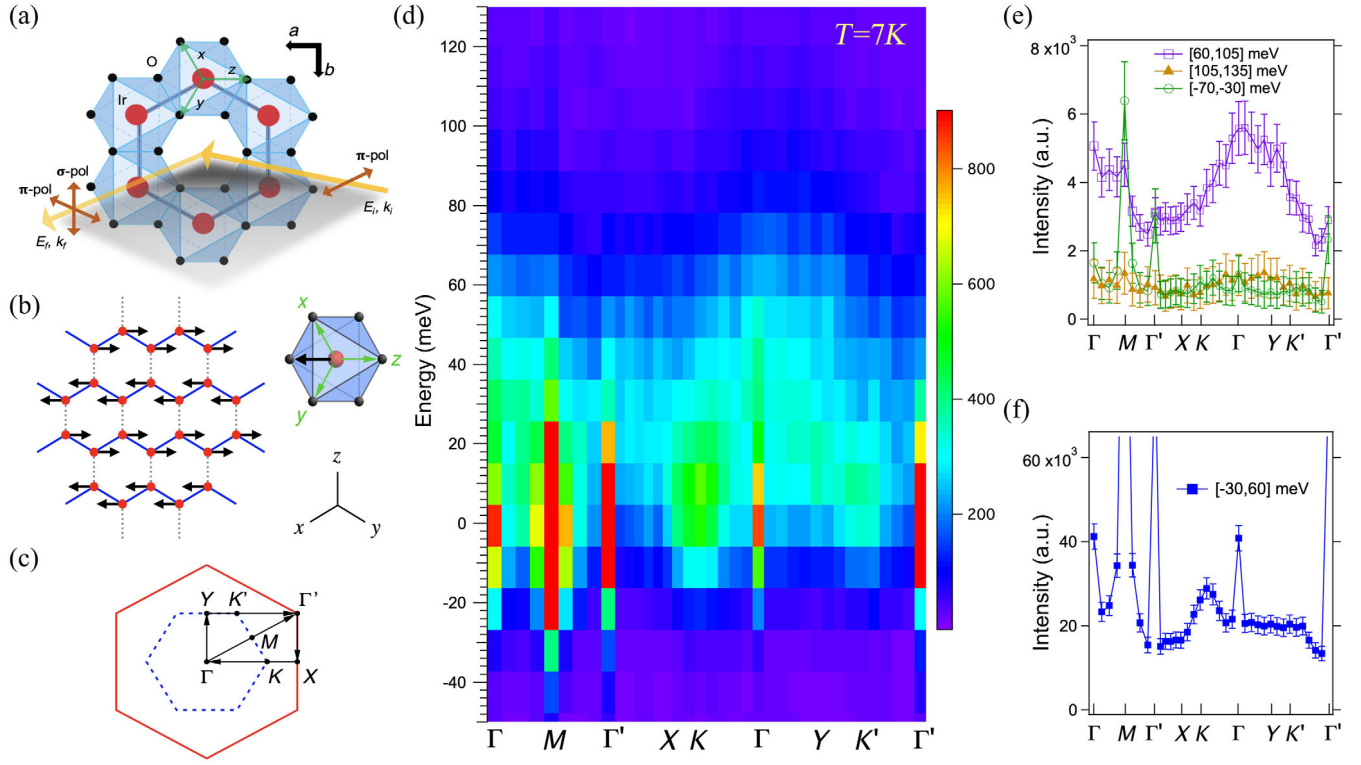

FIG. 1. Magnetic excitation spectra in Na_2IrO_3 along high-symmetry Brillouin zone directions taken at $T = 7$ K. (a) Scattering geometry. Yellow arrows indicate incident and scattered x rays, which define the scattering plane (gray). Brown arrows indicate x-ray polarizations. Green arrows indicate the cubic axes (x, y, z) with respect to the octahedra (all of them point above the paper plane). (b) One of the collinear zigzag patterns and the corresponding direction of the ordered moments. The left-facing arrows have an out-of-plane component pointing above the paper plane; i.e., the corresponding moment direction lies approximately between the x and y axes. (c) Two-dimensional reciprocal space diagram showing the measured path along the symmetry directions. The inner hexagon (blue dashed line) indicates the first Brillouin zone of the honeycomb lattice. (d) RIXS intensity map of magnetic excitations in Na_2IrO_3 as functions of the wave vector and energy loss. (e) The intensity profiles integrated over [60, 105] (open squares) and [105, 135] meV (filled triangles) show that the high-energy spectral intensities are broadly peaked at the Γ point, extending up to 105 meV. (f) The intensity profile integrated over $[-30, 60]$ meV (filled squares) shows a distinctive distribution of the spectral weight along the K-Γ-Y-K'-Γ' path. Passing through the K point, the excitation intensity rapidly increases and then decreases, which is followed by a near-constant intensity along the Γ-Y-K' path. Large intensities at the Γ and Γ' wave vectors correspond to elastic scatterings. The zero-energy loss intensity at the M point is the diffuse magnetic Bragg peak. In the used scattering geometry, the magnetic Bragg peak at the Y point is suppressed.

momentum transfer as shown in Fig. 1(c). These RIXS spectra are obtained from a standard setup with conventional 25 meV resolution using a Si(844) diced spherical analyzer [47,48]. The out-of-plane momentum transfer is varied to keep the scattering angle close to 90° to minimize elastic scatterings. Singular intensities at zero energy loss at Γ (Γ′) and M originate from a specular elastic scattering and a static zigzag magnetic order [11–14], respectively. Polarization factors in the current scattering geometry depicted in Fig. 1(a) lead to a vanishing magnetic Bragg peak at the Y point and a weak scattering intensity at the K' point relative to the K point [15].

The main dispersing feature is observed in the first BZ along the K-Γ-Y-K' path below approximately 60 meV. An intense low-energy excitation around 10 meV is clearly seen near the K point. The spectral intensity moves to higher energy along the K-Γ path, reaching its highest energy at the Γ point, and disperses toward lower energy along the Γ-Y-K' path.

For each wave vector, the intensity is integrated over an energy window of interest to obtain the distribution of the spectral weight in the BZ. Figure 1(e) shows the intensity profiles on the high-energy loss and the energy gain sides. The intensity over the far energy loss region ([105, 135] meV, filled triangles) shows a nearly constant value which is comparable to that of the far energy gain region ($[-70, -30]$ meV, open circles). The intensity profile integrated over [60, 105] meV (open squares) in Fig. 1(f) shows a distribution, peaked broadly around the BZ center Γ. These indicate that the spectral intensity of the observed excitation extends roughly to 105 meV.

Figure 1(f) shows the intensity distribution of the main feature ($[-30, 60]$ meV, filled squares) which reveals a distinctive distribution of the spectral weight as a function of the wave vector. Weak intensities are seen along the Γ′-X line (outside the first Brillouin zone). Passing through the K point, the excitation intensity rapidly increases and then decreases, which is followed by a nearly constant intensity along the Γ-Y-K' path. The intensity is weakened as it approaches the Γ′ point.

B. High-energy resolution RIXS spectra

Recently, a higher energy resolution has been achieved for the Ir L_3 RIXS by using the quartz(309) crystal [45,46]. In this work, the high-resolution quartz analyzer is used to better examine spectral widths of magnetic excitations at the Γ, near M, Y, and K wave vectors, where prominent low-energy spectral weights below 20 meV are seen from the 25 meV RIXS spectra in Fig. 1(d). The measured energy resolution function of the quartz analyzer is plotted at the bottom in Fig. 2(a), which can be described with the pseudo-Voigt function with a 12 meV full width at half maximum (FWHM).

Strong elastic scatterings at $\mathbf{Q} = (0\,0\,6.75)$ (Γ) and (0.45 0.45 6.5) (near M) are due to a specular scattering and a quasielastic scattering due to the diffuse magnetic peak, respectively. At both wave vectors, resolution-limited peaks characteristic of coherent spin waves are not found, but broad incoherent scatterings are seen at high energies. At the Γ, the broad incoherent scattering has a clear peak structure at around 40 meV. At $\mathbf{Q} = (0\,1\,6.5)$ (Y), a glimpse of a low-energy peak is detected, and a broad peak is centered around 50 meV. On the other hand, a narrow width peak below 20 meV is clearly revealed at the $\mathbf{Q} = (0.67\,0\,6.6)$ (K) point, which is also followed by a broad feature.

Figure 2(b) shows the Γ point spectrum with a fit in which the elastic peak is fitted to the pseudo-Voigt resolution function and the broad incoherent peak is fitted by a damped harmonic oscillator (DHO) function convoluted by the pseudo-Voigt resolution function. Note that the high-resolution data have rather a large ratio of background to signal and poor statistics. The background level is determined in a way that the energy gain data below −30 meV are distributed around the zero, and such a background is subtracted from the raw data. The DHO function is expressed as $An(T)\gamma\{1/[(E-E_0)^2+\gamma^2]-1/[(E+E_0)^2+\gamma^2]\}$, where A is the amplitude, $n(T)$ is the Bose factor, E_0 is the peak energy, and γ is the peak width. The fitted curves are overlaid with the Γ point data in Fig. 2(b). A damped peak of $(E_0, \gamma) = (36, 22)$ meV is used to describe the broad incoherent peak. Figure 2(c) shows the K point spectrum, where the background level estimated for the Γ spectrum is assumed. The low-energy peak is described by a narrow width peak of $(E_0, \gamma) = (3, 7)$ meV. The broad feature is fit by the $(E_0, \gamma) = (38, 20)$ meV DHO.

Figure 2(d) shows the temperature dependence of the high-resolution RIXS spectrum at the K point. Na_2IrO_3 is a Mott-like correlated insulator with a 340 meV energy gap [49]. Within the Mott gap of 340 meV, the lattice and spin degrees of freedom could be associated with the appearance of excitations. The temperature dependence data in Fig. 2(d), for example, provide a means to distinguish excitations of distinct origins. If the lattice degree of freedom is involved, the Bose population factor leads to an increasing intensity with an increasing temperature. On the other hand, at a temperature above a characteristic spin exchange energy, the contribution of the spin degree of freedom vanishes.

The low-energy peak in Fig. 2(d) clearly decreases at $T = 70$ K and becomes featureless at $T = 150$ K. The long-range zigzag order disappears above 15 K, but the diffuse magnetic scattering study finds that the short-range zigzag correlations survive at least up to 70 K [15]. Thus, this temperature dependence data establish that the low-energy peak is a magnon peak of the zigzag magnetic order. On the other hand, the broad feature intensity barely changes between 7 and 150 K. This observation is in contrast to the previous RIXS study [43], which finds a temperature-dependent broad scattering and interprets it as a resonant phonon contribution. However, a more recent

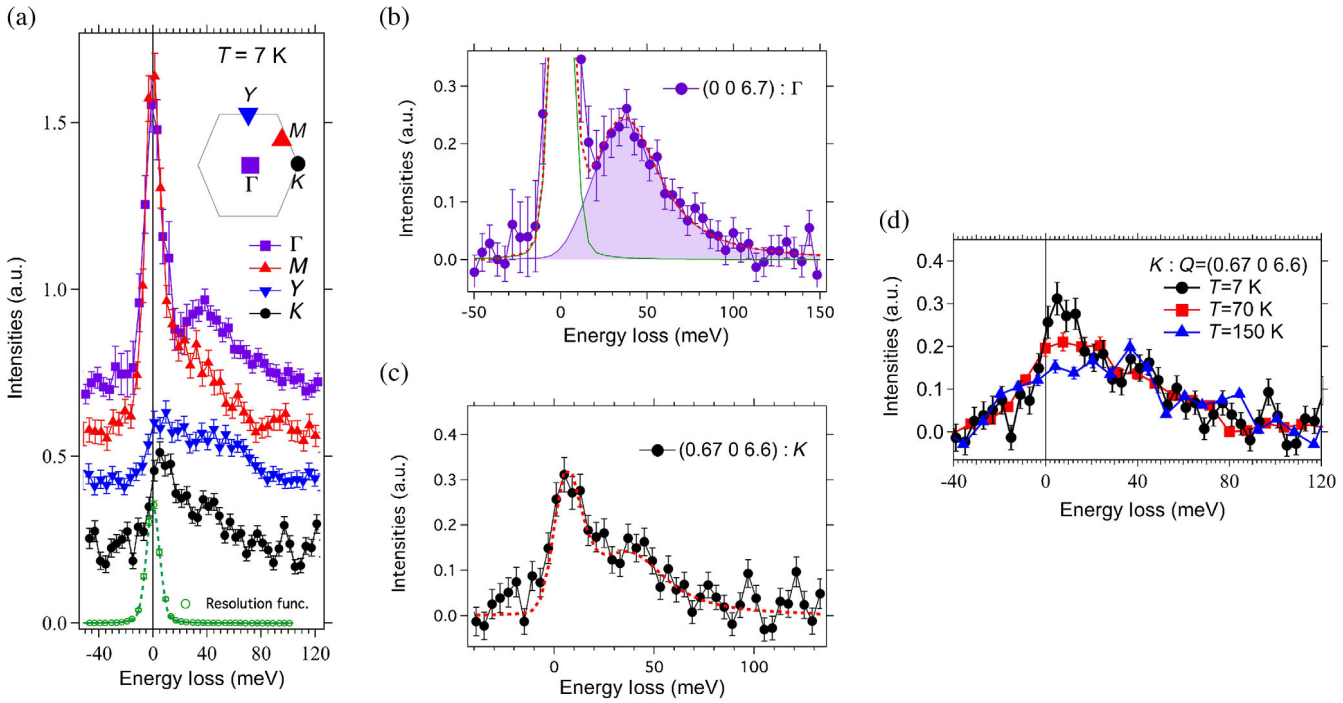

FIG. 2. High-resolution RIXS spectra recorded at $T = 7$ K. (a) The measured energy resolution function of the quartz analyzer is plotted at the bottom. At $\mathbf{Q} = (0\,0\,6.75)$ (Γ), an elastic scattering is followed by a broad excitation without any indication of a narrow excitation. At $\mathbf{Q} = (0.45\,0.45\,6.5)$ (near M), a soft low-energy excitation is unresolved with 12 meV energy resolution, and a quasielastic scattering is followed by a broad shoulder excitation. At $\mathbf{Q} = (0\,1\,6.5)$ (Y), a low-energy excitation is seen with a broad high-energy feature. At $\mathbf{Q} = (0.67\,0\,6.6)$ (K), a narrow excitation is discovered at a low energy. (b),(c) The measured RIXS spectra at the Γ and K wave vectors, respectively, are fit by the pseudo-Voigt function (elastic scattering) and damped harmonic oscillator (DHO) function convoluted by the 12 meV resolution function. (d) Temperature dependence of the RIXS excitation spectrum at the K point. The low-energy peak shows a clear decrease at $T = 70$ K and becomes featureless at $T = 150$ K, indicating that it is an excitation peak of the zigzag magnetic order.

RIXS [44] reports that the broad scattering intensity hardly changes between 5 and 90 K and persists up to 300 K, which is consistent with the current observation. This recent RIXS work rules out the phonon interpretation of the low-energy excitation and claims the magnetic origin of the broad scattering intensity by showing different peak energies of isostructural Na_2IrO_3 and Li_2IrO_3 and the same resonance behavior of all low-energy signals [44]. Here, we assign the broad feature as having a magnetic origin and discuss in more detail in the next two sections.

III. MODEL DESCRIPTION OF THE LOW-T RIXS SPECTRA

A. Spin Hamiltonian

To perform a quantitative model analysis of the magnetic excitations as observed by RIXS, we adopt the extended Kitaev-Heisenberg model for $J_{\mathrm{eff}} = 1/2$ pseudospins [7,16,50]. Compared to the originally proposed Kitaev-Heisenberg model for Na_2IrO_3 [4] comprising a dominant Kitaev interaction supplemented by a smaller Heisenberg interaction, the model is extended by two kinds of off-diagonal exchange interactions. The nearest-neighbor Hamiltonian for the pseudospins $\boldsymbol{S}$ then takes the form

$$\mathcal{H}_{ij}^{(z)} = KS_i^zS_j^z + J\boldsymbol{S}_i\cdot\boldsymbol{S}_j + \Gamma(S_i^xS_j^y + S_i^yS_j^x) + \Gamma'(S_i^xS_j^z + S_i^zS_j^x + S_i^yS_j^z + S_i^zS_j^y) \quad (1)$$

shown here for a z bond [vertical bond in Fig. 1(b); the bond direction is perpendicular to the z axis]. In the case of the other bond directions, a cyclic permutation of the pseudospin components is applied. Various *ab initio* estimates of the interaction parameters (e.g., Refs. [8,16,17]) generally suggest a dominant ferromagnetic (FM) Kitaev interaction ($K < 0$) and a positive off-diagonal Γ interaction. This parameter setup, combined with suitable values of the smaller interaction parameters J and Γ', favors the zigzag magnetic order with the magnetic moments pointing approximately in between the x and y axes (assuming the zigzag order with FM x and y bonds) which corresponds to the experimental situation [15]. In addition, motivated by sizable further-neighbor interactions found by the *ab initio* estimates (see, e.g., Ref. [17]), we also include isotropic

Heisenberg interactions among second and third nearest neighbors and arrive at the full model Hamiltonian

$$\mathcal{H} = \sum_{\langle ij\rangle\in \mathrm{NN}} \mathcal{H}_{ij}^{(\gamma)} + \sum_{\langle ij\rangle\in 2^{\mathrm{nd}}\mathrm{NN}} J_2 \boldsymbol{S}_i \cdot \boldsymbol{S}_j + \sum_{\langle ij\rangle\in 3^{\mathrm{rd}}\mathrm{NN}} J_3 \boldsymbol{S}_i \cdot \boldsymbol{S}_j, \tag{2}$$

where γ labels the nearest-neighbor (NN) bond direction. Following the prevailing expectations, in our analysis we assume that the main interactions are K, Γ, and J, while Γ', J_2, and J_3 are significantly smaller in magnitude.

B. Simulations of the low-temperature RIXS data

We simulate the RIXS spectra by calculating the dynamical pseudospin structure factor and combining its components according to the recipes given in Refs. [51,52]. Namely, we utilize the effective RXS operator expressed within the Kramers doublet manifold via

$$\mathcal{R} \propto i(\boldsymbol{\varepsilon} \times \boldsymbol{\varepsilon}') \cdot (f_{ab} \boldsymbol{S}_{ab} + f_{\perp} \boldsymbol{S}_{\perp}). \tag{3}$$

Here, $\boldsymbol{\varepsilon}$ and $\boldsymbol{\varepsilon}'$ are the polarization vectors of the incident and scattered x rays, respectively, and $\boldsymbol{S}_{ab}$ and $\boldsymbol{S}_{\perp}$ denote the component of the pseudospin lying within the honeycomb plane (crystallographic ab) and being perpendicular to it, respectively. For the L_3 edge resonant process, the factors connecting the pseudospin and the RXS operators read as $f_{ab} = \frac{1}{2} + (5/6\sqrt{2}) \sin 2\vartheta - \frac{1}{6}\cos 2\vartheta$ and $f_{\perp} = 1 + \frac{2}{3}\cos 2\vartheta - (1/3\sqrt{2}) \sin 2\vartheta$ with the angle $\tan 2\vartheta = 2\sqrt{2}/(1 + 2\Delta/\lambda)$ being determined by the ratio of the trigonal field Δ and the spin-orbit coupling constant λ [51,52]. The values of ϑ for Na_2IrO_3 can be estimated from the splitting $\Delta_{BC} \approx 0.1$ eV of the $J_{\mathrm{eff}} = 3/2$ quartet [53], leading to slightly anisotropic $f_{ab} \approx 0.91$ and $f_{\perp} \approx 1.15$.

The RIXS intensity is then calculated as the dynamical correlation function of the $\mathcal{R}$ operator: $I(\boldsymbol{q}, \omega) \propto \chi''_{\mathcal{R}}(\boldsymbol{q}, \omega)$ with $\chi_{\mathcal{R}}(\boldsymbol{q}, \omega) = i\langle[\mathcal{R}_{\boldsymbol{q}}(t), \mathcal{R}_{-\boldsymbol{q}}(0)]\rangle_{\omega}$. This quantity can be conveniently expressed via the pseudospin susceptibility tensor $\chi_{\alpha\beta}(\boldsymbol{q}, \omega) = i\langle[S^{\alpha}_{\boldsymbol{q}}(t), S^{\beta}_{-\boldsymbol{q}}(0)]\rangle_{\omega}$ calculated either by exact diagonalization (ED) on small clusters (see Appendix B for details) or within the linear spin-wave (LSW) approximation. For the geometry shown in Fig. 1(b), the RIXS intensity is roughly proportional to $\frac{1}{2}(\chi''_{xx} + \chi''_{yy}) + \chi''_{zz}$ (neglecting the small off-diagonal contribution and summing up the $\pi - \pi'$ and $\pi - \sigma'$ scattering channels to account for the unpolarized detection).

C. Identification of relevant parameter regime

To narrow down the parameter regime consistent with the experimental data, we perform a systematic scan through the parameter space of the model, inspecting the type of the magnetic order and the excitation spectra obtained by ED. As the six parameters present in the model make this scan a challenging task, we use fixed small values of the subsidiary interactions (Γ' and $J_{2,3}$) and vary only the main ones (J, K, and Γ). This limitation is not severe, since the overall dispersion and intensity distribution in the calculated RIXS spectra is determined by the dominant interactions, while the smaller ones affect only finer details of the spin dynamics not resolved in the experiment. Despite that, the Γ' and $J_{2,3}$ interactions still play important roles in stabilizing the zigzag phase and extending it to the regime where the dominant interactions can reproduce the RIXS data.

The phase diagram focusing on the zigzag phase is presented in Fig. 3. To construct it, we assume small $\Gamma' < 0$ associated with the trigonal compression [50] that is fixed at $\Gamma' = -0.1A$ with A being the overall energy scale of the dominant interactions defined as $A = \sqrt{J^2 + K^2 + \Gamma^2}$. Similarly, the further-neighbor interactions J_2 and J_3 are fixed at $J_2 = 0.05A$ and $J_3 = 0.1A$, respectively, putting thus more emphasis on the third-neighbor interaction as suggested by *ab initio* estimates [17]. The main interactions are parametrized using two angles θ, ϕ as $(J, K, \Gamma) = (A\sin\theta\cos\phi, A\sin\theta\sin\phi, A\cos\theta)$ with the ranges $\theta \in [0, \pi/2]$ and $\phi \in [0, 2\pi]$ covering the entire $JK\Gamma$ parameter space with $\Gamma > 0$. The resulting phase diagram in Fig. 3 shows two zigzag regions connected by a narrow "neck" which substantially differ in the direction of the ordered moments. Let us consider for concreteness one of the degenerate zigzag patterns with zigzag chains running along the x and y bonds shown in Fig. 1(b). The ordered moments in the upper zigzag phase are then found close to the z axis, while the lower zigzag phase is characterized by the moment direction pointing roughly in between the x and y axes. These observations can be understood using simple energy-based arguments when comparing Fig. 1(b) and Eq. (1). The zigzag order of the upper phase found for $K > 0$ and $J < 0$ fully satisfies the AFM K interaction on the z bonds, where it picks up the dominant z component of the ordered moments as seen in Eq. (1). The energy gain from the remaining x and y bonds is due to FM J interaction. In the bottom zigzag phase covering mainly the $K < 0$ and $\Gamma > 0$ case, the FM Kitaev interaction profits from the FM bonds within the chains by using the x and y components of the pseudospins separately. The positive Γ interaction brings energy gain on the AFM interchain z bonds by utilizing the simultaneous presence of the x and y components. This phase is also significantly supported by the negative Γ' interaction (see Ref. [54] for a more detailed discussion). The longer-range AFM interactions J_2 and particularly J_3 further stabilize the zigzag state—now independently on the moment direction due to their isotropic character—and expand significantly the zigzag phases in the parameter space.

The experimentally determined direction of the ordered moments as given by Ref. [15] is consistent with the bottom zigzag region. Using the precise ordered moment direction

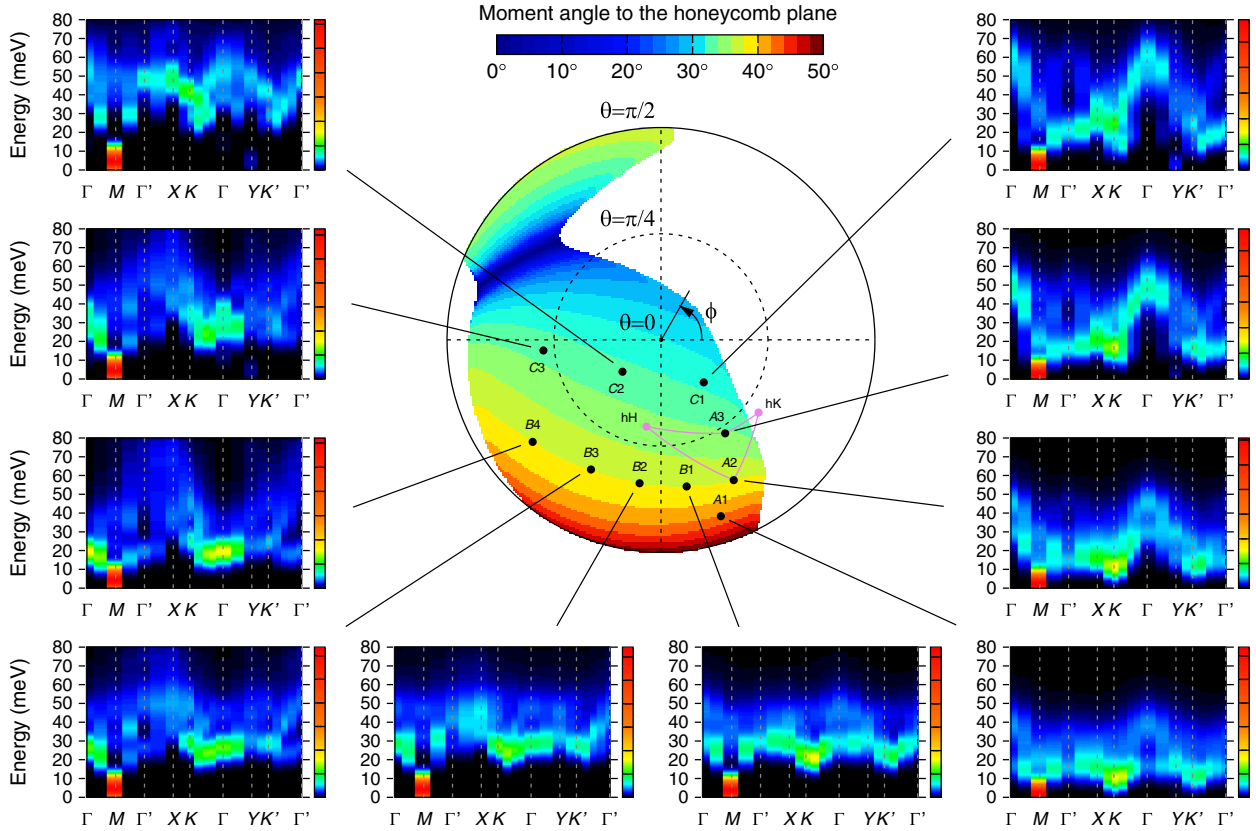

FIG. 3. Zigzag phase in the phase diagram of the extended Kitaev-Heisenberg model with the main interactions parametrized using the radial coordinate θ and the azimuth ϕ as $J = A\sin\theta\cos\phi$, $K = A\sin\theta\sin\phi$, $\Gamma = A\cos\theta$, and the smaller interactions kept constant: $\Gamma' = -0.1A$, $J_2 = 0.05A$, and $J_3 = 0.1A$. Here, A is the overall energy scale, which is irrelevant for the phase diagram but determines the characteristic energies of the magnetic excitations. The color indicates the angle of the zigzag-ordered moments to the honeycomb plane. The data are obtained using the exact-diagonalization-based method in Ref. [51]. Small panels around the phase diagram show, for selected parameter points, the theoretical RIXS intensity maps calculated by exact diagonalization of the extended Kitaev-Heisenberg model on 24- and 32-site clusters (see Appendix B for details). We assume the scattering geometry depicted in Fig. 1(a) and present a sum of $\pi - \pi'$ and $\pi - \sigma'$ scattering channels (imitating an unpolarized detection) plotted along the same path through the Brillouin zone as in Fig. 1. The energies are determined by taking the value $A = 29$ meV giving the best match between the $A2$ parameter point and the experimental data. Gaussian broadening with a FWHM of 25 meV is applied to the spectra. Finally, the violet lines show the pathways in the parameter space connecting the selected points $A2$ and $A3$ with the points of hidden symmetry utilized in Sec. III D 2. They should be understood as projections only, since the hidden Heisenberg point (hH) has $\Gamma' \approx -0.4A$, whereas the hidden Kitaev point (hK) has $\Gamma' \approx -0.3A$, and $J_{2,3} = 0$ for both points.

as a very sensitive probe of the anisotropic exchange interactions, a further refinement of the relevant parameter regime is possible. Namely, we can utilize the angle of the ordered moments to the honeycomb plane which is estimated in a subsequent analysis of the experimental data in Ref. [15] to be around 38°–40° [51]. The theoretical values of this angle obtained by ED through the zigzag phase are indicated in Fig. 3. Considering solely the experimental moment direction, the matching parameter sets form a strip near the $A2$ and $B1$–$B4$ points in Fig. 3.

Let us now focus on the phase diagram in Fig. 3 from the point of view of our RIXS data. We calculate RIXS maps via ED for several selected parameter points assuming the same scattering geometry as in the experiment. Because of the finite size of the clusters used in ED, their ground states entering the calculation of the dynamic response comprise all possible zigzag patterns in an equal-weight superposition. This mixing actually imitates the experimental conditions, since below T_N the long-range zigzag order in the sample is, in fact, accompanied by short-range zigzag orders with the complementary directions of the zigzag chains [15]. The maps, presented in Fig. 3, can thus be directly compared to the data in Fig. 1(d) up to the energy scale that is flexible by tuning A. Within the bottom zigzag phase, which covers a broad range of parameters, several kinds of spin-excitation behavior can be observed. The differences concern the wave vectors away from the M point that universally hosts an intense low-energy magnon through the whole zigzag phase.

In the left part of the phase diagram with significant negative J (representative $B4$ and $C3$ points), the overall

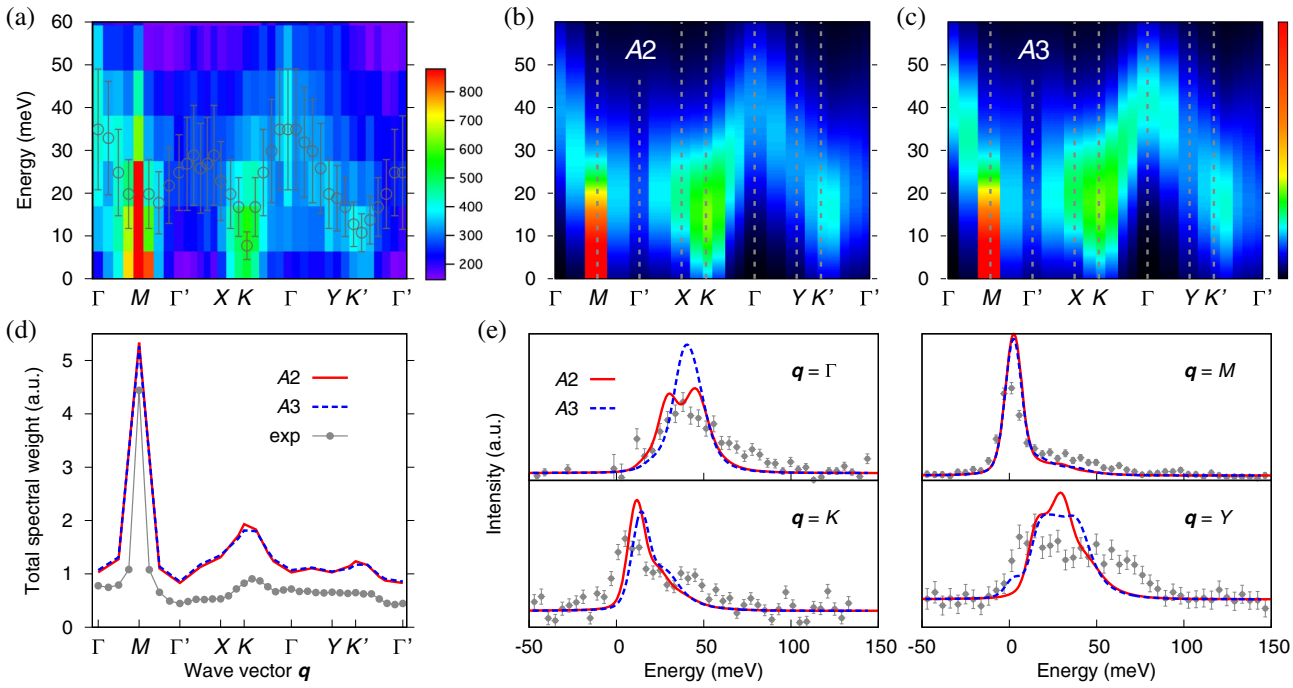

FIG. 4. (a) Experimental RIXS intensity map for $T = 7$ K with the positions of the intensity maxima for the individual wave vectors indicated as open circles. (b) Theoretical RIXS intensity map calculated for the parameter values corresponding to the $A2$ point in Fig. 3 and the energy scale $A = 29$ meV, which gives $J \approx 12$ meV, $K \approx -24$ meV, $\Gamma \approx 11$ meV, $\Gamma' \approx -3$ meV, $J_2 \approx 1.5$ meV, and $J_3 \approx 3$ meV. The scattering geometry depicted in Fig. 1(a) is assumed, and a sum of $\pi - \pi'$ and $\pi - \sigma'$ scattering channels is taken, corresponding to an unpolarized detection. The spectra are broadened in energy by Gaussians with a FWHM of 25 meV to imitate the experimental resolution as in (a). (c) The same as in (b) but for the parameter values corresponding to the $A3$ point in Fig. 3 and the energy scale of $A = 24$ meV: $J \approx 10$ meV, $K \approx -15$ meV, $\Gamma \approx 16$ meV, $\Gamma' = -2.4$ meV, $J_2 = 1.2$ meV, and $J_3 = 2.4$ meV. (d) Energy-integrated RIXS response (total spectral weight) corresponding to (a)–(c). The experimental data, obtained by integrating in the $[-30, 60]$ meV range, are arbitrarily scaled with respect to theoretical ones. (e) RIXS intensity profiles at selected wave vectors. High-resolution experimental data (gray dots) are compared to theoretical spectra for the above parameters (red and blue lines). The theoretical spectra are broadened by the experimental resolution function of the high-resolution setup.

shape of the intensity cloud hints to the proximity of the FM phase. There are intense low-energy excitations around the Γ point whose dispersion goes up toward the AFM wave vector Γ′—such features are shared with FM magnons. In the bottom part, one can notice a shift to the magnon breakdown regime reported for α-$RuCl_3$ by Ref. [32] (representative $B3$, $B2$, and $B1$ points). It is most apparent near the $J = 0$ line ($B1$ and $B2$ points), which shows a rather flat dispersion of excitations with a pronounced high-energy tail. Yet more incoherent scattering is seen at Kitaev-dominant point $A1$. The most robust features of the experimental RIXS spectra in Fig. 1(d) are the dispersing excitations in the K-Γ-Y-K' part, reaching the maximum energy at the Γ point and maximum intensity at the K point. This feature can be clearly observed in the theoretical maps on the right corresponding to the parameter points with a sizable AFM $J > 0$ ($C1$, $A3$, and $A2$ points). A hint of this feature is displayed also at the $A1$ and $C2$ points of the highly dominant Γ interaction and FM $J < 0$. In the $C2$ case, the intensity resides at relatively high energies, being connected to the M-point magnons by a steep excitation branch.

Taking into account also the experimental constraint on the ordered moment angle to the honeycomb plane, the suggested parameter range for Na_2IrO_3 lies around points $A2$ and $A3$ in Fig. 3, i.e., in the regime with Γ comparable to or somewhat less than $|K|$ and quite sizable AFM $J > 0$. For the $A2$ point, the moment angle to the honeycomb plane fits well the experimental value; the $A3$ point may seem to match slightly better the experimental RIXS map. In the following, we thus discuss both these points in parallel to give a broader picture of the relevant parameter range.

To enable a one-to-one comparison, Figs. 4(b) and 4(c) present the theoretical RIXS spectra for the $A2$ and $A3$ points, respectively, with the resolution matching the experimental one and with the values of the energy scale A tuned to fit the position of the main peak at the $\boldsymbol{q} = 0$ wave vector (Γ point). Figure 4(a) shows the experimental RIXS intensity map for $T = 7$ K with the positions of the intensity maxima for the individual wave vectors indicated as open circles, where the specular elastic scattering peaks at Γ and Γ′ are subtracted. The broad maps in Figs. 4(a)–4(c) show a good overall agreement of the theoretical maps with the RIXS data in both the dispersion

and intensity distribution in the Brillouin zone. The latter is supported by the total spectral weight (energy-integrated spectra) in Fig. 4(d), which seems to match quite well to the corresponding experimental data in Fig. 1(f). Here, essentially no difference between $A2$ and $A3$ points is observed.

Figure 4(e) compares the high-resolution experimental RIXS spectra in Fig. 2(a) to the theoretical spectra convoluted with the experimental resolution function. The main incoherent and coherent features of the Γ and K spectra are well captured by the theoretical spectra. A discrepancy is that the theoretical spectra show relatively less spectral weight in high-energy parts. At the M point, the incoherent high-energy part is reasonably reproduced by the model. At the Y point, the discrepancy in the incoherent high-energy intensity seems bigger. Overall, the theoretical spectra clearly capture the main features of the spectra at the individual wave vectors including, to some extent, also the shape of intensity profiles following the central peaks.

Since the data for the various cluster sizes and shapes seem to be quite consistent in the energy ranges and profiles of the modes, we cannot attribute the discrepancy in the incoherent high-energy parts solely to finite-size effects. Even though the extended Kitaev-Heisenberg model captures the essential dynamics of the $J_{\mathrm{eff}} = 1/2$ pseudospins, it may lack certain scattering processes that lead to the enhancement of the high-energy tails. One such mechanism may be a magnetoelastic coupling that comes into play due to the large orbital component of the $J_{\mathrm{eff}} = 1/2$ pseudospins and may act as an additional decay channel. Pronounced effects of coupled lattice and pseudospin dynamics are observed, for example, in phonon line shapes in Raman spectra of perovskite iridates [55,56]. Reference [43] introduces the phonon contributions as producing a series of harmonic peaks to describe the incoherent high-energy scatterings. Few facts, however, suggest that there are no big direct phonon contributions to the incoherent high-energy parts. It is known that the resonant phonon contribution becomes visible when the inverse core-hole lifetime is in the range of a few hundred meV, and a 1 eV detuning of the lifetime leads to a near-zero cross section [57]. At the Ir L_3, the inverse core-hole lifetime is more than 5 eV [58], and this shorter-lived core hole state is not expected to provide sufficient time for the lattice to respond. A majority of optical phonon modes of Na_2IrO_3 and Li_2IrO_3 reside around 60 meV [59]. Recent O K-edge RIXS on Li_2IrO_3 report the resonant phonon spectra where the fundamental phonon is at 70 meV [60]. The Ir L_3-edge RIXS on Li_2IrO_3 [44], on the other hand, shows that the low-energy excitation feature is centered at 20 meV, which is notably lower than 70 meV and so of a different origin from phonon. Our high-resolution spectra in Fig. 4(e) do not show maximum intensities at this energy range but show decreasing intensities, for example, at Γ, K, and M. As mentioned earlier, Ref. [44] argues against the phonon interpretation by showing that the energy scale of the incoherent feature is very different in two isostructural Na_2IrO_3 and Li_2IrO_3. Hence, we assign the incoherent high-energy scattering as of magnetic origin.

The x-ray and neutron diffraction studies [11,13,14] show that there are inherent imperfections in crystal structure such as stacking faults and site disorders, which result in a structural diffuse scattering and a remaining short-range order below the ordering temperature [13,15]. Small variations in the structure can alter various exchange interactions in Na_2IrO_3. So it is possible that the current single parameter set should be supplemented with nearby parameter sets among many in Fig. 3 to explain the discrepancy in the incoherent high-energy parts and fully reproduce the whole observed spectra.

D. Nature of the spin excitations

Having the main magnetic intensity in the RIXS spectra below approximately 60 meV reasonably well captured by the excitations of the extended Kitaev-Heisenberg model, it is natural to ask what the character is of those excitations. In the following, we address this issue by comparing ED results to the linear spin-wave approximation and by inspecting the evolution of the spectra when moving in the parameter space toward points of hidden symmetry. In the latter case, we use a nearby hidden Heisenberg point where a magnon picture is valid and a nearby hidden Kitaev point with the excitations carried by Majorana fermions.

1. Comparison to linear spin-wave approximation

Each of Figs. 5(a) and 5(b) presents fine energy-resolved RIXS spectra obtained by ED and LSW calculation for the $A2$ and $A3$ points, respectively, used also in Figs. 4(b) and 4(c). In the case of the $A3$ point with $\Gamma \approx |K|$ shown in Fig. 5(b), the LSW approximation seems quite successful in capturing the overall dispersion and intensity of the spin excitations, the main difference being the high-energy magnon branches that get significantly renormalized in terms of both the energy shift and broadening. Figure 5(d) shows that the distributions of the total spectral weight are in excellent agreement between ED and LSW. In the case of the $A2$ point with $\Gamma \approx \frac{1}{2}|K|$ shown in Fig. 5(a), the agreement is spoiled by the fact that LSW places this parameter point closer to a competing order with the characteristic wave vector K. The reason is that the minimization of purely classical energy in the LSW approximation completely neglects quantum fluctuations supporting the zigzag phase. As a consequence, LSW brings down the excitations at both K and K' and lifts the M-point magnon. There is also an associated shift of the spectral weight from the M point to the K and K' points as shown in Fig. 5(c). This result is in contrast to the ED calculations, which give similar low-energy spectra for both $A2$ and $A3$ points. However, apart from these trends related to a phase boundary shift, the LSW description of the $A2$ point successfully gives a rough picture

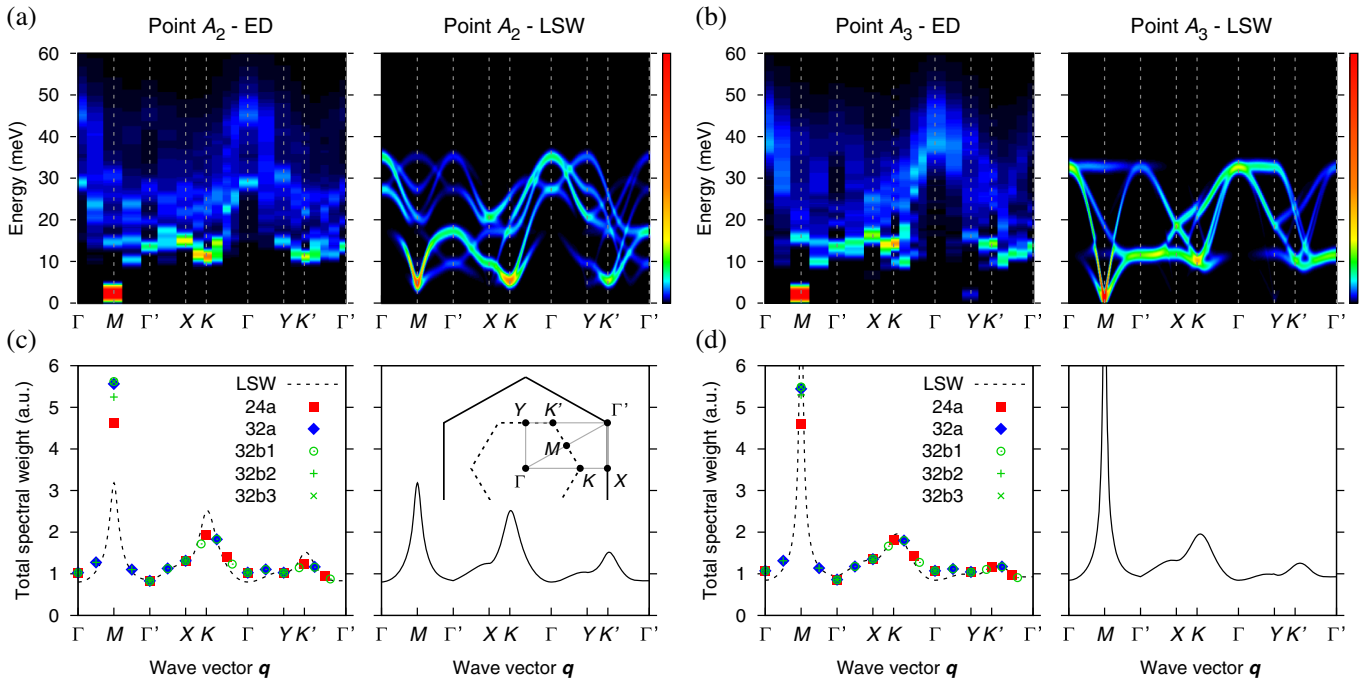

FIG. 5. (a) RIXS intensity maps for the parameter point $A2$ and the same energy scale as in Fig. 4(b). The left and right are obtained by exact diagonalization and the linear spin-wave approach, respectively. To better resolve the finer features, Gaussian broadening with a small FWHM of only 2 meV is used in both cases. In the case of LSW, the spectra are averaged by equally employing all three possible zigzag pattern directions. This procedure leads to a map that could be directly compared to the ED one, since the cluster ground state used in ED contains all zigzag pattern in an equal-weight superposition. (b) The same for the parameter point $A3$ and the energy scale as in Fig. 4(c). (c) Energy-integrated RIXS response (total spectral weight) corresponding to (a). Data for all the clusters are presented, showing negligible finite-size effects on the spectral weight. The curve obtained by the linear spin-wave approach (right) is shown also on the left by a dashed line. (d) Total spectral weight for the data in (b).

of the excitation branches. The high-energy branches at the Γ point are now visibly split. According to the LSW calculation, the lower branch corresponds to oscillations of the moment angle to the honeycomb plane and the upper one to the oscillations in the in-plane direction perpendicular to the zigzag chains.

Based on the above results, it seems quite likely that the spin-excitation spectra could be reproduced when going beyond LSW and include the anharmonic effects, e.g., by correcting the dispersions via the self-consistent spin-wave theory and by implementing finite magnon lifetimes due to magnon decay processes [31]. An attempt to evaluate the magnon decay in a Kitaev system, utilizing the so-called imaginary self-consistent Dyson equation approach, was recently performed by Winter *et al.* [32] when interpreting the neutron data on α-$RuCl_3$. Note that in their case the multimagnon contribution seems stronger (Fig. 6 in Ref. [32]) due to a different parameter regime within the zigzag phase.

2. *Proximate hidden Kitaev and Heisenberg points*

The applicability of the magnon picture can be further checked by inspecting the evolution of the calculated RIXS spectra when going through the parameter space toward suitable reference points. The parameter region identified as relevant for Na_2IrO_3 lies close to two of the points of special symmetry [61], where the nearest-neighbor extended Kitaev-Heisenberg model can be exactly mapped to either the Kitaev or Heisenberg model. Since in both the pure Kitaev and Heisenberg cases the spin excitations are well known, the special-symmetry points provide convenient references for us. In the following, we keep the discussion of both special-symmetry points very brief; further details can be found in Appendix C or the original Ref. [61].

Working in the representation utilizing the energy scale A, our point $A2$ corresponds to

$$(J, K, \Gamma, \Gamma')_{A2} \approx (0.4, -0.8, 0.4, -0.1)A \tag{4}$$

complemented by the small $J_{2,3}$. Similarly, for the $A3$ point, we have

$$(J, K, \Gamma, \Gamma')_{A3} \approx (0.4, -0.6, 0.7, -0.1)A. \tag{5}$$

The hidden Kitaev point is obtained for the parameter set

$$(J, K, \Gamma, \Gamma')_{\mathrm{hK}} \approx (0.6, -0.5, 0.6, -0.3)A, \tag{6}$$

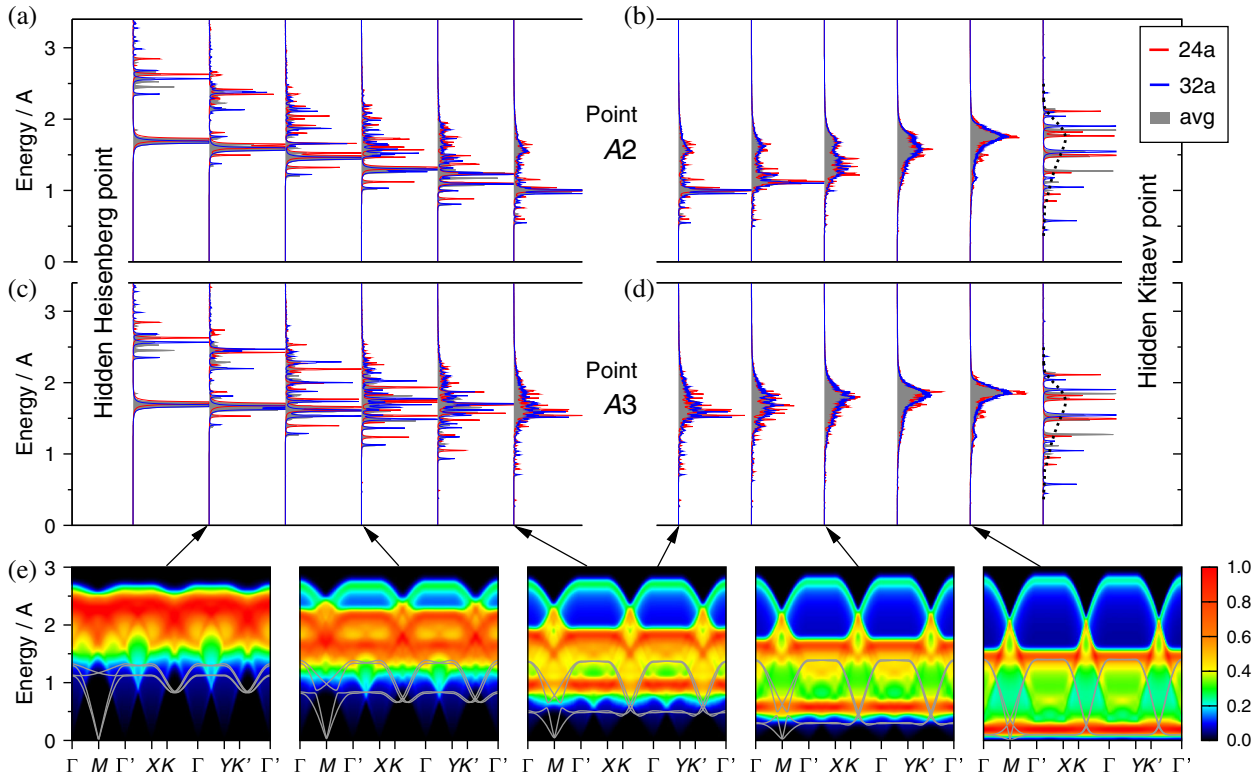

FIG. 6. (a) Evolution of the theoretical Γ-point ($\boldsymbol{q} = 0$) RIXS intensity on a line through the parameter space going from the hidden Heisenberg point $(J, K, \Gamma, \Gamma') \approx (-0.1, -0.6, 0.8, -0.4)A$ to the point $A2$ of Fig. 3. The line lies completely in the zigzag phase. Finite-size effects can be estimated by comparing data for various clusters shown in Appendix B. The average is taken over all of them (i.e., 24a, 32a, and 32b1 to 32b3). The spectra are presented in units of the energy scale A and only a tiny broadening is used to resolve the structure of the continuum. (b) The same for a line connecting the point $A2$ and the hidden Kitaev point $(J, K, \Gamma, \Gamma') \approx (0.6, -0.5, 0.6, -0.3)A$. Apart from the last point, the ground state remains zigzag ordered. The dotted line indicates scaled exact solution in the AFM Kitaev limit [63]. (c,d) Same as panels (a,b) but for the $A3$ point of Fig. 3. (e) Two-magnon density of states for selected points of panels (c) and (d) calculated using the linear spin-wave dispersions (gray lines). Single zigzag pattern of Fig. 1(b) was assumed, its Bragg spots correspond to the Y points.

where J_2 and J_3 are zeros as the longer-range interactions are absent at this special-symmetry point. It may be derived by taking the canonical Kitaev model and rotating the interaction axes x, y, and z by 180° around the axis perpendicular to the honeycomb plane (see Appendix C for a detailed discussion). This way, we arrive at the extended Kitaev-Heisenberg model with the above parameter set. Since the transformation is exact, all the features including, e.g., the fermionic excitation spectrum, are exactly preserved. At the hidden Kitaev point, we thus find the behavior of the extended Kitaev-Heisenberg model to be identical to the Kitaev model with interaction parameter $K_0 \approx 1.4A$, up to a simple global rotation. At the second considered hidden-symmetry point with the parameter set

$$(J, K, \Gamma, \Gamma')_{\mathrm{hH}} \approx (-0.1, -0.6, 0.8, -0.4)A, \qquad (7)$$

the extended Kitaev-Heisenberg model exactly maps to the Heisenberg model with the interaction constant $J_0 \approx 0.9A$. In this case, the derivation is more complicated and includes a four-sublattice transformation connecting zigzag and Néel order (cf. Refs. [61,62] and Appendix C). The spin-excitation spectra are then directly linked to those of the simple Heisenberg antiferromagnet on the honeycomb lattice, but a momentum shift by $\boldsymbol{q} = M$ and equivalent wave vectors is involved.

Figure 6 presents the parameter evolution of the RIXS response, focusing on the Γ-point ($\boldsymbol{q} = 0$) intensity containing the prominent high-energy feature that is a signature of the lack of the global rotational symmetry of the model. The model parameter sets are linearly interpolated between the $A2$ and $A3$ points and the hidden-symmetry points, all given by Eqs. (4)–(7). Note that the latter parameter points differ essentially in J only while having roughly the same $\Gamma/|K|$ ratio as our $A3$ point and an enhanced negative value of Γ' compared to $A2$ and $A3$. An explicit plot of the parameters used in Fig. 6 can be found in Appendix C, and the corresponding pathways are indicated in the overall phase diagram in Fig. 3 in a projected form (note that Γ' and $J_{2,3}$ change once we depart from the $A2$ and $A3$ points).

The evolution from the hidden Heisenberg point toward the $A2$ and $A3$ points shown in Figs. 6(a) and 6(c), respectively, starts with a simple response profile containing a sharp magnon peak and a two-magnon continuum characteristic for the Heisenberg model. The magnon at the Γ point calculated for the zigzag phase is, in fact, a copy of the Néel AFM magnon at the M point shifted by means of the hidden-symmetry transformation. Therefore, it appears at a high energy ($\sqrt{2}J_0$ in the LSW approximation). Going away from the hidden Heisenberg point, the high-energy magnon branches get broadened via magnon scattering and slowly merge with the two-magnon continuum forming the broad high-energy features observed at our points. The gradual onset of the magnon scattering is further illustrated in Fig. 6(e) by comparing the LSW dispersions and the two-magnon density of states (DOS): $\mathcal{D}_2(\omega) = \sum_{n\boldsymbol{q},n'\boldsymbol{q}'} \delta(\omega - \omega_{n\boldsymbol{q}} - \omega_{n'\boldsymbol{q}'})$, where $\omega_{n\boldsymbol{q}}$ stands for the dispersion of the nth magnon branch. Neglecting the magnon-magnon interaction vertex, this quantity indicates the strength of the scattering continuum accessible when keeping the kinematic constraint [31]. It becomes gradually activated as we depart from the hidden Heisenberg point, where the two-magnon decay does not occur and the basic decay channel involves three-magnon processes [31,32].

Continuing further from our points to the hidden Kitaev point, Figs. 6(b) and 6(d) show that the zigzag order is maintained almost up to the hidden Kitaev point. This result is natural, since the hidden KQSL comes with an antiferromagnetic effective Kitaev interaction. As revealed by the study of the Kitaev-Heisenberg model [62], the AFM KQSL phase has a limited extent compared to the FM KQSL phase because of a stronger competition with the surrounding phases that gain energy due to quantum fluctuations [64]. The high-energy continuum in the Γ-point response is present up to the zigzag to KQSL boundary with moderate changes in its shape that seem to be correlated with the two-magnon DOS. Upon entering the KQSL, there is an abrupt change in the character of the spectrum that later only negligibly evolves when approaching the exact hidden AFM Kitaev point as shown in Figs. 6(b) and 6(d). The continuum spreads over a larger spectral range and becomes composed of sharp peaks reflecting the excitations being carried by (almost) noninteracting Majorana fermions with a set of possible momenta strongly limited by the cluster. Nevertheless, the overall distribution of the spectral weight can be successfully compared to the exact result for an infinite lattice [63].

The above observations suggest that the picture of renormalized magnons adequately captures the spin excitations within the extended Kitaev-Heisenberg model in the parameter regime matching the low-temperature RIXS data below $\lesssim$60 meV. This suggestion is supported by the good overall agreement of LSW dispersions, intensity, and spectral weight distribution in the Brillouin zone with the ED results. Moreover, the magnon broadening seems to correlate well with the two-magnon DOS that gives hints about the decay rates of the individual magnon branches. Compared to the recent analysis of spin excitations in α-$RuCl_3$ [32] that placed α-$RuCl_3$ to the regime of magnon "breakdown" within the same spin model as used here, we encounter better-defined magnons with a less extended background of the multimagnon character.

Despite the relative proximity of the KQSL associated with the hidden Kitaev point, in particular, for the $A3$ point, the model spectra for zero temperature do not clearly bear the features characteristic for the Kitaev limit, most importantly, the flat dispersions of the spin excitations that are seen in the exact results for the Kitaev model [63,65] or the study of its perturbed variant [66]. An interesting result in this context is the recent finding by Gohlke *et al.* [20] that the K-Γ-only model shows signatures of a spin-liquid ground state in a wide parameter range. A later study by Wang, Normand, and Liu [67] using the variational quantum Monte Carlo method revisits those results and finds a proximate Kitaev spin liquid with a different structure than KQSL for negative K and $\Gamma/|K|$ up to roughly 0.6. In the parameter area that we identify as relevant for Na_2IrO_3, the large K and Γ are complemented by sizable J and a number of smaller interactions; nevertheless, the spin dynamics within the K-Γ-only model and a possible connection to our case is a highly relevant problem.

IV. MAGNETIC EXCITATION SPECTRA AT A HIGH TEMPERATURE

A. Temperature evolution of magnetic excitation spectra

A defining feature of quantum spin liquids is an emergent magnetic excitation carrying fractional quantum numbers. In the case of KQSL, the fractionalized magnetic excitations are represented by Majorana fermions [1–3]. When a conventional magnetic order is thermally melted, a signature of QSL may be found in the spin dynamics over a wide temperature range. A recent INS study of α-$RuCl_3$ reports a highly unusual temperature-stable signal around the zone center, which is interpreted as a dynamical response of the Majorana fermions of the KQSL due to thermal fluctuations of fluxes [27–30,35,68]. The recent RIXS work [44] on Na_2IrO_3 suggests that the dynamical spin-spin correlation of the broad scattering is restricted to nearest neighbors and phenomenologically similar to the unusual broad INS scattering of α-$RuCl_3$. In Fig. 2(d), the broad scattering at the K point is presented to survive up to 150 K, showing that Na_2IrO_3 also has a highly unusual temperature-stable signal. In this section, we present the temperature evolution of the RIXS spectra over the full Brillouin zone up to 280 K to show the thermal characteristics of dynamic spin correlations in a paramagnetic phase of Na_2IrO_3.

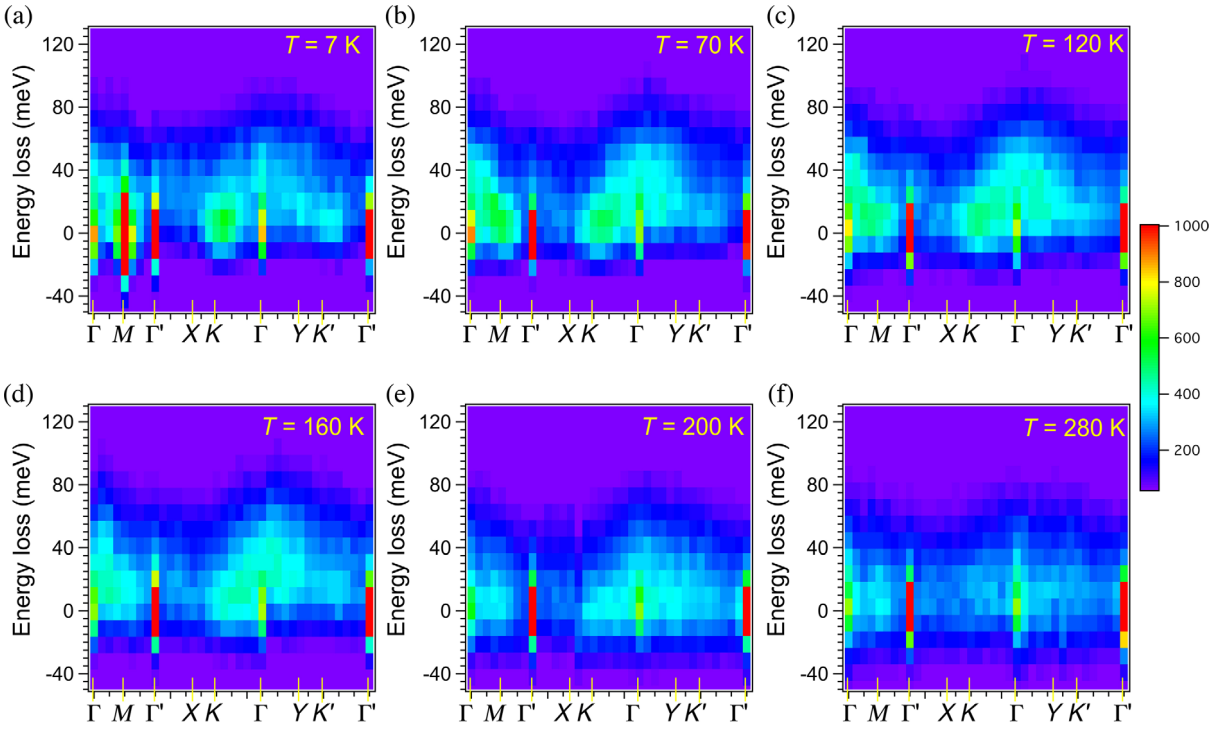

FIG. 7. Temperature evolution of magnetic excitation spectra. (a) $T = 7$ K. (b) $T = 70$ K. The magnetic Bragg peak at the M disappears, indicating disappearing zigzag correlations. Spectral intensities fill in between Γ and all first Brillouin zone symmetric points (M, K, K', and Y), connecting the high-energy feature at the Γ to the low-energy features at the M, K, and Y. This trend becomes more pronounced at (c) $T = 120$ K and (d) $T = 160$ K. (e) $T = 200$ K. Spectral intensities move toward lower energy. (f) $T = 280$ K. The RIXS intensity over the whole Brillouin zone substantially diminishes.

Figure 7(b) shows an intensity color map of RIXS spectra at $T = 70$ K. The specular elastic peaks at Γ and Γ′ are seen as in the $T = 7$ K map in Fig. 7(a). Because the short-range zigzag order disappears at this temperature, the magnetic Bragg peak at the M point is largely suppressed, exposing an underneath low-energy excitation [15]. The low-energy excitation at the K, Y, and K' and the high-energy excitation at the Γ stay more or less the same at $T = 70$ K. On the other hand, it is seen that the spectral intensity near the Γ point unusually grows up at $T = 70$ K, connecting the high-energy excitation at the Γ to the low-energy excitations at the M, K, Y, and K' points. This temperature evolution of the spectral intensity distribution becomes more pronounced up to $T = 160$ K as shown in Figs. 7(c) and 7(d).

Noticeable changes are observed at $T = 200$ K. The overall RIXS scattering intensity becomes weakened and moves toward lower energy, confining its significant weight within 60 meV as shown in Fig. 7(e). The scattering intensity displays a triangular shape along the K-Γ-Y-K' path. At $T = 280$ K, the RIXS scattering intensity over the whole Brillouin zone substantially diminishes, resulting in a featureless spectrum as in a paramagnet as shown in Fig. 7(f). The weakening RIXS intensity at a high temperature is at odds with the Ref. [43] RIXS work but consistent with Ref. [44]. As discussed in Secs. II B and III C, it is not necessary to invoke the lattice degrees of freedom to describe our spectra, and the observed excitations are assigned as of magnetic origin.

In a two-dimensional system, short-ranged spin correlations above the long-range order temperature are visible as a diffusive scattering at the vicinity of characteristic points in the Brillouin zone. As the temperature increases further, the short-range order dies and the corresponding spectral weight disappears. Seemingly, the temperature dependencies of the low-energy spectral weights around the M and K points follow this general tendency. However, the observed intensity modulations in other areas than the K and M are unusual. In particular, this temperature-dependent intensity modulation is seen at a high energy, whose energy is beyond the thermal energy of room temperature. Magnetic excitations at intermediate temperatures are broad in energy and momentum and remind us of unusual scatterings over a large energy interval revealed in α-$RuCl_3$ through the INS [27,29,30].

B. Dynamic spin correlations in a paramagnetic phase

In this section, we discuss the observation that the spectral intensity in a large region surrounding the Γ point unusually grows up to 160 K, connecting the high-energy feature at the Γ point to the low-energy feature at the M, K, and Y points and becomes a diffusive low-energy scattering

with negligible momentum dependence at 280 K (Fig. 7). As the ED calculations in Fig. 6 show, the broad feature below the ordering temperature contains the spontaneous magnon decay into a two-magnon continuum. Two-magnon excitations include pairs of very short wavelength spin waves and can remain at higher temperatures than single-magnon excitations. However, two-magnon scattering cannot explain the increasing spectral weights over the large Brillouin region, because the zigzag correlations decrease as the temperature increases as evidenced by decreasing intensities near the K and M points.

In a frustrated spin system above the ordering temperature, the larger interactions can keep short-range correlations up to quite high temperatures comparable to the energy scale of these interactions. The corresponding fragments of a few specifically correlated spins have a specific dynamics determined by the dominant interactions. In our case, the dynamics at elevated temperatures may be influenced by the proximity of hidden KQSL in the parameter space as well as the large scales of K and Γ that are suggestive of a possible connection to spin-liquid ground states in the K-Γ model that are currently being investigated [20,67,69]. Reliable finite-temperature calculations of the dynamic response are challenging and out of the scope of the present ED scheme. Fortunately, a number of results exist for the integrable pure Kitaev model. An exact solution for spin dynamics at zero temperature is known [63,65], and detailed finite-temperature behaviors of the FM and AFM Kitaev systems are available from studies combining the cluster dynamical mean-field theory and the continuous-time quantum Monte Carlo method (CDMFT + CTQMC) [35,70]. Given the connections mentioned above, here we discuss our observations in the context of Kitaev systems at a finite temperature.

The thermal characteristics of Kitaev systems are understood in terms of fractionalization of spins $\frac{1}{2}$ into itinerant Majorana fermions coupled to Z_2 fluxes represented by localized Majorana fermions [1]. Two characteristic crossover temperatures appear [68]. At the lowest temperatures below $T_L \approx 0.012$ K related to the Z_2 flux gap, an almost flux-free state is found, with only low-energy itinerant Majorana fermions being thermally excited. Intermediate temperatures are characterized by thermally activated Z_2 fluxes, but the itinerant Majorana fermions still retain their coherence. Finally, around $T_H \approx 0.375$ K, the fluxes and Majorana fermions recombine into spins, the nearest-neighbor spin correlations decay, and the system is adiabatically connected to a conventional spin-$\frac{1}{2}$ paramagnet.

Much of this physics is discussed in the context of α-$RuCl_3$. The successive thermal fractionalization finds its thermodynamic signatures in magnetic specific heat data in α-$RuCl_3$ where two separated broad peaks exist and a plateau in between two peaks is pinned at half of the ideal $R\ln 2$ magnetic entropy [30,35,70]. Raman scattering observes a polarization-independent broad continuum [33] successfully interpreted as due to pairs of itinerant Majorana fermions [34]. Banerjee *et al.* report a highly unusual scattering in α-$RuCl_3$ through the INS which is broad in energy and momentum and remains at a high temperature, stimulating much research directed at identifying unique dynamic correlations of emergent Majorana fermions in systems close to KQSL [27,29]. Theoretical works indicate that the characteristic broad scattering of the KQSL is preserved in a proximate phase with long-range ordered spins (proximate KQSL) [37]. The proximate KQSL picture has been further elaborated experimentally and theoretically to understand the finite-temperature behavior [30,35,65,70].

Similarly to α-$RuCl_3$, Na_2IrO_3 shows properties in the paramagnetic phase that can be interpreted as arising from the fractionalization to Majorana fermions. The two separated broad maxima in magnetic specific heat are also present in Na_2IrO_3 with one around 20 K and the other around 110 K [40]. Half of the ideal $R\ln 2$ entropy is gained at around 60 K, and the full $R\ln 2$ entropy is recovered at more than 150 K, whose behavior is in good agreement with theoretical predictions [68,71]. Signatures of Kitaev-like correlations are seen in Raman scattering [38]. In this work, we measure the low-energy RIXS response, which, adopting the fast-collision approximation, is closely related to the dynamic structure factor by the INS [52,72]. The momentum- and energy-resolved magnetic excitation spectra show that magnetic excitations in Na_2IrO_3 are broad in energy and momentum at intermediate temperatures, reminding of the unusual scatterings over a large energy interval in INS on α-$RuCl_3$ [27,29].

An apparent difference between Na_2IrO_3 and α-$RuCl_3$ is in the energy scales. Magnetic excitations in Na_2IrO_3 are observed at a much higher energy than those in α-$RuCl_3$ which are confined within the 15 meV energy window [27–30,43]. The broad excitation at the Γ point [Fig. 2(b)] locates at 36 meV, while the one in α-$RuCl_3$ can be viewed as a diffusive quasielastic scattering. The short-ranged correlations of three spin domains carrying their own zigzags persist at a much higher temperature than in α-$RuCl_3$ [15]. The attempts to quantify the interactions based on the INS data in α-$RuCl_3$ produce $(J,K) = (-4.6, 7)$ meV in the J-K model, $(K,\Gamma) = (-6.8, 9.5)$ meV in the K-Γ model, and $(J,K,\Gamma) = (-0.5, -5, 2.5)$ meV in the nearest-neighbor model Hamiltonian [27,28,32], while our analysis of the RIXS data in Na_2IrO_3 gives larger values; for example, the $A2$ and $A3$ points correspond to $(J,K,\Gamma) = (12, -24, 11)$ and $(10, -15, 16)$ meV, respectively. Related to the discussion in terms of the Kitaev model, the hidden KQSL found near our fit point is driven by the effective Kitaev interaction of AFM type with the strength of about $K_0 \approx 35$–40 meV (see Appendix C), giving, e.g., the crossover temperature of $T_H \approx 140$–170 K.

In studies of α-$RuCl_3$, the temperature evolution of the broad scattering features is described by the isotropic

Kitaev model with an FM Kitaev interaction, $K = -16.5$ meV [30]. The CDMFT + CTQMC calculation on the FM Kitaev system finds that a quasielastic response at zero energy is large around the Γ point at a low temperature and becomes diffusively broadened in energy at a high temperature, ending up in a conventional paramagnetic phase, which is consistent with the experimental observations by the INS [30,35,70]. On the other hand, the CDMFT + CTQMC calculation on the AFM Kitaev system shows that an incoherent flat feature at $\omega \sim K_0$ is seen around the Γ point at a low temperature, while a quasielastic response is distributed on the Brillouin zone boundary [35,70]. As the temperature increases, the incoherent feature becomes diffusively broadened in energy and is connected to the quasielastic response on the Brillouin zone boundary, losing its flat dispersion. The incoherent broad feature at $\omega \sim K_0$ merges to a diffusive response at zero energy when the AFM Kitaev system adiabatically enters into a conventional paramagnetic phase. These finite-temperature behaviors of the AFM Kitaev system bear a similarity to the observed temperature evolution of our magnetic excitation spectra. The spectral intensity in a large region surrounding the Γ unusually grows up to 160 K, connecting the high-energy feature at the Γ to the low-energy feature at the M, K, and Y points as shown in Fig. 7. The overall spectral weight moves toward lower energy at 200 K and shows a diffusive response with negligible momentum dependence at 280 K.

V. CONCLUSION AND OUTLOOK

In this study, magnetic excitation spectra in a honeycomb lattice Na_2IrO_3 were obtained for the wide-range reciprocal space up to the second Brillouin zone using the RIXS spectrometer. The state-of-the-art 12 meV measurements could identify the low-energy sharp magnon peak below the AFM order temperature and verify the broad widths of magnetic excitations. These sets of data allow a detailed comparison with theoretical calculations. The dispersion and spectral intensity distribution in the reciprocal space of RIXS spectra are well reproduced by the simulation using the exact diagonalization method on finite-size clusters. The parameter regime is characterized by large $K < 0$ and $\Gamma > 0$ complemented by sizable $J > 0$ with small J_2 and J_3, and $\Gamma' < 0$. We examine two of the points of special symmetry, i.e., AFM Heisenberg and AFM Kitaev, close to the parameter region of Na_2IrO_3 and investigate the evolution of the spin excitations along paths connecting the special-symmetry points and the parameter points of Na_2IrO_3. This inspection suggests that the main magnetic intensity below the ordering temperature can be reasonably explained by the picture of renormalized magnons.

Magnetic excitation spectra in Na_2IrO_3 show unusual spectral intensity modulations in a large region surrounding the Γ point at elevated temperatures. Finite-temperature calculations of the complex spin Hamiltonian are challenging and not available at the moment. We conjecture that the dominant nearest-neighbor interactions keep short-range correlations up to quite high temperatures with a specific short-range dynamics which has a possible connection to a proximate spin-liquid phase. An interesting experimental direction is given by a theoretical suggestion that the full continuum of the Majorana fermions of the KQSL can be mapped without interference with flux excitations using the spin-conserving scattering of the RIXS [72]. The spin-conserving measurements require two instrumental capabilities which cannot be achieved using a standard (spherical-analyzer-based) RIXS spectrometer: a high-energy resolution and an efficient scattered x-ray polarization analysis [73,74]. Recently, a new flat crystal RIXS analyzer system was developed, which provides a polarization analysis without compromising the energy resolution and with high efficiency [46]. If successful, the spin-conserving RIXS measurements will give a transparent description of the existence of a proximate KQSL in Na_2IrO_3.

ACKNOWLEDGMENTS

The use of the Advanced Photon Source at the Argonne National Laboratory was supported by the U.S. Department of Energy under Contract No. DE-AC02-06CH11357. J. C. acknowledges support by Czech Science Foundation (GAČR) under Project No. 19-16937S and MŠMT ČR under NPU II Project No. CEITEC 2020(LQ1601). Computational resources were supplied by the Ministry of Education, Youth and Sports of the Czech Republic under the Project CERIT-Scientific Cloud (Project No. LM2015085) provided within the program Projects of Large Research, Development and Innovations Infrastructures.

APPENDIX A: SAMPLE AND RIXS MEASUREMENT

Single-domain single crystals of Na_2IrO_3 are grown by the self-flux. Powders of Na_2CO_3 are mixed with 10%–20% excess IrO_2 and are calcined at 700 °C for 24 h. Single crystals are grown on top of a powder matrix in subsequent heating at 1050 °C. Platelike crystals with typical dimensions of 5 mm × 5 mm × 0.1 mm are physically extracted. The sample is mounted in a Displex closed-cycle cryostat. The RIXS measurements are performed using the RIXS spectrometer at the 27-ID beam line of the Advanced Photon Source where the sample, analyzer, and detector are positioned in the Rowland geometry. The diamond(111) high-heat-load monochromator reflects x rays from two in-line undulators into a high-resolution monochromator. The two-bounce monochromator of single monolithic Si(844) channel-cut crystal produces an energy bandpass of 14.8 meV. The four-bounce monochromator of two monolithic Si(844) channel-cut crystals results in an energy bandpass of 8.9 meV. The beam is then focused by a set of

Kirkpatrick-Baez mirrors, yielding a typical spot size of $10 \times 40\ \mu\text{m}^2$ FWHM ($v \times h$) at the sample. A horizontal scattering geometry is used with the incident photon polarization in the scattering plane. Mapping of the full Brillouin zone is carried out within only a few degrees of 90° scattering geometry to minimize the contribution from the Thompson elastic scattering. For the 25 meV RIXS measurement, a Si(844) diced spherical analyzer with 1-in diameter and a position-sensitive silicon microstrip detector are used with the 14.8 meV incident bandpass. For the 12 meV RIXS measurement, a quartz(309) diced spherical analyzer with 1-in diameter is used with the 8.9 meV incident bandpass.

APPENDIX B: EXACT DIAGONALIZATION ON FINITE CLUSTERS

The theoretical RIXS intensity is obtained by combining the components of the pseudospin susceptibility tensor calculated for zero temperature:

$$\chi_{\alpha\beta}(\boldsymbol{q},\omega) = i\int_0^\infty \langle \mathrm{GS}|[S^\alpha_{\boldsymbol{q}}(t), S^\beta_{-\boldsymbol{q}}(0)]|\mathrm{GS}\rangle e^{i\omega t}dt, \quad \text{(B1)}$$

where

$$S^\alpha_{\boldsymbol{q}} = \frac{1}{\sqrt{N_{\mathrm{site}}}}\sum_{\boldsymbol{R}} S^\alpha_{\boldsymbol{R}} e^{-i\boldsymbol{q}\cdot\boldsymbol{R}}. \quad \text{(B2)}$$

The ground state $|\mathrm{GS}\rangle$ and, subsequently, the dynamic response embodied in $\chi_{\alpha\beta}(\boldsymbol{q},\omega)$ are evaluated by the standard Lanczos exact diagonalization method [75] based on periodic tiling of the honeycomb lattice with small clusters. Since the intensity profiles contain broad features corresponding to continua of densely spaced levels, to achieve convergence, we use a large number of Lanczos steps in the calculation—500 to get the data in Fig. 4 and 1200 to get the fine-resolved data presented in Fig. 6. A combination of symmetric hexagonal clusters 24a and 32a and rectangular clusters 32b1–32b3 shown in Fig. 8 enable us to access a number of wave vectors along the Γ-M-Γ'-X-K-Γ-Y-K'-Γ' path used to plot the maps. The maps are constructed by nearest-point interpolation with an additional averaging if the given wave vector is compatible with several clusters.

To account for the simultaneous presence of the three zigzag patterns in the sample—one long-range and two short-range correlated [15]—the response for the three possibilities with different directions of zigzag chains needs to be averaged. This average is, in fact, automatically included in the exact diagonalization calculation, because the symmetry is not spontaneously broken and the cluster ground state is a superposition of the zigzag patterns (equal-weight superposition in the case of 24a and 32a and approximately equal-weight for 32b). The explicit averaging is performed in the case of the linear spin-wave calculation only.

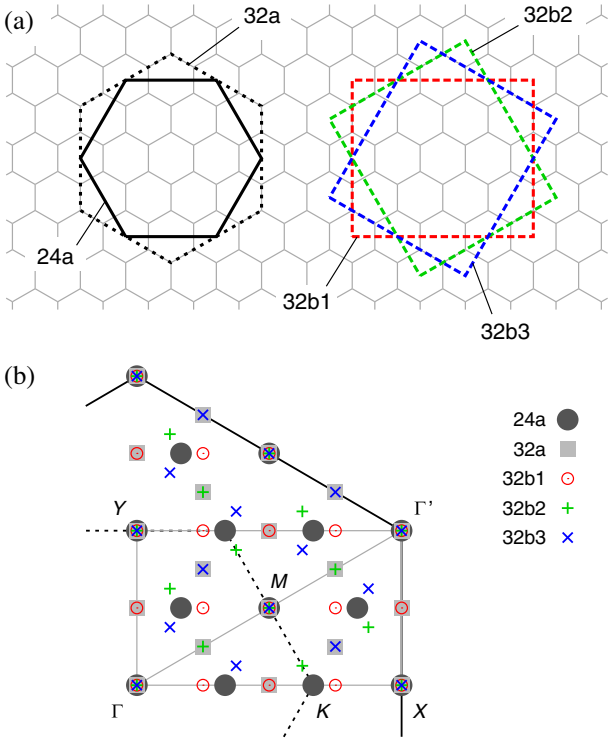

FIG. 8. (a) Clusters used in the exact diagonalization calculations: fully symmetric hexagonal 24- and 32-site clusters and a rectangular 32-site cluster in three possible orientations with respect to the honeycomb lattice. (b) Wave vectors compatible with periodic boundary conditions applied to the individual clusters. They are shown in one quadrant of the first Brillouin zone of the honeycomb lattice (dashed black line) and that of the completed triangular lattice (solid black line). High-symmetry points and the path along which the measured or simulated data are presented (gray line) are indicated [cf. Fig. 1(a)].

A side note on the selection of the clusters is in order: Even though there are other 24-site clusters (of elongated or asymmetric shape) that could bring better $\boldsymbol{q}$ resolution, their dynamic response contains artifacts, e.g., due to the creation of very short zigzag chain loops of just a few bonds when periodic boundary conditions are applied. When compared to the dataset for 24a, 32a, and 32b, the corresponding intensity profiles clearly stand out and are thus not included as unreliable.

APPENDIX C: HIDDEN HEISENBERG AND KITAEV POINTS

In this Appendix, we briefly elaborate on the points of hidden symmetry and the links between the excitation spectra of the extended Kitaev-Heisenberg model and the "hidden" models. The hidden-symmetry points are revealed by rotating spin axes, either globally or in a sublattice-dependent fashion, to convert the extended Kitaev-Heisenberg model

with a particular set of parameters to a simpler model [61]. This one-to-one correspondence enables us to transfer the known features such as the excitation spectra of the simpler model to the extended Kitaev-Heisenberg one.

We start with the hidden Kitaev point. To reveal its presence, one has to utilize the self-dual transformation [61] of the pseudospin Hamiltonian between the original axes xyz used in Eq. (1) and the new axes $x'y'z'$ that are 180° rotated around the axis perpendicular to the honeycomb plane (see the insets in Fig. 9). The two reference frames for the spins are linked by the relation

$$\begin{pmatrix} S^{x'} \\ S^{y'} \\ S^{z'} \end{pmatrix} = \frac{1}{3}\begin{pmatrix} -1 & 2 & 2 \\ 2 & -1 & 2 \\ 2 & 2 & -1 \end{pmatrix}\begin{pmatrix} S^{x} \\ S^{y} \\ S^{z} \end{pmatrix}. \quad \text{(C1)}$$

Applying the transformation to the case of Ising-type interaction in the new coordinate system $x'y'z'$, we find the correspondence

$$S_i^{z'}S_j^{z'} = -\frac{1}{3}S_i^zS_j^z + \frac{4}{9}\boldsymbol{S}_i\cdot\boldsymbol{S}_j + \frac{4}{9}(S_i^xS_j^y + S_i^yS_j^x) - \frac{2}{9}(S_i^xS_j^z + S_i^zS_j^x + S_i^yS_j^z + S_i^zS_j^y). \quad \text{(C2)}$$

The 180° rotation is compatible with the cyclic permutation among xyz and $x'y'z'$ axes so that similar relations can be found for $S_i^{x'}S_j^{x'}$ and $S_i^{y'}S_j^{y'}$ interactions. Altogether, the Ising-type interaction distributed on x, y, and z bonds constitutes the Kitaev model, while the right-hand side of the relation (C2) (and the two other ones) is just the extended Kitaev-Heisenberg model with a particular combination of parameters. Therefore, at the hidden Kitaev point given by the parameters $J = \frac{4}{9}K_0$, $K = -\frac{1}{3}K_0$, $\Gamma = \frac{4}{9}K_0$, and $\Gamma' = -\frac{2}{9}K_0$, the extended Kitaev-Heisenberg model exactly maps to a Kitaev model with the interaction constant K_0. Since the transformation is just a global rotation of the spin axes, all the features of the Kitaev model are exactly reproduced at the hidden Kitaev point. In particular, the excitation spectra are identical, and the spin susceptibility is obtained from that of the Kitaev model by a simple linear combination of the components.

The hidden Heisenberg point is given by the parameters $J = -\frac{1}{9}J_0$, $K = -\frac{2}{3}J_0$, $\Gamma = \frac{8}{9}J_0$, and $\Gamma' = -\frac{4}{9}J_0$, where J_0 is the effective Heisenberg interaction constant. Here, the connection is less apparent, since, by applying the above global rotation (C1), we get to the Kitaev-Heisenberg model only. Its parameters read as $K' = 2J_0$ and $J' = -J_0$ (Γ and Γ' are zero). To establish the relation to the final Heisenberg model, we have to invoke the four-sublattice transformation connecting zigzag and Néel order [5,61,76]. It is depicted in Fig. 9(a) and consists of 180° rotations around one of the cubic axes or identity applied on the respective sublattices. This transformation preserves the form of the Kitaev-Heisenberg model but changes the balance between the Kitaev and Heisenberg term and, for the above parameters K' and J', leads to a pure Heisenberg model with the exchange parameter J_0. Again, all the

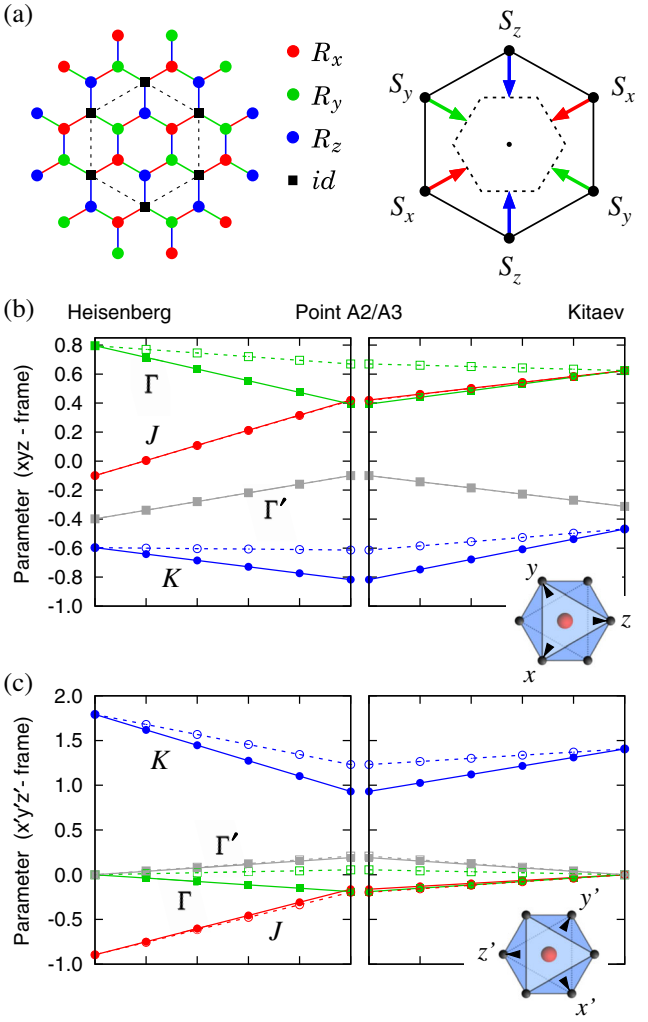

FIG. 9. (a) Four-sublattice transformation used in the text. At the individual sublattices, the spin axes are rotated by 180° around the cubic axes x, y, and z or left intact. In the momentum space (right), the spin components are shifted by the zigzag ordering vectors. (b) Model parameter values along the lines used in Fig. 6. The values are expressed using the original xyz-coordinate system for the spins. The full lines and symbols correspond to Figs. 6(a) and 6(b), and dashed lines and open symbols to Figs. 6(c) and 6(d). The figure is organized like Fig. 6 with $A2$ or $A3$ parameters being in the middle and the evolution toward the hidden Heisenberg (Kitaev) point corresponding to the left (right) direction from the middle. Only nearest-neighbor interaction parameters $JK\Gamma\Gamma'$ are presented; $J_{2,3}$ linearly vanish when approaching the points of hidden symmetry. The marked parameter points correspond to the spectra shown in Fig. 6. (c) The same lines through the parameter space but expressed using the $x'y'z'$-coordinate system rotated by 180° around the axis perpendicular to the honeycomb plane. In both xyz and $x'y'z'$ frames depicted by the insets, the axes point above the paper plane.

features of the Heisenberg model such as the magnon spectra can be transferred to the hidden Heisenberg point. However, due to the four-sublattice transformation, momentum shifts depicted in Fig. 9(a) are involved. The Fourier components of S^x, S^y, and S^z are shifted by wave vectors with the directions identical to the corresponding bond directions of the honeycomb lattice [61]. The intense AFM Heisenberg magnons residing at the Γ' points in the corners of the extended Brillouin zone are then translated to the zigzag M points.

In the main text, we study the parameter evolution of the $\boldsymbol{q} = 0$ spectra when going toward the hidden Heisenberg and Kitaev points. The corresponding parameter values are shown in Fig. 9(b) in the xyz reference frame and in Fig. 9(c) also rotated via Eq. (C1) to the $x'y'z'$ reference frame. Note that, in the $x'y'z'$ frame, the dominant interaction at our points $A2$ and $A3$ is $K > 0$, accompanied by small $J < 0$ and Γ and Γ' interactions. The calculated response is thus similar to the one obtained for the upper zigzag phase in Fig. 3 that is stabilized in the Kitaev-Heisenberg model itself.

[1] A. Kitaev, *Anyons in an Exactly Solved Model and Beyond*, Ann. Phys. (Amsterdam) **321**, 2 (2006).

[2] S. R. Elliott and M. Franz, *Colloquium: Majorana Fermions in Nuclear, Particle, and Solid-State Physics*, Rev. Mod. Phys. **87**, 137 (2015).

[3] A. Yu. Kitaev, *Fault-Tolerant Quantum Computation by Anyons*, Ann. Phys. (Amsterdam) **303**, 2 (2003).

[4] G. Jackeli and G. Khaliullin, *Mott Insulators in the Strong Spin-Orbit Coupling Limit: From Heisenberg to a Quantum Compass and Kitaev Models*, Phys. Rev. Lett. **102**, 017205 (2009).

[5] J. Chaloupka, G. Jackeli, and G. Khaliullin, *Kitaev-Heisenberg Model on a Honeycomb Lattice: Possible Exotic Phases in Iridium Oxides* A_2IrO_3, Phys. Rev. Lett. **105**, 027204 (2010).

[6] I. Kimchi and Y.-Z. You, *Kitaev-Heisenberg-*J_2*-*J_3 *Model for the Iridates* A_2IrO_3, Phys. Rev. B **84**, 180407(R) (2011).

[7] J. G. Rau, E. K.-H. Lee, and H.-Y. Kee, *Generic Spin Model for the Honeycomb Iridates beyond the Kitaev Limit*, Phys. Rev. Lett. **112**, 077204 (2014).

[8] Y. Yamaji, Y. Nomura, M. Kurita, R. Arita, and M. Imada, *First-Principles Study of the Honeycomb-Lattice Iridates* Na_2IrO_3 *in the Presence of Strong Spin-Orbit Interaction and Electron Correlations*Phys. Rev. Lett. **113**, 107201 (2014).

[9] K. Shinjo, S. Sota, and T. Tohyama, *Density-Matrix Renormalization Group Study of the Extended Kitaev-Heisenberg Model*, Phys. Rev. B **91**, 054401 (2015).

[10] E. Sela, H.-C. Jiang, M. H. Gerlach, and S. Trebst, *Order-by-Disorder and Spin-Orbital Liquids in a Distorted Heisenberg-Kitaev Model*, Phys. Rev. B **90**, 035113 (2014).

[11] Y. Singh and P. Gegenwart, *Antiferromagnetic Mott Insulating State in Single Crystals of the Honeycomb Lattice Material* Na_2IrO_3, Phys. Rev. B **82**, 064412 (2010).

[12] X. Liu, T. Berlijn, W.-G. Yin, W. Ku, A. Tsvelik, Y.-J. Kim, H. Gretarsson, Y. Singh, P. Gegenwart, and J. P. Hill, *Long-Range Magnetic Ordering in* Na_2IrO_3, Phys. Rev. B **83**, 220403(R) (2011).

[13] F. Ye, S. Chi, H. Cao, B. C. Chakoumakos, J. A. Fernandez-Baca, R. Custelcean, T. F. Qi, O. B. Korneta, and G. Cao, *Direct Evidence of a Zigzag Spin-Chain Structure in the Honeycomb Lattice: A Neutron and x-ray Diffraction Investigation of Single-Crystal* Na_2IrO_3, Phys. Rev. B **85**, 180403(R) (2012).

[14] S. K. Choi, R. Coldea, A. N. Kolmogorov, T. Lancaster, I. I. Mazin, S. J. Blundell, P. G. Radaelli, Y. Singh, P. Gegenwart, K. R. Choi, S.-W. Cheong, P. J. Baker, C. Stock, and J. Taylor, *Spin Waves and Revised Crystal Structure of Honeycomb Iridate* Na_2IrO_3, Phys. Rev. Lett. **108**, 127204 (2012).

[15] S. H. Chun, J.-W. Kim, J. Kim, H. Zheng, C. Stoumpos, C. Malliakas, J. F. Mitchell, K. Mehlawat, Y. Singh, Y. Choi, T. Gog, A. Al-Zein, M. M. Sala, M. Krisch, J. Chaloupka, G. Jackeli, G. Khaliullin, and B. J. Kim, *Direct Evidence for Dominant Bond-Directional Interactions in a Honeycomb Lattice Iridate* Na_2IrO_3, Nat. Phys. **11**, 462 (2015).

[16] V. M. Katukuri, S. Nishimoto, V. Yushankhai, A. Stoyanova, H. Kandpal, S. Choi, R. Coldea, I. Rousochatzakis, L. Hozoi, and J. van den Brink, *Kitaev Interactions between* $J = 1/2$ *Moments in Honeycomb* Na_2IrO_3 *are Large and Ferromagnetic: Insights from ab initio Quantum Chemistry Calculations*, New J. Phys. **16**, 013056 (2014).

[17] S. M. Winter, Y. Li, H. O. Jeschke, and R. Valentí, *Challenges in Design of Kitaev Materials: Magnetic Interactions from Competing Energy Scales*, Phys. Rev. B **93**, 214431 (2016).

[18] S. M. Winter, A. A. Tsirlin, M. Daghofer, J. van den Brink, Y. Singh, P. Gegenwart, and R. Valentí, *Models and Materials for Generalized Kitaev Magnetism*, J. Phys. Condens. Matter **29**, 493002 (2017).

[19] I. Rousochatzakis and N. B. Perkins, *Classical Spin Liquid Instability Driven by Off-Diagonal Exchange in Strong Spin-Orbit Magnets*, Phys. Rev. Lett. **118**, 147204 (2017).

[20] M. Gohlke, G. Wachtel, Y. Yamaji, F. Pollmann, and Y. B. Kim, *Quantum Spin Liquid Signatures in Kitaev-Like Frustrated Magnets*, Phys. Rev. B **97**, 075126 (2018).

[21] Y. Singh, S. Manni, J. Reuther, T. Berlijn, R. Thomale, W. Ku, S. Trebst, and P. Gegenwart, *Relevance of the Heisenberg-Kitaev Model for the Honeycomb Lattice Iridates* A_2IrO_3, Phys. Rev. Lett. **108**, 127203 (2012).

[22] T. Takayama, A. Kato, R. Dinnebier, J. Nuss, H. Kono, L. S. I. Veiga, G. Fabbris, D. Haskel, and H. Takagi, *Hyperhoneycomb Iridate* β*-*Li_2IrO_3 *as a Platform for Kitaev Magnetism*, Phys. Rev. Lett. **114**, 077202 (2015).

[23] K. A. Modic, T. E. Smidt, I. Kimchi, N. P. Breznay, A. Biffin, S. Choi, R. D. Johnson, R. Coldea, P. Watkins-Curry, G. T. McCandless, J. Y. Chan, F. Gandara, Z. Islam, A. Vishwanath, A. Shekhter, R. D. McDonald, and J. G. Analytis, *Realization of a Three-Dimensional Spin–Anisotropic Harmonic Honeycomb Iridate*, Nat. Commun. **5**, 4203 (2014).

[24] M. Abramchuk, C. Ozsoy-Keskinbora, J. W. Krizan, K. R. Metz, D. C. Bell, and F. Tafti, Cu_2IrO_3*: A New Magnetically*

Frustrated Honeycomb Iridate, J. Am. Chem. Soc. **139**, 15371 (2017).

[25] K. Kitagawa, T. Takayama, Y. Matsumoto, A. Kato, R. Takano, Y. Kishimoto, S. Bette, R. Dinnebier, G. Jackeli, and H. Takagi, *A Spin–Orbital-Entangled Quantum Liquid on a Honeycomb Lattice*, Nature (London) **554**, 341 (2018).

[26] K. W. Plumb, J. P. Clancy, L. J. Sandilands, V. V. Shankar, Y. F. Hu, K. S. Burch, H.-Y. Kee, and Y.-J. Kim, *α-$RuCl_3$: A Spin-Orbit Assisted Mott Insulator on a Honeycomb*, Phys. Rev. B **90**, 041112(R) (2014).

[27] A. Banerjee, C. A. Bridges, J.-Q. Yan, A. A. Aczel, L. Li, M. B. Stone, G. E. Granroth, M. D. Lumsden, Y. Yiu, J. Knolle, S. Bhattacharjee, D. L. Kovrizhin, R. Moessner, D. A. Tennant, D. G. Mandrus, and S. E. Nagler, *Proximate Kitaev Quantum Spin Liquid Behaviour in a Honeycomb Magnet*, Nat. Mater. **15**, 733 (2016).

[28] K. Ran, J. Wang, W. Wang, Z.-Y. Dong, X. Ren, S. Bao, S. Li, Z. Ma, Y. Gan, Y. Zhang, J. T. Park, G. Deng, S. Danilkin, S.-L. Yu, J.-X. Li, and J. Wen, *Spin-Wave Excitations Evidencing the Kitaev Interaction in Single Crystalline α-$RuCl_3$*, Phys. Rev. Lett. **118**, 107203 (2017).

[29] A. Banerjee, J. Yan, J. Knolle, C. A. Bridges, M. B. Stone, M. D. Lumsden, D. G. Mandrus, D. A. Tennant, R. Moessner, and S. E. Nagler, *Neutron Scattering in the Proximate Quantum Spin Liquid α-$RuCl_3$*, Science **356**, 1055 (2017).

[30] S.-H. Do, S.-Y. Park, J. Yoshitake, J. Nasu, Y. Motome, Y. S. Kwon, D. T. Adroja, D. J. Voneshen, K. Kim, T.-H. Jang, J.-H. Park, K.-Y. Choi, and S. Ji, *Majorana Fermions in the Kitaev Quantum Spin System α-$RuCl_3$*, Nat. Phys. **13**, 1079 (2017).

[31] M. E. Zhitomirsky and A. L. Chernyshev, *Colloquium: Spontaneous Magnon Decays*, Rev. Mod. Phys. **85**, 219 (2013).

[32] S. M. Winter, K. Riedl, P. A. Maksimov, A. L. Chernyshev, A. Honecker, and R. Valentí, *Breakdown of Magnons in a Strongly Spin-Orbital Coupled Magnet*, Nat. Commun. **8**, 1152 (2017).

[33] L. J. Sandilands, Y. Tian, K. W. Plumb, Y.-J. Kim, and K. S. Burch, *Scattering Continuum and Possible Fractionalized Excitations in α-$RuCl_3$*, Phys. Rev. Lett. **114**, 147201 (2015).

[34] J. Nasu, J. Knolle, D. L. Kovrizhin, Y. Motome, and R. Moessner, *Fermionic Response from Fractionalization in an Insulating Two-Dimensional Magnet*, Nat. Phys. **12**, 912 (2016).

[35] J. Yoshitake, J. Nasu, and Y. Motome, *Fractional Spin Fluctuations as a Precursor of Quantum Spin Liquids: Majorana Dynamical Mean-Field Study for the Kitaev Model*, Phys. Rev. Lett. **117**, 157203 (2016).

[36] I. A. Leahy, C. A. Pocs, P. E. Siegfried, D. Graf, S.-H. Do, K.-Y. Choi, B. Normand, and M. Lee, *Anomalous Thermal Conductivity and Magnetic Torque Response in the Honeycomb Magnet α-$RuCl_3$*, Phys. Rev. Lett. **118**, 187203 (2017).

[37] M. Gohlke, R. Verresen, R. Moessner, and F. Pollmann, *Dynamics of the Kitaev-Heisenberg Model*, Phys. Rev. Lett. **119**, 157203 (2017).

[38] S. N. Gupta, P. V. Sriluckshmy, K. Mehlawat, A. Balodhi, D. K. Mishra, S. R. Hassan, T. V. Ramakrishnan, D. V. S. Muthu, Y. Singh, and A. K. Sood, *Raman signatures of strong Kitaev exchange correlations in $(Na_{1-x}Li_x)_2IrO_3$: Experiments and theory*, Europhys. Lett. **114**, 47004 (2016).

[39] J. Knolle, G.-W. Chern, D. L. Kovrizhin, R. Moessner, and N. B. Perkins, *Raman Scattering Signatures of Kitaev Spin Liquids in A_2IrO_3 Iridates with A = Na or Li*, Phys. Rev. Lett. **113**, 187201 (2014).

[40] K. Mehlawat, A. Thamizhavel, and Y. Singh, *Heat Capacity Evidence for Proximity to the Kitaev Quantum Spin Liquid in A_2IrO_3 (A = Na, Li)*, Phys. Rev. B **95**, 144406 (2017).

[41] I. A. Leahy, C. A. Pocs, P. E. Siegfried, D. Graf, S.-H. Do, K.-Y. Choi, B. Normand, and M. Lee, *Anomalous Thermal Conductivity and Magnetic Torque Response in the Honeycomb Magnet α-$RuCl_3$*, Phys. Rev. Lett. **118**, 187203 (2017).

[42] S. D. Das, S. Kundu, Z. Zhu, E. Mun, R. D. McDonald, G. Li, L. Balicas, A. McCollam, G. Cao, J. G. Rau, H.-Y. Kee, V. Tripathi, and S. E. Sebastian, *Magnetic Anisotropy of the Alkali Iridate Na_2IrO_3 at High Magnetic Fields: Evidence for Strong Ferromagnetic Kitaev Correlations*, Phys. Rev. B **99**, 081101(R) (2019).

[43] H. Gretarsson, J. P. Clancy, Y. Singh, P. Gegenwart, J. P. Hill, J. Kim, M. H. Upton, A. H. Said, D. Casa, T. Gog, and Y.-J. Kim, *Magnetic Excitation Spectrum of Na_2IrO_3 Probed with Resonant Inelastic x-ray Scattering*, Phys. Rev. B **87**, 220407(R) (2013).

[44] A. Revelli, M. M. Sala, G. Monaco, C. Hickey, P. Becker, F. Freund, A. Jesche, P. Gegenwart, T. Eschmann, F. L. Buessen, S. Trebst, P. H. M. van Loosdrecht, J. van den Brink, and M. Gruninger, Fingerprints of Kitaev Physics in the Magnetic Excitations of Honeycomb Iridates arXiv:1905.13590.

[45] A. H. Said, T. Gog, M. Wieczorek, X. Huang, D. Casa, E. Kasman, R. Divan, and J. H. Kim, *High-Energy-Resolution Diced Spherical Quartz Analyzers for Resonant Inelastic X-ray Scattering*, J. Synchrotron Radiat. **25**, 373 (2018).

[46] J. Kim, D. Casa, A. Said, R. Krakora, B. J. Kim, E. Kasman, X. Huang, and T. Gog, *Quartz-Based Flat-Crystal Resonant Inelastic x-ray Scattering Spectrometer with sub-10 meV Energy Resolution*, Sci. Rep. **8**, 1958 (2018).

[47] T. Gog, D. M. Casa, A. H. Said, M. H. Upton, J. Kim, I. Kuzmenko, X. Huang, and R. Khachatryan, *Spherical Analyzers and Monochromators for Resonant Inelastic Hard X-ray Scattering: A Compilation of Crystals and Reflections*, J. Synchrotron Radiat. **20**, 74 (2013).

[48] Yu. V. Shvyd'ko, J. P. Hill, C. A. Burns, D. S. Coburn, B. Brajuskovic, D. Casa, K. Goetze, T. Gog, R. Khachatryan, J.-H. Kim, C. N. Kodituwakku, M. Ramanathan, T. Roberts, A. Said, H. Sinn, D. Shu, S. Stoupin, M. Upton, M. Wieczorek, and H. Yavas, *Merix—Next Generation Medium Energy Resolution Inelastic X-Ray Scattering Instrument at the APS*, J. Electron Spectrosc. Relat. Phenom. **188**, 140 (2013).

[49] R. Comin, G. Levy, B. Ludbrook, Z.-H. Zhu, C. N. Veenstra, J. A. Rosen, Y. Singh, P. Gegenwart, D. Stricker, J. N. Hancock, D. van der Marel, I. S. Elfimov, and A. Damascelli, *Na_2IrO_3 as a Novel Relativistic Mott Insulator with a 340-meV Gap*, Phys. Rev. Lett. **109**, 266406 (2012).

[50] J. G. Rau and H.-Y. Kee, *Trigonal Distortion in the Honeycomb Iridates: Proximity of Zigzag And Spiral Phases in Na_2IrO_3*, arXiv:1408.4811.

[51] J. Chaloupka and G. Khaliullin, *Magnetic Anisotropy in the Kitaev Model Systems* Na_2IrO_3 *and* $RuCl_3$, Phys. Rev. B **94**, 064435 (2016).

[52] B. J. Kim and G. Khaliullin, *Resonant Inelastic x-ray Scattering Operators for* t_{2g} *Orbital Systems*, Phys. Rev. B **96**, 085108 (2017).

[53] H. Gretarsson, J. P. Clancy, X. Liu, J. P. Hill, E. Bozin, Y. Singh, S. Manni, P. Gegenwart, J. Kim, A. H. Said, D. Casa, T. Gog, M. H. Upton, H.-S. Kim, J. Yu, V. M. Katukuri, L. Hozoi, J. van den Brink, and Y.-J. Kim, *Crystal-Field Splitting and Correlation Effect on the Electronic Structure of* A_2IrO_3, Phys. Rev. Lett. **110**, 076402 (2013).

[54] J. Rusnačko, D. Gotfryd, and J. Chaloupka, *Structural and Magnetic Studies of* Sr_2IrO_4, Phys. Rev. B **99**, 064425 (2019).

[55] H. Gretarsson, N. H. Sung, M. Höppner, B. J. Kim, B. Keimer, and M. Le Tacon, *Two-Magnon Raman Scattering and Pseudospin-Lattice Interactions in* Sr_2IrO_4 *and* $Sr_3Ir_2O_7$, Phys. Rev. Lett. **116**, 136401 (2016).

[56] H. Gretarsson, J. Sauceda, N. H. Sung, M. Höppner, M. Minola, B. J. Kim, B. Keimer, and M. Le Tacon, *Raman Scattering Study of Vibrational and Magnetic Excitations in* $Sr_{2-x}La_xIrO_4$, Phys. Rev. B **96**, 115138 (2017).

[57] L. Braicovich, M. Rossi, R. Fumagalli, Y. Peng, Y. Wang, R. Arpaia, D. Betto, G. M. D. Luca, D. D. Castro, K. Kummer, M. M. Sala, M. Pagetti, G. Balestrino, N. B. Brookes, M. Salluzzo, S. Johnston, J. van den Brink, and G. Ghiringhelli, *Determining the Electron-Phonon Coupling in Superconducting Cuprates by Resonant Inelastic X-ray Scattering: Methods and Results on* $Nd_{1+x}Ba_{2-x}Cu_3O_{7-\delta}$ arXiv: 1906.01270.

[58] M. O. Krause and J. H. Oliver, *Natural Widths of Atomic K and L Levels, Kα X-ray Lines and Several KLL Auger Lines*, J. Phys. Chem. Ref. Data **8**, 329 (1979).

[59] V. Hermann, J. Ebad-Allah, F. Freund, I. M. Pietsch, A. Jesche, A. A. Tsirlin, J. Deisenhofer, M. Hanfland, P. Gegenwart, and C. A. Kuntscher, *High-Pressure versus Isoelectronic Doping Effect on the Honeycomb Iridate* Na_2IrO_3, Phys. Rev. B **96**, 195137 (2017).

[60] J. G. Vale, C. D. Dashwood, E. Paris, L. S. I. Veiga, M. Garcia-Fernandez, A. Nag, A. Walters, K. J. Zhou, I. M. Pietsch, A. Jesche, P. Gegenwart, R. Coldea, T. Schmitt, and D. F. McMorrow, *High-Resolution Resonant Inelastic x-ray Scattering study of the Electron-Phonon Coupling in Honeycomb* α-Li_2IrO_3, Phys. Rev. B **100**, 224303 (2019).

[61] J. Chaloupka and G. Khaliullin, *Hidden Symmetries of the Extended Kitaev-Heisenberg Model: Implications for the Honeycomb-Lattice Iridates* A_2IrO_3, Phys. Rev. B **92**, 024413 (2015).

[62] J. Chaloupka, G. Jackeli, and G. Khaliullin, *Zigzag Magnetic Order in the Iridium Oxide* Na_2IrO_3, Phys. Rev. Lett. **110**, 097204 (2013).

[63] J. Knolle, D. L. Kovrizhin, J. T. Chalker, and R. Moessner, *Dynamics of Fractionalization in Quantum Spin Liquids*, Phys. Rev. B **92**, 115127 (2015).

[64] D. Gotfryd, J. Rusnačko, K. Wohlfeld, G. Jackeli, J. Chaloupka, and A. M. Oleś, *Phase Diagram and Spin Correlations of the Kitaev-Heisenberg Model: Importance of Quantum Effects*, Phys. Rev. B **95**, 024426 (2017).

[65] J. Knolle, D. L. Kovrizhin, J. T. Chalker, and R. Moessner, *Dynamics of a Two-Dimensional Quantum Spin Liquid: Signatures of Emergent Majorana Fermions and Fluxes*, Phys. Rev. Lett. **112**, 207203 (2014).

[66] J. Knolle, S. Bhattacharjee, and R. Moessner, *Dynamics of a Quantum Spin Liquid Beyond Integrability: The Kitaev-Heisenberg-*Γ *Model in an Augmented Parton Mean-Field Theory*, Phys. Rev. B **97**, 134432 (2018).

[67] J. Wang, B. Normand, and Z.-X. Liu, *One Proximate Kitaev Spin Liquid in the K-J-*Γ *Model on the Honeycomb Lattice*, Phys. Rev. Lett. **123**, 197201 (2019).

[68] J. Nasu, M. Udagawa, and Y. Motome, *Thermal Fractionalization Of Quantum Spins in a Kitaev Model: Temperature-Linear Specific Heat and Coherent Transport of Majorana Fermions*, Phys. Rev. B **92**, 115122 (2015).

[69] A. Catuneanu, Y. Yamaji, G. Wachtel, Y. B. Kim, and H.-Y. Kee, *Path to Stable Quantum Spin Liquids in Spin-Orbit Coupled Correlated Materials*, npj Quantum Mater. **3**, 23 (2018).

[70] J. Yoshitake, J. Nasu, Y. Kato, and Y. Motome, *Majorana Dynamical Mean-Field Study of Spin Dynamics at Finite Temperatures in the Honeycomb Kitaev Model*, Phys. Rev. B **96**, 024438 (2017).

[71] Y. Yamaji, T. Suzuki, T. Yamada, S.-I. Suga, N. Kawashima, and M, Imada, *Clues and Criteria for Designing a Kitaev Spin Liquid Revealed by Thermal and Spin Excitations of the Honeycomb Iridate* Na_2IrO_3, Phys. Rev. B **93**, 174425 (2016).

[72] G. B. Halász, N. B. Perkins, and J. van den Brink, *Resonant Inelastic X-Ray Scattering Response of the Kitaev Honeycomb Model*, Phys. Rev. Lett. **117**, 127203 (2016).

[73] K. Ishii, S. Ishihara, Y. Murakami, K. Ikeuchi, K. Kuzushita, T. Inami, K. Ohwada, M. Yoshida, I. Jarrige, N. Tatami, S. Niioka, D. Bizen, Y. Ando, J. Mizuki, S. Maekawa, and Y. Endoh, *Polarization-Analyzed Resonant Inelastic x-ray Scattering of the Orbital Excitations in* $KCuF_3$, Phys. Rev. B **83**, 241101(R) (2011).

[74] X. Gao, D. Casa, J. Kim, T. Gog, C. Li, and C. Burns, *Toroidal Silicon Polarization Analyzer for Resonant Inelastic x-ray Scattering*, Rev. Sci. Instrum. **87**, 083107 (2016).

[75] A. Avella and F. Mancini, *Strongly Correlated Systems: Numerical Methods* (Springer, Berlin, 2013).

[76] G. Khaliullin, *Orbital Order and Fluctuations in Mott Insulators*, Prog. Theor. Phys. Suppl. **160**, 155 (2005).

PHYSICAL REVIEW LETTERS **125,** 047201 (2020)

Kitaev Spin Liquid in 3*d* Transition Metal Compounds

Huimei Liu,[1] Jiří Chaloupka,[2,3] and Giniyat Khaliullin[1]
[1]*Max Planck Institute for Solid State Research, Heisenbergstrasse 1, D-70569 Stuttgart, Germany*
[2]*Department of Condensed Matter Physics, Faculty of Science, Masaryk University, Kotlářská 2, Brno 61137, Czech Republic*
[3]*Central European Institute of Technology, Masaryk University, Kamenice 753/5, Brno 62500, Czech Republic*

(Received 10 February 2020; accepted 2 July 2020; published 21 July 2020)

We study the exchange interactions and resulting magnetic phases in the honeycomb cobaltates. For a broad range of trigonal crystal fields acting on Co^{2+} ions, the low-energy pseudospin-1/2 Hamiltonian is dominated by bond-dependent Ising couplings that constitute the Kitaev model. The non-Kitaev terms nearly vanish at small values of trigonal field Δ, resulting in spin liquid ground state. Considering $Na_3Co_2SbO_6$ as an example, we find that this compound is proximate to a Kitaev spin liquid phase, and can be driven into it by slightly reducing Δ by ∼20 meV, e.g., via strain or pressure control. We argue that, due to the more localized nature of the magnetic electrons in 3*d* compounds, cobaltates offer the most promising search area for Kitaev model physics.

DOI: 10.1103/PhysRevLett.125.047201

The Kitaev honeycomb model [1], demonstrating the key concepts of quantum spin liquids [2] via an elegant exact solution, has attracted much attention (see the recent reviews [3–7]). In this model, the nearest-neighbor (NN) spins $S = 1/2$ interact via a simple Ising-type coupling $S_i^\gamma S_j^\gamma$. However, the Ising axis γ is not global but bond dependent, taking the mutually orthogonal directions (x, y, z) on the three adjacent NN bonds on the honeycomb lattice. Having no unique easy axis and being frustrated, the Ising spins fail to order and form instead a highly entangled quantum many-body state, supporting fractional excitations described by Majorana fermions [1].

Much effort has been made to realize the Kitaev spin liquid (SL) experimentally. From a materials perspective, the Ising-type anisotropy is a hallmark of unquenched orbital magnetism. As the orbitals are spatially anisotropic and bond directional, they naturally lead to the desired bond-dependent exchange anisotropy via spin-orbit coupling [8]. Along these lines, 5*d* iridates have been suggested [9] to host Kitaev model; later, 4*d* $RuCl_3$ was added [10] to the list of candidates. To date, however, the Kitaev SL remains elusive, as this state is fragile and destroyed by various perturbations, such as small admixture of a conventional Heisenberg coupling [11] caused by direct overlap of the *d* orbitals. Even more detrimental to Kitaev SL are the longer range couplings [12], unavoidable in weakly localized 5*d*- and 4*d*-electron systems with the spatially extended *d* wave functions. We thus turn to 3*d* systems with more compact *d* orbitals [13].

While the idea of extending the search area to 3*d* materials is appealing, and plausible theoretically [15,16], it raises an immediate question crucial for experiment: is spin-orbit coupling (SOC) in 3*d* ions strong enough to support the orbital magnetism prerequisite for the Kitaev model design? This is a serious concern, since noncubic crystal fields present in real materials tend to quench orbital moments and suppress the bond dependence of the exchange couplings [8]. In this Letter, we give a positive answer to this question. Our quantitative analysis of the crystal field effects on the magnetism of 3*d* cobaltates shows that the orbital moments remain active and generate a Kitaev model as the leading term in the Hamiltonian. In fact, we identify the trigonal crystal field as the key and experimentally tunable parameter, which decides the strength of the non-Kitaev terms in 3*d* compounds.

Our main results are summarized in Fig. 1, displaying various magnetic phases of spin-orbit entangled pseudospin-1/2 Co^{2+} ions on a honeycomb lattice. The phase diagram is shown as a function of trigonal field Δ, in a window relevant for honeycomb cobaltates, and a ratio of Coulomb repulsion U and the charge-transfer gap Δ_{pd} [17]. From the analysis of experimental data, we find that $Na_3Co_2SbO_6$ [18–20] is located at just ∼20 meV "distance" from the Kitaev SL phase (see Fig. 1), and could be driven there by a *c*-axis compression that reduces Δ. This seems feasible, given that Δ variations within a window of ∼70 meV were achieved by strain control in a cobalt oxide [21].

We now describe our calculations resulting in Fig. 1. In short, we first derive the pseudospin exchange interactions from a microscopic theory, as a function of various

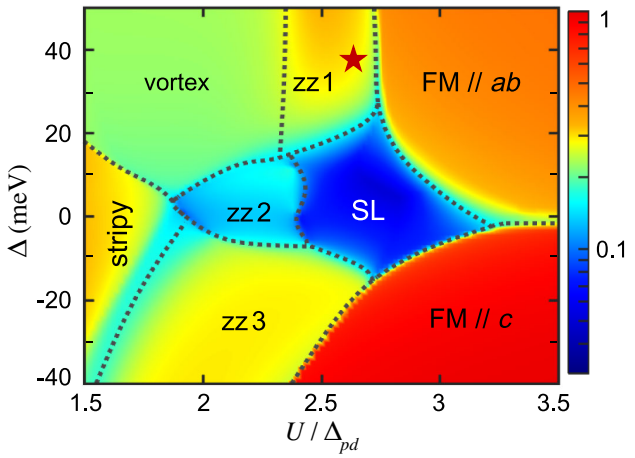

FIG. 1. The calculated magnetic phase diagram of honeycomb cobaltates. The Kitaev SL phase is surrounded by ferromagnetic (FM) states with moments in the honeycomb ab plane and along the c axis, zigzag-type states with moments in the ab plane (zz1), along Co-O bonds (zz2), and in the ac plane (zz3). Vortex- and stripy-type phases take over at smaller U/Δ_{pd}. The color map shows the second-NN spin correlation strength (leading eigenvalue of the correlation matrix $\langle \tilde{S}_i^{\alpha}\tilde{S}_j^{\beta}\rangle$ normalized by $\tilde{S}^2 = 1/4$), which drops sharply in the SL phase. The star indicates the rough position of $Na_3Co_2SbO_6$.

parameters, and then obtain the corresponding ground states numerically by exact diagonalization.

Exchange interactions.—In an octahedral environment, Co^{2+} ion with $t_{2g}^5 e_g^2$ configuration possesses spin $S = 3/2$ and effective orbital moment $L = 1$, which form, via spin-orbit coupling, a pseudospin $\tilde{S} = 1/2$ [14]. Over decades, cobaltates served as a paradigm for quantum magnetism, providing a variety of pseudospin-1/2 models ranging from the Heisenberg model in perovskites with corner-sharing octahedra [22,23] to the Ising model when the CoO_6 octahedra share their edges [24].

A microscopic theory of Co^{2+} interactions in the edge-sharing geometry has been developed just recently [15,16], assuming an ideal cubic symmetry. Here we consider a realistic case of trigonally distorted lattices, where t_{2g} orbitals split as shown in Fig. 2(a). Our goal is to see if such distortions leave enough room for the Kitaev model physics in real compounds. This is decided by the spin-orbital structure of the pseudospin $\tilde{S} = 1/2$ wave functions; in terms of $|S_Z, L_Z\rangle$ states (the trigonal axis $Z \| c$ is perpendicular to the honeycomb plane), they read as:

$$\left|\pm\frac{\tilde{1}}{2}\right\rangle = \mathcal{C}_1\left|\pm\frac{3}{2},\mp 1\right\rangle + \mathcal{C}_2\left|\pm\frac{1}{2},0\right\rangle + \mathcal{C}_3\left|\mp\frac{1}{2},\pm 1\right\rangle. \tag{1}$$

The coefficients $\mathcal{C}_{1,2,3}$ depend on a relative strength Δ/λ of the trigonal field $\Delta(L_Z^2 - \frac{2}{3})$ and SOC $\lambda \boldsymbol{L}\cdot\boldsymbol{S}$ [25,26]. At

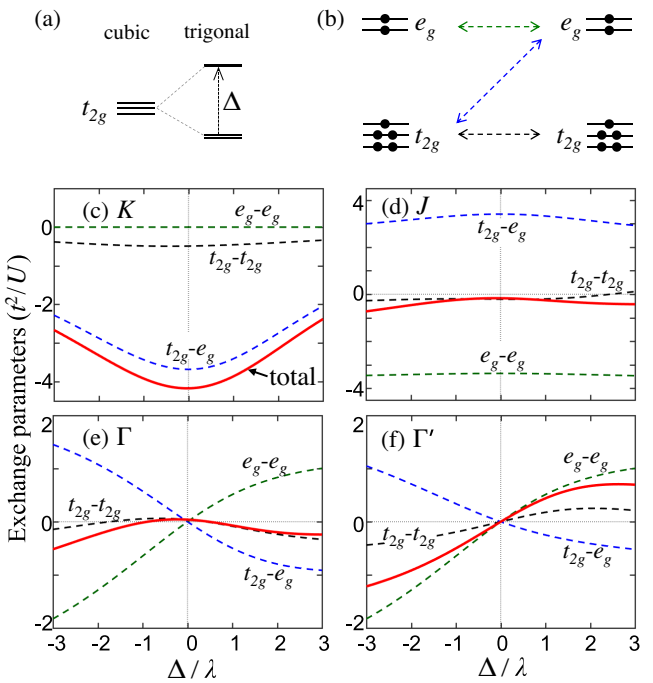

FIG. 2. (a) Splitting of t_{2g}-electron level under trigonal crystal field. (b) Schematic of the spin-orbital exchange channels for d^7 ions. (c)–(f) Exchange parameters K, J, Γ, and Γ' (red solid lines) as a function of Δ/λ, calculated at $U/\Delta_{pd} = 2.5$ and Hund's coupling $J_H = 0.15U$. On each panel, dashed lines show individual contributions of t_{2g}-t_{2g} (black), t_{2g}-e_g (blue), and e_g-e_g (green) exchange channels. The couplings J, Γ, and Γ' nearly vanish in the cubic limit $\Delta = 0$.

$\Delta = 0$, one has $(\mathcal{C}_1, \mathcal{C}_2, \mathcal{C}_3) = (1/\sqrt{2}, -1/\sqrt{3}, 1/\sqrt{6})$, and all the three components of $\boldsymbol{L}$ are equally active. A positive (negative) Δ field tends to quench L_Z ($L_{X/Y}$).

The next step is to project various spin-orbital exchange interactions in cobaltates [15] onto the above pseudospin-1/2 subspace. The calculations are standard but very lengthy; the readers interested in details are referred to the Supplemental Material [26]. At the end, we obtain the $\tilde{S} = 1/2$ Kitaev model $K\tilde{S}_i^{\gamma}\tilde{S}_j^{\gamma}$, supplemented by Heisenberg J and off-diagonal anisotropy Γ, Γ' terms; for $\gamma = z$ type NN bonds, they read as:

$$\begin{aligned}\mathcal{H}_{ij}^{(z)} = {} & K\tilde{S}_i^z\tilde{S}_j^z + J\tilde{\boldsymbol{S}}_i\cdot\tilde{\boldsymbol{S}}_j + \Gamma(\tilde{S}_i^x\tilde{S}_j^y + \tilde{S}_i^y\tilde{S}_j^x) \\ & + \Gamma'(\tilde{S}_i^x\tilde{S}_j^z + \tilde{S}_i^z\tilde{S}_j^x + \tilde{S}_i^y\tilde{S}_j^z + \tilde{S}_i^z\tilde{S}_j^y).\end{aligned} \tag{2}$$

Interactions $\mathcal{H}_{ij}^{(\gamma)}$ for $\gamma = x, y$ type bonds follow from a cyclic permutation among $\tilde{S}_j^x$, $\tilde{S}_j^y$, and $\tilde{S}_j^z$.

While the Hamiltonian (2) is of the same form as in d^5 Ir/Ru systems [5,34], the microscopic origin of its parameters K, J, Γ, Γ' is completely different in d^7 Co compounds. This is due to the spin-active e_g electrons of $Co(t_{2g}^5 e_g^2)$ ions, which generate new spin-orbital exchange

channels t_{2g}-e_g and e_g-e_g, shown in Fig. 2(b), in addition to the t_{2g}-t_{2g} ones operating in d^5 systems with t_{2g}-only electrons. In fact, the new terms make a major contribution to the exchange parameters, as illustrated in Figs. 2(c)–2(f). In particular, Kitaev coupling K comes almost entirely from the t_{2g}-e_g process. It is also noticed that t_{2g}-e_g and e_g-e_g contributions to J, Γ, and Γ' are of opposite signs and largely cancel each other, resulting in only small overall values of these couplings.

Figure 2 shows that the trigonal field Δ, which acts via modification of the pseudospin wave function (1), has an especially strong impact on the non-Kitaev couplings J, Γ, Γ'. As a result, the relative strength (J/K, etc.) of these "undesired" terms is very sensitive to Δ variations. This suggests the orbital splitting Δ as an efficient (and experimentally accessible) parameter that controls the proximity of cobaltates to the Kitaev-model regime.

Another important parameter in the theory is the U/Δ_{pd} ratio. In contrast to Ir/Ru-based Mott insulators with small $U/\Delta_{pd} \sim 0.5$, cobaltates are charge-transfer insulators [17], with typical values of $U/\Delta_{pd} \sim 2$–3 depending on the material chemistry. Including both Mott-Hubbard U and charge-transfer Δ_{pd} excitations, we have calculated [26] the exchange couplings as a function of U/Δ_{pd} and Δ/λ. Figure 3(a) shows that Kitaev coupling K is not much sensitive to U/Δ_{pd} variations. On the other hand, the non-Kitaev terms, especially Heisenberg coupling J, are quite sensitive to U/Δ_{pd}, see Figs. 3(b)–3(d). However, their values relative to K remain small over a broad range of parameters.

Phase diagram.—Having quantified the exchange parameters in Hamiltonian (2), we are now ready to address the corresponding ground states. As Kitaev coupling is the leading term, the model is highly frustrated. We therefore employ exact diagonalization (ED) which has been widely used to study phase behavior of the extended Kitaev-Heisenberg models (see, e.g., Refs. [11,35–39]). In particular, by utilizing the method of coherent spin states [38,39], we can detect and identify the magnetically ordered phases (including easy-axis directions for the ordered moments). When non-Kitaev couplings are small (roughly below 10% of the FM K value), a quantum spin-liquid state is expected. Reflecting the unique feature of the Kitaev model [1], this state is characterized by short-range spin correlations that are vanishingly small beyond nearest-neighbors [11].

The resulting phase diagram, along with the data quantifying spin correlations beyond NN distances, is presented in Figs. 3(e) and 3(f). The main trends in the phase map are easy to understand considering the variations of non-Kitaev couplings with Δ/λ and U/Δ_{pd}. As we see in Figs. 3(c) and 3(d), Γ' exactly vanishes at the $\Delta = 0$ line, and Γ is very small too. Thus, in the cubic limit, the model (2) essentially becomes the well-studied $K-J$ model, with

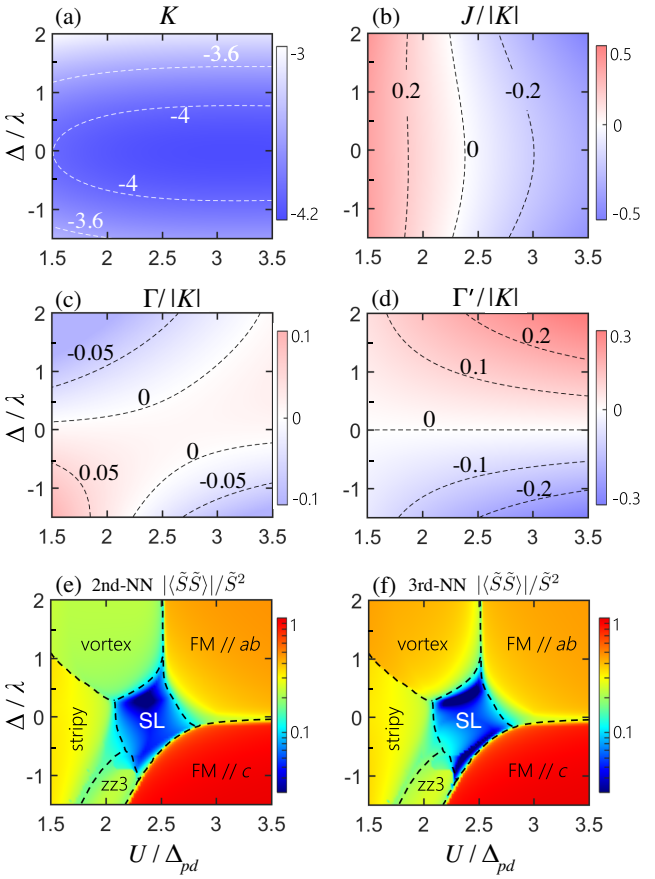

FIG. 3. (a) Kitaev coupling K (in units of t^2/U), and (b)–(d) the relative values of $J/|K|$, $\Gamma/|K|$, and $\Gamma'/|K|$ as a function of Δ/λ and U/Δ_{pd}. For convenience, specific values of parameters are indicated by contour lines. (e)–(f) The corresponding phase diagram obtained by ED of the model on a hexagon-shaped 24-site cluster. As in Fig. 1, the color maps quantify the strength of (e) second-NN and (f) third-NN spin correlations, which drop sharply in the SL phase (small but finite values are due to deviations from the pure Kitaev model [11]).

large FM Kitaev K term, and J correction changing from AF $J > 0$ to FM $J < 0$ as a function of U/Δ_{pd}. Consequently, the ground state changes from stripy AF (at small U/Δ_{pd}) to FM order at large U/Δ_{pd}, through the Kitaev SL phase in between [35]. In the SL phase, spin correlations are indeed short-ranged and bond-selective: for z-type NN bonds, we find $\langle \tilde{S}^z \tilde{S}^z \rangle / \tilde{S}^2 \simeq 0.52$ (as in the Kitaev model), while they nearly vanish at farther distances, see Figs. 3(e) and 3(f).

As we switch on the trigonal field Δ, the Γ' term comes into play confining the SL phase to the window of $|\Delta|/\lambda < 1$ (where $|\Gamma'/K| < 0.1$). In the FM phases, the sign of Γ' decides the direction of the FM moments. On the left-top (left-bottom) part of the phase map, where Heisenberg coupling J is AF, the stripy state gives way to a vortex-type [34] (zigzag-type) ordering, stabilized by the combined effect of Γ and Γ' terms.

To summarize up to now, the nearest-neighbor pseudospin Hamiltonian is dominated by the FM Kitaev model, which appears to be robust against trigonal splitting of orbitals. Subleading terms, represented mostly by J and Γ' couplings, shape the phase diagram, which includes a sizeable SL area. While these observations are encouraging, it is crucial to inspect how the picture is modified by longer range interactions, especially by the third-NN Heisenberg coupling $J_3\tilde{\boldsymbol{S}}_i \cdot \tilde{\boldsymbol{S}}_j$, which appears to be one of the major obstacles on the way to a Kitaev SL in $5d$ and $4d$ compounds [5,12]. We have no reliable estimate for J_3, since long-range interactions involve multiple exchange channels and are thus sensitive to material chemistry details. As such, they have to be determined experimentally. We note that $|J_3/K| \simeq 0.1$ was estimated [40,41] in the $4d$ compound $RuCl_3$; in cobaltates with more localized $3d$ orbitals [13], this ratio is expected to be smaller.

Adding a J_3 term to the model (2), we have reexamined the ground states and found that the Kitaev SL phase is stable up to $|J_3/K| \sim 0.06$ [26]. The modified phase diagram, obtained for a representative value of $J_3 = 0.15t^2/U \simeq 0.04|K|$, is shown in Fig. 1 [42]. Its comparison with Fig. 3 tells that the main effect of J_3 is to support the zigzag-type states (with different orientation of moments) at the expense of other phases. Note also that the SL area is shifted to the right, where FM J and AF J_3 tend to frustrate each other. The phase diagram in Fig. 1 should be generic to Co^{2+} honeycomb systems, and will be used in the following discussion.

Honeycomb lattice cobaltates.—A number of such compounds are known: $A_3Co_2SbO_6$ ($A = Na, Ag, Li$) [18–20,43,44], $Na_2Co_2TeO_6$ [18,45–47], $BaCo_2(XO_4)_2$ ($X = As, P$) [48–51], $CoTiO_3$ [52–54], $CoPS_3$ [55,56]. They are quasi-two-dimensional magnets; within the ab planes, zigzag or FM order is most common.

Traditionally, experimental data in Co^{2+} compounds is analyzed in terms of an effective $\tilde{S} = 1/2$ models of XXZ type [48,50,54,57–59]. As $\tilde{S} = 1/2$ magnons ($\sim$10 meV) are well separated from higher lying spin-orbit excitations ($\sim$30 meV), the pseudospin picture itself is well justified; however, a conventional XXZ model neglects the bond-directional nature of pseudospin $\tilde{S} = 1/2$ interactions. A general message of our work is that a proper description of magnetism in cobaltates should be based on the model of Eq. (2), supplemented by longer-range interactions. We note in passing that the XXZ model also follows from Eq. (2) when the Kitaev-type anisotropy is suppressed [34]; however, such an extreme limit is unlikely for realistic trigonal fields, given the robustness of the K coupling, see Fig. 3.

As an example, we consider $Na_3Co_2SbO_6$ which has low Néel temperature and a reduced ordered moment [20]. Analyzing the magnetic susceptibility data [20] including all spin-orbit levels [26], we obtain a positive trigonal field $\Delta \simeq 38$ meV and $\lambda \simeq 28$ meV; these values are typical for Co^{2+} ions in an octahedral environment (see, e.g., Ref. [54]). With $\Delta/\lambda \simeq 1.36$, we evaluate $\tilde{S} = 1/2$ doublet g factors $g_{ab} \simeq 4.6$ and $g_c \simeq 3$, from which a saturated moment of $2.3\mu_B$, consistent with the magnetization data [20], follows.

Zigzag-ordered moments in $Na_3Co_2SbO_6$ are confined to the ab plane [20]; this corresponds to the zz1 phase in Fig. 1. The easy-plane anisotropy is due to the Γ' term, which is positive for $\Delta > 0$, see Fig. 3(d). Regarding the location of $Na_3Co_2SbO_6$ on the U/Δ_{pd} axis of Fig. 1, we believe it is close to the FM$//ab$ phase, based on the following observations. First, a sister compound $Li_3Co_2SbO_6$ has ab-plane FM order [44] (most likely due to smaller Co-O-Co bond angle, 91° versus 93°, slightly enhancing the FM J value). Second, zigzag order gives way to fully polarized state at small magnetic fields [18,20]. These facts imply that zz1 and FM$//ab$ states are closely competing in $Na_3Co_2SbO_6$.

Based on the above considerations, we roughly locate $Na_3Co_2SbO_6$ in the phase diagram as shown in Fig. 1. In this parameter area, the exchange couplings are $K \simeq -3.6t^2/U$, $J/|K| \sim -0.14$, $\Gamma/|K| \sim -0.03$, and $\Gamma'/|K| \sim 0.16$, see Figs. 3(a)–3(d). The small values of J, Γ, Γ' imply the proximity to the Kitaev model, explaining a strong reduction of the ordered moments from their saturated values [20]. As a crucial test for our theory, we show in Fig. 4 the expected spin excitations. The large FM Kitaev interaction enhances magnon spectral weight near $\boldsymbol{q} = 0$ and leads to its anisotropy in momentum space, see Figs. 4(a) and 4(b).

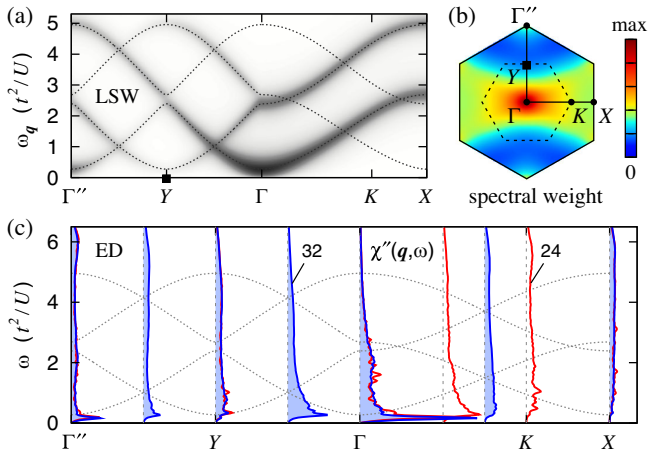

FIG. 4. Spin excitation spectrum expected in $Na_3Co_2SbO_6$. The parameters $K = -3.6$, $J = -0.5$, $\Gamma = -0.1$, $\Gamma' = 0.6$ (in units of t^2/U) follow from our theory, while $J_3 = 0.15$ is added "by hand" [63] to stabilize the zigzag order. (a) Magnon dispersions and intensities from linear spin wave (LSW) theory. (b) The energy-integrated magnon intensity over the Brillouin zone. The intensity is largest around Γ, i.e., away from the Bragg point Y. (c) Exact diagonalization results for hexagonal 24- and 32-site clusters. Plotted is the trace $\chi''(\boldsymbol{q}, \omega)$ of the spin susceptibility tensor [26], which comprises the low-energy magnon peak and a broad continuum.

The ED results in Fig. 4(c) show that, as a consequence of the dominant Kitaev coupling, magnons are strongly renormalized and only survive at low energies, and a broad continuum of excitations [41,60] as in $RuCl_3$ [61,62] emerges. Neutron scattering experiments on $Na_3Co_2SbO_6$ are desired to verify these predictions.

If the above picture is confirmed by experiments, the next step should be to drive $Na_3Co_2SbO_6$ into the Kitaev SL state. As suggested by Fig. 1, this requires a reduction of the trigonal field by ~20 meV, e.g., by means of strain or pressure control. At this point, the relative smallness of SOC for 3*d* Co ions comes as a great advantage: while strong enough to form the pseudospin moments, it makes the lattice manipulation of the $\tilde{S} = 1/2$ wave functions (and hence magnetism) far easier than in iridates [64]. Monitoring the magnetic behavior of $Na_3Co_2SbO_6$ and other honeycomb cobaltates under uniaxial pressure would be thus very interesting.

To conclude, we have presented a comprehensive theory of exchange interactions in honeycomb cobaltates, and studied their magnetic phase behavior. The analysis of $Na_3Co_2SbO_6$ data suggests that this compound is proximate to a Kitaev SL phase and could be driven there by a *c*-axis compression. A broader message is that as one goes from 5*d* Ir to 4*d* Ru and further to 3*d* Co, magnetic *d* orbitals become more localized, and this should improve the conditions for realization of the nearest-neighbor-only interaction model designed by Kitaev.

We thank A. Yaresko, T. Takayama, and A. Smerald for discussions, and M. Songvilay for sharing unpublished data. G. Kh. acknowledges support by the European Research Council under Advanced Grant No. 669550 (Com4Com). J. Ch. acknowledges support by Czech Science Foundation (GAČR) under Project No. GA19-16937S and MŠMT ČR under NPU II Project No. CEITEC 2020 (LQ1601). Computational resources were supplied by the Project "e-Infrastruktura CZ" (No. e-INFRA LM2018140) provided within the program Projects of Large Research, Development and Innovations Infrastructures.

[1] A. Kitaev, Ann. Phys. (N.Y.) **321**, 2 (2006).
[2] L. Savary and L. Balents, Rep. Prog. Phys. **80**, 016502 (2017).
[3] M. Hermanns, I. Kimchi, and J. Knolle, Annu. Rev. Condens. Matter Phys. **9**, 17 (2018).
[4] S. Trebst, arXiv:1701.07056.
[5] S. M. Winter, A. A. Tsirlin, M. Daghofer, J. van den Brink, Y. Singh, P. Gegenwart, and R. Valentí, J. Phys. Condens. Matter **29**, 493002 (2017).
[6] H. Takagi, T. Takayama, G. Jackeli, G. Khaliullin, and S. E. Nagler, Nat. Rev. Phys. **1**, 264 (2019).
[7] Y. Motome and J. Nasu, J. Phys. Soc. Jpn. **89**, 012002 (2020).
[8] G. Khaliullin, Prog. Theor. Phys. Suppl. **160**, 155 (2005).
[9] G. Jackeli and G. Khaliullin, Phys. Rev. Lett. **102**, 017205 (2009).
[10] K. W. Plumb, J. P. Clancy, L. J. Sandilands, V. V. Shankar, Y. F. Hu, K. S. Burch, H.-Y. Kee, and Y.-J. Kim, Phys. Rev. B **90**, 041112(R) (2014).
[11] J. Chaloupka, G. Jackeli, and G. Khaliullin, Phys. Rev. Lett. **105**, 027204 (2010).
[12] S. M. Winter, Y. Li, H. O. Jeschke, and R. Valentí, Phys. Rev. B **93**, 214431 (2016).
[13] Cf. $\langle r^2 \rangle_{3d} = 1.25$ and $\langle r^2 \rangle_{4d} = 2.31$ for Co^{2+} and Ru^{3+} ions (in a.u.), respectively [14].
[14] A. Abragam and B. Bleaney, *Electron Paramagnetic Resonance of Transition Ions* (Clarendon Press, Oxford, 1970).
[15] H. Liu and G. Khaliullin, Phys. Rev. B **97**, 014407 (2018).
[16] R. Sano, Y. Kato, and Y. Motome, Phys. Rev. B **97**, 014408 (2018).
[17] J. Zaanen, G. A. Sawatzky, and J. W. Allen, Phys. Rev. Lett. **55**, 418 (1985).
[18] L. Viciu, Q. Huang, E. Morosan, H. W. Zandbergen, N. I. Greenbaum, T. McQueen, and R. J. Cava, J. Solid State Chem. **180**, 1060 (2007).
[19] C. Wong, M. Avdeev, and C. D. Ling, J. Solid State Chem. **243**, 18 (2016).
[20] J.-Q. Yan, S. Okamoto, Y. Wu, Q. Zheng, H. D. Zhou, H. B. Cao, and M. A. McGuire, Phys. Rev. Mater. **3**, 074405 (2019).
[21] S. I. Csiszar, M. W. Haverkort, Z. Hu, A. Tanaka, H. H. Hsieh, H.-J. Lin, C. T. Chen, T. Hibma, and L. H. Tjeng, Phys. Rev. Lett. **95**, 187205 (2005).
[22] T. M. Holden, W. J. L. Buyers, E. C. Svensson, R. A. Cowley, M. T. Hutchings, D. Hukin, and R. W. H. Stevenson, J. Phys. C **4**, 2127 (1971).
[23] W. J. L. Buyers, T. M. Holden, E. C. Svensson, R. A. Cowley, and M. T. Hutchings, J. Phys. C **4**, 2139 (1971).
[24] R. Coldea, D. A. Tennant, E. M. Wheeler, E. Wawrzynska, D. Prabhakaran, M. Telling, K. Habicht, P. Smeibidl, and K. Kiefer, Science **327**, 177 (2010).
[25] M. E. Lines, Phys. Rev. **131**, 546 (1963).
[26] See the Supplemental Material at http://link.aps.org/supplemental/10.1103/PhysRevLett.125.047201 for Co^{2+} ionic wave functions, computational details of the exchange couplings and phase diagrams, spin excitation spectra, and the analysis of experimental data in $Na_3Co_2SbO_6$, which includes Refs. [27–33].
[27] G. W. Pratt, Jr. and R. Coelho, Phys. Rev. **116**, 281 (1959).
[28] V. I. Anisimov, J. Zaanen, and O. K. Andersen, Phys. Rev. B **44**, 943 (1991).
[29] W. E. Pickett, S. C. Erwin, and E. C. Ethridge, Phys. Rev. B **58**, 1201 (1998).
[30] H. Jiang, R. I. Gomez-Abal, P. Rinke, and M. Scheffler, Phys. Rev. B **82**, 045108 (2010).
[31] K. Foyevtsova, H. O. Jeschke, I. I. Mazin, D. I. Khomskii, and R. Valentí, Phys. Rev. B **88**, 035107 (2013).
[32] J. Chaloupka and G. Khaliullin, Prog. Theor. Phys. Suppl. **176**, 50 (2008).
[33] S. H. Chun, J.-W. Kim, Jungho Kim, H. Zheng, C. C. Stoumpos, C. D. Malliakas, J. F. Mitchell, K. Mehlawat, Y. Singh, Y. Choi, T. Gog, A. Al-Zein, M. Moretti Sala,

M. Krisch, J. Chaloupka, G. Jackeli, G. Khaliullin, and B. J. Kim, Nat. Phys. **11**, 462 (2015).
[34] J. Chaloupka and G. Khaliullin, Phys. Rev. B **92**, 024413 (2015).
[35] J. Chaloupka, G. Jackeli, and G. Khaliullin, Phys. Rev. Lett. **110**, 097204 (2013).
[36] S. Okamoto, Phys. Rev. Lett. **110**, 066403 (2013).
[37] J. G. Rau, Eric Kin-Ho Lee, and H.-Y. Kee, Phys. Rev. Lett. **112**, 077204 (2014).
[38] J. Chaloupka and G. Khaliullin, Phys. Rev. B **94**, 064435 (2016).
[39] J. Rusnačko, D. Gotfryd, and J. Chaloupka, Phys. Rev. B **99**, 064425 (2019).
[40] S. M. Winter, K. Riedl, D. Kaib, R. Coldea, and R. R. Valentí, Phys. Rev. Lett. **120**, 077203 (2018).
[41] S. M. Winter, K. Riedl, P. A. Maksimov, A. L. Chernyshev, A. Honecker, and R. R. Valentí, Nat. Commun. **8**, 1152 (2017).
[42] In Fig. 1, the Δ/λ axis of Fig. 3 is replaced by Δ, using $\lambda = 28$ meV for Co^{2+} ion.
[43] E. A. Zvereva, M. I. Stratan, A. V. Ushakov, V. B. Nalbandyan, I. L. Shukaev, A. V. Silhanek, M. Abdel-Hafiez, S. V. Streltsov, and A. N. Vasiliev, Dalton Trans. **45**, 7373 (2016).
[44] M. I. Stratan, I. L. Shukaev, T. M. Vasilchikova, A. N. Vasiliev, A. N. Korshunov, A. I. Kurbakov, V. B. Nalbandyan, and E. A. Zvereva, New J. Chem. **43**, 13545 (2019).
[45] E. Lefrançois, M. Songvilay, J. Robert, G. Nataf, E. Jordan, L. Chaix, C. V. Colin, P. Lejay, A. Hadj-Azzem, R. Ballou, and V. Simonet, Phys. Rev. B **94**, 214416 (2016).
[46] A. K. Bera, S. M. Yusuf, A. Kumar, and C. Ritter, Phys. Rev. B **95**, 094424 (2017).
[47] W. Yao and Y. Li, Phys. Rev. B **101**, 085120 (2020).
[48] L. P. Regnault, C. Boullier, and J. Y. Henry, Physica (Amsterdam) **385B**, 425 (2006).
[49] R. Zhong, T. Gao, N. P. Ong, and R. J. Cava, Sci. Adv. **6**, eaay6953 (2020).
[50] H. S. Nair, J. M. Brown, E. Coldren, G. Hester, M. P. Gelfand, A. Podlesnyak, Q. Huang, and K. A. Ross, Phys. Rev. B **97**, 134409 (2018).
[51] R. Zhong, M. Chung, T. Kong, L. T. Nguyen, S. Lei, and R. J. Cava, Phys. Rev. B **98**, 220407(R) (2018).
[52] R. E. Newnham, J. H. Fang, and R. P. Santoro, Acta Crystallogr. **17**, 240 (1964).
[53] A. M. Balbashov, A. A. Mukhin, V. Y. Ivanov, L. D. Iskhakova, and M. E. Voronchikhina, Low Temp. Phys. **43**, 965 (2017).
[54] B. Yuan, I. Khait, G.-J. Shu, F. C. Chou, M. B. Stone, J. P. Clancy, A. Paramekanti, and Y.-J. Kim, Phys. Rev. X **10**, 011062 (2020).
[55] R. Brec, Solid State Ionics **22**, 3 (1986).
[56] A. R. Wildes, V. Simonet, E. Ressouche, R. Ballou, and G. J. McIntyre, J. Phys. Condens. Matter **29**, 455801 (2017).
[57] M. T. Hutchings, J. Phys. C **6**, 3143 (1973).
[58] K. Tomiyasu, M. K. Crawford, D. T. Adroja, P. Manuel, A. Tominaga, S. Hara, H. Sato, T. Watanabe, S. I. Ikeda, J. W. Lynn, K. Iwasa, and K. Yamada, Phys. Rev. B **84**, 054405 (2011).
[59] K. A. Ross, J. M. Brown, R. J. Cava, J. W. Krizan, S. E. Nagler, J. A. Rodriguez-Rivera, and M. B. Stone, Phys. Rev. B **95**, 144414 (2017).
[60] M. Gohlke, R. Verresen, R. Moessner, and F. Pollmann, Phys. Rev. Lett. **119**, 157203 (2017).
[61] A. Banerjee, P. Lampen-Kelley, J. Knolle, C. Balz, A. A. Aczel, B. Winn, Y. Liu, D. Pajerowski, J. Yan, C. A. Bridges, A. T. Savici, B. C. Chakoumakos, M. D. Lumsden, D. A. Tennant, R. Moessner, D. G. Mandrus, and S. E. Nagler, npj Quantum Mater. **3**, 8 (2018).
[62] L. J. Sandilands, Y. Tian, K. W. Plumb, Y.-J. Kim, and K. S. Burch, Phys. Rev. Lett. **114**, 147201 (2015).
[63] In fact, the choice of J_3 is dictated by the close proximity of zz1 and FM$//ab$ states in $Na_3Co_2SbO_6$. Classically, they differ by $J - \Gamma + 3J_3$; this gives a rough idea of $J_3 \sim -J/3$ (as Γ is very small).
[64] H. Liu and G. Khaliullin, Phys. Rev. Lett. **122**, 057203 (2019).

Supplemental Material for Kitaev Spin Liquid in $3d$ Transition Metal Compounds

Huimei Liu,[1] Jiří Chaloupka,[2,3] and Giniyat Khaliullin[1]

[1]*Max Planck Institute for Solid State Research, Heisenbergstrasse 1, D-70569 Stuttgart, Germany*
[2]*Department of Condensed Matter Physics, Faculty of Science, Masaryk University, Kotlářská 2, 61137 Brno, Czech Republic*
[3]*Central European Institute of Technology, Masaryk University, Kamenice 753/5, 62500 Brno, Czech Republic*

(Dated: May 6, 2020)

I. Single-ion wavefunctions

The d^7 Co^{2+} ions in an octahedral crystal field have predominantly $t_{2g}^5 e_g^2$ configuration with a high spin $S = 3/2$ [1]. A trigonal distortion along Z-axis splits the t_{2g} manifold into an orbital singlet a_{1g} and a doublet e'_g by energy Δ, see Fig. S1(a,b). In the electron representation, it is captured by the Hamiltonian $H_\Delta = \frac{1}{3}\Delta(2n_{a_{1g}} - n_{e'_g})$. In terms of the effective angular momentum $L = 1$ of the Co^{2+} ions, the a_{1g}-hole configuration corresponds to $L_Z = 0$, while the e'_g doublet hosts the $L_Z = \pm 1$ states. Consequently, the trigonal field Hamiltonian translates into $H_\Delta = \Delta(L_Z^2 - \frac{2}{3})$. The following relations between the L-states and orbitals hold:

$$
\begin{aligned}
|L_Z = 0\rangle &= \frac{1}{\sqrt{3}}\left(|a\rangle + |b\rangle + |c\rangle\right), \\
|L_Z = \pm 1\rangle &= \pm\frac{1}{\sqrt{3}}\left(e^{\pm i\frac{2\pi}{3}}|a\rangle + e^{\mp i\frac{2\pi}{3}}|b\rangle + |c\rangle\right),
\end{aligned}
\tag{S1}
$$

where shorthand notations $a = d_{yz}$, $b = d_{zx}$, and $c = d_{xy}$ are used.

Diagonalization of $H_\Delta = \Delta(L_Z^2 - \frac{2}{3})$ and $H_\lambda = \lambda \boldsymbol{L}\cdot\boldsymbol{S}$ results in a level structure shown in Fig. S1(c). The states are labeled according to the total angular momentum $J_{\rm eff} = \widetilde{\frac{1}{2}}$, $\widetilde{\frac{3}{2}}$, and $\widetilde{\frac{5}{2}}$. The ground state Kramers doublet hosts a pseudospin $\widetilde{S} = 1/2$; its wavefunctions, written in the basis of $|S_Z, L_Z\rangle$, read as:

$$
\left|\widetilde{\frac{1}{2}}, \pm\widetilde{\frac{1}{2}}\right\rangle = \mathcal{C}_1\left|\pm\frac{3}{2}, \mp 1\right\rangle + \mathcal{C}_2\left|\pm\frac{1}{2}, 0\right\rangle + \mathcal{C}_3\left|\mp\frac{1}{2}, \pm 1\right\rangle. \tag{S2}
$$

The coefficients obey a relation $\mathcal{C}_1 : \mathcal{C}_2 : \mathcal{C}_3 = \frac{\sqrt{6}}{r_1} : -1 : \frac{\sqrt{8}}{r_1+2}$, where the parameter $r_1 > 0$ is determined by the equation $\frac{\Delta}{\lambda} = \frac{r_1+3}{2} - \frac{3}{r_1} - \frac{4}{r_1+2}$ [2]. The ground state energy is

$$
E_{\rm GS} = \frac{\Delta}{3} - \frac{\lambda}{2}(r_1 + 3). \tag{S3}
$$

The exchange Hamiltonian between the pseudospins $\widetilde{S} = 1/2$ is obtained by projecting the Kugel-Khomskii type spin-orbital Hamiltonians onto the ground state doublet (S2).

We also specify the excited states, which will be needed in Sec. IV to calculate the magnetic susceptibility. The wavefunctions and energies for $\left|\widetilde{\frac{3}{2}}, \pm\widetilde{\frac{1}{2}}\right\rangle$ and $\left|\widetilde{\frac{5}{2}}, \pm\widetilde{\frac{1}{2}}\right\rangle$ states share the same form as of Eq. S2 and Eq. S3, but with different r_1. Namely, the above equation $\frac{\Delta}{\lambda} = \frac{r_1+3}{2} - \frac{3}{r_1} - \frac{4}{r_1+2}$ has three roots. The root $r_1 > 0$ corresponds to the ground state. The other two roots with $-2 < r_1 < 0$ and $r_1 < -2$ correspond to $\left|\widetilde{\frac{3}{2}}, \pm\widetilde{\frac{1}{2}}\right\rangle$ and $\left|\widetilde{\frac{5}{2}}, \pm\widetilde{\frac{1}{2}}\right\rangle$ states, respectively. The wavefunctions and energies of the remaining states are:

$$
\begin{aligned}
\left|\widetilde{\frac{3}{2}}, \pm\widetilde{\frac{3}{2}}\right\rangle &= c_\varphi\left|\pm\frac{3}{2}, 0\right\rangle - s_\varphi\left|\pm\frac{1}{2}, \pm 1\right\rangle, & E(\widetilde{\tfrac{3}{2}}, \pm\widetilde{\tfrac{3}{2}}) &= -\tfrac{1}{2}\sqrt{\left(\Delta + \tfrac{1}{2}\lambda\right)^2 + 6\lambda^2} + \tfrac{1}{4}\lambda - \tfrac{1}{6}\Delta, \\
\left|\widetilde{\frac{5}{2}}, \pm\widetilde{\frac{3}{2}}\right\rangle &= s_\varphi\left|\pm\frac{3}{2}, 0\right\rangle + c_\varphi\left|\pm\frac{1}{2}, \pm 1\right\rangle, & E(\widetilde{\tfrac{5}{2}}, \pm\widetilde{\tfrac{3}{2}}) &= \tfrac{1}{2}\sqrt{\left(\Delta + \tfrac{1}{2}\lambda\right)^2 + 6\lambda^2} + \tfrac{1}{4}\lambda - \tfrac{1}{6}\Delta, \\
\left|\widetilde{\frac{5}{2}}, \pm\widetilde{\frac{5}{2}}\right\rangle &= \left|\pm\frac{3}{2}, \pm 1\right\rangle, & E(\widetilde{\tfrac{5}{2}}, \pm\widetilde{\tfrac{5}{2}}) &= \tfrac{3}{2}\lambda + \tfrac{2}{3}\Delta.
\end{aligned}
\tag{S4}
$$

Here, $c_\varphi = \cos\varphi$, $s_\varphi = \sin\varphi$, and $\tan 2\varphi = 2\sqrt{6}\lambda/(2\Delta + \lambda)$.

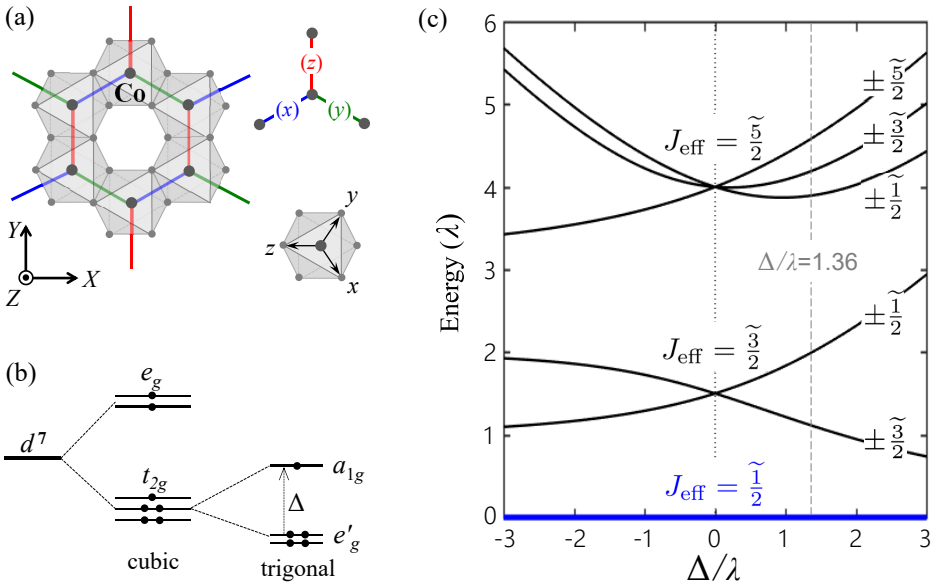

FIG. S1: (a) Top view of the honeycomb cobaltate plane, x, y, and z type NN-bonds are shown in blue, green, and red colors, respectively. The definition of global X, Y, Z and the local cubic x, y, z axes are shown in insets. (b) High-spin $d^7(t_{2g}^5 e_g^2)$ configuration in the trigonal crystal field Δ. (c) Splitting of $S = 3/2$, $L = 1$ manifold of Co^{2+} ion under spin-orbit coupling λ and trigonal field Δ. At $\Delta/\lambda = 1.36$ (appropriate for $Na_3Co_2SbO_6$), the first excited state energy is about $\lambda \sim 30$ meV.

II. Pseudospin $\widetilde{S} = 1/2$ Hamiltonian and calculation of its parameters

In the cubic reference frame, pseudospin-1/2 interactions on z-type bonds have a general form

$$\mathcal{H}_{ij}^{(z)} = K\widetilde{S}_i^z\widetilde{S}_j^z + J\widetilde{\boldsymbol{S}}_i\cdot\widetilde{\boldsymbol{S}}_j + \Gamma(\widetilde{S}_i^x\widetilde{S}_j^y + \widetilde{S}_i^y\widetilde{S}_j^x) + \Gamma'(\widetilde{S}_i^x\widetilde{S}_j^z + \widetilde{S}_i^z\widetilde{S}_j^x + \widetilde{S}_i^y\widetilde{S}_j^z + \widetilde{S}_i^z\widetilde{S}_j^y)\,. \tag{S5}$$

The interactions on x and y type bonds are obtained by cyclic permutations among $\widetilde{S}_j^x$, $\widetilde{S}_j^y$, and $\widetilde{S}_j^z$.

The Hamiltonian in Eq. S5 can also be written in global XYZ reference frame [3]:

$$\begin{aligned}\mathcal{H}_{ij}^{(\gamma)} =& J_{XY}\left(\widetilde{S}_i^X\widetilde{S}_j^X + \widetilde{S}_i^Y\widetilde{S}_j^Y\right) + J_Z\widetilde{S}_i^Z\widetilde{S}_j^Z \\ &+A\left[c_\gamma\left(\widetilde{S}_i^X\widetilde{S}_j^X - \widetilde{S}_i^Y\widetilde{S}_j^Y\right) - s_\gamma\left(\widetilde{S}_i^X\widetilde{S}_j^Y + \widetilde{S}_i^Y\widetilde{S}_j^X\right)\right] \\ &-B\sqrt{2}\left[c_\gamma\left(\widetilde{S}_i^X\widetilde{S}_j^Z + \widetilde{S}_i^Z\widetilde{S}_j^X\right) + s_\gamma\left(\widetilde{S}_i^Y\widetilde{S}_j^Z + \widetilde{S}_i^Z\widetilde{S}_j^Y\right)\right],\end{aligned} \tag{S6}$$

with $c_\gamma \equiv \cos\phi_\gamma$ and $s_\gamma \equiv \sin\phi_\gamma$. The angles $\phi_\gamma = 0, \frac{2\pi}{3}, \frac{4\pi}{3}$ refer to the z, x, and y type bonds, respectively. The transformations between the two sets of parameters entering Eq. S5 and Eq. S6 are:

$$\begin{aligned} J_{XY} &= J + \tfrac{1}{3}K - \tfrac{1}{3}(\Gamma + 2\Gamma')\,, & K &= A + 2B\,, \\ J_Z &= J + \tfrac{1}{3}K + \tfrac{2}{3}(\Gamma + 2\Gamma')\,, & J &= \tfrac{1}{3}(2J_{XY} + J_Z - A - 2B)\,, \\ A &= \tfrac{1}{3}K + \tfrac{2}{3}(\Gamma - \Gamma')\,, & \Gamma &= \tfrac{2}{3}(A - B) + \tfrac{1}{3}(J_Z - J_{XY})\,, \\ B &= \tfrac{1}{3}K - \tfrac{1}{3}(\Gamma - \Gamma')\,, & \Gamma' &= \tfrac{1}{3}(J_Z - J_{XY} + B - A)\,. \end{aligned} \tag{S7}$$

Since the pseudospin wavefunctions (S2) are defined in the trigonal XYZ basis, it is technically simpler to derive $\widetilde{S} = 1/2$ Hamiltonian in a form of (S6), and then convert the results onto a cubic xyz reference frame via Eqs. S7.

As discussed in the main text, there are three basic exchange channels in d^7 systems, which we consider now in detail. General form of the Kugel-Khomskii type spin-orbital Hamiltonians were obtained earlier [4]; for completeness, they will be reproduced below. Here, the major task is to derive the corresponding pseudospin-1/2 Hamiltonians in a realistic case of finite trigonal splitting of t_{2g} orbitals. As the $\widetilde{S} = 1/2$ wavefunctions (S2) are somewhat complicated, the calculations are tedious but can still be done analytically.

1. t_{2g}-t_{2g} exchange contributions

1.1 Intersite U processes

The spin-orbital Hamiltonian for these exchange processes is given by equations (A2) and (3) of Ref. [4]:

$$\begin{aligned}\mathcal{H}_{11}^{(z)} =&\frac{4t^2}{9}\frac{1}{E_1}(\boldsymbol{S}_i\cdot\boldsymbol{S}_j+S^2)(a_i^\dagger b_i a_j^\dagger b_j+b_i^\dagger a_i b_j^\dagger a_j)\\
&+\frac{4t^2}{27}\left(\frac{1}{E_3}+\frac{2}{E_2}\right)(\boldsymbol{S}_i\cdot\boldsymbol{S}_j+S^2)(n_{ia}n_{jb}+n_{ib}n_{ja})\\
&-\frac{t^2}{6}\left(\frac{1}{E_1}-\frac{1}{E_2}\right)(\boldsymbol{S}_i\cdot\boldsymbol{S}_j+S^2)\left[(n_{ia}-n_{jb})^2+(n_{ib}-n_{ja})^2\right]\\
&-\frac{4t^2}{27}\left(\frac{1}{E_2}-\frac{1}{E_3}\right)(\boldsymbol{S}_i\cdot\boldsymbol{S}_j-S^2)(a_i^\dagger b_i b_j^\dagger a_j+b_i^\dagger a_i a_j^\dagger b_j)\\
&+\frac{t^2}{6}\left(\frac{3}{E_1}+\frac{1}{E_2}-\frac{4}{E_3}\right)(n_{ia}n_{jb}+n_{ib}n_{ja})\\
&-\frac{4}{9}\frac{tt'}{U}(\boldsymbol{S}_i\cdot\boldsymbol{S}_j+S^2)\left[(a_i^\dagger c_i c_j^\dagger b_j+c_i^\dagger a_i b_j^\dagger c_j)+(a\leftrightarrow b)\right]\\
&+\frac{4}{9}\frac{t'^2}{U}(\boldsymbol{S}_i\cdot\boldsymbol{S}_j-S^2)\,n_{ic}n_{jc}.\end{aligned}\tag{S8}$$

Here $n_a = a^\dagger a$, etc. denote the orbital occupations, t is the hopping between a and b orbitals via ligand ions, t' is the direct overlap of c orbitals. The Mott-Hubbard excitation energies are $E_1 = U - 3J_H$, $E_2 = U + J_H$, and $E_3 = U + 4J_H$, where U and J_H are Coulomb repulsion and Hund's coupling on Co^{2+} ions.

Now, we need to express various combinations of the spin and orbital operators above in terms of the pseudospins $\widetilde{S} = 1/2$ defined by Eq. S2. To this end, we have derived a general projection table, presented in subsection 4 below. Using this table, we obtain the pseudospin Hamiltonian in the form of Eq. S6, with the following exchange constants:

$$\begin{aligned}J_{11}^{XY} =&\frac{4t^2}{27}\left(\frac{3}{E_1}-\frac{1}{E_2}+\frac{1}{E_3}\right)\left(2u_4^2+2u_6^2-\tfrac{13}{2}u_5^2\right)+\frac{t^2}{27}\left(\frac{9}{E_1}-\frac{1}{E_2}+\frac{4}{E_3}\right)\left(\tfrac{2}{9}u_1^2-u_4^2-\tfrac{1}{2}u_5^2\right)\\
&-\frac{2t^2}{9}\left(\frac{1}{E_1}-\frac{1}{E_2}\right)u_1^2-\frac{4}{9}\frac{tt'}{U}\left(4u_6^2-2u_4^2+\tfrac{13}{2}u_5^2\right)+\frac{4}{9}\frac{t'^2}{U}\left(\tfrac{1}{9}u_1^2+u_4^2+\tfrac{1}{2}u_5^2\right),\\
J_{11}^{Z} =&\frac{4t^2}{27}\left(\frac{3}{E_1}-\frac{1}{E_2}+\frac{1}{E_3}\right)\left[2u_7^2+u_3^2-\tfrac{3}{8}(u_2-1)^2\right]+\frac{t^2}{27}\left(\frac{9}{E_1}-\frac{1}{E_2}+\frac{4}{E_3}\right)\left(\tfrac{2}{9}u_2^2-2u_3^2\right)\\
&-\frac{2t^2}{9}\left(\frac{1}{E_1}-\frac{1}{E_2}\right)u_2^2-\frac{4}{9}\frac{tt'}{U}\left[4u_7^2-u_3^2-\tfrac{3}{4}(u_2-1)^2\right]+\frac{4}{9}\frac{t'^2}{U}\left(\tfrac{1}{9}u_2^2+2u_3^2\right),\\
A_{11} =&-\frac{4t^2}{27}\left(\frac{3}{E_1}-\frac{1}{E_2}+\frac{1}{E_3}\right)\left(4u_4u_6+\tfrac{13}{2}u_5^2\right)+\frac{t^2}{27}\left(\frac{9}{E_1}-\frac{1}{E_2}+\frac{4}{E_3}\right)\left(\tfrac{2}{3}u_1u_4+u_5^2\right)\\
&-\frac{t^2}{3}\left(\frac{1}{E_1}-\frac{1}{E_2}\right)u_1u_4-\frac{4}{9}\frac{tt'}{U}\left(4u_4u_6-13u_5^2\right)+\frac{4}{9}\frac{t'^2}{U}\left(\tfrac{1}{2}u_5^2-\tfrac{2}{3}u_1u_4\right),\\
B_{11} =&\frac{4t^2}{27}\left(\frac{3}{E_1}-\frac{1}{E_2}+\frac{1}{E_3}\right)\left[u_3(u_6-u_4)-\frac{u_5}{\sqrt{2}}\left(u_7-\tfrac{9}{4}u_2+\tfrac{9}{4}\right)\right]+\frac{t^2}{27}\left(\frac{9}{E_1}-\frac{1}{E_2}+\frac{4}{E_3}\right)\left[u_3\left(\tfrac{1}{3}u_1+2u_4\right)-\tfrac{1}{3\sqrt{2}}u_2u_5\right]\\
&-\frac{t^2}{6}\left(\frac{1}{E_1}-\frac{1}{E_2}\right)\left(u_1u_3-\tfrac{1}{\sqrt{2}}u_2u_5\right)+\frac{4}{9}\frac{tt'}{U}\left[u_3(2u_4+u_6)-\frac{u_5}{\sqrt{2}}\left(u_7-\tfrac{9}{4}u_2+\tfrac{9}{4}\right)\right]-\frac{4}{9}\frac{t'^2}{U}\left[u_3\left(\tfrac{1}{3}u_1-u_4\right)-\tfrac{1}{3\sqrt{2}}u_2u_5\right].\end{aligned}\tag{S9}$$

Coefficients u_i $(i = 1, 2, \ldots, 7)$ are given by Eqs. S33 below; they depend on the spatial shape of the pseudospin wavefunctions (S2), and thus decide how the relative values of the pseudospin interactions vary as a function of trigonal field Δ.

1.2 Charge-transfer processes

The spin-orbital Hamiltonian is (Eq. 9 in Ref. [4]):

$$\mathcal{H}_{12}^{(z)} = \frac{4}{9}\frac{t^2}{\Delta_{pd}+\frac{U_p}{2}}(\boldsymbol{S}_i\cdot\boldsymbol{S}_j - S^2)(n_{ia}n_{jb}+n_{ib}n_{ja}) - \frac{2}{9}\frac{t^2\ J_H^p}{(\Delta_{pd}+\frac{U'_p}{2})^2}\ \boldsymbol{S}_i\cdot\boldsymbol{S}_j(n_{ic}+n_{jc}), \tag{S10}$$

where Δ_{pd} is charge-transfer gap. U_p and $U'_p = U_p - 2J_H^p$ are the intra- and inter-orbital Coulomb repulsion of the ligand p orbitals, respectively, and J_H^p is the Hund's coupling.

Using the projection table of subsection 4, we find the exchange constants in the form of Eq. S6:

$$\begin{aligned}
J_{12}^{XY} &= \frac{4}{9}\frac{t^2}{\Delta_{pd}+\frac{U_p}{2}}\left(\tfrac{2}{9}u_1^2 - u_4^2 - \tfrac{1}{2}u_5^2\right) - \frac{4}{27}\frac{t^2\ J_H^p}{(\Delta_{pd}+\frac{U'_p}{2})^2}\ u_1^2\ ,\\
J_{12}^{Z} &= \frac{4}{9}\frac{t^2}{\Delta_{pd}+\frac{U_p}{2}}\left(\tfrac{2}{9}u_2^2 - 2u_3^2\right) - \frac{4}{27}\frac{t^2\ J_H^p}{(\Delta_{pd}+\frac{U'_p}{2})^2}\ u_2^2\ ,\\
A_{12} &= \frac{4}{9}\frac{t^2}{\Delta_{pd}+\frac{U_p}{2}}\left(\tfrac{2}{3}u_1u_4 + u_5^2\right) + \frac{4}{9}\frac{t^2\ J_H^p}{(\Delta_{pd}+\frac{U'_p}{2})^2}\ u_1u_4\ ,\\
B_{12} &= \frac{4}{9}\frac{t^2}{\Delta_{pd}+\frac{U_p}{2}}\left[u_3\left(\tfrac{1}{3}u_1+2u_4\right) - \tfrac{1}{3\sqrt{2}}u_2u_5\right] + \frac{2}{9}\frac{t^2\ J_H^p}{(\Delta_{pd}+\frac{U'_p}{2})^2}\ \left(u_1u_3 - \tfrac{1}{\sqrt{2}}u_2u_5\right).
\end{aligned} \tag{S11}$$

1.3 Cyclic exchange processes

The spin-orbital Hamiltonian is (Eq. 11 in Ref. [4]):

$$\mathcal{H}_{13}^{(z)} = \frac{4}{9}\frac{t^2}{\Delta_{pd}}(\boldsymbol{S}_i\cdot\boldsymbol{S}_j + S^2)(a_i^\dagger b_i a_j^\dagger b_j + b_i^\dagger a_i b_j^\dagger a_j). \tag{S12}$$

After projection, we obtain the exchange constants as:

$$\begin{aligned}
J_{13}^{XY} &= \frac{4}{9}\frac{t^2}{\Delta_{pd}}\left(2u_4^2 + 2u_6^2 - \tfrac{13}{2}u_5^2\right), & J_{13}^{Z} &= \frac{4}{9}\frac{t^2}{\Delta_{pd}}\left[2u_7^2 + u_3^2 - \tfrac{3}{8}(u_2-1)^2\right],\\
A_{13} &= -\frac{4}{9}\frac{t^2}{\Delta_{pd}}\left(4u_4u_6 + \tfrac{13}{2}u_5^2\right), & B_{13} &= \frac{4}{9}\frac{t^2}{\Delta_{pd}}\left[u_3(u_6-u_4) - \frac{u_5}{\sqrt{2}}\left(u_7 - \tfrac{9}{4}u_2 + \tfrac{9}{4}\right)\right].
\end{aligned} \tag{S13}$$

The total contribution from t_{2g}-t_{2g} hopping channel to Eq. S6 is given by

$$\begin{aligned}
J_1^{XY} &= J_{11}^{XY} + J_{12}^{XY} + J_{13}^{XY}\ , & J_1^{Z} &= J_{11}^{Z} + J_{12}^{Z} + J_{13}^{Z}\ ,\\
A_1 &= A_{11} + A_{12} + A_{13}\ , & B_1 &= B_{11} + B_{12} + B_{13}\ .
\end{aligned} \tag{S14}$$

The corresponding K, J, Γ, and Γ' values can be obtained using Eqs. S7.

2. t_{2g}-e_g exchange contributions

2.1 Intersite U processes

The corresponding spin-orbital exchange Hamiltonian is (Eq. A5 in Ref. [4]):

$$\mathcal{H}_{21}^{(z)} = \frac{4\alpha_1}{9}\frac{tt_e}{\widetilde{U}}(\boldsymbol{S}_i\cdot\boldsymbol{S}_j - S^2)(n_{ic}+n_{jc}) - \frac{tt_e}{6}\frac{\Delta_e}{\Delta_{pd}}\left(\frac{1}{E_1+D} - \frac{1}{E_2+D}\right)\boldsymbol{S}_i\cdot\boldsymbol{S}_j\ (2-n_{ic}-n_{jc}). \tag{S15}$$

Here, $t_e = t_{pd\sigma}^2/\Delta_e$, with $t_{pd\sigma}$ representing hopping between p and e_g orbitals via the charge-transfer gap $\Delta_e = \Delta_{pd}+D$. Parameter D is the splitting between t_{2g} and e_g levels. The constants α_1 and $1/\widetilde{U}$ are:

$$\alpha_1 = 1 - \frac{D^2}{2\Delta_{pd}\Delta_e}\left(\frac{\Delta_{pd}+\Delta_e}{U+2J_H} - 1\right), \qquad \frac{1}{\widetilde{U}} = \frac{1}{6}\left(\frac{2}{E_2+D} + \frac{1}{E_3+D} + \frac{3}{U+2J_H-D}\right). \tag{S16}$$

After projection onto pseudospin-1/2 doublet (S2), we get the exchange constants in the form of Eq. S6:

$$\begin{aligned}
J_{21}^{XY} &= \left[\frac{8\alpha_1}{27}\frac{tt_e}{\widetilde{U}} - \frac{2tt_e}{9}\frac{\Delta_e}{\Delta_{pd}}\left(\frac{1}{E_1+D}-\frac{1}{E_2+D}\right)\right]u_1^2\,,\\
J_{21}^{Z} &= \left[\frac{8\alpha_1}{27}\frac{tt_e}{\widetilde{U}} - \frac{2tt_e}{9}\frac{\Delta_e}{\Delta_{pd}}\left(\frac{1}{E_1+D}-\frac{1}{E_2+D}\right)\right]u_2^2\,,\\
A_{21} &= -\left[\frac{8\alpha_1}{9}\frac{tt_e}{\widetilde{U}} + \frac{tt_e}{3}\frac{\Delta_e}{\Delta_{pd}}\left(\frac{1}{E_1+D}-\frac{1}{E_2+D}\right)\right]u_1u_4\,,\\
B_{21} &= \left[\frac{4\alpha_1}{9}\frac{tt_e}{\widetilde{U}} + \frac{tt_e}{6}\frac{\Delta_e}{\Delta_{pd}}\left(\frac{1}{E_1+D}-\frac{1}{E_2+D}\right)\right]\left(\frac{u_2u_5}{\sqrt{2}}-u_1u_3\right).
\end{aligned} \tag{S17}$$

2.2 Charge-transfer processes

The spin-orbital Hamiltonian describing these processes is (Eq. 19 in Ref. [4]):

$$\mathcal{H}_{22}^{(z)} = \frac{8\alpha_2}{9}\frac{tt_e}{\Delta_{pd}+\frac{U_p}{2}}(\boldsymbol{S}_i\cdot\boldsymbol{S}_j - S^2)(n_{ic}+n_{jc}) - \frac{2\alpha_3}{9}\frac{tt_e\,J_H^p}{(\Delta_{pd}+\frac{D+U_p'}{2})^2}\,\boldsymbol{S}_i\cdot\boldsymbol{S}_j\,(2-n_{ic}-n_{jc}), \tag{S18}$$

where

$$\alpha_2 = 1 - \frac{D}{4(\Delta_e+\frac{U_p}{2})} + \frac{D\,U_p}{8\Delta_{pd}(\Delta_e+\frac{U_p}{2})} - \frac{D}{4\Delta_e}, \qquad \alpha_3 = \frac{(\Delta_{pd}+\Delta_e)^2}{4\Delta_{pd}\Delta_e}\,. \tag{S19}$$

The corresponding pseudospin exchange constants are:

$$\begin{aligned}
J_{22}^{XY} &= \left[\frac{16\alpha_2}{27}\frac{tt_e}{\Delta_{pd}+\frac{U_p}{2}} - \frac{8\alpha_3}{27}\frac{tt_e\,J_H^p}{(\Delta_{pd}+\frac{D+U_p'}{2})^2}\right]u_1^2\,,\\
J_{22}^{Z} &= \left[\frac{16\alpha_2}{27}\frac{tt_e}{\Delta_{pd}+\frac{U_p}{2}} - \frac{8\alpha_3}{27}\frac{tt_e\,J_H^p}{(\Delta_{pd}+\frac{D+U_p'}{2})^2}\right]u_2^2\,,\\
A_{22} &= -\left[\frac{16\alpha_2}{9}\frac{tt_e}{\Delta_{pd}+\frac{U_p}{2}} + \frac{4\alpha_3}{9}\frac{tt_e\,J_H^p}{(\Delta_{pd}+\frac{D+U_p'}{2})^2}\right]u_1u_4\,,\\
B_{22} &= \left[\frac{8\alpha_2}{9}\frac{tt_e}{\Delta_{pd}+\frac{U_p}{2}} + \frac{2\alpha_3}{9}\frac{tt_e\,J_H^p}{(\Delta_{pd}+\frac{D+U_p'}{2})^2}\right]\left(\frac{u_2u_5}{\sqrt{2}}-u_1u_3\right).
\end{aligned} \tag{S20}$$

2.3 Cyclic exchange processes

The corresponding spin-orbital Hamiltonian is (Eq. 22 in Ref. [4]):

$$\mathcal{H}_{23}^{(z)} = -\frac{2\alpha_4}{9}\frac{tt_e}{\Delta_{pd}}(\boldsymbol{S}_i\cdot\boldsymbol{S}_j + S^2)(n_{ic}+n_{ic}), \tag{S21}$$

with $\alpha_4 = 1-\frac{1}{2}\frac{D}{\Delta_{pd}+D}$.

After projection onto pseudospin-1/2 doublet, we obtain:

$$\begin{aligned}
J_{23}^{XY} &= -\frac{4\alpha_4}{27}\frac{tt_e}{\Delta_{pd}}u_1^2\,, & J_{23}^{Z} &= -\frac{4\alpha_4}{27}\frac{tt_e}{\Delta_{pd}}u_2^2\,,\\
A_{23} &= \frac{4\alpha_4}{9}\frac{tt_e}{\Delta_{pd}}u_1u_4\,, & B_{23} &= -\frac{2\alpha_4}{9}\frac{tt_e}{\Delta_{pd}}\left(\frac{u_2u_5}{\sqrt{2}}-u_1u_3\right).
\end{aligned} \tag{S22}$$

The total contribution from t_{2g}-e_g exchange channel to Eq. S6 is given by

$$\begin{aligned}
J_2^{XY} &= J_{21}^{XY}+J_{22}^{XY}+J_{23}^{XY}\,, & J_2^{Z} &= J_{21}^{Z}+J_{22}^{Z}+J_{23}^{Z}\,,\\
A_2 &= A_{21}+A_{22}+A_{23}\,, & B_2 &= B_{21}+B_{22}+B_{23}\,.
\end{aligned} \tag{S23}$$

3. e_g-e_g exchange contribution

The corresponding Hamiltonian is very simple (see Eq. 27 in Ref. [4]):

$$\mathcal{H}_3^{(z)} = -\frac{4}{9}\frac{t_e^2\, J_H^p}{(\Delta_e + \frac{U_p'}{2})^2}\, \boldsymbol{S}_i \cdot \boldsymbol{S}_j. \tag{S24}$$

Note that no orbital operators are involved in this interaction and thus it has no bond-dependence. This is because e_g doublet hosts two electrons with parallel spins, leaving no e_g-orbital degeneracy. After projecting Eq. S24 onto pseudospin subspace, we find

$$J_3^{XY} = -\frac{4}{9}\frac{t_e^2\, J_H^p}{(\Delta_e + \frac{U_p'}{2})^2} u_1^2\,, \qquad J_3^{Z} = -\frac{4}{9}\frac{t_e^2\, J_H^p}{(\Delta_e + \frac{U_p'}{2})^2} u_2^2\,, \tag{S25}$$

while the bond-dependent terms $A_3 = B_3 = 0$. The latter implies that e_g-e_g interaction channel supports the XXZ-type model. In the cubic reference frame, Eq. S5, this translates into $K = 0$ and $\Gamma = \Gamma'$.

Total values of the exchange constants are obtained by summing up t_{2g}-t_{2g}, t_{2g}-e_g, and e_g-e_g contributions [Eqs. S14, S23, and S25, respectively], and converted into K, J, Γ, and Γ' using Eqs. S7.

4. Projection table

Calculating the matrix elements of spin-orbital operators within the pseudospin $\widetilde{S} = 1/2$ doublet (S2), we obtain the correspondence:

$$S_+ = u_1 \widetilde{S}_+\,, \quad S_- = u_1 \widetilde{S}_-\,, \quad S_Z = u_2 \widetilde{S}_Z\,, \tag{S26}$$

$$\begin{aligned}
S_+ n_a &= \sqrt{2} u_3 e^{i\frac{2\pi}{3}} \widetilde{S}_Z + \frac{u_1}{3}\widetilde{S}_+ - u_4 e^{i\frac{4\pi}{3}} \widetilde{S}_-\,, \\
S_- n_a &= \sqrt{2} u_3 e^{-i\frac{2\pi}{3}} \widetilde{S}_Z + \frac{u_1}{3}\widetilde{S}_- - u_4 e^{-i\frac{4\pi}{3}} \widetilde{S}_+\,, \\
S_Z n_a &= \frac{u_2}{3}\widetilde{S}_Z + \frac{u_5}{2}(\widetilde{S}_X - \sqrt{3}\widetilde{S}_Y)\,,
\end{aligned} \tag{S27}$$

$$\begin{aligned}
S_+ n_b &= \sqrt{2} u_3 e^{-i\frac{2\pi}{3}} \widetilde{S}_Z + \frac{u_1}{3}\widetilde{S}_+ - u_4 e^{-i\frac{4\pi}{3}} \widetilde{S}_-\,, \\
S_- n_b &= \sqrt{2} u_3 e^{i\frac{2\pi}{3}} \widetilde{S}_Z + \frac{u_1}{3}\widetilde{S}_- - u_4 e^{i\frac{4\pi}{3}} \widetilde{S}_+\,, \\
S_Z n_b &= \frac{u_2}{3}\widetilde{S}_Z + \frac{u_5}{2}(\widetilde{S}_X + \sqrt{3}\widetilde{S}_Y)\,,
\end{aligned} \tag{S28}$$

$$\begin{aligned}
S_+ n_c &= \sqrt{2} u_3 \widetilde{S}_Z + \frac{u_1}{3}\widetilde{S}_+ - u_4 \widetilde{S}_-\,, \\
S_- n_c &= \sqrt{2} u_3 \widetilde{S}_Z + \frac{u_1}{3}\widetilde{S}_- - u_4 \widetilde{S}_+\,, \\
S_Z n_c &= \frac{u_2}{3}\widetilde{S}_Z - u_5 \widetilde{S}_X\,,
\end{aligned} \tag{S29}$$

$$\begin{aligned}
a^\dagger b &= \tfrac{i}{2\sqrt{3}}[(1-u_2)\widetilde{S}_Z - 6u_5\widetilde{S}_X]\,, \qquad & S_+ a^\dagger b &= -\frac{u_3}{\sqrt{2}}\widetilde{S}_Z + u_6\widetilde{S}_+ - u_4\widetilde{S}_-\,, \\
S_- a^\dagger b &= -\frac{u_3}{\sqrt{2}}\widetilde{S}_Z + u_6\widetilde{S}_- - u_4\widetilde{S}_+\,, \qquad & S_Z a^\dagger b &= u_7\widetilde{S}_Z + \frac{u_5}{2}\widetilde{S}_X\,,
\end{aligned} \tag{S30}$$

$$\begin{aligned}
b^\dagger c &= \tfrac{i}{2\sqrt{3}}[(1-u_2)\widetilde{S}_Z - 3u_5(\sqrt{3}\widetilde{S}_Y - \widetilde{S}_X)]\,, \qquad & S_+ b^\dagger c &= \frac{u_3}{\sqrt{2}} e^{-i\frac{\pi}{3}}\widetilde{S}_Z + u_6\widetilde{S}_+ - u_4 e^{-i\frac{2\pi}{3}}\widetilde{S}_-\,, \\
S_- b^\dagger c &= \frac{u_3}{\sqrt{2}} e^{i\frac{\pi}{3}}\widetilde{S}_Z + u_6\widetilde{S}_- - u_4 e^{i\frac{2\pi}{3}}\widetilde{S}_+\,, \qquad & S_Z b^\dagger c &= u_7\widetilde{S}_Z - \frac{u_5}{4}(\widetilde{S}_X - \sqrt{3}\widetilde{S}_Y)\,,
\end{aligned} \tag{S31}$$

$$c^\dagger a = \tfrac{i}{2\sqrt{3}}[(1-u_2)\widetilde{S}_Z + 3u_5(\sqrt{3}\widetilde{S}_Y + \widetilde{S}_X)] \,, \qquad S_+c^\dagger a = \frac{u_3}{\sqrt{2}}e^{i\frac{\pi}{3}}\widetilde{S}_Z + u_6\widetilde{S}_+ - u_4 e^{i\frac{2\pi}{3}}\widetilde{S}_- \,,$$
$$S_-c^\dagger a = \frac{u_3}{\sqrt{2}}e^{-i\frac{\pi}{3}}\widetilde{S}_Z + u_6\widetilde{S}_- - u_4 e^{-i\frac{2\pi}{3}}\widetilde{S}_+ \,, \qquad S_Zc^\dagger a = u_7\widetilde{S}_Z - \frac{u_5}{4}(\widetilde{S}_X + \sqrt{3}\widetilde{S}_Y) \,, \tag{S32}$$

The parameters u_i $(i = 1, 2, \ldots, 7)$ are determined by the pseudospin wavefunction (S2) parameters $\mathcal{C}_{1,2,3}$ as:

$$u_1 = 2\sqrt{3}\mathcal{C}_1\mathcal{C}_3 + 2\mathcal{C}_2^2 \,, \quad u_2 = 1 + 2(\mathcal{C}_1^2 - \mathcal{C}_3^2) \,, \quad u_3 = \tfrac{2\sqrt{2}}{3}\mathcal{C}_2\mathcal{C}_3 - \sqrt{\tfrac{2}{3}}\mathcal{C}_1\mathcal{C}_2 \,, \quad u_4 = \tfrac{2}{3}\mathcal{C}_3^2 \,,$$
$$u_5 = \tfrac{2}{3}\mathcal{C}_2\mathcal{C}_3 \,, \quad u_6 = \tfrac{2}{3}\mathcal{C}_2^2 - \tfrac{1}{\sqrt{3}}\mathcal{C}_1\mathcal{C}_3 \,, \quad u_7 = \tfrac{1}{3}\mathcal{C}_2^2 + \tfrac{1}{6}\mathcal{C}_3^2 - \tfrac{1}{2}\mathcal{C}_1^2 \,. \tag{S33}$$

In the cubic limit, where $(\mathcal{C}_1, \mathcal{C}_2, \mathcal{C}_3) = (\frac{1}{\sqrt{2}}, \frac{-1}{\sqrt{3}}, \frac{1}{\sqrt{6}})$, they are

$$u_1 = u_2 = \frac{5}{3} \,, \quad u_3 = u_4 = \frac{1}{9} \,, \quad u_5 = -\frac{\sqrt{2}}{9} \,, \quad u_6 = \frac{1}{18} \,, \quad u_7 = -\frac{1}{9} \,. \tag{S34}$$

5. Microscopic parameters used in the calculations

Apart from an overall energy scale t^2/U, a number of microscopic parameters appeared in the above expressions for exchange constants. Hund's coupling $J_H \sim 0.8$ eV follows from optical data in CoO [5]; cubic splitting D for $3d$ ions is of the order of $1.0 - 1.5$ eV. With the *ab initio* estimates of $U \sim 5.0 - 7.8$ eV [6–8], this gives $J_H/U \sim 0.1 - 0.2$ and $D/U \sim 0.13 - 0.30$. Specifically, we set $J_H/U = 0.15$ and $D/U = 0.20$. Hund's coupling on oxygen is large, $J_H^p \sim 1.2 - 1.6$ eV [9], while U_p is about ~ 4 eV, so we use the representative values of $J_H^p/U_p = 0.3$ and $U_p/U = 0.7$. We set a direct hopping $t' = 0.2t$ (i.e. smaller than in $5d/4d$ compounds [10]), but this value is nearly irrelevant here since t_{2g}-t_{2g} exchange is of minor importance anyway, see Fig. 2 of the main text. A ratio $t_{pd\sigma}/t_{pd\pi} = 2$ [11] is used. Regarding Δ/λ and U/Δ_{pd} values, we vary them rather broadly, as they most sensitively control the exchange interactions. With the above input parameters, we arrive at K, J, Γ, and Γ' values presented in the main text. We have verified that while variations of the input parameters result in some changes of the exchange constants, they do not affect the overall picture and conclusions.

III. Exact diagonalization: Phase diagrams based on static correlations and coherent-state analysis

We consider the nearest-neighbor (NN) interaction model (Eq. 2 of the main text or S5 in the previous section), supplemented by the third-NN Heisenberg exchange J_3 that appears as the major one among the long-range interactions in ab-initio studies [10]. In this section we show the full evolution of the phase diagram with the parameter J_3 and also demonstrate the robustness of our picture with respect to variations of the Hund's exchange J_H. The data presented here complements Fig. 1 and Fig. 3(e,f) of the main manuscript.

To determine the magnetic state, we have performed exact diagonalization using the values of exchange parameters derived in Sec. II. Utilizing the Lanczos method, we have obtained exact ground states of the exchange Hamiltonian for a symmetric, hexagon-shaped cluster containing 24 sites. Periodic boundary conditions were applied, corresponding to a periodic tiling of an infinite lattice. Since the small cluster does not allow for spontaneous symmetry breaking, we inspect its magnetic state by analyzing the static spin correlations and by employing the method of coherent spin states introduced in Ref. [12].

We focus on real-space correlations that enable us to judge the extent of the Kitaev spin liquid phase which should be characterized by vanishing correlations beyond nearest neighbors. By evaluating the static spin correlations in momentum space, we would be able to detect the magnetically ordered states that show peaks at the characteristic momenta of the particular ordering pattern. Here, however, it is favorable to utilize the method of coherent spin states that provides a better access to the magnetic order encoded in the complex cluster wavefunction. In essence, it constructs "classical" states (coherent spin states) with spins pointing in prescribed directions and identifies a "classical" state having maximum overlap with the exact cluster ground state. Thanks to its full flexibility in the individual spin directions, the method can precisely determine both collinear patterns as well as non-collinear ones. The "classical" trial state is a product state of spins pointing in prescribed directions (in the sense of finding spin up with 100% probability when measuring in that particular direction) and as such it excludes quantum fluctuations. The maximum overlap is therefore a useful indicator of the amount of quantum fluctuations. For a fluctuation-free state and non-degenerate cluster ground state, the corresponding probability reaches the value 1/(number of degenerate patterns).

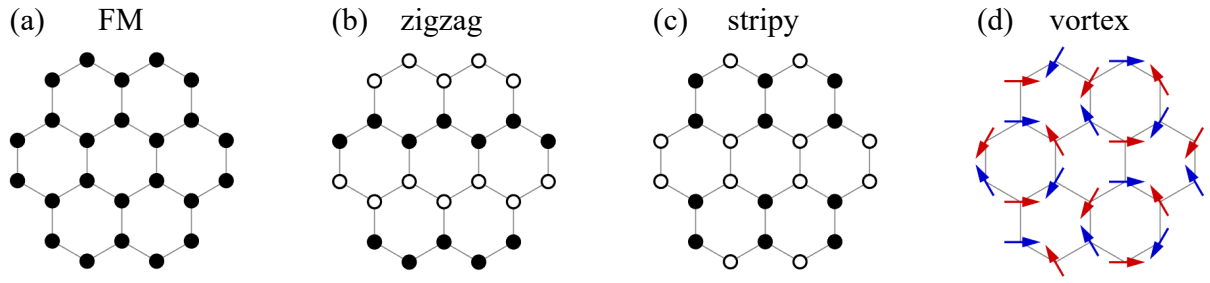

FIG. S2: Sketch of the magnetic structures for (a) FM, (b) zigzag, (c) stripy, and (d) vortex orders. Open and closed circles represent opposite spin directions.

In contrast, Kitaev spin liquid is highly fluctuating and does not contain a pronounced "classical" state which leads to a tiny maximum overlap (see [12, 13] for details).

Figures S3 and S4 show phase diagram data as functions of U/Δ_{pd} and Δ/λ for several values of J_3. The static correlations up to fourth NN presented in upper three rows of panels clearly localize the Kitaev spin liquid phase spreading in the area with dominant K. It is surrounded by several phases with long-range correlations that are identified by the method of coherent spin states. For $J_3 = 0$, these include two types of FM orders with the magnetic moments lying in the honeycomb plane and perpendicular to it, respectively, stripy phase, zigzag phase zz3, and finally a vortex phase of the type depicted in Fig. S2.

The effect of nonzero antiferromagnetic J_3 may be estimated by considering the correlations of third NN in the individual phases. Strongly supported by J_3 is the zigzag phase that is characterized by AF oriented spins on all third-neighbor bonds. Similarly, a large suppression may be expected for FM and stripy phases that have FM aligned third NN spins. The effect on the vortex phase is weak as each spin has one FM aligned third neighbor and two third neighbors at an angle of 120°, leading to a cancellation of J_3 in energy on classical level. Finally, in the Kitaev spin liquid phase the third neighbors are not correlated at all, so that small J_3 has a moderate negative impact when trying to align them in AF fashion. The consequences of the above energetics are well visible in Figs. S3 and S4. Once including nonzero J_3, the Kitaev spin liquid phase slightly grows first, at the expense of FM and stripy phases. At the same time, the Kitaev spin liquid phase is also being expelled from the bottom left corner by the expanding zz3 phase. With increasing J_3 between $J_3 = 0.05$ and 0.15 in t^2/U units, two new zigzag phases zz1 and zz2 around Kitaev SL are successively formed. Once J_3 reaches $0.25t^2/U$, the zigzag order quickly takes over, suppressing the Kitaev SL phase completely.

In the large area covered by the zigzag order, various ratios and combinations of signs of the nearest-neighbor interactions are realized. This is the origin of three distinct zigzag phases zz1, zz2, and zz3, differing in their moment directions as seen in bottom panels of Figs. S3 and S4. Negative Γ and positive Γ' found in zz1 phase space [see Fig. 3(c,d) of the main text] lead to the ab-plane moment direction. The zz3 phase is characterized by opposite signs of Γ and Γ' interactions which stabilizes the zigzag order as in Na_2IrO_3 [12, 14]. Finally, in the zz2 phase, Γ and Γ' terms maintain only small values and moment directions pointing along cubic axes x, y, z are selected by order-from-disorder mechanism [12].

To check the robustness of our picture, we have also performed the exact diagonalization for a different J_H value. The trends discussed above remain quite similar as demonstrated in Figs. S5 and S6 calculated for $J_H/U = 0.2$. Roughly speaking, when we increase the J_H/U value, the whole scenario merely shifts to smaller U/Δ_{pd} region.

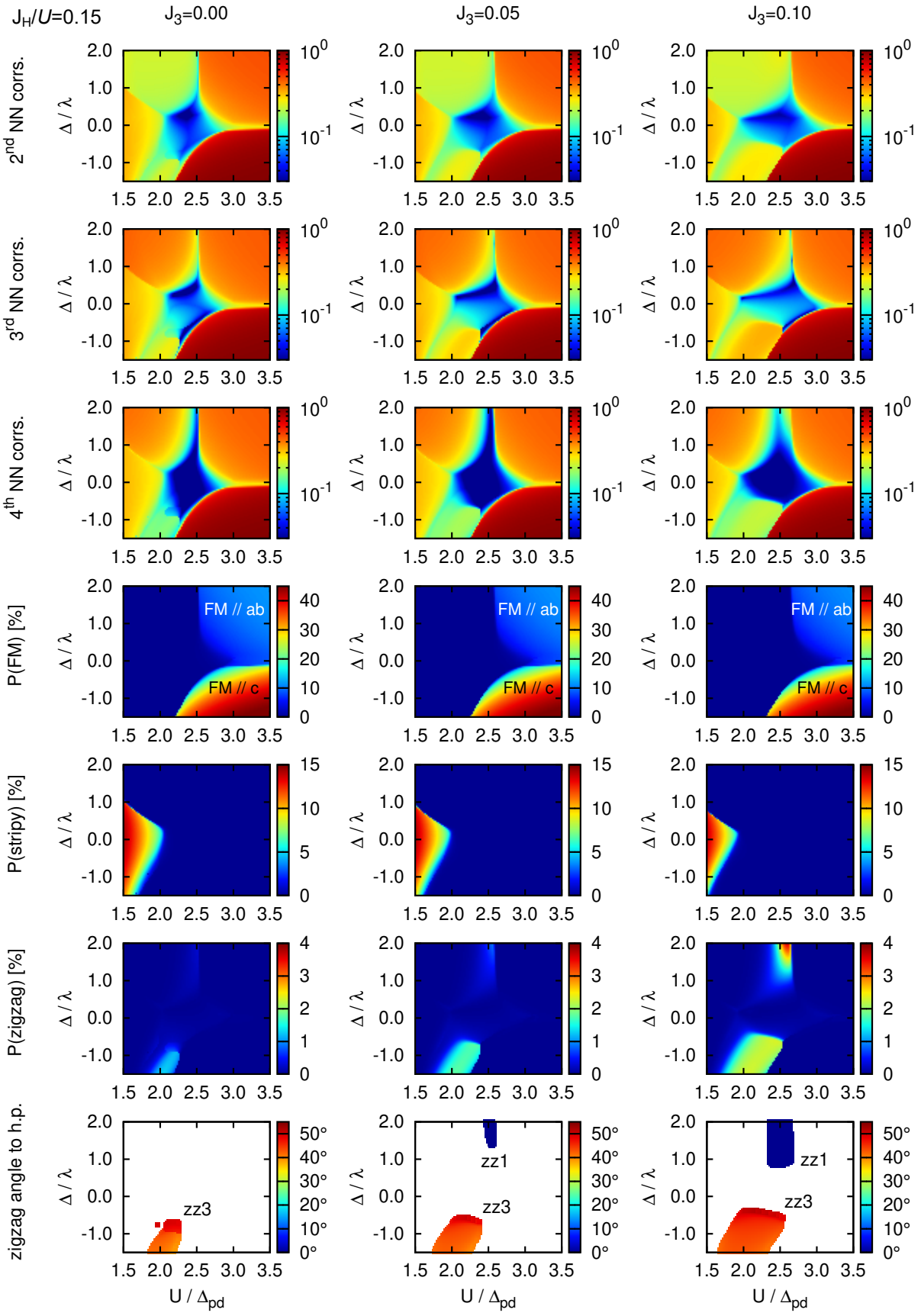

FIG. S3: The first three rows present second-NN, third-NN and fourth-NN spin correlations. The color indicates the largest absolute value among the eigenvalues of the 3×3 spin correlation matrix for the respective bond. It is normalized by the maximum possible value of $\widetilde{S}^2 = 0.25$. The next three rows are the probability of FM, stripy, and zigzag classical states contained in the cluster ground state as determined by the method of coherent spin states. The last row shows the angle between the honeycomb plane (h.p.) and the magnetic moments for the zigzag order. $J_H/U = 0.15$ is fixed and three columns correspond to $J_3 = 0$, $J_3 = 0.05$, and $J_3 = 0.1$ in units of t^2/U.

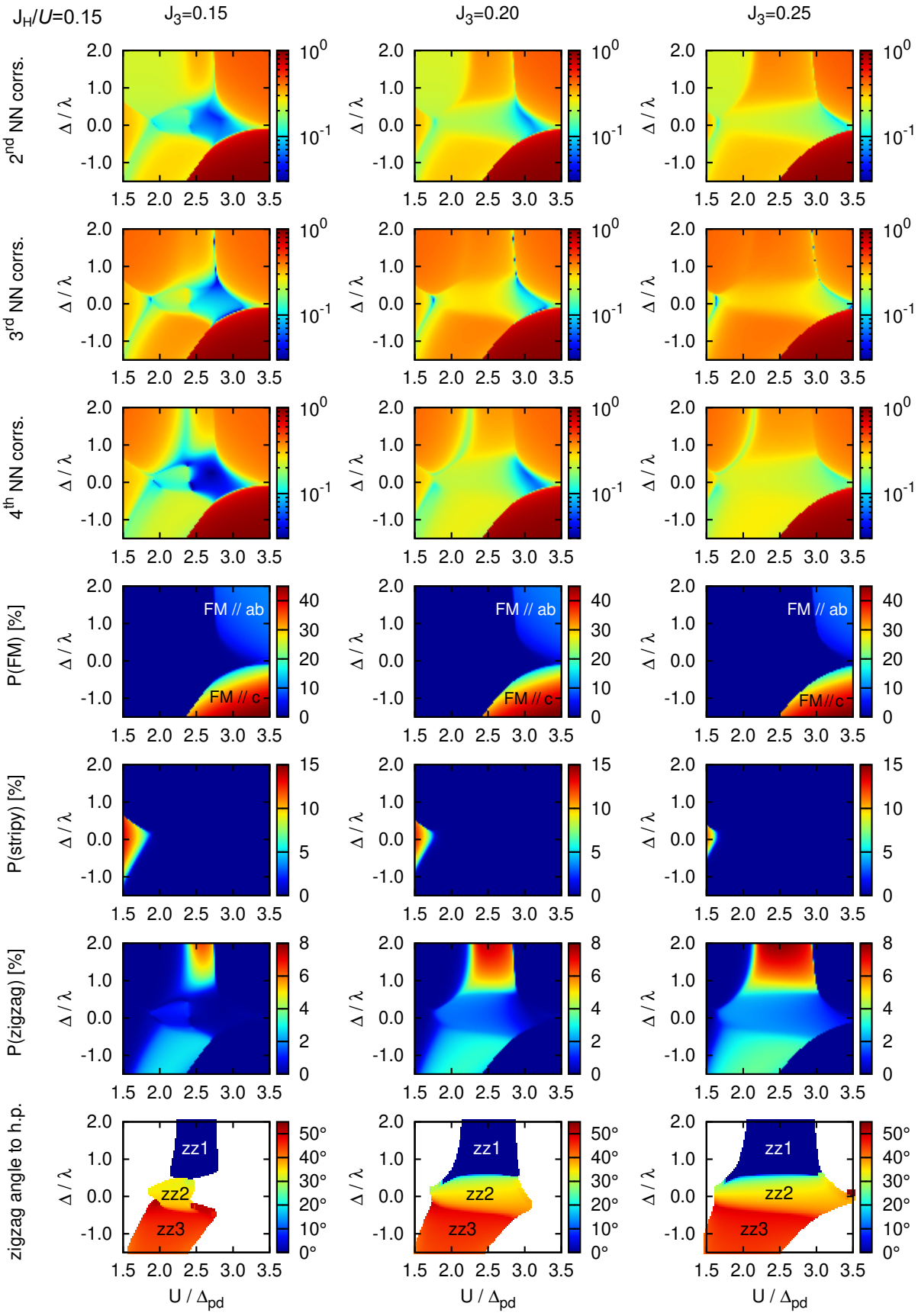

FIG. S4: The same as in Fig. S3 for larger J_3 values. The three columns correspond to $J_3 = 0.15$, 0.20, and 0.25 (t^2/U).

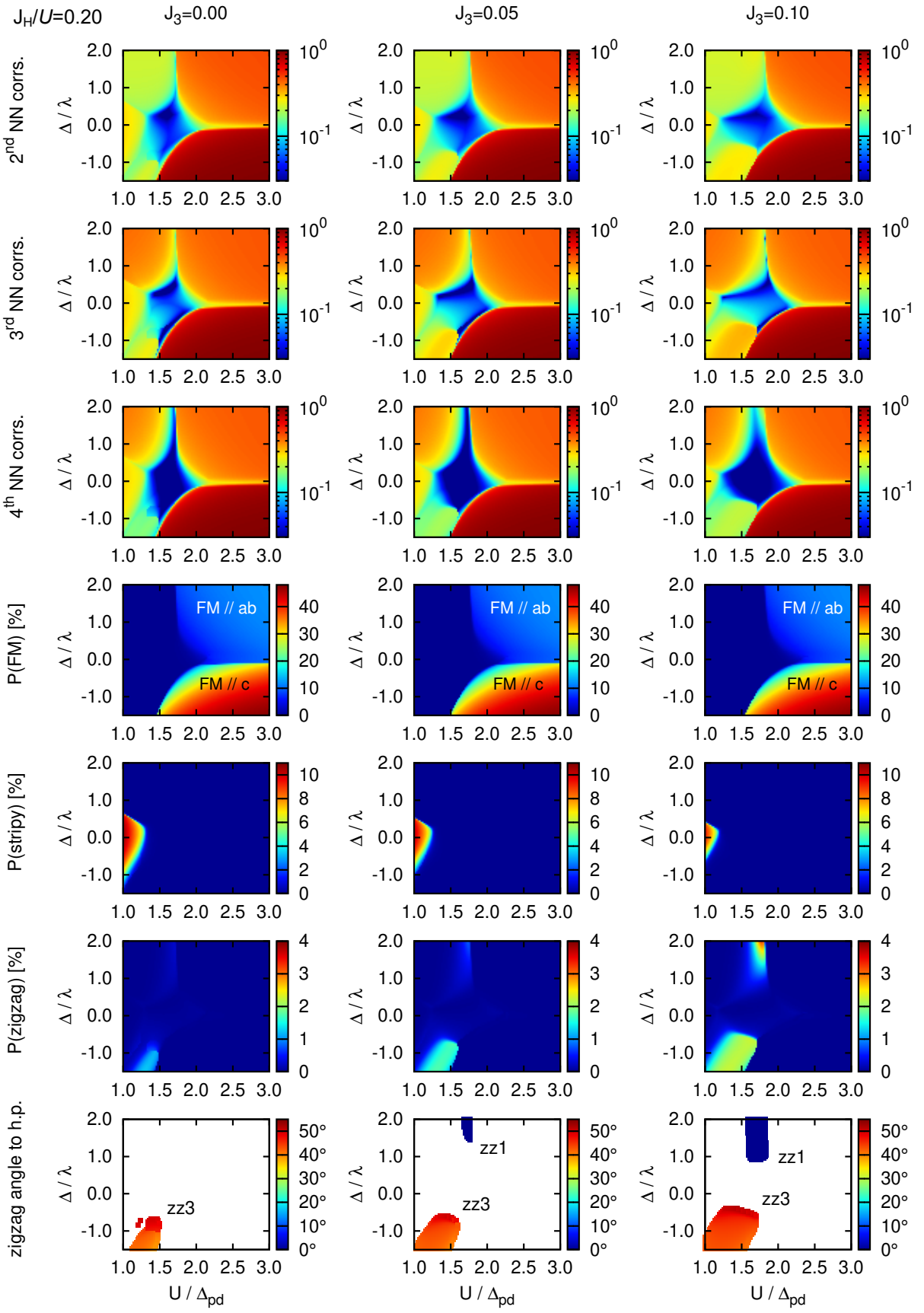

FIG. S5: The same as in Fig. S3 for a larger value $J_H/U = 0.2$. The three columns correspond to $J_3 = 0$, $J_3 = 0.05$, and $J_3 = 0.1$ (t^2/U).

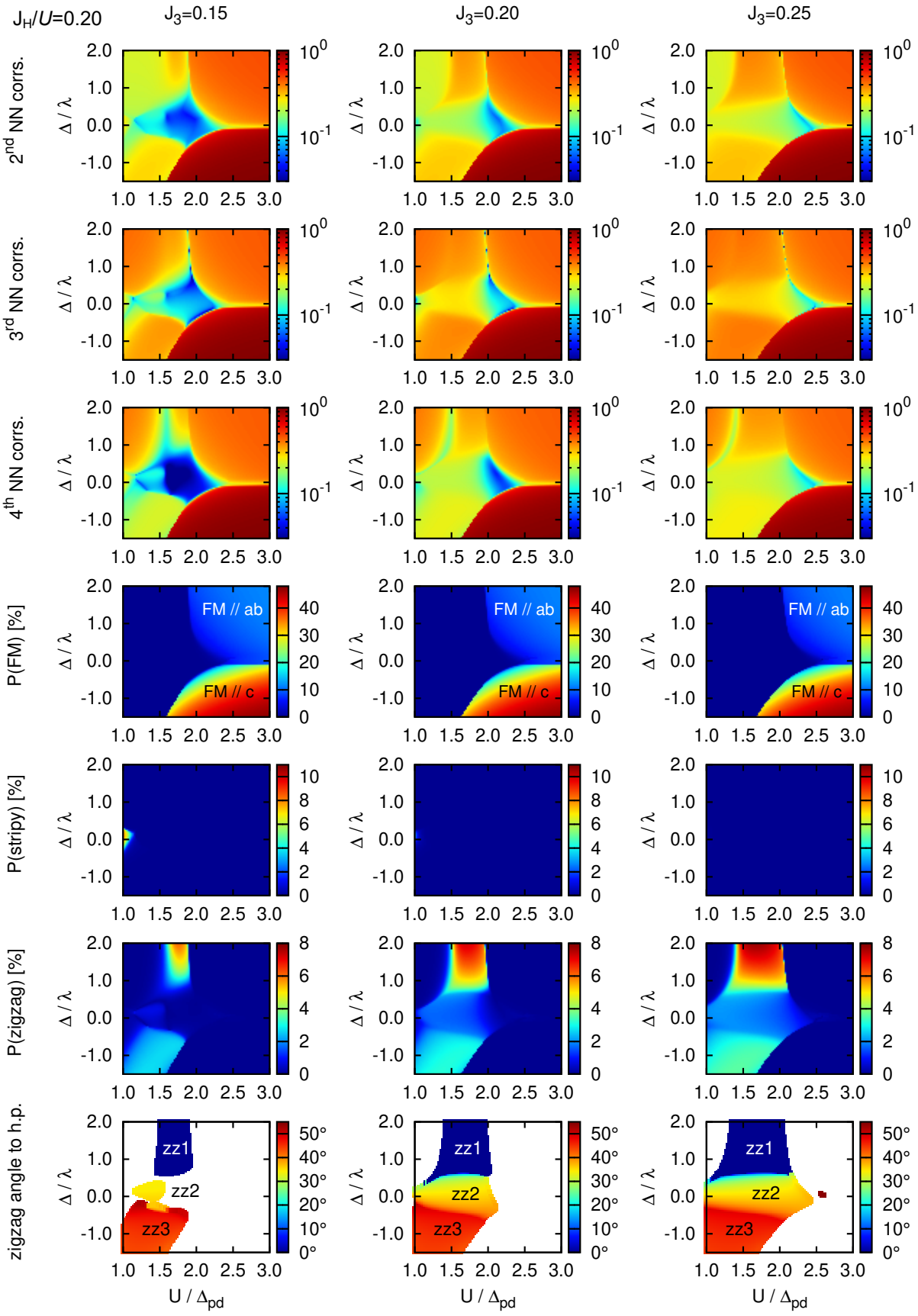

FIG. S6: The same as in Fig. S5 for larger J_3 values. The three columns correspond to $J_3 = 0.15$, 0.20, and 0.25 (t^2/U).

IV. Trigonal crystal field Δ in $Na_3Co_2SbO_6$

The parameter Δ determines the effective magnetic moment values $\mu^{\alpha}_{\rm eff}$ ($\alpha = ab$ or c), and thus can be obtained from paramagnetic susceptibility $\chi^{\alpha}(T)$. One has to keep in mind that extracting the moments from a standard Curie-Weiss fit $\chi(T) = C/(T-\Theta) + \chi_0$ assumes that the excited levels are high in energy (as compared to k_BT) and hence thermally unpopulated. The Curie constant C is then indeed temperature independent, providing the ground state g-factors and moments. For Co^{2+} ions, where the excited level at ~ 30 meV is thermally activated already at the room temperature, we have to use instead a general expression for a single-ion susceptibility:

$$\chi^{\alpha}_{\rm ion} = \frac{1}{Z(T)} \sum_{n,m} \frac{e^{-\beta E_n} - e^{-\beta E_m}}{E_m - E_n} (M^{\alpha}_{nm})^2. \tag{S35}$$

Here, n and m run over all the 12 states (6 doublets in Fig. S1), with the wavefunctions and energies calculated in Sec. I. The partition function $Z(T) = \sum_n e^{-\beta E_n}$, and $\beta = 1/k_BT$. $M^{\alpha}_{nm} = \langle n|M_{\alpha}|m\rangle$ is matrix element of the magnetic moment operator $\boldsymbol{M} = (2\boldsymbol{S} - \frac{3}{2}\kappa\boldsymbol{L})$ (in units of Bohr magneton μ_B). We use the covalency reduction factor $\kappa = 0.8$ typical for Co^{2+} ion [1]. $\chi^{\alpha}_{\rm ion}$ includes both the Curie and Van-Vleck contributions and depends on two parameters, Δ and λ.

We have fitted the data of Ref. [15] with $\chi^{\alpha}(T) = \chi^{\alpha}_{\rm ion} + \chi^{\alpha}_0$, and obtained a fair agreement with experiment for both χ^{ab} and χ^{c}, using $\Delta = 38$ meV and $\lambda = 28$ meV, see Fig. S7(a,b). In particular, the characteristic changes in the slopes of both $1/\chi^{ab}$ and $1/\chi^{c}$ data are well reproduced by the calculations. In fact, this behavior is common for layered cobaltates and deserves some discussion.

It is instructive to divide Eq. S35 into two parts, $\chi^{\alpha}_{\rm ion} = \chi^{\alpha}_1 + \chi^{\alpha}_2$, where χ^{α}_1 term accounts for the transitions within $\widetilde{S} = 1/2$ doublet. Using the wavefunctions (S2), we obtain

$$\chi^{\alpha}_1 = p_{1/2}\, \frac{(\mu^{\alpha}_{\rm eff})^2}{3k_BT}\ . \tag{S36}$$

The effective moments $\mu^{\alpha}_{\rm eff} = g_{\alpha}\sqrt{\widetilde{S}(\widetilde{S}+1)}$, with the $\widetilde{S} = 1/2$ doublet g-factors given by

$$\begin{aligned} g_{ab} &= 4\sqrt{3}\mathcal{C}_1\mathcal{C}_3 + 4\mathcal{C}_2^2 - 3\sqrt{2}\kappa\mathcal{C}_2\mathcal{C}_3\ , \\ g_{c} &= (6+3\kappa)\mathcal{C}_1^2 + 2\mathcal{C}_2^2 - (2+3\kappa)\mathcal{C}_3^2\ . \end{aligned} \tag{S37}$$

In Eq. S36, $p_{1/2} = 2/Z(T)$ measures the occupation of the ground state. As the excited levels of Co^{2+} are relatively low, the weight $p_{1/2}$ of the Curie term, as well as Van-Vleck contribution χ^{α}_2 of the excited states depend on temperature. The characteristic changes in the slopes of $1/\chi^{ab}$ ($1/\chi^{c}$) around 200 K (100 K) originate from the interplay between $\chi_1(T)$ and $\chi_2(T)$ which become of a similar order at these temperatures, see Fig. S7(c,d).

The g-factors (S37) are plotted in Fig. S7(g); with Δ and λ values obtained above, we get $g_{ab} \simeq 4.6$ and $g_c \simeq 3$. This gives the in-plane saturated magnetic moment $M_{ab} = g_{ab}\widetilde{S} = 2.3\mu_B$ consistent with experiment [15].

Apparent deviations at low temperatures are due to short-range correlations between the pseudospins, which can partially be accounted for in a molecular field approximation, i.e. replacing the Curie term χ^{α}_1 by $\chi^{\alpha}_1 \cdot T/(T-\Theta_{\alpha})$. The result is shown in Fig. S7(e,f). The paramagnetic Curie temperatures $\Theta_{ab} = 17$K and $\Theta_c = 6$K are rather small and anisotropic. We can evaluate Θ values using our theoretical exchange constants given in Fig. 4 caption of the main text; the result is:

$$\begin{aligned} \Theta_{ab} &= -\tfrac{3}{4}\left[J + J_3 + \tfrac{1}{3}K - \tfrac{1}{3}(\Gamma + 2\Gamma')\right] \simeq 1.4\ (t^2/U), \\ \Theta_{c} &= -\tfrac{3}{4}\left[J + J_3 + \tfrac{1}{3}K + \tfrac{2}{3}(\Gamma + 2\Gamma')\right] \simeq 0.6\ (t^2/U). \end{aligned} \tag{S38}$$

Curiously enough, this gives the Θ-anisotropy close to what we get from the susceptibility fits. This comparison also suggests the energy scale of $t^2/U \sim 1$ meV, setting thereby the magnon bandwidth of the order of 10 meV. The relative smallness of t^2/U is due to large U and more localized nature of $3d$ orbitals.

It is worth to comment on a positive sign of $\Delta > 0$ in $Na_3Co_2SbO_6$. Within a simple model only considering contribution from O_6 octahedron, which is slightly compressed along the c-axis [15], one would find a negative $\Delta < 0$ instead. However, this approximation is too crude in layered structures, where the non-cubic Madelung potential of more distant ions has to be considered. In $Na_3Co_2SbO_6$, we think that $\Delta > 0$ is due to a positive contribution of the high-valence Sb^{5+} ions residing within the ab-plane. A c-axis compression would enhance a negative contribution of the oxygen octahedra, reducing thereby a total value of the trigonal field Δ.

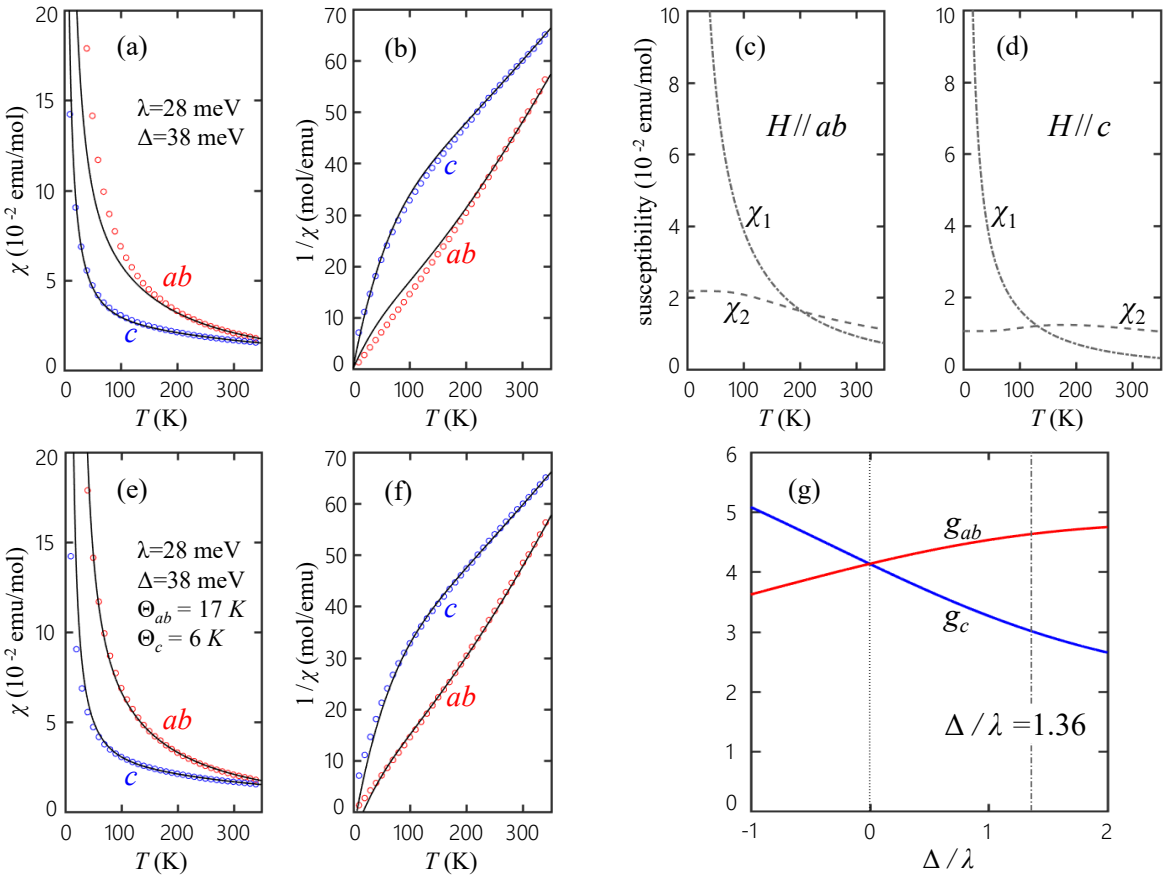

FIG. S7: (a),(b) Temperature dependence of magnetic susceptibility χ and its inverse $1/\chi$ in $Na_3Co_2SbO_6$. Open circles represent the experimental data extracted from Ref. [15], and solid lines are the fits using single-ion approximation $\chi^\alpha = \chi^\alpha_{\rm ion} + \chi^\alpha_0$, with $\chi^{ab}_0 = -10^{-3}$ emu/mol and $\chi^c_0 = 1.5 \times 10^{-3}$ emu/mol. (c),(d) Decomposition of single-ion susceptibility $\chi^\alpha_{\rm ion}$ into pseudospin-1/2 χ_1 and Van-Vleck χ_2 contributions. (e),(f) The fitting results including the pseudospin interactions within a molecular field approximation. Here, $\chi^{ab}_0 = -1.5 \times 10^{-3}$ emu/mol and $\chi^c_0 = 1.5 \times 10^{-3}$ emu/mol. (g) The g-factors g_{ab} (red) and g_c (blue) as a function of Δ/λ. $\Delta/\lambda = 1.36$ corresponds to $Na_3Co_2SbO_6$.

V. Dynamical spin susceptibility

1. Linear spin wave theory

The dispersions and intensities of magnons presented in Fig. 4(a,b) of the main text were determined by standard linear spin wave (LSW) theory. Zigzag pattern with FM x and y bonds was assumed, i.e. the zigzags are running along the X direction in Fig. S1(a). By applying Holstein-Primakoff transformation, harmonic expansion, and Bogoliubov transformation numerically, we have calculated diagonal components of the spin susceptibility tensor and evaluated its trace that is plotted in Fig. 4(a,b), including artificial lorentzian broadening with FWHM of 0.4 in units of t^2/U.

2. Exact diagonalization

The dynamical spin susceptibility profiles presented in Fig. 4(c) of the main text were determined by exact diagonalization (ED) using the hexagonal clusters with $N = 24$ and $N = 32$ sites shown in Fig. S8(a) and (b), respectively. Utilizing Lanczos algorithm, we have obtained the exact cluster ground state $|\mathrm{GS}\rangle$ and calculated the dynamical spin susceptibility tensor $\chi_{\alpha\beta}(\boldsymbol{q},\omega) = i\int \langle \mathrm{GS}|[S^\alpha_{\boldsymbol{q}}(t), S^\beta_{-\boldsymbol{q}}(0)]|\mathrm{GS}\rangle \exp(i\omega t)\theta(t)dt$. Here $S^\alpha_{\boldsymbol{q}} = \sum_{\boldsymbol{R}} S^\alpha_{\boldsymbol{R}} \exp(-i\boldsymbol{q}\boldsymbol{R})/\sqrt{N}$ is the Fourier component combining spin operators at cluster sites $\boldsymbol{R}$. The accessible wavevectors $\boldsymbol{q}$ that are compatible with periodic tiling of the honeycomb lattice by the clusters are depicted in Fig. S8(c). As in the case of the LSW theory, in Fig. 4(c) we have plotted the imaginary part of the trace of the spin susceptibility tensor: $\chi''(\boldsymbol{q},\omega) = \mathrm{Im}\sum_\alpha \chi_{\alpha\alpha}(\boldsymbol{q},\omega)$.

The spectra were broadened by lorentzians with FWHM of 0.1 in units of t^2/U and the quasielastic peaks at momenta corresponding to the zigzag Bragg points were removed.

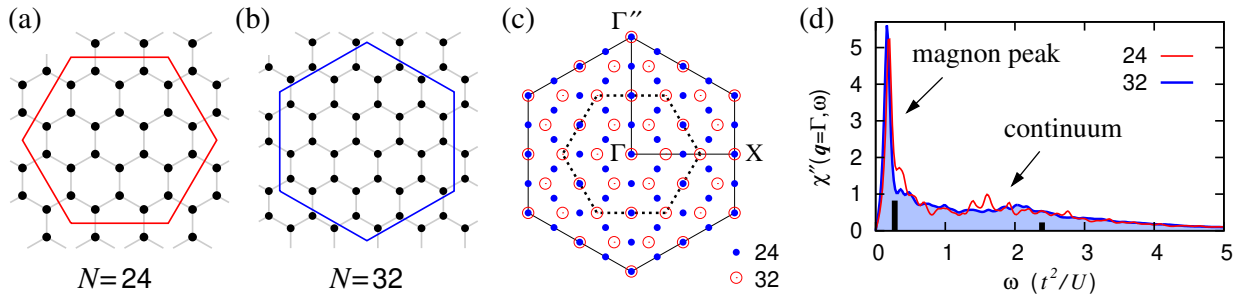

FIG. S8: (a) 24-site cluster used in ED to obtain phase diagrams and spin susceptibility. (b) 32-site cluster used in ED calculations of the spin susceptibility. (c) Wavevectors compatible with the periodic tiling of the honeycomb lattice by 24- and 32-site clusters. Inner dotted hexagon indicates the Brillouin zone of the honeycomb lattice, outer hexagon corresponds to the Brillouin zone of the triangular lattice formed when adding sites at hexagon centers to the honeycomb lattice. (d) Imaginary part of the trace of the spin susceptibility tensor at $\boldsymbol{q} = \Gamma = 0$ calculated by ED for 24- and 32-site clusters. The values of model parameters are the same as in Fig. 4 of the main text. The thick black bars show the positions and relative spectral weights of the magnon peaks obtained within LSW theory. Note that the ED results for 24- and 32-site clusters are qualitatively similar to each other.

Compared to the LSW approximation result, the ED profiles show highly renormalized magnons that only survive at low energies, and broad continua of excitations that emerge as a consequence of the dominant Kitaev interactions. In fact, the most spectral weight is taken by the continuum. This is illustrated in detail for the FM wavevector $\boldsymbol{q} = \Gamma = 0$ in Fig. S8(d) and can be seen in Fig. 4(c) of the main text for other wavevectors $\boldsymbol{q}$ as well. To properly capture such broad continua, we have used 1000 Lanczos steps in the dynamical susceptibility evaluation.

Finally, we want to notice an important aspect that one has to keep in mind while comparing the above results with the experimental data. Namely, the cluster ground state is fully symmetric and contains all degenerate ordering patterns. In our case these correspond to the three possible zigzag directions that are represented with equal weights for the hexagonal shape clusters. As a result, the dynamical spin susceptibility obtained via ED contains contributions from all these zigzag patterns. In practice, this would correspond to the dynamical spin structure factor measured on the twinned samples with three types of zigzag domains. On the other hand, the intensities calculated using the LSW theory correspond to a single-domain crystal with one particular zigzag pattern.

[1] A. Abragam and B. Bleaney, *Electron Paramagnetic Resonance of Transition Ions* (Clarendon Press, Oxford, 1970).
[2] M. E. Lines, Phys. Rev. **131**, 546 (1963).
[3] J. Chaloupka and G. Khaliullin, Phys. Rev. B **92**, 024413 (2015).
[4] H. Liu and G. Khaliullin, Phys. Rev. B **97**, 014407 (2018).
[5] G. W. Pratt Jr. and R. Coelho, Phys. Rev. **116**, 281 (1959).
[6] V. I. Anisimov, J. Zaanen, and O. K. Andersen, Phys. Rev. B **44**, 943 (1991).
[7] W. E. Pickett, S. C. Erwin, and E. C. Ethridge, Phys. Rev. B **58**, 1201 (1998).
[8] H. Jiang, R. I. Gomez-Abal, P. Rinke, and M. Scheffler, Phys. Rev. B **82**, 045108 (2010).
[9] K. Foyevtsova, H. O. Jeschke, I. I. Mazin, D. I. Khomskii, and R. Valentí, Phys. Rev. B **88**, 035107 (2013).
[10] S. M. Winter, Y. Li, H. O. Jeschke, and R. Valentí, Phys. Rev. B **93**, 214431 (2016).
[11] J. Chaloupka and G. Khaliullin, Prog. Theor. Phys. Suppl. **176**, 50 (2008).
[12] J. Chaloupka and G. Khaliullin, Phys. Rev. B **94**, 064435 (2016).
[13] J. Rusnačko, D. Gotfryd, and J. Chaloupka, Phys. Rev. B **99**, 064425 (2019).
[14] S. H. Chun, J.-W. Kim, Jungho Kim, H. Zheng, C. C. Stoumpos, C. D. Malliakas, J. F. Mitchell, K. Mehlawat, Y. Singh, Y. Choi, T. Gog, A. Al-Zein, M. Moretti Sala, M. Krisch, J. Chaloupka, G. Jackeli, G. Khaliullin, and B. J. Kim, Nature Phys. **11**, 462 (2015).
[15] J.-Q. Yan, S. Okamoto, Y. Wu, Q. Zheng, H. D. Zhou, H. B. Cao, and M. A. McGuire, Phys. Rev. Materials **3**, 074405 (2019).

6 Papers addressing the singlet–triplet model

- *Spin-State Crossover Model for the Magnetism of Iron Pnictides*

  J. Chaloupka and G. Khaliullin

  Physical Review Letters **110**, 207205 (2013) DOI: 10.1103/PhysRevLett.110.207205

  This paper represents our first attempt to employ the ideas of triplon condensation within singlet-triplet model, here in the context of iron pnictides. The singlet and triplet states correspond to low-spin and intermediate-spin states of $3d^6$ configuration of Fe^{2+} ions that get dynamically mixed by superexchange processes. We have demonstrated that the unusual features of the iron-pnictide magnetism can be explained by AF condensate with a large quadrupolar component. Such a situation can be effectively described by a spin-1 system with a significant biquadratic interaction.

- *Doping-Induced Ferromagnetism and Possible Triplet Pairing in d^4 Mott Insulators*

  J. Chaloupka and G. Khaliullin

  Physical Review Letters **116**, 017203 (2016) DOI: 10.1103/PhysRevLett.116.017203

  In this paper we study a doped variant of the singlet-triplet model for d^4 systems where large-enough spin orbit coupling forms $J = 0$ ionic ground state. We find that the doped electrons strongly affect the triplon condensation supporting the FM order. Already a modest amount of doping may convert the AF condensate into FM one or induce FM condensation in the nonmagnetic phase. In the vicinity of the FM phase, the low-energy spin response is dominated by intense paramagnons. We have explored a scenario where these excitations serve as mediators of triplet pairing.

- *Higgs mode and its decay in a two-dimensional antiferromagnet*

  A. Jain, M. Krautloher, J. Porras, G. H. Ryu, D. P. Chen, D. L. Abernathy, J. T. Park, A. Ivanov, J. Chaloupka, G. Khaliullin, B. Keimer, and B. J. Kim

  Nature Physics **13**, 633 (2017) DOI: 10.1038/NPHYS4077

  This paper presents results of inelastic neutron scattering on Ca_2RuO_4 that are interpreted along the lines of singlet-triplet model (more precisely, we use the refined model of Sec. 4.2). We demonstrate the peculiar spectrum of magnetic excitations including the amplitude ("Higgs") mode associated with triplon condensate that appears in the longitudinal spin response, as well as magnons with unusual dispersion having a maximum at $\boldsymbol{q} = 0$. The interplay of the amplitude mode with the two-magnon continuum is observed, leading to a broadening of the longitudinal mode that largely depends on the position in the Brillouin zone.

- *Raman Scattering from Higgs Mode Oscillations in the Two-Dimensional Antiferromagnet Ca_2RuO_4*

  S.-M. Souliou, J. Chaloupka, G. Khaliullin, G. Ryu, A. Jain, B. J. Kim, M. Le Tacon, and B. Keimer

  Physical Review Letters **119**, 067201 (2017) DOI: 10.1103/PhysRevLett.119.067201

  In this paper we demonstrate that the Raman scattering on Ca_2RuO_4 can be successfully interpreted in terms of the magnetic model introduced in the above Ref. [101] to fit the neutron data. We present the temperature-dependent Raman spectra in B_{1g} and A_g channels, identify their magnetic parts, and interpret the magnetic features in terms of magnons and the amplitude mode. Most importantly, the A_g spectrum is shown to directly reveal the amplitude mode without a parasitic excitation of the two-magnon continuum as in the longitudinal spin response.

- *Highly frustrated magnetism in relativistic d^4 Mott insulators: Bosonic analog of the Kitaev honeycomb model*

  J. Chaloupka and G. Khaliullin

  Physical Review B **100**, 224413 (2019) DOI: 10.1103/PhysRevB.100.224413

  The paper analyzes the singlet-triplet model for d^4 compounds with the honeycomb lattice. We focus on the limit of dominant direct hopping between t_{2g} orbitals which leads to Kitaev-like frustration of exchange interactions. The symmetry of the model is explored in detail, the links to the Kitaev honeycomb model are discussed, and effective models emerging in various parameter regimes are identified. We construct the overall phase diagram of the model based on numerical simulations complemented by the above symmetry analysis and discuss possible implications for the magnetism of honeycomb ruthenium oxides.

PRL 110, 207205 (2013) PHYSICAL REVIEW LETTERS week ending 17 MAY 2013

Spin-State Crossover Model for the Magnetism of Iron Pnictides

Jiří Chaloupka[1,2] and Giniyat Khaliullin[1]

[1]*Max Planck Institute for Solid State Research, Heisenbergstrasse 1, D-70569 Stuttgart, Germany*
[2]*Central European Institute of Technology, Masaryk University, Kotlářská 2, 61137 Brno, Czech Republic*

(Received 18 March 2013; published 14 May 2013)

We propose a minimal model describing magnetic behavior of Fe-based superconductors. The key ingredient of the model is a dynamical mixing of quasidegenerate spin states of Fe^{2+} ion by intersite electron hoppings, resulting in an effective local spin $S_{\rm eff}$. The moments $S_{\rm eff}$ tend to form singlet pairs and may condense into a spin nematic phase due to the emergent biquadratic exchange couplings. The long-range ordered part m of $S_{\rm eff}$ varies widely, $0 \leq m \leq S_{\rm eff}$, but magnon spectra are universal and scale with $S_{\rm eff}$, resolving the puzzle of large but fluctuating Fe moments. Unusual temperature dependences of a local moment and spin susceptibility are also explained.

DOI: 10.1103/PhysRevLett.110.207205 PACS numbers: 75.10.Jm, 71.27.+a, 74.70.Xa

Since the discovery of superconductivity (SC) in doped LaFeAsO [1], a number of Fe-based SCs have been found and studied [2]. Evidence is mounting that quantum magnetism is an essential part of the physics of Fe-based SCs. However, the origin of magnetic moments and the mechanisms that suppress their long-range order (LRO) in favor of SC are still not well understood.

The magnetic behavior of Fe-based SCs is unusual. The ordered moments range from 0.1–0.4$\mu_{\rm B}$, as in spin-density wave (SDW) metals like Cr, to 1–2$\mu_{\rm B}$ typical for Mott insulators, causing debates whether the spin-Heisenberg [3–8] or fermionic-SDW pictures [9–13] are more adequate. At the same time, irrespective of the strength or very presence of LRO, the Fe-ions possess the fluctuating moments $\sim$1–2$\mu_{\rm B}$ [14,15], even in apparently "nonmagnetic" LiFeAs and FeSe. In fact, it was noticed early on that the Fe-moments, "formed independently on fermiology" [16] and "present all the time," [3] are instrumental to reproduce the measured bond lengths and phonon spectra [3,16–18]. Recent experiments [19–21] observe intense high-energy spin waves that are almost independent of doping, further supporting a notion of local moments induced by Hund's coupling [22] and coexisting [23–25] with metallic bands.

While the formation of the local moments in multiorbital systems is natural, it is puzzling that these moments (residing on a simple square lattice) may remain quantum disordered in a broad phase space despite a sizable interlayer coupling; moreover, the Fe-pnictides are semimetals with strong tendency of the electron-hole pairs to form SDW state, further supporting classical LRO of the underlying moments. A fragile nature of the magnetic-LRO in Fe-pnictides thus implies the presence of a strong quantum disorder effects, not captured by *ab initio* calculations that invariably lead to magnetic order over an entire phase diagram. The ideas of domain wall motion [17] and local spin fluctuations [22] were proposed as a source of spin disorder, but no clear and tractable model of quantum magnetism in Fe-based SCs has emerged to date. Here we propose such a model.

Since Fe pnictides are distinct among the other (Mn, Co, Ni) families, their unique physics should be rooted in specific features of the Fe ion itself. In fact, Fe^{2+} is famous for its spin crossover [26]; it may adopt either of $S = 0$, 1, 2 states depending on orbital splitting, covalency, and Hund's coupling. As the ionic radius of Fe is sensitive to its spin, Fe-X bond length (X is a ligand) is also crucial. In oxides, $S = 2$ is typical and $S = 0$,1 occur at high pressures only [27]. In compounds with more covalent Fe-X bonds (X = S, As, Se), $S = 0$ is more common while $S = 1$, 2 levels are higher. The basic idea of this Letter is that when the covalency and Hund's coupling effects compete, the many-body ground state (GS) is a coherent superposition of different spin states intermixed by electron hoppings, resulting in an *average* effective spin $S_{\rm eff}$ whose length depends on pressure, etc. We explore this dynamical spin-crossover idea, and find that (i) local moment $S_{\rm eff}$ may increase with temperature explaining recent data [28], (ii) interactions between $S_{\rm eff}$ contain large biquadratic exchange, and resulting spin-nematic correlations compete with magnetic LRO, (iii) the ordered moment m varies widely, but magnon spectra are universal and scale with $S_{\rm eff}$ as observed [19,20,29], and (iv) singlet correlations among $S_{\rm eff}$ lead to the increase of the spin susceptibility with temperature [30].

The Fe ions in pnictides have a formal valence state $Fe^{2+}(d^6)$. Among its possible spin states [Fig. 1(a)], low-spin ones are expected to be favored; otherwise, the ordered moment would be too large and robust. The $S = 0$, 1 states, "zoomed-in" further in Fig. 1(b), are most important since they can overlap in the many-body GS by an exchange of just two electrons between ions; see Fig. 1(c). The corresponding κ process converts Fe($S = 0$)-Fe($S = 0$) pair into Fe($S = 1$)-Fe($S = 1$) singlet pair and vice versa; this requires the interorbital hopping which is perfectly allowed for $\sim$109° Fe-As-Fe

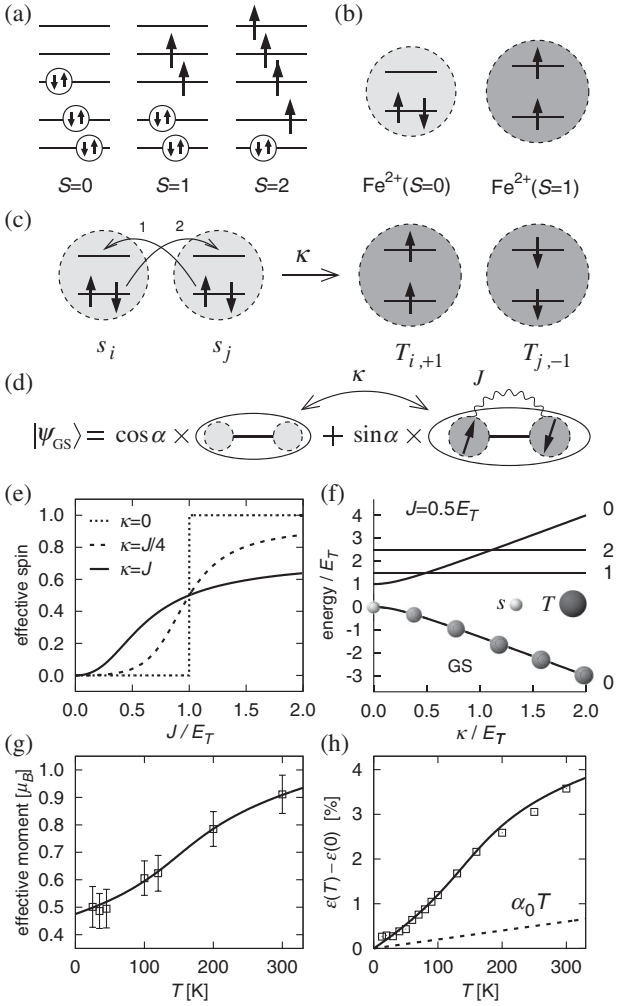

FIG. 1. (a) Schematic view of low ($S = 0$), intermediate ($S = 1$), and high ($S = 2$) spin states of $Fe^{2+}(3d^6)$. (b) $S = 0$ and $S = 1$ states differ in two electrons (out of six) occupying either the same or two different t_{2g} orbitals. The $S = 1$ state has a larger ionic radius. (c) The κ process generating a singlet pair of $S = 1$ triplets T of two Fe^{2+} ions, both originally in the $S = 0$ state (denoted by s). (d) The GS wave function of a Fe^{2+}-Fe^{2+} pair is a coherent superposition of two total-singlet states. (e) Effective spin (average occupation of $S = 1$ state) depending on the ratio of the coupling J between $S = 1$ states and their energy E_T. (f) Energy levels labeled by the total spin value of the Fe^{2+}-Fe^{2+} pair. Only singlet pairs are affected by κ. With increasing κ, the $S = 1$ states are gradually mixed into the GS. (g) Temperature dependence of the local magnetic moment $2n_T$, and (h) the c axis thermal expansion. Squares in (g,h) represent experimental data on $Ca_{0.78}La_{0.22}Fe_2As_2$ [28]. Dashed line in (h) is a thermal expansion excluding magnetoelastic term.

bonding. Basically, κ is a part of usual exchange process when local Hilbert space includes different spin states $S = 0,1$; hence, $\kappa \sim J$. Coupling J between $S = 1$ triplets is contributed also by their indirect interaction via the electron-hole Stoner continuum and, as expected, it reduces with doping [31] as the electron-hole balance of a parent semimetal becomes no longer perfect.

The Hamiltonian describing the above physics comprises the following three terms: on-site energy E_T of $S = 1$ triplet T relative to $S = 0$ singlet s, and the bond interactions κ, J,

$$\mathcal{H} = E_T \sum_i n_{T_i} + \sum_{\langle ij \rangle} [-\kappa_{ij}(D_{ij}^\dagger s_i s_j + \text{H.c.}) + J_{ij} \boldsymbol{S}_i \cdot \boldsymbol{S}_j]. \quad (1)$$

The operator $D_{ij}^\dagger$ creates a singlet pair of spin-full T particles on bond $\langle ij \rangle$. For a general spin S of T particles, $D_{ij} = \sum_M (-1)^{M+S} T_{i,+M} T_{j,-M}$ with $M = -S, \ldots, S$ denoting the $N = 2S + 1$ projections; physically, $N = 3$. The constraint $n_{si} + n_{Ti} = 1$ is implied [32,33].

The above model rests on three specific features of Fe pnictides or chalcogenides: (i) spin-state flexibility of Fe^{2+} that can be tuned by pressure increasing E_T, (ii) edge-sharing FeX_4 tetrahedral structure allowing "spin-mixing" κ term, and (iii) semimetallic nature which makes J values to decrease upon doping [31].

Figures 1(d)–1(f) demonstrate the behavior of spin-1 T particles ($N = 3$) on a single bond. The GS wave function $|\psi_{GS}\rangle = \cos\alpha|A\rangle + \sin\alpha|B\rangle$ is a superposition of two singlets $A = s_1^\dagger s_2^\dagger$ and $B = -(1/\sqrt{3}) \sum_M (-1)^M T_{1,M}^\dagger T_{2,-M}^\dagger$, with the "spin-mixing" angle $\tan 2\alpha = \sqrt{3}\kappa/(E_T - J)$. The GS energy $E_{GS} = (E_T - J) - \sqrt{(E_T - J)^2 + 3\kappa^2}$. At $\kappa = 0$, there is a sudden jump [Fig. 1(e)] from $S = 0$ state to $S = 1$ once the J-energy compensates the cost of having two T particles. At finite κ, the dynamical mixing of spin states converts this transition into a spin-crossover, where the effective spin-length $S_{\text{eff}} = n_T = \sin^2\alpha$ increases gradually. Figure 1(f) shows that κ term strongly stabilizes the singlet pair of T particles; this leads (see later) to a large biquadratic coupling $(\boldsymbol{S}_1 \cdot \boldsymbol{S}_2)^2$ which is essential in Fe pnictides [31,34,35].

We are ready to show the model in action, explaining recent observation of an unusual increase of the local moment upon warming [28]. This fact is at odds with Heisenberg and SDW pictures but easy to understand within the spin-crossover model. Indeed, the spin-length S_{eff} may vary as a function of E_T which, in turn, is sensitive to lattice expansion; in fact, Gretarsson *et al.* found that the moment value follows c-axis thermal expansion $\epsilon = \delta c/c$. We add (magnetoelastic) coupling $-A\epsilon n_T$ in Eq. (1), affecting E_T value, and evaluate ϵ and $\langle n_T \rangle_\epsilon$ self-consistently. This is done by minimizing the elastic energy $(1/2)K\epsilon^2 - K\alpha_0 T\epsilon + (1/4)Q\epsilon^4$ (α_0 is the usual thermal expansion coefficient), together with the GS energy E_{GS} given above. This results in a linear relation $\epsilon \simeq \alpha_0 T + (A/K)\langle n_T \rangle_\epsilon$ between the magnetic moment ($= 2n_T$) and lattice expansion. They both strongly increase with temperature if lattice is "soft" enough (i.e., small K), as demonstrated in Figs. 1(g) and 1(h) by employing

the parameters $E_T - J = 160$ meV, $\kappa = 60$ meV, $A = 1.5$ eV, $K = 4.55$ eV, $Q = 250$ eV, and $\alpha_0 = 0.2 \times 10^{-4}$ K^{-1}, providing a good fit to the experimental data of Ref. [28].

Turning to collective behavior of the model, we notice first that for $N \to \infty$ and large κ, the GS is dominated by tightly bound singlet dimers derived from the single-bond solution. The resonance of dimers on square-lattice plaquettes then supports a columnar state [36] breaking lattice symmetry without magnetic LRO [33]. In the opposite limit of $N = 1$, the model shows a condensation of T bosons. We found that the $N = 3$ model relevant here is also unstable towards a condensation of T particles with $S = 1$. This condensate hosts interesting properties not present in a conventional Heisenberg model. We discuss them based on the following wave function describing Gutzwiller-projected condensate of spin-1 T bosons:

$$|\Psi\rangle = \prod_i \left[\sqrt{1-\rho}\, s_i^\dagger + \sqrt{\rho} \sum_{\alpha=x,y,z} d_{\alpha i}^* T_{\alpha i}^\dagger\right] |\text{vac}\rangle, \quad (2)$$

where $\rho \in [0, 1]$ is the condensate density to be understood as the effective spin-length S_{eff}. The complex unit vectors $\boldsymbol{d}_i = \boldsymbol{u}_i + i\boldsymbol{v}_i$ ($u_i^2 + v_i^2 = 1$) determine the spin structure of the condensate in terms of the coherent states of spin-1 [37,38] corresponding to $T_x = (T_{+1} - T_{-1})/\sqrt{2}i$, $T_y = (T_{+1} + T_{-1})/\sqrt{2}$, $T_z = iT_0$. The GS phase diagram obtained by minimizing $\langle\Psi|\mathcal{H}|\Psi\rangle$ and cross-checked by an exact diagonalization on a small cluster is presented in Fig. 2. We have included nearest-neighbor (NN) and next-NN interactions and fixed their ratio at $J_2/J_1 = \kappa_2/\kappa_1 = 0.7$, reflecting large next-NN overlap via As ions. Like in $J_1 - J_2$ model, this ratio decides between (π, π) and $(\pi, 0)$ order. Figures 2(a) and 2(b) contain, apart from a disordered (uncondensed) phase ($\rho = 0$) at small κ, J, three distinct phases depending on κ/E_T and J/E_T values. (i) Ferroquadrupolar (FQ) phase with $\boldsymbol{u}_i = \boldsymbol{u}$ and $\boldsymbol{v}_i = 0$. This phase has zero magnetization and is characterized by the quadrupolar order parameter $\langle S^\alpha S^\beta - (1/3)S^2\delta_{\alpha\beta}\rangle = \rho((1/3)\delta_{\alpha\beta} - u_\alpha u_\beta)$ with $\boldsymbol{u}$ playing the role of the *director* [38]. This state, often referred to as "spin nematic," appears in biquadratic exchange [37–40] and optical lattice models [41–44]. (ii) Nonsaturated antiferromagnetic (ns-AF) phase with stripy magnetic order, specified by $\boldsymbol{u}_i = (0, 0, u)$ and $\boldsymbol{v}_i = (0, v, 0)e^{i\boldsymbol{Q}\cdot\boldsymbol{R}_i}$ with $\boldsymbol{Q} = (\pi, 0)$. The LRO moment $\langle\boldsymbol{S}\rangle$ given by $m = 2\rho uv$ can take values from 0 to $S_{\text{eff}} = \rho$. (iii) Saturated antiferromagnet (AF) with the same $\boldsymbol{Q}$ vector, but now with $u = v = 1/\sqrt{2}$ and $m = S_{\text{eff}} = 1$.

The part of the phase diagram relevant to pnictides is shown in Fig. 2(d). The decrease of J is associated with doping that changes the nesting conditions [31], while the increase of E_T is related to external or chemical pressure. Figures 2(e) and 2(f), shows that the LRO moment m quickly vanishes as J (E_T) values decrease (increase); however, the spin-length $S_{\text{eff}} = \rho$ remains almost constant

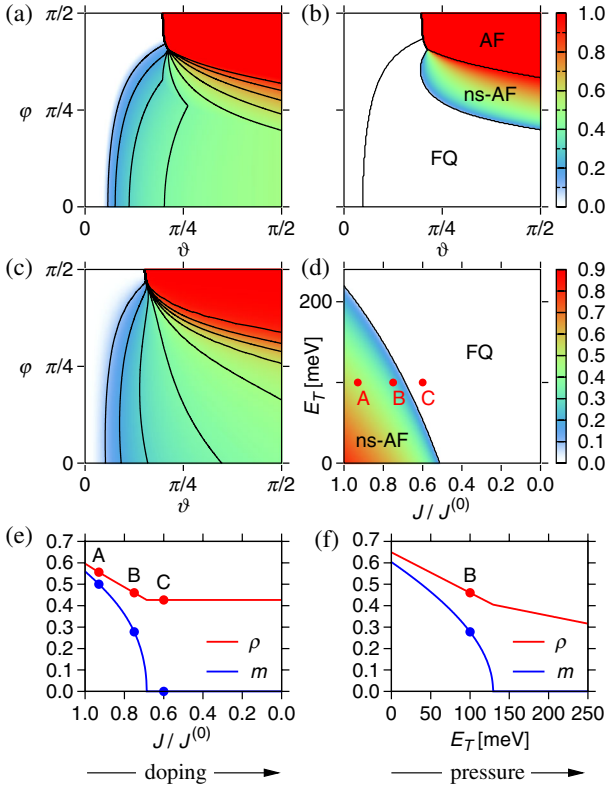

FIG. 2 (color online). (a) Condensate density $\rho(\equiv S_{\text{eff}})$ obtained from Eq. (2) as a function of angles ϑ, φ which parametrize the model (1) via $E_T = \cos\vartheta$, $\kappa_1 = \sin\vartheta\cos\varphi$, and $J_1 = \sin\vartheta\sin\varphi$. We set $\kappa_2/\kappa_1 = J_2/J_1 = 0.7$. (b) The ordered spin moment value m. (c) T occupation per site n_T obtained by an exact diagonalization of 12-site cluster, to be compared with ρ of panel (a). (d) The ordered moment m as a function of E_T and relative J-strength for fixed $\kappa_1 = 100$ meV, $\kappa_2 = 0.7\kappa_1$, $J_1^{(0)} = 140$ meV, $J_2^{(0)} = 0.7J_1^{(0)}$. (e,f) Effective spin length $\rho = S_{\text{eff}}$ and ordered moment m at the (e) $E_T = 100$ meV and (f) $J/J^{(0)} = 0.75$ lines through the phase diagram in (d).

($\sim 1/2$), corresponding to a fluctuating magnetic moment $\sim 1\mu_B$. This quantum state is driven by the κ process, which generates the spin-1 states in a form of singlet pairs.

We consider now the excitation spectrum. It is convenient to separate fast (density) and slow (spin) fluctuations. We introduce pseudospin $\tau = 1/2$ indicating the presence of a T particle, and a vector field $\boldsymbol{d}$ defining the spin-1 operator as $\boldsymbol{S} = -i(\boldsymbol{d}^\dagger \times \boldsymbol{d})$. The resulting Hamiltonian,

$$\mathcal{H} = E_T \sum_i \left(\frac{1}{2} - \tau_i^z\right) - \sum_{\langle ij\rangle} \kappa_{ij}(\tau_i^+ \tau_j^+ \boldsymbol{d}_i \cdot \boldsymbol{d}_j + \text{H.c.}) - \sum_{\langle ij\rangle} J_{ij}\left(\frac{1}{2} - \tau_i^z\right)\left(\frac{1}{2} - \tau_j^z\right)(\boldsymbol{d}_i^\dagger \times \boldsymbol{d}_i)\cdot(\boldsymbol{d}_j^\dagger \times \boldsymbol{d}_j) \quad (3)$$

is decoupled on a mean-field level. The condensate spin dynamics is then given by $O(3)$-symmetric Hamiltonian

$$\mathcal{H}_d = -\sum_{\langle ij\rangle} \tilde{\kappa}_{ij}(\boldsymbol{d}_i \cdot \boldsymbol{d}_j + \text{H.c.}) - \sum_{\langle ij\rangle} \tilde{J}_{ij}(\boldsymbol{d}_i^\dagger \times \boldsymbol{d}_i)\cdot(\boldsymbol{d}_j^\dagger \times \boldsymbol{d}_j) \tag{4}$$

with the renormalized $\tilde{\kappa}_{ij} = \kappa_{ij}\langle\tau_i^+\tau_j^+\rangle \approx \kappa_{ij}(1-\rho)\rho$ and $\tilde{J}_{ij} \approx J_{ij}\rho^2$. The excitations are found by introducing a, b, c bosons according to $\boldsymbol{d} = (d_x, d_y, d_z) = (a, ub - ive^{i\boldsymbol{Q}\cdot\boldsymbol{R}}c, -ive^{i\boldsymbol{Q}\cdot\boldsymbol{R}}b + uc)$ and replacing the condensed one as c, $c^\dagger \to \sqrt{1-n_a-n_b}$. The resulting ($a$, b) Hamiltonian is solved by the Bogoliubov transformation. A similar approach is used for the τ sector describing the condensate density fluctuations $\delta\rho = \delta S_{\text{eff}}$.

Shown in Fig. 3 is the excitation spectra for several points of the phase diagram. The spin-length fluctuations δS_{eff} are high in energy. Figure 3(b) focuses on the magnetic excitations. In the FQ phase, quadrupole and magnetic modes are degenerate and gapless at $\boldsymbol{q} = 0$. As the AF phase is approached, the gap at $\boldsymbol{Q}$ decreases and closes upon entering the magnetic phase. However, the higher energy magnons (which scale with S_{eff}) are not much affected by transition, apart from getting (softer) harder in a (dis)ordered phase; this explains the persistence of well-defined high-energy magnons into nonmagnetic phases [19,20].

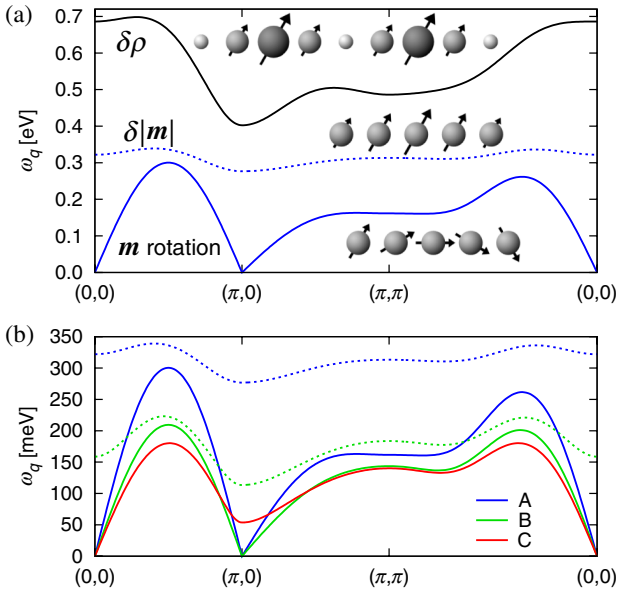

FIG. 3 (color online). (a) Dispersion of the condensate density ($\delta\rho$, solid-black) and the ordered moment-length ($\delta|\mathbf{m}|$, dotted-blue) fluctuations, and the magnon dispersion (solid-blue), at the point A in the phase diagram of Fig. 2(d). All three modes are active in resonant x-ray scattering, and the latter two in neutron scattering. (b) Evolution of the magnetic excitations going from FQ to the ns-AF phase [$C \to B \to A$ in Fig. 2(d)]. Twofold degenerate quadrupole waves (C) split into the magnon (solid lines) and the $\delta|\mathbf{m}|$ mode (dotted lines). The latter represents oscillations between the nematic and magnetic orderings and is gapful.

The magnetic modes in Fig. 3(b) resemble excitations of bilinear-biquadratic spin model [38]. In fact, the dispersion in FQ phase can be exactly reproduced [45] from an effective spin-1 model $\sum_{\langle ij\rangle}\tilde{J}_{ij}\boldsymbol{S}_i\cdot\boldsymbol{S}_j - \tilde{\kappa}_{ij}(\boldsymbol{S}_i\cdot\boldsymbol{S}_j)^2$, with $\tilde{J}$ and $\tilde{\kappa}$ given above. A large biquadratic coupling was indeed found to account for many observations in Fe pnictides [8,31,34]. We note, however, that this model possesses FQ and AF phases only and misses the ns-AF phase, where the ordered moment is reduced already at the classical level; also, it does not contain the key notion of the original model, i.e., formation of the effective spin S_{eff} and its fluctuations.

Singlet correlations inherent to the model may also lead to an increase of the paramagnetic susceptibility $\chi(T)$ with temperature [30]. Considering the nonmagnetic phase, we find that for the field parallel to the director $\boldsymbol{u}$, χ is temperature dependent, $\chi_\parallel = \frac{1}{2T}\int d\omega\, \mathcal{N}(\omega)\sinh^{-2}\frac{\omega}{2T}$, where $\mathcal{N}(\omega) = \sum_{\boldsymbol{q}}\delta(\omega - \omega_{\boldsymbol{q}})$ is the density of states (DOS) of magnetic excitations, while $\chi_\perp$ is constant. The average $\chi = (\chi_\parallel + 2\chi_\perp)/3$ (with additional factor of $4\rho^2\mu_B^2 N_A$) gives the measured $\chi(T)$, assuming slow rotations of the director. The DOS shown in Fig. 4(a) is contributed mainly by the regions around $(\pi, 0)$ and $(0, \pi)$ hosting AF correlations. The corresponding thermal excitations lead to the increase of χ [Fig. 4(b)].

To conclude, we proposed the model describing quantum magnetism of Fe pnictides. Their universal magnetic spectra, wide-range variations of the LRO moments, and emergent biquadratic-spin couplings are explained. The model stands also on its own: extending the Heisenberg models to the case of "mixed-spin" ions, it represents a novel many-body problem. Of particular interest is the effect of band fermions, which should have a strong impact on low-energy dynamics of the model, e.g., converting the $\boldsymbol{q} = 0$ Goldstone modes into overdamped spin-nematic fluctuations. Understanding the effects of coupling between local moments and band fermions, including

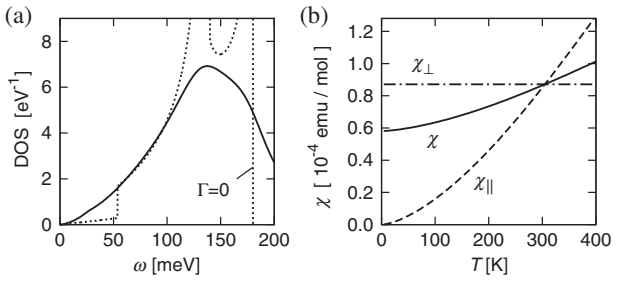

FIG. 4. (a) Density of states of the magnetic excitations calculated for the point C of Fig. 2(d). We included the damping (e.g., due to coupling to the Stoner continuum) in a form $\Gamma(\omega) = \min(\omega, \Gamma)$ with $\Gamma = \omega_{\boldsymbol{Q}}/2$. The result with $\Gamma = 0$ is shown for comparison. (b) Temperature dependence of the uniform susceptibility χ. The components $\chi_\parallel$ ($\chi_\perp$) parallel (perpendicular) to the local director $\boldsymbol{u}$ are also shown.

implications for SC, should be the next step towards a complete theory of Fe pnictides.

J. C. acknowledges support by the Alexander von Humboldt Foundation, ERDF under project CEITEC (CZ.1.05/1.1.00/02.0068) and EC 7th Framework Programme (286154/SYLICA).

[1] Y. Kamihara, T. Watanabe, M. Hirano, and H. Hosono, J. Am. Chem. Soc. **130**, 3296 (2008).
[2] For a review of the experimental data, see, e.g., D. C. Johnston, Adv. Phys. **59**, 803 (2010).
[3] T. Yildirim, Physica (Amsterdam) **469C**, 425 (2009).
[4] C. Xu, M. Müller, and S. Sachdev, Phys. Rev. B **78**, 020501(R) (2008).
[5] Q. Si and E. Abrahams, Phys. Rev. Lett. **101**, 076401 (2008).
[6] C. Fang, H. Yao, W. F. Tsai, J. P. Hu, and S. A. Kivelson, Phys. Rev. B **77**, 224509 (2008).
[7] G. Uhrig, M. Holt, J. Oitmaa, O. P. Sushkov, and R. R. P. Singh, Phys. Rev. B **79**, 092416 (2009).
[8] D. Stanek, O. P. Sushkov, and G. S. Uhrig, Phys. Rev. B **84**, 064505 (2011).
[9] I. I. Mazin, D. J. Singh, M. D. Johannes, and M. H. Du, Phys. Rev. Lett. **101**, 057003 (2008).
[10] K. Kuroki, S. Onari, R. Arita, H. Usui, Y. Tanaka, H. Kontani, and H. Aoki, Phys. Rev. Lett. **101**, 087004 (2008).
[11] A. V. Chubukov, D. V. Efremov, and I. Eremin, Phys. Rev. B **78**, 134512 (2008).
[12] S. Graser, T. A. Maier, P. J. Hirschfeld, and D. J. Scalapino, New J. Phys. **11**, 025016 (2009).
[13] E. Kaneshita, T. Morinari, and T. Tohyama, Phys. Rev. Lett. **103**, 247202 (2009).
[14] H. Gretarsson *et al.*, Phys. Rev. B **84**, 100509(R) (2011).
[15] P. Vilmercati *et al.*, Phys. Rev. B **85**, 220503(R) (2012).
[16] M. D. Johannes, I. I. Mazin, and D. S. Parker, Phys. Rev. B **82**, 024527 (2010).
[17] I. I. Mazin and M. D. Johannes, Nat. Phys. **5**, 141 (2009).
[18] D. Reznik *et al.*, Phys. Rev. B **80**, 214534 (2009).
[19] M. Liu *et al.*, Nat. Phys. **8**, 376 (2012).
[20] K.-J. Zhou *et al.*, Nat. Commun. **4**, 1470 (2013).
[21] M. Wang *et al.*, arXiv:1303.7339.
[22] Z. P. Yin, K. Haule, and G. Kotliar, Nat. Mater. **10**, 932 (2011).
[23] J. Dai, Q. Si, J.-X. Zhu, and E. Abrahams, Proc. Natl. Acad. Sci. U.S.A. **106**, 4118 (2009).
[24] S.-P. Kou, T. Li, and Z.-Y. Weng, Europhys. Lett. **88**, 17010 (2009).
[25] W. Lv, F. Krüger, and P. Phillips, Phys. Rev. B **82**, 045125 (2010).
[26] *Spin Crossover in Transition Metal Compounds I*, edited by P. Gütlich and H. A. Goodwin (Springer, Berlin, 2004).
[27] S. Stackhouse, Nat. Geosci. **1**, 648 (2008).
[28] H. Gretarsson, S. R. Saha, T. Drye, J. Paglione, J. Kim, D. Casa, T. Gog, W. Wu, S. R. Julian, and Y.-J. Kim, Phys. Rev. Lett. **110**, 047003 (2013).
[29] J. T. Park *et al.*, Phys. Rev. B **86**, 024437 (2012).
[30] R. Klingeler *et al.*, Phys. Rev. B **81**, 024506 (2010).
[31] A. N. Yaresko, G.-Q. Liu, V. N. Antonov, and O. K. Andersen, Phys. Rev. B **79**, 144421 (2009).
[32] See Supplemental Material at http://link.aps.org/supplemental/10.1103/PhysRevLett.110.207205 for derivation of the Hamiltonian (1) from a two-orbital Hubbard model.
[33] To address a tetra/ortho structural (''orbital order'') transition, we may include also xz/yz orbital degeneracy of $S = 1$ triplets; this is left for future work.
[34] A. L. Wysocki, K. D. Belashchenko, and V. P. Antropov, Nat. Phys. **7**, 485 (2011).
[35] R. Yu, Z. Wang, P. Goswami, A. H. Nevidomskyy, Q. Si, and E. Abrahams, Phys. Rev. B **86**, 085148 (2012).
[36] N. Read and S. Sachdev, Phys. Rev. Lett. **62**, 1694 (1989).
[37] B. A. Ivanov and A. K. Kolezhuk, Phys. Rev. B **68**, 052401 (2003).
[38] A. Läuchli, F. Mila, and K. Penc, Phys. Rev. Lett. **97**, 087205 (2006).
[39] H. Tsunetsugu and M. Arikawa, J. Phys. Soc. Jpn. **75**, 083701 (2006).
[40] K. Harada and N. Kawashima, Phys. Rev. B **65**, 052403 (2002).
[41] E. Demler and F. Zhou, Phys. Rev. Lett. **88**, 163001 (2002); A. Imambekov, M. Lukin, and E. Demler, Phys. Rev. A **68**, 063602 (2003).
[42] S. K. Yip, Phys. Rev. Lett. **90**, 250402 (2003).
[43] C. M. Puetter, M. J. Lawler, and H.-Y. Kee, Phys. Rev. B **78**, 165121 (2008).
[44] M. Serbyn, T. Senthil, and P. A. Lee, Phys. Rev. B **84**, 180403(R) (2011).
[45] This can be understood using the identity $(\boldsymbol{S}_i \cdot \boldsymbol{S}_j)^2 = |\boldsymbol{d}_i \cdot \boldsymbol{d}_j|^2 + 1$. If $v \ll u \approx 1$, like in the FQ phase or close to it in the ns-AF phase, we recover the κ term of Eq. (4), $(\boldsymbol{S}_i \cdot \boldsymbol{S}_j)^2 \approx \boldsymbol{d}_i \cdot \boldsymbol{d}_j + \boldsymbol{d}_i^\dagger \cdot \boldsymbol{d}_j^\dagger$.

Supplemental Material for

Spin-state crossover model for the magnetism of iron pnictides

Jiří Chaloupka[1,2] and Giniyat Khaliullin[1]

[1] *Max Planck Institute for Solid State Research, Heisenbergstrasse 1, D-70569 Stuttgart, Germany*
[2] *Central European Institute of Technology, Masaryk University, Kotlářská 2, 61137 Brno, Czech Republic*

Here we analyze two-orbital Hubbard model in the regime of large Hund's coupling and large interorbital hopping, and explicitly demonstrate the emergence of the effective model proposed in the main paper. We also provide estimates of the model parameters in terms of the microscopic parameters of the Hubbard model.

Based on the "orbital-differentiation" mechanism – which is particularly pronounced in multiorbital systems with large Hund's coupling (see Ref. [1] for recent discussion) – we assume a coexistence of strongly correlated orbitals (hosting magnetic moments) and more itinerant bands (responsible for the charge transport and Fermi-surface related physics). For the Fe-pnictide/chalcogenide families, a minimal model for the "magnetic" sector is a two-orbital Hubbard model which may accommodate magnetic moments ranging from zero to $2\mu_{\rm B}$ per Fe-ion, depending on the parameter regime. This possible moment-window is what observed in Fe-pnictide/chalcogenides [2] (and also consistent with the model of the main text). We assume that these two orbitals (labeled a and b below) are populated by two electrons per site on average, while the remaining four electrons out of Fe-d^6 configuration form a semimetallic band structure. The itinerant bands are not a prime source of magnetic moments but, as noticed in the main text, we keep in mind that they may mediate the interactions between local moments and hence support their long-range order [3, 4].

Let us focus now on the "magnetic" sector, i.e. two-orbital Hubbard Hamiltonian. As usual, it comprises two parts, local interactions and intersite hoppings: $\mathcal{H} = \mathcal{H}_{\rm loc} + \mathcal{H}_{\rm kin}$. Its local part includes the crystal field splitting Δ between a and b orbitals (their precise structure in terms of original d states is not essential here) and local correlations:

$$\mathcal{H}_{\rm loc} = \frac{\Delta}{2}\sum_i (n_{ib} - n_{ia}) + U \sum_{i,\gamma=a,b} n_{i\gamma\uparrow} n_{i\gamma\downarrow} + \sum_i \Big[U' - J_H\Big(2\boldsymbol{S}_{ia}\cdot\boldsymbol{S}_{ib} + \tfrac{1}{2}\Big)\Big] n_{ia} n_{ib} \ . \tag{S1}$$

The local pair-hopping term is neglected, and the relation $U' = U - 2J_H$ between inter- and intra-orbital Coulomb interactions will be used. The kinetic term $\mathcal{H}_{\rm kin}$ of the Hamiltonian contains the intersite hopping of both intra- and inter-orbital character

$$\mathcal{H}_{\rm kin} = -t \sum_{\langle ij\rangle,\sigma} \left(a^\dagger_{i\sigma} a_{j\sigma} + b^\dagger_{i\sigma} b_{j\sigma} + \text{h.c.}\right) - \tilde{t} \sum_{\langle ij\rangle,\sigma} \left(a^\dagger_{i\sigma} b_{j\sigma} + b^\dagger_{i\sigma} a_{j\sigma} + \text{h.c.}\right) \ . \tag{S2}$$

Similar model was recently considered in Ref. [5] to address the spin-transition physics in cobaltates. The key difference of our model is the presence of interorbital hopping $\tilde{t}$, which converts the transitions found in Ref. [5] into a smooth spin-crossover such that the ground state magnetic moment length (not long-range order parameter!) may acquire any value from zero to $2\,\mu_{\rm B}$.

Our aim is to obtain the model Hamiltonian of the main paper as an effective low-energy Hamiltonian resulting from $\mathcal{H} = \mathcal{H}_{\rm loc} + \mathcal{H}_{\rm kin}$ in the appropriate regime of parameters Δ, J_H, etc. This is achieved by a standard procedure – we select the relevant $d_i^2 - d_j^2$ bond states from the eigenbasis of $\mathcal{H}_{\rm loc}$ and obtain effective interactions on the bonds by eliminating $\mathcal{H}_{\rm kin}$ perturbatively, employing the low-energy $d_i^3 - d_j^1$ and $d_i^1 - d_j^3$ configurations as the intermediate states. To check the validity of this approach, the exact eigenstates of $\mathcal{H}$ on a single bond are calculated and the results compared with those of the effective Hamiltonian $\mathcal{H}_{\rm eff}$ we have derived.

In the spin-crossover regime discussed in the main paper, large Hund's coupling nearly compensates the crystal field splitting (i.e., $\Delta \sim 3J_H$) and makes the on-site singlet $|s\rangle = a^\dagger_\uparrow a^\dagger_\downarrow |\,\rangle$ and the three triplet

states $|T_{+1}\rangle = a^\dagger_\uparrow b^\dagger_\uparrow |\,\rangle$, $|T_0\rangle = \frac{1}{\sqrt{2}}(a^\dagger_\uparrow b^\dagger_\downarrow + a^\dagger_\downarrow b^\dagger_\uparrow)|\,\rangle$, and $|T_{-1}\rangle = a^\dagger_\downarrow b^\dagger_\downarrow |\,\rangle$ quasidegenerate. These states thus form the relevant low-energy sector while the other states (such as $a^\dagger_\uparrow b^\dagger_\downarrow |\,\rangle$) are much higher in energy and can be ignored.

To be able to extract the effective Hamiltonian on a bond, it is convenient to consider the subspaces with total spin $S_{\rm tot} = 0, 1, 2$ separately. In $S_{\rm tot} = 0$ sector, the relevant bond states are the two $d^2_i - d^2_j$ configurations depicted in Fig. S1(a, b): $|ss\rangle = |s\rangle_i|s\rangle_j$ with the local energy $E_{ss} = 2U - 2\Delta$, and $|TT\rangle = \frac{1}{\sqrt{3}}\big(|T_{+1}\rangle_i|T_{-1}\rangle_j - |T_0\rangle_i|T_0\rangle_j + |T_{-1}\rangle_i|T_{+1}\rangle_j\big)$ with the local energy $E_{TT} = E_{ss} + 2(\Delta - 3J_H)$. The bond interaction originates from virtual processes employing as the intermediate states mainly the low-lying $d^3_i - d^1_j$ and $d^1_i - d^3_j$ configurations presented in Fig. S1(c, d). They are denoted as $|A\rangle$ and $|B\rangle$ and their local energy amounts to $E_A = E_B = E_{ss} + U' + \Delta - 3J_H$. The other bond states have a negligible contribution to the groundstate, due to their high energy or due to kinematic (no hopping) reasons. The lowest state in the $S_{\rm tot} = 1$ sector is composed of a pair of on-site triplets $|T\rangle$ and states analogous to $|A\rangle$ and $|B\rangle$ but having total spin one. Finally, the only states in the $S_{\rm tot} = 2$ are the combinations of two on-site triplets. These states are unaffected by hopping.

The validity of the above classification of low-energy levels of Hubbard model is demonstrated in Fig. S2 showing the results of an exact diagonalization of full two-orbital model $\mathcal{H}$ on a single bond. We consider a representative set of parameters Δ and J_H such that a spin-crossover regime, where the on-site singlet and triplet states are quasidegenerate, is realized: $\Delta - 3J_H = 0.1$ eV. Focusing on $S_{\rm tot} = 0$ sector in Fig. S2(b), we can observe that with increasing $\tilde{t}$, the state $|TT\rangle$ gets gradually involved into the groundstate, which becomes a mixture of $|ss\rangle$, $|TT\rangle$ and the higher energy states $|A\rangle$, $|B\rangle$ serving as the intermediate states for the κ-processes. The contribution of the other states, which are neglected in our derivation of the effective Hamiltonian below, is indeed negligible.

Having selected our basis states and evaluated their local energy, we proceed now by incorporating the intersite hopping within this basis. First, the initial Hamiltonian $\mathcal{H}$ is projected to the selected subspace of total spin $S_{\rm tot}$ and denoted accordingly as $\mathcal{H}^{(S)}$ (where $S = 0, 1, 2$). In the next step, the intermediate states are eliminated from $\mathcal{H}^{(S)}$-matrix by perturbation theory. After these steps, we will obtain an effective Hamiltonian $\mathcal{H}^{(S)}_{\rm eff}$ that operates within $d^2_i - d^2_j$ configuration alone, and compare it with the model Hamiltonian $\mathcal{H}_{\rm model}$ used in the main paper.

In the most interesting $S_{\rm tot} = 0$ subspace, after the elimination of intermediate states, the Hamiltonian $\mathcal{H}$ projected to the subspace spanned by $|ss\rangle$, $|TT\rangle$, $|A\rangle$, $|B\rangle$ states

$$\mathcal{H}^{(0)} = \begin{pmatrix} E_{ss} & 0 & -\sqrt{2}\,\tilde{t} & -\sqrt{2}\,\tilde{t} \\ 0 & E_{TT} & -\sqrt{\tfrac{3}{2}}\,\tilde{t} & -\sqrt{\tfrac{3}{2}}\,\tilde{t} \\ -\sqrt{2}\,\tilde{t} & -\sqrt{\tfrac{3}{2}}\,\tilde{t} & E_A & 0 \\ -\sqrt{2}\,\tilde{t} & -\sqrt{\tfrac{3}{2}}\,\tilde{t} & 0 & E_B \end{pmatrix} \quad \text{becomes} \quad \mathcal{H}^{(0)}_{\rm eff} = \begin{pmatrix} E_{ss} - \dfrac{4\tilde{t}^2}{\varepsilon} & -\dfrac{2\sqrt{3}\,\tilde{t}^2}{\varepsilon} \\ -\dfrac{2\sqrt{3}\,\tilde{t}^2}{\varepsilon} & E_{TT} - \dfrac{3\tilde{t}^2}{\varepsilon} \end{pmatrix} \tag{S3}$$

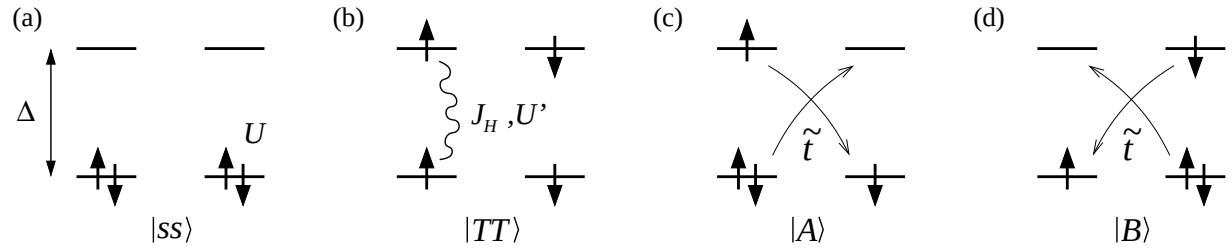

Figure S1: Basis states dominating the groundstate of the Hubbard model in the discussed spin-crossover regime. All the states have zero total spin. The two $d^2_i - d^2_j$ configurations $|ss\rangle$ and $|TT\rangle$ are shown in panels (a) and (b), respectively, together with a schematic depiction of the microscopic parameters. The $d^3_i - d^1_j$ configuration $|A\rangle$ and $d^1_i - d^3_j$ configuration $|B\rangle$, shown in panels (c) and (d), respectively, are connected to the $d^2_i - d^2_j$ configurations by virtue of the interorbital hoppings $\tilde{t}_{ab}$ or $\tilde{t}_{ba}$ indicated by arrows.

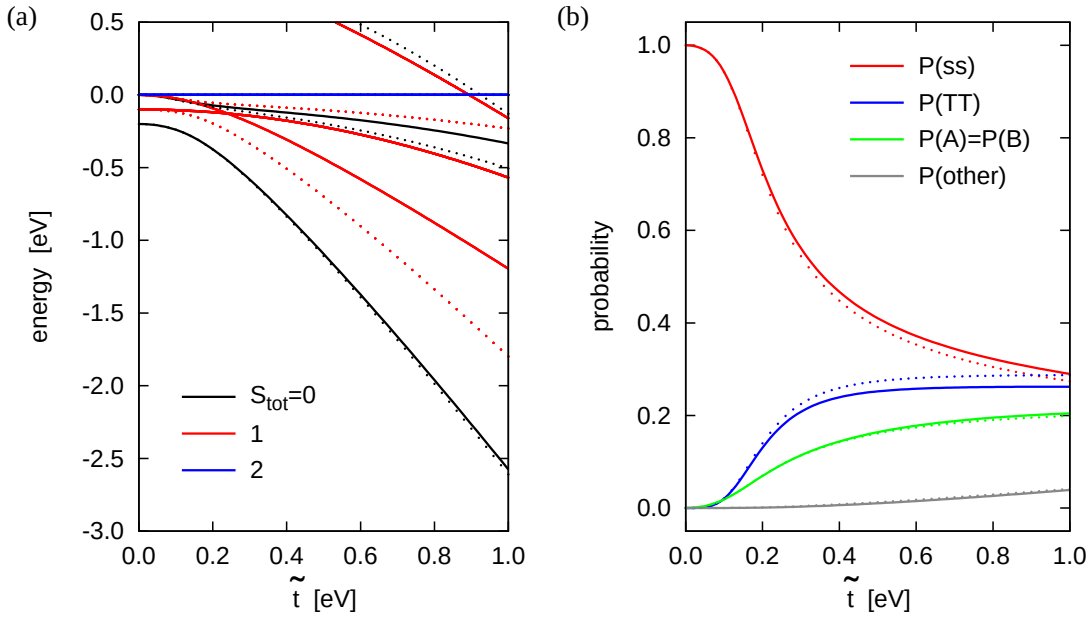

Figure S2: (a) Exact energy levels on the bond as a function of interorbital hopping $\tilde{t}$ for $U = 3$ eV, $J_H = 1$ eV, $\Delta - 3J_H = 0.1$ eV, and $t = 0$ (solid lines) and $t = 0.5\,\tilde{t}$ (dotted lines). States with different values of the total spin are distinguished by color. (b) Probabilities of selected basis states $|ss\rangle$, $|TT\rangle$, $|A\rangle$, and $|B\rangle$ in the groundstate. The other states ignored in the effective model derivation have a negligible total weight [see corresponding P(other) curve]. For a moderate value of t, the energy and the composition of the groundstate remains practically unaffected.

operating now within the $|ss\rangle$ and $|TT\rangle$ singlet states of $d_i^2 - d_j^2$ configuration. Here, $\varepsilon = E_A - E = E_B - E$ denotes the excitation energy. In the second order perturbation theory $E = E_{ss}$, but by diagonalizing the energy dependent $\mathcal{H}_{\rm eff}^{(0)}$ self-consistently, one can exactly reproduce the groundstate energy and the ratio of $|ss\rangle$ and $|TT\rangle$ coefficients obtained by diagonalizing the original matrix $\mathcal{H}^{(0)}$. In the following, we therefore take $E = E_{\rm GS}$ with $E_{\rm GS}$ being the groundstate energy of $\mathcal{H}_{\rm eff}^{(0)}$.

Using the same procedure, the pairs of local triplets T of total spin $S_{\rm tot} = 1$ obtain an energy $\mathcal{H}_{\rm eff}^{(1)} = E_1 = E_{TT} - 2\tilde{t}^2/\varepsilon'$ with $\varepsilon' = E_A - E_1$ being the excitation energy, and those of total spin $S_{\rm tot} = 2$ remain at an energy $\mathcal{H}_{\rm eff}^{(2)} = E_{TT}$.

The effective Hamiltonian $\mathcal{H}_{\rm eff}$ can now be exactly mapped to the model Hamiltonian $\mathcal{H}_{\rm model}$ proposed in the main paper. For a single bond, using the same notations, the corresponding matrix elements of $\mathcal{H}_{\rm model}$ read as

$$\mathcal{H}_{\rm model}^{(0)} = \begin{pmatrix} 0 & -\sqrt{3}\,\kappa \\ -\sqrt{3}\,\kappa & 2E_T - 2J - 4K \end{pmatrix}, \quad \mathcal{H}_{\rm model}^{(1)} = 2E_T - J - K\,, \quad \mathcal{H}_{\rm model}^{(2)} = 2E_T + J - K\,. \tag{S4}$$

To make the correspondence between $\mathcal{H}_{\rm eff}$ and $\mathcal{H}_{\rm model}$ matrices complete, we had to include small biquadratic exchange $-K(\boldsymbol{S}_1 \cdot \boldsymbol{S}_2)^2$. The term-by-term comparison of the matrix elements of $\mathcal{H}_{\rm eff}^{(S)}$ and $\mathcal{H}_{\rm model}^{(S)}$ yields the following values of the model parameters

$$\kappa = \frac{2\tilde{t}^2}{\varepsilon}\,, \qquad J = \frac{\tilde{t}^2}{\varepsilon'}\,, \qquad K = \tilde{t}^2\left(\frac{1}{\varepsilon} - \frac{1}{\varepsilon'}\right), \qquad E_T = (\Delta - 3J_H) + \tilde{t}^2\left(\frac{5}{2\varepsilon} - \frac{1}{\varepsilon'}\right). \tag{S5}$$

As evidenced by Fig. S3(a), the effective model gives an adequate description of the lowest states of the Hubbard model. The obtained model parameters entering Eqs. (S4) and (S5) are presented in Fig. S3(b) as functions of the interorbital hopping amplitude $\tilde{t}$. The realistic range of $E_T \approx 0.1 - 0.2$ eV and $\kappa, J \approx 0.05 - 0.20$ eV is obtained by taking $\tilde{t} \approx 0.2 - 0.4$ eV. The small biquadratic exchange contained in $\mathcal{H}_{\rm eff}$ can be neglected at this point because the much larger effective biquadratic contribution is in fact generated by the κ-processes dynamically (see main text).

It is worth noticing that the strength κ of the key process of the model is finite due to interorbital hopping $\tilde{t}$. This process is thus ineffective in perovskite lattices, but it is perfectly allowed for the Fe-(As/Te)-Fe bonding geometry of Fe-pnictides/chalcogenides and leads to the spin-crossover mechanism ("soft" magnetism) in these compounds (see main text). Concerning the role of intra-orbital t-hopping in the mapping, it did not enter the above formulas, since t does not connect any pair of the selected low energy states. The intermediate states that can be reached by t have an energy higher by Δ than those involved by $\tilde{t}$, so that the t-effect on κ and E_T values is relatively weak. It is only found to increase J by about $2t^2/(\Delta + E_A - E_{TT})$.

To conclude, we have shown that the model Hamiltonian proposed in the paper naturally emerges from the two-orbital Hubbard model with strong Hund's coupling, when a regime of spin-state quasidegeneracy is realized. The model parameters that follow from this derivation are well within the ranges that we have explored in our study.

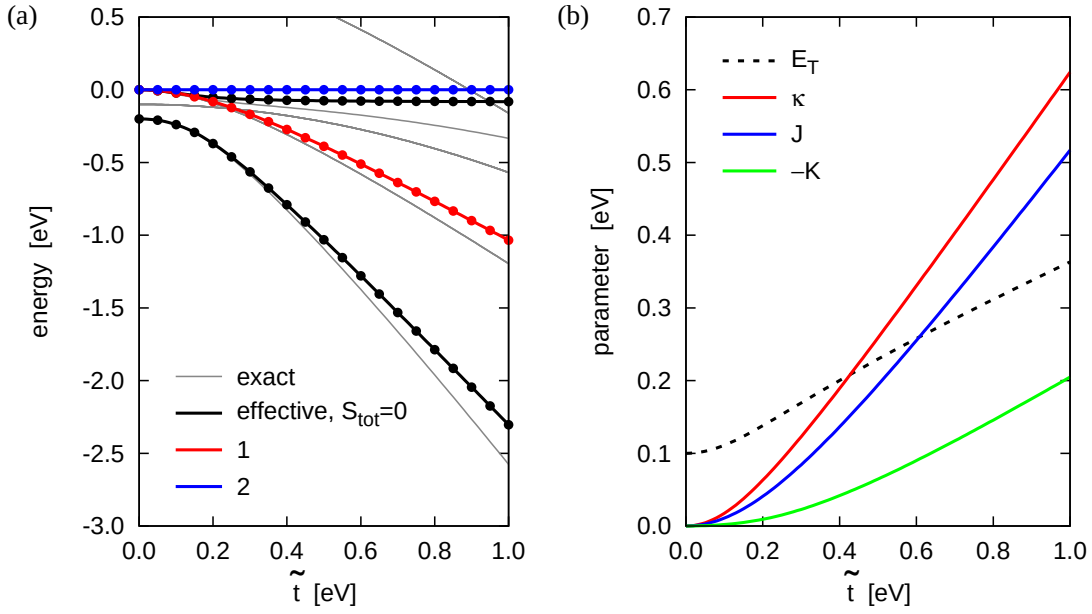

Figure S3: (a) Energy levels resulting from the diagonalization of $\mathcal{H}_{\text{eff}}$ compared to the exact levels of the original Hubbard Hamiltonian. The same parameters as in Fig. S2 are used and $t = 0$. (b) Values of the effective model parameters as functions of interorbital hopping $\tilde{t}$.

References

[1] A. Georges, L. de' Medici, and J. Mravlje, arXiv:1207.3033.

[2] H. Gretarsson *et al.*, Phys. Rev. B **84**, 100509(R) (2011).

[3] M.D. Johannes, I.I. Mazin, and D.S. Parker, Phys. Rev. B **82**, 024527 (2010).

[4] M.D. Johannes and I.I. Mazin, Phys. Rev. B **79**, 220510(R) (2009).

[5] J. Kuneš and V. Křápek, Phys. Rev. Lett. **106**, 256401 (2011).

PRL 116, 017203 (2016) PHYSICAL REVIEW LETTERS week ending 8 JANUARY 2016

Doping-Induced Ferromagnetism and Possible Triplet Pairing in d^4 Mott Insulators

Jiří Chaloupka[1] and Giniyat Khaliullin[2]
[1]Central European Institute of Technology, Masaryk University, Kotlářská 2, 61137 Brno, Czech Republic
[2]Max Planck Institute for Solid State Research, Heisenbergstrasse 1, D-70569 Stuttgart, Germany
(Received 26 October 2015; published 8 January 2016)

We study the effects of electron doping in Mott insulators containing d^4 ions such as Ru^{4+}, Os^{4+}, Rh^{5+}, and Ir^{5+} with $J = 0$ singlet ground state. Depending on the strength of the spin-orbit coupling, the undoped systems are either nonmagnetic or host an unusual, excitonic magnetism arising from a condensation of the excited $J = 1$ triplet states of t_{2g}^4. We find that the interaction between J excitons and doped carriers strongly supports ferromagnetism, converting both the nonmagnetic and antiferromagnetic phases of the parent insulator into a ferromagnetic metal, and further to a nonmagnetic metal. Close to the ferromagnetic phase, the low-energy spin response is dominated by intense paramagnon excitations that may act as mediators of a triplet pairing.

DOI: 10.1103/PhysRevLett.116.017203

A distinct feature of Mott insulators is the presence of low-energy magnetic degrees of freedom, and their coupling to doped charge carriers plays the central role in transition metal compounds [1]. In large spin systems like manganites, this coupling converts parent antiferromagnet (AF) into a ferromagnetic (FM) metal and gives rise to large magnetoresistivity effects. The doping of spin one-half compounds like cuprates and titanites, on the other hand, suppresses magnetic order and a paramagnetic (PM) metal emerges. In general, the fate of magnetism upon charge doping is dictated by the spin-orbital structure of parent insulators.

In compounds with an even number of electrons on the d shell, one may encounter a curious situation when the ionic ground state has no magnetic moment at all, yet they may order magnetically by virtue of low-lying magnetic levels with finite spin, if the exchange interactions are strong enough to overcome the single-ion magnetic gap. The d^4 ions such as Ru^{4+}, Os^{4+}, Rh^{5+}, Ir^{5+} possess exactly this type of level structure [2] due to spin-orbit coupling $\lambda(\boldsymbol{S}\cdot\boldsymbol{L})$: the spin $S = 1$ and orbital $L = 1$ moments form a nonmagnetic ground state with total $J = 0$ moment, separated from the excited level $J = 1$ by λ. A competition of the exchange and spin-orbit couplings results then in a quantum critical point (QCP) between the nonmagnetic Mott insulator and the magnetic order [3,4]. Since the magnetic order is due to the condensation of the virtual $J = 1$ levels and hence "soft," the amplitude (Higgs) mode is expected. The corollary of the "d^4 excitonic magnetism" [3] is the presence of the magnetic QCP that does not require any special lattice geometry, and the energy scales involved are large. The recent neutron scattering data [5] in d^4 Ca_2RuO_4 seem to support the theoretical expectations.

As we show in this Letter, the unusual magnetism of d^4 insulators, where the soft J spins fluctuate between 0 and 1, results also in anomalous doping effects that differ drastically from conventional cases as manganites and cuprates. Indeed, while common wisdom suggests that the PM phase with yet uncondensed J moments near QCP would get even "more PM" upon doping, we find that mobile carriers induce long-range order instead. The order is of the FM type and is promoted by the carrier-driven condensation of J moments. By the same mechanism, the exchange dominated AF phase also readily switches to the FM metal, as observed in La-doped Ca_2RuO_4 [6,7]. The theory might be relevant also to the electric-field-induced FM of Ca_2RuO_4 [8] and the FM state of the RuO_2 planes in oxide superlattices [9]. Further doping suppresses any magnetic order, and we suggest that residual FM correlations may lead to a triplet superconductivity (SC).

Model.—There are a number of d^4 compounds, magnetic as well nonmagnetic, with various lattice structures [10–17]. To be specific, we consider a square lattice d^4 insulator lightly doped by electrons. Assuming relatively large spin-orbit coupling (SOC), the relevant states are pseudospin $J = 0, 1$ states of t_{2g}^4 and $J = 1/2$ states of t_{2g}^5 [see Fig. 1(a)]. The d^4 singlet s ($J = 0$) and triplon $T_{0,\pm1}$ ($J = 1$) states obey the Hamiltonian derived in Ref. [3]. Adopting the Cartesian basis $T_x = (T_1 - T_{-1})/\sqrt{2}i$, $T_y = (T_1 + T_{-1})/\sqrt{2}$, and $T_z = iT_0$, it can be written as

$$\mathcal{H}_{d^4} = \lambda\sum_i \boldsymbol{T}_i^\dagger\cdot\boldsymbol{T}_i + \frac{1}{4}K\sum_{\langle ij\rangle}\Big[s_i s_j^\dagger\Big(\boldsymbol{T}_i^\dagger\cdot\boldsymbol{T}_j - \frac{1}{3}T_{i\gamma}^\dagger T_{j\gamma}\Big) - s_i^\dagger s_j^\dagger\Big(\frac{5}{6}\boldsymbol{T}_i\cdot\boldsymbol{T}_j - \frac{1}{6}T_{i\gamma}T_{j\gamma}\Big) + \text{H.c.}\Big], \quad (1)$$

where γ is determined by the bond direction. The model shows the AF transition due to a condensation of $\boldsymbol{T}$ at a critical value $K_c = \frac{6}{11}\lambda$ of the interaction parameter $K = 4t_0^2/U$. The degenerate $T_{x,y,z}$ levels split upon material-dependent lattice distortion, affecting the details of the model behavior [18]. We will consider the cubic

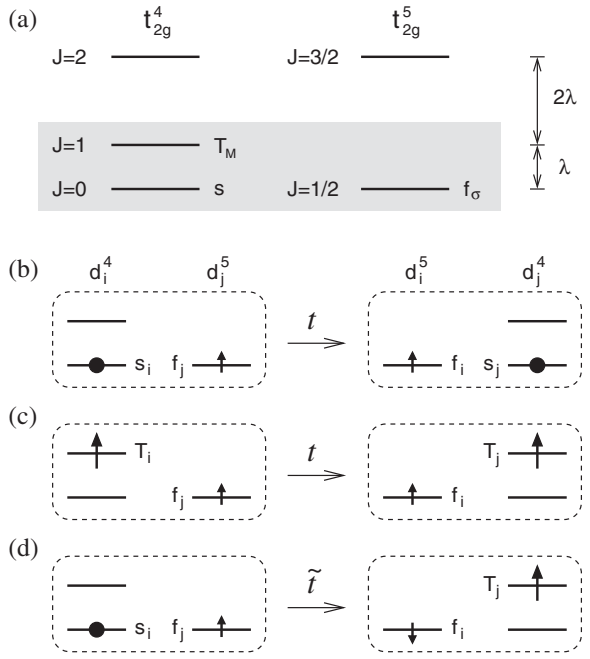

FIG. 1. (a) Spin-orbital level structure of t_{2g}^4 and t_{2g}^5 configurations. The lowest states including singlet s and triplet T_M states of d^4, and pseudospin $1/2$ f_σ states of d^5 configurations form a basis for the effective low-energy Hamiltonian. (b)–(d) Schematics of electron hoppings that lead to Eqs. (2) and (3): (b) Free motion of a doped fermion f_σ in a singlet background. (c) The fermion hopping is accompanied by a triplon backflow supporting the double-exchange type ferromagnetism. (d) Fermionic hopping generates a singlet-triplet excitation. This process leads to a coupling between the Stoner continuum and T moments promoting magnetic condensation.

symmetry case and make a few comments on the possible effects of the tetragonal splitting.

The d^4 system is doped by introducing a small number of d^5 objects—fermions f_σ carrying the pseudospin $J = 1/2$ of t_{2g}^5. The on-site constraint $n_s + n_T + n_f = 1$ is implied. The Hamiltonian describing the correlated motion of f is derived by calculating matrix elements of the nearest-neighbor hopping $\hat{T}_{ij} = -t_0(a_{i\sigma}^\dagger a_{j\sigma} + b_{i\sigma}^\dagger b_{j\sigma})$ between multielectron configurations $\langle d_i^5 d_j^4 | \hat{T}_{ij} | d_i^4 d_j^5 \rangle$. Here, a and b are the t_{2g} orbitals active on a given bond, e.g., xy and zx for x bonds. The resulting hopping Hamiltonian comprises three contributions, $\mathcal{H}_{d^4-d^5} = \sum_{ij}(h_1 + h_2 + h_3)_{ij}^{(\gamma)}$. The first one, depicted schematically in Figs. 1(b) and 1(c), is a spin-independent motion of f, accompanied by a backflow of s and $\boldsymbol{T}$:

$$h_1^{(\gamma)} = -t f_{i\sigma}^\dagger f_{j\sigma}\left[s_j^\dagger s_i + \frac{15}{16}\left(\boldsymbol{T}_j^\dagger \cdot \boldsymbol{T}_i - \frac{3}{5} T_{j\gamma}^\dagger T_{i\gamma}\right)\right]. \quad (2)$$

The second contribution is a spin-dependent motion of f generating $J = 0 \leftrightarrow J = 1$ magnetic excitation in the d^4 background [see Fig. 1(d)]:

$$h_2^{(\gamma)} = i\tilde{t}\left[\sigma_{ij}^\gamma (s_j^\dagger T_{i\gamma} - T_{j\gamma}^\dagger s_i) - \frac{1}{3}\boldsymbol{\sigma}_{ij} \cdot (s_j^\dagger \boldsymbol{T}_i - \boldsymbol{T}_j^\dagger s_i)\right]. \quad (3)$$

Here, $\boldsymbol{\sigma}_{ij} = f_{i\alpha}^\dagger \boldsymbol{\tau}_{\alpha\beta} f_{j\beta}$ with Pauli matrices τ denotes the bond-spin operator. The derivation for the cubic symmetry gives $t = \frac{4}{9}t_0$ and $\tilde{t} = (1/\sqrt{6})t_0$ with the ratio $\tilde{t}/t \approx 1$. However, these values are affected by the lattice distortions (via the pseudospin wave functions) and f-band renormalization reducing the effective t. We thus consider $\tilde{t}/t$ as a free parameter and set $\tilde{t} = 1.5t$ below. The last contribution to $\mathcal{H}_{d^4-d^5}$ reads as coupling between the bond spins residing in f and T sectors: $h_3^{(\gamma)} = \frac{9}{16}t(\sigma_{ij}^\gamma J_{ji}^\gamma + \frac{1}{3}\boldsymbol{\sigma}_{ij} \cdot \boldsymbol{J}_{ji})$, where $\boldsymbol{J}_{ji} = -i(\boldsymbol{T}_j^\dagger \times \boldsymbol{T}_i)$. At small doping and near QCP where the density of $\boldsymbol{T}$ excitons is small, the scattering term h_3 can be neglected.

Phase diagram.—We first inspect the phase behavior of the model as a function of doping x and interaction parameters K and $\tilde{t}$. The magnetic order is linked to the condensation of triplons induced by their mutual interactions and the interaction with the doped fermions f. In contrast to the cubic lattice where all the $\boldsymbol{T}$ flavors are equivalent, on the two-dimensional square lattice the T_z flavor experiences the strongest interactions and is selected to condense, provided that it is not suppressed by a large tetragonal distortion. We thus focus on T_z and omit the index z.

Following the standard notation for spin-1 condensates, we express complex $\boldsymbol{T} = \boldsymbol{u} + i\boldsymbol{v}$ using two real fields $\boldsymbol{u}, \boldsymbol{v}$. The ordered dipolar moment residing on Van Vleck transition $s \leftrightarrow \boldsymbol{T}$ is then $\boldsymbol{m} = 2\sqrt{6}\boldsymbol{v}$ [3]. Assuming either FM order (condensation prescribed by $T \to iv$) or AF order ($T \to \pm iv$ in a Néel pattern), we evaluate the classical energy of the T condensate and add the energy of the f bands polarized due to the condensed T. Doing so, we replace s_i by $\sqrt{1 - x - v^2}$ to incorporate the constraint, on average. The resulting total energy $E(v) = E_T + E_{\text{band}}$ is minimized with respect to the condensate strength v and compared for the individual phases: FM, AF, and PM ($v = 0$). The condensate energy amounts to $E_T = [\lambda \pm \frac{11}{6}K(1 - x - v^2)]v^2$, with the $+$ ($-$) sign for FM (AF) phase, respectively. The band energy $E_{\text{band}} = \sum_{k\sigma}\varepsilon_{k\sigma}n_{k\sigma}$ is calculated for a particular doping level $x = \sum_{k\sigma}n_{k\sigma}$ using the band dispersion $\varepsilon_{k\sigma} = -4(t_1 - \sigma t_2)\gamma_k$, where $\gamma_k = \frac{1}{2}(\cos k_x + \cos k_y)$. The hopping parameter t_1 stemming from h_1 reads as $t_1 \simeq t(1 - x)$ and $t_1 \simeq t(1 - x - 2v^2)$ for FM and AF, respectively. This captures the double-exchange nature of h_1—only FM-aligned T allow for a free motion of f, while the AF order of T blocks it. The parameter t_2 quantifies the polarization of the bands by virtue of h_2 and is nonzero in the FM case only: $t_2 = \frac{2}{3}\tilde{t}v\sqrt{1 - x - v^2}$.

Shown in Fig. 2 are the resulting phase diagrams along with the total ordered moment $m[\mu_B] = 2\sqrt{6}v + n_\uparrow - n_\downarrow$.

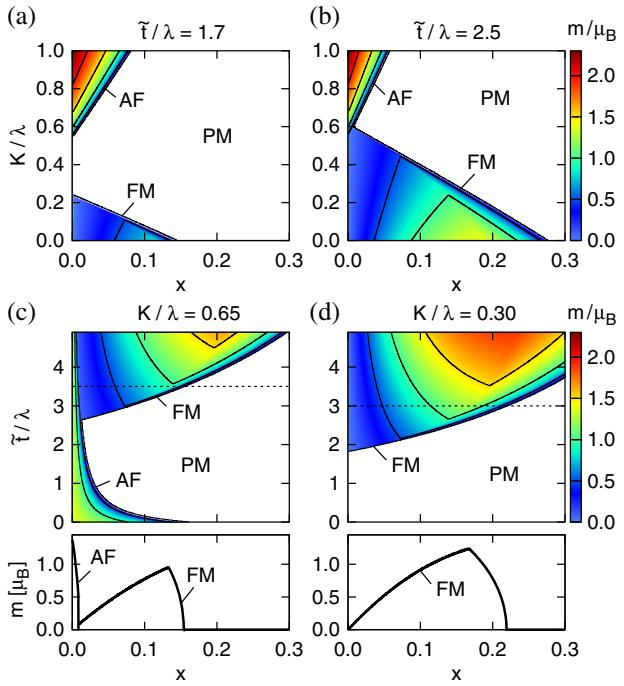

FIG. 2. (a),(b) Phase diagrams and the ordered magnetic moment value for varying doping x and K/λ keeping fixed $\tilde{t}/\lambda$ of 1.7 and 2.5. (c) Phase diagram for varying doping and $\tilde{t}/\lambda$ and fixed $K = 0.65\lambda$ above the critical $K_c = \frac{6}{11}\lambda$ of the d^4 system. The bottom panel shows $m(x)$ along the cut at $\tilde{t}/\lambda = 3.5$. (d) The same for $K = 0.3\lambda$ and the cut at $\tilde{t}/\lambda = 3$.

In both phase diagrams for constant $\tilde{t}/\lambda$ [Figs. 2(a) and 2(b)] at $x = 0$ we recover the QCP of the d^4 model. Nonzero doping causes a suppression of the AF phase via the double-exchange mechanism in h_1, and an appearance of the FM phase strongly supported by h_2 that directly couples the moment $\boldsymbol{m} \sim \boldsymbol{v}$ of $\boldsymbol{T}$ exciton to the fermionic spin $\boldsymbol{\sigma}_{ij}$, promoting magnetic condensation. With an increasing $\tilde{t}$ the FM phase quickly extends as seen also in Figs. 2(c) and 2(d) containing the phase diagrams for constant $K/\lambda = 0.65$ (selected to roughly reproduce the experimental value 1.3 μ_B for Ca_2RuO_4 [19]) and $K/\lambda = 0.30$. The constant $\tilde{t}/\lambda$ cut in Fig. 2(c) is strongly reminiscent of the phase diagram of La-doped Ca_2RuO_4 [6,7,20], where the AF phase is almost immediately replaced by the FM phase present up to a certain doping level. To estimate realistic values of $\tilde{t}/\lambda$, we assume $t_0 \sim 300$ meV. The large SOC in d^4 Ir^{5+} with $\lambda \sim 200$ meV [22–24] leads to $\tilde{t}/\lambda \sim 1$ and places it strictly to the AF/PM (c) or PM/PM (d) regime. In contrast to this, the moderate $\lambda \sim 70$–80 meV in Ru^{4+} [2,25] makes the FM phase easily accessible.

Spin susceptibility, emergence of paramagnons.—The tendency toward FM ordering naturally manifests itself in the dynamic spin response of the coupled $\boldsymbol{T}$ exciton and f-band system. Here we study it in detail for the PM phase, focusing again on T_z being the closest to condense. The magnetic moment $\boldsymbol{m}$ is carried mainly by the dipolar component $\boldsymbol{v} = (\boldsymbol{T} - \boldsymbol{T}^\dagger)/2i$ of triplons so that the dominant contribution to the spin susceptibility is given by the $\boldsymbol{v}$ susceptibility $\chi(\boldsymbol{q}, \omega)$. To evaluate it, we replace $s_i \to \sqrt{1 - x - n_{Ti}}$, and decouple h_1 (3) into f and T parts on a mean-field level. This yields a fermionic Hamiltonian $\mathcal{H}_f = \sum_{k\sigma} \varepsilon_k f^\dagger_{k\sigma} f_{k\sigma}$ with $\varepsilon_k = -4t(1-x)\gamma_k$, and a quadratic form for T_z boson: $\mathcal{H}_T = \sum_q [A_q T^\dagger_q T_q - \frac{1}{2} B_q (T_q T_{-q} + T^\dagger_q T^\dagger_{-q})]$. Here, $A_q = \lambda + 4t\langle n_{ij}\rangle(1-\gamma_q) + K(1-x)\gamma_q$, $B_q = \frac{5}{6}K(1-x)\gamma_q$, and $\langle n_{ij}\rangle = \sum_{k\sigma}\gamma_k n_{k\sigma}$. Bogoliubov diagonalization provides the bare triplon dispersion $\omega_q = (A_q^2 - B_q^2)^{1/2}$ and the bare v susceptibility $\chi_0(\boldsymbol{q}, \omega) = \frac{1}{2}(A_q - B_q)/[\omega_q^2 - (\omega + i\delta)^2]$. The susceptibility is further renormalized by the coupling h_2 (3), which can be viewed as an interaction between a dipolar component v of the triplons and the Stoner continuum of f fermions:

$$\mathcal{H}_{\text{int}} = g \sum_q v_q \tilde{\sigma}_{-q}, \qquad \tilde{\sigma}_{-q} = \sum_k \Gamma_{kq} f^\dagger_{k+q,\alpha} \tau^z_{\alpha\beta} f_{k,\beta}. \tag{4}$$

The coupling constant $g = \frac{8}{3}\tilde{t}\sqrt{1-x}$, and the vertex $\Gamma_{kq} = \frac{1}{2}(\gamma_k + \gamma_{k+q})$ is close to 1 in the limit of small $\boldsymbol{k}$, $\boldsymbol{q}$. By treating this coupling on a RPA level, we arrive at the full v susceptibility $\chi = \chi_0/(1 - \chi_0\Pi)$ with the v self-energy

$$\Pi(\boldsymbol{q}, \omega) = g^2 \sum_{k\sigma} \Gamma^2_{kq} \frac{n_{k\sigma} - n_{k+q\sigma}}{\varepsilon_{k+q} - \varepsilon_k - \omega - i\delta}. \tag{5}$$

The interplay of the coupled excitonic and band spin responses is demonstrated in Fig. 3. The high-energy component of χ linked to χ_0 follows the bare triplon dispersion ω_q. In an undoped system, due to the AF K interaction, ω_q has a minimum at $\boldsymbol{q} = (\pi, \pi)$ and χ_0 would be most intense there. By doping, the double exchange mechanism in h_1 disfavoring AF correlations pushes ω_q up near (π, π). Further, due to a dynamical mixing [Eqs. (3) and (4)] of triplons with the fermionic continuum, the low-energy component of χ gains spectral weight as $\tilde{t}/\lambda$ approaches the critical value, and a gradually softening FM paramagnon is formed [see Fig. 3(b)]. The emergence of the paramagnon and the increase of its spectral weight is shown in detail in Fig. 3(e). Finally, once the critical $\tilde{t}/\lambda$ is reached, triplons, whose spectral weight was pulled down by the coupling to the Stoner continuum, condense and the FM order sets in, signaled by the divergence of $\chi(\boldsymbol{q} = 0, \omega = 0)$ [cf. Figs. 3(c) and 3(d)].

Triplet pairing.—Intense paramagnons emerging in the proximity to the FM phase may serve as mediators of a triplet pairing interaction [26]. In the following, we perform semiquantitative estimates for this triplet SC.

While the dominant contribution to the pairing strength is due to the v_z fluctuations, in order to assess the structure of the triplet order parameter, the full coupling $\mathcal{H}_{\text{int}} = g\sum_q \boldsymbol{v}_q \cdot \tilde{\boldsymbol{\sigma}}_{-q}$ leading to the effective interaction $-\frac{1}{2}g^2 \sum_{q\alpha} \chi_\alpha(\boldsymbol{q}, \omega = 0)\tilde{\sigma}^\alpha_q \tilde{\sigma}^\alpha_{-q}$ has to be considered. The

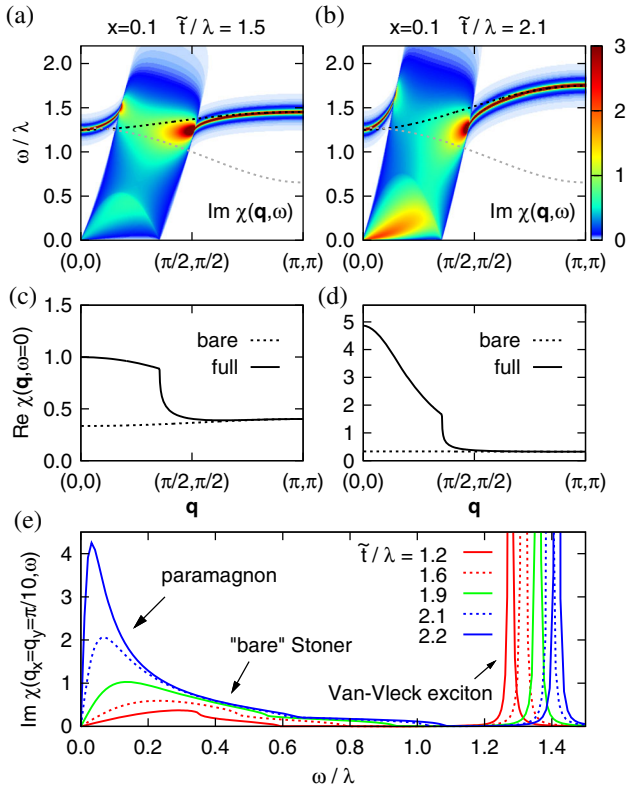

FIG. 3. (a) Imaginary part of the v_z susceptibility $\chi(\boldsymbol{q},\omega)$ in the (π,π) direction calculated for $x=0.1$, $\tilde{t}/\lambda=1.5$, $K/\lambda=0.3$. $\chi(\boldsymbol{q},\omega)$ is shown in units of λ^{-1}. The black (gray) dashed line shows the bare triplon dispersion for $x=0.1$ ($x=0$). (b) The same for $\tilde{t}/\lambda=2.1$ closer to the FM transition point $\tilde{t}/\lambda\approx 2.25$. (c),(d) The static susceptibility corresponding to panels (a) and (b). (e) Imaginary part of $\chi(\boldsymbol{q},\omega)$ at $\boldsymbol{q}=(\pi/10,\pi/10)$ for several values of $\tilde{t}/\lambda$ gradually approaching the FM transition point.

v_α susceptibility χ_α for $\alpha=x,y$ may be calculated the same way as χ_z above, using now $A^\alpha_{\boldsymbol{q}}=A^z_{\boldsymbol{q}}+[\frac{6}{5}t\langle n_{ij}\rangle-\frac{1}{6}K(1-x)]\cos q_\alpha$ and $B^\alpha_{\boldsymbol{q}}=B^z_{\boldsymbol{q}}-\frac{1}{12}K(1-x)\cos q_\alpha$. The coupling vertex for v_x and v_y obtains an additional contribution, $\Gamma^\alpha_{\boldsymbol{kq}}=\Gamma^z_{\boldsymbol{kq}}-\frac{3}{4}[\cos k_\alpha+\cos(k_\alpha+q_\alpha)]$. The resulting BCS interaction in terms of $t_{+1\boldsymbol{k}}=f_{\boldsymbol{k}\uparrow}f_{-\boldsymbol{k}\uparrow}$, $t_{0\boldsymbol{k}}=\frac{1}{\sqrt{2}}(f_{\boldsymbol{k}\downarrow}f_{-\boldsymbol{k}\uparrow}+f_{\boldsymbol{k}\uparrow}f_{-\boldsymbol{k}\downarrow})$, and $t_{-1\boldsymbol{k}}=f_{\boldsymbol{k}\downarrow}f_{-\boldsymbol{k}\downarrow}$ takes the form

$$\begin{aligned}\mathcal{H}_{\rm BCS}=-\frac{1}{2}\sum_{\boldsymbol{kk}'}&[V_z(t_1^\dagger t_1+t_{-1}^\dagger t_{-1})_{\boldsymbol{kk}'}\\&+(V_x-V_y)(t_1^\dagger t_{-1}+t_{-1}^\dagger t_1)_{\boldsymbol{kk}'}\\&+(V_x+V_y-V_z)t_{0\boldsymbol{k}}^\dagger t_{0\boldsymbol{k}'}],\end{aligned}\tag{6}$$

where V_α denotes the properly symmetrized $V_{\alpha\boldsymbol{kk}'}=g^2(\Gamma^\alpha_{\boldsymbol{k},\boldsymbol{k}'-\boldsymbol{k}})^2\frac{1}{2}[\chi_\alpha(\boldsymbol{k}-\boldsymbol{k}')-\chi_\alpha(\boldsymbol{k}+\boldsymbol{k}')]$. Decomposed into the Fermi surface harmonics, the BCS interaction is well approximated by $V_{z\boldsymbol{kk}'}\approx 2V_0\cos(\phi_{\boldsymbol{k}}-\phi_{\boldsymbol{k}'})$ and $(V_x-V_y)_{\boldsymbol{kk}'}\approx 2V_1\cos(\phi_{\boldsymbol{k}}+\phi_{\boldsymbol{k}'})$ with $V_{0,1}>0$ [see Figs. 3(d) and 4(a)]. The relatively small $V_1\ll V_0$ fixes the relative phase of the t_{+1} and t_{-1} pairs so that the SC order parameter becomes $\Delta_{\pm 1\boldsymbol{k}}=\Delta e^{\pm i\phi_{\boldsymbol{k}}}$. This ordering type is captured by the $\boldsymbol{d}$ vector $\boldsymbol{d}=-i\Delta(\sin\phi_{\boldsymbol{k}},\cos\phi_{\boldsymbol{k}},0)\sim\hat{x}k_y+\hat{y}k_x$ shown in Fig. 4(b). In the classification of Ref. [28], it forms the Γ_4^- irreducible representation of tetragonal group D_{4h}. However, this result applies to the cubic symmetry case. Lattice distortions that cause splitting among $T_{x,y,z}$ and modify the pseudospin wave functions may in fact offer a possibility to "tune" the symmetry of the order parameter. If distortions favor $T_{x,y}$, the potentials $V_{x,y}$ are expected to dominate in Eq. (6), supporting the chiral t_0 pairing represented by the last term in (6).

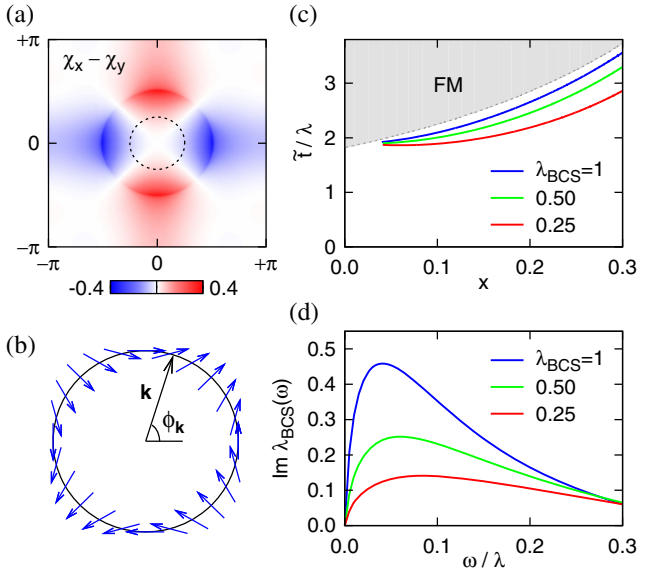

FIG. 4. (a) Combination $(\chi_x-\chi_y)_{\omega=0}$ that determines the symmetry of the pairing potential V_x-V_y. The parameters are the same as in Figs. 3(b) and 3(d). The dashed circle indicates the Fermi surface. (b) Representation of $\Delta_{\pm 1\boldsymbol{k}}=\Delta e^{\pm i\phi_{\boldsymbol{k}}}$ using the $\boldsymbol{d}$ vector along the Fermi surface. (c) Contours of $\lambda_{\rm BCS}=V_0N$ in the phase diagram of Fig. 2(d). (d) Imaginary part of ω-dependent $\lambda_{\rm BCS}(\omega)$ for $x=0.1$ and the values of $\tilde{t}/\lambda$ corresponding to $\lambda_{\rm BCS}=1$, 0.5, and 0.25.

Data in Figs. 4(c) and 4(d) serve as a basis for a rough T_c estimate. Figure 4(c) shows the BCS parameter $\lambda_{\rm BCS}\approx V_0N$ (N is DOS per spin component of the f band) which attains sizable values near the FM phase boundary, where the paramagnons are intense. To avoid complex physics near the very vicinity of the FM QCP [29–31], we take a conservative upper limit $\lambda_{\rm BCS}\approx 0.5$. Extending V_0 by the ω dependence of the underlying $\chi_z(\boldsymbol{q},\omega)$, we define $\lambda_{\rm BCS}(\omega)$. Its imaginary part to be understood as the conventional α^2F is plotted in Fig. 4(d) yielding an estimate of the BCS cutoff $\Omega\lesssim 0.1\lambda$. With $\lambda\sim 100$ meV, this gives $T_c\approx\Omega e^{-1/\lambda_{\rm BCS}}$ of about 10 K.

In conclusion, we have explored the doping effects in spin-orbit d^4 Mott insulators. The results show that the doped electrons moving in the d^4 background firmly favor ferromagnetism, explaining, e.g., the observed behavior of

La-doped Ca_2RuO_4. In the paramagnetic phase near the FM QCP, the incipient FM correlations are manifested by intense paramagnons that may provide a triplet pairing.

We thank G. Jackeli for useful comments. J. C. acknowledges support by the Czech Science Foundation (GA ČR) under Project No. 15-14523Y and ERDF under Project CEITEC (CZ.1.05/1.1.00/02.0068).

[1] M. Imada, A. Fujimori, and Y. Tokura, Rev. Mod. Phys. **70**, 1039 (1998).
[2] A. Abragam and B. Bleaney, *Electron Paramagnetic Resonance of Transition Ions* (Clarendon, Oxford, 1970).
[3] G. Khaliullin, Phys. Rev. Lett. **111**, 197201 (2013).
[4] O. N. Meetei, W. S. Cole, M. Randeria, and N. Trivedi, Phys. Rev. B **91**, 054412 (2015).
[5] A. Jain, M. Krautloher, J. Porras, G. H. Ryu, D. P. Chen, D. L. Abernathy, J. T. Park, A. Ivanov, J. Chaloupka, G. Khaliullin, B. Keimer, and B. J. Kim, arXiv:1510.07011.
[6] G. Cao, S. McCall, V. Dobrosavljevic, C. S. Alexander, J. E. Crow, and R. P. Guertin, Phys. Rev. B **61**, R5053 (2000).
[7] G. Cao, C. S. Alexander, S. McCall, J. E. Crow, and R. P. Guertin, J. Magn. Magn. Mater. **226–230**, 235 (2001).
[8] F. Nakamura, M. Sakaki, Y. Yamanaka, S. Tamaru, T. Suzuki, and Y. Maeno, Sci. Rep. **3**, 2536 (2013).
[9] C. R. Hughes, T. Harada, R. Ashoori, A. V. Boris, H. Hilgenkamp, M. E. Holtz, L. Li, J. Mannhart, D. A. Muller, D. G. Schlom, A. Soukiassian, X. Renshaw Wang, and H. Boschker (unpublished).
[10] S. Nakatsuji, S. Ikeda, and Y. Maeno, J. Phys. Soc. Jpn. **66**, 1868 (1997).
[11] Y. Miura, Y. Yasui, M. Sato, N. Igawa, and K. Kakurai, J. Phys. Soc. Jpn. **76**, 033705 (2007).
[12] M. Bremholm, S. E. Dutton, P. W. Stephens, and R. J. Cava, J. Solid State Chem. **184**, 601 (2011).
[13] G. Cao, T. F. Qi, L. Li, J. Terzic, S. J. Yuan, L. E. DeLong, G. Murthy, and R. K. Kaul, Phys. Rev. Lett. **112**, 056402 (2014).
[14] Y. Shi, Y. Guo, Y. Shirako, W. Yi, X. Wang, A. A. Belik, Y. Matsushita, H. L. Feng, Y. Tsujimoto, M. Arai, N. Wang, M. Akaogi, and K. Yamaura, J. Am. Chem. Soc. **135**, 16507 (2013).
[15] P. Khalifah, R. Osborn, Q. Huang, H. W. Zandbergen, R. Jin, Y. Liu, D. Mandrus, and R. J. Cava, Science **297**, 2237 (2002).
[16] S. Lee, J.-G. Park, D. T. Adroja, D. Khomskii, S. Streltsov, K. A. McEwen, H. Sakai, K. Yoshimura, V. I. Anisimov, D. Mori, R. Kanno, and R. Ibberson, Nat. Mater. **5**, 471 (2006).
[17] Hua Wu, Z. Hu, T. Burnus, J. D. Denlinger, P. G. Khalifah, D. G. Mandrus, L.-Y. Jang, H. H. Hsieh, A. Tanaka, K. S. Liang, J. W. Allen, R. J. Cava, D. I. Khomskii, and L. H. Tjeng, Phys. Rev. Lett. **96**, 256402 (2006).
[18] A. Akbari and G. Khaliullin, Phys. Rev. B **90**, 035137 (2014).
[19] M. Braden, G. André, S. Nakatsuji, and Y. Maeno, Phys. Rev. B **58**, 847 (1998).
[20] For a detailed comparison, one has to keep in mind polaronic and phase coexistence effects [21] generic to weakly doped Mott insulators, and deviations from two dimensionality.
[21] W. Brzezicki, A. M. Oleś, and M. Cuoco, Phys. Rev. X **5**, 011037 (2015).
[22] B. N. Figgis and M. A. Hitchman, *Ligand Field Theory and Its Applications* (Wiley-VCH, New York, 2000).
[23] J. Kim, D. Casa, M. H. Upton, T. Gog, Y.-J. Kim, J. F. Mitchell, M. van Veenendaal, M. Daghofer, J. van den Brink, G. Khaliullin, and B. J. Kim, Phys. Rev. Lett. **108**, 177003 (2012).
[24] Note a relation $\lambda = \xi/2S$ between spin-orbit coupling constant λ for spin $S = 1$ and the single-electron one ξ [2].
[25] T. Mizokawa, L. H. Tjeng, G. A. Sawatzky, G. Ghiringhelli, O. Tjernberg, N. B. Brookes, H. Fukazawa, S. Nakatsuji, and Y. Maeno, Phys. Rev. Lett. **87**, 077202 (2001).
[26] We recall that the pseudospins are spin-orbit entangled objects [27], and hence a pseudospin triplet is in fact a mixture of real-spin singlets and triplets.
[27] G. Khaliullin, Prog. Theor. Phys. Suppl. **160**, 155 (2005).
[28] M. Sigrist and K. Ueda, Rev. Mod. Phys. **63**, 239 (1991).
[29] A. V. Chubukov, A. M. Finkel'stein, R. Haslinger, and D. K. Morr, Phys. Rev. Lett. **90**, 077002 (2003).
[30] A. V. Chubukov, C. Pépin, and J. Rech, Phys. Rev. Lett. **92**, 147003 (2004).
[31] A. V. Chubukov and D. L. Maslov, Phys. Rev. Lett. **103**, 216401 (2009).

nature physics

LETTERS

PUBLISHED ONLINE: 27 MARCH 2017 | DOI: 10.1038/NPHYS4077

Higgs mode and its decay in a two-dimensional antiferromagnet

A. Jain[1,2†], M. Krautloher[1†], J. Porras[1†], G. H. Ryu[1‡], D. P. Chen[1], D. L. Abernathy[3], J. T. Park[4], A. Ivanov[5], J. Chaloupka[6], G. Khaliullin[1], B. Keimer[1*] and B. J. Kim[1,7*]

Condensed-matter analogues of the Higgs boson in particle physics allow insights into its behaviour in different symmetries and dimensionalities[1]. Evidence for the Higgs mode has been reported in a number of different settings, including ultracold atomic gases[2], disordered superconductors[3], and dimerized quantum magnets[4]. However, decay processes of the Higgs mode (which are eminently important in particle physics) have not yet been studied in condensed matter due to the lack of a suitable material system coupled to a direct experimental probe. A quantitative understanding of these processes is particularly important for low-dimensional systems, where the Higgs mode decays rapidly and has remained elusive to most experimental probes. Here, we discover and study the Higgs mode in a two-dimensional antiferromagnet using spin-polarized inelastic neutron scattering. Our spin-wave spectra of Ca_2RuO_4 directly reveal a well-defined, dispersive Higgs mode, which quickly decays into transverse Goldstone modes at the antiferromagnetic ordering wavevector. Through a complete mapping of the transverse modes in the reciprocal space, we uniquely specify the minimal model Hamiltonian and describe the decay process. We thus establish a novel condensed-matter platform for research on the dynamics of the Higgs mode.

For a system of interacting spins, amplitude fluctuations of the local magnetization—the Higgs mode—can exist as well-defined collective excitations near a quantum critical point (QCP). We consider here a magnetic instability driven by the intra-ionic spin–orbit coupling, which tends towards a non-magnetic state through complete cancellation of orbital (L) and spin (S) moments when they are antiparallel and of equal magnitude[5,6]. This mechanism should be broadly relevant for d^4 compounds of such ions as Ir(V), Ru(IV), Os(IV) and Re(III) with sizable spin–orbit coupling but remains little explored. We investigate the magnetic insulator Ca_2RuO_4, a quasi-two-dimensional antiferromagnet[7] with nominally $L = 1$ and $S = 1$ (Fig. 1). Because the local symmetry around the Ru(IV) ion is very low[8,9] (having only inversion symmetry), it is widely believed that the orbital moment is completely quenched by the crystalline electric field[10–13], which is dominated by the compressive distortion of the RuO_6 octahedra along the c-axis (Fig. 1). In the absence of an orbital moment, the nearest-neighbour magnetic exchange interaction is necessarily isotropic. Deviations from this behaviour are a sensitive indicator of an unquenched orbital moment. If this moment is sufficiently strong, it can drive Ca_2RuO_4 close to a QCP with novel Higgs physics.

Our comprehensive set of time-of-flight (TOF) inelastic neutron scattering (INS) data over the full Brillouin zone (Fig. 2a) indeed reveal qualitative deviations of the transverse spin-wave dispersion from those of a Heisenberg antiferromagnet. In particular, the global maximum of the dispersion is found at $\mathbf{q} = (0,0)$, in sharp contrast to a Heisenberg antiferromagnet, which has a minimum there (Fig. 1). This striking manifestation of orbital magnetism in Ca_2RuO_4 leads us to consider the limit of strong spin–orbit coupling described in terms of a singlet and a triplet separated in energy by λ (Fig. 1), which was estimated in earlier experiments[14–16] to be in the range ∼75–100 meV. In this limit, the ground state is non-magnetic with zero total angular momentum, and therefore a QCP separating it from a magnetically ordered phase is expected as a matter of principle. Although this QCP can be pre-empted by an insulator–metal transition[17,18] or rendered first-order by coupling to the lattice or other extraneous factors, it is sufficient that the system is reasonably close to the hypothetical QCP.

To assess the proximity to the QCP and the possibility of finding the Higgs mode, we first reproduce the observed transverse spin-wave modes by applying the spin-wave theory[19,20] to the following phenomenological Hamiltonian dictated by general symmetry considerations:

$$H = J\sum_{\langle ij\rangle}(\tilde{\mathbf{S}}_{\mathbf{i}}\cdot\tilde{\mathbf{S}}_{\mathbf{j}} - \alpha\tilde{S}_{zi}\tilde{S}_{zj}) + E\sum_i \tilde{S}_{zi}^2 + \epsilon\sum_i \tilde{S}_{xi}^2 \mp A\sum_{\langle ij\rangle}(\tilde{S}_{xi}\tilde{S}_{yj} + \tilde{S}_{yi}\tilde{S}_{xj}) \quad (1)$$

Here, $\tilde{\mathbf{S}}$ denotes a pseudospin-1 operator describing the entangled spin and orbital degrees of freedom. This model includes single-ion terms (E and ϵ) of tetragonal ($z \parallel c$) and orthorhombic ($x \parallel a$) symmetries, correspondingly, as well as an XY-type exchange anisotropy ($\alpha > 0$) and the bond-directional pseudodipolar interaction (A); note that its sign depends on the bond. Also symmetry allowed—but neglected here—are the Dzyaloshinskii–Moriya interaction (which can be gauged out by a suitable local coordinate transformation) and further-neighbour interactions.

[1]Max Planck Institute for Solid State Research, Heisenbergstraße 1, D-70569 Stuttgart, Germany. [2]Solid State Physics Division, Bhabha Atomic Research Centre, Mumbai 400085, India. [3]Quantum Condensed Matter Division, Oak Ridge National Laboratory, Oak Ridge, Tennessee 37831, USA. [4]Heinz Maier-Leibnitz Zentrum, TU München, Lichtenbergstraße 1, D-85747 Garching, Germany. [5]Institut Laue-Langevin 6, rue Jules Horowitz, BP 156, 38042 Grenoble Cedex 9, France. [6]Central European Institute of Technology, Masaryk University, Kotlářská 2, 61137 Brno, Czech Republic. [7]Department of Physics, Pohang University of Science and Technology, Pohang 790-784, Republic of Korea. [†]These authors contributed equally to this work. [‡]Present address: Max-Planck-Institute for Chemical Physics of Solids, Nöthnitzerstraße 40, D-01187 Dresden, Germany. *e-mail: B.Keimer@fkf.mpg.de; bjkim@fkf.mpg.de

NATURE PHYSICS DOI: 10.1038/NPHYS4077

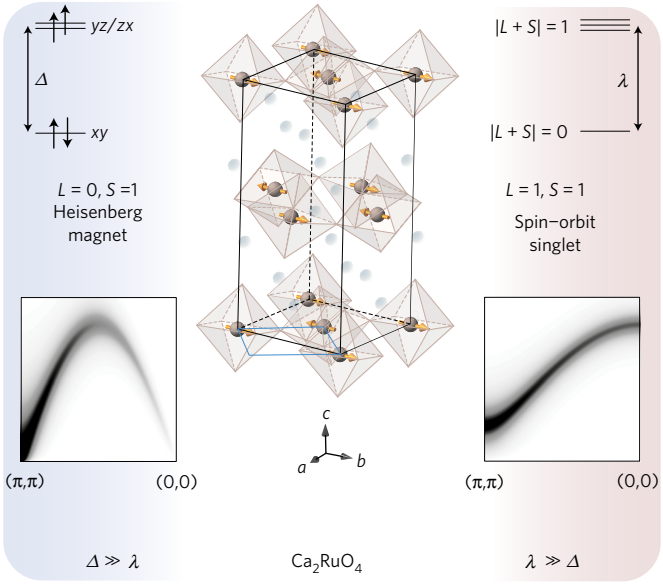

Figure 1 | Crystal, magnetic, and electronic structures of Ca_2RuO_4. Ca_2RuO_4 crystallizes in the orthorhombic *Pbca* space group, a distorted variant of the layered perovskite structure with a quasi-two-dimensional square lattice. For clarity, Ca ions are shown as small, light grey balls and oxygen ions, at all corners of the octahedra, are not shown. The distortion involves 2% compression of the RuO_6 octahedra along the *c*-axis, and their rotation about the *c*-axis and tilting about an axis that lies in the *a*–*b* plane[8,9]. The unit cell for the undistorted square lattice is shown as the blue square. (π,π) magnetic order develops below $T_N \approx 110$ K with the moment (orange arrow) aligned approximately along the *b*-axis. The compressive distortion of the RuO_6 octahedra leads to the splitting Δ between the orbitals of *xy* and *yz*/*zx* symmetry. If Δ is much larger than the spin-orbit splitting (λ), the orbital degrees of freedom are completely quenched and a $S=1$ Heisenberg magnet is obtained. In the other limit $\lambda \gg \Delta$, a non-magnetic singlet ground state is stabilized. These two distinct phases exhibit qualitatively different magnetic excitation spectra. See Supplementary Figs 1 and 2 for the evolution of the electronic structure and the spin-wave dispersions between these two limiting cases. Error bars denote one standard deviation.

The coupling constants resulting from fits of the model to the measured spectra are provided in the caption of Fig. 2. We stress that this model gives the unique minimal description of the system, which we also derive explicitly starting from the microscopic electronic structure (see Supplementary Information).

We find that the single-ion term E overwhelms all other coupling constants, particularly the nearest-neighbour exchange coupling J, and thus confines the pseudospins to the *a*–*b* basal plane. This accounts for the XY-like dispersion, which has a maximum at $\mathbf{q}=(0,0)$. This important aspect was missed in a recent INS study of Ca_2RuO_4, because the dispersion along the path $(\frac{\pi}{2},\frac{\pi}{2})$–(0,0) was not measured[21]. The large E implies unquenched spin–orbit coupling; in cubic symmetry E is λ itself (see Supplementary Fig. 1). This term also acts towards suppressing the magnetic order by favouring the $\tilde{S}_z = 0$ singlet ground state—known in the literature as 'spin nematic'[22]—and is responsible for the significant reduction of the moment size from the nominal $2\mu_B$ for pure $S=1$ moments to approximately $1.3\mu_B$ (ref. 8). Other terms allow fine tuning of the spin-wave dispersions; the pseudodipolar term accounts for the weak dispersion along the magnetic zone boundary $(\frac{\pi}{2},\frac{\pi}{2})$-$(\pi,0)$, and ϵ is responsible for gapping the transverse mode. The latter means that the Goldstone bosons acquire a finite mass through the explicit breaking of the continuous symmetry, the significance of which for the Higgs mode decay will be discussed later on. Our calculation (Fig. 2b) predicts an intense Higgs mode in this parameter regime, visible as a longitudinal spin wave, which heralds a proximate QCP. Although not evident in the image plot in Fig. 2a, a peak that matches well the predicted position of the Higgs mode is clearly seen in the energy spectra plotted in Fig. 2c.

We further pursue the Higgs mode using spin-polarized INS, using the scattering geometry that maximizes its neutron cross-section. We use the standard XYZ-difference method to filter out all non-magnetic and incoherent scattering signals and to resolve all three spin-wave polarizations: the longitudinal mode (L) oscillates along the crystallographic *b*-axis, and the transverse Goldstone modes (T and T′) along the *a*- and *c*-axes. Because our sample mosaic consisting of ∼100 crystals is 'twinned'—that is, approximately half of them are rotated 90° about the *c*-axis with respect to the other half—we can distinguish only between in-plane (*a*–*b*) and out-of-plane (*c*) polarized modes. However, this is sufficient to identify the Higgs mode (see Supplementary Information).

Figure 3a shows the measured (symbols with error bars) and calculated (solid lines) dynamical susceptibility at $\mathbf{q}=(0,0)$. We observe three peaks in total as expected, but not all of them were clearly seen in the TOF data (see also Supplementary Fig. 3) because their intensities are maximized in different scattering geometries. The highest-energy peak at approximately 52 meV is unambiguously identified as the Higgs mode by its magnetic and in-plane-polarized character, because the second in-plane-polarized mode at approximately 45 meV has already been identified as the T mode (Fig. 2). Further, the data are in excellent accord with the model calculation, which has no adjustable parameter after fitting the dispersion of the T modes. The intensity ratio between the L and T modes is 0.55 ± 0.11, which is a quantitative measure of the proximity to the QCP (Supplementary Fig. 7), at which the distinction between the L and T modes vanishes and their intensities become identical.

Having established the existence of the Higgs amplitude mode, we now look at its long-wavelength behaviour. It is at the ordering wavevector where the stability of the Higgs mode critically depends on the dimensionality of the system. In three dimensions, earlier INS studies on a dimerized quantum magnet have established a well-defined Higgs mode[4], which was then used to study its critical behaviour across a QCP[23,24]. In sharp contrast, our in-plane-polarized spectrum measured at $\mathbf{q}=(\pi,\pi)$ shows only one clear peak for the T mode at approximately 14 meV, followed by a broad magnetic intensity distribution in the energy range 20–50 meV, which is, however, well above the detection limit (Fig. 3b). The Higgs mode has decayed to the extent that a high-flux spin-polarized neutron spectrometer is required to detect its trace—although in retrospect a hint of this feature could be found in the unpolarized data shown in Fig. 3c.

However, it is also known that the response of the Higgs mode depends strongly on the symmetry of the probe being used. Therefore, its rapid decay in the longitudinal susceptibility measured by INS does not necessarily imply its instability in two dimensions. In fact, it has been shown in other two-dimensional systems, such as disordered superconductors[3] and superfluids of cold atoms[2], that the Higgs mode is clearly visible in the scalar susceptibility with its characteristic $\sim\omega^3$ onset in the energy spectrum. Indeed, theory predicts a contrasting behaviour of the Higgs mode in the scalar and longitudinal susceptibilities; in the latter, the Higgs mode quickly loses its coherence by decaying into a pair of Goldstone modes[25,26]. This results in an infrared divergence in two dimensions and renders the Higgs mode elusive.

Conversely, the INS spectrum at $\mathbf{q}=(\pi,\pi)$ encodes detailed information on the decay process of the Higgs mode that is not available from other measurements. To model the decay process, we go beyond the harmonic approximation used in the spin-wave

NATURE PHYSICS DOI: 10.1038/NPHYS4077

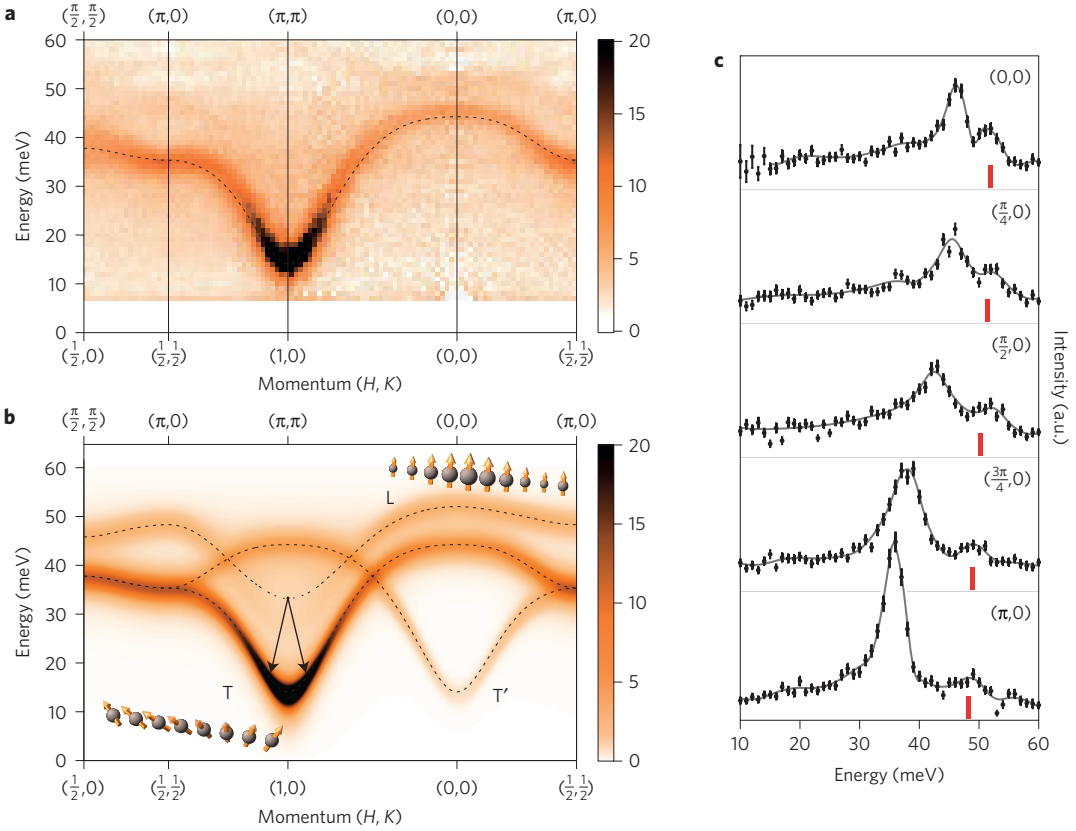

Figure 2 | Spin-wave dispersions strongly deviating from the Heisenberg model. a, TOF INS spectra along high-symmetry directions measured at $T = 5$ K (see Supplementary Fig. 3 for more details). The momenta indicated on the top axis refer to the undistorted square lattice unit cell (see Fig. 1), which is doubled for the magnetic unit cell. The dotted line is from **b** for direct comparison between theory and experiment. **b**, The excitation spectra of the model in equation (1) calculated with the parameters $E \simeq 25$ meV, $J \simeq 5.8$ meV, $\alpha = 0.15$, $\epsilon \simeq 4.0$ meV and $A \simeq 2.3$ meV. The spectra were convolved with the instrumental resolution (4.2 meV full-width at half-maximum). Transverse and longitudinal modes are labelled as 'T' and 'L', respectively, and their motions are depicted. The T′ mode arises from back-folding of the T mode by the magnetic (π,π) scattering and thus its intensity vanishes when approaching the QCP. The L mode carries the Higgs amplitude oscillation. The latter is not subject to the back-folding because it is insensitive to the staggered vector field. The black arrows show the momentum- and energy-conserving decay process of the L mode into a pair of T modes. The total momentum of the pair is that of the L mode shifted by (π,π) momentum provided by the condensate (see Supplementary Information). **c**, Energy spectra for several $\mathbf{q}$ points along (0,0)–$(\pi,0)$ obtained using an integration window of ± 0.0475 in H and K after symmetrization. The integration ranges were doubled for $\mathbf{q} = (0,0)$ to obtain similar statistics. The red marks indicate the position of the longitudinal mode as calculated by theory. The black solid curves are a guide to the eye. Error bars denote one standard deviation.

theory to include the coupling of the longitudinal mode to the two-magnon continuum (see Supplementary Information). The solid lines in Fig. 3 show the result of the final calculation, which give an excellent description of the data both at $\mathbf{q} = (0,0)$ and $\mathbf{q} = (\pi,\pi)$; the decay process (Fig. 2b) is kinematically restricted away from the ordering wavevector, and the Higgs mode is well identified at $\mathbf{q} = (0,0)$. Although continuum structures are generic to low-dimensional quantum magnets (for example, Haldane chains[27,28]), the present case is distinct because the continuum structure near $\mathbf{q} = (\pi,\pi)$ is derived from a Higgs mode that exists as a well-defined quasiparticle away from the ordering wavevector.

As mentioned earlier, we have a rather unusual situation where all the transverse modes are massive (gapped), as a result of the orthorhombic symmetry of the crystal structure parameterized by ϵ, which significantly modifies the Higgs mode decay process at low energies. The transverse gap cuts off the infrared singularity and the spectral weight piles up at non-zero energy. We illustrate this point in Fig. 4 by simulating the change in the longitudinal spectrum as the system approaches the QCP. At $\mathbf{q} = (\pi,\pi)$, the decay of the Higgs mode into a pair of minimum-energy transverse modes is still the dominant channel, which generates a 'resonance' at twice the energy of the gap. This resonance steals much of the spectral weight from the bare longitudinal mode, thus obscuring its spectral signature, especially near the QCP. As the system moves away from the QCP, the longitudinal mode progressively hardens and becomes weaker, and its spectral weight spans a larger energy range. The spectral evolution at $\mathbf{q} = (0,0)$ shows this trend with the decay process suppressed; the Higgs mode remains a well-defined excitation even away from the QCP, although its intensity quickly diminishes.

Now that we have established a two-dimensional material system, future studies can reveal further aspects of the Higgs mode. In particular, it is uncertain at this point whether the decay process considered above fully describes its dynamics. In addition to the multimagnon continuum[27–30], other channels such as decays into vortex-like excitations are conceivable in two-dimensional planar magnets and require further investigation. It would be also interesting to compare the results presented herein with the spectra from resonant inelastic X-ray scattering, which can in principle access both the scalar and longitudinal susceptibilities. Finally, it is interesting to note that the Higgs boson in particle physics is detected through its decay products, such as pairs of photons, W and Z bosons, or leptons. The Higgs potential can be determined through the decay rates and branching ratios of these processes, which have been calculated to very high precision. Our

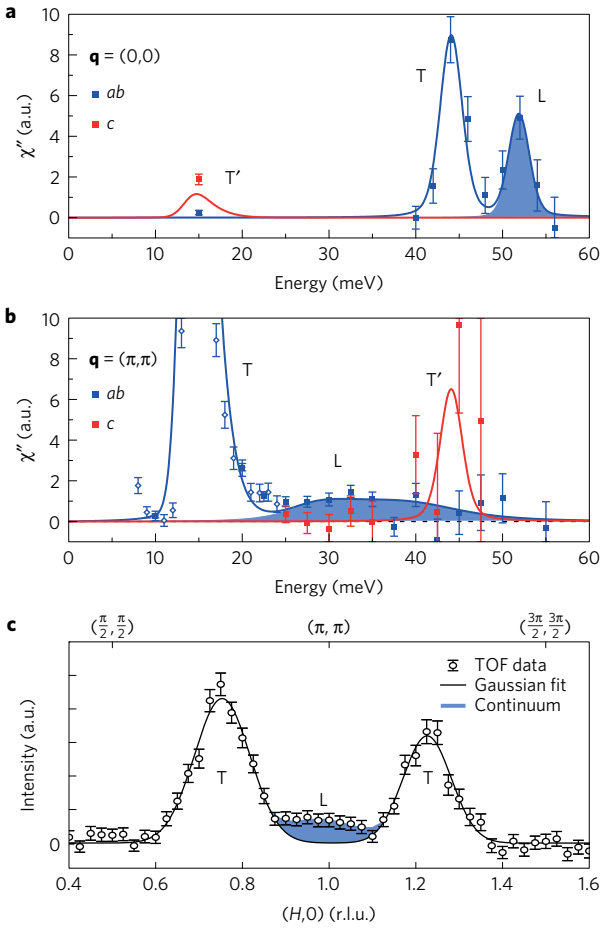

Figure 3 | Identification of the magnetic modes with polarized INS and their comparison to model calculation. a,**b**, Imaginary part of the dynamic spin susceptibility obtained by normalizing the INS spectra measured at $T = 2$ K at $\mathbf{q} = (0,0)$ (**a**)(Supplementary Fig. 5) and $\mathbf{q} = (\pi,\pi)$ (**b**) (Supplementary Fig. 6) with respect to the orientation factor and the isotropic form factor of the Ru ion (Supplementary Fig. 4). Blue (red) symbols indicate in-plane (out-of-plane) polarized magnetic intensities. Solid symbols show data with the background removed by taking the difference between two spin-flip channels, and open symbols show data from a single spin-flip channel (see Supplementary Information). Solid lines show the calculated spectra, which were convolved using Gaussian functions with 0.19π and 2.5 meV full-width at half-maximum to account for the instrumental momentum and energy resolutions, respectively. The decay process of the L mode into T modes is described in the Supplementary Information. The shaded area indicates the spectral weight of the L mode. The intensities in **a**,**b** are in the same arbitrary units. The T′ mode arises from back-folding of the T mode by the magnetic (π,π) scattering. **c**, A feature consistent with the L mode in the unpolarized data; an H-cut obtained by integrating the data in the range $25 \leq E \leq 31$ meV, $-0.05 \leq K \leq 0.05$, and $0 \leq L \leq 6$. A quadratic background has been fitted and subtracted. The solid line is a Gaussian fit to single magnon peaks (T), and the shaded region indicates the intensity not accounted for by the T magnons but instead consistent with the longitudinal mode. Error bars denote one standard deviation.

study represents the first step towards a parallel development in condensed-matter physics.

Methods

Methods, including statements of data availability and any associated accession codes and references, are available in the online version of this paper.

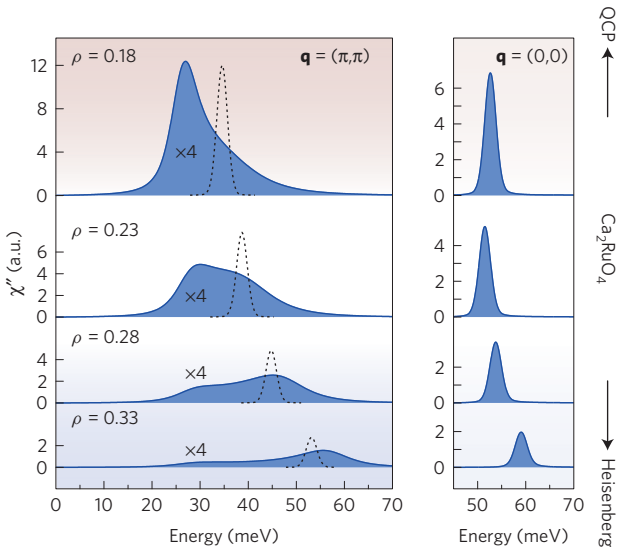

Figure 4 | Evolution of the Higgs mode towards the QCP. Imaginary part of the longitudinal susceptibility calculated for several values of J/E, which can be expressed in terms of the condensate density ρ via the relation $\rho = 1/2(1 - E/8J)$. The ρ values of 0.18, 0.23, 0.28, 0.33 approximately correspond to $J/E = 0.20$, 0.23, 0.28, 0.37, respectively. The dotted lines show the bare susceptibility before taking the decay process into account.

Received 19 February 2016; accepted 22 February 2017; published online 27 March 2017

References

1. Pekker, D. & Varma, C. M. Amplitude/Higgs modes in condensed matter physics. *Annu. Rev. Condens. Matter Phys.* **6,** 269–297 (2014).
2. Endres, M. *et al*. The 'Higgs' amplitude mode at the two-dimensional superfluid/Mott insulator transition. *Nature* **487,** 454–458 (2012).
3. Sherman, D. *et al*. The Higgs mode in disordered superconductors close to a quantum phase transition. *Nat. Phys.* **11,** 188–192 (2015).
4. Rüegg, C. *et al*. Quantum magnets under pressure: controlling elementary excitations in $TlCuCl_3$. *Phys. Rev. Lett.* **100,** 205701 (2008).
5. Khaliullin, G. Excitonic magnetism in Van Vleck-type d^4 Mott insulators. *Phys. Rev. Lett.* **111,** 197201 (2013).
6. Meetei, O. N., Cole, W. S., Randeria, M. & Trivedi, N. Novel magnetic state in d^4 Mott insulators. *Phys. Rev. B* **91,** 054412 (2015).
7. Nakatsuji, S., Ikeda, S. I. & Maeno, Y. Ca_2RuO_4: new Mott insulators of layered ruthenate. *J. Phys. Soc. Jpn* **66,** 1868–1871 (1997).
8. Braden, M., André, G., Nakatsuji, S. & Maeno, Y. Crystal and magnetic structure of Ca_2RuO_4: magnetoelastic coupling and the metal-insulator transition. *Phys. Rev. B* **58,** 847–861 (1998).
9. Friedt, O. *et al*. Structural and magnetic aspects of the metal-insulator transition in $Ca_{2-x}Sr_xRuO_4$. *Phys. Rev. B* **63,** 174432 (2001).
10. Anisimov, V. I., Nekrasov, I. A., Kondakov, D. E., Rice, T. M. & Sigrist, M. Orbital-selective Mott-insulator transition in $Ca_{2-x}Sr_xRuO_4$. *Eur. Phys. J. B* **25,** 191–201 (2002).
11. Fang, Z., Nagaosa, N. & Terakura, K. Orbital-dependent phase control in $Ca_{2-x}Sr_xRuO_4$. *Phys. Rev. B* **69,** 045116 (2004).
12. Liebsch, A. & Ishida, H. Subband filling and Mott transition in $Ca_{2-x}Sr_xRuO_4$. *Phys. Rev. Lett.* **98,** 216403 (2007).
13. Gorelov, E. *et al*. Nature of the Mott transition in Ca_2RuO_4. *Phys. Rev. Lett.* **104,** 226401 (2010).
14. Mizokawa, T. *et al*. Spin–orbit coupling in the Mott insulator Ca_2RuO_4. *Phys. Rev. Lett.* **87,** 077202 (2001).
15. Haverkort, M. W., Elfimov, I. S., Tjeng, L. H., Sawatzky, G. A. & Damascelli, A. Strong spin–orbit coupling effects on the Fermi surface of Sr_2RuO_4 and Sr_2RhO_4. *Phys. Rev. Lett.* **101,** 026406 (2008).
16. Fatuzzo, C. G. *et al*. Spin–orbit-induced orbital excitations in Sr_2RuO_4 and Ca_2RuO_4: a resonant inelastic X-ray scattering study. *Phys. Rev. B* **91,** 155104 (2015).
17. Taniguchi, H. *et al*. Anisotropic uniaxial pressure response of the Mott insulator Ca_2RuO_4. *Phys. Rev. B* **88,** 205111 (2013).
18. Nakamura, F. *et al*. From Mott insulator to ferromagnetic metal: a pressure study of Ca_2RuO_4. *Phys. Rev. B* **65,** 220402(R) (2002).

19. Matsumoto, M., Normand, B., Rice, T. M. & Sigrist, M. Field- and pressure-induced magnetic quantum phase transitions in $TlCuCl_3$. *Phys. Rev. B* **69,** 054423 (2004).
20. Sommer, T., Vojta, M. & Becker, K. Magnetic properties and spin waves of bilayer magnets in a uniform field. *Eur. Phys. J. B* **23,** 329–339 (2001).
21. Kunkemöller, S. *et al*. Highly anisotropic magnon dispersion in Ca_2RuO_4: evidence for strong spin orbit coupling. *Phys. Rev. Lett.* **115,** 247201 (2015).
22. Podolsky, D. & Demler, E. Properties and detection of spin nematic order in strongly correlated electron systems. *New J. Phys.* **7,** 59 (2005).
23. Giamarchi, T., Rüegg, C. & Tchernyshyov, O. Bose–Einstein condensation in magnetic insulators. *Nature* **4,** 198–204 (2008).
24. Merchant, P. *et al*. Quantum and classical criticality in a dimerized quantum antiferromagnet. *Nat. Phys.* **10,** 373–379 (2014).
25. Podolsky, D., Auerbach, A. & Arovas, D. P. Visibility of the amplitude (Higgs) mode in condensed matter. *Phys. Rev. B* **84,** 174522 (2011).
26. Gazit, S., Podolsky, D. & Auerbach, A. Fate of the Higgs mode near quantum criticality. *Phys. Rev. Lett.* **110,** 140401 (2013).
27. Kenzelmann, M. *et al*. Multiparticle states in the $S=1$ chain system $CsNiCl_3$. *Phys. Rev. Lett.* **87,** 017201 (2001).
28. Zaliznyak, I. A., Lee, S.-H. & Petrov, S. V. Continuum in the spin-excitation spectrum of a Haldane chain observed by neutron scattering in $CsNiCl_3$. *Phys. Rev. Lett.* **87,** 017202 (2001).
29. Stone, M. B., Zaliznyak, I. A., Hong, T., Broholm, C. L. & Reich, D. H. Quasiparticle breakdown in a quantum spin liquid. *Nature* **440,** 187–190 (2006).
30. Masuda, T. *et al*. Dynamics of composite Haldane spin chains in IPA-$CuCL_3$. *Phys. Rev. Lett.* **96,** 047210 (2006).

Acknowledgements
We acknowledge financial support from the German Science Foundation (DFG) via the coordinated research programme SFB-TRR80, and from the European Research Council via Advanced Grant 669550 (Com4Com). The experiments at Oak Ridge National Laboratory's Spallation Neutron Source were sponsored by the Division of Scientific User Facilities, US DOE Office of Basic Energy Sciences. J.C. was supported by GACR (project no. GJ15-14523Y) and by MSMT CR under NPU II project CEITEC 2020 (LQ1601).

Author contributions
M.K., G.H.R. and D.P.C. grew the single crystals. A.J., M.K. and J.P. characterized and co-aligned the crystals. A.J., M.K., J.P. and B.J.K. performed INS experiments and analysed the data. D.L.A., J.T.P. and A.I. supported the INS experiments. G.K. developed the theoretical model. J.C. and B.J.K. performed the numerical calculations. B.J.K. wrote the manuscript with contributions from G.K., J.C., B.K., J.P., A.J. and M.K. and discussions with all authors. B.J.K. and B.K. managed the project.

Additional information
Supplementary information is available in the online version of the paper. Reprints and permissions information is available online at www.nature.com/reprints. Publisher's note: Springer Nature remains neutral with regard to jurisdictional claims in published maps and institutional affiliations. Correspondence and requests for materials should be addressed to B.K. or B.J.K.

Competing financial interests
The authors declare no competing financial interests.

Methods

Sample synthesis and characterization. Single crystals of Ca_2RuO_4 were grown by the floating zone method with RuO_2 self-flux[31]. The lattice parameters $a = 5.409$ Å, $b = 5.505$ Å, and $c = 11.9312$ Å were determined by X-ray powder diffraction, in good agreement with the parameters reported in the literature[8] for the 'S' phase with short c-axis lattice parameter. The magnetic ordering temperature $T_N = 110$ K was determined using magnetization measurements in a Quantum Design SQUID-VSM device. Polarized neutron diffraction measurements indicate that most of the array orders in the 'A-centred' magnetic structure with magnetic ordering vector $\mathbf{Q} = (1,0,0)$[8]. The fraction of the sample with ordering vector $\mathbf{Q} = (0,1,0)$, that is, 'B-centred', is estimated to be less than 5%.

Time-of-flight inelastic neutron scattering. For the TOF measurements, we co-aligned about 100 single crystals with a total mass of ∼1.5 g into a mosaic on Al plates. Approximately half of the crystals were rotated 90° about the c-axis from the other half (Supplementary Fig. 2). The in-plane and c-axis mosaicities of the aligned crystal assembly were $\lesssim$3.2° and $\lesssim$2.7°, respectively. The measurements were performed on the ARCS time-of-flight chopper spectrometer at the Spallation Neutron Source, Oak Ridge National Laboratory, Tennessee, USA. The incident neutron energy was 100 meV. The Fermi chopper and T_0 chopper frequencies were set to 600 and 90 Hz, respectively, to optimize the neutron flux and energy resolution. The measurements were carried out at $T = 5$ K. The sample was mounted with the $(H,0,L)$ plane horizontal. The sample was rotated over 90° about the vertical c-axis with a step size of 1°. At each step data were recorded over a deposited proton charge of 3 Coulombs (∼45 minutes) and then converted into 4D $S(\mathbf{Q},\omega)$ using the HORACE software package[32] and normalized using a vanadium calibration.

Polarized inelastic neutron scattering. Preliminary triple-axis measurements, to reproduce the TOF results and determine the feasibility of the polarized experiment, were done on the thermal triple-axis spectrometer PUMA at the FRM-II, Garching, Germany. The measurements were done on crystals from the same batch as the ones used for the TOF experiment. To optimize the flux and energy resolution, double-focused PG (002) and Cu (220) monochromators, for measurements below and above 30 meV, respectively, and a double-focused PG (002) analyser were used, keeping $k_f = 2.662$ Å^{-1} constant. For the polarized triple-axis measurement we remounted the crystals from the TOF experiment on Si plates and increased the number of crystals to obtain a total sample mass of ∼3 g. The mosaicity of this sample was $\lesssim$3.2° and $\lesssim$2.6° for in-plane and c-axis, respectively. The experiment was performed on the IN20 three-axis spectrometer at the Institute Laue-Langevin, Grenoble, France. For the XYZ polarization analysis, we used a Heusler (111) monochromator and analyser in combination with Helmholtz coils at the sample position. Throughout the experiment we used a fixed $k_f = 2.662$ Å^{-1} and performed polarization analysis in energy and H scans at (π,π) and (0,0), keeping L as small as permitted by kinematic constraints. The measurements were carried out at $T = 2$ K.

Data availability. The data that support the plots within this paper and other findings of this study are available from the corresponding author upon reasonable request. The polarized inelastic neutron scattering data are available at http://doi.ill.fr/10.5291/ILL-DATA.4-01-1431.

References

31. Nakatsuji, S. & Maeno, Y. Synthesis and single-crystal growth of $Ca_{2-x}Sr_xRuO_4$. *J. Solid State Chem.* **156,** 26–31 (2001).
32. Ewings, R. A. *et al*. HORACE: software for the analysis of data from single crystal spectroscopy experiments at time-of-flight neutron instruments. *Nucl. Instrum. Methods Phys. Res. A* **884,** 132–142 (2016).

nature physics

SUPPLEMENTARY INFORMATION

DOI: 10.1038/NPHYS4077

In the format provided by the authors and unedited.

Higgs mode and its decay in a two-dimensional antiferromagnet

A. Jain, M. Krautloher, J. Porras, G. H. Ryu, D. P. Chen, D. L. Abernathy, J. T. Park, A. Ivanov, J. Chaloupka, G. Khaliullin, B. Keimer, and B. J. Kim

A. Microscopic model

We derive here the phenomenological model in eq. (1) starting from the microscopic electronic structure. The compressive tetragonal distortion Δ, is the key parameter that determines the proximity of Ca_2RuO_4 to the QCP, because the spin-orbit splitting λ is known for Ru(IV) ion, and the nearest-neighbor exchange coupling J is to a large extent fixed by the measured bandwidth $W \simeq 2zJ$ of the spin-wave (z is the coordination number). In the absence of Δ, the low energy physics is described in terms of a singlet-triplet model[7], formally similar to that used for dimerized quantum magnets[23], such as $TlCuCl_3$ and $BaCuSi_2O_6$. The magnetic transitions in these systems have been extensively studied as a Bose-Einstein condensation of triplons, where the magnetic field H plays the role of the chemical potential μ. In our case, Δ plays the role of μ (see Fig. S1); it splits the triplets into a doublet and a singlet and thereby lowers the energy cost E to create an exciton (T_x or T_y). The quantum phase transition occurs when $E \simeq W$; the equality holds for classical consideration. With the free-ion value $\lambda \approx 75$ meV and $W \approx 45$ meV, we estimate that QCP is at $\delta(\equiv\Delta/2\lambda) \approx 1$.

Because Ca_2RuO_4 is on the right hand side of the QCP where the T_z singlet is in very high energy and hence can be neglected, the low-energy physics of Ca_2RuO_4 can be described by the three levels $\{s, T_x, T_y\}$. These three levels constitute the effective $S = 1$ degrees of freedom in the phenomenological model in eq. (1). We note that the large energy scale of E microscopically originates from λ and depends on δ.

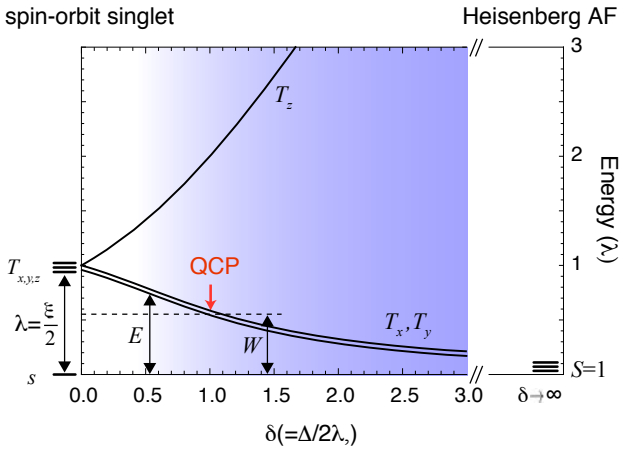

FIG. S1. **Microscopic mechanism of the QCP driven by tetragonal lattice distortion.** Crystal-field splitting of the triplet effectively lowers the energy scale of SOC from λ to E. λ is equal to one-half of the single-electron SOC ξ for d^4 low-spin electron configuration. The QCP occurs when E becomes equal to the strength of the exchange field $W \approx 2zJ$. The blue shading indicates the region where the effective $S = 1$ model is valid.

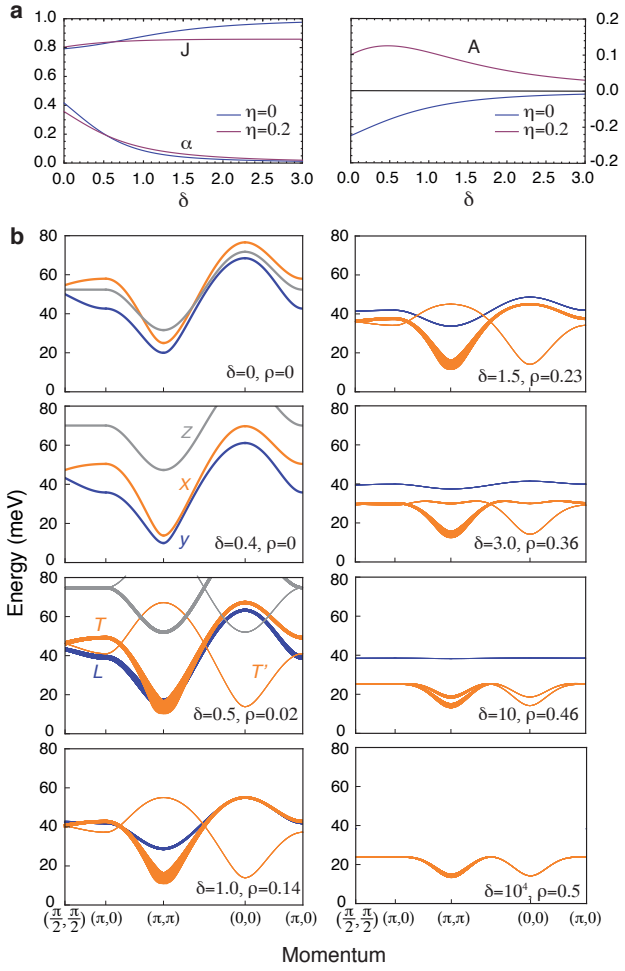

FIG. S2. **Coupling constants and spin-wave dispersion from the microscopic model. a,** J and A (see eq. 1) are in units of t^2/U. **b,** Evolution of the spin-wave dispersions from the non-magnetic spin-orbit singlet to the Heisenberg limit as a function of δ. $\eta = 0.25$ was used. A non-zero ρ, the condensate density, indicates the magnetic order. At $\delta = 0.5$, the magnetic order has set in; now the T_x becomes the transverse mode and T_y the longitudinal mode. At $\delta = 1.5$, the simulation is very similar to the experimental data. Further increase of δ leads to a development of a local minimum at $\mathbf{q} = (0,0)$, and eventually to a Heisenberg-like dispersion.

DOI: 10.1038/NPHYS4077

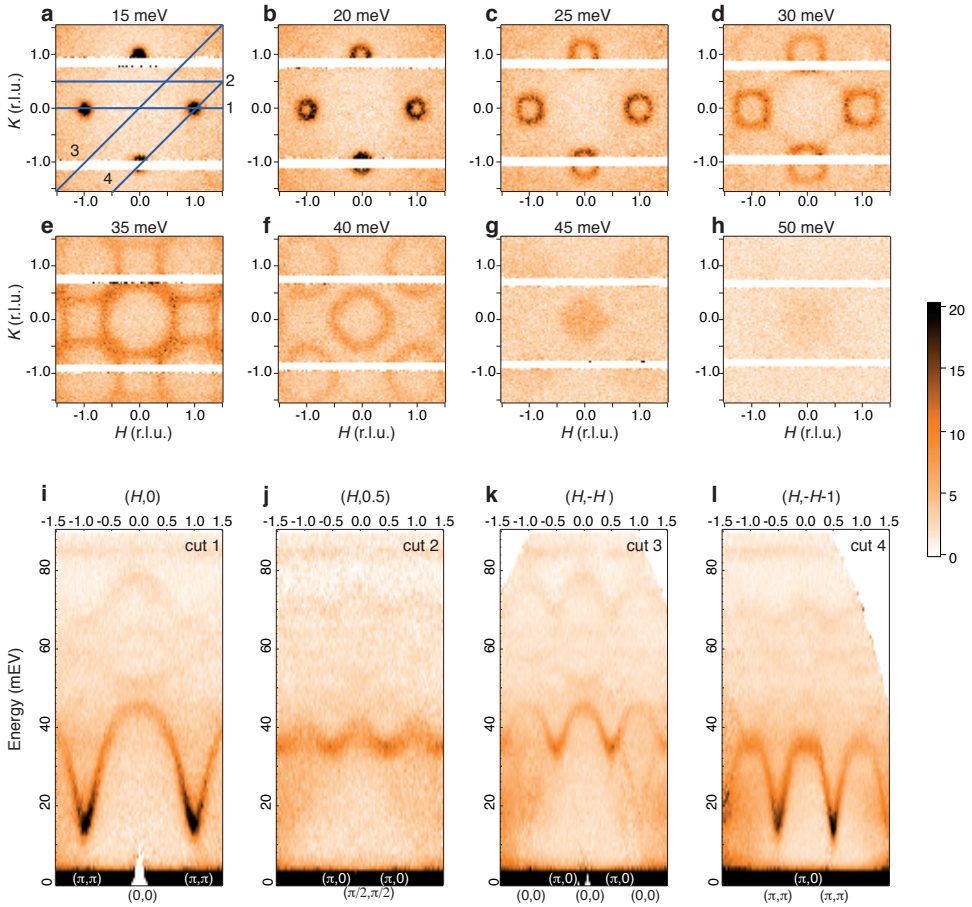

FIG. S3. **Time-of-flight INS spectra of Ca_2RuO_4. a-h,** Constant energy maps of INS intensity in the (H,K) plane with L integrated over the range $0 \le L \le 6$. The wave-vectors are expressed in reciprocal lattice units (r.l.u.) of a tetragonal cell with $a^* = b^* = 1.16\,\text{Å}^{-1}$ and $c^* = 0.53\,\text{Å}^{-1}$. At $E = 14$ meV, intense spin waves are observed at the reduced wave-vectors $(\pm 1, 0)$ and $(0, \pm 1)$, which correspond to the antiferromagnetic ordering wave-vector (π, π) for the 2D square lattice Brillouin-zone. **i-l,** Energy spectra along high-symmetry directions as shown in blue lines in panel **a**. The intensity is in arbitrary units.

In terms of the z projections of the S=1 and L=1 moments $|S_M, L_M\rangle$, the wave functions for the basis states $\{s, T_x, T_y\}$ with $T_x = \frac{1}{i\sqrt{2}}(T_1 - T_{-1})$, $T_y = \frac{1}{\sqrt{2}}(T_1 + T_{-1})$ are given by

$$|s\rangle = \sin\theta_0 \tfrac{1}{\sqrt{2}}(|1,-1\rangle + |-1,1\rangle) - \cos\theta_0\,|0,0\rangle\,, \quad (1)$$

$$|T_{+1}\rangle = \cos\theta_1|1,0\rangle - \sin\theta_1|0,1\rangle\,, \quad (2)$$

$$|T_{-1}\rangle = \sin\theta_1|0,-1\rangle - \cos\theta_1|-1,0\rangle. \quad (3)$$

Here the angles θ_0, θ_1 are defined through

$$\tan\theta_1 = \frac{1}{\delta + \sqrt{1+\delta^2}}\,, \quad \tan\theta_0 = \sqrt{1+\beta^2} - \beta, \quad (4)$$

where $\beta = \frac{1}{\sqrt{2}}(\delta - \frac{1}{2})$. The energy E in eq. (1) and Fig. S1 is given by

$$E = \frac{\xi}{2}\left(\frac{\sqrt{2}}{\beta + \sqrt{1+\beta^2}} - \frac{1}{\delta + \sqrt{1+\delta^2}}\right). \quad (5)$$

Using the above wavefunctions in the standard second-order perturbation theory, we calculate the coupling constants incorporating the Hund's coupling $\eta = J_H/U$ measured in units of the Coulomb interaction U. Figure S2a shows the exchange constant J, two-ion XY-type anisotropy α, and pseudodipolar interaction A as functions of δ, for $\eta = 0$ and $\eta = 0.2$; the latter would be more realistic. The calculation shows that $\alpha \ll 1$ in the entire range of δ where the model is relevant to Ca_2RuO_4, insensitive to the value of η, confirming that the XY-type anisotropy due to two-ion exchange is small. Thus, the single-ion term E is mostly responsible for the XY-type anisotropy.

Using these coupling constants, we simulate in Fig. S2b the evolution of the spin-wave spectra over the entire phase diagram from the non-magnetic singlet to the Heisenberg limit using δ as the only tuning parameter. In the simulation, we used $\lambda = 50$ meV, $\eta = 0.25$, and $t^2/U = 5.75$ meV. Additionally the ϵ term in eq. (1) was added to reproduce the transverse mode gap of ≈14 meV. Note that at $\delta = 1.5$, the simulated spectra becomes very similar to the experimental spectra. The above parameters translate to $J \simeq 5.2$ meV, $\alpha = 0.1$, $E = 21.5$ meV and

DOI: 10.1038/NPHYS4077

$A \simeq 1.0$ meV, which are in excellent agreement with those found from the fitting, considering that the model is minimal and the coupling constants absorb various renormalization effects in the solid not taken into account in the microscopic model. In particular, A absorbs the effect of further neighboring couplings, which also contribute to the dispersion along the magnetic zone boundary $(\pi/2,\pi/2)$-$(\pi,0)$.

B. Time-of-flight inelastic neutron scattering

Figures S3a-h and S3i-l exhibit constant-energy maps and energy spectra along high-symmetry directions, respectively, measured by TOF INS comprising spin-wave dispersions in the energy range $14 \lesssim \hbar\omega \lesssim 45$ meV and phonon modes above ∼50 meV. The magnetic nature of the former is explicitly confirmed by using spin-polarized neutrons (Fig. 3), and the non-magnetic nature of the latter is inferred from exhaustion of all magnetic modes and also through comparison with the known phonon modes. The data has been integrated along L because the magnetic excitations are close to the 2D limit, which can also be seen from the narrow linewidth of the excitations after the integration. Indeed, a recent INS study shows that the excitations at (π,π) are almost dispersionless (less than 1 meV), with no significant change in amplitude[21]. Figures S3m and S3n show energy spectra and an H-cut, respectively, indicated in which are intensities consistent with the longitudinal mode.

C. Polarization analysis

In the standard reference frame for the neutron polarization with $\hat{x} \parallel \mathbf{Q}$, $\hat{y} \perp \mathbf{Q}$ in the scattering plane of the spectrometer and $\hat{z} = \hat{x} \times \hat{y}$, the magnetic intensity in the spin flip channels is extracted from the differences:

$$M_y = I_x - I_y, \qquad (6)$$
$$M_z = I_x - I_z,$$

where I_x, I_y, I_z are the raw intensities of the respective polarizations. Note that any contribution from the background is suppressed in the difference. For conversion from INS intensity to dynamic spin susceptibility, we used the isotropic form factor for Ru^+, which gave a good description of the data at 15 meV (Fig. S4).

C.1 Flipping ratio

The flipping ratio is estimated using the strong magnetic signal at 15 meV to be around $F = 10$; minor differences in the flipping ratio for different channels $F_x = 14.8$, $F_y = 14.4$ and $F_z = 14.1$ measured using several nuclear Bragg reflections, do not alter the analysis significantly. All data were taken in regions where the signal in the non-spin flip channel $\hat{x}$ was at the background level, and therefore any leakage from non-spin flip processes can be neglected in the differences.

C.2 Twinning ratio

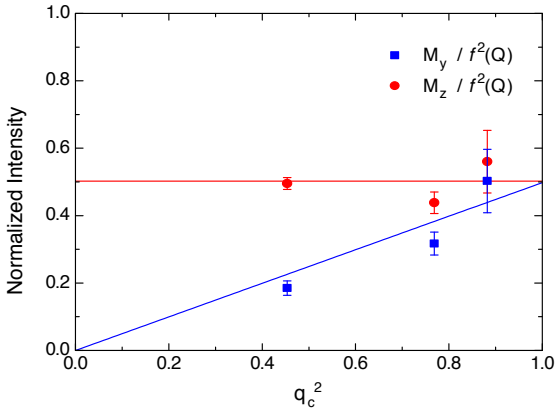

FIG. S4. **Determination of the twinning ratio.** Magnetic intensities M_y(blue squares) and M_z(red circles) normalized by the squared magnetic form factor as a function of q_c^2 at $\mathbf{Q} = (1,0,L)$ with $L = 2$, 4, and 6 at energy transfer 15 meV. For one type of domain the intensity is constant, and for the other type of domain the intensity increases linearly with q_c^2. A one-parameter fit (red and blue solid lines) to the data points determines the twinning ratio p.

In this study the a and b orientation of the crystals in the array are not distinguished. In other words, for the volume fraction p of the sample the scattering plane is $(H,0,L)$, and for the fraction $(1-p)$ the scattering plane is $(0,H,L)$. Taking into account the polarization factor, the intensities in each channel are related to excitations M_a, M_b and M_c along the crystallographic directions by:

$$M_y = q_c^2 \left[p\ M_a + (1-p)\ M_b\right] + \left(1 - q_c^2\right) M_c \qquad (7)$$
$$M_z = (1-p)\ M_a + p\ M_b$$

where $q_c^2 = (Q_c/|\mathbf{Q}|)^2$.

The twinning ratio p can be estimated from rocking scans through the Bragg reflections (4,0,0) and (0,4,0) where the separation in the scattering angle is large enough to distinguish the two peaks (not shown). Alternatively, p can be estimated from the inelastic measurements by considering the L-dependence of the 15 meV feature at (π,π) as shown in Fig. S4. Since this is an in-plane transverse mode, M_b and M_c vanish and eq. (14) greatly simplifies. From the one-parameter fit to the data, a twinning ratio $p = 0.498 \pm 0.014$ is determined, consistent with the first method. For the analysis we used $p = 0.5$.

From polarization analysis on this "twinned" array, only in-plane (ab) or out-of-plane (c) polarization can be distinguished, as M_a and M_b give equal contributions in each channel. Nevertheless, two in-plane-polarized modes T and L and one out-of-plane-polarized mode T′ are expected which are non-degenerate. We can indeed distinguish them from the energy scans at (0,0) and (π,π).

C.3 Energy scans at $\mathbf{q} = (0,0)$

For the energy scans at $\mathbf{q} = (0,0)$, it is useful to use two

DOI: 10.1038/NPHYS4077

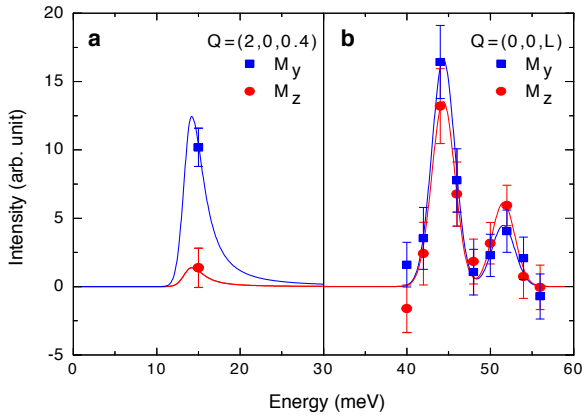

FIG. S5. **Energy scans at $\mathbf{q}=(0,0)$.** Magnetic intensities **a,** at $\mathbf{Q}=(2,0,0.4)$, and **b,** at $\mathbf{Q}=(0,0,L)$. The value of L was varied along the scan to minimize the magnitude of $\mathbf{Q}$. Blue squares denote M_y, red circles M_z, and the lines are guides to the eye.

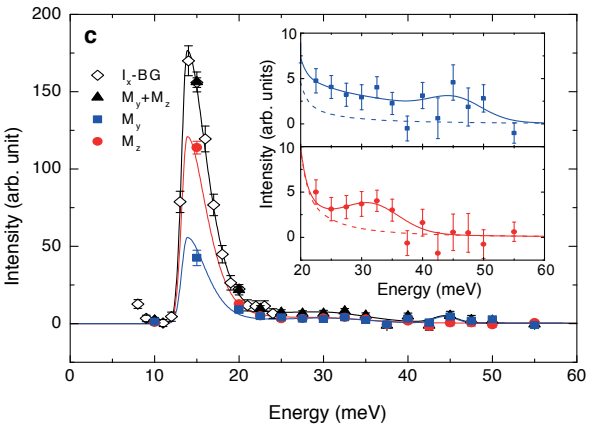

FIG. S6. **Energy scan at $\mathbf{q}=(\pi,\pi)$.** The value of L was varied along the scan to minimize the magnitude of $\mathbf{Q}$. The data denoted I_x-BG (empty black diamonds) is obtained from the raw data in the M_x channel after subtraction of a small background; this method is only reliable when the signal is much larger than the background. The intensities M_y+M_z(filled black triangles), M_y (blue squares), and M_z(red circles) are obtained using eq. (6) and the lines are guides to the eye. The inset shows in detail the region above 20 meV for M_y (top) and M_z(bottom). Dashed lines represent the tail of the main transverse mode.

different Brillouin zones to maximize the intensity for the different modes. The measurements at $\mathbf{Q}=(2,0,0.4)$ at 15 meV give conclusive evidence for the folded mode T′ (Fig. S5a), as the out-of-plane polarization gives rise to a signal in M_y but not in M_z. We confirmed that the signal is peaked at (2,0,0.4) by scanning along the H direction (not shown). To avoid a sharp spurion a small L component was used. For the energy scan at $\mathbf{Q}=(0,0,L)$, shown in Fig. S5b, the signal exclusively originates from in-plane polarized modes. We observe two magnetic excitations clearly separated in energy, both with equal contributions from the M_y and M_z channels. Given the dispersion obtained from TOF, the peak at 45 meV is unambiguously assigned to the transverse mode T; thus the peak at 52 meV must be associated with the longitudinal mode L.

C.4 Energy scans at $\mathbf{q}=(\pi,\pi)$

Energy scans at $\mathbf{Q}=(1,0,L)$ shown in Fig. S6, corresponding to $\mathbf{q}=(\pi,\pi)$ of the tetragonal unit cell, reveal three magnetic excitations above a gap of 14 meV. For the two features lowest in energy we observe a signal in both M_y and M_z channels, characterizing them as in-plane polarized magnetic excitations. The third mode is unambiguously identified as the folded mode as the polarization factor suppresses the intensity in the M_z channel completely for out-of-plane excitations. The M_y and M_z signals allow separation of the in-plane and out-of-plane responses, because the M_y signal exclusively originates from in-plane polarized modes, whereas the M_z signal has contributions from both in-plane and out-of-plane polarized modes.

D. Proximity to the QCP

To quantify the proximity to the QCP, we introduce $\tau = J/J_{cr} \approx 8J/E$. At the QCP ($\tau=1$), where the distinction between transverse and amplitude modes vanishes, their intensity ratio at $\mathbf{q}=(0,0)$ is $\simeq 1$ (equality holds when the gap is zero), and approaches zero as the moment saturates (Fig. S7). The measured intensity ratio of 0.55 ± 0.11 translates to $\tau \approx 1.8$. In principle, the size of the static moment contains the same information, but only after corrections due to g-factors, covalency, and quantum fluctuations, have been properly taken into account, which are model-dependent and fraught with systematic uncertainties.

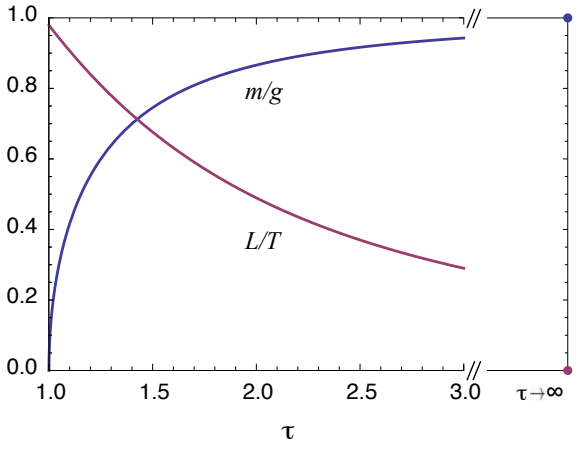

FIG. S7. **Quantification of the proximity to the QCP.** Evolution of the intensity ratio between the amplitude (L) and the transverse (T) modes at $\mathbf{q}=(0,0)$, and the static magnetic moment normalized by the in-plane g-factor as a function of $\tau = J/J_{cr}$. $\tau=1$ at the QCP.

DOI: 10.1038/NPHYS4077

E. Mode dispersions and intensities

The excitation spectra for the model in eq. (1) formulated in the basis $\{s, T_x, T_y\}$ were calculated using the modified spin-wave theory for the models where the QCP is associated with triplet condensation (see refs. 19,20). The energy and magnetic intensity of the longitudinal mode obtained within the harmonic approximation reads as

$$\omega_{L\mathbf{q}} = W\sqrt{1+\frac{\gamma_{\mathbf{q}}}{\tau^2}}\,, \quad I_{L\mathbf{q}} \propto \frac{1}{\tau}\frac{1}{\sqrt{\tau^2+\gamma_{\mathbf{q}}}}\,, \tag{8}$$

where $W = 8J$ is the energy scale and $\gamma_{\mathbf{q}} = \frac{1}{2}(\cos q_x + \cos q_y)$. This mode is most dispersive and intense near the QCP ($\tau \sim 1$) while in the rigid-spin limit ($\tau \gg 1$), it flattens and vanishes. To describe the main (T) and folded (T′) transverse modes, we introduce two auxiliary quantities

$$\begin{aligned} a_{\mathbf{q}} &= \tfrac{1}{2}W(1+\tfrac{1}{\tau})(1+\gamma_{\mathbf{q}}) + \epsilon\,, \\ b_{\mathbf{q}} &= \tfrac{1}{2}W(1+\tfrac{1}{\tau})\left[1-\tfrac{\tau-1}{\tau+1}(1-\alpha)\gamma_{\mathbf{q}}\right] + \epsilon\,. \end{aligned} \tag{9}$$

Then the energy and intensity of the T mode may be expressed as

$$\omega_{T\mathbf{q}} = \sqrt{a_{\mathbf{q}}b_{\mathbf{q}}}\,, \quad I_{T\mathbf{q}} \propto \frac{1}{\tau}\frac{\tau+1}{2}\sqrt{\frac{b_{\mathbf{q}}}{a_{\mathbf{q}}}} \tag{10}$$

and for the T′ mode we have

$$\omega_{T'\mathbf{q}} = \omega_{T\tilde{\mathbf{q}}}\,, \quad I_{T'\mathbf{q}} \propto \frac{1}{\tau}\frac{\tau-1}{2}\sqrt{\frac{a_{\tilde{\mathbf{q}}}}{b_{\tilde{\mathbf{q}}}}}\,, \tag{11}$$

where $\tilde{\mathbf{q}} = \mathbf{q} + (\pi,\pi)$. The intensity contrast between the T and T′ modes is most pronounced in the soft-spin situation where $\tau \sim 1$. At the crossing point of their dispersions, $\mathbf{q} = (\frac{\pi}{2}, \frac{\pi}{2})$, $\gamma_{\mathbf{q}}$ is zero and $I_{T'}/I_T$ becomes $(\tau-1)/(\tau+1)$, vanishing as $\tau \to 1$. Note that in the standard Heisenberg or XY models the intensity ratio is 1 (consider $\tau \to \infty$). For the relative intensity of the L and T mode at $\mathbf{q} = (0,0)$, used to quantify the proximity to the QCP, we get $I_L/I_T = 2/\sqrt{(\tau+1)(\tau^2+1)}$ ($\alpha = 0$, $\epsilon = 0$) corrected by a multiplicative factor $1 - \frac{\tau^2}{2(\tau+1)}\frac{\epsilon}{W}$ for small nonzero ϵ. Non-zero pseudodipolar term in eq. (1) mixes the L mode and T mode leading to two modes with the modified dispersions

$$\omega^2_{1,2\mathbf{q}} = \frac{\omega^2_{L\mathbf{q}} + \omega^2_{T\mathbf{q}}}{2} \pm \sqrt{\left(\frac{\omega^2_{L\mathbf{q}} - \omega^2_{T\mathbf{q}}}{2}\right)^2 + c^2_{\mathbf{q}}}\,, \tag{12}$$

where $c^2_{\mathbf{q}} = W^3 b_{\mathbf{q}}(A/2J\tau)^2(\cos q_x - \cos q_y)^2$. Due to the d-wave type form-factor $(\cos q_x - \cos q_y)$, this correction is only relevant near the $(\pi, 0)$ area.

The two-dimensional situation requires us to go beyond the harmonic approximation for the amplitude mode. Its coupling to the two-magnon continuum modifies the bare susceptibility

$$\chi_{L0}(\mathbf{q},\omega) = \frac{W}{2(\omega^2_{L\mathbf{q}} - \omega^2)} \tag{13}$$

associated with the amplitude mode as $\chi_L^{-1} = \chi_{L0}^{-1} - \Pi_L$. Collecting the leading terms, the self-energy Π is obtained as

$$\Pi_L(\mathbf{q},\omega) = \sum_{\mathbf{k}} \frac{M^2_{L\mathbf{k}\mathbf{k}'} b_{\mathbf{k}} b_{\mathbf{k}'} (\omega^{-1}_{T\mathbf{k}} + \omega^{-1}_{T\mathbf{k}'})}{(\omega_{T\mathbf{k}} + \omega_{T\mathbf{k}'})^2 - (\omega + i\Gamma)^2}\,. \tag{14}$$

Here $\mathbf{k}' = -\mathbf{k} + \mathbf{q} + (\pi,\pi)$ and the matrix element

$$M^2_{L\mathbf{k}\mathbf{k}'} = \frac{W^2}{4}\left(1 - \frac{1}{\tau^2}\right)\left(\frac{\gamma_{\mathbf{q}}}{\tau} + \frac{\gamma_{\mathbf{k}} + \gamma_{\mathbf{k}'}}{2}\right)^2\,. \tag{15}$$

Note that the (π,π) shift in the momentum conservation relation above arises due to the condensate acting as a source and sink of the (π,π) momentum. In the calculations, we have used the broadening parameter $\Gamma = 6\,\mathrm{meV}$. The self-energy is largest for $\mathbf{q} \approx (\pi,\pi)$, where the dominant contribution comes from $\mathbf{k} \approx -\mathbf{k}' \approx (\pi,\pi)$ (supported by both small ω_T and large $M^2_{\mathbf{k}\mathbf{k}'}$), and turns the amplitude mode into a broad feature. A sizable gap $\omega_{T(\pi,\pi)}$ of the spin-wave dispersion prevents the infrared singularity of Π, whose imaginary part would diverge like $1/\omega$ in the gapless case. In our case it is zero below the cutoff energy $2\omega_{T(\pi,\pi)}$ comparable to W making the above perturbative approach well controlled.

The T mode is the subject of a similar, albeit much smaller renormalization due to a coupling to the L mode. The relevant bare susceptibility $\chi_{T0}(\mathbf{q},\omega) = \frac{1}{2}b_{\mathbf{q}}/(\omega^2_{T\mathbf{q}} - \omega^2)$ is modified according to $\chi_T^{-1} = \chi_{T0}^{-1} - \Pi_T$ by employing the self-energy

$$\Pi_T(\mathbf{q},\omega) = \sum_{\mathbf{k}} \frac{M^2_{T\mathbf{k}\mathbf{k}'} W b_{\mathbf{k}'} (\omega^{-1}_{L\mathbf{k}} + \omega^{-1}_{T\mathbf{k}'})}{(\omega_{L\mathbf{k}} + \omega_{T\mathbf{k}'})^2 - (\omega + i\Gamma)^2} \tag{16}$$

containing the matrix element

$$M^2_{T\mathbf{k}\mathbf{k}'} = \frac{W^2}{8}\frac{\tau+1}{\tau^2(\tau-1)}\left(1 + \gamma_{\mathbf{q}} - \gamma_{\mathbf{k}} - \gamma_{\mathbf{q}-\mathbf{k}} + 2\tau\frac{\epsilon}{W}\right)^2\,. \tag{17}$$

Note that, as a consequence of the rotational symmetry, this coupling vanishes for the $\mathbf{q} = (\pi,\pi)$ magnons in the gapless situation ($\epsilon = 0$).

PRL 119, 067201 (2017) PHYSICAL REVIEW LETTERS week ending 11 AUGUST 2017

Raman Scattering from Higgs Mode Oscillations in the Two-Dimensional Antiferromagnet Ca_2RuO_4

Sofia-Michaela Souliou,[1,2] Jiří Chaloupka,[3,4] Giniyat Khaliullin,[1] Gihun Ryu,[1] Anil Jain,[1,6] B. J. Kim,[1,7,8] Matthieu Le Tacon,[1,5] and Bernhard Keimer[1]

[1]*Max Planck Institute for Solid State Research, Heisenbergstrasse 1, D-70569 Stuttgart, Germany*
[2]*European Synchrotron Radiation Facility, BP 220, F-38043 Grenoble Cedex, France*
[3]*Central European Institute of Technology, Masaryk University, Kamenice 753/5, 62500 Brno, Czech Republic*
[4]*Department of Condensed Matter Physics, Faculty of Science, Masaryk University, Kotlářská 2, 61137 Brno, Czech Republic*
[5]*Karlsruhe Institute of Technology, Institut für Festkörperphysik, D-76021 Karlsruhe, Germany*
[6]*Solid State Physics Division, Bhabha Atomic Research Centre, Mumbai 400085, India*
[7]*Department of Physics, Pohang University of Science and Technology, Pohang 790-784, Republic of Korea*
[8]*Center for Artificial Low Dimensional Electronic Systems, Institute for Basic Science (IBS), 77 Cheongam-Ro, Pohang 790-784, Republic of Korea*

(Received 12 April 2017; revised manuscript received 30 May 2017; published 8 August 2017)

We present and analyze Raman spectra of the Mott insulator Ca_2RuO_4, whose quasi-two-dimensional antiferromagnetic order has been described as a condensate of low-lying spin-orbit excitons with angular momentum $J_{\rm eff} = 1$. In the A_g polarization geometry, the amplitude (Higgs) mode of the spin-orbit condensate is directly probed in the scalar channel, thus avoiding infrared-singular magnon contributions. In the B_{1g} geometry, we observe a single-magnon peak as well as two-magnon and two-Higgs excitations. Model calculations using exact diagonalization quantitatively agree with the observations. Together with recent neutron scattering data, our study provides strong evidence for excitonic magnetism in Ca_2RuO_4 and points out new perspectives for research on the Higgs mode in two dimensions.

DOI: 10.1103/PhysRevLett.119.067201

The notion of Goldstone and Higgs modes, corresponding to phase and amplitude oscillations of a condensate of quantum particles, appears in many areas of physics including magnetism [1]. In quantum magnets, especially near quantum criticality [2], the magnetization density is far from being saturated and, hence, allowed to oscillate near its mean value, forming a collective amplitude mode.

The "magnetic" Higgs mode has been observed [3] in quantum dimer systems, where the magnetic order is due to Bose-Einstein condensation of spin-triplet excitations [4]. A conceptually similar, but physically distinct case is expected in Van Vleck–type Mott insulators, where the "soft" moments result from condensation of spin-orbit excitons [5], that is, magnetic transitions between spin-orbit $J_{\rm eff} = 0$ and $J_{\rm eff} = 1$ levels propagating via exchange interactions. Recent inelastic neutron scattering (INS) experiments [6] on Ca_2RuO_4 have indeed revealed Higgs oscillations of the magnetization in this material, which is based on nominally nonmagnetic, spin-orbit singlet Ru^{4+} ions. A detailed analysis of the dispersion relations of the Higgs mode and magnons determined by INS showed that Ca_2RuO_4 is close to a quantum critical point associated with the condensation of $J_{\rm eff} = 1$ excitons [6].

The unique aspect of Ca_2RuO_4 is that it hosts Higgs physics in a two-dimensional setting, which has been a focus of many theoretical studies [7–15]. As the magnetization density is not a conserved quantity, the Higgs mode is not symmetry protected, and various decay processes convert it into a many-body resonance with $\sim\omega^3$ onset. It was also emphasized [7] that the actual appearance of this resonance strongly depends on the symmetry of the probe. In INS experiments, which probe the longitudinal magnetic susceptibility, the low-energy behavior of the Higgs resonance is masked by the infrared-singular two-magnon contribution. To avoid contamination by the Goldstone modes, the probe should couple to the condensate in the scalar channel (i.e., insensitively to the phase or direction). Precisely this type of experiment has been done in ultracold atomic systems [16].

In this Letter, we demonstrate that Raman light scattering in the fully symmetric, i.e., A_g channel can serve as a scalar probe in magnetic systems, thus providing direct access to Higgs oscillations of soft moments. While in conventional Heisenberg magnets with rigid spins (such as La_2CuO_4 or Sr_2IrO_4) the A_g channel is magnetically silent, the size of the local moments, and hence the magnetization density in excitonic systems is determined by a balance between the spin-orbit λ and exchange J interactions [5,6], and the A_g modulation of the latter directly shakes the condensate density.

The Raman scattering data in Ca_2RuO_4 presented below indeed reveal a pronounced magnetic contribution in the A_g channel, which we identify and describe using the same excitonic model that has already been parametrized in the INS study [6]. In the B_{1g} channel, we observe the expected

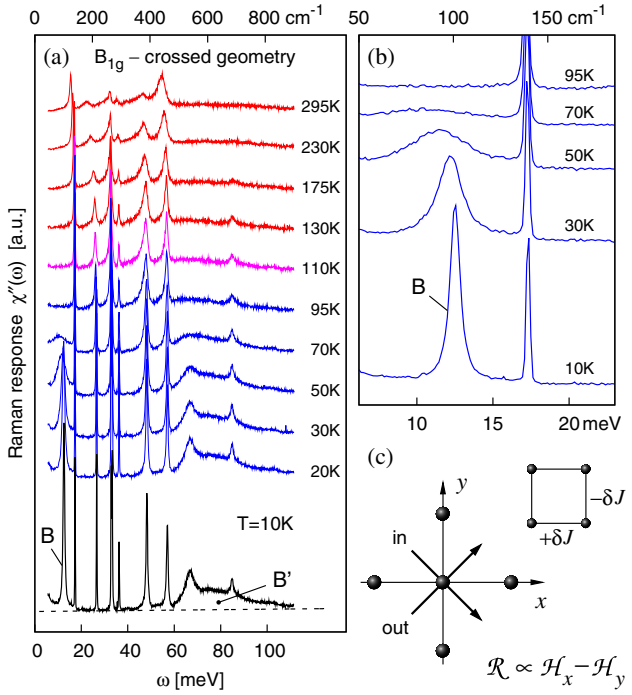

FIG. 1. (a) Raman spectra in B_{1g} scattering geometry with two magnetic features B, B' appearing below T_N. The background (dashed line) is subtracted in further analysis. (b) Detailed view on the feature B. (c) Polarization vectors of incoming and outgoing photons with respect to the Ru lattice. In the Raman process, the exchange is modulated with opposite signs on x and y bonds leading to the Raman operator $\mathcal{R} \propto \mathcal{H}_x - \mathcal{H}_y$.

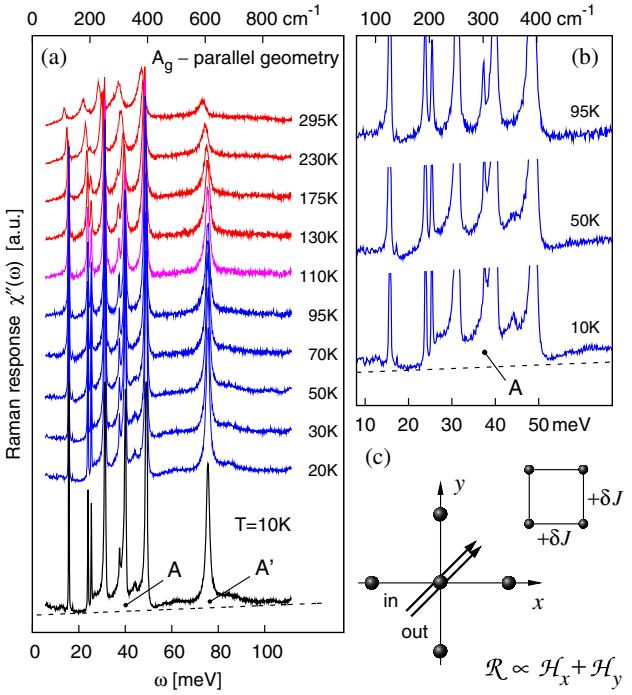

FIG. 2. (a) Raman spectra in A_g scattering geometry with two magnetic features A, A' appearing below T_N. (b) Detailed view on the feature A. (c) The polarization vectors in the A_g setup. In this case, the exchange is modulated equally on x and y bonds and the Raman operator $\mathcal{R} \propto \mathcal{H}_x + \mathcal{H}_y$.

two-magnon scattering and an additional two-Higgs scattering contribution, as well as a single-magnon peak. All the observations are coherently explained by model calculations.

Experiment.—Single crystals of Ca_2RuO_4 with $T_N = 110$ K were grown by a floating zone method, as described elsewhere [17]. The Raman data were recorded on a Labram (Horiba Jobin-Yvon) single-grating Raman spectrometer, using the 632.817 nm line of a He^+/Ne^+ mixed gas laser. The experiments were performed in backscattering geometry along the crystallographic c axis. Ca_2RuO_4 crystallizes in the orthorhombic $Pbca$-D_{2h}^{15} space group. Excitations in the B_{1g} and A_g representations of the point group D_{2h} were probed in crossed and parallel configurations, respectively, with the polarization of the incident light at 45° to the Ru-Ru bonds [see Figs. 1(c) and 2(c)]. The spectra were corrected for the Bose thermal factor to obtain the Raman response functions $\chi''(\omega)$.

Temperature-dependent $\chi''(\omega)$ spectra in the range of 5 to 110 meV are plotted in Figs. 1 and 2. The frequencies of the observed phonon modes are in good agreement with previous Raman studies [18]. The phonon modes are superimposed on top of a broad continuum. As the temperature is lowered, the continuum evolves into distinct spectral features B, B' (Fig. 1) and A, A' (Fig. 2). The temperature dependence of the new features follows closely that of the magnetic order parameter and strongly suggests their magnetic origin. The fact that these excitations are well inside the optical gap exceeding 0.5 eV [19] further supports this interpretation.

More specifically, in the B_{1g} channel, the feature B appears around 12 meV and gradually sharpens [Fig. 1(b)]. Earlier Raman studies attributed it either to two-magnon scattering [20,21] or to a zone-boundary folded phonon in the magnetically ordered state [18]. However, we find below that the two-magnon scattering is represented by the B' structure around 80 meV, while the B peak is identified as a single-magnon excitation.

In the A_g channel, the A structure in the range of 25 to 50 meV develops in the magnetically ordered state [Fig. 2(b)]. The phonon modes in this spectral region exhibit pronounced Fano-type asymmetric line shapes—a clear signature of the presence of a continuum of excitations coupled to the phonons. As noticed above, the large optical gap implies a magnetic origin of the continuum.

Extraction of the magnetic response.—We adopt the Green's function approach [22–24] to the Raman response of the coupled system of phonons and a continuum. We describe the system by a matrix propagator whose inverse $G^{-1}(\omega)$ contains the response functions of the magnetic $[G^{-1}(\omega)]_{00} = R(\omega) + iS(\omega)$ and phonon $[G^{-1}(\omega)]_{nn} = \omega_n - \omega - i\Gamma_n$ $(n = 1 \ldots N)$ subsystems as the diagonal elements. The coupling between phonon n and the continuum is provided by nondiagonal matrix elements

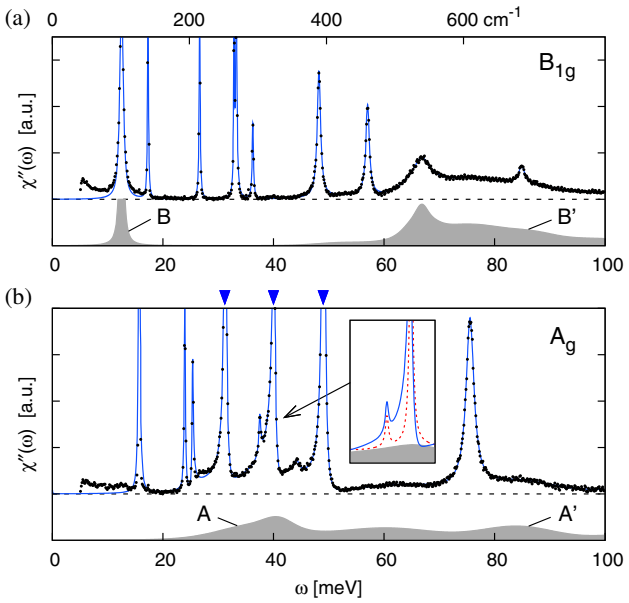

FIG. 3. Fits of $T = 10$ K Raman spectra in B_{1g} (a) and A_g (b) channels using a model of phonons interacting with a magnetic continuum. The model response (blue) is compared to the experimental points (black). The obtained magnetic signal $S(\omega)$ is indicated by shading. The A_g phonons marked by blue triangles are most strongly affected by the spin-phonon interaction which changes their line shape dramatically compared to the noninteracting case (red dashed line in the inset). The associated spectral-weight transfer is moderate only.

$[G^{-1}(\omega)]_{n0} = [G^{-1}(\omega)]_{0n} = V_n$. After inverting $G^{-1}(\omega)$, the Raman response is obtained as $\chi''(\omega) = \sum_{j=0}^{N} W_j [\mathrm{Im}G(\omega)]_{jj}$, where W_j are spectral weights of the normal modes of the coupled spin-phonon system.

The magnetic response functions $S(\omega)$, determined by fitting $\chi''(\omega)$ to the low-temperature spectra, are presented in Fig. 3. While in the B_{1g} case the above procedure just confirms the expected result, in the A_g case it proved essential to obtain the actual $S(\omega)$ profile. The feature A is found to be peaked at about 40 meV and has a long tail that merges with the high-energy continuum (A'), much flatter than the B_{1g} one (B').

Magnetic model.—In the following, we give a quantitative interpretation of the magnetic features using the excitonic model of Ref. [5], refined further by a comparison to INS data [6]. The model utilizes the local basis depicted in Fig. 4(b) stabilized by intraionic spin-orbit coupling. The dominant energy scale corresponds to the energy cost E_T of a triplon T (derived from $J_{\mathrm{eff}} = 1$ states) relative to that of the singlet ground state s ($J_{\mathrm{eff}} = 0$). Its competition with the spin-orbital exchange interaction results in a quantum critical point separating the paramagnetic phase (dilute "gas" of T on top of an s background) and the antiferromagnetic phase (condensate with coherently mixed T and s). In terms of hardcore bosons s and $T_{x/y}$ associated with the relevant low-energy

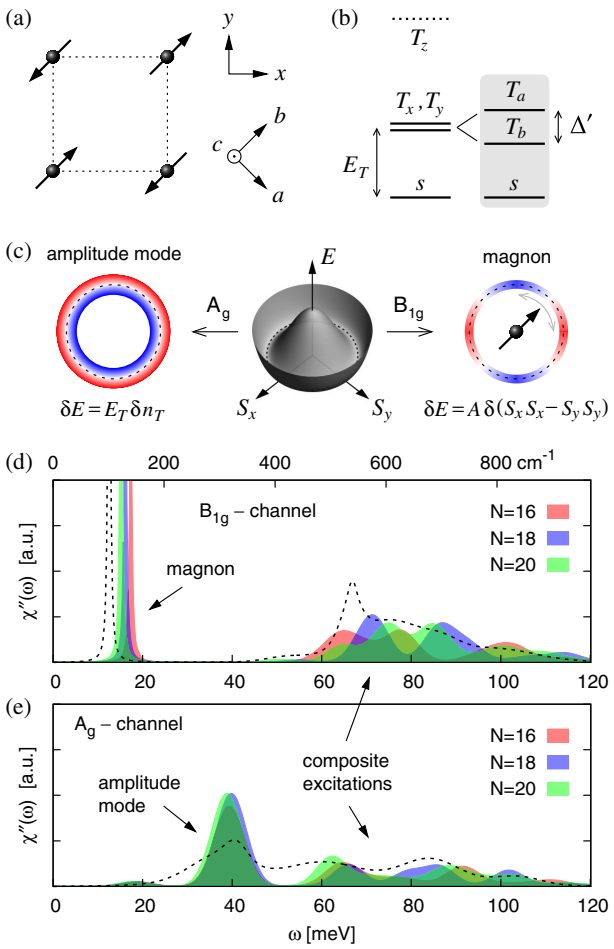

FIG. 4. (a) Coordinate frames for the Ru lattice. The ordered moments point along the b axis. (b) Multiplet structure of Ru^{4+} ions with a ground-state singlet s with $J_{\mathrm{eff}} = 0$ and higher-lying magnetic states derived from $J_{\mathrm{eff}} = 1$ triplet. A tetragonal crystal field removes the degeneracy of the triplet states T by lifting up T_z [6]. An orthorhombic distortion further splits $T_{x/y}$ into $T_{a/b} = (T_x \mp T_y)/\sqrt{2}$ levels forming together with s the basis for the low-energy model (shaded). (c) Modulation of the condensate energy (Mexican-hat potential) in the Raman process leading to an excitation of the amplitude mode (A_g channel). Note that $\delta n_T \equiv \delta(S_x^2 + S_y^2)$, i.e., the A_g coupling is rotationally invariant. In contrast, the B_{1g} coupling leads to the shape deformations, leaving the condensate density intact. A single magnon is excited instead of the amplitude mode. (d),(e) Raman spectra obtained by exact diagonalization on clusters with $N = 16$, 18, and 20 sites [25] using $E_T = 31$ meV, $J = 7.5$ meV, $A = 2.3$ meV, $\alpha = 0.15$, and $\Delta' = 4$ meV. The ED data for B_{1g} (a) and A_g (b) channels are presented in identical scales and overlayed by the magnetic $S(\omega)$ from Figs. 3(a), 3(b) (dashed line).

levels and obeying the local constraint $n_s + n_T = 1$, these main constituents of the model are expressed as

$$\mathcal{H} = E_T \sum_i n_{T_i} + J \sum_{\langle ij\rangle,\gamma=x,y} (T^\dagger_{\gamma i} s_i s^\dagger_j T_{\gamma j} - T^\dagger_{\gamma i} s_i T^\dagger_{\gamma j} s_j + \mathrm{H.c.}). \quad (1)$$

The exchange interaction J comprises triplon hopping and pair creation or annihilation which act together to form AF-aligned pairs of Van Vleck moments.

The full model is most conveniently expressed using a pseudospin $S=1$ formed by the three levels $\{s, T_x, T_y\}$ [6]. The corresponding in-plane operators $S_\gamma = -i(s^\dagger T_\gamma - T_\gamma^\dagger s)$ for $\gamma = x,\ y$ are directly linked to the dominating Van Vleck part of the magnetic moment, while $S_z = -i(T_x^\dagger T_y - T_y^\dagger T_x)$ is related to the moment residing in the excited T levels. In this basis, the J term in Eq. (1) takes a form of the XY model $J(S_i^x S_j^x + S_i^y S_j^y)$. Supplemented by the bond-directional interaction A and coupling between the out-of-plane S_z components, the exchange Hamiltonian for the x bonds reads as

$$\mathcal{H}_x = \sum_{\langle ij\rangle \| x} [(J+A)S_i^x S_j^x + (J-A)S_i^y S_j^y + J(1-\alpha)S_i^z S_j^z]. \tag{2}$$

The signs of the A terms are opposite for y bonds. The $T_{x/y}$-level orthorhombic splitting [see Figs. 4(a), 4(b)] orienting the moments along the b axis translates into a single-ion anisotropy $\mathcal{H}_{\Delta'} = -\Delta'(S_x S_y + S_y S_x) = \frac{1}{2}\Delta'(S_a^2 - S_b^2)$. The full Hamiltonian used below is then $\mathcal{H} = E_T n_T + \mathcal{H}_x + \mathcal{H}_y + \mathcal{H}_{\Delta'}$, with $n_T = S_z^2$.

Model calculations and interpretation of the data.— We employ the Loudon-Fleury [26] Raman scattering operator $\mathcal{R} \propto \sum_{\langle ij\rangle}(\boldsymbol{\epsilon}_{\rm in}\cdot\boldsymbol{r}_{ij})(\boldsymbol{\epsilon}_{\rm out}\cdot\boldsymbol{r}_{ij})\mathcal{H}_{ij}$, which modulates the exchange interactions $\mathcal{H}_{ij}$ in a way determined by the incoming $\boldsymbol{\epsilon}_{\rm in}$ and outgoing $\boldsymbol{\epsilon}_{\rm out}$ polarization vectors [27]. Specifying $\boldsymbol{\epsilon}_{\rm in}$ ($\boldsymbol{\epsilon}_{\rm out}$) by its angle φ (φ') to the a axis, $\mathcal{R}$ becomes

$$\mathcal{R} \propto \cos(\varphi-\varphi')(\mathcal{H}_x+\mathcal{H}_y) + \sin(\varphi+\varphi')(\mathcal{H}_x-\mathcal{H}_y). \tag{3}$$

For B_{1g} ($\varphi = 0$, $\varphi' = \pi/2$) and A_g ($\varphi = \varphi' = \pi/2$) symmetries, only the $\mathcal{H}_x - \mathcal{H}_y$ or $\mathcal{H}_x + \mathcal{H}_y$ term above is active, respectively.

We first discuss the implications of Eq. (3) on a qualitative level. Consider the A_g scattering channel with $\mathcal{R} \propto \mathcal{H}_x + \mathcal{H}_y$. While in the usual rigid spin systems (e.g., cuprates) this operator is proportional to the Hamiltonian itself and does not bring any dynamics, here we may replace it by its complement in the Hamiltonian, i.e., $\mathcal{R} \propto E_T n_T$ (and a small Δ' term), and obtain a nontrivial spectrum. Most importantly, $E_T n_T$ globally changes the balance between the s and $T_{x/y}$ components coherently mixed in the condensate, exciting thus directly the amplitude mode of the condensate. This A_g Raman process may be intuitively understood as a forced expansion and contraction of the Mexican-hat potential in Fig. 4(c). In contrast to INS, the amplitude mode is probed here in a rotationally invariant way, using a scalar coupling to the condensate density. We thus avoid the contamination by the two-magnon response that leads to a drastic broadening of the longitudinal mode in the dynamical spin susceptibility.

In the B_{1g} channel, the modulation of the exchange J contained in $\mathcal{R} \propto \mathcal{H}_x - \mathcal{H}_y$ produces a high-energy two-magnon continuum, as in usual Heisenberg magnets. Here it is additionally supported by other composite excitations such as a two-Higgs continuum (similar to what was found in a soft-spin model [28]). A special role is played by the bond-anisotropic A term contributing to $\mathcal{R}$ as $A\sum_{\langle ij\rangle}(S_i^x S_j^x - S_i^y S_j^y)$. The resulting quadrupolar modulation of the condensate energy [see Fig. 4(c)] drives the ordered moment toward the x or y directions, hence exciting a magnon.

To confirm the above expectations and make a quantitative comparison to the experiment, in Figs. 4(d), 4(e) we show Raman spectra calculated by exact diagonalization (ED). The best fit to the magnetic intensity extracted in Fig. 3 is obtained for the parameters $E_T = 31$ meV, $J = 7.5$ meV, $A = 2.3$ meV, $\alpha = 0.15$, and $\Delta' = 4$ meV, well matching those from the INS data [6]. The small differences in E_T and J are due to the different methods—the spin-wave approach [6] versus ED used here.

In accord with the above discussion, the B_{1g} model spectrum in Fig. 4(d) contains a high-energy continuum and a single-magnon peak due to the bond-directional A part of $\mathcal{R}$ that sums up to $A\sum_{\langle ij\rangle}(S_i^a S_j^b + S_i^a S_j^b)$. Approximating S along the ordered moment direction by $S_{\boldsymbol{R}}^b \approx \langle S_\parallel\rangle e^{i\boldsymbol{Q}\cdot\boldsymbol{R}}$ with $\boldsymbol{Q} = (\pi,\pi)$, this part becomes $A\langle S_\parallel\rangle S_{\boldsymbol{Q}}^a$, thus probing the magnon at the ordering vector. The energy of the experimental feature B of about 12.5 meV indeed agrees with that of the INS (π,π)-magnon peak [6,29]. The spectral weight (SW) of the peak B is roughly proportional to A^2, enabling us to estimate A by comparing the SW of B and that of the B' continuum. The experimental SW ratio obtained from Fig. 3(a) amounts to 0.27. In the model calculations, the average over the three clusters gives a consistent value of 0.30, confirming $A \simeq 2.3$ meV taken from INS fits.

In the A_g channel, the model spectrum in Fig. 4(e) is dominated by the amplitude mode appearing at 40 meV in agreement with the expected position of the bare amplitude mode based on INS (see Fig. 4 of Ref. [6]). The amplitude mode peak is accompanied by a high-energy continuum [Fig. 4(e)]. Since it is a part of the n_T susceptibility, its profile is rather different from that of the (mainly) two-magnon continuum in the B_{1g} channel. The limited scattering possibilities on the small clusters do not allow us to access the mode profile by ED in detail. The available results for the relativistic quantum $O(N)$ model in $2+1$ dimensions [11–14] suggest a Higgs peak with $\sim\omega^3$ onset and an extended tail, which is in qualitative agreement with $S(\omega)$ extracted in Fig. 3(b).

Finally, we comment on the notable interplay of phonons with the amplitude mode observed in Fig. 3(b). First, A_g

phonons involving rotations and tiltings of RuO_6 octahedra modify the Ru-O-Ru bond angle, thus modulating the exchange J in a symmetric fashion. Second, deformations of the octahedra affect the splitting among t_{2g} orbitals, thus modulating E_T owing to the different orbital composition of the s and $T_{x/y}$ states. Both mechanisms provide a natural coupling of phonons to oscillations of the condensate density that is determined by the ratio E_T/J.

In conclusion, we have presented Raman light scattering data on Ca_2RuO_4 and fully interpreted its magnetic features in terms of the excitonic model [5,6]. As demonstrated, the A_g scattering channel enables direct access to the amplitude (Higgs) mode of the spin-orbit condensate. In contrast to INS, the Higgs mode is probed here via a scalar coupling and is not obscured by the two-magnon continuum. The overall agreement with both the neutron and Raman experiments strongly supports the excitonic picture as the basis for magnetism of Ca_2RuO_4. More generally, our results encourage future experimental efforts to explore other compounds based on Van Vleck-type ions such as Ru^{4+}, Os^{4+}, and Ir^{5+}.

J. C. acknowledges support by the Czech Science Foundation (GAČR) under Project No. GJ15-14523Y and MŠMT ČR under NPU II project CEITEC 2020 (LQ1601). B. K. acknowledges support by the European Research Council under Advanced Grant No. 669550 (Com4Com) and by the German Science Foundation (DFG) under the coordinated research program SFB-TRR80.

[1] D. Pekker and C. M. Varma, Annu. Rev. Condens. Matter Phys. **6**, 269 (2015).
[2] S. Sachdev and B. Keimer, Phys. Today **64**, 29 (2011).
[3] Ch. Rüegg, B. Normand, M. Matsumoto, A. Furrer, D. F. McMorrow, K. W. Krämer, H.-U. Güdel, S. N. Gvasaliya, H. Mutka, and M. Boehm, Phys. Rev. Lett. **100**, 205701 (2008).
[4] T. Giamarchi, Ch. Rüegg, and O. Tchernyshyov, Nat. Phys. **4**, 198 (2008).
[5] G. Khaliullin, Phys. Rev. Lett. **111**, 197201 (2013).
[6] A. Jain, M. Krautloher, J. Porras, G. H. Ryu, D. P. Chen, D. L. Abernathy, J. T. Park, A. Ivanov, J. Chaloupka, G. Khaliullin, B. Keimer, and B. J. Kim, Nat. Phys. **13**, 633 (2017).
[7] D. Podolsky, A. Auerbach, and D. P. Arovas, Phys. Rev. B **84**, 174522 (2011).
[8] D. Podolsky and S. Sachdev, Phys. Rev. B **86**, 054508 (2012).
[9] L. Pollet and N. Prokof'ev, Phys. Rev. Lett. **109**, 010401 (2012).
[10] K. Chen, L. Liu, Y. Deng, L. Pollet, and N. Prokof'ev, Phys. Rev. Lett. **110**, 170403 (2013).
[11] S. Gazit, D. Podolsky, and A. Auerbach, Phys. Rev. Lett. **110**, 140401 (2013).
[12] S. Gazit, D. Podolsky, A. Auerbach, and D. P. Arovas, Phys. Rev. B **88**, 235108 (2013).
[13] A. Rançon and N. Dupuis, Phys. Rev. B **89**, 180501(R) (2014).
[14] F. Rose, F. Léonard, and N. Dupuis, Phys. Rev. B **91**, 224501 (2015).
[15] Y. T. Katan and D. Podolsky, Phys. Rev. B **91**, 075132 (2015).
[16] M. Endres, T. Fukuhara, D. Pekker, M. Cheneau, P. Schauß, Ch. Gross, E. Demler, S. Kuhr, and I. Bloch, Nature (London) **487**, 454 (2012).
[17] S. Nakatsuji and Y. Maeno, J. Solid State Chem. **156**, 26 (2001).
[18] H. Rho, S. L. Cooper, S. Nakatsuji, H. Fukazawa, and Y. Maeno, Phys. Rev. B **71**, 245121 (2005).
[19] J. H. Jung, Z. Fang, J. P. He, Y. Kaneko, Y. Okimoto, and Y. Tokura, Phys. Rev. Lett. **91**, 056403 (2003).
[20] C. S. Snow, S. L. Cooper, G. Cao, J. E. Crow, H. Fukazawa, S. Nakatsuji, and Y. Maeno, Phys. Rev. Lett. **89**, 226401 (2002).
[21] H. Rho, S. L. Cooper, S. Nakatsuji, H. Fukazawa, and Y. Maeno, Phys. Rev. B **68**, 100404(R) (2003).
[22] A. Nitzan, Mol. Phys. **27**, 65 (1974).
[23] M. V. Klein, in *Light Scattering in Solids*, edited by M. Cardona (Springer-Verlag, Heidelberg, 1975).
[24] X. K. Chen, E. Altendorf, J. C. Irwin, R. Liang, and W. N. Hardy, Phys. Rev. B **48**, 10530 (1993).
[25] Clusters 16A, 18A, and 20A from D. D. Betts, H. Q. Lin, and J. S. Flynn, Can. J. Phys. **77**, 353 (1999) were used. The spectra were broadened by Gaussians (FWHM = 8 meV), apart from the low-energy B_{1g} peak whose line shape is taken from the B feature in Fig. 3(a).
[26] P. A. Fleury and R. Loudon, Phys. Rev. **166**, 514 (1968).
[27] Note that a direct excitation of the magnetic continuum requires $\boldsymbol{\epsilon}_{\text{in}}$ and $\boldsymbol{\epsilon}_{\text{out}}$ to be in the xy plane. We have verified that the feature A and the associated Fano asymmetries are indeed absent in the zz-polarized Raman spectra (not shown).
[28] S. A. Weidinger and W. Zwerger, Eur. Phys. J. B **88**, 237 (2015).
[29] S. Kunkemöller, D. Khomskii, P. Steffens, A. Piovano, A. A. Nugroho, and M. Braden, Phys. Rev. Lett. **115**, 247201 (2015).

PHYSICAL REVIEW B **100**, 224413 (2019)

Highly frustrated magnetism in relativistic d^4 Mott insulators: Bosonic analog of the Kitaev honeycomb model

Jiří Chaloupka [1,2] and Giniyat Khaliullin [3]

[1]*Department of Condensed Matter Physics, Faculty of Science, Masaryk University, Kotlářská 2, 61137 Brno, Czech Republic*

[2]*Central European Institute of Technology, Masaryk University, Kamenice 753/5, 62500 Brno, Czech Republic*

[3]*Max Planck Institute for Solid State Research, Heisenbergstrasse 1, D-70569 Stuttgart, Germany*

(Received 24 September 2019; published 16 December 2019)

We study the orbitally frustrated singlet-triplet models that emerge in the context of spin-orbit coupled Mott insulators with t_{2g}^4 electronic configuration. In these compounds, low-energy magnetic degrees of freedom can be cast in terms of three-flavor "triplon" operators describing the transitions between spin-orbit entangled $J = 0$ ionic ground state and excited $J = 1$ levels. In contrast to a conventional, flavor-isotropic O(3) singlet-triplet models, spin-orbit entangled triplon interactions are flavor-and-bond selective and thus highly frustrated. In a honeycomb lattice, we find close analogies with the Kitaev spin model—an infinite number of conserved quantities, no magnetic condensation, and spin correlations being strictly short-ranged. However, due to the bosonic nature of triplons, there are no emergent gapless excitations within the spin gap, and the ground state is a strongly correlated paramagnet of dense triplon pairs with no long-range entanglement. Using exact diagonalization, we study the bosonic Kitaev model and its various extensions, which break exact symmetries of the model and allow magnetic condensation of triplons. Possible implications for magnetism of ruthenium oxides are discussed.

DOI: 10.1103/PhysRevB.100.224413

I. INTRODUCTION

Frustrated magnets where competing exchange interactions result in exotic orderings and spin-liquid phases [1–3] has been a subject of active research over the years. In general, the magnetic moments in solids are composed of spin and orbital angular momentum, with rather different symmetry properties of interactions in spin and orbital sectors. While the spin-exchange processes are described by isotropic Heisenberg model, the orbital moment interactions are far more complex—they are strongly anisotropic in real and magnetic spaces [4–6] and frustrated even on simple cubic lattices. The physical origin of this frustration is that the orbitals are spatially anisotropic and hence cannot simultaneously satisfy all the interacting bond directions in a crystal.

In late transition metal ion compounds, the bond directionality and frustration of the orbital interactions are inherited by the total angular momentum $J = L + S$ [5]. Consequently, the low-energy "pseudospin" J models may obtain nontrivial symmetries and host exotic ground states. The best example of this sort is the emergence of the Kitaev honeycomb model [7] in spin-orbit coupled Mott insulators of transition metal ions with low-spin $d^5(S = 1/2, L = 1)$ [8,9] and high-spin $d^7(S = 3/2, L = 1)$ [10,11] electronic configurations, both possessing pseudospin $J = 1/2$ Kramers doublet in the ground state.

The present paper studies the consequences of orbital frustration in another class of spin-orbit Mott insulators, which are based on transition metal ions with low-spin d^4 ($S = 1$, $L = 1$) electronic configuration such as $4d$ Ru^{4+} and $5d$ Ir^{5+}. In these compounds, spin-orbit coupling $\lambda \boldsymbol{L} \cdot \boldsymbol{S}$ favors nonmagnetic $J = 0$ ionic ground state, and magnetic order—if any—is realized via the condensation of excited $J = 1$ triplet states [12,13]. Near a magnetic quantum critical point, where spin-orbit coupling and exchange interactions are of a similar strength and compete, magnetic condensate can strongly fluctuate both in phase and amplitude, as it has been observed in d^4 Mott insulator Ca_2RuO_4 [14,15].

A minimal low-energy model describing the $J = 0$ Mott insulators is a singlet-triplet model, which can be written down in terms of three-flavor "triplon" operators T_α with $\alpha = x, y, z$ [12]. Distinct from a conventional triplet excitations in spin-only models, the spin-orbit entangled triplons keep track of the spatial shape of the t_{2g} orbitals. Therefore their dynamics is expected to be flavor-and-bond selective and frustrate the triplon condensation process. In broader terms, $J = 0$ Mott insulators provide a natural route to a phenomenon of frustrated magnetic criticality [3].

The bond-directional nature of triplon dynamics is most pronounced in compounds with 90°-exchange geometry as, e.g., in honeycomb lattice Li_2RuO_3 [16] with RuO_6 octahedra sharing the edges. Previous work [12,17] has already addressed singlet-triplet honeycomb models, and found that the frustration effects can strongly delay triplon condensation, or suppress it completely in the limit when only one particular triplon flavor out-of-three T_α is active on a given bond. Here, we perform a comprehensive symmetry analysis and exact diagonalization of the model in this limit, where it features a number of properties of Kitaev model. For instance, we observe that the model has an extensive number of conserved quantities, magnetic correlations are highly anisotropic and confined to nearest-neighbor sites. We also find that the model is closely related to the bilayer spin-1/2 Kitaev model [18–20]. However, unlike the Kitaev spin-liquid with emergent nonlocal excitations, the ground state of the model

is a strongly correlated paramagnet smoothly connected to the noninteracting triplon gas, and the lowest excitations are of a single-triplon character at any strength of the exchange interactions.

We analyze the model behavior also in the parameter regime where singlet-triplet level is reversed (formally corresponding to the sign-change of spin-orbit coupling), and find that triplon pairs condense into a valence-bond-solid (VBS). This state is identical to the plaquette-VBS phase of hard-core bosons on kagome lattice [21]; this is not accidental, since the symmetry properties of the model allow a mapping of triplon-pair configurations on honeycomb lattice to a system of spinless bosons on dual kagome lattice. Further, adding the terms that relax the model symmetries, we find a rich phase diagram including the magnetic and quadrupolar orderings.

The paper is organized as follows. Section II introduces the model and sketches its derivation. In Sec. III, we analyze the model symmetries and find analogies to the Kitaev honeycomb model. The phase diagrams and spin excitations are studied in Secs. IV and V—for the simpler one-dimensional (1D) analog of the model providing useful insights, and the full model on the honeycomb lattice, respectively. Section VI summarizes the main results.

II. HONEYCOMB SINGLET-TRIPLET MODEL

We consider a transition metal ion with four electrons on t_{2g} level, e.g., Ru^{4+}. Spin-orbit coupling results in a multiplet structure shown in Fig. 1(a). A minimal model for magnetism of such van Vleck-type ions includes the lowest excited $J_{\rm eff}=1$ states $|T_{\pm1}\rangle$ and $|T_0\rangle$, in addition to the ground state $J_{\rm eff}=0$ singlet $|s\rangle$. It is convenient to work with three triplon operators T_α of Cartesian flavors ("colors") $\alpha = x, y, z$. Using the above J_z eigenstates, they are defined as

$$\begin{aligned} T_x &= \frac{1}{i\sqrt{2}}(T_1 - T_{-1}),\\ T_y &= \frac{1}{\sqrt{2}}(T_1 + T_{-1}),\\ T_z &= iT_0, \end{aligned} \tag{1}$$

and together form a Cartesian vector $\boldsymbol{T}$. A constraint $n_x + n_y + n_z + n_s = 1$ with $n_\alpha = T_\alpha^\dagger T_\alpha$ and $n_s = s^\dagger s$ is implied. Spin-orbit splitting reads then as a chemical potential for T_α bosons: $\lambda\, n_T = \lambda\,(n_x + n_y + n_z)$.

As illustrated in Fig. 1(b), local magnetic moment is composed of two terms, $\boldsymbol{M} = \boldsymbol{M}_1 + \boldsymbol{M}_2$, where $\boldsymbol{M}_1$ originates from dipolar-active transitions between s and T_α states [12]:

$$\boldsymbol{M}_1 = 2\sqrt{6}\,\boldsymbol{v} = -\sqrt{6}\,i\,(s^\dagger \boldsymbol{T} - \boldsymbol{T}^\dagger s), \tag{2}$$

while $\boldsymbol{M}_2$ is derived from triplon-spin $\boldsymbol{J} = -i(\boldsymbol{T}^\dagger \times \boldsymbol{T})$ with g factor $1/2$:

$$\boldsymbol{M}_2 = \tfrac{1}{2}\boldsymbol{J} = -\tfrac{1}{2}\,i\,(\boldsymbol{T}^\dagger \times \boldsymbol{T}). \tag{3}$$

In Eq. (2), $\boldsymbol{v} = -\frac{1}{2}i(s^\dagger \boldsymbol{T} - \boldsymbol{T}^\dagger s)$ keeps track of the imaginary part of $\boldsymbol{T}$ (real part of $\boldsymbol{T}$ carries a quadrupolar moment).

Triplon interactions are derived from Kugel-Khomskii-type exchange Hamiltonian, projected onto singlet-triplet basis [12,17]. In honeycomb lattice of the edge-shared RuO_6 octahedra, see Fig. 1(c), there are two types of electron exchange processes, generated by (i) a direct hopping t of d electrons between nearest-neighbor (NN) Ru ions, and (ii) indirect hopping $\tilde{t}$ via oxygen ions, as depicted in Fig. 1(d).

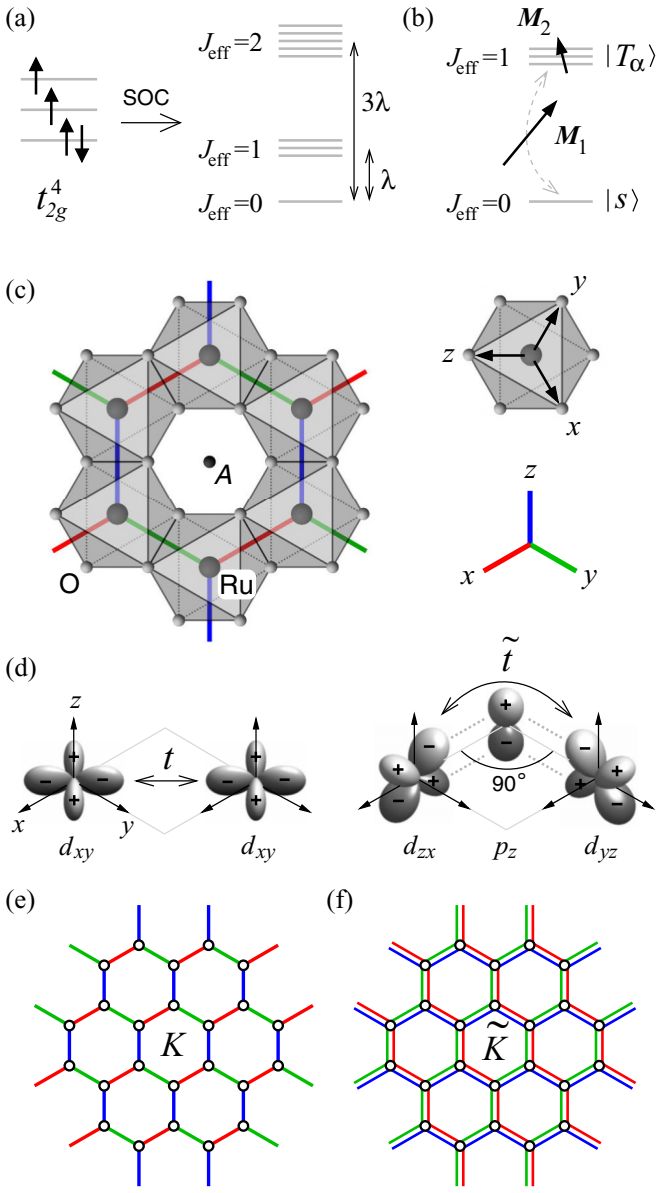

FIG. 1. (a) Energy levels of t_{2g}^4 configuration in LS coupling scheme. Low-energy $J_{\rm eff}=0$ singlet and $J_{\rm eff}=1$ triplet form the local basis of our effective model. (b) The magnetic moment consists of dominant van Vleck-type contribution $\boldsymbol{M}_1$ residing on the $J_{\rm eff} = 0 \leftrightarrow 1$ transition, and a smaller contribution $\boldsymbol{M}_2$ carried by $J_{\rm eff}=1$ triplet. (c) Top view of the honeycomb lattice of edge-shared RuO_6 octahedra in A_2RuO_3. Cubic axes x, y, z pointing from Ru towards O ions, as well as the three types (red, green, blue) of nearest-neighbor bonds in the honeycomb lattice are indicated. (d) Hopping within Ru_2O_2 plaquette of a z bond proceeds through direct overlap of d orbitals (left) or indirectly via oxygen ions (right). (e) Kitaev-like pattern of active bond colors for the interaction K in Eq. (10) in the direct-hopping case. On z bonds, the blue-color triplons T_z are active, etc. (f) Complementary xy-type pattern for the interaction $\tilde{K}$ emerging in the case of indirect hopping; on z bonds, the red (T_x) and green (T_y) color triplons are active.

Consider, for example, direct t hopping; for a z-type bond, it reads as $-t(d^\dagger_{xy,i}d_{xy,j}+\text{H.c.})$. Second-order perturbation theory gives the exchange Hamiltonian, written in terms of spin $S=1$ and orbital $L=1$ operators of d^4 configuration:

$$\mathcal{H}^{(z)}_{ij}=\frac{t^2}{U}\left[(\boldsymbol{S}_i\cdot\boldsymbol{S}_j+1)L^2_{zi}L^2_{zj}-L^2_{zi}-L^2_{zj}\right]. \tag{4}$$

Next, one has to calculate the matrix elements of operators in Eq. (4) between $J_{\rm eff}=0$ and $J_{\rm eff}=1$ wave functions [12], and represent them in terms T_α and s. For example, $S^zL^2_z=\sqrt{\frac{8}{3}}\,v_z$, while $S^{x/y}L^2_z=\sqrt{\frac{2}{3}}\,v_{x/y}+\frac{1}{2}J_{x/y}$, with "van-Vleck" moments $\boldsymbol{v}$ and triplon-spin $\boldsymbol{J}$ already defined above. The projected Hamiltonian (4) takes the form of $\mathcal{H}^{(z)}_{ij}=\frac{8}{3}\frac{t^2}{U}(h_2+h_3+h_4)^{(z)}_{ij}$. It contains two-, three-, and four-triplon operator terms:

$$h^{(z)}_2=v_{zi}v_{zj}+\frac{1}{4}(v_{xi}v_{xj}+v_{yi}v_{yj}), \tag{5}$$

$$h^{(z)}_3=\frac{1}{8}\sqrt{\frac{3}{2}}(v_{xi}J_{xj}+v_{yi}J_{yj})+(i\leftrightarrow j), \tag{6}$$

$$h^{(z)}_4=\frac{3}{32}(J_{xi}J_{xj}+J_{yi}J_{yj})+\frac{1}{32}\,Q_{3i}Q_{3j}, \tag{7}$$

where $Q_3=(n_x+n_y-2n_z)/\sqrt{3}$ is a quadrupole operator of E_g symmetry. Interactions $\mathcal{H}^{(x)}_{ij}$ and $\mathcal{H}^{(y)}_{ij}$ for x- and y-type bonds follow from symmetry. The largest term in the above Hamiltonian is represented by $v_{zi}v_{zj}$ coupling in h_2; physically, this is Ising-type coupling between van-Vleck moments.

Indirect hopping via ligands $-\tilde{t}(d^\dagger_{yz,i}d_{zx,j}+\text{H.c.})$ generates triplon Hamiltonian of the same form, $\tilde{\mathcal{H}}^{(z)}_{ij}=3\frac{\tilde{t}^2}{U}(\tilde{h}_2+\tilde{h}_3+\tilde{h}_4)^{(z)}_{ij}$. In contrast to the above case, however, a dominant term here is represented by xy-type coupling $(v_{xi}v_{xj}+v_{yi}v_{yj})$ in $\tilde{h}_2$ (explicit forms of the other terms can be found in Ref. [12]).

The full models $\mathcal{H}$ and $\tilde{\mathcal{H}}$ are clearly rich but complicated; considering their dominant terms represented by Ising- and xy-type couplings between v-moments should provide some useful insights. Even though these couplings look as simple quadratic forms, the hard-core nature of triplons and their bond-directional anisotropy lead to nontrivial consequences [12,17].

We introduce the bond operator $\mathcal{O}^\alpha_{ij}=4v_{\alpha i}v_{\alpha j}$, which in terms of singlet s and triplon T_α operators reads as

$$\mathcal{O}^\alpha_{ij}=T^\dagger_{\alpha i}s_is^\dagger_jT_{\alpha j}-T^\dagger_{\alpha i}s_iT^\dagger_{\alpha j}s_j+\text{H.c.} \tag{8}$$

We recall that s and T_α are subject to local constraint $n_s+n_T=1$. Alternatively,

$$\mathcal{O}^\alpha_{ij}=\mathcal{T}^\dagger_{\alpha i}\mathcal{T}_{\alpha j}-\mathcal{T}^\dagger_{\alpha i}\mathcal{T}^\dagger_{\alpha j}+\text{H.c.}, \tag{9}$$

where $\mathcal{T}^\dagger=T^\dagger s$ is a hard-core boson with $n_{\mathcal{T}}\leqslant 1$. In terms of $\mathcal{O}^\alpha_{ij}$, a minimal singlet-triplet model Hamiltonian can concisely be written as

$$\mathcal{H}=\sum_i E_T\,n_{T_i}+\sum_{\langle ij\rangle_\alpha}\left[K\mathcal{O}^\alpha_{ij}+\tilde{K}\left(\mathcal{O}^{\bar{\alpha}}_{ij}+\mathcal{O}^{\bar{\bar{\alpha}}}_{ij}\right)\right]. \tag{10}$$

Here, the color $\alpha\in\{x,y,z\}$ is given by the direction of the bond $\langle ij\rangle$, and $\bar{\alpha}$, $\bar{\bar{\alpha}}$ are the two complementary colors; e.g., for z-type bond $\langle ij\rangle_z$ one has $\alpha=z$, while $\bar{\alpha}=x$ and $\bar{\bar{\alpha}}=y$. As derived, the model parameters are $E_T=\lambda$, $K=\frac{2}{3}t^2/U$, and $\tilde{K}=\frac{1}{4}K+\frac{3}{4}\tilde{t}^{\,2}/U$.

The K ($\tilde{K}$) term in Eq. (10) features Kitaev-like (xy-type) symmetry, with one (two) active components of $\boldsymbol{T}$ vector on a given bond. The resulting color-and-bond selective interaction patterns K and $\tilde{K}$ are shown in Figs. 1(e) and 1(f), correspondingly. At $K=\tilde{K}$, the model is equivalent to a conventional O(3) singlet-triplet models [22] that appear, e.g., in low-energy description of a bilayer Heisenberg system. In this isotropic limit, the model is free of frustration and would undergo a magnetic transition at large enough coupling strength $K\sim E_T$. In this paper, the Kitaev-like model with K term, where triplon dynamics is most frustrated, is of primary interest. In particular, we are interested in the nature of magnetically disordered ground state at strong coupling limit of $K\gg E_T$. In real materials, an admixture of the complementary interaction $\tilde{K}$ is expected, and we will consider its impact on the phase behavior of the model.

III. SYMMETRY PROPERTIES AND LINKS TO KITAEV HONEYCOMB MODEL

The color-bond correspondence of the above model in the $K\neq 0$, $\tilde{K}=0$ case is strongly reminiscent of the Kitaev honeycomb model. In this section, we focus exclusively on this limit, draw the corresponding analogies, and find an exact link between our model and a particular variant of bilayer Kitaev model.

A. Extensive number of conserved quantities

In the Kitaev-like limit of the model in Eq. (10), i.e., $\tilde{K}=0$, the number of T_α stays either even (0 and 2) or odd (1) on a bond of direction α. The parity of this number is thus a conserved Z_2 quantity that can be formally written as

$$P_{ij}=(1-2n_{\alpha i})(1-2n_{\alpha j}) \tag{11}$$

with $n_{\alpha i}$ counting T_α-triplon number on site i. Being associated with the individual bonds, the parities form an extensive set of conserved Z_2 quantities that decompose the Hilbert space into subspaces with fixed bond-parity configurations. The total Hilbert space dimension equals 4^N for a system with N sites. With one Z_2 conserved quantity per bond (amounting to $3/2$ per site), the average subspace dimension is reduced to $4^N/2^{\frac{3N}{2}}=(\sqrt{2})^N$. This is actually the same scaling as in the case of the Kitaev honeycomb model [7], where the conserved Z_2 quantities are associated with hexagonal plaquettes (giving $1/2$ of Z_2 quantity per site) and the average subspace dimension thus becomes $2^N/2^{\frac{N}{2}}=(\sqrt{2})^N$. In accord with intuitive expectation, our numerical calculations found the ground state to have *all-even* bond-parity configuration.

B. Mapping to hardcore bosons on a dual lattice

When working in the subspaces with fixed bond parities, most of the 4^N configurations of triplons on the honeycomb lattice of size N are irrelevant. To remove this redundancy in the description, here we develop an auxiliary particle representation by mapping to a system of spinless hardcore bosons on dual (kagome) lattice.

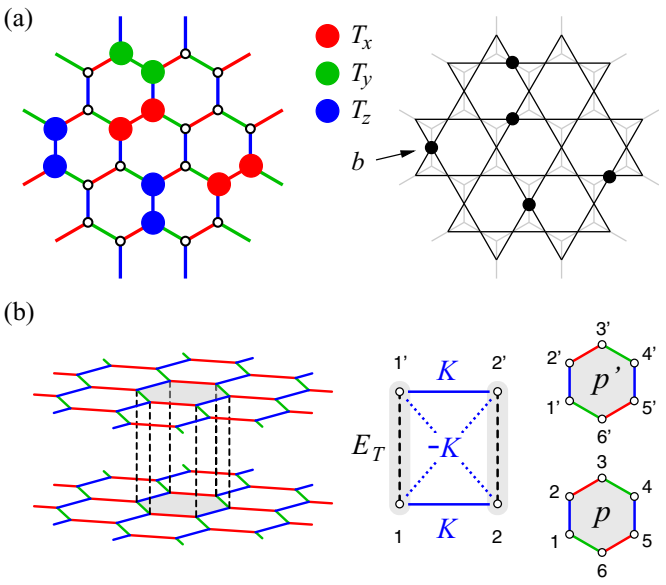

FIG. 2. (a) Sample triplon configuration on the honeycomb lattice (left) and the corresponding configuration of spinless hardcore bosons b (black dots) on a dual kagome lattice (right). In the case of all-even bond parities depicted here, the presence of a T dimer with a proper color (i.e., same as that of the bond) is represented by b boson on the dual lattice. No nearest-neighbor pairs of b on a kagome lattice is allowed. (b) Equivalent spin-1/2 bilayer model realizing the singlet-triplet basis on interlayer vertical bonds that are subject to Heisenberg interaction $J = E_T$. In the model, Kitaev interaction K active on intralayer bonds (such as 1-2 and 1′-2′) is complemented by a Kitaev interaction $-K$ of opposite sign, acting on interlayer cross links (such as 1-2′ and 1′-2). Vertically adjacent hexagonal plaquettes p, p' are used to construct the conserved quantities.

For simplicity, we limit ourselves to the case of *all-even* bond parities, similar one-to-one mappings can be found also in the other cases. The mapping is illustrated in Fig. 2(a). A given bond of the honeycomb lattice can either be occupied by a pair of triplons of the proper color or be empty. These two states are represented by the presence/absence of a hardcore boson b on the corresponding dual lattice site. Starting from a b configuration, the state of a given honeycomb site can be uniquely reconstructed by checking the surrounding kagome sites for b bosons. Either (i) one of them is found, selecting one of the T_α states with α depending on the bond occupied by the b boson, or (ii) none is present, corresponding to the "empty" states s. The constraint for the b bosons is now evident—a nearest-neighbor pair of b at the dual lattice is forbidden.

Altogether, we can formulate the Hamiltonian for the b bosons on the dual lattice as

$$\mathcal{H}_{\rm dual} = \sum_i [2E_T n_b - K(b + b^\dagger)]_i + U \sum_{\langle ij \rangle} n_{bi} n_{bj}, \qquad (12)$$

where i runs through the sites of the kagome lattice, and the repulsive interaction with $U \to \infty$ enforces the constraint of "no nearest-neighbor occupation" for b bosons. Without this constraint, the sum of local Hamiltonians in Eq. (12) would be easy to diagonalize leading to bond eigenstates that involve $|ss\rangle$ and $|T_\alpha T_\alpha\rangle$ pairs. In the form of Eq. (12), the peculiarity of the model is fully exposed—the K interaction forms bond dimers that communicate via constraint only. Adding intersite hopping terms $b_i^\dagger b_j$ in the model would generate boson dispersion and phase relations between them on different sites, leading to a superfluid condensate; however, we have so far no clear microscopic mechanism that would result in such a triplon-pair hopping process.

Finally, let us recall that the above $\mathcal{H}_{\rm dual}$ is valid for the all-even sector only; the formulation of the constraint in the other cases is more complicated.

C. Local nature of the spin correlations

Similarly to the Kitaev model, the presence of the local conserved quantities has consequences for the spin correlations, both of van Vleck moments of Eq. (2) as well as triplon spins entering Eq. (3). Let us consider static correlations of the type $\langle M_\alpha M_\alpha \rangle = Z^{-1} \sum_n \langle n|M_\alpha M_\alpha|n\rangle \, \mathrm{e}^{-\beta E_n}$ or the corresponding dynamic correlations. The eigenstates $|n\rangle$ of Eq. (10) with $\tilde{K} = 0$ have fixed bond-parity configurations. When acting by the α-component of the van Vleck moment operator $M_{1\alpha} \propto (s^\dagger T_\alpha - T_\alpha^\dagger s)$ on a given site, the bond parity of the attached α bond is switched. Bond parities are conserved by the Hamiltonian, the introduced parity defect is thus immobile, and to get back to original parity configuration, one has to act with $M_{1\alpha}$ either at the same site or on the second site of the affected α bond. Therefore $\langle M_\alpha M_\alpha \rangle$ correlator is strictly zero beyond a nearest-neighbor distance. Similarly, the triplon spin operator $-i(\boldsymbol{T}^\dagger \times \boldsymbol{T})$ flips parities of two attached bonds, the original bond-parity configuration therefore has to be restored by acting at the same site. As a result, the Kitaev-like limit of the model is characterized by nearest-neighbor only correlations of the magnetic moments (stemming from the van Vleck component matching the bond color), and a localized nature of the dynamic spin response. This mechanism is completely analogous to the Kitaev model, where a spin flip introduces two localized fluxes [7].

D. Links to the Kitaev honeycomb model

In the previous Secs. III A and III C, we have noticed several striking similarities between the bosonic K model and Kitaev's model for spins-1/2 residing on the honeycomb lattice. A deeper connection of the two models can be thus anticipated, motivating the search for a spin-1/2 equivalent of our model that could reveal such a link. A natural search direction is the class of bilayer spin-1/2 systems with Heisenberg interlayer interaction forming a local singlet-triplet basis on the interlayer rungs.

Indeed, the Hamiltonian in Eq. (10) can be exactly mapped onto spin-1/2 bilayer honeycomb system with the interactions K and $\tilde{K}$ transforming into nearest-neighbor intralayer links and second nearest-neighbor interlayer links as depicted in Fig. 2(b). For $\tilde{K} = 0$, the Hamiltonian involving the nearest-neighbor bond 1-2 and the adjacent one 1′-2′ in the other layer reads as

$$\mathcal{H}_{121'2'} = E_T(\boldsymbol{S}_1\boldsymbol{S}_{1'} + \boldsymbol{S}_2\boldsymbol{S}_{2'}) + K\left(S_1^\alpha S_2^\alpha + S_{1'}^\alpha S_{2'}^\alpha\right) - K\left(S_1^\alpha S_{2'}^\alpha + S_{1'}^\alpha S_2^\alpha\right). \qquad (13)$$

The first two terms form nothing but a pair of Kitaev models linked by vertical Heisenberg bonds. This so-called bilayer Kitaev model was recently studied in Refs. [18–20]. The last term in Eq. (13) provides additional Kitaev-like cross-links of the sign opposite to the intra-layer Kitaev interaction and, as we find later, drastically changes the behavior of the system from that of standard bilayer Kitaev model.

With the above mapping, we are ready to consider the relations between various local conserved quantities. The single layer Kitaev model conserves the product of spin operators at a hexagonal plaquette [see Fig. 2(b)]

$$W_p = 2^6 S_1^x S_2^y S_3^z S_4^x S_5^y S_6^z. \tag{14}$$

In a bilayer Kitaev model, one has to construct products $W_p W_{p'}$ of Kitaev's W_p for vertically adjacent plaquettes [18]. These conserved Z_2 quantities bring about certain features of Kitaev physics to the bilayer Kitaev model. In the case of our model (13), the extra Kitaev-like crosslinks are present. However, the products $W_p W_{p'}$ are still conserved, as can be verified by a direct calculation. Surprisingly, this does not make them yet another set of conserved quantities. In fact, it turns out that $W_p W_{p'}$ are merely products of our bond parities P_{ij}

$$W_p W_{p'} = P_{12} P_{23} P_{34} P_{45} P_{56} P_{61} \tag{15}$$

in the original formulation, and appear as a simple consequence of the bond-parity conservation in the model. The above connection also translates the all-even parity configuration of the ground state into the absence of fluxes in the ground state, i.e., $W_p W_{p'} = +1$ for all plaquettes. The local symmetries of our model are thus more powerful than in the Kitaev model or its simple bilayer extension. Intuitively it may be expected that this denser covering by local conserved quantities will lead to less entangled (more factorized) ground states, as we indeed find below.

As a side remark, we note that while the Hamiltonian (10) contains a balanced combination of hopping and pair terms, differing only by the sign [see Eq. (9)], it is possible to generalize the above mapping to the case $A\, T_\alpha^\dagger T_\alpha - B\, T_\alpha^\dagger T_\alpha^\dagger +$ H.c. with $A \neq B$. The resulting spin-1/2 interactions consist of $\mathcal{H}_{121'2'}$ of Eq. (13) with $K = \frac{1}{2}(A + B)$ and an additional four-spin interaction

$$\Delta\mathcal{H}_{121'2'} = 2(A - B)(\boldsymbol{S}_1 \times \boldsymbol{S}_{1'})^\alpha (\boldsymbol{S}_2 \times \boldsymbol{S}_{2'})^\alpha. \tag{16}$$

By introducing symmetric off-diagonal exchange $\Gamma_{ij} = S_i^x S_j^y + S_i^y S_j^x$ (for a z bond, x and y-bond expressions are obtained by cyclic permutation), it can be brought to a form $2(B - A)(\Gamma_{12}\Gamma_{1'2'} - \Gamma_{12'}\Gamma_{1'2})$ resembling somewhat the structure in Eq. (13). All the arguments concerning conserved quantities remain valid also in the $A \neq B$ case, because the original interactions in expressed using the T particles manifestly conserve bond parities. For example, despite the complicated structure of Eq. (16), it commutes with the plaquette products $W_p W_{p'}$ keeping them still conserved.

IV. KITAEV-LIKE SINGLET-TRIPLET ZIGZAG CHAIN

Before studying the full model on the honeycomb lattice, we first focus on its one-dimensional analog. The 1D system is more accessible to numerics and enables easier insights. As an example of such an approach in the context of the Kitaev-Heisenberg model, Ref. [23] studies the corresponding 1D chains and subsequently makes an interpretation of the 2D honeycomb model behavior in terms of coupled 1D chains.

To form a 1D model analogous to the honeycomb one, we remove T_z triplon and keep only one zigzag chain of the honeycomb lattice, consisting of x and y bonds. In the Kitaev-like limit $\tilde{K} = 0$, these two changes are equivalent as only T_z is active on the z bonds. Going away from the Kitaev-like limit, as an alternative to the complementary $\tilde{K}$ interaction, it is more transparent here to add bond-independent $J_{\rm XY}$ interaction. Instead of the model in Eq. (10), we therefore deal with

$$\mathcal{H} = \sum_i E_T\, n_{T_i} + \sum_{\langle ij\rangle_\alpha} \left[K\mathcal{O}_{ij}^\alpha + J_{\rm XY}\left(\mathcal{O}_{ij}^x + \mathcal{O}_{ij}^y\right)\right] \tag{17}$$

formulated for a zigzag chain of alternating x and y bonds with the bond direction determining again the color α. Note that for $J_{\rm XY} \neq 0$, a slight change to the original parametrization occurs: $K = (K - \tilde{K})_{\rm orig}$ and $J_{\rm XY} = \tilde{K}_{\rm orig}$.

Having now only three levels s, T_x, and T_y in the 1D model, it is possible to convert it to a spin-1 chain using the transformation

$$S^x = -i(s^\dagger T_x - T_x^\dagger s), \tag{18}$$

$$S^y = -i(s^\dagger T_y - T_y^\dagger s), \tag{19}$$

$$S^z = -i(T_x^\dagger T_y - T_y^\dagger T_x), \tag{20}$$

where the first two components of the effective spin-1 correspond to van Vleck moments $\boldsymbol{v}$ while the last one is linked to the triplon spin $\boldsymbol{J}$ [see Eqs. (2) and (3)]. The resulting equivalent spin-1 model is a Kitaev-XY spin-1 chain with single-ion anisotropy E_T:

$$\mathcal{H} = \sum_i E_T \left(S_i^z\right)^2 + \sum_{\langle ij\rangle_\alpha} \left[K S_i^\alpha S_j^\alpha + J_{\rm XY}\left(S_i^x S_j^x + S_i^y S_j^y\right)\right]. \tag{21}$$

The phase diagram of this model for the $K = 0$ case (no bond-alternation) was thoroughly explored in the context of spin-1 XXZ chain with single-ion anisotropy (see, e.g., Refs. [24–27]). Later in Sec. IV B, we will use these corresponding studies as a reference.

A. Chain with pure Kitaev-like interaction

As the first step, we consider the Kitaev-like limit of the model (17), i.e., neglecting J_{XY} term. In general, the behavior of all our models is determined by a competition of the triplon energy cost E_T with the energy gain due to the interactions. One can thus expect a quantum critical point (QCP) separating a triplon gas phase with small triplon densities (dominant E_T regime) from a phase characterized by strongly interacting triplons at larger densities (dominant K regime).

Such a competition is captured by Fig. 3 presenting an evolution for varying K to E_T ratio. For a better understanding and to actually reach the QCP in this case, we have extended the parameter range to the (nonrealistic in the present physical context but interesting theoretically) regime of $E_T < 0$ with reversed s and T levels. The data obtained by exact diagonalization (ED) are shown for two chain lengths to assess the finite-size effects that are quite small here. As seen in

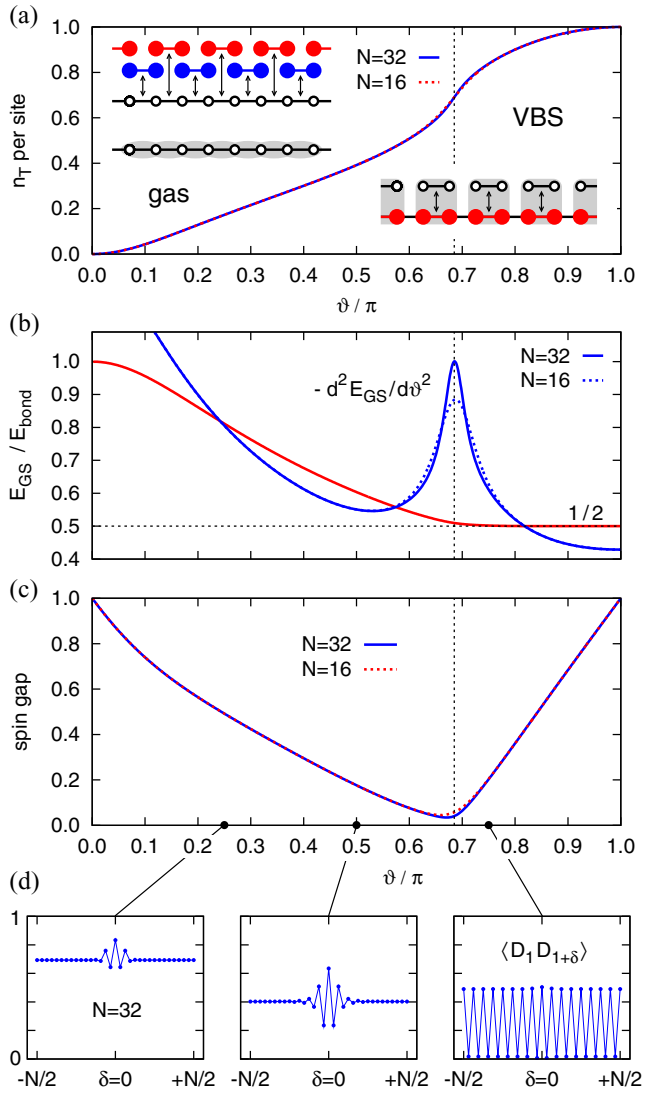

FIG. 3. (a) Occupation of the triplon states $T_{x,y}$ within the chain model parametrized as $E_T = \cos\vartheta$, $K = \sin\vartheta$ obtained by exact diagonalization. Results for the chains of the length $N = 16$ and $N = 32$ are nearly identical. The insets show a cartoon picture of the ground state. At positive $E_T \gg K$, each bond can be predominantly in the bonding state as it is mostly composed of s. At negative E_T with $|E_T| \gg K$, the bonding states are incompatible and are realized only on every second bond creating thus a valence bond solid. (b) Ground-state energy per bond E_{GS} measured by bonding state energy E_{bond} (red) and the second derivative of E_{GS} with respect to ϑ revealing the quantum critical point (blue). (c) Spin gap obtained as the difference of ground-state energies within all-even sector and the sector with a single odd-parity bond. (d) Examples of bond-dimer correlations $\langle D_1 D_{1+\delta} \rangle$ with the dimer operator defined as a projector to the bonding state of Eq. (22): $D = |B\rangle\langle B|$. The value of the correlator at $\delta = 0$ gives the probability of the bonding state P_B, at large distances it approaches P_B^2 in the gas phase. Oscillations near $\delta = 0$ growing with ϑ are due to the increasing incompatibility of bonding states at adjacent bonds. The correlation length diverges approaching the QCP and long-range correlations are seen in the VBS phase.

Fig. 3(a), for an increasing interaction strength K, the triplon density n_T gradually increases with just a single hint of a change of the regime located already at negative E_T. This QCP is clearly revealed by the second derivative of the ground-state energy E_{GS} with respect to model parameters as presented in Fig. 3(b).

To understand the energetics of the evolution together with the nature of the two phases, it is convenient to measure the chain E_{GS} per bond by a ground-state energy of an isolated bond, as it is done in Fig. 3(b). The ground state of a single bond—the bonding state—mixes a pair of proper-color triplons and a pair of s in the wave function

$$|B\rangle = \cos\phi\,|ss\rangle + \sin\phi\,|T_\alpha T_\alpha\rangle \tag{22}$$

with ϕ given by $\tan 2\phi = K/E_T$, and has the energy $E_{bond} = E_T - \sqrt{E_T^2 + K^2}$. This approximately evaluates to $-K^2/2E_T$ for small K, capturing the perturbative incorporation of a triplon pair (energy $2E_T$) by a process with an amplitude K. The orthogonal combination to $|B\rangle$ is the antibonding state $|A\rangle = \cos\phi\,|T_\alpha T_\alpha\rangle - \sin\phi\,|ss\rangle$ whose energy starts at $2E_T$ in $K \to 0$ limit. Similarly to n_T, the ground-state energy measured by E_{bond} shows a gradual evolution with the model parameters for most of the parameter range apart from a change at QCP [see Fig. 3(b)]. In the $E_T \gg K$ regime, E_{GS} reveals the dominance of the bonding states that seem to fill up the system. This is possible since the bonding states are composed mostly of s states that can be shared by the neighboring bonds. For increasing K and thus an increasing admixture of T pairs with bond-dependent color, the bonding states at neighboring bonds have less overlap and the energy gain from K is reduced compared to that of isolated bonds. At the QCP, E_{GS}/E_{bond} approaches $1/2$ and stays flat indicating a valence bond solid (VBS) phase with a rigid structure where every second bond hosts a bonding state. A more detailed inspection shows that in the VBS phase, E_{GS}/E_{bond} positively deviates from $1/2$ with the difference scaling as K^6. This energy gain can be understood within second order perturbation theory as an effect of virtual processes where two neighboring T pairs disappear to make space for an emerging middle T pair (total amplitude is K^3) being an intermediate state.

Interestingly, the smooth evolution observed in Fig. 3 suggests a picture of the dilute triplon gas at $E_T \gg K$ being continuously connected with the dense triplon state close to the QCP. It is further supported by a gradual reduction of the spin gap closing at QCP Fig. 3(c) and an exponential decay of dimer correlations [Fig. 3(d)] with the decay length diverging at QCP when the VBS is formed.

In the Kitaev model, the spin gap separates the flux-free ground state from the topological sector with two fluxes. Within this gap, excitations from the flux-free sector carried by itinerant Majorana fermions can be found. In our model, the spin gap shown in Fig. 3(c) separates the ground state with all-even bond configuration and the sector with one odd bond that is being flipped by the van Vleck moment operator. However, in contrast to the Kitaev model, here the excitation to one-odd sector is lower than excitations within all-even sector all the way up to QCP. In other words, no modes (e.g., Majorana bands) are present within the spin gap. At the QCP, the lowest excitations merge, including also partly the lowest excitations to the other sectors with more odd bonds. The special role of the QCP will be further demonstrated in the next section—an antiferromagnetic condensate will be found

to emanate from it and an intuitive picture of the critical excitations near QCP will be inferred.

B. Extension towards XY chain

Having explored the Kitaev-like limit of the model on the chain, we now consider its extension by J_{XY} interaction introduced in Eqs. (17) and (21). As our main interest is the qualitative illustration of the concepts that appear in the honeycomb case as well, we do not focus on the specifics that are related to one-dimensionality but rather on the generic features that will be inherited by the 2D lattice case.

Let us start the discussion with the pure XY-limit where our model can be related to spin-1 XXZ chain with single-ion anisotropy for which extensive studies are available [24–28], mainly in the connection with the Haldane gap problem. Its phase diagram is quite complex containing a number of phases depending on the J_Z/J_{XY} ratio and single-ion anisotropy D [corresponding to our E_T in Eq. (21)]: large-D phase, Haldane phase, two XY phases, the ferromagnetic phase, and the Néel phase [27]. For the relevant $J_Z = 0$ case that matches to our model, it shows two quantum critical points. The first one at $E_T \approx 0.34 J_{XY}$ corresponds to the transition between the large-D phase and the Haldane phase and its precise determination requires the detection of topological features of the Haldane phase such as the edge spin-1/2 pair [27]. The second transition to the Néel phase occurs at $E_T \approx -2J_{XY}$ and in contrast to the first one is easy to capture precisely [28].

The XY-limit of our model is numerically studied in Fig. 4(a) by means of spin correlations obtained by ED. Since the local conserved quantities are lost when introducing the J_{XY} interaction, we are now limited to a shorter chain length (at most $N = 20$ sites) compared to the previous paragraph. We employ both van Vleck moments [S^x and S^y components of the effective spin-1 defined by Eqs. (18) and (19)] and triplon spin [S^z component defined in Eq. (20)]. The static correlators $\langle S^\alpha_q S^\alpha_{-q}\rangle$ of their Fourier components $S^\alpha_q = \sum_{l=1}^N S^\alpha_l \exp(-iql)/\sqrt{N}$ at the characteristic momentum $q = \pi$ are plotted for two different lengths of the chain and subtracted. The difference uncovers a correlation contribution scaling with the system size (on top of a size-independent contribution) that we regard as a signature of a particular phase. Though oversimplified compared to a full finite-size scaling analysis, this approach will later provide a rough sketch of the phase diagram of the model in its entire parameter space.

Figure 4(a) shows three regimes of the correlations for the XY limit. The first one for $E_T \gg J_{XY}$ corresponds to the triplon gas with the correlations generated exclusively by triplon excitations. It is quickly replaced at about $E_T \approx 1.5 J_{XY}$ with a triplon condensate characterized by antiferromagnetic (AF) correlations of van Vleck moments $M_{1\alpha} \propto (s^\dagger T_\alpha - T^\dagger_\alpha s)$. An intuitive picture of the condensate can be based on a trial ground-state wave function that explicitly mixes the condensed T states into a "pool" of s states

$$|\Psi\rangle = \prod_{l=1}^{N} (\sqrt{1-\rho}\,|s\rangle + \sqrt{\rho}\; i\,e^{i\pi l}\,|T\rangle)_l, \qquad (23)$$

creating thus van Vleck moments. Here $|T\rangle$ stands for any normalized combination of $|T_x\rangle$ and $|T_y\rangle$ and ρ is the condensate density, $0 \leqslant \rho \leqslant 1$. At each site l the hardcore condition $n_T \leqslant 1$ is obeyed. While the wave function (23) is more appropriate for the 2D case with static long-range AF order, it

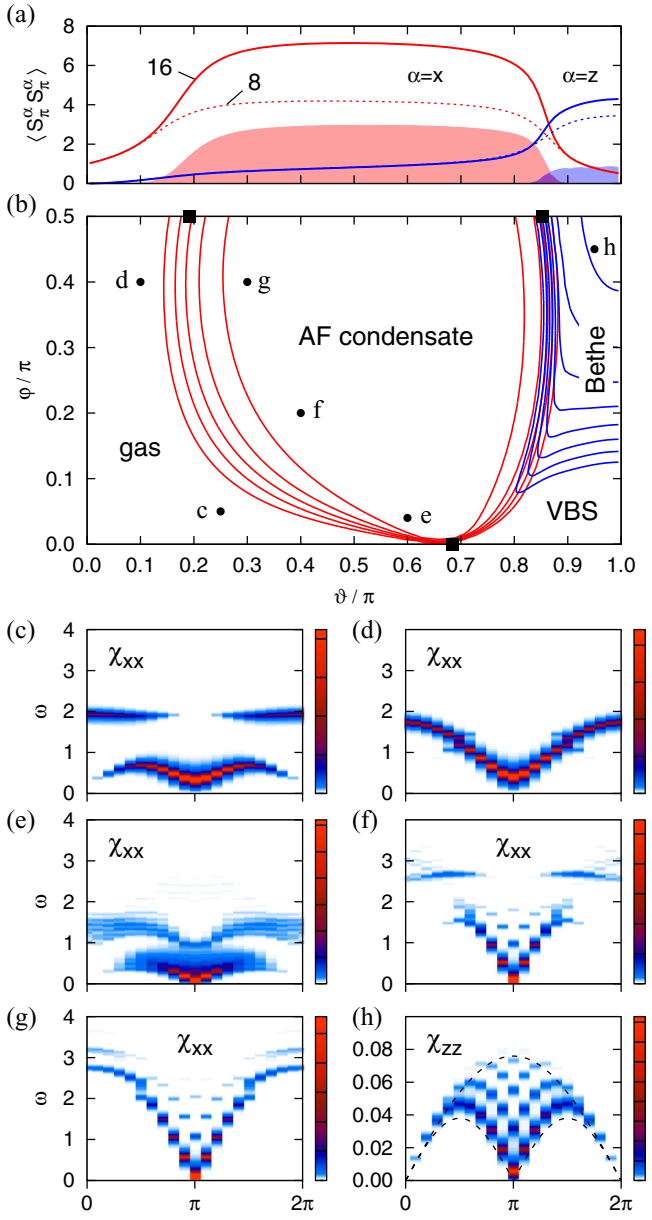

FIG. 4. (a) Correlations $\langle S^\alpha_q S^\alpha_{-q}\rangle$ with $q = \pi$ for the chain model with $K = 0$ parametrized as $E_T = \cos\vartheta$, $J_{XY} = \sin\vartheta$. Data for chains of the length $N = 16$ and 8 are shown. Their difference (shaded areas) represents the part of the correlations scaling with the system size and could be used to estimate the extent of the corresponding phases. (b) Approximate phase diagram of E_T-K-J_{XY} model parametrized as $E_T = \cos\vartheta$, $K = \sin\vartheta\cos\varphi$, $J_{XY} = \sin\vartheta\sin\varphi$. The contours capture the difference of the correlations $\langle S^\alpha_\pi S^\alpha_\pi\rangle$ between $N = 16$ and 8 chains. Red and blue lines are based on S^x and S^z correlations, respectively. Black squares are reference points from Langari *et al.* [28] ($\varphi = \pi/2$ line) and from Fig. 3 ($\varphi = 0$ line). The top line with $\varphi = \pi/2$ matches panel (a). [(c)–(h)] Imaginary part of S^x or S^z susceptibilities calculated for a chain with $N = 20$ sites at the selected parameter points marked in (b). (h) shows also the boundaries (dashed lines) of the excitation continuum for the effective spin-1/2 Heisenberg chain.

still captures the transition between the regime of a triplon gas ($\rho = 0$) and the condensate with pronounced AF correlations ($\rho > 0$) and gives a very crude estimate $E_T = 4J_{XY}$ of the transition point. This is based on minimizing the energy per site $E_T\rho - 4J_{XY}\rho(1-\rho)$ with respect to the variational parameter ρ. Later in Sec. V B, we will develop a quantitative mean-field treatment of the honeycomb model based on the same type of condensation.

The second quantum phase transition (QPT) appearing at $E_T \approx -2J_{XY}$ is to a phase associated with the limit of large negative E_T. At this transition, the energy gain from negative E_T overcomes the energy gain from correlated van Vleck moments and the system collapses to a state full of T_x and T_y triplons leaving the triplon color as the only active degree of freedom. The costly s state can be integrated out leading to an effective interaction among pseudospins $1/2$ describing the T_x, T_y doublets. In the isotropic XY case under consideration, the resulting effective model valid for $J_{XY} \ll -E_T$ is simply a spin-$1/2$ Heisenberg chain with the exchange parameter $J_{\text{eff}} = J_{XY}^2/|E_T|$. It can be obtained by removing s via second order perturbation theory and introducing the sublattice dependent mapping

$$|T_x\rangle \to |\uparrow\rangle, \quad |T_y\rangle \to |\downarrow\rangle \quad \text{(even sites)}, \tag{24}$$

$$|T_x\rangle \to |\downarrow\rangle, \quad |T_x\rangle \to -|\uparrow\rangle \quad \text{(odd sites)}. \tag{25}$$

Because of the connection to the exactly solvable spin-$1/2$ Heisenberg chain, hereafter we call the corresponding phase the Bethe phase (Néel phase in the context of spin-1 XXZ chains).

It has to be noted that while our second QPT for negative E_T well corresponds to the reference data by Chen *et al.* [27], the first change of the regime occurs for much smaller J_{XY} in our data than in Ref. [27]. On the other hand, we obtain a good agreement with the quantum renormalization group (QRG) and ED study [28] of the ground-state fidelity. This may be interpreted within the triplon condensation picture as follows. The true Haldane phase appears around $E_T \approx 0.34J_{XY}$ but this QPT is preceded much earlier by our "transition" associated with the onset of van Vleck correlations and corresponding to the emergence of a triplon (quasi)condensate. Such a change in the ground-state structure is also reflected in the ground-state fidelity inspected in Ref. [28]. While probably not a real QPT, it is a crossover determined by the energy balance of the triplon cost and the energy gain due to a formation of correlated van Vleck moments. In nonfrustrated situations, this energy balance shall lead to a crossover/transition at similar J/E_T ratios, depending mainly on the connectivity of the particular lattice. Therefore the apparent discrepancy is not essential because in the 2D honeycomb case, the emergence of the condensate will correspond to establishing a real long-range AF order of van Vleck moments.

After discussing both the Kitaev-like limit explored in Sec. IV A and the XY limit in the above, we now extend the correlation-based approach to the full E_T-K-J_{XY} model to obtain a sketch of the phase diagram presented in Fig. 4(b).

The topology of the phase diagram follows from the features already met above when inspecting the limiting cases. Most of the phase diagram, in particular all of its physically sensible part ($E_T > 0$), is taken up by the competition of the triplon gas and the triplon condensate with AF correlations of van Vleck moments—components S^x, S^y of the effective spin-1. The crossover is more and more delayed when going from the XY limit ($\varphi/\pi = 0.5$) to the Kitaev-like one ($\varphi = 0$). This is easily understood by an increasing frustration in this direction and thus a smaller gain from creating correlated van Vleck moments. A larger interaction strength is thus needed to overcome the E_T cost. The remaining phases are restricted to the area of large negative E_T. Depending on the balance between K and J_{XY}, the system selects either the VBS phase with every second bond essentially inactivated, or the Bethe phase linked to the hidden effective spin-$1/2$ model—a Heisenberg chain—and revealed by AF correlations of S^z components of the effective spin-1.

To complement the phase diagram, Figs. 4(c)–4(h) present dynamical correlations $\chi_{\alpha\alpha}(q,\omega) = \langle S^\alpha_q S^\alpha_{-q}\rangle_\omega$, i.e., spin susceptibility associated with the effective spin-1, calculated for several points in the phase diagram. The gapped van Vleck susceptibility $\chi_{xx} = \chi_{yy}$ in Figs. 4(c) and 4(d) for the triplon gas phase shows the difference between the local-like response consisting of two flat parts in the Kitaev-like limit [Fig. 4(c)] and (almost) continuous dispersion at large J_{XY} [Fig. 4(d)]. Similarly, Figs. 4(e)–4(g) capture the evolution from the Kitaev-like to the XY-limit response of the AF condensate. Here the low-energy part is dominated by an intense linear mode centered at the AF wave vector $q = \pi$. Extrapolation of data up to $N = 20$ suggests gapless response inside the AF condensate region, within the precision limited by finite-size effects that are pronounced mainly in the transition region. Finally, inspecting the susceptibility χ_{zz} for a point deep inside the Bethe phase, we notice that the dynamical response clearly reveals the hidden spin-$1/2$ Heisenberg chain. For example, its excitation continuum perfectly matches the expected analytical boundaries obtained using $J_{\text{eff}} = J_{XY}^2/|E_T|$, see the dashed lines in Fig. 4(h).

An interesting feature is the "emanation" of the AF condensate from the QCP of the Kitaev-like model. Around that point, indicated by a black square on $\varphi = 0$ line of Fig. 4(b), the triplon gas consists of bonding states that are about to form VBS, while for the AF condensate above QCP we expect the state of the type (23). A naive picture of the link between the two states that is related to low-energy van Vleck excitations observed in Fig. 3(c) can be constructed as follows. For simplicity, let us consider mixing of s and T states in 1:1 ratio and ignore the triplon color. Adopting the condensate wave function (23) with $\rho = \frac{1}{2}$, at two neighboring sites l, $l+1$ we have a state proportional to

$$\begin{aligned}|\text{cond}\rangle &\propto (|s\rangle + i|T\rangle)_l \otimes (|s\rangle - i|T\rangle)_{l+1} \\ &= [|ss\rangle + |TT\rangle - i(|sT\rangle - |Ts\rangle)]_{l,l+1}.\end{aligned} \tag{26}$$

On the other hand, the bonding state with 1:1 mixing is $|B\rangle \propto |ss\rangle + |TT\rangle$. Applying the van Vleck operator $M_q \propto -i\sum_{l=1}^{N} e^{-iql}(s_l^\dagger T_l - T_l^\dagger s_l)$ with the critical $q = \pi$ on $|B\rangle$, we obtain $-2i(|sT\rangle - |Ts\rangle)$ which is exactly the missing part to get bond state $|\text{cond}\rangle$ of (26). The presence of low-energy van Vleck excitations that become gapless at the QCP of the Kitaev-like limit therefore makes the "pool" of bonding states

susceptible to the formation of the AF condensate of the type (23) and this condensate is indeed formed once J_{XY} is added.

V. HONEYCOMB LATTICE CASE

With the basic physical features of our model being illustrated by the 1D simplified case, we now focus on its original version on the honeycomb lattice. While the 2D lattice and one more degree of freedom bring an increased complexity compared to what discussed in Sec. IV, the overall behavior will turn out to be rather similar.

A. The case of pure Kitaev-like interaction

This similarity is seen already in Figs. 5(a) and 5(b) which is a direct analogy of Figs. 3(a) and 5(b) capturing the competition between the gas and VBS phase in the Kitaev-like limit of the model. Again a single QCP is detected, now with a position shifted to a smaller $K/|E_T|$ ratio in the negative E_T region. The reduction of the VBS phase is a consequence of the lattice connectivity—the VBS state can only host a bonding state on one third of the bonds compared to one half in the chain case, leading to a less competitive energy gain. The formation of VBS consisting of maximum geometrically possible number of dimers (bonding states), i.e., $N_{\rm bond}/3$, is seen also in the GS energy per bond measured by $E_{\rm bond}$. This quantity stays close to $1/3$ and there is again a small positive deviation scaling as K^6 that indicates residual interactions among the dimers. They establish a specific dimer arrangement that we detect in Fig. 5(c) using dual b-boson representation on the kagome lattice as described in Sec. III B (note that all the bond parities are even in the case inspected). The VBS phase is marked by size-dependent reciprocal-space correlations of the b-boson density n_b at the characteristic momenta $\boldsymbol{q} = K'$ lying in the corners of the extended Brillouin zone of the kagome lattice. This suggests the real-space pattern shown in Fig. 5(d) that is also the most probable b configuration in the ground state. Translating it into the T-dimer picture, we obtain the pattern in Fig. 5(e) which maximizes the number of plaquettes carrying three dimers. However, the true structure of the ground state is more complicated and requires the following deeper analysis.

In fact, working in the basis of maximum dimer coverings, an effective quantum dimer model (QDM) with $\mathcal{O}(K^6)$ interactions can be formulated. This QDM "lives" in the all-even parity sector and captures both the ground state and the lowest excitations. Leaving the details aside, we note that the dimer model involves two kinds of interactions. First, there is an energy gain $\propto K^6$ from dimer-dimer bonds which is constant for all the coverings and which was already noticed in the 1D case with just two trivial dimer coverings. The second contribution, being the actual driving force stabilizing the VBS pattern, is enabled by the geometry of the honeycomb lattice and corresponds to hexagonal plaquette flips with an amplitude $\propto K^6$. They are captured by the QDM Hamiltonian

$$\mathcal{H}_{\rm QDM} = -t \sum_{\rm plaquettes} \left(\left| \hexagon \right\rangle \left\langle \hexagon \right| + \text{H.c.} \right), \qquad (27)$$

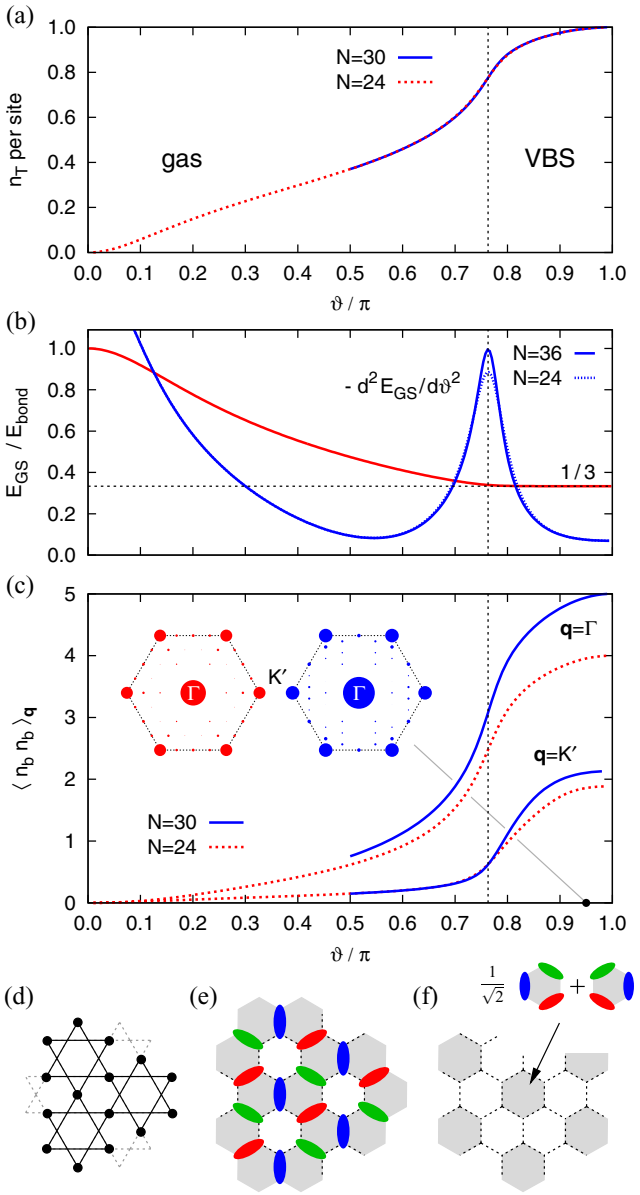

FIG. 5. (a) Occupation of the triplet state within the honeycomb model parametrized as $E_T = \cos\vartheta$, $K = \sin\vartheta$. Presented for a hexagonal 24-site cluster and rectangular 30-site cluster. (b) Ground-state energy per bond $E_{\rm GS}$ measured by bonding-state energy $E_{\rm bond}$ (red) and the second derivative of $E_{\rm GS}$ with respect to ϑ revealing the quantum critical point (blue). (c) Correlations $\langle n_b n_b \rangle_{\boldsymbol{q}}$ of the bosons b on the dual kagome lattice. Size-dependent correlations at the characteristic vector $\boldsymbol{q} = K'$ detect the VBS state. The insets show the correlations at $\vartheta = 0.95\pi$ plotted in the extended Brillouin zone of the kagome lattice at all momenta accessible when using the 24- and 30-site clusters, respectively. (d) Static pattern of the b bosons on the dual lattice suggested by their reciprocal-space correlations. (e) Corresponding arrangement of T dimers in the original representation. Red, green, and blue ellipses represent bonding states involving T_x, T_y, and T_z, respectively. The shaded hexagons indicate flippable plaquettes. (f) The actual plaquette order in VBS phase. The shaded hexagons indicate resonating plaquettes.

with $t = 3K^6/16|E_T|^5$, i.e., by the kinetic term of the Rokhsar–Kivelson (RK) model for the honeycomb lattice [29,30]. Using the connection to this well-studied model we

can fix the type of order in the VBS phase now. The phase diagram of the honeycomb RK model, depending on the ratio of the flippable plaquette energy cost V and the flipping amplitude t, was precisely determined by Monte Carlo simulations [30–32]. Our $V/t = 0$ case falls into the interval between $(V/t)_c \approx -0.23$ [32] and the RK point $V/t = 1$ where the honeycomb RK model supports a triangular covering by resonating plaquettes ("plaquette" order) depicted approximately in Fig. 5(f) which is the true VBS order for our model. The anticipated "columnar" order of Fig. 5(e) only appears below the (rather close) critical point $(V/t)_c$ of the RK model where the sufficiently large negative potential energy of the plaquettes wins.

Finally, we conclude the comparison to the Kitaev-like 1D model by a remark that the spin gap behavior for the honeycomb lattice strongly resembles that of the 1D chain case [see Fig. 3(c)], i.e., the spin gap gradually closes as we approach the QCP from both the gas as well as VBS phases.

B. Full honeycomb model

In this section, we explore the phase diagram and to a limited extent also the excitations of the full model of Eq. (10) containing both the Kitaev-like interaction K and the complementary one $\tilde{K}$. We do not go up to the dominant $\tilde{K}$ regime characterized by strongly interacting quasi-one-dimensional condensates hosted by zigzag chains in the honeycomb lattice [12]. Instead, similarly to the chain case, we interpolate between the Kitaev-like limit and the isotropic limit $K = \tilde{K}$, being both positive as derived. Phase diagram for arbitrary $\tilde{K}/K$ ratio and positive $E_T > 0$ sector can be found in Ref. [17].

1. Phase diagram

Figure 6(a) presents the phase diagram of the E_T-K-$\tilde{K}$ model estimated by the method of Sec. IV B, i.e., by tracking the cluster-size-dependent correlations characteristic to the individual phases. Due to a larger local basis of four states, lack of symmetries, and many points to be analyzed, we had to resort to a combination of small six-site and 12-site clusters. This makes the phase diagram rather semi-quantitative as seen for example by comparing the position of the QCP in the Kitaev-like limit obtained for much bigger clusters in Sec. V A. Nevertheless, four phases in an arrangement resembling that of Fig. 4(b) can be identified. Two of them—gas and VBS phases—were already encountered in the previous Sec. V A.

The left part of the phase diagram ($E_T > 0$) is a playground for a competition between the AF correlations and Kitaev-like frustration of the interactions. In the isotropic $K = \tilde{K}$ limit [top line in Fig. 6(a)] where the bond interactions handle all the triplon colors equally, the situation is analogous to the square-lattice case discussed in the context of Ca_2RuO_4 [12,14,15]. Since the honeycomb lattice is not geometrically frustrated, it can easily host an antiferromagnetic phase associated with a bipartite condensation of triplons captured by a wave function similar to that of Eq. (23). This AF phase with "soft" (i.e., far from saturated) van Vleck moments $\boldsymbol{M}_1$ actually takes the largest portion of the entire phase diagram in Fig. 6(a). Going down to the region with strong Kitaev-like

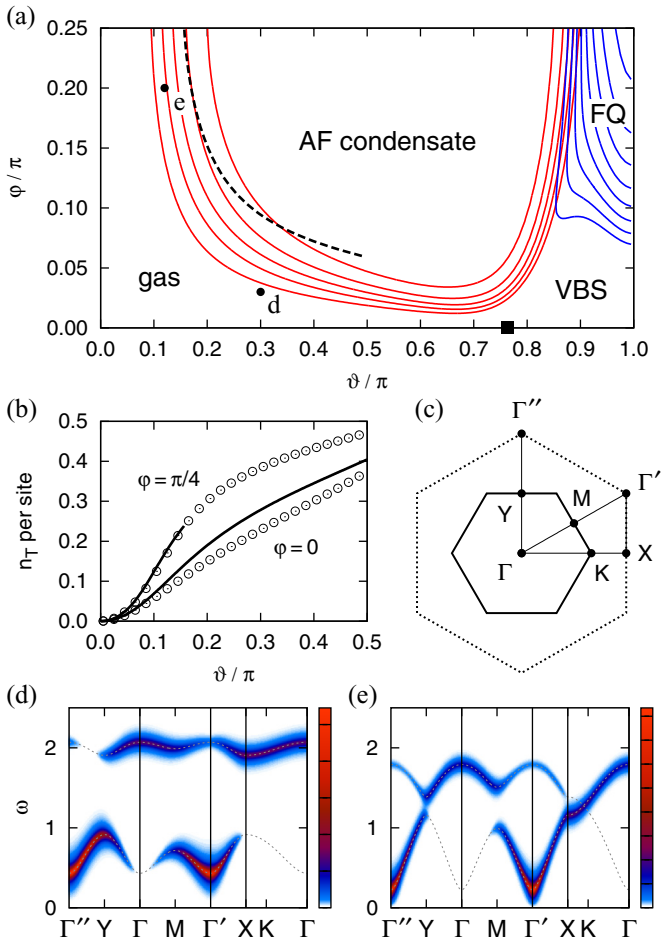

FIG. 6. (a) Approximate phase diagram of E_T-K-$\tilde{K}$ model up to $\tilde{K} = K$ estimated as in Fig. 4(b) via size-dependent characteristic correlations. Hexagonal six-site cluster and rectangular 12-site cluster were used. The model is parametrized as $E_T = \cos\vartheta$, $K = \sin\vartheta\cos\varphi$, $\tilde{K} = \sin\vartheta\sin\varphi$. Red lines show contours of the increase of the van Vleck correlations $\langle S^x_{\boldsymbol{q}} S^x_{-\boldsymbol{q}}\rangle$ at the antiferromagnetic (AF) momentum $\boldsymbol{q} = \Gamma'$ when going from 6- to 12-site cluster. The correlations detecting the ferroquadrupolar (FQ) phase (blue contours) were estimated as described in the text. Black square is the extrapolated position of the QCP for pure Kitaev-like (K only) model [see Fig. 5(b)]. The dashed line indicates the transition between the gas phase and AF condensate obtained using Gutzwiller-type treatment of the hardcore constraint. (b) Comparison of mean-field (solid line) and ED results (circles, 12-site cluster) for n_T at the top ($\varphi = \pi/4$) and bottom line ($\varphi = 0$) of the phase diagram. (c) Brillouin zone of the honeycomb lattice (solid) and completed triangular lattice (dotted) with indicated special points and the path used in the next panels. (d),(e) Imaginary part of van Vleck spin susceptibility $\chi_{zz}(\boldsymbol{q}, \omega)$ calculated in the mean-field approximation for the two points marked by d and e in panel (a) and artificially broadened. The dotted lines indicate the dispersions of Eq. (33) with $\alpha = z$.

anisotropy of the interactions and the resulting frustration, the AF phase gets largely suppressed. One of the highlights of the soft-moment magnetism based on spin-orbit triplon condensation is the presence of both transverse magnon modes as well as an intense amplitude mode (dubbed "Higgs mode" in this context), that have been observed experimentally in Ca_2RuO_4

[14,15]. It is an interesting and nontrivial problem for a future study to analyze the effect of the Kitaev-like frustration on such magnetic excitation spectra. Later in Sec. V B 2, we only make an attempt to address the gas phase close to the AF phase boundary, by inspecting the excitation spectrum close to the point where the condensate is formed.

Focusing now on the large negative E_T limit, we can again notice similarities to the 1D chain case of Sec. IV B. In this limit the singlets s can be integrated out leaving us with an effective spin-1 model where the spin now coincides with the triplon spin $-i(\boldsymbol{T}^\dagger \times \boldsymbol{T})$. The nature of this model changes with the $\tilde{K}/K$ ratio. For the strongly anisotropic K-only case, one formally obtains a biquadratic Kitaev-like model as a leading term:

$$\mathcal{H}_{\mathrm{bqK}} = -\frac{K^2}{2|E_T|}\sum_{\langle ij\rangle}\left(S_i^\alpha S_j^\alpha\right)^2, \tag{28}$$

with the active component $\alpha \in \{x, y, z\}$ given by the bond direction as before. Compared to the usual bilinear spin-one Kitaev model (see, e.g., Ref. [33] and references therein), the behavior of the biquadratic model is rather trivial. In the original language, it simply counts the number of proper-color T dimers and associates an energy gain $K^2/2|E_T|$ with each of them. This selects a large number of degenerate T-dimer coverings as the model ground state. At this level of approximation which misses the $\mathcal{O}(K^6)$ interactions, the true VBS ground state cannot be resolved. Furthermore, the low-lying excitations with the energies $\propto K^6$ are not captured. Hence, in the Kitaev-like limit, spin-1 is not a suitable elementary object and bonding-state dimers should be used instead, leading to the effective quantum dimer model which we extensively discussed in Sec. V A.

In contrast to that, the isotropic limit $K = \tilde{K}$ can be expected to be adequately captured by a simple isotropic spin-1 model. Indeed, the preference of the total-singlet T pairs that may virtually transform into s pairs and back gives rise to biquadratic interaction described by the effective Hamiltonian

$$\mathcal{H}_{\mathrm{bq}} = -\frac{K^2}{2|E_T|}\sum_{\langle ij\rangle}(\boldsymbol{S}_i\boldsymbol{S}_j)^2 \tag{29}$$

at the isotropic point $K = \tilde{K}$. Model of this kind is a special case of bilinear-biquadratic spin-1 models that were thoroughly explored for various lattices. On a nonbipartite, geometrically frustrated triangular lattice [34,35] its ground state shows a ferroquadrupolar (FQ) order [36–38] which does not break time-reversal symmetry but introduces a preferential plane in spin space where the spins can be found with a higher probability. For a nonfrustrated lattice such as square [37,39] or honeycomb [40–42], the AF phase is more competitive and the biquadratic model is just on the verge of the FQ and AF order. This type of order, labeled as FQ in Fig. 6(a) for simplicity, therefore replaces the Bethe phase of the 1D chain [compare Fig. 4(b)]. Note that here we refer to the AF phase of triplon spins $-i(\boldsymbol{T}^\dagger \times \boldsymbol{T})$; this should not be confused with the neighboring AF phase of correlated van Vleck moments $\boldsymbol{M}_1$ which reside on the $J = 0 \leftrightarrow 1$ transitions. The detection of the "edge-case" FQ/AF order is somewhat complicated, also due to the incompatible geometry of the two clusters (six-site hexagon and 12-site rectangle) that we use to check the size-scaling of the characteristic correlations. To this end, as the characteristic quantity we take the contribution to FQ correlations $\langle Q_{\boldsymbol{q}} Q_{-\boldsymbol{q}}\rangle$ with $\boldsymbol{q} = 0$ that is carried by triplon spins at AF momentum $\boldsymbol{q} = \Gamma'$. More explicitly, we decompose the various quadrupole operators Q containing $S^\alpha S^\beta$ terms (see, e.g., Ref. [34] for their explicit forms) into a momentum sum $Q_{\boldsymbol{q}} \sim \sum_{\boldsymbol{q}'} S^\alpha_{\boldsymbol{q}-\boldsymbol{q}'} S^\beta_{\boldsymbol{q}'}$ and evaluate the four-spin correlators of the type $\langle S^\alpha_{\boldsymbol{q}-\boldsymbol{q}'} S^\beta_{\boldsymbol{q}'} S^\gamma_{-\boldsymbol{q}-\boldsymbol{q}''} S^\delta_{\boldsymbol{q}''}\rangle$ constituting $\langle Q_{\boldsymbol{q}} Q_{-\boldsymbol{q}}\rangle$. The contribution with all the momenta being equal to the AF one is found to dominate and behave well at the reference $K = \tilde{K} \ll |E_T|$ point described by $\mathcal{H}_{\mathrm{bq}}$ of Eq. (29). The resulting correlations obtained as a difference between 12-site and six-site cluster are shown in Fig. 6(a). They suggest that FQ/AF phase extends slightly further from its reference point than the VBS one, though this result may be potentially biased as the small clusters can not properly accommodate the VBS state. As a general remark on biquadratic spin models such as (29), it is worth noticing that while they are typically very weak in conventional spin systems, they emerge naturally in singlet-triplet level systems; see yet another example in Ref. [43].

2. *Dynamical Gutzwiller treatment and excitations*

As argued in Sec. III C, the Kitaev-like anisotropy of the interactions should manifest itself by the localized nature of the dynamic spin response which translates to the flat dispersions of the spin excitations. Having now covered the entire interval from the Kitaev-like limit to the isotropic limit, one might wonder about the corresponding evolution of the spin excitations. Due to the limited cluster size, ED calculations do not provide a sufficient resolution to study such effects.

Here we adopt instead a dynamical Gutzwiller treatment combined with selfconsistent mean-field approximation formulated for the triplon gas phase. Besides the excitation spectrum, this enables us to obtain the gas/AF transition point as a function of non-Kitaev term $\tilde{K}$. The derivation starts with a replacement of s implicitly contained in Eq. (10) by the operator $\sqrt{1-n_T}$ which dynamically accounts for the triplon hardcore constraint. The resulting Hamiltonian is expanded and a mean-field decoupling is applied leading to the quadratic Hamiltonian

$$\mathcal{H}_{\mathrm{MF}} = \sum_i (E_T + \Lambda)\, n_{T_i} + \sum_{\langle ij\rangle_\alpha}\langle 1 - n_T\rangle\left[K\mathcal{O}^\alpha_{ij} + \tilde{K}\left(\mathcal{O}^{\bar{\alpha}}_{ij} + \mathcal{O}^{\bar{\bar{\alpha}}}_{ij}\right)\right], \tag{30}$$

where all the s, $s^\dagger$ operators in $\mathcal{O}$ are left out. At this point, we have already relaxed the hardcore constraint. Two effects of the hardcore nature of the triplons got captured at the level of $\mathcal{H}_{\mathrm{MF}}$: (i) effective triplon cost is increased by an energy

$$\Lambda = -\frac{1}{2}\sum_{\delta_\alpha}\left[K\langle\mathcal{O}^\alpha_{i,i+\delta}\rangle + \tilde{K}\left(\langle\mathcal{O}^{\bar{\alpha}}_{i,i+\delta}\rangle + \langle\mathcal{O}^{\bar{\bar{\alpha}}}_{i,i+\delta}\rangle\right)\right] \tag{31}$$

(δ runs through all nearest neighbors) and (ii) the interactions K and $\tilde{K}$ are reduced by a factor $1 - \langle n_T\rangle$ that embodies the probability of another triplon blocking the interaction process on the particular bond. After a conversion to momentum

space, we obtain

$$\mathcal{H}_{\rm MF} = \sum_{k\alpha} E\,(\alpha^\dagger_{1k}\alpha_{1k} + \alpha^\dagger_{2k}\alpha_{2k}) + [\kappa_{\alpha k}(\alpha^\dagger_{1k}\alpha_{2k} - \alpha_{1,-k}\alpha_{2k}) + \text{H.c.}], \quad (32)$$

where the unconstrained triplons are labeled by their color $\alpha = x, y, z$ and the index 1 or 2 referring to the two sites in the unit cell of the honeycomb lattice. It is convenient to choose the unit cell for triplons of color α as a bond of direction α. In this convention, the on-site triplon energy $E = E_T + \Lambda$ entering Eq. (32) is complemented by the interaction term $\kappa_{\alpha k} = \langle 1 - n_T\rangle(K + \tilde{K}\eta_{\alpha k})$ with the form factor η_{zk} given by $\eta_{zk} = 2\cos(\frac{\sqrt{3}}{2}k_x)\exp(-i\frac{3}{2}k_y)$, and η_{xk} and η_{yk} being simply rotated by multiples of $2\pi/3$. Note that $\kappa_{\alpha k}$ depends on momentum k via non-Kitaev $\tilde{K}$ term only.

The 4×4 problem contained in Eq. (32) can be diagonalized explicitly and yields the dispersions of the bosonic quasiparticles

$$\omega_{B\alpha k} = \sqrt{E(E - 2|\kappa_{\alpha k}|)},$$
$$\omega_{A\alpha k} = \sqrt{E(E + 2|\kappa_{\alpha k}|)}. \quad (33)$$

The averages entering all the equations starting from Eq. (30) have to be calculated self consistently via

$$\langle n_T\rangle = \frac{1}{4}\sum_{k\alpha}\left(\frac{E - |\kappa_{\alpha k}|}{\omega_{B\alpha k}} + \frac{E + |\kappa_{\alpha k}|}{\omega_{A\alpha k}} - 2\right), \quad (34)$$

$$\Lambda = \frac{1}{4}\sum_{k\alpha}|K + \tilde{K}\eta_{\alpha k}|\left(\frac{E}{\omega_{B\alpha k}} - \frac{E}{\omega_{A\alpha k}}\right). \quad (35)$$

The above approach is applicable through the entire gas phase where the excitations are found to be gapped ($\omega_{B\alpha k}$ and $\omega_{A\alpha k} > 0$). Once the lower-energy $\omega_{B\alpha k}$ touches zero at some point of the Brillouin zone, the triplon condensation occurs with the condensate structure being similar to the one of Eq. (23). The corresponding condition $E = 2|\kappa_{\alpha k}|$ is first met at $\boldsymbol{k} = 0$ which results in the following equation:

$$E_T + \Lambda = 2\langle 1 - n_T\rangle(K + 2\tilde{K}), \quad (36)$$

determining the points where AF condensate starts to form. The gas/AF phase boundary obtained this way is presented as a dashed line in Fig. 6(a). It shows a good overall agreement with the estimate by ED, correctly capturing the physical trend of a delayed condensation when the frustration increases approaching the Kitaev-like limit. As expected, the best agreement is obtained near the isotropic limit which is also illustrated in Fig. 6(b) where the isotropic-limit data ($\varphi = \pi/4$) of the self-consistent $\langle n_T\rangle$ perfectly match the ED values. In the Kitaev-like limit ($\varphi = 0$), the deviation is already significant but still acceptable for our semiquantitative analysis.

With an adequate description of the excitations in the gas phase at hand, we are now ready to inspect an analogy to Figs. 4(c) and 4(d) presenting the dynamical spin susceptibility for the gas phase of the 1D chain model. To this end we express the Fourier component of the van Vleck moment operator $\propto -i(s^\dagger T_\alpha - T^\dagger_\alpha s)$ in terms of the unconstrained triplons as

$$S^\alpha_{\boldsymbol{q}} \propto -i\big[\alpha_{1\boldsymbol{q}} - \alpha^\dagger_{1,-\boldsymbol{q}} + \big(\alpha_{2\boldsymbol{q}} - \alpha^\dagger_{2,-\boldsymbol{q}}\big)e^{-i\boldsymbol{q}\cdot\boldsymbol{\delta}_\alpha}\big], \quad (37)$$

where $\boldsymbol{\delta}_\alpha$ is a unit vector in the direction of α bonds. Next, we use the eigenspectrum of $\mathcal{H}_{\rm MF}$ to find the dynamic correlation function $\chi_{\alpha\alpha}(\boldsymbol{q}, \omega) = \langle S^\alpha_{\boldsymbol{q}} S^\alpha_{-\boldsymbol{q}}\rangle_\omega$ shown in Figs. 6(d) and 6(e) for two selected points in the phase diagram.

Similarly to the chain case, the vicinity of the Kitaev-like limit [Fig. 6(d)] is characterized by flat dispersion of excitations with the modulation being generated by nonzero $\tilde{K}$ only as it is evident from Eq. (33) and the form of $\kappa_{\alpha k}$. Flat dispersions are the fingerprints of underlying frustrations, and resemble the Kitaev-Heisenberg model magnons characterized by two different energy scales [44]. The excitations in Eq. (33) have two branches for each triplon color α that cover the entire Brillouin zone associated with the completed triangular lattice [dotted hexagon in Fig. 6(c)] by periodic copies of the smaller Brillouin zone of the honeycomb lattice [full hexagon in Fig. 6(c)]. The intensity of these excitations in the dynamic spin susceptibility varies through the Brillouin zone—while the upper branch dominates around the $\boldsymbol{q} = \Gamma$ point, the lower branch is most intense around the AF wave vector $\boldsymbol{q} = \Gamma'$. At the latter point (equivalent to $\boldsymbol{q} = \Gamma = 0$ in terms of the bosonic excitations), the magnetic excitations will eventually touch zero energy signaling the transition into long-range AF phase as $\tilde{K}$ increases. This is also observed near the isotropic limit [see Fig. 6(e)] where the modulation of the originally flat dispersions by the complementary interaction $\tilde{K}$ leads to a merging of the two excitation branches and the result starts to resemble the excitonic magnon dispersion. In contrast to the Heisenberg model at the same lattice, it is characterized by a maximum at Γ point, as has been seen experimentally in the square-lattice case of Ca_2RuO_4 [14].

The observed features of the presented gas-phase spectra close to the AF transition are expected to be already quite indicative for the AF phase. After the condensation, an additional excitation branch corresponding to the amplitude (Higgs) mode will develop [a hint of this can be noticed in the chain case when comparing Figs. 4(d) and 4(g)]. Besides that, there will be also an ongoing redistribution of the spectral weight in the magnon branch.

VI. CONCLUSIONS

We have studied singlet-triplet models that describe magnetism of spin-orbit coupled d^4 Mott insulators, such as ruthenium Ru^{4+} or iridium Ir^{5+} compounds. Singlet-triplet models appear in various physical contexts (see, e.g., Refs. [22,43,45,46]) and are of general interest because they host—by very construction—a quantum phase transition from triplon gas to the ordered state of soft moments, when exchange interactions overcome a singlet-triplet spin gap. The models considered here bring a new feature into this physics: a magnetic frustration that originates from bond-directional nature of orbital interactions [5]. Similar to the case of spin-orbit pseudospin $J = 1/2$ Mott insulators with bond-directional Ising couplings [8–11] on a honeycomb lattice, the orbital frustration has a strong impact on magnetism of singlet-triplet models [12,17].

The main aim of the present work was to understand how a triplon gas evolves into a dense system of strongly interacting particles, in particular when bond-directional anisotropy of the exchange interactions are taken to the extreme as in Kitaev

model. We find that this evolution is continuous and results in a strongly correlated paramagnet smoothly connected to a triplon gas. Even though this paramagnet misses the defining features of genuine spin liquids (many-body entanglement and emergent quasiparticles) [2], it is far from being trivial. In contrast to a conventional O(3) singlet-triplet systems, spin correlations here are highly anisotropic and strictly short-ranged even in the limit of strong exchange interactions where the spin gap is very small. As in the Kitaev model, these peculiar features of spin correlations follow from the symmetry properties of the model—an extensive number of conserved Z_2 quantities that decompose the Hilbert space into subspaces with fixed bond-parity configurations. We have also shown that the model can be mapped to a bilayer version of Kitaev model, but with some additional terms in the interlayer couplings which act to suppress gas-to-liquid phase transition in a bilayer Kitaev model [18–20]. Exact diagonalization of the model in 1D-zigzag chain as well as on honeycomb lattice show that the lowest energy excitations are in the spin sector (and always gapped). This is different from the Kitaev model with Majorana bands within the spin gap.

Going away from Kitaev-like symmetry of the exchange interactions towards isotropic O(3) limit, we find that triplons condense into AF ordered phase at finite critical value of non-Kitaev $\tilde{K}$ term. At $\tilde{K} < K$ regime (and close to phase transition), spin excitations show two distinct branches of weakly dispersive modes [Fig. 6(d)]; however, this result is obtained within a mean-field treatment of the hard-core constraint neglecting any multi-particle scattering processes. A quantitative description of the highly frustrated magnetic condensate and its excitations in the regime of $\tilde{K} < K$ remains an open theoretical problem.

Considering the model at negative E_T values, we observe the links to some exotic models such as biquadratic spin-1 and quantum dimer models. At negative E_T and small $\tilde{K}$ regime, we find a quantum phase transition from strongly correlated paramagnetic phase to a plaquette-VBS state of the triplon dimers.

Apart from a theoretical interest in frustrated singlet-triplet models, this study was partly motivated by magnetic properties of honeycomb lattice ruthenium compounds, in particular $Ag_3LiRu_2O_6$ [47–49]. This compound is derived from Li_2RuO_3 by substituting Ag ions for those Li ions which reside between the Ru-honeycomb planes. As a result, a structural transition observed in Li_2RuO_3 [16] is completely suppressed, suggesting $Ag_3LiRu_2O_6$ as a nearly ideal honeycomb lattice system to study the interplay between spin-orbit coupling and exchange interactions. Current data [47–49] show that this compound is insulating and has no magnetic order, which would be consistent with the (correlated) triplon-gas phase where interactions are either too weak to overcome the spin-orbit gap, or they are strongly frustrated preventing triplon condensation. As $4d$-electron wave functions are rather extended in space, a direct overlap processes can be sizable in ruthenates [50], thus raising the possibility of bond-directional triplon dynamics in this material. Future experiments probing magnetic dynamics are necessary to identify symmetry of the dominant exchange interactions in $Ag_3LiRu_2O_6$. Metallic states induced by electron doping of this material could bring some surprises as well.

Overall, the orbitally frustrated singlet-triplet models show a rich physics, interesting theoretically and also relevant to spin-orbit coupled $J_{\text{eff}} = 0$ Mott insulators based on, e.g., ruthenium Ru^{4+} and iridium Ir^{5+} ions.

ACKNOWLEDGMENTS

We would like to thank P. Anisimov, M. Daghofer, and T. Takayama for useful discussions. J.C. acknowledges support by Czech Science Foundation (GAČR) under Project No. GA19-16937S and MŠMT ČR under NPU II project CEITEC 2020 (LQ1601). Computational resources were supplied by the Ministry of Education, Youth and Sports of the Czech Republic under the Projects CESNET (Project No. LM2015042) and CERIT-Scientific Cloud (Project No. LM2015085) provided within the program Projects of Large Research, Development and Innovations Infrastructures. G.K. acknowledges support by the European Research Council under Advanced Grant 669550 (Com4Com).

[1] L. Balents, Nature (London) **464**, 199 (2010).
[2] L. Savary and L. Balents, Rep. Prog. Phys. **80**, 016502 (2017).
[3] M. Vojta, Rep. Prog. Phys. **81**, 064501 (2018).
[4] K. I. Kugel and D. I. Khomskii, Sov. Phys. Usp. **25**, 231 (1982).
[5] G. Khaliullin, Prog. Theor. Phys. Suppl. **160**, 155 (2005).
[6] Z. Nussinov and J. van den Brink, Rev. Mod. Phys. **87**, 1 (2015).
[7] A. Kitaev, Ann. Phys. **321**, 2 (2006).
[8] G. Jackeli and G. Khaliullin, Phys. Rev. Lett. **102**, 017205 (2009).
[9] J. Chaloupka, G. Jackeli, and G. Khaliullin, Phys. Rev. Lett. **105**, 027204 (2010).
[10] H. Liu and G. Khaliullin, Phys. Rev. B **97**, 014407 (2018).
[11] R. Sano, Y. Kato, and Y. Motome, Phys. Rev. B **97**, 014408 (2018).
[12] G. Khaliullin, Phys. Rev. Lett. **111**, 197201 (2013).
[13] O. N. Meetei, W. S. Cole, M. Randeria, and N. Trivedi, Phys. Rev. B **91**, 054412 (2015).
[14] A. Jain, M. Krautloher, J. Porras, G. H. Ryu, D. P. Chen, D. L. Abernathy, J. T. Park, A. Ivanov, J. Chaloupka, G. Khaliullin, B. Keimer, and B. J. Kim, Nat. Phys. **13**, 633 (2017).
[15] S.-M. Souliou, J. Chaloupka, G. Khaliullin, G. Ryu, A. Jain, B. J. Kim, M. Le Tacon, and B. Keimer, Phys. Rev. Lett. **119**, 067201 (2017).
[16] Y. Miura, Y. Yasui, M. Sato, N. Igawa, and K. Kakurai, J. Phys. Soc. Jpn. **76**, 033705 (2007).
[17] P. S. Anisimov, F. Aust, G. Khaliullin, and M. Daghofer, Phys. Rev. Lett. **122**, 177201 (2019).
[18] H. Tomishige, J. Nasu, and A. Koga, Phys. Rev. B **97**, 094403 (2018).
[19] U. F. P. Seifert, J. Gritsch, E. Wagner, D. G. Joshi, W. Brenig, M. Vojta, and K. P. Schmidt, Phys. Rev. B **98**, 155101 (2018).
[20] H. Tomishige, J. Nasu, and A. Koga, Phys. Rev. B **99**, 174424 (2019).

[21] X.-F. Zhang, Y.-C. He, S. Eggert, R. Moessner, and F. Pollmann, Phys. Rev. Lett. **120**, 115702 (2018).
[22] T. Giamarchi, Ch. Rüegg, and O. Tchernyshyov, Nat. Phys. **4**, 198 (2008).
[23] C. E. Agrapidis, J. van den Brink, and S. Nishimoto, Sci. Rep. **8**, 1815 (2018).
[24] R. Botet, R. Jullien, and M. Kolb, Phys. Rev. B **28**, 3914 (1983).
[25] H. J. Schulz, Phys. Rev. B **34**, 6372 (1986).
[26] M. den Nijs and K. Rommelse, Phys. Rev. B **40**, 4709 (1989).
[27] W. Chen, K. Hida, and B. C. Sanctuary, Phys. Rev. B **67**, 104401 (2003).
[28] A. Langari, F. Pollmann, and M. Siahatgar, J. Phys.: Condens. Matter **25**, 406002 (2013).
[29] D. S. Rokhsar and S. A. Kivelson, Phys. Rev. Lett. **61**, 2376 (1988).
[30] R. Moessner, S. L. Sondhi, and P. Chandra, Phys. Rev. B **64**, 144416 (2001).
[31] T. Schlittler, T. Barthel, G. Misguich, J. Vidal, and R. Mosseri, Phys. Rev. Lett. **115**, 217202 (2015).
[32] T. M. Schlittler, R. Mosseri, and T. Barthel, Phys. Rev. B **96**, 195142 (2017).
[33] T. Minakawa, J. Nasu, and A. Koga, arXiv:1909.10170.
[34] A. Läuchli, F. Mila, and K. Penc, Phys. Rev. Lett. **97**, 087205 (2006).
[35] H. Tsunetsugu and M. Arikawa, J. Phys. Soc. Jpn. **75**, 083701 (2006).
[36] H. H. Chen and P. M. Levy, Phys. Rev. B **7**, 4267 (1973).
[37] K. Harada and N. Kawashima, Phys. Rev. B **65**, 052403 (2002).
[38] B. A. Ivanov and A. K. Kolezhuk, Phys. Rev. B **68**, 052401 (2003).
[39] T. A. Tóth, A. M. Läuchli, F. Mila, and K. Penc, Phys. Rev. B **85**, 140403(R) (2012).
[40] Y.-W. Lee and M.-F. Yang, Phys. Rev. B **85**, 100402(R) (2012).
[41] H. H. Zhao, C. Xu, Q. N. Chen, Z. C. Wei, M. P. Qin, G. M. Zhang, and T. Xiang, Phys. Rev. B **85**, 134416 (2012).
[42] P. Corboz, M. Lajkó, K. Penc, F. Mila, and A. M. Läuchli, Phys. Rev. B **87**, 195113 (2013).
[43] J. Chaloupka and G. Khaliullin, Phys. Rev. Lett. **110**, 207205 (2013).
[44] J. Chaloupka, G. Jackeli, and G. Khaliullin, Phys. Rev. Lett. **110**, 097204 (2013).
[45] T. Sommer, M. Vojta, and K. W. Becker, Eur. Phys. J. B **23**, 329 (2001).
[46] G. Chen, L. Balents, and A. P. Schnyder, Phys. Rev. Lett. **102**, 096406 (2009).
[47] S. A. J. Kimber, C. D. Ling, D. J. P. Morris, A. Chemseddine, P. F. Henry, and D. N. Argyriou, J. Mater. Chem. **20**, 8021 (2010).
[48] R. Kumar, T. Dey, P. M. Ette, K. Ramesha, A. Chakraborty, I. Dasgupta, J. C. Orain, C. Baines, S. Tóth, A. Shahee, S. Kundu, M. Prinz-Zwick, A. A. Gippius, N. Büttgen, P. Gegenwart, and A. V. Mahajan, Phys. Rev. B **99**, 054417 (2019).
[49] T. Takayama *et al.* (unpublished).
[50] S. V. Streltsov and D. I. Khomskii, Phys. Usp. **60**, 1121 (2017).

7 Conclusions and outlook

In this thesis we have illustrated the route to unusual kinds of magnetic phenomena where the spin-orbit coupling plays the role of a key ingredient. Spin-orbit coupling enters in a twofold way here. First, it rearranges the ionic energy level structure and forms new local degrees of freedom that serve as a basis for the low-energy collective behavior. In our examples, these were represented by pseudospins $J = 1/2$ or the singlet-triplet $J = 0, 1$ basis. Second, through the spin-orbit entangled wavefunctions associated with these new degrees of freedom, spin-orbit coupling unifies the spin and orbital subspaces and imprints the well-known anisotropy of orbital interactions into the pseudospin interactions. This may in certain cases give rise to highly anisotropic bond-selective interactions that do not appear in conventional magnetic systems based on pure spins. The systems discussed here were limited to either rigid pseudospin-1/2 moments being subject to frustrated superexchange interactions or the quasidegenerate singlet-triplet basis, whose members got dynamically mixed by superexchange in a non-frustrated setting. There are many ways to go beyond these two situations. Several promising directions that await detailed exploration, both experimental and theoretical, include:

(i) *Combining quantum critical behavior of soft-spin systems with frustration*: In the soft-spin d^4 system studied in Sec. 4, the energy gain due to a dynamic mixing of the singlets and triplets via superexchange interactions competed with the triplet cost, resulting in a quantum critical behavior. It would be interesting to transfer such a competition into a frustrated setting. This is readily available thanks to the spin-orbit entangled nature of the singlet-triplet basis states that produces various kinds of highly anisotropic bond-selective interactions when considering 90° metal-oxygen-metal bonds [98, 100]. The case of geometrically non-frustrated honeycomb lattice where a bosonic model with Kitaev-type frustrations emerges was already inspected in Ref. [100]. This work can be continued by, e.g., exploration of the effects of trigonal distortion or extension to other kinds of lattices with 90° bonds, like it happened in the case of Kitaev pseudospin-1/2 systems.

(ii) *Lattice control of interactions*: As we have seen in Secs. 3.2.1 and 4.2, the spin-orbit entangled wavefunctions sensitively react to changes in the crystal field induced for instance by trigonal or tetragonal deformations. By changing the orbital composition, these crystal fields have a direct impact on the interactions between pseudospin moments. These effects open a possibility to tune the interactions by e.g. strain in the material to a larger extent than in the conventional spin systems. Not only the strength of the interactions would be affected but, more importantly, the balance between the various anisotropic contributions could be changed. In the soft-spin systems, such manipulations with the crystal field could be used to tune the quantum critical point.

(iii) *Heterostructuring*: The materials discussed here are of a natural quasi-2D character enforced by their crystal structures consisting of active layers sandwiched between "inert" separating layers. However, such an arrangement can be produced also artificially by growing a superlattice of two materials [112]. The resulting reduced dimensionality achieved by heterostructuring, as well as the associated interface effects may bring new physical phenomena not present in the bulk of the constituent materials. An example is our early proposal [113] of imitating cuprate physics by heterostructuring nickelates which triggered rather intense experimental activities.

(iv) *Doping*: Perhaps the richest area of future research are doped variants of the systems with large spin-orbit coupling. Both the doped carriers as well as the states forming the background could be complex spin-orbit entangled objects, as it happens for instance in the case of electron doping of d^4 compounds where the mobile objects carry pseudospin-1/2 while the back-

ground realizes singlet-triplet physics. Such situations lead to highly non-trivial interactions of the doped carriers with the background and unusual behavior may occur. One of the attractive options are various forms of unconventional superconductivity that were predicted both for the doped Kitaev honeycomb systems [114–116] and the square-lattice singlet-triplet systems [117]. Despite being promising theoretically, the preparation of doped materials for the experimental studies faces severe challenges. The usual chemical doping by element substitution introduces disorder that may inhibit some more fragile phenomena, unconventional superconductivity included. Fortunately, there exist clever alternatives, such as those applied to pseudospin $J = 1/2$ prototype system Sr_2IrO_4 [118] that is expected to be akin to high-T_c cuprates – surface doping by potassium deposition [119] on the surface of parent Sr_2IrO_4 or ionic liquid gating [120].

Bibliography

[1] M. Imada, A. Fujimori, and Y. Tokura, Rev. Mod. Phys. **70**, 1039 (1998).

[2] S. Maekawa, T. Tohyama, S. E. Barnes, S. Ishihara, W. Koshibae, and G. Khaliullin, *Physics of Transition Metal Oxides* (Springer, Berlin, 2004).

[3] D. Khomskii, *Transition Metal Compounds* (Cambridge University Press, Cambridge, 2014).

[4] J.R. Schrieffer (editor), *Handbook of High-Temperature Superconductivity* (Springer, New York, 2007).

[5] N. Plakida, *High-Temperature Cuprate Superconductors* (Springer, Berlin, 2010).

[6] M. B. Salamon and M. Jaime, Rev. Mod. Phys. **73**, 583 (2001).

[7] D. Khomskii, Physics **2**, 20 (2009).

[8] W. Witczak-Krempa, G. Chen, Y. B. Kim, and L. Balents, Annu. Rev. Condens. Matter Phys. **5**, 57 (2014).

[9] L. Savary and L. Balents, Rep. Prog. Phys. **80**, 016502 (2017).

[10] H. Takagi, T. Takayama, G. Jackeli, G. Khaliullin, and S. E. Nagler, Nature Reviews Physics **1**, 264 (2019).

[11] P. A. M. Dirac, *The Principles of Quantum Mechanics* (Oxford University Press, Oxford, 1958).

[12] H. B. Nielsen and S. Chadha, Nucl. Phys. B **105**, 445 (1976).

[13] H. Watanabe and H. Murayama, Phys. Rev. Lett. **108**, 251602 (2012).

[14] H. J. Liao, Z. Y. Xie, J. Chen, Z. Y. Liu, H. D. Xie, R. Z. Huang, B. Normand, and T. Xiang, Phys. Rev. Lett. **118**, 137202 (2017).

[15] S. R. White and A. L. Chernyshev, Phys. Rev. Lett. **99**, 127004 (2007).

[16] J.-F. Yu and Y.-J. Kao, Phys. Rev. B **85**, 094407 (2012).

[17] H.-C. Jiang, H. Yao, and L. Balents, Phys. Rev. B **86**, 024424 (2012).

[18] A. Kitaev, Ann. Phys. **321**, 2 (2006).

[19] E. Ising, Zeitschrift für Physik **31**, 253 (1925).

[20] G. Jackeli and G. Khaliullin, Phys. Rev. Lett. **102**, 017205 (2009).

[21] J. J. Sakurai and J. Napolitano, *Modern Quantum Mechanics* (Cambridge University Press, Cambridge, 2017).

[22] Y. Tanabe and S. Sugano, J. Phys. Soc. Jpn. **9**, 753 (1954), *ibid.* **9**, 766 (1954), *ibid.* **11**, 864 (1956).

[23] T. Inui, Y. Tanabe, Y. Onodera, *Group Theory and Its Applications in Physics* (Springer, Berlin, 1990).

[24] G. Racah, Phys. Rev. **61**, 186 (1942), *ibid.* **62**, 438 (1942), *ibid.* **63**, 367 (1943), *ibid.* **76**, 1352 (1949).

[25] J. S. Griffith, *The Theory of Transition-Metal Ions* (Cambridge University Press, Cambridge, 1971).

[26] J. Kanamori, Prog. Theor. Phys. **30**, 275 (1963).

[27] N. W. Ashcroft, N. D. Mermin, *Solid State Physics* (Holt, Rinehart and Winston, New York, 1976).

[28] P. Gütlich and H. A. Goodwin (Eds.), *Spin Crossover in Transition Metal Compounds I* (Springer, Berlin, 2004).

[29] V. B. Berestetskii, E. M. Lifshitz, and L. P. Pitaevskii, *Quantum Electrodynamics* (Pergamon Press, Oxford, 1982).

[30] L. D. Landau and E. M. Lifshitz, *Quantum Mechanics – Non-relativistic Theory* (Pergamon Press, Oxford, 1977).

[31] A. Abragam and B. Bleaney, *Electron Paramagnetic Resonance of Transition Ions* (Clarendon Press, Oxford, 1970).

[32] S. Sugano, Y. Tanabe, and H. Kamimura, *Multiplets of Transition-Metal Ions in Crystals* (Academic Press, New York, 1970).

[33] J. C. Slater and G. F. Koster, Phys. Rev. **94** 1498 (1954).

[34] J. B. Torrance, P. Lacorre, A. I. Nazzal, E. J. Ansaldo, and Ch. Niedermayer, Phys. Rev. B **45**, 8209(R) (1992).

[35] J. Zaanen, G. A. Sawatzky, and J. W. Allen, Phys. Rev. Lett. **55**, 418 (1985).

[36] J. Zaanen and G. A. Sawatzky, J. Solid State Chem. **88**, 8 (1990).

[37] S. Yamada, T. Imamura, T. Kano, Y. Ohashi, H. Matsumoto, and M. Mahida, Journal of the Earth Simulator **7**, 23 (2007).

[38] M. Machida, S. Yamada, Y. Ohashi, and H. Matsumoto, Phys. Rev. Lett. **93**, 200402 (2004).

[39] H. A. Kramers, Physica **1**, 182 (1934).

[40] P. W. Anderson, Phys. Rev. **79**, 350 (1950).

[41] P. W. Anderson, Phys. Rev. **115**, 2 (1959).

[42] H. Feshbach, Ann. Phys. **5**, 357 (1958).

[43] H. Feshbach, Ann. Phys. **19**, 287 (1962).

[44] P. O. Löwdin, J. Math. Phys. **3**, 969 (1962).

[45] P. O. Löwdin, Phys. Rev. **139**, A357 (1965).

[46] H. Eskes and J. H. Jefferson, Phys. Rev. B **48**, 9788 (1993).

[47] B. Lake, D. A. Tennant, C. D. Frost, and S. E. Nagler, Nature Materials **4**, 329 (2005).

[48] K. Hirakawa and Y. Kurogi, Prog. Theor. Phys. Suppl. **46**, 147 (1970).

[49] Z. Nussinov and J. van den Brink, Rev. Mod. Phys. **87**, 1 (2015).

[50] J. G. Rau, E. K.-H. Lee, and H.-Y. Kee, Annu. Rev. Condens. Matter Phys. **7**, 195 (2016).

[51] R. Schaffer, E. K.-H. Lee, B.-J. Yang, and Y. B. Kim, Rep. Prog. Phys. **79**, 094504 (2016).

[52] S. Trebst, arXiv:1701.07056 [cond-mat.str-el].

[53] S. M. Winter, A. A. Tsirlin2, M. Daghofer, J. van den Brink, Y. Singh, P. Gegenwart, and R. Valentí, J. Phys.: Condens. Matter **29**, 493002 (2017).

[54] M. Hermanns, I. Kimchi, and J. Knolle, Annu. Rev. Condens. Matter Phys. **9**, 17 (2018).

[55] Y. Motome and J. Nasu, J. Phys. Soc. Jpn. **89**, 012002 (2020).

[56] T. Takayama, A. Kato, R. Dinnebier, J. Nuss, H. Kono, L. S. I. Veiga, G. Fabbris, D. Haskel, and H. Takagi, Phys. Rev. Lett. **114**, 077202 (2015).

[57] K. A. Modic, T. E. Smidt, I. Kimchi, N. P. Breznay, A. Biffin, S. Choi, R. D. Johnson, R. Coldea, P. Watkins-Curry, G. T. McCandless, J. Y. Chan, F. Gandara, Z. Islam, A. Vishwanath, A. Shekhter, R. D. McDonald, and J. G. Analytis, Nat. Comm. **5**, 4203 (2014).

[58] I. Rousochatzakis, U. K. Rössler, J. van den Brink, and M. Daghofer, Phys. Rev. B **93**, 104417 (2016).

[59] K. Morita, M. Kishimoto, and T. Tohyama, Phys. Rev. B **98**, 134437 (2018).

[60] B. J. Kim, Hosub Jin, S. J. Moon, J.-Y. Kim, B.-G. Park, C. S. Leem, Jaejun Yu, T. W. Noh, C. Kim, S.-J. Oh, J.-H. Park, V. Durairaj, G. Cao, and E. Rotenberg, Phys. Rev. Lett. **101**, 076402 (2008).

[61] B. J. Kim, H. Ohsumi, T. Komesu, S. Sakai, T. Morita, H. Takagi, and T. Arima, Science **323**, 1329 (2009).

[62] H. Liu and G. Khaliullin, Phys. Rev. B **97**, 014407 (2018).

[63] R. Sano, Y. Kato, and Y. Motome, Phys. Rev. B **97**, 014408 (2018).

[64] H. Liu, J. Chaloupka, and G. Khaliullin, Phys. Rev. Lett. **125**, 047201 (2020).

[65] S. M. Winter, Y. Li, H. O. Jeschke, and R. Valentí, Phys. Rev. B **93**, 214431 (2016).

[66] H. Gretarsson, J. P. Clancy, X. Liu, J. P. Hill, E. Bozin, Y. Singh, S. Manni, P. Gegenwart, J. Kim, A. H. Said, D. Casa, T. Gog, M. H. Upton, H.-S. Kim, J. Yu, V. M. Katukuri, L. Hozoi, J. van den Brink, and Y.-J. Kim, Phys. Rev. Lett. **110**, 076402 (2013).

[67] J. Nasu, M. Udagawa, and Y. Motome, Phys. Rev. B **92**, 115122 (2015).

[68] J. Knolle, D. L. Kovrizhin, J. T. Chalker, and R. Moessner, Phys. Rev. Lett. **112**, 207203 (2014).

[69] J. Knolle, D. L. Kovrizhin, J. T. Chalker, and R. Moessner, Phys. Rev. B **92**, 115127 (2015).

[70] J. Nasu, M. Udagawa, and Y. Motome, Phys. Rev. Lett. **113**, 197205 (2014).

[71] X. Liu, T. Berlijn, W.-G. Yin, W. Ku, A. Tsvelik, Y.-J. Kim, H. Gretarsson, Y. Singh, P. Gegenwart, and J. P. Hill, Phys. Rev. B **83**, 220403(R) (2011).

[72] F. Ye, S. Chi, H. Cao, B. C. Chakoumakos, J. A. Fernandez-Baca, R. Custelcean, T. F. Qi, O. B. Korneta, and G. Cao, Phys. Rev. B **85**, 180403(R) (2012).

[73] S. K. Choi, R. Coldea, A. N. Kolmogorov, T. Lancaster, I. I. Mazin, S. J. Blundell, P. G. Radaelli, Y. Singh, P. Gegenwart, K. R. Choi, S.-W. Cheong, P. J. Baker, C. Stock, and J. Taylor, Phys. Rev. Lett. **108**, 127204 (2012).

[74] R. D. Johnson, S. C. Williams, A. A. Haghighirad, J. Singleton, V. Zapf, P. Manuel, I. I. Mazin, Y. Li, H. O. Jeschke, R. Valentí, and R. Coldea, Phys. Rev. B **92**, 235119 (2015).

[75] S. C. Williams, R. D. Johnson, F. Freund, Sungkyun Choi, A. Jesche, I. Kimchi, S. Manni, A. Bombardi, P. Manuel, P. Gegenwart, and R. Coldea, Phys. Rev. B **93**, 195158 (2016).

[76] M. Gohlke, G. Wachtel, Y. Yamaji, F. Pollmann, and Y. B. Kim, Phys. Rev. B **97**, 075126 (2018).

[77] J. Wang, B. Normand, and Z.-X. Liu, Phys. Rev. Lett. **123**, 197201 (2019).

[78] J. M. Luttinger and L. Tisza, Phys. Rev. **70**, 954 (1946).

[79] Z. Friedman and J. Felsteiner, Phil. Mag. **29**, 957 (1974).

[80] J. Chaloupka and G. Khaliullin, Phys. Rev. B **92**, 024413 (2015).

[81] J. Chaloupka and G. Khaliullin, Phys. Rev. B **94**, 064435 (2016).

[82] H.-C. Jiang, Z.-C. Gu, X.-L. Qi, and S. Trebst, Phys. Rev. B **83**, 245104 (2011).

[83] J. O. Iregui, P. Corboz, and M. Troyer, Phys. Rev. B **90**, 195102 (2014).

[84] J. Lou, L. Liang, Y. Yu, and Y. Chen, ArXiv e-prints (2015), arXiv:1501.06990 [cond-mat.str-el].

[85] J. Rusnačko, D. Gotfryd, and J. Chaloupka, Phys. Rev. B **99**, 064425 (2019).

[86] S. H. Chun, J. W. Kim, J. Kim, H. Zheng, C. C. Stoumpos, C. D. Malliakas, J. F. Mitchell, K. Mehlawat, Y. Singh, Y. Choi, T. Gog, A. Al-Zein, M. M. Sala, M. Krisch, J. Chaloupka, G. Jackeli, G. Khaliullin, and B. J. Kim, Nature Phys. **11**, 462 (2015).

[87] S. M. Winter, K. Riedl, P. A. Maksimov, A. L. Chernyshev, A. Honecker, and R. Valentí, Nature Comm. **8**, 1152 (2017).

[88] S. M. Winter, K. Riedl, D. Kaib, R. Coldea, and R. Valentí, Phys. Rev. Lett. **120**, 077203 (2018).

[89] J. Jaklič and P. Prelovšek, Phys. Rev. B **49**, 5065 (1994).

[90] J. Jaklič and P. Prelovšek, Adv. Phys. **49**, 1 (2000).

[91] M. Aichhorn, M. Daghofer, H. G. Evertz, W. von der Linden, Phys. Rev. B **67**, 161103(R) (2003).

[92] J. Kim, J. Chaloupka, Y. Singh, J. W. Kim, B. J. Kim, D. Casa, A. Said, X. Huang, and T. Gog, Phys. Rev. X **10**, 021034 (2020).

[93] C. S. Alexander, G. Cao, V. Dobrosavljevic, S. McCall, J. E. Crow, E. Lochner, and R. P. Guertin, Phys. Rev. B **60**, R8422 (1999).

[94] S. Nakatsuji, S. Ikeda, and Y. Maeno, J. Phys. Soc. Jpn. **66**, 1868 (1997).

[95] G. Cao, S. McCall, M. Sheppard, J. E. Crow, and R. P. Guertin, Phys. Rev. B **56**, R2916 (1997).

[96] M. Braden. G. André, S. Nakatsuji, and Y. Maeno, Phys. Rev. B **58**, 847 (1998).

[97] T. Mizokawa, L. H. Tjeng, G. A. Sawatzky, G. Ghiringhelli, O. Tjernberg, N. B. Brookes, H. Fukazawa, S. Nakatsuji, and Y. Maeno, Phys. Rev. Lett. **87**, 077202 (2001).

[98] G. Khaliullin, Phys. Rev. Lett. **111**, 197201 (2013).

[99] P. S. Anisimov, F. Aust, G. Khaliullin, and M. Daghofer, Phys. Rev. Lett. **122**, 177201 (2019).

[100] J. Chaloupka and G. Khaliullin, Phys. Rev. B **100**, 224413 (2019).

[101] A. Jain, M. Krautloher, J. Porras, G. H. Ryu, D. P. Chen, D. L. Abernathy, J. T. Park, A. Ivanov, J. Chaloupka, G. Khaliullin, B. Keimer, and B. J. Kim, Nature Phys. **13**, 633 (2017).

[102] K. I. Kugel and D. I. Khomskii, Sov. Phys. Usp. **25**, 231 (1982).

[103] D. Pekker and C. M. Varma, Annu. Rev. Condens. Matter Phys. **6**, 269 (2015).

[104] Ch. Rüegg, B. Normand, M. Matsumoto, A. Furrer, D. F. McMorrow, K. W. Krämer, H.-U. Güdel, S. N. Gvasaliya, H. Mutka, and M. Boehm, Phys. Rev. Lett. **100**, 205701 (2008).

[105] U. Bissbort, S. Götze, Y. Li, J. Heinze, J. S. Krauser, M. Weinberg, C. Becker, K. Sengstock, and W. Hofstetter, Phys. Rev. Lett. **106**, 205303 (2011).

[106] D. Podolsky, A. Auerbach, and D. P. Arovas, Phys. Rev. B **84**, 174522 (2011).

[107] S. Gazit, D. Podolsky, and A. Auerbach, Phys. Rev. Lett. **110**, 140401 (2013).

[108] A. Rançon and N. Dupuis, Phys. Rev. B **89**, 180501(R) (2014).

[109] F. Rose, F. Léonard, and N. Dupuis, Phys. Rev. B **91**, 224501 (2015).

[110] P. A. Fleury and R. Loudon, Phys. Rev. **166**, 514 (1968).

[111] S.-M. Souliou, J. Chaloupka, G. Khaliullin, G. Ryu, A. Jain, B. J. Kim, M. Le Tacon, and B. Keimer, Phys. Rev. Lett. **119**, 067201 (2017).

[112] H. Y. Hwang, Y. Iwasa, M. Kawasaki, B. Keimer, N. Nagaosa, and Y. Tokura, Nature Mater. **11**, 103 (2012).

[113] J. Chaloupka and G. Khaliullin, Phys. Rev. Lett. **100**, 016404 (2008).

[114] T. Hyart, A. R. Wright, G. Khaliullin, and B. Rosenow, Phys. Rev. B **85**, 140510(R) (2012).

[115] Y.-Z. You, I. Kimchi, and A. Vishwanath, Phys. Rev. B **86**, 085145 (2012).

[116] S. Okamoto, Phys. Rev. Lett. **110**, 066403 (2013).

[117] J. Chaloupka and G. Khaliullin, Phys. Rev. Lett. **116**, 017203 (2016).

[118] J. Bertinshaw, Y. K. Kim, G. Khaliullin, and B. J. Kim, Annu. Rev. Condens. Matter Phys. **10**, 315 (2019).

[119] Y. K. Kim, O. Krupin, J. D. Denlinger, A. Bostwick, E. Rotenberg, Q. Zhao, J. F. Mitchell, J. W. Allen, and B. J. Kim, Science **345**, 187 (2014).

[120] C. Lu, S. Dong, A. Quindeau, D. Preziosi, N. Hu, and M. Alexe, Phys. Rev. B **91**, 104401 (2015).